IBRACON
Instituto Brasileiro do Concreto

REVISTA IBRACON DE ESTRUTURAS E MATERIAIS

IBRACON STRUCTURES AND MATERIALS JOURNAL

Volume 13, Number 3

June, 2020

ISSN 1983-4195

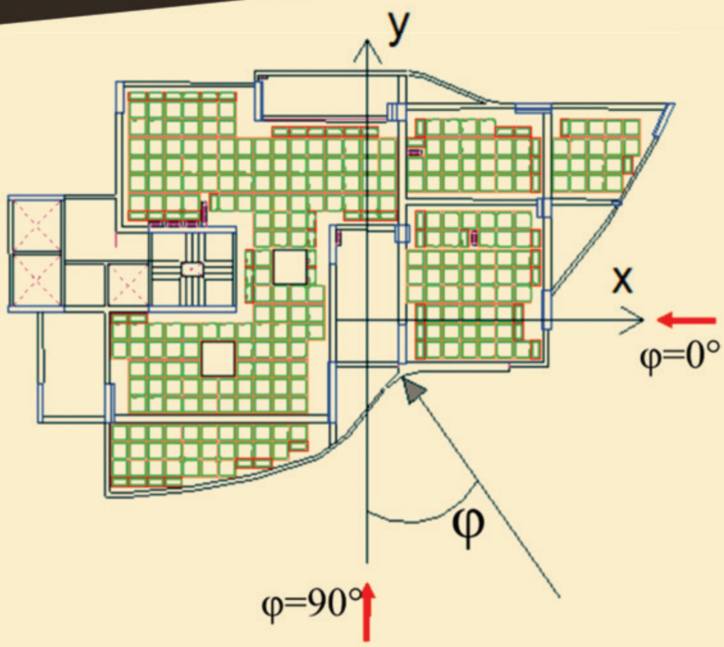

(a) Floor plan and wind incidence angle φ

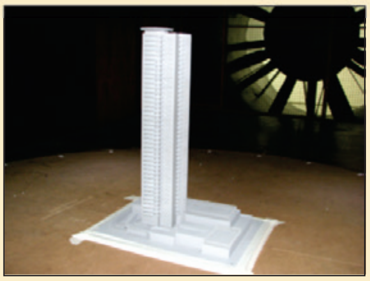

(b) Wind tunnel test model

(c) Ground roughness detail

(d) Pressure sensors

(e) Building details

Contents

Editorial

The IBRACON Structures and Materials Journal, published every two months, is a scientific and international journal, published by the Brazilian Concrete Institute, the largest Latin American Concrete Institute. Recently this journal has implemented some changes. The article submission now uses the Scholar One Manuscripts managing system, available at https://mc04.manuscriptcentral.com/riem-scielo. Reviewers can choose if they wish to be acknowledged in the publons website. Only papers submitted in English are now accepted and a new paper template is available. The Journal is increasing the number of published paper per year to 90, due to the high-qualified demand of paper submissions. Annually, close to 250 papers are received. Starting in the next issue, V13 n.4, the volumes will be published using the continuous flow system. This will reduce the time between submission and on-line availability of accepted articles. We would like to thank Professor José Luis Antunes de Oliveira e Souza, Editor-emeritus, who, together with other Editors, for more than 12 years, built the reputation of the IBRACON Journal.

We acknowledge the dedication of authors and reviewers, fundamental to the quality of the Journal.

The Editors

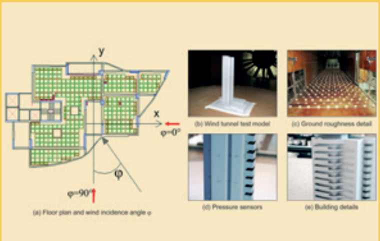

Cover: WIND TUNNEL TEST AND DETAILS

Courtesy: C. V. S. SARMENTO, A. O. C. FONTE, L. J. PEDROSO AND P. M. V. RIBEIRO

Ibracon Structures and Materials Journal
is published bimonthly
(February, April, June, August, October and December) by IBRACON.

IBRACON
Instituto Brasileiro do Concreto
Founded in 1972

Av. Queiroz Filho, nº 1700 — sala 407/408
Torre D — Villa Lobos Office Park
CEP 05319-000 — São Paulo, SP — Brasil
Phone: +55 11 3735-0202
Fax: +55 11 3733-2190
E-mail: arlene@ibracon.org.br
Website: http://www.ibracon.org.br

Volume 13, Number 3
June 2020
ISSN: 1983-4195

REVISTA IBRACON DE ESTRUTURAS E MATERIAIS

IBRACON STRUCTURES AND MATERIALS JOURNAL

Contents

Aims and Scope

Aims and Scope

The IBRACON Structures and Materials Journal is a technical and scientifical divulgation vehicle of IBRACON (Brazilian Concrete Institute). Each issue of the periodical has 5 to 8 papers and, possibly, a technical note and/or a technical discussion regarding a previously published paper. All contributions are reviewed and approved by reviewers with recognized scientific competence in the area.

Objectives

The IBRACON Structures and Materials Journal´s main objectives are:

- Present current developments and advances in the area of concrete structures and materials;
- Make possible the better understanding of structural concrete behavior, supplying subsidies for a continuous interaction among researchers, producers and users;
- Stimulate the development of scientific and technological research in the areas of concrete structures and materials, through papers peer-reviewed by a qualified Editorial Board;
- Promote the interaction among researchers, constructors and users of concrete structures and materials and the development of Civil Construction;
- Provide a vehicle of communication of high technical level for researchers and designers in the areas of concrete structures and materials.

Submission Procedure

The procedure to submit and revise the contributions, as well as the formats, are detailed on IBRACON's WebSite (www.ibracon.org.br). The papers and the technical notes are revised by at least three reviewers indicated by the editors. The discussions and replies are accepted for publication after a revision by the editors and at least one member of the Editorial Board. In case of disagreement between the reviewer and the authors, the contribution will be sent to a specialist in the area, not necessarily linked to the Editorial Board.

Contribution Types

The periodical will publish original papers, short technical notes and paper discussions. Announcements of conferences and meetings, information about book reviews, events and contributions related to the area will also be available in the periodical's WebSite. All contributions will be revised and only published after the Editorial and Reviewers Boards approve the paper. Restrictions of content and space (size) are imposed to the papers. The contributions will be accepted for review in Portuguese, Spanish or English. The abstracts are presented in Portuguese or Spanish, and in English, independently of the language in which the paper is written. After the review process, papers originally written in Portuguese or Spanish should be translated into English, which is the official language of the IBRACON Structures and Materials Journal. Optionally, papers are also published in Portuguese or Spanish.

Original papers will be accepted as long as they are in accordance with the objectives of the periodical and present quality of information and presentation. The instructions to submit a paper are detailed in the template (available on IBRACON's WebSite).

The length of the papers must not exceed 20 pages.

A technical note is a brief manuscript. It may present a new feature of research, development or technological application in the areas of Concrete Structures and Materials, and Civil Construction. This is an opportunity to be used by industries, companies, universities, institutions of research, researchers and professionals willing to promote their works and products under development. The instructions to submit a technical note are detailed on IBRACON's WebSite.

A discussion is received no later than 3 months after the publication of the paper or technical note. The instructions to submit a discussion are detailed on IBRACON's WebSite. The discussion must be limited to the topic addressed in the published paper and must not be offensive. The right of reply is guaranteed to the Authors. The discussions and the replies are published in the subsequent issues of the periodical.

Internet Access

IBRACON Structural Journal Page in http://www.ibracon.org.br

Subscription rate

All IBRACON members have free access to the periodical contents through the Internet. Non-members have limited access to the published material, but are able to purchase isolated issues through the Internet. The financial resources for the periodical´s support are provided by IBRACON and by research funding agencies. The periodical will not receive any type of private advertisement that can jeopardize the credibility of the publication.

Photocopying

Photocopying in Brazil. Brazilian Copyright Law is applicable to users in Brazil. IBRACON holds the copyright of contributions in the journal unless stated otherwise at the bottom of the first page of any contribution. Where IBRACON holds the copyright, authorization to photocopy items for internal or personal use, or the internal or personal use of specific clients, is granted for libraries and other users registered at IBRACON.

IBRACON

Av. Queiroz Filho, 1700 – sala 407/408 – Torre D
Villa Lobos Office Park
05319-000 – Vila Hamburguesa
São Paulo – SP
Phone: +55 (11) 3735-0202
E-mail: arlene@ibracon.org.br.

Disclaimer

Papers and other contributions and the statements made or opinions expressed therein are published on the understanding that the authors of the contribution are the only responsible for the opinions expressed in them and that their publication does not necessarily reflect the support of IBRACON or the journal.

Objetivos e Escopo

A Revista IBRACON de Estruturas e Materiais é um veículo de divulgação técnica e científica do IBRACON (Instituto Brasileiro do Concreto). Cada número do periódico tem 5 a 8 artigos e, possivelmente, uma nota técnica e/ou uma discussão técnica sobre um artigo publicado anteriormente. Todas as contribuições são revistas e aprovadas por revisores com competência científica reconhecida na área.

Objetivos

Os objetivos principais da Revista IBRACON de Estruturas e Materiais são:

- Apresentar desenvolvimentos e avanços atuais na área de estruturas e materiais de concreto;
- Possibilitar o melhor entendimento do comportamento do concreto estrutural, fornecendo subsídios para uma interação contribua entre pesquisadores, produtores e usuários;
- Estimular o desenvolvimento de pesquisa científica e tecnológica nas áreas de estruturas de concreto e materiais, através de artigos revisados por um corpo de revisores qualificado;
- Promover a interação entre pesquisadores, construtores e usuários de estruturas e materiais de concreto, e o desenvolvimento da Construção Civil;
- Prover um veículo de comunicação de alto nível técnico para pesquisadores e projetistas nas áreas de estruturas de concreto e materiais.

Submissão de Contribuições

O procedimento para submeter e revisar as contribuições, assim como os formatos, estão detalhados na página Internet do IBRACON (www.ibracon.org.br). Os artigos e as notas técnicas são revisadas por, no mínimo, três revisores indicados pelos editores. As discussões e réplicas são aceitas para publicação após uma revisão pelo editores e no mínimo um membro do Corpo Editorial. No caso de desacordo entre revisor e autores, a contribuição será enviada a um especialista na área, não necessariamente do Corpo Editorial.

Tipos de Contribuição

O periódico publicará artigos originais, notas técnicas curtas e discussões sobre artigos. Anúncios de congressos e reuniões, informação sobre revisão de livros e contribuições relacionadas à área serão também disponibilizadas na página Internet da revista. Todas as contribuições serão revisadas e publicadas apenas após a aprovação dos revisores e do Corpo Editorial. Restrições de conteúdo e espaço (tamanho) são impostas aos artigos. As contribuições serão aceitas para revisão em português, espanhol ou inglês. Os resumos serão apresentados em português ou espanhol, e em inglês, independentemente do idioma em que o artigo for escrito. Após o processo de revisão, artigos originalmente escritos em português ou espanhol deverão ser traduzidos para inglês, que é o idioma oficial da Revista IBRACON de Estruturas e Materiais. Opcionalmente, os artigos são também publicados em português ou espanhol.

Artigos originais serão aceitos desde que estejam de acordo com os objetivos da revista e apresentam qualidade de informação e apresentação. As instruções para submeter um artigo estão detalhadas em um gabarito (disponível no sítio do IBRACON).

A extensão dos artigos não deve exceder 20 páginas.

Um nota técnica é um manuscrito curto. Deve apresentar uma nova linha de pesquisa, desenvolvimento ou aplicação tecnológica nas áreas de Estruturas de Concreto e Materiais, e Construção Civil. Esta é uma oportunidade a ser utilizada por indústrias, empresas, universidades, instituições de pesquisa, pesquisadores e profissionais que desejem promover seus trabalhos e produtos em desenvolvimento. As instruções para submissão estão detalhadas na página de Internet do IBRACON.

Uma discussão é recebida não mais de 3 meses após a publicação do artigo ou nota técnica. As instruções para submeter uma discussão estão detalhadas na página de Internet do IBRACON. A discussão deve se limitar ao tópico abordado no artigo publicado e não pode ser ofensivo. O direito de resposta é garantido aos autores. As discussões e réplicas são publicadas nos números subseqüentes da revista.

Acesso via Internet

Página da Revista IBRACON de Estruturas e Materiais em http://www.ibracon.org.br

Assinatura

Todos os associados do IBRACON têm livre acesso ao conteúdo do periódico através da Internet. Não associados têm acesso limitado ao material publicado, mas podem adquirir números isolados pela Internet. O financiamento para suporte à revista é provido pelo IBRACON e por agências de financiamento à pesquisa. A revista não receberá qualquer tipo de anúncio privado que possa prejudicar a credibilidade da publicação.

Fotocópias

Fotocópias no Brasil, A Lei Brasileira de Direitos Autorais é aplicada a usuários no Brasil. O IBRACON detém os direitos autorais das contribuições na revista a menos que haja informação em contrário no rodapé da primeira página da contribuição. Onde o IBRACON detém os direitos autorais, autorização para fotocopiar itens para uso interno ou pessoal, ou uso interno ou pessoal de clientes específicos, é concedida para bibliotecas e outros usuários registrados no IBRACON.

IBRACON

Av. Queiroz Filho, 1700 – sala 407/408 – Torre D
Villa Lobos Office Park
05319-000 – Vila Hamburguesa
São Paulo – SP
Phone: +55 (11) 3735-0202
E-mail: arlene@ibracon.org.br.

Aviso Legal

Artigos e outras contribuições e declarações feitas ou opiniões expressas aqui são publicadas com o entendimento que os autores da contribuição são os únicos responsáveis pelas opiniões expressas neles e que sua publicação não necessariamente reflete o apoio do IBRACON ou da revista.

Diretoria
Biênio 2020/2021

Diretor Presidente
Paulo Helene

Diretor 1º Vice-Presidente
Julio Timerman

Diretor 2º Vice-Presidente
Enio José Pazini Figueiredo

Diretor 1º Secretário
Cláudio Sbrighi Neto

Diretor 2º Secretário
Carlos José Massucato

Diretor 1º Tesoureiro
Julio Timerman

Diretor 2º Tesoureiro
Hugo Armelin

Diretora de Marketing
Jéssika Pacheco

Assessor da Diretoria de Marketing
Guilherme Covas

Diretor de Publicações
Guilherme Parsekian

Assessor da Diretoria de Publicações
Tulio Nogueira Bittencourt

Diretor de Eventos
Rafael Timerman

Assessor da Diretoria de Eventos
Luis César De Luca

Diretor Técnico
José Tadeu Balbo

Assessor da Diretoria Técnica
Selmo Chapira Kuperman

Diretor de Relações Institucionais
Cesar Henrique Daher

Assessor da Diretoria de Relações Internacionais
José Vanderley de Abreu

Diretor de Cursos
Leandro Moura Trautwein

Assessor da Diretoria de Cursos
Antonio Carlos dos Santos

Diretora de Atividades Estudantis
Jéssica Andrade Dantas

Assessora da Diretoria de Atividades Estudantis
Sandra Regina Bertocini

Diretor de Certificação de Pessoal
Adriano Damasio Soterio

Assessor da Diretoria de Certificação de Pessoal
Gilberto Antonio Giuzio

Diretor de Pesquisa e Desenvolvimento
Bernardo Tutikian

Assessor da Diretoria de Pesquisa e Desenvolvimento
Roberto Christ

Conselho Diretor
Biênio 2020/2021

Assessores da Presidência

Antonio Domingues de Figueiredo
Íria Lícia Oliva Doniak
Jairo Abud
Jorge Batlouni Neto
Luiz Aurélio Fortes da Silva
Mario William Esper
Maurice Antonie Traboulsi
Paula Baillot
Simão Priszkulnik

Sócios Individuais

Inês Laranjeira da Silva Battagin
Antônio Carlos dos Santos
Antônio Domingues de Figueiredo
Vladimir Antônio Paulon
Iria Licia Oliva Doniak
Arnaldo Forti Battagin
Luiz Prado Vieira Júnior
José Tadeu Balbo
Mário William Esper
Hugo da Costa Rodrigues Filho

Sócios Mantenedores e Coletivos

ABCP
Associação Brasileira de Cimento Portland

ABECE
Associação Brasileira de Engenharia e Consultoria Estrutural

IPT
Instituto de Pesquisas Tecnológicas do Estado de São Paulo

TQS Informática Ltda

EPUSP
Escola Politécnica da Universidade de São Paulo

ABCIC
Associação Brasileira da Construção Industrializada de Concreto

PhD Engenharia Ltda

FURNAS Centrais Elétricas S/A

ABESC
Associação Brasileira das Empresas de Serviços de Concretagem

L. A. FALCÃO BAUER Centro Tecnológico

VOTORANTIM Cimentos S/A

Volume 13, Number 3 (June 2020) p. 464 – 482 • ISSN 1983-4195
http://dx.doi.org/10.1590/S1983-41952020000300002

IBRACON

REVISTA IBRACON DE ESTRUTURAS E MATERIAIS
IBRACON STRUCTURES AND MATERIALS JOURNAL

Evaluation of the impact of two types of steel fibers (SE), mono and 3D, on concrete properties, when added isolated or blended

Avaliação do impacto de dois tipos de fibras de aço, simples e espaciais, nas propriedades do concreto, quando inseridas separadamente ou de forma combinada





A. L. BAUER [a]
andersonbauer1995@gmail.com
https://orcid.org/0000-0002-7633-618X

H. EHRENBRING [a]
hzamis@unisinos.br
https://orcid.org/0000-0002-0339-9825

D. SCHNEIDER [a]
diegosch@unisinos.br
https://orcid.org/0000-0002-8810-460X

U. C. M. QUININO [a]
uquinino@unisinos.br
https://orcid.org/0000-0002-6488-9828

B. TUTIKIAN [a]
bftutikian@unisinos.br
https://orcid.org/0000-0003-1319-0547

Abstract

The brittle behavior of concrete can be compensated by the addition of reinforcements, providing benefits such as improved crack control, residual strength and increased flexural strength. It is usual to apply mono fibers to concrete, but their positioning in the matrix may not be homogeneous, consequently increasing the susceptibility to fracture planes with fewer reinforcements. This study aimed to evaluate the use and behavior of simple (mono) and space (3D) steel fibers (SE), in order to achieve a more homogeneous mixture, increase the effectiveness of fibers in restricting cracks and improve mechanical properties. The fresh-state was assessed through slump and VeBe tests, whereas the hardened-state tests comprised axial compressive strength, flexural strength and the flexural toughness factor. The volume content of simple and space fibers varied from 0 to 0.93%. Based on the results, it can be stated that space and simple fiber contents improved rheological and mechanical properties of the composite in isolated (0.29%) and hybrid (0.64%) combinations, since their overall performance exceeded the other mixtures'. However, space fibers caused considerable workability losses compared to the conventional concrete, hindering its casting and harming its hardened-state properties.

Keywords: fiber-reinforced concrete, space fiber, simple fibers, hybrid mixtures.

Resumo

O comportamento frágil de concretos pode ser compensado com a inserção de reforços, proporcionando benefícios no que tange ao controle de fissuração, ganho de tenacidade, aumento da resistência à tração, entre outros. Comumente, aplicam-se fibras isoladas em concretos, porém o seu posicionamento na matriz pode não ser homogêneo e, consequentemente, facilita-se o surgimento de planos de ruptura com baixo número de reforços. Assim, o trabalho em questão teve como objetivo avaliar a aplicação e comportamento de fibras simples e espaciais em aço, a fim de proporcionar uma mistura mais homogênea, aumentar a área de atuação da fibra na contenção de fissuras e melhorias nas propriedades mecânicas. Os ensaios no estado fresco foram de consistência do compósito, por meio do abatimento do tronco de cone e do VeBe, e, no estado endurecido, avaliou-se a resistência à compressão axial, resistência à tração na flexão e o fator de tenacidade. Variou-se o teor de adição das fibras uni (simples) e espaciais, em volume, de 0 até 0,93%. Com base nos resultados, pode-se afirmar que os teores de fibras espaciais e simples foram benéficos às propriedades reológicas e mecânicas do compósito na combinação isolada (0,29%) e híbrida (0,64%), dado que demonstraram desempenho geral superior às demais misturas. Entretanto, as fibras espaciais acarretam consideráveis perdas da trabalhabilidade, comparado ao concreto tradicional sem fibras, dificultando o seu lançamento e, consequentemente, propriedades no estado endurecido.

Palavras-chave: concreto reforçado com fibras, fibra espacial, fibras simples, misturas híbridas.

[a] *Unisinos, itt Performance, São Leopoldo, RS, Brazil.*

Received: 14 Aug 2018 • Accepted: 30 Sep 2019 • Available Online: 26 May 2020

1. Introduction

Concrete is a material with sensitive behavior that relies on other components that can change its failure mode [1]. Steel reinforcements are then specified to increase tensile strength, even though this type of stress acts in a concentrated way, which is not effective to mitigate localized cracks, impacting the durability of the system. The addition of fibers to concrete aims to amend these deficiencies, since it is supposed to make the material isotropic, improving its performance when subjected to mechanical actions and increasing the area that fends off cracking [2].
According to Ibrahim et al. [3], the use of SE fibers as concrete matrix reinforcement brings about a series of benefits to its hardened state, such as the increase of load-bearing capacity and fracture strength, while improving the control of cracks, which in turn extends the composite's life span. As for fresh state, the fibers themselves form an internal mesh that hinders the movement of the coarse aggregates within the mixture. This action may impair the processes of casting the composite in the molds, as microfibers make it harder for coarse aggregates to homogenize with the other materials [4, 5]. It should be noted that the fiber reinforcement acts as a stress transfer bridge that limits the appearance of fracture planes and restrain crack propagation, hence increasing tensile failure stress and causing the composite to change from a state of brittleness to one of pseudo-ductility [6]. The current literature widely covers the advantage of using numerous types of mono-fibers [7, 8, 9], which are distributed separately within the matrix, whereas each one acts in a single direction that is typified by the mobility of reinforcements inside the matrix. Researchers in the field of aerospace engineering have developed structural sets capable of acting in multiple directions, as to increase the mechanical strength of other composites [10, 11], although such reinforcement has not been added to cement matrices yet. Even if the identified results are interesting, there is still a gap concerning the performance of concrete reinforced with space fibers, which are marked by a specific setting that is structured with simple fibers acting in 3 directions (3D). It is expected that this new reinforcement model may increase the number and/or efficiency of fibers in the fracture plane, since their arrangement gets better controlled and the set is theoretically more effective. Therefore, it can be assured that the fracture plane will tend to be intercepted by space fibers no matter the placement, since the set has rigid fiber bindings that are orthogonal to each other and act as 3D reinforcements, increasing the strength of the matrix fracture plane.
Studies on the use of 2D fibers were developed as well, exemplified by the textile-reinforced concrete [12, 13], which brings along a series of advantages compared to conventional and reinforced concretes. Some of these advantages are great tensile and compressive performances, high durability, owing to the matrix having low water-cement ratio (<0.30), and the fibers used do not require corrosion protection, allowing for a reduction of the weight of structures [14]. Another benefit of these composites is the possibility of subjecting the pieces to geometric forming.
In order to achieve even higher gains, two or more fibers can be blended in a same matrix to enhance the composite's performance. This fiber blend is also known as hybridization. The types of material of each fiber and their geometry are often varied. However, it is still necessary to figure out the best way to blend the effects of fibers that act in different directions, to reach maximum interaction and so achieve optimal performance [2, 15].
Quinino [2] explains that the hybridization of polypropylene (PP) and SE fibers, working together and in proper amounts, improves the performance of the matrix, as PP microfibers hinder the formation of microcracks and can even restrict likely differential displacements that take place within the composite during formation and propagation of cracks, while SE macrofibers stay in charge of "sewing" cracks up, hindering their opening and extension.
Banthia and Sappakittipakorn [16] also reached promising results when they evaluated the hybridization of matrices with two types of corrugated SE fibers, varying only the aspect ratio, fixing fiber length, demonstrating positive effects on the mechanical properties of concrete.
For this purpose, the experimental procedure was designed to evaluate the influence on fresh state and mechanical properties of cement matrices reinforced with simple and space fibers in varied amounts, isolated and with fiber hybridization.

2. Experimental procedure

The experimental procedure regards the analysis of the physical behavior of a conventional concrete when reinforced with simple

Table 1
Steel fiber content in the mixture of each composite of this study

Mixture	Fiber content		Fiber type			
			Simple		Space	
	kg/m³	% in volume	kg/m³	% in volume	kg/m³	% in volume
MR	0	0.00%	0	0.00%	0	0.00%
M1	10	0.14%	10	0.14%	0	0.00%
M2	20	0.29%	20	0.29%	0	0.00%
M3	40	0.52%	10	0.14%	30	0.38%
M4	50	0.67%	20	0.29%	30	0.38%
M5	60	0.78%	10	0.14%	50	0.64%
M6	70	0.93%	20	0.29%	50	0.64%
M7	30	0.38%	0	0.00%	30	0.38%
M8	50	0.64%	0	0.00%	50	0.64%

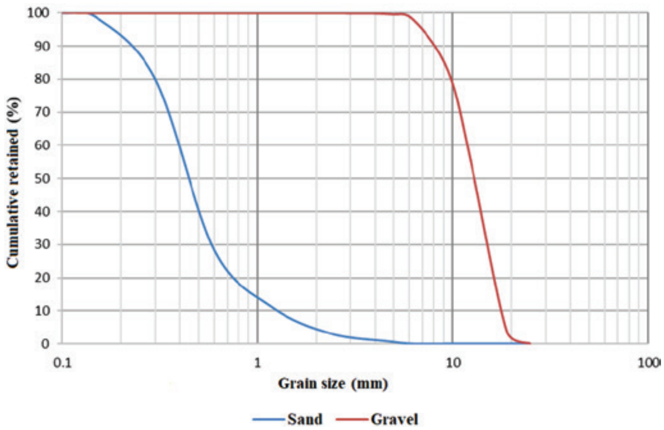

Figure 1
Particle-size distribution of fine and coarse aggregates

and space SE fibers, forming a fiber reinforced concrete (FRC). The composites were crafted with 25-MPa conventional concrete dosed as per the method of Tutikian and Helene (IBRACON Method) [17]. So, 9 different mixtures were molded, one for the unreinforced reference concrete (MR) and the other 8 were reinforced with fibers (M1 – M8). The fresh-state characteristics were evaluated through the slump and VeBe methods. The mechanical properties under analysis comprised axial compressive strength, flexural strength and flexural toughness, all of which were tested at 28 days. Table 1 presents the SE fiber content of each mixture in volume with mass compensation.

The fiber contents were chosen based on usual average consumptions that range from 10 to 70 kg/m³, in accordance with Banthia and Sappakittipakorn [16], Boulekbache et al. [18] and Quinino [2]. Mixtures M3, M4, M5 and M6 were subjected to fiber hybridization with varied contents of simple and space fibers. Both simple and space fibers were made of SE and had hooked ends that were able to improve the performance of the composite by reducing the likelihood of the reinforcement being expelled from the cement matrix as tensile stresses increase. The following items cover the materials and methods that were used along this research.

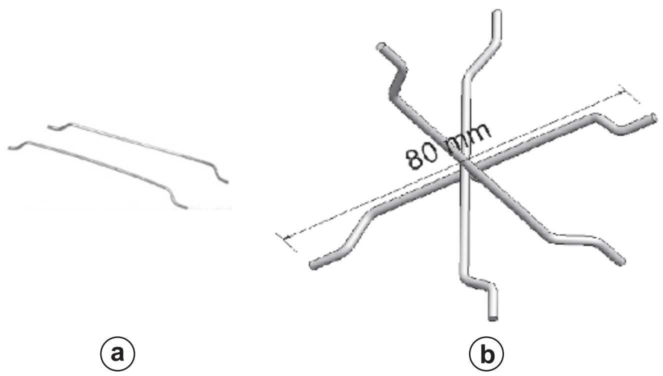

Figure 2
Shape of (a) simple and (b) space fibers

2.1 Materials used

All mixtures were made with type-III Portland cement, specified by ASM C150:2018 [19]. The density of the material was 3.04 g/cm³, with surface area of 4936 cm²/g. The quartzous fine aggregate used had maximum grain size of 4.8 mm and fineness modulus of 2.22. The specific gravity of this material was assessed as per ASTM C128:2015 [20] and yielded the value of 2.63 g/cm³. Regarding unit weight, the value of 1.54 g/cm³ was identified by following the procedures prescribed by ASTM C29:2017 [21]. As for the natural coarse aggregate, its maximum size and fineness modulus were 19.0 mm and 6.86 respectively. The specific gravity was equals 2.69 g/cm³, according to methods of ASTM C127:2015 [22]. The unit weight of gravel was determined in accordance with ASTM C29:2017 [2017], resulting in 1.45 g/cm³.

The natural aggregates were graded under the parameters set by ASTM C33:2018 [23] and ASTM C136:2014 [24]. Figure 1 then depicts the particle-size distribution of fine and coarse aggregates. Simple fibers (Figure 2-a) with length of 60 mm were adopted due to their compatibility with the coarse aggregate, hence allowing the fiber to perform well as a structural reinforcement for concrete [25]. Moreover, these fibers had diameter of 0.75 mm, which yields an aspect ratio of 80. The space fibers (Figure 2-b) had length of 80 mm and diameter of 1.8 mm, which means an aspect ratio of 44. The simple fiber had strength of 1000 MPa, just like the filaments used in the production of space fibers. It should be noted that space fibers are new reinforcements with specific arrangements, which, for the purpose of this study, were manually crafted to allow their assessment, since they have not been made available for purchase in the market yet. Hence, 3 fiber were used per arrangement, interconnected with solder and oriented at 90°. This orthogonality between fibers remained during the operations of concrete mixing, casting and consolidation. The dimensions of these fibers had to be greater than those of simple fibers in order to achieve the proper soldering. Nevertheless, the filaments applied to the space fibers were type A and class I (A-I), according to definitions of ABNT NBR 15530:2007 [26]. The technical naming used in this study to distinguish the fibers was “simple” and “space”, as to discriminate the way each type of fiber acts.

2.2 Dosing method and mixing process

The reference concrete was dosed with the intent of achieving compressive strength of 25 MPa, adopting cement content of 280 kg/m³ and water-cement ratio of 0.66. The reference mix ratio was 1: 2.51: 3.43 (cement: sand: gravel). The mixtures had the same base cement matrix, changing the type of reinforcement in use. The fiber content was determined according to the mass of reinforcements per cubic meter, ranging from 10 to 70 kg/m³. The slump of the reference matrix was fixed to reach class S160 (160 ≤ s ≤ 220 mm) and plastic workability for the VeBe test, and just the same for FRC. Moreover, during the homogenization of materials, the formation of lumps, that is, localized agglomeration of fibers, could not be noted. Table 2 presents the parameters for classifying the workability of the cement matrices used as reference in this study.

Table 2
Workability classified by the VeBe test

Classification	Slump (mm)	VeBe (s)
Extremely dry	–	32 to 18
Very stiff (maintains shape)	–	18 to 10
Stiff	0 to 25	10 to 5
Stiff plastic	25 to 75	5 to 3
Plastic	75 to 125	3 to 0
Very plastic	125 to 190	–

Source: Adapted from ACI 211.R3-02 [30]

2.3 Specimen produce and curing

For the 28-day compressive strength test, two cylindrical specimens were molded per mixture, with 100 mm of diameter and 200 mm of height, as per specifications of ASTM C192:2016 [27]. Then, the samples remained for 24 hours at room temperature, covered with a glass plate. After this period, they were unmolded and stored in a curing chamber with temperature of 21 ± 2°C and humidity of 95 ± 3%, remaining there until they had reached the testing age.
The dimensions of the flexural strength and flexural toughness test samples followed the recommendations of JSCE-SF4:1984 [28], so two prismatic specimens were molded with dimensions of 150x150x500 mm. The molding process was conducted under recommendations of ASTM C192:2016 [27]. Then, the curing procedure followed the same requirements as the cylindrical specimens.

2.4 Fresh-state concrete

Concrete workability was analyzed by slump and dynamic VeBe tests. The first is guided by ASTM C143:2015 [29], while the latter is specified by ACI 211.3R-02:2009 [30] and DNIT 064:2004 [31].

2.5 Hardened concrete

2.5.1 Compressive strength

The simple compressive strength was assessed under recommendations of ASTM C39:2018 [32]. The specimens were ground to improve the distribution of loads during the test, being subjected to testing in a hydraulic press with capacity of 2000 kN. Load was applied with a velocity of 0.45 ± 0.15 MPa/s until failure. The specimens were tested at 28 days, 2 specimens per mixture, yielding a total of 18 samples.

2.5.2 Equivalent flexural strength and flexural toughness factor

The flexural strength and flexural toughness tests abided by JSCE-SF4:1984 [28]. For the first, the test setting consists of laying the beam over two punches and then apply load through two other punches placed on top of the beam, at the mid one-third of the span, as depicted in Figure 3. The method specified by the standard states that the test span must be thrice the height of the specimen, so the dimensions were 450 mm of length span, 150 mm of height and 150 mm of width. A 2000-kN Shimadzu press was used, and the load was applied by prescribed displacement, at 28 days, two specimens per mixture, leading to a total of 18 samples.

3. Results and discussions

3.1 Fresh-state Properties

Table 3 shows the fresh-state concrete test results. It can be noted

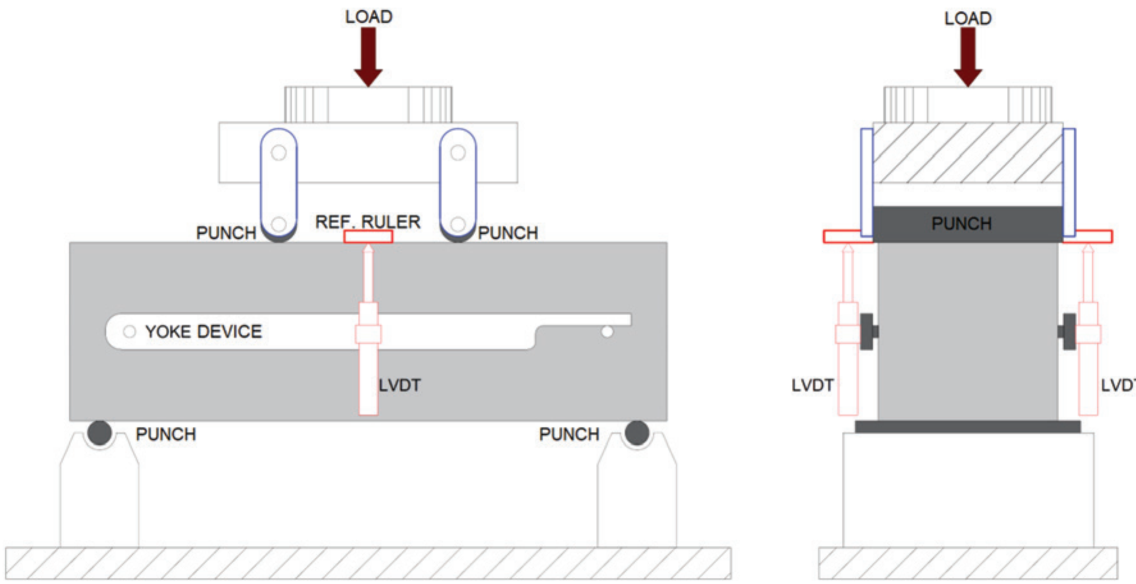

Figure 3
Test apparatus – four-point bending
Source: Adapted by the authors from JSCE-SF4 (1984)

Table 3
Fresh-state results of the mixtures

Mixture	Steel fiber (kg/m³)		Total (kg/m³)	Blended	Slump (mm)	VeBe (s)
	Space	Simple				
MR	0	0	0	–	170	1.5
M1	0	10	10	E0+M10	170	1.4
M2	0	20	20	E0+M20	130	1.6
M3	30	10	40	E30+M10	20	5.31
M4	30	20	50	E30+M20	40	3.19
M5	50	10	60	E50+M10	20	4.56
M6	50	20	70	E50+M20	20	4.63
M7	30	0	30	E30+M0	50	4.32
M8	50	0	50	E50+M0	20	4.34

that the addition of fibers reduced the workability of the composite, and the values were consistent with those found by Abbass et al. [33]. Akcay and Tasdemir [34] and Banthia et al. [15]. Velasco [35] stated that fiber-reinforced concrete tends to lose workability and fluidity, a loss that becomes clearer as fiber content increases. This workability loss is even more evident for mixtures reinforced with space fibers, as the VeBe test values increased by 184.7% and 200.7% for mixtures with 30 kg/m³ and 50 kg/m³ of space fibers respectively. The rates show that space fibers exceed the shear strength of fresh-state mixtures, hindering particle dispersion and raising the need for alternatives that promote fluidity for handling. Under these circumstances, it is recommended to use mechanical consolidation with proper devices [36], or even change the composition of the cement matrix. Such change concerns the increase of mortar content, which increases the mobility of materials added to concrete, by means of lubrication, reducing internal friction between particles, hence allowing the proper consolidation that fiber-reinforced concrete needs.
This behavior can be justified by the low mobility of space fiber-reinforced composites, since these fibers are formed by a set of three simply interconnected fibers, so they end up requiring more energy to be moved than simple fibers. This leads to a structured mixture that limits the fluidity of the matrix.
Figure 4 compares the fresh-state concrete test results and shows that space fibers cause considerable influence on the workability of the matrix as there was an average reduction of 174% based on the matrices studied. This behavior was observed in the VeBe test for mixtures with 30 kg/m³ and 50 kg/m³ of space fibers. Moderate decreases were also identified when simple fibers were hybridized. So, among the mixtures with space fibers, matrix M4 yielded the best results, while matrix M3, which contained 40 kg/m³, attained the worst results due to its limited consolidation. Lastly, mixtures M8, M5 and M6, which contained 50 kg/m³ of space fibers, behaved similarly with respect to each other.

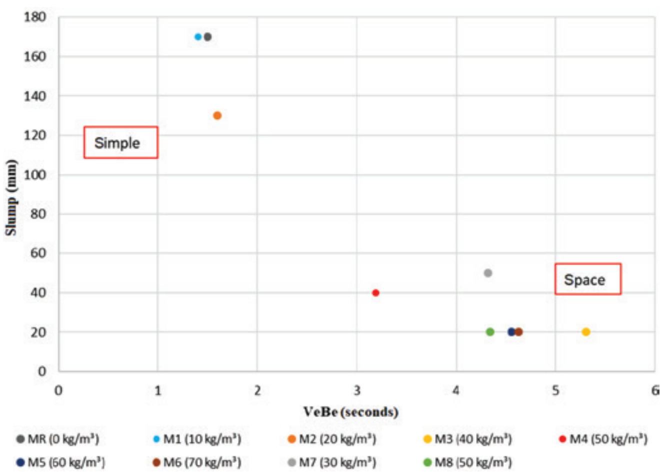

Figure 4
Relation between slump and VeBe tests

3.2 Compressive strength

Table 4 presents the potential compressive strength of the mixtures. These values correspond to the highest strength attained by each composite and are followed by their respective standard deviation. The tests were performed at 28 days, along with the prismatic specimens that were tested for flexural strength.
It is noteworthy that none of the fiber-reinforced mixtures reached values that exceed the reference, indicating that the addition of these elements did not contribute to the increase of compressive strength, agreeing with [33, 34, 36, 37]. Additionally, the standard deviation of fiber-reinforced samples was higher than that of the

Table 4
Potential compressive strength of each composite

Mixture	Fiber content (kg/m³)	f_c (MPa)
MR	0	36.4 ± 2.5
M1	10	32.3 ± 3.1
M2	20	30.2 ± 2.8
M3	40	33.1 ± 3.3
M4	50	35.4 ± 3.5
M5	60	31.4 ± 2.9
M6	70	29.7 ± 3.2
M7	30	30.6 ± 1.9
M8	50	26.9 ± 2.6

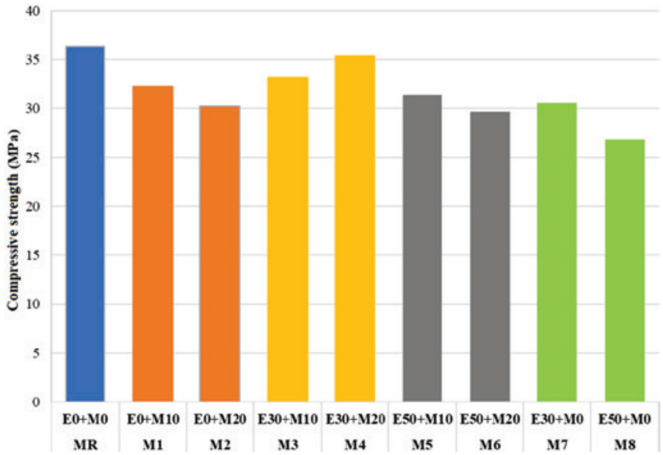

Figure 5
Potential compressive strength

reference matrix due to the instability that is inherent to this casting process. The addition of fibers caused average decreases of 14.3%. Analyzing non hybridized mixtures, the fibers decreased compressive strength by up to 17.0% for mixtures with simple fibers, while mixtures with space fibers reached higher decreases, ranging from 15.9% to 26.1%, which represent matrices M7 and M8 respectively. Hybridization lessened these decreases though, since mixtures M3 and M4, with 30 kg/m³ of space fibers, yielded decreases of 8.8% and 2.5% respectively. On the other hand, mixtures M5 and M6, which contained 50 kg/m³ of space fibers, reached decreases of 13.7% and 18.4% respectively. Mixture M4 performed well in the end, in spite of the hybridized mixtures with 50 kg/m³ of space fibers, which presented the highest compressive strength losses. The compressive strength results have been plotted in Figure 5.

3.3 Flexural strength

Table 5 demonstrates the flexural strength test results. Mixture M6, which contained 70 kg/m³, yielded the best performance as it achieved a flexural strength gain of 32.3% compared to the reference concrete. Quinino [2] explains that, the higher the fiber content, the higher the number of filaments that act directly on the fracture plane as stress transfer bridges, and so, the higher the strength of the matrix. Additionally, mixture M2, whose fiber content was 3.5 times smaller than matrix M6, showed a strength increase of 24.8%, only 7.5 percentage points lower than M6. This suggests that simple SE fibers are more efficient concerning flexural strength, considering that, excluding mixture M6, matrix M2 attained the highest value for flexural strength. The proportional increase of flexural strength with respect to the increase of fiber content was identified by Jang and Yun [38], Khaloo et al. [39], Lee, Cho and Choi [40], Pająk and Ponikiewski [41] and Ehrenbring et al. [42] as well.

Table 5
Average flexural strength

Mixture	Fiber content (kg/m³)	f_t (MPa)
MR	0	3.03 ± 0.12
M1	10	3.52 ± 0.09
M2	20	3.78 ± 0.25
M3	40	3.54 ± 0.27
M4	50	3.58 ± 0.17
M5	60	3.57 ± 0.33
M6	70	4.01 ± 0.39
M7	30	3.64 ± 0.37
M8	50	3.30 ± 0.02

The flexural performance was similar for hybrid matrices M3, M4 and M5, which reached an average ft of 3.55 MPa. Composite M3 stands out among these three as it presented the best value. It should be noted that mixtures M2 and M7 reached higher tensile strength values, that is, 7.78 MPa and 3.64 MPa respectively, despite their lower fiber contents. Therefore, the high values of this study have hindered the molding and the distribution of fibers along the samples, affecting the mechanical properties, in accordance with Pacheco et al. [43].

3.4 Flexural toughness

The flexural toughness behavior is presented in Table 6 and Figure 6, which was obtained when the composites were subjected

Table 6
Average toughness values

Mixture	Fiber content (kg/m³)	Toughness		
		Max. load (kN)	FT (MPa)	Efficiency (kg/m³.MPa)
MR	0	22.69 ± 0.87	0.00 ± 0	-
M1	10	26.35 ± 0.72	0.84 ± 0.23	11.9
M2	20	28.32 ± 1.87	1.30 ± 0.59	15.4
M3	40	26.58 ± 2.02	1.56 ± 0.16	25.6
M4	50	26.83 ± 1.27	2.58 ± 0.13	19.4
M5	60	26.75 ± 2.43	2.47 ± 0.51	24.3
M6	70	30.09 ± 2.81	2.96 ± 0.63	23.6
M7	30	27.33 ± 2.75	1.70 ± 1.20	17.6
M8	50	24.69 ± 0.16	2.26 ± 0.30	22.1

to the test for determination of equivalent flexural strength. Curves have been depicted for the two specimens of each mixture, and the average results were used for calculation.

After the tests, it was noted that the reference matrix (MR) presented null flexural toughness factor, as expected. This result was reached because the matrix was not reinforced, so its failure was brittle due to its low capacity to deform as more stressed were added along the test. It became evident that the area under the curves increased after the addition of fibers, mainly for samples with higher fiber contents. The hybrid mixtures (M3, M4, M5 and M6) underwent different behaviors, considering that M6 yielded the highest flexural toughness factor, equals 2.96 MPa. In contrast, matrix M3 presented the lowest flexural toughness factor among hybrid mixtures, despite reaching the most efficient factor (25.6 kg/m³.MPa).

It was then possible to extract the area below the load-displacement curve to calculate the flexural toughness factor, by means of the formulas of JSCE – SF4:1981 [28]. Table 6 expresses the results for the mixture toughness analysis.

The flexural toughness factor, which relates the amount of energy absorbed by the specimen, just like in studies of Banthia et al. [15], Lee, Cho and Choi [40] and Carrillo, Cárdenas Pulido and Aperador [44], turned out to increase gradually along with the fiber content. Evaluating the improvement of this property with respect to matrix M1, the increases were 54.8% for mixture M2 and 251.8% for M6, demonstrating performance gains as fiber content increases. On the other hand, the mixtures with lower fiber contents (M1, M2 and M7) achieved the best yields, since their efficiency exceeds the others', so they require a fewer fibers per strength unit (MPa).

Mixture M4 presented the second-highest flexural toughness factor, but the lowest efficiency among hybrid mixtures (19.4 kg/m³.MPA). Mixture M3 stood out as the most efficient. This behavior shows that M3 was able to transfer and absorb stresses more easily, what is related to their placement inside the matrix, supplying a

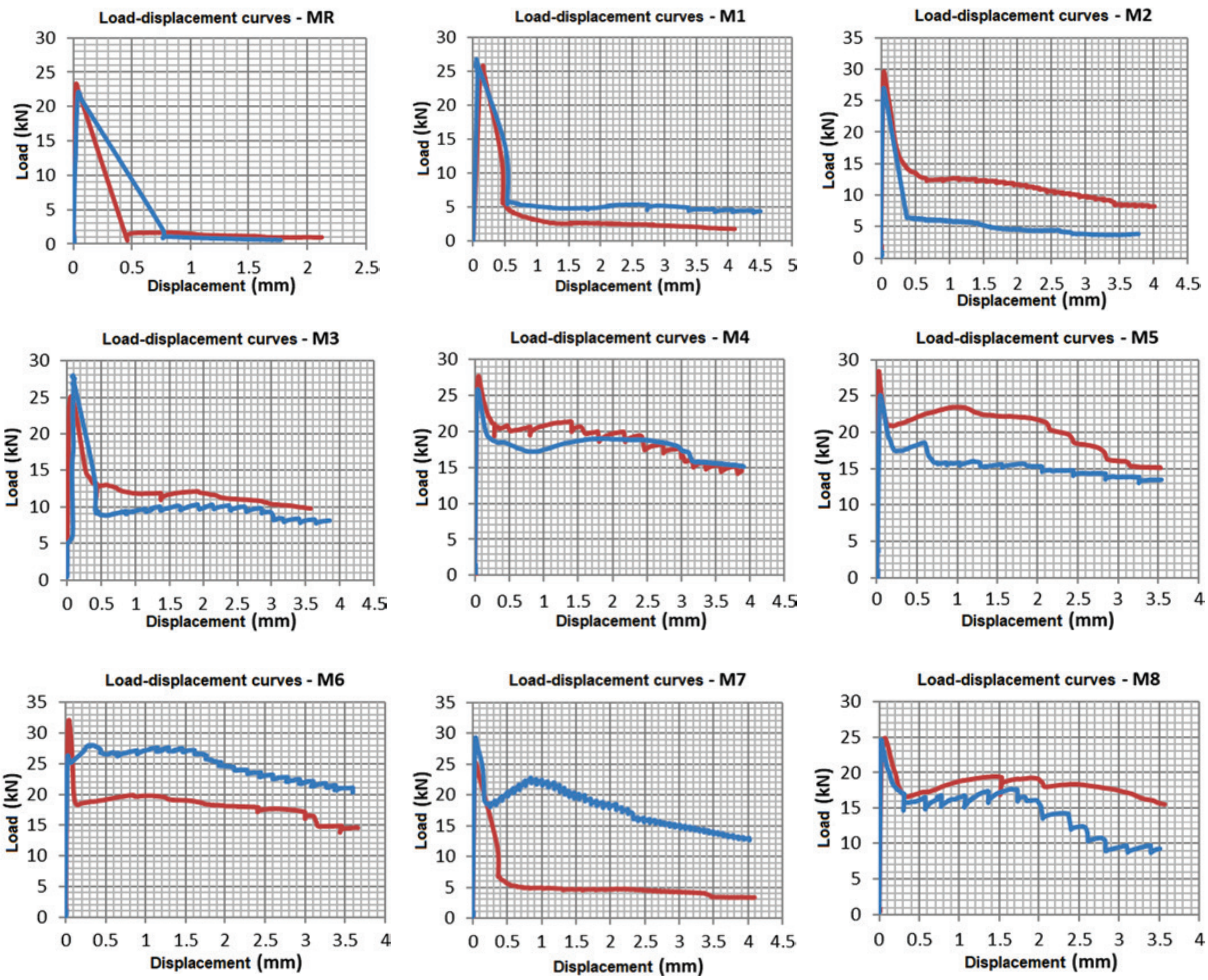

Figure 6
Load-displacement curves

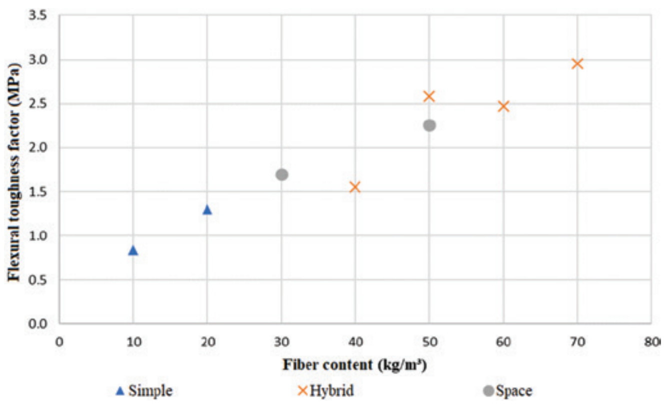

Figure 7
Increase of fiber content and flexural toughness factor

greater number of fibers that act on the fracture plane and, consequently, improve stress distribution, as Gil et al. [45] also identified. Another finding was that flexural toughness increased along with fiber content, as expected. Figure 7 depicts the correlation between flexural toughness factor and fiber content.
It shows a linear behavior that grows as the content of fibers increases, despite the discontinuity yielded by matrix M3 (40kg/m³). Finally, space fibers attained better values, although smaller than those of hybrid mixtures.

4. Conclusions

Based on the results and discussions of this study, it can be stated that adding space fibers to concrete has led to improvements to flexural strength and flexural toughness factor, despite the loss of workability and compressive strength. Matrix M4, a hybrid mixture with 30 kg/m³ of space fibers and 20 kg/m³ of simple fibers, achieved the best overall performance among the matrices that were tested, demonstrating the acceptable compatibility of this matrix with simple and space fiber contents.

5. References

[1] YOO, D.-Y. et al. Effect of fiber orientation on the rate-dependent flexural behavior of ultra-high-performance fiber-reinforced concrete. Composite Structures, v. 157, p. 62–70, 1 dez. 2016.
[2] QUININO, U. C. M. Investigação experimental das propriedades mecânicas de compósitos de concreto com adições híbridas de fibras. 2015. Thesis (Civil Engineering PhD) – Civil Engineering Graduate Program, Universidade Federal do Rio Grande do Sul (UFRGS), Porto Alegre, 2015.
[3] IBRAHIM, M. A. et al. Effect of Material Constituents on Mechanical and Fracture Mechanics Properties of Ultra-High-Performance Concrete. Materials Journal, v. 114, n. 3, p. 453- 465, 2017.
[4] FIGUEIREDO, A. D.; CECCATO, M. R. Workability Analysis of Steel Fiber Reinforced Concrete Using Slump and Ve-Be Test. Materials Research, 18 (2015), n. 6, pp. 1284-1290.
[5] EHRENBRING, H. Z. Comportamento de concreto reforçados com microfibras de polipropileno (PP), álcool polivinílico (PVA) e recicladas de poliéster (POL) em relação à retração por secagem restringida e às propriedades mecânicas. 2017. 165 s. Thesis (Civil Engineering Master's) – Civil Engineering Graduate Program, Universidade do Vale do Rio dos Sinos, São Leopoldo, 2017.
[6] BENTUR, A.; MINDESS, S. Fibre reinforced cementitious composites. 2.Ed., Modern Concrete Technology Series, Taylor&Francis, 2007.
[7] GÜNEYISI, E. et al. Combined effect of steel fiber and metakaolin incorporation on mechanical properties of concrete. Composites Part B: Engineering, v. 56, p. 83–91, 01 Jan. 2014.
[8] WU, Z. et al. Effects of steel fiber content and shape on mechanical properties of ultra high performance concrete. Construction and Building Materials, v. 103, p. 8–14, 30 Jan. 2016.
[9] YOO, D.-Y.; PARK, J.-J.; KIM, S.-W. Fiber pullout behavior of HPFRCC: Effects of matrix strength and fiber type. Composite Structures, v. 174, p. 263–276, 15 Aug. 2017.
[10] PARDINI, L. C. Preformas para compósitos estruturais. Polímeros, v. 10, n. 2, p. 100–109, June. 2000.
[11] RIBEIRO, J. L. P.; GREGORI, M. L.; PARDINI, L. C. Predição das propriedades elásticas de compósitos termoestruturais com reforço multidirecional. Matéria (Rio de Janeiro), v. 13, n. 1, p. 33–48, Mar. 2008.
[12] DU, Y. et al. Experimental study on basalt textile reinforced concrete under uniaxial tensile loading. Construction and Building Materials, v. 138, p. 88–100, 01 May 2017.
[13] WILLIAMS PORTAL, N.; NYHOLM THRANE, L.; LUNDGREN, K. Flexural behaviour of textile reinforced concrete composites: experimental and numerical evaluation. Materials and Structures, v. 50, n. 1, p. 1–14, Aug. 2017.
[14] COLOMBO, I. G. et al. Textile Reinforced Concrete: experimental investigation on design parameters. Materials and Structures, v. 46, n. 11, p. 1933–1951, 2013.
[15] BANTHIA, N. et al. Fiber synergy in Hybrid Fiber Reinforced Concrete (HyFRC) in flexure and direct shear. Cement and Concrete Composites, v. 48, p. 91–97, 01 Apr. 2014.
[16] BANTHIA, N.; SAPPAKITTIPAKORN, M. Toughness enhancement in steel fiber reinforced concrete through fiber hybridization. Cement and Concrete Research, v. 37, n. 9, p. 1366–1372, 01 Sept. 2007.
[17] TUTIKIAN, B. F.; HELENE, P. Dosagem dos concretos de cimento Portland. In: ISAIA, Geraldo Cechella. Concreto: Ciência e Tecnologia. São Paulo: IBRACON, 2011. Ch. 12. P. 415-452.
[18] BOULEKBACHE, B. et al. Flexural behaviour of steel fibre-reinforced concrete under cyclic loading. Construction and Building Materials, v. 126, p. 253–262, 15 Nov. 2016.
[19] AMERICAN SOCIETY FOR TESTING AND MATERIALS. Standard Specification for Portland Cement. C150/C150M, ASTM, Pennsylvania, 2018.
[20] AMERICAN SOCIETY FOR TESTING AND MATERIALS. Standard Test Method for Relative Density (Specific

Gravity) and Absorption of Fine Aggregate. C128, ASTM, Pennsylvania, 2015.

[21] AMERICAN SOCIETY FOR TESTING AND MATERIALS. Standard Test Method for Bulk Density ("Unit Weight") and Voids in Aggregate. C29/C29M, ASTM, Pennsylvania, 2017.

[22] AMERICAN SOCIETY FOR TESTING AND MATERIALS. Standard Test Method for Relative Density (Specific Gravity) and Absorption of Coarse Aggregate. C127, ASTM, Pennsylvania, 2015.

[23] AMERICAN SOCIETY FOR TESTING AND MATERIALS. Standard Specification for Concrete Aggregates. C33/C33M, ASTM, Pennsylvania, 2018.

[24] AMERICAN SOCIETY FOR TESTING AND MATERIALS. Standard Test Method for Sieve Analysis of Fine and Coarse Aggregates. C136/C136M, ASTM, Pennsylvania, 2014.

[25] FIGUEIREDO, A. D. Concreto reforçado com fibras. Thesis (habilitation) – Civil Construction Engineering Department, Escola Politécnica de São Paulo, São Paulo, 2011.

[26] ASSOCIAÇÃO BRASILEIRA DE NORMAS TÉCNICAS (ABNT). NBR 15530: Fibras de Aço para concreto. Rio de Janeiro, 2007.

[27] AMERICAN SOCIETY FOR TESTING AND MATERIALS. Standard Practice for Making and Curing Concrete Test Specimens in the Laboratory. C192/C192M, ASTM, Pennsylvania, 2016.

[28] JAPAN SOCIETY OF CIVIL ENGINEERS. Method of tests for flexural strength and flexural toughness of steel fiber reinforced concrete. JSCE-SF4. Concrete Library of JSCE. Part III-2 Method of tests for steel fiber reinforced concrete. № 3 June 1984. p.58-61.

[29] AMERICAN SOCIETY FOR TESTING AND MATERIALS. Standard Test Method for Slump of Hydraulic-Cement Concrete. C143/C143M, ASTM, Pennsylvania, 2015.

[30] AMERICAN CONCRETE INSTITUTE. Guide for Selecting Proportions for No-Slump Concrete (ACI 211.3R-02). ACI Committee 211. Detroit, USA, 2009.

[31] DEPARTAMENTO NACIONAL DE INFRA-ESTRUTURA DE TRANSPORTES. DIRETORIA DE PLANEJAMENTO E PESQUISA. INSTITUTO DE PESQUISAS RODOVIÁRIA. DNIT 064: Pavimento rígido – Determinação da consistência do concreto pelo consistômetro VeBe – Método de ensaio. Rio de Janeiro, 2004.

[32] AMERICAN SOCIETY FOR TESTING AND MATERIALS. Standard Test Method for Compressive Strength of Cylindrical Concrete Specimens. C39/C39M, ASTM, Pennsylvania, 2018.

[33] ABBASS, W.; KHAN, M. I.; MOURAD, S. Evaluation of mechanical properties of steel fiber reinforced concrete with different strengths of concrete. Construction and Building Materials, v. 168, p. 556–569, 2018.

[34] AKCAY, B.; TASDEMIR, M. A. Mechanical behaviour and fibre dispersion of hybrid steel fibre reinforced self-compacting concrete. Construction and Building Materials, v. 28, n. 1, p. 287–293, 2012.

[35] VELASCO, R.V. Concretos auto-adensáveis reforçados com elevadas frações volumétricas de fibras de aço: propriedades reológicas, físicas, mecânicas e térmicas. Thesis (Civil Engineering PhD) – Civil Engineering Graduate Program, Universidade Federal do Rio de Janeiro, Rio de Janeiro, 2008.

[36] TABATABAEIAN, M. et al. Experimental investigation on effects of hybrid fibers on rheological, mechanical, and durability properties of high-strength SCC. Construction and Building Materials, v. 147, p. 497–509, 2017.

[37] PRATHAP, P.; NARESH KUMAR, T.; NARAYANA, S. M. V. Evaluation of Mechanical Properties of Concrete using Silica fume and Steel fibers. International Journal of Scientific & Engineering Research, v. 8, n. 5, p. 332–338, 2017.

[38] JANG, S. J.; YUN, H. D. Combined effects of steel fiber and coarse aggregate size on the compressive and flexural toughness of high-strength concrete. Composite Structures, v. 185, p. 203–211, 01 Feb. 2018.

[39] KHALOO, A. et al. Mechanical performance of self-compacting concrete reinforced with steel fibers. Construction and Building Materials, v. 51, p. 179–186, 31 Jan. 2014.

[40] LEE, J.-H.; CHO, B.; CHOI, E. Flexural capacity of fiber reinforced concrete with a consideration of concrete strength and fiber content. Construction and Building Materials, v. 138, p. 222–231, 01 May 2017.

[41] PAJĄK, M.; PONIKIEWSKI, T. Flexural behavior of self-compacting concrete reinforced with different types of steel fibers. Construction and Building Materials, v. 47, p. 397–408, 01 Oct. 2013.

[42] EHRENBRING H. Z.; DE MEDEIROS QUININO, U. C.; OLIVEIRA, L. F. S.; TUTIKIAN, B. F. Experimental method for investigating the impact of the addition of polymer fibers on drying shrinkage and cracking of concrete. *Structural Concrete*, 2019; 20 pp. 1064–1075. https://doi.org/10.1002/suco.201800228

[43] PACHECO, F.; CHRIST, R.; GIL, A. M.; TUTIKIAN, B. F. Aplicação de MEV e microtomografia 3D na investigação da distribuição de fibras em compósitos cimentícios avançados. *Rev. IBRACON Estrut. Mater.*, São Paulo, v. 9, n. 6, p. 824-841, Dec. 2016.

[44] CARRILLO, J.; CÁRDENAS PULIDO, J.; APERADOR, W. Flexural mechanical properties of steel fiber reinforced concrete under corrosive environments. Revista Ingeniería de Construcción, v. 32, n. 2, p. 59–72, 2017.

[45] GIL, A. M.; KHAYAT, K. H.; TUTIKIAN, B. F. An experimental approach to design self-consolidating concrete. Construction and Building Materials, v. 229, n. 30, 2019. https://doi.org/10.1016/j.conbuildmat.2019.116939

Volume 13, Number 3 (June 2020) p. 464 – 482 • ISSN 1983-4195
http://dx.doi.org/10.1590/S1983-41952020000300002

IBRACON

REVISTA IBRACON DE ESTRUTURAS E MATERIAIS
IBRACON STRUCTURES AND MATERIALS JOURNAL

Evaluation of the impact of two types of steel fibers (SE), mono and 3D, on concrete properties, when added isolated or blended

Avaliação do impacto de dois tipos de fibras de aço, simples e espaciais, nas propriedades do concreto, quando inseridas separadamente ou de forma combinada





A. L. BAUER [a]
andersonbauer1995@gmail.com
https://orcid.org/0000-0002-7633-618X

H. EHRENBRING [a]
hzamis@unisinos.br
https://orcid.org/0000-0002-0339-9825

D. SCHNEIDER [a]
diegosch@unisinos.br
https://orcid.org/0000-0002-8810-460X

U. C. M. QUININO [a]
uquinino@unisinos.br
https://orcid.org/0000-0002-6488-9828

B. TUTIKIAN [a]
bftutikian@unisinos.br
https://orcid.org/0000-0003-1319-0547

Abstract

The brittle behavior of concrete can be compensated by the addition of reinforcements, providing benefits such as improved crack control, residual strength and increased flexural strength. It is usual to apply mono fibers to concrete, but their positioning in the matrix may not be homogeneous, consequently increasing the susceptibility to fracture planes with fewer reinforcements. This study aimed to evaluate the use and behavior of simple (mono) and space (3D) steel fibers (SE), in order to achieve a more homogeneous mixture, increase the effectiveness of fibers in restricting cracks and improve mechanical properties. The fresh-state was assessed through slump and VeBe tests, whereas the hardened-state tests comprised axial compressive strength, flexural strength and the flexural toughness factor. The volume content of simple and space fibers varied from 0 to 0.93%. Based on the results, it can be stated that space and simple fiber contents improved rheological and mechanical properties of the composite in isolated (0.29%) and hybrid (0.64%) combinations, since their overall performance exceeded the other mixtures'. However, space fibers caused considerable workability losses compared to the conventional concrete, hindering its casting and harming its hardened-state properties.

Keywords: fiber-reinforced concrete, space fiber, simple fibers, hybrid mixtures.

Resumo

O comportamento frágil de concretos pode ser compensado com a inserção de reforços, proporcionando benefícios no que tange ao controle de fissuração, ganho de tenacidade, aumento da resistência à tração, entre outros. Comumente, aplicam-se fibras isoladas em concretos, porém o seu posicionamento na matriz pode não ser homogêneo e, consequentemente, facilita-se o surgimento de planos de ruptura com baixo número de reforços. Assim, o trabalho em questão teve como objetivo avaliar a aplicação e comportamento de fibras simples e espaciais em aço, a fim de proporcionar uma mistura mais homogênea, aumentar a área de atuação da fibra na contenção de fissuras e melhorias nas propriedades mecânicas. Os ensaios no estado fresco foram de consistência do compósito, por meio do abatimento do tronco de cone e do VeBe, e, no estado endurecido, avaliou-se a resistência à compressão axial, resistência à tração na flexão e o fator de tenacidade. Variou-se o teor de adição das fibras uni (simples) e espaciais, em volume, de 0 até 0,93%. Com base nos resultados, pode-se afirmar que os teores de fibras espaciais e simples foram benéficos às propriedades reológicas e mecânicas do compósito na combinação isolada (0,29%) e híbrida (0,64%), dado que demonstraram desempenho geral superior às demais misturas. Entretanto, as fibras espaciais acarretam consideráveis perdas da trabalhabilidade, comparado ao concreto tradicional sem fibras, dificultando o seu lançamento e, consequentemente, propriedades no estado endurecido.

Palavras-chave: concreto reforçado com fibras, fibra espacial, fibras simples, misturas híbridas.

[a] *Unisinos, itt Performance, São Leopoldo, RS, Brazil.*

Received: 14 Aug 2018 • Accepted: 30 Sep 2019 • Available Online: 26 May 2020

1. Introdução

O concreto é um material de comportamento frágil e depende de outros componentes que permitam alterar sua forma de ruptura [1]. Assim, as armaduras metálicas são especificadas para prover aumentos na resistência à tração. Porém, este tipo de reforço atua de forma concentrada, sendo ineficiente na mitigação de fissuras localizadas, impactando na durabilidade do sistema. A adição de fibras no concreto tem o intuito de suprir tais deficiências, uma vez que se espera torná-lo um material isotrópico, melhorando seu comportamento, quando submetido às ações mecânicas e aumentando a área de combate à nucleação de fissuras [2].
Conforme Ibrahim et al. [3], a utilização de fibras de aço como reforço da matriz de concreto traz uma série de benefícios no estado endurecido, como o aumento da capacidade de carga, da energia de ruptura, bem como proporciona um maior controle de fissuração e, por sua vez, um aumento na vida útil do compósito. Já no estado fresco, há a criação de uma malha interna formada pelas próprias fibras, a qual interfere na movimentação dos agregados no interior da mistura. Essa ação pode prejudicar os processos de moldagem e o adensamento do compósito nas fôrmas, tendo as microfibras como elementos que dificultam a homogeneização dos agregados graúdos com o restante dos materiais [4, 5].
Salienta-se que fibras incorporadas à matriz atuam como pontes de transferência de tensões e, na medida em que limitam a abertura dos planos de ruptura, atenuam a propagação da anomalia, aumentando a energia de ruptura à tração e alterando a forma de fragilização do compósito para o estado pseudo-dúctil [6]. A vasta literatura atual aborda as vantagens do emprego de diferentes tipos de fibras simples [7, 8, 9], sendo essas distribuídas separadamente ao longo da matriz e, consequentemente, atuando individualmente em direção única. A mobilidade dos reforços no interior da matriz caracterizará a direção que cada um atuará.
Na área de engenharia aeroespacial, pesquisas têm desenvolvido conjuntos estruturais capazes de atuarem em várias direções, a fim de agregar a resistência mecânica de outros compósitos [10, 11], no entanto, ainda não ocorreu a inserção desse tipo de reforços em matrizes cimentícias. Mesmo que os resultados identificados sejam atrativos, ainda há uma lacuna acerca do desempenho do concreto com adição de fibras espaciais, as quais são caracterizadas por um arranjo específico estruturado com fibras simples atuantes em 3 direções. Tem-se uma expectativa que este novo modelo de reforço possa aumentar o número e/ou eficiência das fibras no plano de fratura, uma vez que o seu posicionamento é mais bem controlado e o conjunto, teoricamente, é mais efetivo. Assim, é possível assegurar que o plano de ruptura tenderá a ser interceptado pelas fibras espaciais independentemente da localização, visto que o conjunto tem a união rígida entre fibras formatadas ortogonalmente entre si, contribuindo como reforço em 3 direções e elevando a resistência do plano de fratura da matriz.
Também foram desenvolvidos estudos em torno do emprego de fibras bidirecionais, a exemplo do concreto têxtil [12, 13], que traz uma série de vantagens em relação ao concreto convencional e armado. Algumas dessas vantagens são o ótimo comportamento na tração, à compressão e elevada durabilidade, visto que a matriz possui baixa relação a/c (< 0,30) e as fibras empregadas não necessitam de proteção contra corrosão, permitindo a redução do peso das estruturas [14]. Outro benefício desses compósitos é a possibilidade de conformação geométrica das peças.
Para obter um aproveitamento ainda maior, pode ser realizada a combinação de duas ou mais fibras em uma mesma matriz, a fim de potencializar o desempenho do compósito. Esta combinação de fibras é também conhecida como hibridização. Comumente, são variados os tipos de material em cada reforço, bem como a geometria dos mesmos. No entanto, há ainda a necessidade de se conhecer a melhor forma de combinar o efeito de fibras que atuam em diferentes direções, de modo a alcançar a sinergia máxima e, assim, proporcionar um comportamento otimizado [2, 15].
Quinino [2] explica que a hibridização de microfibras de polipropileno e metálicas, trabalhando em conjunto e nas proporções adequadas, resultam em uma melhora de desempenho da matriz, uma vez que as microfibras de polipropileno retardam a formação de microfissuras, podendo restringir possíveis deslocamentos diferenciais no interior do compósito durante a formação e propagação de fissuras, enquanto as macrofibras metálicas têm a função de "costurar" as fissuras, retardando sua abertura e extensão.
Banthia e Sappakittipakorn [16] também obtiveram resultados promissores ao avaliar a hibridização de matrizes com dois tipos de fibras metálicas, ambas ondulares, variando apenas o fator de

Tabela 1
Teor de adição de fibras de aço nos traços dos compósitos utilizados na pesquisa

Misturas	Teor de adição		Tipo de fibra			
			Simples		Espacial	
	kg/m³	% em volume	kg/m³	% em volume	kg/m³	% em volume
MR	0	0,00%	0	0,00%	0	0,00%
M1	10	0,14%	10	0,14%	0	0,00%
M2	20	0,29%	20	0,29%	0	0,00%
M3	40	0,52%	10	0,14%	30	0,38%
M4	50	0,67%	20	0,29%	30	0,38%
M5	60	0,78%	10	0,14%	50	0,64%
M6	70	0,93%	20	0,29%	50	0,64%
M7	30	0,38%	0	0,00%	30	0,38%
M8	50	0,64%	0	0,00%	50	0,64%

forma, mantendo-se o comprimento das fibras, demonstrando efeitos benéficos nas propriedades mecânicas do concreto.
Com esse propósito, foi elaborado o programa experimental para avaliar a influência no estado fresco e as propriedades mecânicas de matrizes cimentícias com a incorporação de fibras simples e espaciais em proporções variadas, de maneira individual e com hibridização entre as fibras.

2. Programa experimental

O programa experimental da pesquisa está voltado à análise do comportamento físico de uma matriz cimentícia padrão quando reforçada com fibras de aço simples e espaciais. Os compósitos estudados foram constituídos de um concreto convencional de resistência à compressão característica de 25 MPa, sendo sua dosagem estabelecida por meio do método de Tutikian e Helene [17]. Moldou-se 9 misturas distintas, uma do concreto referência sem fibra (MR) e as oito restantes com fibras simples e espaciais (M1 – M8). As características no estado fresco foram avaliadas pelo método do tronco de cone e VeBe. As propriedades mecânicas analisadas, resistência à compressão axial, à tração na flexão e o fator de tenacidade, foram testadas aos 28 dias. A Tabela 1 apresenta o teor de adição, em volume com compensação de massa, de fibras de aço em cada uma das misturas estudadas.
A escolha dos teores de adição teve como base os consumos médios usuais, estando na faixa de 10 a 70 kg/m3, conforme constatam as pesquisas de Banthia e Sappakittipakorn [16], Boulekbache et al. [18] e Quinino [2]. Nas misturas denominadas M3, M4, M5 e M6 houve a hibridização dos tipos de reforços, variando um teor de fibras simples com as espaciais. Ambas fibras em simples ou espaciais eram de aço e apresentavam ancoragem nas extremidades, o que contribui para o desempenho do compósito, pelo fato de diminuir o potencial de desprendimento do reforço à matriz cimentícia, à medida em que se elevam as tensões de tração. Os itens a seguir apresentam os materiais e métodos aplicados no desenvolvimento dessa pesquisa.

2.1 Materiais utilizados

Em todas as misturas utilizou-se cimento Portland tipo III, especificado pela ASTM C150:2018 [19]. A densidade do material correspondeu a 3,04 g/cm³ e área superficial equivalente a 4936 cm²/g. O agregado miúdo quartzoso utilizado possuía dimensão máxima dos grãos de 4,8 mm e módulo de finura de igual a 2,22. A massa específica desse material foi avaliada conforme ASTM C128:2015 [20], obtendo um valor equivalente a 2,63 g/cm³. Quanto a massa unitária, identificou-se o valor de 1,54 g/cm³, conforme os procedimentos prescritos pela ASTM C29:2017 [21]. Já para o agregado graúdo natural, os valores encontrados para a dimensão máxima e módulo de finura foram 19,0 mm e 6,86, respectivamente. A sua massa específica correspondeu a 2,69 g/cm³, de acordo com os métodos da ASTM C127:2015 [22]. A massa unitária da brita foi determinada de acordo com a ASTM C29:2017 [21], tendo como resultado 1,45 g/cm³.
A composição granulométrica dos agregados naturais foi realizada seguindo os parâmetros prescritos na ASTM C33:2018 [23] e ASTM C136:2014 [24]. A distribuição granulométrica dos agregados miúdo e graúdo é apresentada na Figura 1.

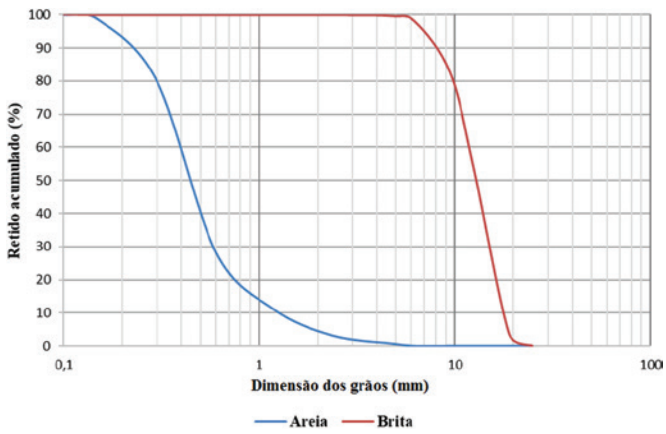

Figura 1
Distribuição granulométrica dos agregados miúdo e graúdo

Foram adotadas fibras simples (Figura 2-a) de comprimento de 60 mm, devido a compatibilidade com o agregado graúdo, garantindo assim o bom desempenho da fibra como reforço estrutural do concreto [25]. Estas fibras apresentam ainda diâmetro de 0,75 mm, o que resulta em um fator de forma de 80. Já as fibras espaciais (Figura 2-b) tem comprimento de 80 mm e diâmetro de 1,8 mm, tendo um fator de forma igual à 44. A fibra simples tem resistência de 1000 MPa, bem como os filamentos utilizados na produção da fibra espaciais. Salienta-se que as fibras espaciais são novos reforços, na forma de arranjos, os quais, para essa pesquisa, foram manualmente produzidos para viabilizar a sua avaliação, uma vez que ainda não são comercializados no mercado. Utilizaram-se 3 fibras por arranjo, interligadas com solda e orientadas à 90º. Essa ortogonalidade entre as fibras se manteve durante as operações de mistura, lançamento e adensamento do concreto. As dimensões dessas fibras necessitaram ser maiores que as fibras simples em virtude de obter uma soldagem satisfatória. Todavia, os filamentos aplicados nas fibras espaciais são classificados como tipo A e classe I (A-I), conforme as definições da ABNT NBR 15530:2007 [26]. A nomenclatura técnica adotada nesse trabalho para distinguir as fibras foi “simples” e “espaciais” de maneira a

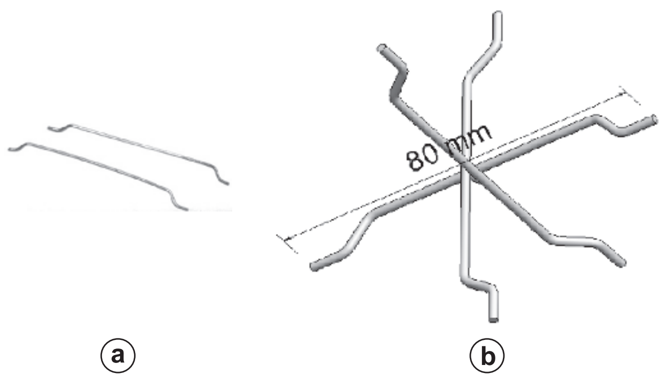

Figura 2
Formato das fibras (a) simples e (b) espaciais

Tabela 2
Classificação de consistência pelo ensaio de VeBe

Classificação	Abatimento (mm)	VeBe (s)
Extremamente seco	–	32 a 18
Muito rígido (mantém formato)	–	18 a 10
Rígido	0 a 25	10 a 5
Pouco fluido	25 a 75	5 a 3
Fluido	75 a 125	3 a 0
Muito fluido	125 a 190	–

Fonte: Adaptado de ACI 211.R3-02 [30]

distinguir o modo de atuação de cada fibra, simples e espacial, respectivamente.

2.2 Método de dosagem e processo de mistura

A dosagem do concreto referência teve como objetivo atingir a resistência à compressão de 25 MPa, adotando o consumo de cimento igual a 280 kg/m³ e relação água/cimento da mistura equivalente a 0,66. A proporção referencial praticada foi de 1: 2,51: 3,43 (cimento: areia: brita). As misturas contaram com a mesma matriz cimentícia de base, alterando o tipo de reforço aplicado. O teor de adição das fibras foi determinado em função da massa de reforços por metro cúbico, partindo de 10 até 70 kg/m³. O abatimento da matriz referência foi fixado para atingir a classe S160 (160 ≤ a < 220 mm) e comportamento fluído para o ensaio VeBe, bem como para os concretos reforçados com fibras. É importante ressaltar que, no decorrer da homogeneização dos materiais, não foi possível visualizar a formação de grumos, ou seja, aglomeração localizada de fibras. A Tabela 2 ilustra os parâmetros de classificação da fluidez de matrizes cimentícias utilizados como referência nesta pesquisa.

2.3 Moldagem e cura dos corpos de prova

Para o ensaio de resistência à compressão aos 28 dias, foram moldados dois corpos de prova cilíndricos por mistura, tendo dimensões de 100 mm de diâmetro e 200 mm de altura, conforme especifica a ASTM C192:2016 [27]. Posteriormente, as amostras permaneceram por 24 horas em temperatura ambiente, cobertas por uma placa de vidro. Passado o período, foram desmoldadas e dispostas em uma câmara de cura com temperatura de 21 ± 2ºC e umidade de 95 ± 3%, onde permaneceram até a idade de ensaio. Para os ensaios de tração na flexão e o fator de tenacidade, as dimensões adotadas das amostras são recomendadas pela norma JSCE – SF4:1984 [28], sendo moldados dois corpos de prova prismáticos, com dimensões de 150x150x500 mm. O processo de moldagem foi realizado conforme as recomendações da ASTM C192:2016 [27]. Posteriormente, o procedimento de cura seguiu os mesmos requisitos dos corpos de prova cilíndricos.

2.4 Concreto no estado fresco

A análise da consistência do concreto ocorreu pelo ensaio de abatimento do tronco de cone e o ensaio dinâmico de VeBe. O primeiro é regido pela ASTM C143:2015 [29], já o segundo é especificado pela ACI 211.3R-02:2009 [30] e DNIT 064:2004 [31].

2.5 Concreto no estado endurecido

2.5.1 Resistência à compressão axial

A resistência à compressão simples foi avaliada seguindo as

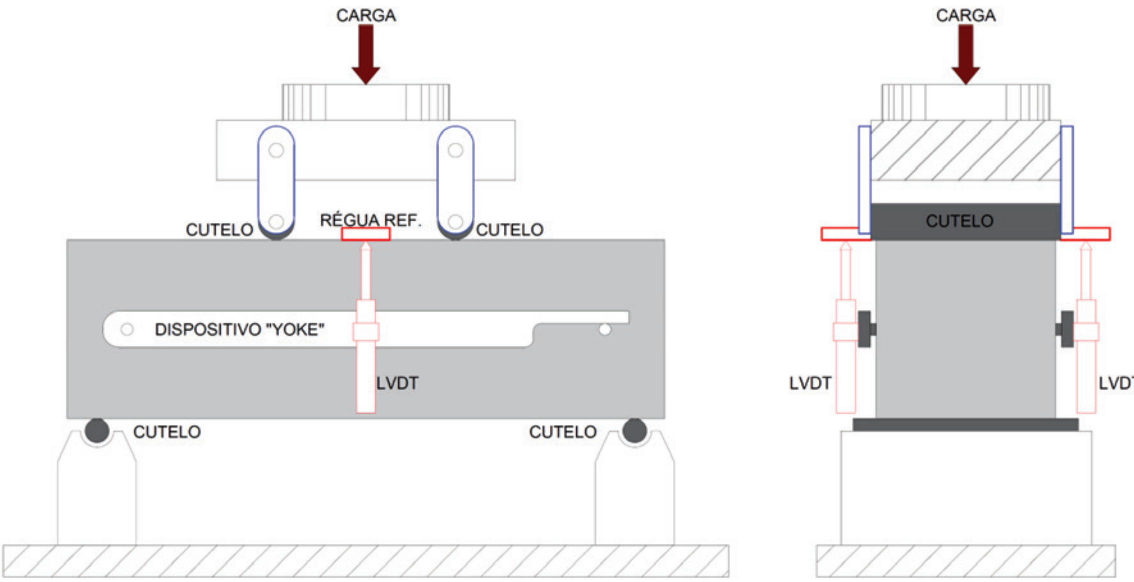

Figura 3
Configuração de ensaio – flexão em quatro pontos
Fonte: JSCE-SF4 (1984); adaptado pelos autores

Tabela 3
Resultados do estado fresco das misturas

Misturas	Fibra de aço (kg/m³)		Total (kg/m³)	Combinação	Abatim. (mm)	VeBe (s)
	Espacial	Simples				
MR	0	0	0	–	170	1,5
M1	0	10	10	E0+M10	170	1,4
M2	0	20	20	E0+M20	130	1,6
M3	30	10	40	E30+M10	20	5,31
M4	30	20	50	E30+M20	40	3,19
M5	50	10	60	E50+M10	20	4,56
M6	50	20	70	E50+M20	20	4,63
M7	30	0	30	E30+M0	50	4,32
M8	50	0	50	E50+M0	20	4,34

recomendações da ASTM C39:2018 [32]. Os corpos de prova foram retificados para melhor distribuição do carregamento de ensaio, sendo submetidos ao ensaio com uma prensa hidráulica com capacidade de 2000 kN. A velocidade de aplicação de carga foi de 0,45 ± 0,15 MPa/s, até o rompimento. A idade ensaiada foi de 28 dias, sendo ensaiados 2 corpos de prova por mistura, totalizando 18 amostras.

2.5.2 Fator de tenacidade e resistência à tração na flexão equivalente

Para os ensaios de tração na flexão e tenacidade, a norma utilizada foi a japonesa JSCE-SF4:1984 [28]. Com relação à tração na flexão, a configuração do ensaio consiste em apoiar a viga em dois cutelos e aplicar o carregamento através de outros dois cutelos, posicionados na parte superior da viga, no terço médio do vão, como apresentado na Figura 3. O método especificado pela norma prevê que o vão de ensaio deve apresentar três vezes a altura do corpo de prova, sendo assim, as dimensões foram de 450 mm de comprimento, 150 mm de altura e 150 mm de largura. A prensa utilizada foi uma Shimadzu de 2000 kN, sendo a aplicação da carga efetuada por deslocamento prescrito, aos 28 dias, sendo 2 corpos de prova por mistura, totalizando 18 amostras.

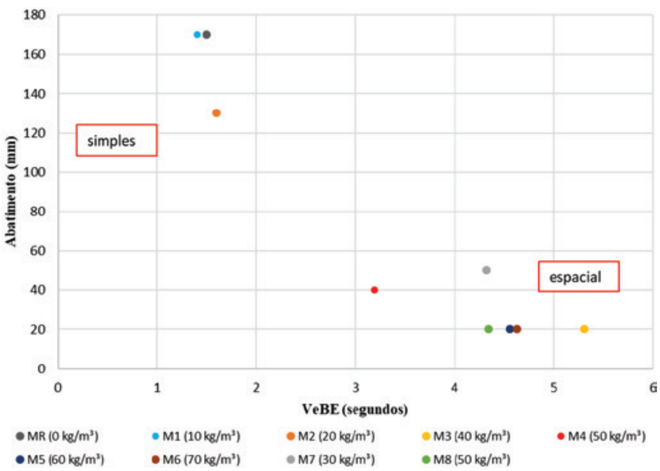

Figura 4
Relação entre ensaio de abatimento e VeBe

3. Resultados e discussões

3.1 *Propriedades no estado fresco*

A Tabela 3 mostra os resultados obtidos durante os ensaios do concreto no estado fresco.
Analisando os resultados, é possível perceber que, com a inserção das fibras, a consistência do compósito diminuiu, e os valores foram condizentos aos encontrados por Abbass et al. [33], Akcay e Tasdemir [34] e Banthia et al. [15]. Velasco [35] afirmou que o concreto com inserção de fibras tende a perder a consistência e fluidez, sendo mais notável à medida que o teor de fibras é acrescido. Essa perda de consistência fica ainda mais evidente nas misturas com a presença das fibras espaciais, visto que os valores para o ensaio de VeBe aumentaram em 184,7% e 200,7%, para as misturas com 30 kg/m³ e 50 kg/m³ de fibras espaciais, respectivamente. Os índices demonstram que as fibras espaciais superam a resistência ao cisalhamento da mistura no estado fresco, dificultando a dispersão das partículas e necessitando de alternativas que promovam fluidez para seu manuseio. Nessas condições, recomenda-se o uso de adensamento mecânico por meio de dispositivos adequados [36], ou ainda, interferir na composição da

Tabela 4
Resistência potencial à compressão de cada compósito

Mixture	Teor de fibras (kg/m³)	f_c (MPa)
MR	0	36,4 ± 2,5
M1	10	32,3 ± 3,1
M2	20	30,2 ± 2,8
M3	40	33,1 ± 3,3
M4	50	35,4 ± 3,5
M5	60	31,4 ± 2,9
M6	70	29,7 ± 3,2
M7	30	30,6 ± 1,9
M8	50	26,9 ± 2,6

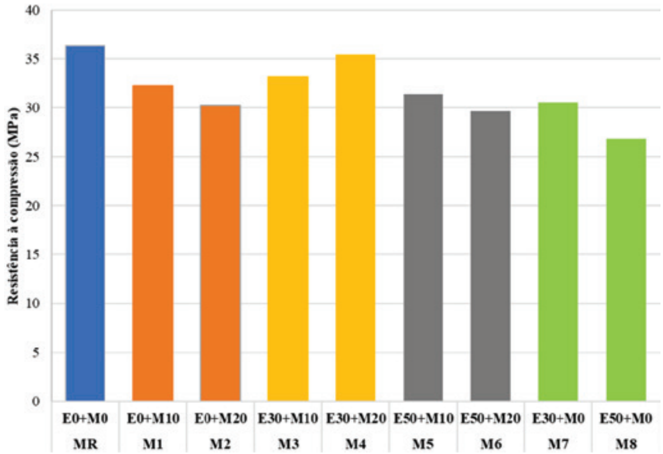

Figura 5
Resistência potencial à compressão axial

matriz cimentícia. Essa adequação na mistura volta-se ao aumentando do seu teor de argamassa, a fim de facilitar a mobilização dos materiais inseridos no concreto, por meio da lubrificação, diminuindo o atrito interno entre partículas e possibilitando um adequado adensamento do concreto reforçado com fibras (CRF).
Tal comportamento pode ser justificado pela baixa mobilidade dos compósitos com fibras espaciais, dado que as mesmas são formadas por um conjunto de três fibras simples interligadas entre si e, consequentemente, o esforço necessário para movimentá-las é maior do que para apenas uma fibra simples. Assim, tem-se uma mistura estruturada, que limita a fluidez da matriz.
A Figura 4 apresenta uma comparação dos resultados dos ensaios do concreto no estado fresco. Pode-se constatar que as fibras espaciais exercem uma influência considerável na trabalhabilidade da matriz do concreto, podendo ser apontada uma redução média de 174% com base nas matrizes estudadas. Esse comportamento é percebido no ensaio VeBe, tanto para as misturas com 30 kg/m³, quanto para as misturas contendo 50 kg/m³ de fibras espaciais. Também são identificados moderados decrementos ao se hibridizar as fibras. Percebe-se que, dentre as misturas com fibras espaciais, a matriz M4 apresentou os melhores resultados, enquanto a matriz M3, contento 40 kg/m³, apresentou piores resultados, devido a dificuldade de adensamento. Já as misturas M8, M5 e M6, contendo 50 kg/m³ de fibras espaciais, demonstraram comportamento semelhantes entre si.

Tabela 5
Resistência média à tração na flexão

Misturas	Teor de fibras (kg/m³)	f_t (MPa)
MR	0	3,03 ± 0,12
M1	10	3,52 ± 0,09
M2	20	3,78 ± 0,25
M3	40	3,54 ± 0,27
M4	50	3,58 ± 0,17
M5	60	3,57 ± 0,33
M6	70	4,01 ± 0,39
M7	30	3,64 ± 0,37
M8	50	3,30 ± 0,02

3.2 Resistência à compressão

A Tabela 4 apresenta os resultados potenciais obtidos no ensaio de compressão axial de cada mistura estudada. Esses valores correspondem às maiores resistências atingidas pelos compósitos e são acompanhados de seu respectivo desvio-padrão. Os ensaios foram realizados aos 28 dias, juntamente com os corpos de prova prismáticos ensaiados para a resistência à tração na flexão. Observa-se que nenhuma das misturas com presença de fibras apresentou valor superior ao traço referência, indicando que a adição desses elementos não contribuiu para o aumento da resistência à compressão, como já havia sido ressaltado por [33, 34, 36, 37]. Também, notou-se que o desvio-padrão das misturas com fibras foi superior ao da matriz referência, devido a instabilidade inerente a esse processo de inclusão. A incorporação de fibras ocasionou reduções médias de 14,3%. Analisando as misturas não hibridizadas, percebe-se que as fibras apresentaram redução na resistência à compressão em até 17,0% para as misturas com fibras simples, enquanto as misturas com fibras espaciais tiveram reduções maiores, nas proporções de 15,9% a 26,1%, referente às matrizes M7 e M8, respectivamente. Todavia, a hibridização atenuou estes decréscimos, dado que as misturas M3 e M4, contendo 30 kg/m³ de fibras

Tabela 6
Resistência média de tenacidade

Misturas	Teor de fibra (kg/m³)	Tenacidade		
		Carga (kN)	FT (MPa)	Eficiência (kg/m³.MPa)
MR	0	22,69 ± 0,87	0,00 ± 0	–
M1	10	26,35 ± 0,72	0,84 ± 0,23	11,9
M2	20	28,32 ± 1,87	1,30 ± 0,59	15,4
M3	40	26,58 ± 2,02	1,56 ± 0,16	25,6
M4	50	26,83 ± 1,27	2,58 ± 0,13	19,4
M5	60	26,75 ± 2,43	2,47 ± 0,51	24,3
M6	70	30,09 ± 2,81	2,96 ± 0,63	23,6
M7	30	27,33 ± 2,75	1,70 ± 1,20	17,6
M8	50	24,69 ± 0,16	2,26 ± 0,30	22,1

espaciais, apresentaram reduções de 8,8%, 2,5%, respectivamente. Já as misturas M5 e M6, contendo 50 kg/m³ de fibras espaciais, apresentaram reduções de 13,7% e 18,4%, respectivamente. Novamente, observou-se o bom desempenho da mistura M4. Nota-se ainda que as misturas hibridizadas, contendo 50 kg/m³ de fibras espaciais, demonstraram as maiores perdas de resistência à compressão. Os resultados de resistência à compressão estão apresentados graficamente na Figura 5.

3.3 *Resistência à tração na flexão*

Os resultados para os ensaios de tração na flexão são demonstrados na Tabela 5.

Na Tabela 5 é possível constatar que a mistura M6, a qual contém 70 kg/m³, apresentou o melhor desempenho, demonstrando um ganho de resistência à tração na flexão de 32,3% em relação ao concreto referência. Quinino [2] explica que, quanto maior o teor de fibras, maior será a quantidade de filmentos que atuam diretamente no plano de fratura como ponte de transferência de tensão e, consequentemente, proverá maior resistência à matriz. Pode-se destacar a mistura M2, que contém uma concentração de fibras 3,5 vezes menor do que a matriz M6, mostrou um incremento de resistência de 24,8%, apenas 7,5% menos que a mistura M6. Este fato evidencia que as fibras de aço, em formato simples, apresentam performance mais eficiente no que tange a resistência à tração por flexão, visto que a matriz M2 demonstrou, salvo a mistura M6, o maior valor de resistência a tração na flexão. Foi observado um aumento da resistência proporcionalmente ao aumento do teor de fibras, conforme os estudos de Jang e Yun[38], Khaloo et al. [39], Lee, Cho e Choi [40], Pająk e Ponikiewski [41] e Ehrenbring et al. [42] demonstraram.

Observa-se ainda que o desempenho à tração foi semelhante entre as misturas M3, M4 e M5, matrizes híbridas, atingindo um ft médio

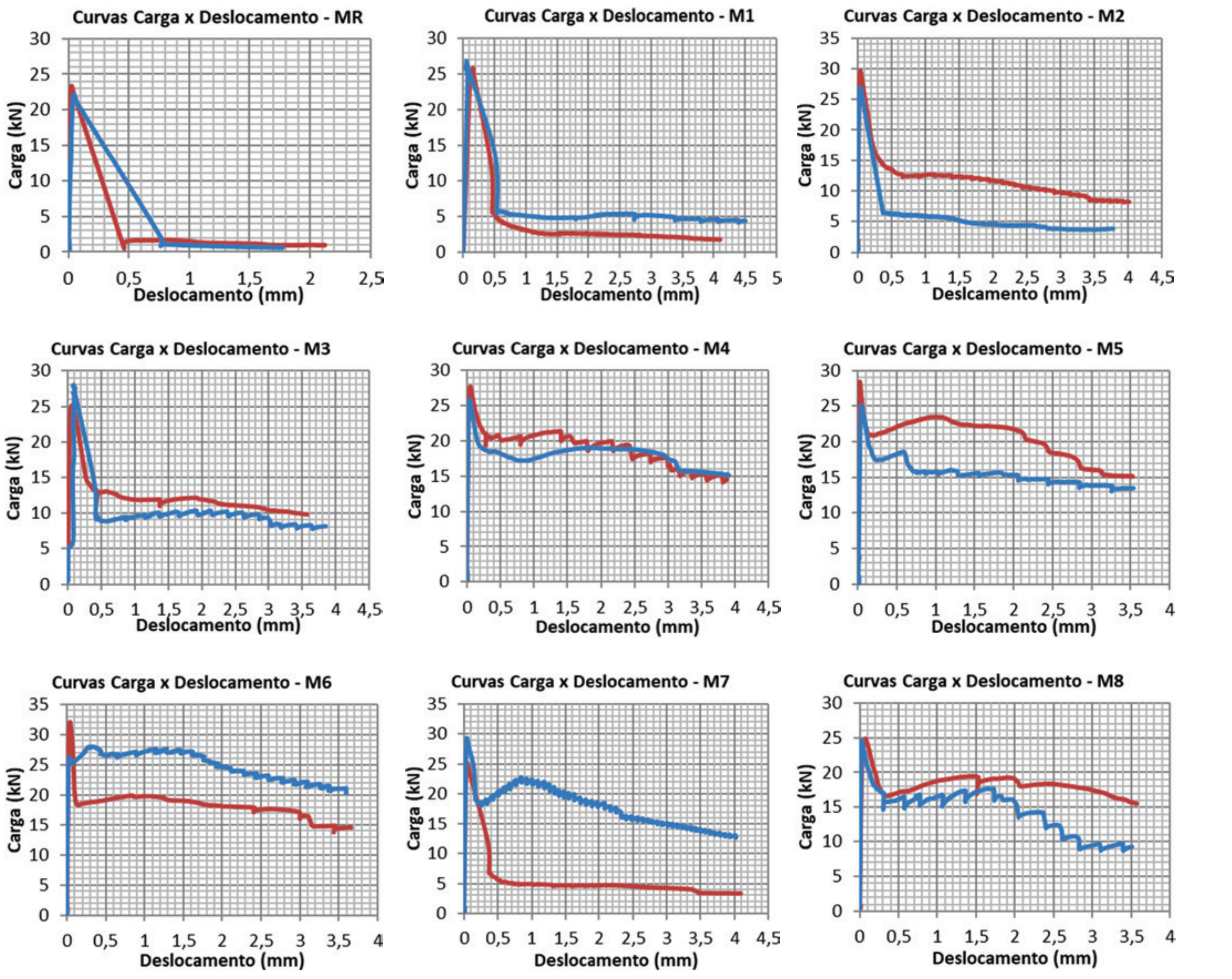

Figura 6
Curvas Carga x Deslocamento

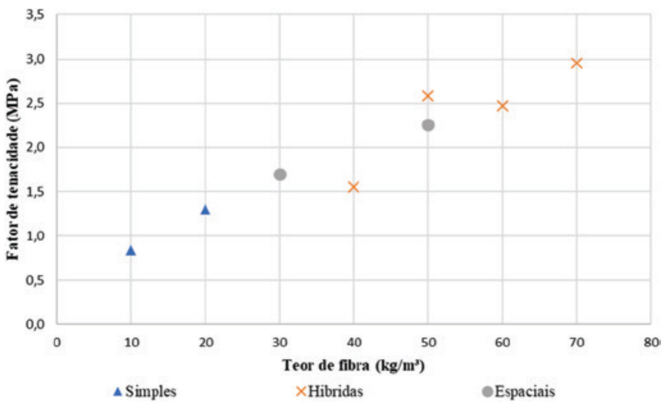

Figura 7
Aumento do teor de fibras e o aumento fator de tenacidade

de 3,55 MPa. Dentre estes compósitos híbridos, destaca-se o compósito M3, por apresentar o melhor aproveitamento das fibras. É interessante ressaltar que as misturas M2 e M7, com baixos teores de adição, alcançaram os maiores valores à tração, 3,78 MPa e 3,64 MPa, respectivamente. Pode-se entender que os altos teores da pesquisa prejudicaram a moldagem e distribuição das fibras nas amostras, refletindo nas propriedades mecânicas, de acordo com Pacheco et al. [43].

3.4 Tenacidade

O comportamento da tenacidade dos compósitos é apresentado na Tabela 6 e Figura 6, quando submetidos ao ensaio de flexão para determinação da resistência à flexão equivalente. Estão apresentadas as curvas dos dois corpos de prova para cada mistura, sendo utilizado os resultados médios para os cálculos.
Após a realização dos ensaios, notou-se que a matriz referência (MR) apresentou um fator de tenacidade nulo, o que já era esperado. Esse resultado foi atingido, uma vez que essa matriz não recebeu reforços e apresentou ruptura frágil devido a sua baixa capacidade de deformação com o acréscimo de tensões durante o ensaio. É perceptível o acréscimo da área sob as curvas após a incorporação de fibras, sendo mais notável este comportamento para as misturas contendo os maiores teores de incorporação. As misturas híbridas (M3, M4, M5 e M6) obtiveram comportamento distinto, sendo que a M6 obteve o maior fator de tenacidade, equivalente a 2,96 MPa. Já a matriz M3 apresentou o menor fator de tenacidade entre as híbridas, todavia o teor de maior eficiência (25,6 kg/m^3.MPa).
Com base nas curvas carga x deslocamento é possível extrair a área sob elas, e calcular o valor da resistência à flexão equivalente, aplicando a formulação da norma Japonesa JSCE – SF4:1984 [28]. A Tabela 6 expressa os resultados obtidos na análise da tenacidade das misturas.
O fator de tenacidade, que relaciona a quantidade de energia absorvida pelo corpo de prova, como nas pesquisas de Banthia et al. [15], Lee, Cho e Choi [40] e Carrillo, Cárdenas Pulido e Aperador [44], demonstrou aumentos gradativos conforme o teor de fibras foi incrementado. Avaliando a melhoria desta propriedade em relação a matriz M1, constata-se aumentos nas proporções de 54,8% para a mistura M2 e 251,8% para a mistura M6, tendenciando a melhoria do desempenho à medida que a matriz recebe maior teor de fibras. Entretanto, percebe-se que as misturas com menores teores de fibras (M1, M2 e M7) obtiveram os melhores aproveitamentos, visto que estas apresentaram eficiência superiores as demais, dado que é necessária uma menor quantidade de fibras por unidade de resistência (MPa).
A mistura M4, a qual apresentou o segundo maior índice de tenacidade, mas a menor eficiência, de 19,4 kg/m^3.MPa, entre o grupo das misturas híbridas. Destaca-se a mistura M3, tendo a maior eficiência da pesquisa. Esse comportamento demonstrou que a mistura M3 apresentou maior eficiência na transferência e absorção de esforços, o que está associado ao seu posicionamento dentro da matriz, propiciando um maior número de fibras que atuam no plano de ruptura e, consequentemente, geram uma melhor distribuição das tensões, como indetificou Gil et al. [45] em sua pesquisa.
Ainda, foi percebido o aumento da tenacidade à medida que o teor de fibras aumentou, como era esperado. A Figura 7 ilustra a correlação entre o fator de tenacidade e o teor de fibras incorporado. É possível perceber um comportamento linear crescente à medida que a concentração de fibras aumenta, apresentando apenas uma descontinuidade da matriz M3 (40 kg/m^3). Observou-se que as fibras espaciais apresentaram melhores índices, porém, ainda inferiores do que as misturas híbridas.

4. Conclusões

Com base nos resultados e discussões apresentadas nesse artigo, foi possível verificar que a adição de fibras espaciais em concretos trouxe melhoras na resistência à tração na flexão e no índice de tenacidade, porém, prejudicaram a trabalhabilidade das misturas e resistência à compressão. A matriz M4, uma mistura hibrida com 30 kg/m^3 de fibras espaciais e 20 kg/m^3 de fibras simples, demonstrou o melhor desempenho geral dentre as matrizes estudadas, denotando a boa compatibilização obtida desta matriz com os teores de fibras, espaciais e simples, empregados na hibridização.

5. Referências bibliográficas

[1] YOO, D.-Y. et al. Effect of fiber orientation on the rate-dependent flexural behavior of ultra-high-performance fiber-reinforced concrete. Composite Structures, v. 157, p. 62–70, 1 dez. 2016.
[2] QUININO, U. C. M. Investigação experimental das propriedades mecânicas de compósitos de concreto com adições híbridas de fibras. 2015. Thesis (Civil Engineering PhD) – Civil Engineering Graduate Program, Universidade Federal do Rio Grande do Sul (UFRGS), Porto Alegre, 2015.
[3] IBRAHIM, M. A. et al. Effect of Material Constituents on Mechanical and Fracture Mechanics Properties of Ultra-High-Performance Concrete. Materials Journal, v. 114, n. 3, p. 453- 465, 2017.
[4] FIGUEIREDO, A. D.; CECCATO, M. R. Workability Analysis of Steel Fiber Reinforced Concrete Using Slump and Ve-Be Test. Materials Research, 18 (2015), n. 6, pp. 1284-1290.

[5] EHRENBRING, H. Z. Comportamento de concreto reforçados com microfibras de polipropileno (PP), álcool polivinílico (PVA) e recicladas de poliéster (POL) em relação à retração por secagem restringida e às propriedades mecânicas. 2017. 165 s. Thesis (Civil Engineering Master's) – Civil Engineering Graduate Program, Universidade do Vale do Rio dos Sinos, São Leopoldo, 2017.
[6] BENTUR, A.; MINDESS, S. Fibre reinforced cementitious composites. 2.Ed., Modern Concrete Technology Series, Taylor&Francis, 2007.
[7] GÜNEYISI, E. et al. Combined effect of steel fiber and metakaolin incorporation on mechanical properties of concrete. Composites Part B: Engineering, v. 56, p. 83–91, 01 Jan. 2014.
[8] WU, Z. et al. Effects of steel fiber content and shape on mechanical properties of ultra high performance concrete. Construction and Building Materials, v. 103, p. 8–14, 30 Jan. 2016.
[9] YOO, D.-Y.; PARK, J.-J.; KIM, S.-W. Fiber pullout behavior of HPFRCC: Effects of matrix strength and fiber type. Composite Structures, v. 174, p. 263–276, 15 Aug. 2017.
[10] PARDINI, L. C. Preformas para compósitos estruturais. Polímeros, v. 10, n. 2, p. 100–109, June. 2000.
[11] RIBEIRO, J. L. P.; GREGORI, M. L.; PARDINI, L. C. Predição das propriedades elásticas de compósitos termoestruturais com reforço multidirecional. Matéria (Rio de Janeiro), v. 13, n. 1, p. 33–48, Mar. 2008.
[12] DU, Y. et al. Experimental study on basalt textile reinforced concrete under uniaxial tensile loading. Construction and Building Materials, v. 138, p. 88–100, 01 May 2017.
[13] WILLIAMS PORTAL, N.; NYHOLM THRANE, L.; LUNDGREN, K. Flexural behaviour of textile reinforced concrete composites: experimental and numerical evaluation. Materials and Structures, v. 50, n. 1, p. 1–14, Aug. 2017.
[14] COLOMBO, I. G. et al. Textile Reinforced Concrete: experimental investigation on design parameters. Materials and Structures, v. 46, n. 11, p. 1933–1951, 2013.
[15] BANTHIA, N. et al. Fiber synergy in Hybrid Fiber Reinforced Concrete (HyFRC) in flexure and direct shear. Cement and Concrete Composites, v. 48, p. 91–97, 01 Apr. 2014.
[16] BANTHIA, N.; SAPPAKITTIPAKORN, M. Toughness enhancement in steel fiber reinforced concrete through fiber hybridization. Cement and Concrete Research, v. 37, n. 9, p. 1366–1372, 01 Sept. 2007.
[17] TUTIKIAN, B. F.; HELENE, P. Dosagem dos concretos de cimento Portland. In: ISAIA, Geraldo Cechella. Concreto: Ciência e Tecnologia. São Paulo: IBRACON, 2011. Ch. 12. P. 415-452.
[18] BOULEKBACHE, B. et al. Flexural behaviour of steel fibre-reinforced concrete under cyclic loading. Construction and Building Materials, v. 126, p. 253–262, 15 Nov. 2016.
[19] AMERICAN SOCIETY FOR TESTING AND MATERIALS. Standard Specification for Portland Cement. C150/C150M, ASTM, Pennsylvania, 2018.
[20] AMERICAN SOCIETY FOR TESTING AND MATERIALS. Standard Test Method for Relative Density (Specific Gravity) and Absorption of Fine Aggregate. C128, ASTM, Pennsylvania, 2015.
[21] AMERICAN SOCIETY FOR TESTING AND MATERIALS. Standard Test Method for Bulk Density ("Unit Weight") and Voids in Aggregate. C29/C29M, ASTM, Pennsylvania, 2017.
[22] AMERICAN SOCIETY FOR TESTING AND MATERIALS. Standard Test Method for Relative Density (Specific Gravity) and Absorption of Coarse Aggregate. C127, ASTM, Pennsylvania, 2015.
[23] AMERICAN SOCIETY FOR TESTING AND MATERIALS. Standard Specification for Concrete Aggregates. C33/C33M, ASTM, Pennsylvania, 2018.
[24] AMERICAN SOCIETY FOR TESTING AND MATERIALS. Standard Test Method for Sieve Analysis of Fine and Coarse Aggregates. C136/C136M, ASTM, Pennsylvania, 2014.
[25] FIGUEIREDO, A. D. Concreto reforçado com fibras. Thesis (habilitation) – Civil Construction Engineering Department, Escola Politécnica de São Paulo, São Paulo, 2011.
[26] ASSOCIAÇÃO BRASILEIRA DE NORMAS TÉCNICAS (ABNT). NBR 15530: Fibras de Aço para concreto. Rio de Janeiro, 2007.
[27] AMERICAN SOCIETY FOR TESTING AND MATERIALS. Standard Practice for Making and Curing Concrete Test Specimens in the Laboratory. C192/C192M, ASTM, Pennsylvania, 2016.
[28] JAPAN SOCIETY OF CIVIL ENGINEERS. Method of tests for flexural strength and flexural toughness of steel fiber reinforced concrete. JSCE-SF4. Concrete Library of JSCE. Part III-2 Method of tests for steel fiber reinforced concrete. № 3 June 1984. p.58-61.
[29] AMERICAN SOCIETY FOR TESTING AND MATERIALS. Standard Test Method for Slump of Hydraulic-Cement Concrete. C143/C143M, ASTM, Pennsylvania, 2015.
[30] AMERICAN CONCRETE INSTITUTE. Guide for Selecting Proportions for No-Slump Concrete (ACI 211.3R-02). ACI Committee 211. Detroit, USA, 2009.
[31] DEPARTAMENTO NACIONAL DE INFRA-ESTRUTURA DE TRANSPORTES. DIRETORIA DE PLANEJAMENTO E PESQUISA. INSTITUTO DE PESQUISAS RODOVIÁRIA. DNIT 064: Pavimento rígido – Determinação da consistência do concreto pelo consistômetro VeBe – Método de ensaio. Rio de Janeiro, 2004.
[32] AMERICAN SOCIETY FOR TESTING AND MATERIALS. Standard Test Method for Compressive Strength of Cylindrical Concrete Specimens. C39/C39M, ASTM, Pennsylvania, 2018.
[33] ABBASS, W.; KHAN, M. I.; MOURAD, S. Evaluation of mechanical properties of steel fiber reinforced concrete with different strengths of concrete. Construction and Building Materials, v. 168, p. 556–569, 2018.
[34] AKCAY, B.; TASDEMIR, M. A. Mechanical behaviour and fibre dispersion of hybrid steel fibre reinforced self-compacting concrete. Construction and Building Materials, v. 28, n. 1, p. 287–293, 2012.
[35] VELASCO, R.V. Concretos auto-adensáveis reforçados com elevadas frações volumétricas de fibras de aço:

propriedades reológicas, físicas, mecânicas e térmicas. Thesis (Civil Engineering PhD) – Civil Engineering Graduate Program, Universidade Federal do Rio de Janeiro, Rio de Janeiro, 2008.

[36] TABATABAEIAN, M. et al. Experimental investigation on effects of hybrid fibers on rheological, mechanical, and durability properties of high-strength SCC. Construction and Building Materials, v. 147, p. 497–509, 2017.

[37] PRATHAP, P.; NARESH KUMAR, T.; NARAYANA, S. M. V. Evaluation of Mechanical Properties of Concrete using Silica fume and Steel fibers. International Journal of Scientific & Engineering Research, v. 8, n. 5, p. 332–338, 2017.

[38] JANG, S. J.; YUN, H. D. Combined effects of steel fiber and coarse aggregate size on the compressive and flexural toughness of high-strength concrete. Composite Structures, v. 185, p. 203–211, 01 Feb. 2018.

[39] KHALOO, A. et al. Mechanical performance of self-compacting concrete reinforced with steel fibers. Construction and Building Materials, v. 51, p. 179–186, 31 Jan. 2014.

[40] LEE, J.-H.; CHO, B.; CHOI, E. Flexural capacity of fiber reinforced concrete with a consideration of concrete strength and fiber content. Construction and Building Materials, v. 138, p. 222–231, 01 May 2017.

[41] PAJĄK, M.; PONIKIEWSKI, T. Flexural behavior of self-compacting concrete reinforced with different types of steel fibers. Construction and Building Materials, v. 47, p. 397–408, 01 Oct. 2013.

[42] EHRENBRING H. Z.; DE MEDEIROS QUININO, U. C.; OLIVEIRA, L. F. S.; TUTIKIAN, B. F. Experimental method for investigating the impact of the addition of polymer fibers on drying shrinkage and cracking of concrete. *Structural Concrete*, 2019; 20 pp. 1064–1075. https://doi.org/10.1002/suco.201800228

[43] PACHECO, F.; CHRIST, R.; GIL, A. M.; TUTIKIAN, B. F. Aplicação de MEV e microtomografia 3D na investigação da distribuição de fibras em compósitos cimentícios avançados. *Rev. IBRACON Estrut. Mater.*, São Paulo, v. 9, n. 6, p. 824-841, Dec. 2016.

[44] CARRILLO, J.; CÁRDENAS PULIDO, J.; APERADOR, W. Flexural mechanical properties of steel fiber reinforced concrete under corrosive environments. Revista Ingeniería de Construcción, v. 32, n. 2, p. 59–72, 2017.

[45] GIL, A. M.; KHAYAT, K. H.; TUTIKIAN, B. F. An experimental approach to design self-consolidating concrete. Construction and Building Materials, v. 229, n. 30, 2019. https://doi.org/10.1016/j.conbuildmat.2019.116939

Volume 13, Number 3 (June 2020) p. 483 – 500 • ISSN 1983-4195
http://dx.doi.org/10.1590/S1983-41952020000300003

REVISTA IBRACON DE ESTRUTURAS E MATERIAIS
IBRACON STRUCTURES AND MATERIALS JOURNAL

Characterization of pervious concrete focusing on non-destructive testing

Caracterização do concreto permeável com foco em ensaios não destrutivos




S. T. MARTINS FILHO [a]
sergiotunis@hotmail.com
https://orcid.org/0000-0002-4334-399X

E. M. BOSQUESI [a]
eduardobosquesi@gmail.com
https://orcid.org/0000-0003-3802-0288

J. R. FABRO [a]
julianofabro@hotmail.com
https://orcid.org/0000-0002-1680-9627

R. PIERALISI [b]
ricpieralisi@ufpr.br
https://orcid.org/0000-0001-8339-5324

Abstract

This study aims to investigate the properties of pervious concrete focusing on characterization tests by the Ultrasound Method. For this, three mixtures were produced with the paste/aggregate (P/Ag) ratio ranging from 0.45 to 0.65, water to cement ratio (w/c) of 0.3, and all the specimens were compacted with a steel rod. The application of the ultrasound method deserves special attention for the characterization of pervious concrete, due to a lack of research and the potential to develop analytical models for predicting properties from ultrasonic pulse velocity (UPV) as an independent variable. The UPV obtained in this study ranged from 3642 to 4262 m/s for an approximately 12% reduction in porosity, with a correlation (R^2) of 0.91. It is noteworthy that the high porosity of pervious concrete causes attenuation of the ultrasonic wave. The measurements of UPV had higher values for specimens with higher densities (R^2=0.87), higher compressive and tensile strengths (R^2 of 0.79 and 0.84, resp.), and lower permeability (R^2 = 0.91).

Keywords: pervious concrete, ultrasound method, porosity, permeability, compressive strength.

Resumo

Neste estudo, objetiva-se investigar as propriedades do concreto permeável com foco nos ensaios de caracterização pelo Método do Ultrassom. Para isso, foram produzidos três traços com a relação pasta/agregado variando de 0,45 a 0,65, relação a/c de 0,3 e compactados por haste. A aplicação do Método do Ultrassom merece atenção especial para caracterização do concreto permeável, com carência de pesquisas e com potencial de desenvolver modelos analíticos de previsão das propriedades a partir da velocidade de pulsos ultrassônicos (VPU) como uma variável independente. A VPU variou de 3642 até 4262 m/s para uma redução de aproximadamente 12% na porosidade, com alta correlação (R^2) de 0,91 e destaca-se que a alta porosidade do concreto provoca atenuação da onda ultrassônica. As medições da VPU retrataram valores maiores para os CPs com maiores densidades (R^2=0,87), maiores resistências à compressão e à tração (R^2 de 0,79 e 0,84, resp.), e menores permeabilidades (R^2=0,91).

Palavras-chave: concreto permeável, método do ultrassom, porosidade, permeabildiade, resistência à compressão.

[a] *Universidade Tecnológica Federal do Paraná, Coordenação de Engenharia Civil, Apucarana, PR, Brasil;*
[b] *Universidade Federal do Paraná, Centro de Estudos de Engenharia Civil, Programa de Pós-Graduação em Engenharia de Construção Civil, Curitiba, PR, Brasil.*

Received: 05 Aug 2019 • Accepted: 10 Dec 2019 • Available Online: 26 May 2020

1. Introduction

Currently, pervious concrete is used in pavement construction in urban areas, as a way to minimize the impacts caused by conventional impermeable paving. During heavy rainfall, impervious paving contributes to increased runoff of surface waters and potential for sudden flooding [1, 2], and is an effective way to meet growing environmental demands.
Permeability is an intrinsic property of pervious concrete that allows fluid (water) to pass through its matrix [3]. This feature is attributed to the fact that pervious concrete has a network of interconnected macropores that form channels that allow water to drain. Moreover, permeability may be used as a drainage device in retaining walls [4].
Also, pervious concrete is used to reduce the formation of heat islands in cities [5], and helps as a sound barrier, absorbing noise caused by the interaction between tire and pavement [6]. However, pervious concrete is generally used for low traffic demand pavements, since its high porosity decreases its compressive strength [5, 7, 8].
Allied to the environmental aspects, the technical characteristics of pervious concrete arouse an increasing interest for its use in sustainable construction, being promoted by building certification systems (such as the Green Building Council's LEED [1]). Pervious concrete may contribute to some categories in LEED certification, namely: Sustainable Sites; Water efficiency; Materials and Resources; and Design Innovation [9].
In order to optimize the percentage of interconnected pores relative to the total element volume, the traditional mix design philosophies for pervious concrete [10] suggest that the composition is formed by coarse aggregates, a minimal amount of fine aggregates (or, even, no fine aggregates), and cement paste volume sufficient to involve the coarse aggregates. Due to this proportion of materials, pervious concrete has a dry consistency with a slump close to zero [10-12].

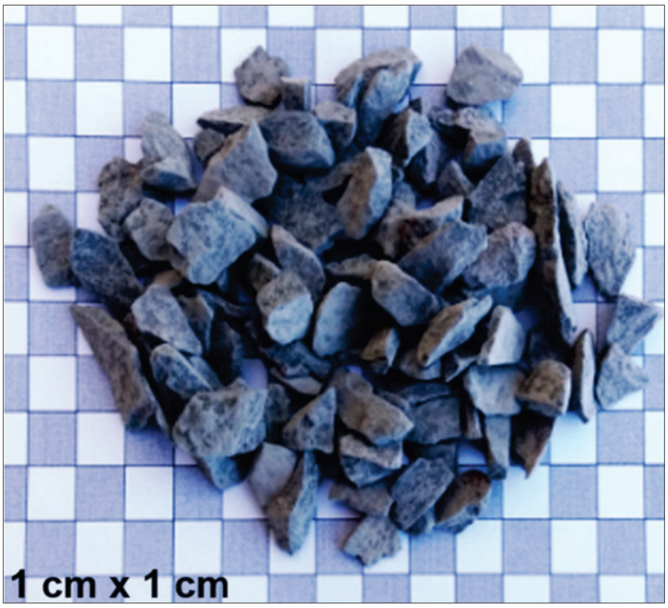

Figure 1
Surface aspect of the particle size fraction: range 6.3 to 9.5 mm

The porosity of pervious concrete is a relevant factor in its performance and is related to other properties, such as permeability [12-14]. It is noteworthy that, currently, there is no guideline that regulates the test procedure for the characterization of permeability of pervious concrete in the laboratory. However, for some researchers [12, 15-19], the permeability test may be performed with constant-head permeameter for specimens with high porosity and high permeability. On the other hand, other authors [20-23] perform the test using falling-head permeameter, regardless of the porosity level of the specimens.
In this sense, mix design philosophies of pervious concrete are limited. There is no consolidated and universally accepted theoretical knowledge that relates the mix proportion of the materials and the consolidation process to the hardened properties of the pervious concrete [24]. Moreover, according to ACI 522R-10 [10] pervious concrete mix design has an empirical component based on the experiments already performed. In the usual applications among researchers, it is noted mass mixtures ranging from 1:2 to 1:12, with cement consumption ranging from 150 to 700 kg/m³ and w/c ratio from 0.2 to 0.5, which conduct to porosities up to 42% and permeability up to 33 mm/s [2].
The first published guidelines for pervious concrete were: PCP manual [1]; and ACI 522R-10 [10]. Both address technical aspects of the material, the constituents, simplified mix design methods, and characterization tests.
In recent years, the American Society for Testing and Materials (ASTM) has released a collection of standards for pervious concrete characterization: ASTM C1754 [25], to determine the density and void content of pervious concrete in the hardened state; ASMT C1747 [26], to determine the degradation resistance of impact and abrasion pervious concrete; ASTM C1688 [27], to determine the density and void content of fresh pervious concrete; ASTM C1701 [28], to determine the permeability of pervious concrete. Recently, the Brazilian Association of Technical Standards (ABNT) also published a standard on pervious concrete, ABNT NBR 16416 [29], which deals with pervious pavement requirements, focusing on interlocking blocks and the *in situ* permeability characterization test. Although there are standards related to properties characterization of pervious concrete, there are no in-depth standards nor guidelines in the literature on the use of non-destructive tests for indirect characterization of pervious concrete.
The Ultrasound Method is a relevant non-destructive test for the characterization and investigation of conventional concrete [30, 47]. Regarding pervious concrete, there is a little research about this topic, which opens the possibility of developing prediction equations that can help in determining its properties.
The use of an ultrasound test allows the characterization of concrete, detecting flaws, and monitoring its state of deterioration, in addition to estimate its mechanical properties. Generally, the frequency of the transducers used in the tests ranges from 25 to 100 kHz and the ultrasonic pulse velocity (UPV) for conventional concrete is different depending on the mix constitution, its proportion, and the physical characteristics of the aggregates [31]. The

Table 1
Dimensions and shape index of the particle size range

Particle size (mm)	Length (l)	Width (w)	Thickness (t)	Shape index (SI)	Sphericity (standard deviation)	Unit mass (kg / m³) (standard deviation)	Voids index
	Average (mm) (standard deviation)						
6.3 - 9.5	15.96 (2.92)	10.08 (1.58)	5.09 (1.64)	3.29 (1.03)	0.59 (0.09)	1,374.01 (2.35)	0.544

standard for determining ultrasonic pulse velocity (UPV) in concrete follow ASTM C 597 [32]
Because pervious concrete has a high level of porosity, it causes attenuation of the ultrasonic wave. This characteristic leads to an amplification factor between 50 and 60 dB [33] in order to measure the UPV. In the literature [34, 35] was found that for a higher pervious concrete density, lower porosity and higher compressive strength, the greater the UPV. Also, the authors [34, 35] highlighted the feasibility of using the ultrasound method to perform periodic evaluations on pervious concrete pavements, preserving it from the need for core extraction. From the current state of the art, this paper aims to investigate the properties of pervious concrete focusing on characterization tests by the ultrasound method.

2. Materials and methods

2.1 Materials

The coarse aggregate was obtained by a sieving process from a granular set of basaltic origin acquired in a quarry located in the region of Apucarana/PR (Brazil). The sieving process followed the recommendations of ABNT NBR NM 248 [36]. The result was the particle size fraction between 6.3 and 9.5 mm. Figure 1 shows the superficial aspect of coarse aggregates.
The obtained particle size fraction was characterized by the following tests: Unit mass, ABNT NBR NM 45 [37]; Shape Index (SI), ABNT NBR 7809 [38]; and Zingg Method [39]. In this sense, three measurements (length, width, and thickness) of 200 aggregates, random selected, were made. Table 1 shows the physical characteristics of the aggregates.
According to the Zinng classification [39], obtained by the values of elongation (ratio between thickness and width) and flatness (ratio between width and length) of the aggregates, the predominant aspect of the aggregates is lamellar elongation. The aggregate classification is important for the understanding of the properties of pervious concrete, which its physical characteristics influence in the compaction process, adversely affecting the contact area between the aggregates and thus leading to different densities and strength [10, 40, 44].
The material compositions used were defined in order to emulate typical dosages found in pervious concrete applications. According to the literature recommendations [17, 22, 40-42], the aggregates with uniform diameter were selected. The value of Paste/Aggregate (P/Ag) ratios was defined in order to obtain pervious concretes with porosity and permeability compatible with the practical application.
Table 2 shows the 3 mix composition defined in this study. The P/Ag volume ranged from 0.45 to 0.65, assigning the nomenclature to the three mixture of T0.45, T0.55, and T0.65. The particle size range used was uniform, with diameters between 6.3 and 9.5 mm, the water/cement ratio (w/c) was constant for all compositions, and the Portland Cement CP II-Z regulated by ABNT NBR 16697 [43] was used.
The pervious concrete mixing process followed the recommendations of SCHAEFER et al. [44]. After concrete preparation, a visual inspection was performed and it was found that the w/c ratio used to lead to the aggregates entirely covered with paste and in the consolidation process the paste did not segregate, following the recommendations of TENNIS et al. [1]. The consolidation process was performed by throwing the concrete into the cylindrical mold in three layers, each layer was compacted with 25 blows with a steel rod, following the rules of ABNT NBR 45 [37]. In total, 36 cylindrical specimens (100 mm in diameter and 200 mm in height) were produced.

2.2 Methods

All the specimens had their density and porosity in the fresh and hardened state, permeability, compressive and tensile strength, and UPV characterized. The density and porosity in the fresh state were obtained using the procedure described by ASTM C1688 [27]. The procedures proposed by ASTM C1754 [25] were used to calculate the density and porosity in the hardened state.
The permeability of pervious concrete was obtained through the constant-head permeameter, which is recommended in the

Table 2
Mixture proportion of the pervious concrete: the first experimental campaign

Mixture	P/Ag ratio by mass	Aggregate consumption (kg/m³)	Cement consumption (kg/m³)	Mixture by mass		
				Cement	Aggregate	w/c
T0.45	0.45	1,305.91	452.26	1	2.9	0.3
T0.55	0.55	1,306.85	553.35	1	2.4	0.3
T0.65	0.65	1,218.81	609.40	1	2.0	0.3

(a) (b) (c)

Figure 2
Process for mounting the permeability test

Figure 3
Ultrasound test: reading by direct longitudinal transmission

literature [12,15-19]. Figure 2 shows the constant-head permeameter developed for the test. The permeability results presented in this study were calculated with a hydraulic load of 30 cm.

Once the specimen was coupled with the apparatus, the opening of the bottom tube was closed. Next, the volume of water necessary to fill the bottom tube and the pore spaces of the specimen was measured (q_1). Then, the apparatus was completely filled with water and the bottom tube was opened. Finally, the volume of water that passed through the specimen in 60 s was measured (q_2).

The permeability (k) was estimated using Darcy's Law according to Equation 1. In this equation q is the difference between both measured volumes of water (q_2 - q_1), h is the heigth specimen (L_s) plus the hydraulic load (30 cm), and t is time interval (60 s).

$$k = \frac{4.q.L_s}{\pi.\emptyset_s^2.h.t} \tag{1}$$

The compressive strength was determined according to ABNT NBR 5739 [45]. The bottom and top surfaces of the specimens were regularized with plaster. The tensile strength was determined by diametric compression according to the recommendations of ABNT NBR 7222 [46].

The Ultrasonic Pulse Velocity (UPV) was determined using the PROCEQ/Pundit Lab ultrasound device, following the procedures established in ASTM C597 [32]. The ultrasound measurement was performed in the longitudinal direction (around 20 cm) of the specimens, with an ultrasonic wave vibration frequency of 24 kHz and a receiver amplification factor of 500 (which corresponds to 54 dB). The test setup consisted of two plates with holes to support the ultrasound transducers for direct measurement, this ensured that the transducers were concentric to the specimen (see Figure 3). According to Chandrappa and Biligiri [34], it is required to apply a thick layer of gel on the top and bottom surfaces of the specimen where the transducers are placed. Finally, the average of three measurements was used as a single UPV value.

Table 3
Properties of pervious concrete

Mixture	Fresh state density (kg/m^3)	Hardened state density (kg/m^3)	Total porosity (%)	Compressive strength (MPa)	Tensile strength (MPa)	Permeability height 30 cm (mm/s)	UPV (m/s)
T0.45	1,914.85 (23.48)	1,893.84 (23.71)	28.44 (1.05)	7.77 (0.46)	1.49 (0.20)	8.31 (0.77)	3,719.79 (48.91)
T0.55	2,046.04 (32.80)	2,026.20 (32.41)	20.97 (1.62)	10.65 (1.07)	2.36 (0.34)	2.37 (0.99)	4,063.50 (73.28)
T0.65	2,035.27 (42.38)	2,004.08 (42.21)	20.93 (2.14)	11.73 (1.72)	2.33 (0.41)	3.15 (0.82)	4,163.00 (97.70)

3. Results e discussions

Table 3 shows the average and standard deviations (in parenthesis below average) of density (fresh and hardened states), porosity, compressive strength, tensile strength, permeability, and UPV value. From the data obtained in the characterization by the ultrasound method, some correlations can be made in order to understand the behavior of pervious concrete using a nondestructive method.

Figure 4a shows the relation between UPV and total porosity, notice that the UPV increases as porosity decreases. This behavior is expected because the voids cause attenuation of the ultrasonic wave velocity. Besides, mixtures with a higher P/Ag ratio lead to a low level of porosities, which increase the possibility of the wave to find shorter paths for its propagation and increase the UPV value. Equation 2 presents the relation to obtain total porosity (P) through the independent variables UPV and P/Ag ratio.

$$P = 105.7576 + 11.8586 \cdot P/Ag - 0.022308 \cdot UPV \quad (2)$$

Figure 4b presents a comparison between the average experimental and estimated porosity for all specimens, including an equivalence line. Results reveal a relative prediction error of the estimation is 0,24%, and a coefficient of correlation (R2) of 0.91.

Figure 5a shows the relation between UPV and density at the hardened state. The observed behavior is the opposite of the relation between UPV and Porosity, which means that samples with higher densities (or lower porosities) conduct to higher values of UPV. Equation 3 presents the relation to obtaining density at the hardened state (DE) through the independent variables UPV and P/Ag.

$$DE = 413,28 - 457,86 \cdot P/Ag + 0.45534 \cdot UPV \quad (3)$$

Figure 5b presents a comparison between the average experimental and estimated densities for all specimens, including an equivalence line. Results reveal a relative prediction error of the estimation is 0,01%, and a coefficient of correlation (R2) of 0.87.

Figure 6a presents the comparison between the permeability (k) depending on UPV value. It is observed that specimens with higher

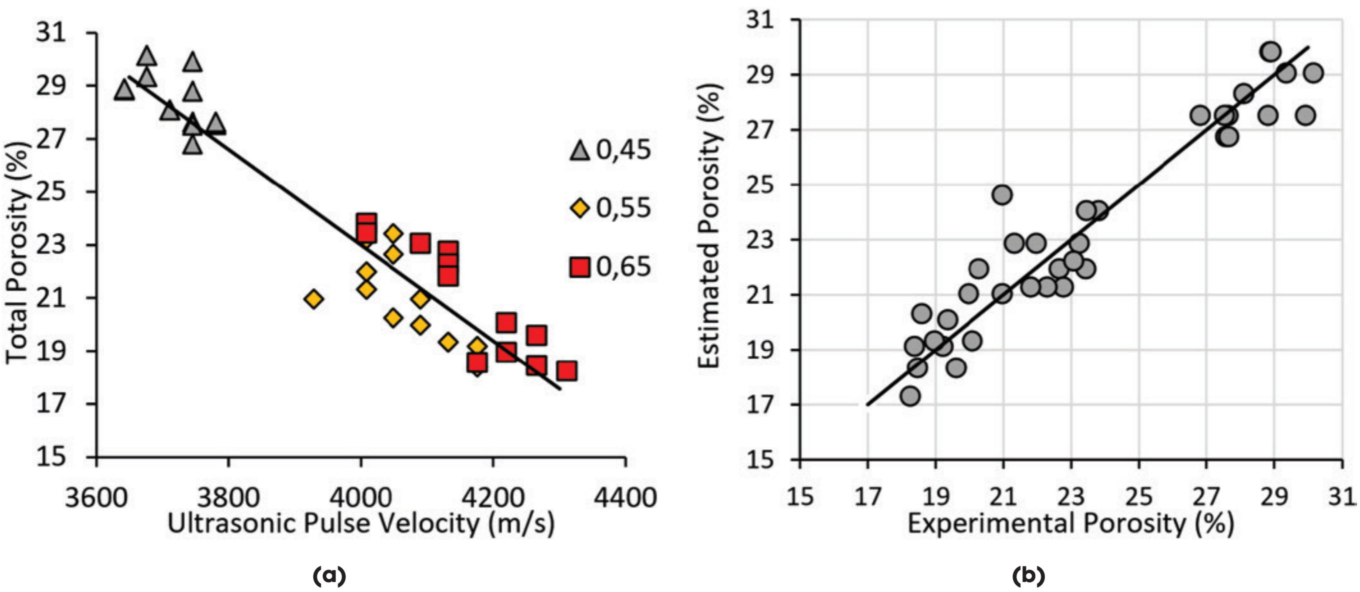

Figure 4
Relation between total porosity and ultrasonic pulse velocity (a) and validation of experimental and estimated data (b)

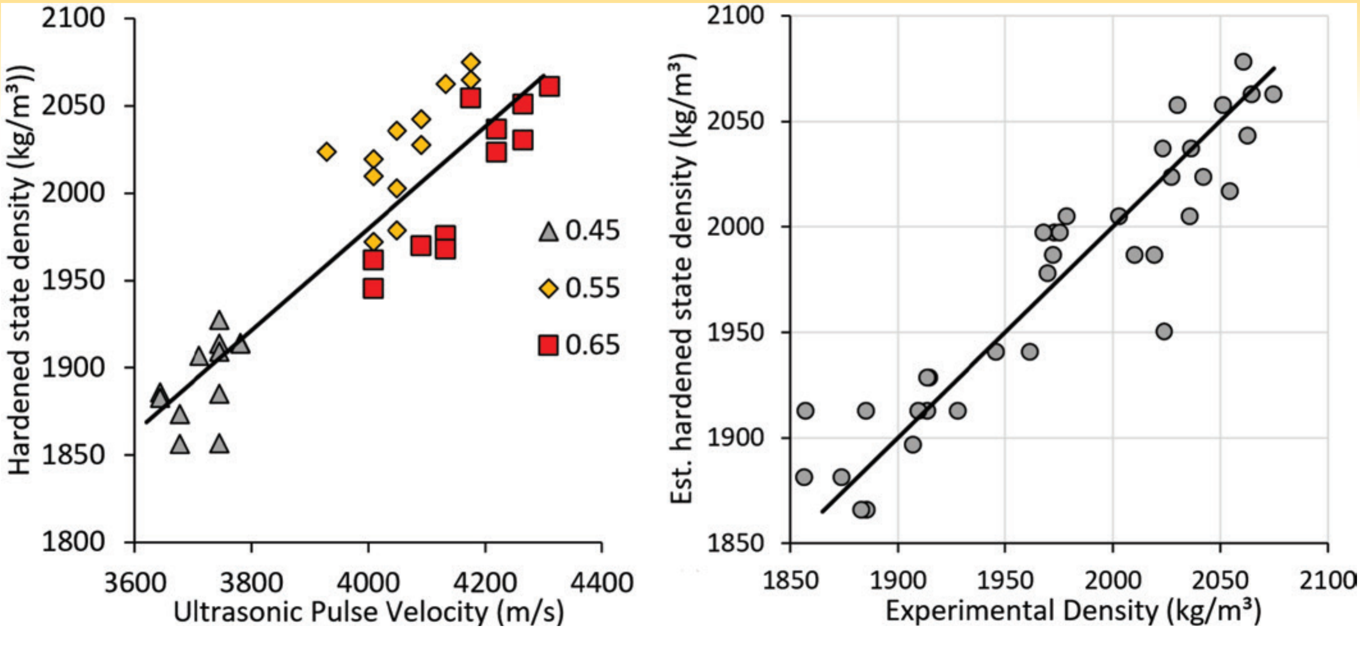

(a)

(b)

Figure 5
Hardened state density and ultrasonic pulse velocity (a) and validation of experimental and estimated data (b)

permeability lead to a lower value of UPV, which is related to higher porosities. This sheds light on the possibility of estimate the permeability of the pervious concrete with nondestructive tests. It is possible to estimate permeability (k) through the independent variables UPV and P/Ag ratio by Equation 4.

$$k = 65.842 + 10.089 \cdot P/Ag - 0.01677 \cdot UPV \quad (4)$$

Figure 6b presents a comparison between the average experimental and estimated permeability for all specimens, including an equivalence line. Results reveal a relative prediction error of the estimation is 5,06%, and a coefficient of correlation (R2) of 0.91.
Figure 7 shows the comparison between compressive and tensile strengths depending on the UPV. This correlation provides an estimation of these properties without the need for destructive tests.

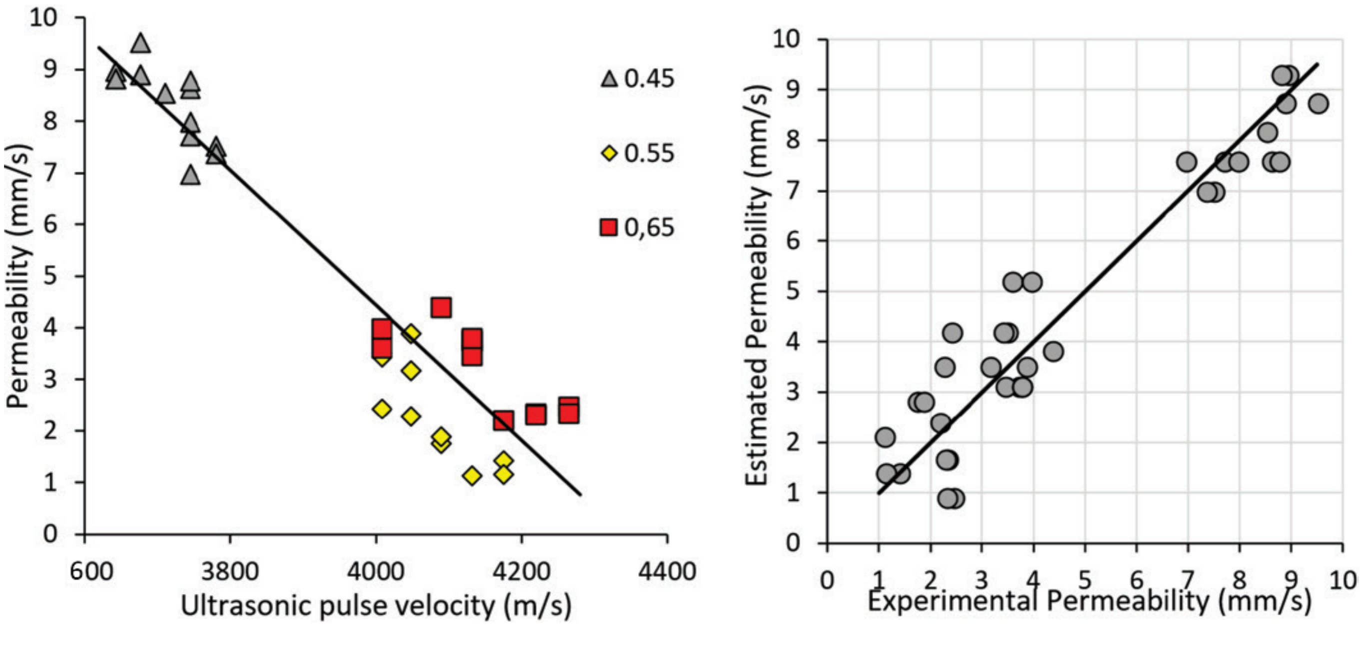

(a)

(b)

Figure 6
Relation between permeability and ultrasonic pulse velocity (a) and validation of experimental and estimated data (b)

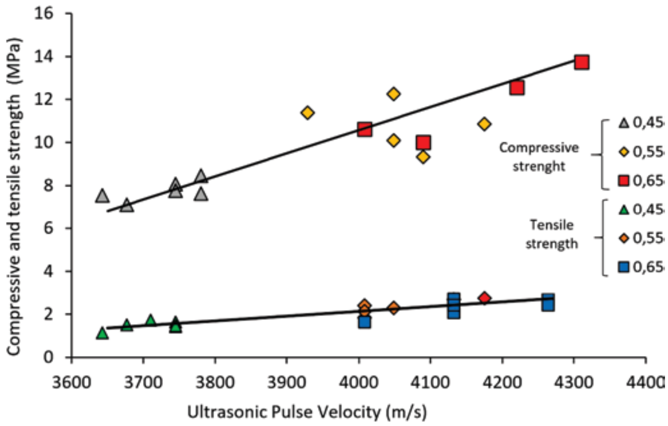

Figure 7
Relation between compressive strength and tensile strength with ultrasonic pulse velocity for three volumes P/Ag

Equations 5 and 6 present the relations to obtain the compressive and tensile strength, respectively, through the independent variables UPV and P/Ag ratio.
Figure 8 presents a comparison between the average experimental and estimated compressive and tensile strength for all specimens, including an equivalence line. Results reveal relative prediction errors of the estimations are 0,63% and 0,81%, and coefficients of correlations (R^2) of 0.79 and 0.84 for compressive and tensile strength, respectively.

$$\sigma_C = -18.56 + 6.418 \cdot P/Ag + 0.006297 \cdot UPV \quad (5)$$

$$\sigma_T = -9.4996 - 3.237 \cdot P/Ag + 0.003354 \cdot UPV \quad (6)$$

It is worth highlighting a particular characteristic of pervious concrete concerning its rupture, in which predominantly it was the coarse aggregates that failed and not the P/Ag bonding layer, a behavior also observed by other authors [21].
The correlations presented suggest the potential that the application of nondestructive tests has to characterize pervious concrete, avoiding the need for core extraction and allowing to establish correlations with its properties. Thus, deeper studies are required to verify the influence of the pervious concrete constituent materials on the UPV. It is emphasized that all presented equations are only compatible with the materials used in this research. So, concretes produced with materials of different physical and chemical characteristics need to be tested and validated for the presented equations.

4. Conclusions

The application of the ultrasound method deserves special attention for the characterization of pervious concrete, due to the potential to develop analytical models for predicting properties from UPV. Ultrasonic pulse velocity results were between 3642 and 4262 m/s for a variation of approximately 12% in porosity. Specimens with higher permeability presented higher porosity which leads to a higher value of UPV because the voids cause attenuation of the ultrasonic wave velocity. Moreover, the mechanical properties (compressive and tensile strengths) are inversely proportional to the UPV. With the UPV values of all mixtures, multivariable linear regressions were performed to estimate the properties of the pervious concrete, obtaining a high correlation coefficient, as follows: 0.91 (Porosity); 0.87 (Density); 0.91 (permeability); 0.79 and 0.84 (Compressive and tensile strength, respectively).

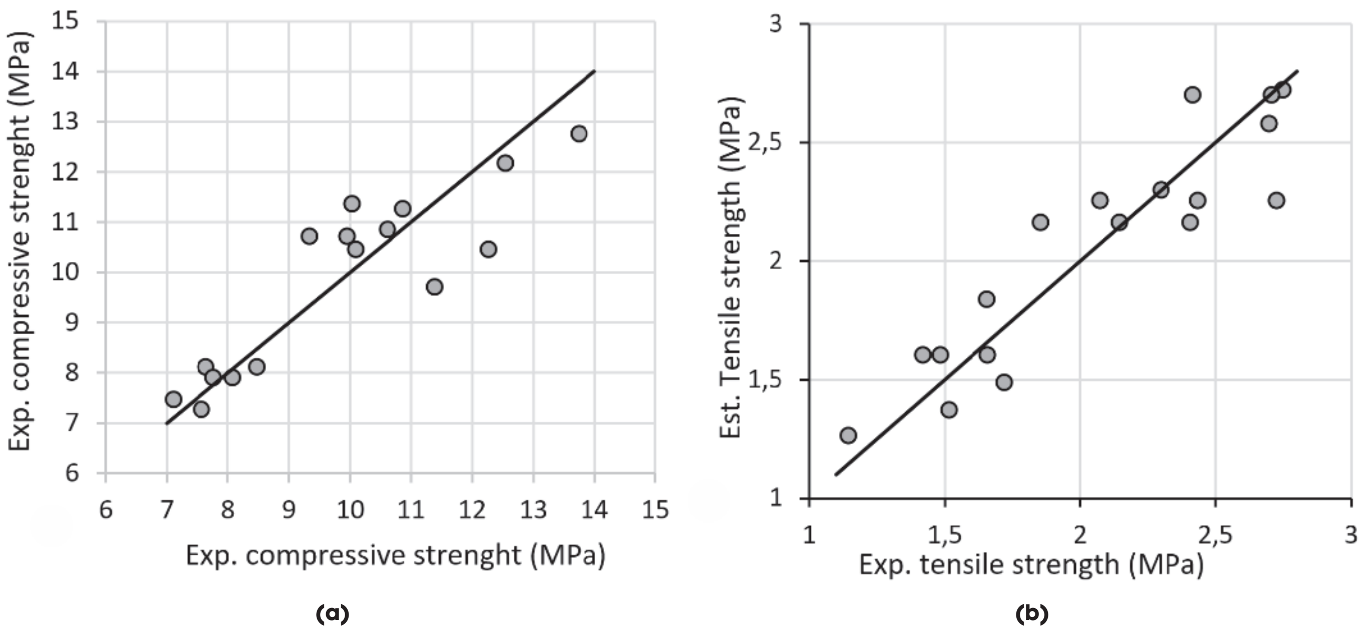

Figure 8
Validation of compressive (a) and tensile (b) strength, estimated and experimental

5. Acknowledgment

The authors thank the Postgraduate Program in Civil Construction Engineering (PPGECC) at the Federal University of Paraná (UFPR) and the Department of Civil Engineering of UTFPR / Apucarana.

6. Bibliographic references

[1] TENNIS, P. D.; LEMING, M. L.; AKERS, D. J. Pervious concrete pavements. Technical report, EB302.02. Portland Cement Association, Skokie, Illinois, and National Ready Mixed Concrete Association, Silver Spring, Maryland, 32p, 2004.

[2] KIA, A.; WONG, H. S.; CHEESEMAN, C.R. Clogging in permeable concrete: A review. Journal of Environmental Management, v.193, p. 221-233, 2017.

[3] CAPUTO, H.P. Mecânica dos Solos e suas Aplicações-Fundamentos, v. 1, 234p, Rio de Janeiro, 1988.

[4] OSPINA, C. M. M.; ERAZO, C. H. B. Resistencia mecánica y condiciones de obra del concreto poroso en los pavimentos según el tipo de granulometría. Medellín, 2007.

[5] FERGUSON, B. K. Porous pavements, Boca Raton: CRC Press, London, 577p, 2005.

[6] KIM, H. K.; LEE, H. K. Influence of cement flow and aggregate type on the mechanical and acoustic characteristics of porous concrete. Applied Acoustics, v. 71, p. 607-615, 2010.

[7] HAGER, A. S. Sustainable Design of Pervious Concrete Pavements. PhD Dissertation, University of Colorado Denver, Department of Civil Engineering, Denver, CO, 2009.

[8] SABNIS G.M. Green building with concrete. Sustainable design and construction, 1nEd. Boca Raton, 320p, 2012.

[9] ASHLEY, E. Using Pervious Concrete to Achieve LEED Points. Concrete Infocus. National Ready Mixed Concrete Association, Silver Spring, MD, p. 1-6, 2008.

[10] AMERICAN CONCRETE INSTITUTE (ACI), 2010. Report on Pervious Concrete. ACI Committee 522. Report number: ACI 522R-10.

[11] NEITHALATH N.; DEO, O. Compressive response of pervious concretes proportioned for desired porosities. Construction and Building Materials, v. 25, p. 4181–4189, 2011.

[12] PIERALISI, R.; CAVALARO, S.H.P.; AGUADO. A Advanced numerical assessment of the permeability of pervious concrete. Cement and Concrete Research, v. 102, p. 149-160, 2017.

[13] MEININGER, R. C. No-Fines Pervious Concrete for Paving. Concrete International, v.10, p. 20-27, 1988.

[14] GHAFOORI, N.; DUTTA, S. Laboratory Investigation of Compacted No-Fines Concrete for Paving Materials. Journal of Materials in Civil Engineering, v. 7, n. 3, p. 183–191, 1995a.

[15] THO-IN, T.; SATA, V.; CHINDAPRASIRT, P.; JATURAPITAKKUL, C. Pervious highcalcium fly ash geopolymer concrete. Construction and Building Materials, v. 30, p. 366-371, 2012.

[16] SATA, V.; WONGSA, A.; CHINDAPRASIRT, P. Properties of pervious geopolymer concrete using recycled aggregates. Construction and Building Materials, v. 42, p. 33–39, 2013.

[17] ZAETANG, Y.; WONGSA, A.; SATA, V.; CHINDAPRASIRT, P. Use of lightweight aggregates in pervious concrete. Construction and Building Materials, v. 48, p. 585–591, 2013.

[18] BHUTTA, M. A. R.; HASANAH, N.; FARHAYU, N.; HUSSIN, M. W.; TAHIR, M. B. M.; MIRZA, J. Properties of porous concrete from waste crushed concrete (recycled aggregate). Construction and Building Materials, v. 47, p. 1243-1248, 2013.

[19] KUO, W. T.; LIU, C. C.; SU, D. S. Use of washed municipal solid waste incinerator bottom ash in pervious concrete. Cement and Concrete Composites, v.37, p. 328–335, 2013.

[20] NEITHALATH, N.; SUMANASOORIYA, M. S.; DEO, O. Characterizing pore volume, sizes, and connectivity in pervious concretes for permeability prediction. Materials Characterization, v. 61, p. 802-813, 2010.

[21] YAHIA, A.; KABAGIRE, D. New approach to proportion pervious concrete. Construction and Building Materials, v. 62, p. 38–46, 2014.

[22] NGUYEN, D. H.; SEBAIBI, N.; BOUTOUIL. M.; LELEYTER, L.; BARAUD, F. A modified method for the design of pervious concrete mix. Construction and Building Materials, v. 73, p. 271–282, 2014.

[23] COSTA, F. B. P.; LORENZI, A.; HASELBACH, L.; SILVA FILHO, L. C. P. Best practices for pervious concrete mix design and laboratory tests. REVISTA IBRACON DE ESTRUTURAS E MATERIAIS, v. 11, n. 5, p. 1151-1159, 2018.

[24] CAVALARO, S. H. P.; BLANCO, A.; PIERALISI, R. Holistic modelling approach for special concrete: from fresh-to hardened-state. RILEM Technical Letters, v. 3. p. 84-90, 2018.

[25] AMERICAN SOCIETY FOR TESTING AND MATERIALS.. ASTM C1754 / C1754M, Standard Test Method for Density and Void Content of Hardened Pervious Concrete, ASTM International, West Conshohocken, PA, 2012.

[26] AMERICAN SOCIETY FOR TESTING AND MATERIALS. ASTM C1747 / C1747M, Standard Test Method for Determining Potential Resistance to Degradation of Pervious Concrete by Impact and Abrasion, ASTM International, West Conshohocken, PA, 2013.

[27] AMERICAN SOCIETY FOR TESTING AND MATERIALS. ASTM C1688 / C1688M, Standard Test Method for Density and Void Content of Freshly Mixed Pervious Concrete, ASTM International, West Conshohocken, PA, 2014.

[28] AMERICAN SOCIETY FOR TESTING AND MATERIALS...ASTM C1701 / C1701M, Standard Test Method for Infiltration Rate of In Place Pervious Concrete, ASTM International, West Conshohocken, PA, 2017.

[29] ASSOCIAÇÃO BRASILEIRA DE NORMAS TÉCNICAS. NBR 16416: Pavimentos permeáveis de concreto - Requisitos e procedimentos, Rio de Janeiro, 2015.

[30] OHDAIRA, E.; MASUZAWA, N. Water content and its effect on ultrasound propagation in concrete —the possibility of NDE. Ultrasonics, v. 38, p. 546-552, 2000.

[31] MALHOTRA, V.M., N. J. E. CARINO, N. J. E. Handbook of Nondestructive Testing of Concrete, CRC Press, Boca Raton, FL, USA, 2nd edition, 2004.

[32] AMERICAN SOCIETY FOR TESTING AND MATERIALS.

ASTM C597, Pulse velocity through concrete, ASTM International, West Conshohocken, PA, 1989.
[33] CHANDRAPPA, A. K.; BILIGIRI, K. P. Investigations on Pervious Concrete Properties Using Ultrasonic Wave Applications. Journal of Testing and Evaluation, v. 45, n.5, p.1736-1749, 2017.
[34] CHANDRAPPA, A. K.; BILIGIRI, K. P. Influence of mix parameters on pore properties and modulus of pervious concrete: an application of ultrasonic pulse velocity. Materials and Structures, v. 49, p. 5255-5271, 2016c.
[35] AMINI, K.; WANG, X.; DELATTE, N. Statistical Modeling of Hydraulic and Mechanical Properties of Pervious Concrete Using Nondestructive Tests. Journal of Materials in Civil Engineering, v. 30, n. 6, p. 1-8, 2018.
[36] ASSOCIAÇÃO BRASILEIRA DE NORMAS TÉCNICAS. NBR NM 248: Agregados -Determinação da composição granulométrica, Rio de Janeiro, 2003.
[37] ASSOCIAÇÃO BRASILEIRA DE NORMAS TÉCNICAS. NBR NM 45: Agregados – Determinação da massa unitária e do volume de vazios. Rio de Janeiro, 2006.
[38] ASSOCIAÇÃO BRASILEIRA DE NORMAS TÉCNICAS.. NBR 7809: Agregado graúdo - Determinação do índice de forma pelo método do paquímetro - Método de ensaio, Rio de Janeiro, 2006.
[39] ZINGG, T. Beiträg zur schotteanalysis. Diss.-Druckerei A.-O. Gebr. Leemann & Co., 107p., 1935.
[40] LIAN, C.; ZHUGE, Y. Optimum mix design of enhanced permeable concrete – An experimental investigation. Journal of Environmental Management, v.193, p. 221-233, 2017.
[41] LIM, E.; TWAN, K. H.; FWA, T. F. Effect of mix proportion on strength and permeability of pervious concrete for use in pavement. Journal of the Eastern Asia Society for Transportation Studies, v. 9, p. 1565-1575, 2013.
[42] IBRAHIM, A.; MAHMOUD, E.; YAMIN, M.; PATIBANDLA, V. C. Experimental study on Portland cement pervious concrete mechanical and hydrological properties, Construction and Building Materials, v. 50, p. 524–529, 2014.
[43] ASSOCIAÇÃO BRASILEIRA DE NORMAS TÉCNICAS. NBR 16697: Cimento Portland- Requisitos, Rio de Janeiro, 2018.
[44] SCHAEFER, V.; WANG, K.; SULEIMAN, M.; KEVERN, J. Mix design development for pervious concrete in cold weather climates. National Concrete Pavement Technology Center, 83p, 2006.
[45] ASSOCIAÇÃO BRASILEIRA DE NORMAS TÉCNICAS. NBR 5739: Concreto - Ensaio de compressão de corpos de prova cilíndricos, Rio de Janeiro, 1994.
[46] ASSOCIAÇÃO BRASILEIRA DE NORMAS TÉCNICAS. NBR 7222: Concreto e argamassa - Determinação da resistência à tração por compressão diametral de corpos de prova cilíndricos, Rio de Janeiro, 2011.
[47] CARRIÓN, A.; GENOVÉS, V.; GOSÁLBEZ, J.; MIRALLES, R.; PAYÁ, J. Ultrasonic signal modality: A novel approach for concrete damage evaluation. Cement and Concrete Research, v. 101, p. 25-32, 2017.

Volume 13, Number 3 (June 2020) p. 483 – 500 • ISSN 1983-4195
http://dx.doi.org/10.1590/S1983-41952020000300003

REVISTA IBRACON DE ESTRUTURAS E MATERIAIS
IBRACON STRUCTURES AND MATERIALS JOURNAL

Characterization of pervious concrete focusing on non-destructive testing

Caracterização do concreto permeável com foco em ensaios não destrutivos




S. T. MARTINS FILHO [a]
sergiotunis@hotmail.com
https://orcid.org/0000-0002-4334-399X

E. M. BOSQUESI [a]
eduardobosquesi@gmail.com
https://orcid.org/0000-0003-3802-0288

J. R. FABRO [a]
julianofabro@hotmail.com
https://orcid.org/0000-0002-1680-9627

R. PIERALISI [b]
ricpieralisi@ufpr.br
https://orcid.org/0000-0001-8339-5324

Abstract

This study aims to investigate the properties of pervious concrete focusing on characterization tests by the Ultrasound Method. For this, three mixtures were produced with the paste/aggregate (P/Ag) ratio ranging from 0.45 to 0.65, water to cement ratio (w/c) of 0.3, and all the specimens were compacted with a steel rod. The application of the ultrasound method deserves special attention for the characterization of pervious concrete, due to a lack of research and the potential to develop analytical models for predicting properties from ultrasonic pulse velocity (UPV) as an independent variable. The UPV obtained in this study ranged from 3642 to 4262 m/s for an approximately 12% reduction in porosity, with a correlation (R^2) of 0.91. It is noteworthy that the high porosity of pervious concrete causes attenuation of the ultrasonic wave. The measurements of UPV had higher values for specimens with higher densities (R^2=0.87), higher compressive and tensile strengths (R^2 of 0.79 and 0.84, resp.), and lower permeability (R^2 = 0.91).

Keywords: pervious concrete, ultrasound method, porosity, permeability, compressive strength.

Resumo

Neste estudo, objetiva-se investigar as propriedades do concreto permeável com foco nos ensaios de caracterização pelo Método do Ultrassom. Para isso, foram produzidos três traços com a relação pasta/agregado variando de 0,45 a 0,65, relação a/c de 0,3 e compactados por haste. A aplicação do Método do Ultrassom merece atenção especial para caracterização do concreto permeável, com carência de pesquisas e com potencial de desenvolver modelos analíticos de previsão das propriedades a partir da velocidade de pulsos ultrassônicos (VPU) como uma variável independente. A VPU variou de 3642 até 4262 m/s para uma redução de aproximadamente 12% na porosidade, com alta correlação (R^2) de 0,91 e destaca-se que a alta porosidade do concreto provoca atenuação da onda ultrassônica. As medições da VPU retrataram valores maiores para os CPs com maiores densidades (R^2=0,87), maiores resistências à compressão e à tração (R^2 de 0,79 e 0,84, resp.), e menores permeabilidades (R^2=0,91).

Palavras-chave: concreto permeável, método do ultrassom, porosidade, permeabildiade, resistência à compressão.

[a] *Universidade Tecnológica Federal do Paraná, Coordenação de Engenharia Civil, Apucarana, PR, Brasil;*
[b] *Universidade Federal do Paraná, Centro de Estudos de Engenharia Civil, Programa de Pós-Graduação em Engenharia de Construção Civil, Curitiba, PR, Brasil.*

Received: 05 Aug 2019 • Accepted: 10 Dec 2019 • Available Online: 26 May 2020

1. Introdução

Atualmente, o concreto permeável é utilizado nas construções de pavimentos em áreas urbanas, sendo uma maneira de minimizar os impactos provocados pela pavimentação convencional impermeável. Durante chuvas intensas, a pavimentação impermeável contribui para o aumento do escoamento das águas superficiais e com potencial de inundações repentinas [1, 2], sendo uma maneira eficaz para atender às crescentes demandas ambientais.

A permeabilidade é uma propriedade intrínseca do concreto permeável que permite a passagem de um fluido (água) por meio de sua matriz [3]. Essa característica é atribuída ao fato de possuir uma rede de macro-poros interconectados que formam canais permitindo a drenagem da água. Ainda relacionado a sua capacidade permeável, pode ser utilizado como dispositivo de drenagem em muros de arrimo [4].

O concreto permeável é utilizado para reduzir a formação de ilhas de calor em cidades [5], e auxilia como barreira de som, absorvendo o ruído provocado pela interação entre pneu e pavimento [6]. No entanto, geralmente o concreto permeável não é utilizado para pavimentos com alta solicitação de tráfego, uma vez que sua alta porosidade diminui sua resistência à compressão [5, 7, 8].

Aliado aos aspectos ambientais, as características técnicas do concreto permeável despertam um interesse cada vez maior para seu emprego em construções sustentáveis, sendo promovidas pelos sistemas de certificação de edifícios, como o LEED da Green Building Council [1]. O concreto permeável pode contribuir para algumas categorias na certificação do LEED, sendo: Locais Sustentáveis; Eficiência Hídrica; Materiais e Recursos; e Inovação em Design [9].

Visando otimizar a porcentagem de poros interconectados em relação ao volume total do elemento, as filosofias de dosagem mais tradicionais ACI 522R-10 [10] sugerem que sua composição seja formada por uma quantidade mínima ou nula de areia e o volume de pasta apenas o suficiente para envolver os agregados graúdos. Devido a essa proporção de materiais, possui uma consistência seca, com abatimento do tronco cone (*slump test)* próximo a zero [10-12]. A porosidade do concreto permeável é um fator relevante em seu desempenho e possui relação com outras propriedades, como a permeabilidade [12-14]. Destaca-se que atualmente não há uma normativa que regulamente o procedimento de ensaio para caracterização da permeabilidade do concreto permeável em laboratório. No entanto, para alguns pesquisadores [12, 15-19], o ensaio de permeabilidade pode ser realizado com permeâmetro de carga constante para conjuntos granulares com alta porosidade e alta permeabilidade. Por outro lado, outros autores [20-23] realizam o ensaio utilizando permeâmetro de carga variável.

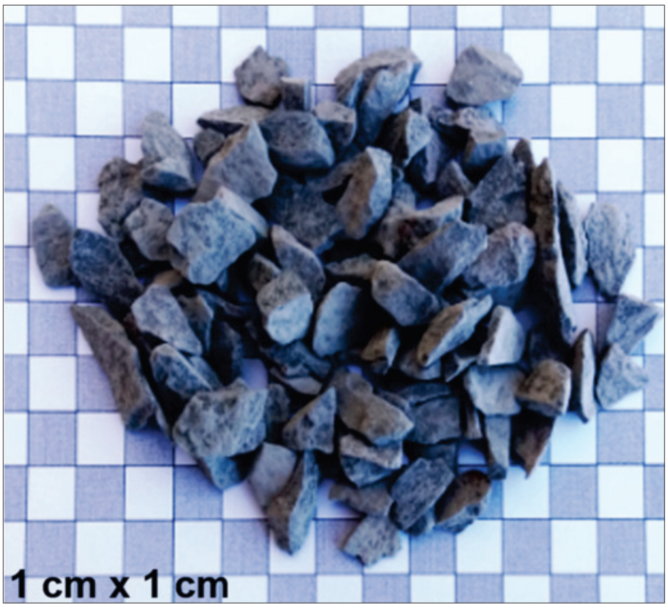

Figura 1
Aspecto superficial da fração granulométrica: faixa 6,3 a 9,5 mm

As filosofias de dosagem do concreto permeável são limitadas. Não há um conhecimento teórico consolidado e universalmente aceito que relacione os materiais constituintes e seu processo de confecção com suas propriedades [24]. Além disso, segundo a ACI 522R-10 [10] as dosagens do concreto permeável têm um grande componente empírico com base nas experiências já realizadas. Nas aplicações usuais entre os pesquisadores, nota-se traços, em massa, variando 1:2 a 1:12, com consumo de cimento variando de 150 a 700 kg/m³ e relação a/c de 0,2 a 0,5, podendo obter como características porosidades de até 42 % e permeabilidade de até 33 mm/s [2].

As primeiras recomendações normativas para o concreto permeável publicadas foram: manual da PCP [1]; e ACI 522R-10 [10]. Ambas abordam aspectos técnicos do material e seus constituintes, métodos simplificados de dosagem e ensaios de caracterização.

Nos últimos anos, a ASTM (*American Society for Testing and Materials)* lançou uma coletânea de normativas para caracterização do concreto permeável: ASTM C1754 [25], para determinar a densidade e conteúdo de vazios do concreto permeável no estado endurecido; a ASMT C1747 [26], para determinar a resistência a degradação do concreto permeável por impacto e abrasão; a ASTM C1688 [27], para determinar a densidade e conteúdo de vazios do concreto permeável no estado fresco; ASTM C1701 [28], para determinar a permeabilidade do concreto permeável. Recentemente, a ABNT (Associação Brasileira de Normas Técnicas), também, publicou uma normativa sobre concretos permeáveis a ASTM NBR 16416 [29], que aborda requisitos e procedimentos dos pavimentos permeáveis, com enfoque dado para blocos intertravados e o ensaio de caracterização da permeabilidade. Embora tenha normativas para caracterização do concreto permeável, não há normas ou abordagens aprofundadas na literatura sobre a utilização de ensaios não destrutivos para uma caracterização direta do concreto permeável.

O Método de Ultrassom é um ensaio não destrutivo relevante para caracterização e investigação do concreto convencional [30,47]. Em relação ao concreto permeável, existem poucas pesquisas nesta linha, o que abre possibilidade de desenvolver equações de previsão que podem auxiliar na determinação de suas propriedades.

A utilização do ultrassom permite a caracterização do concreto, detectando falhas, e monitorando seu estado de deterioração, além de obter suas propriedades mecânicas. Geralmente a frequência dos transdutores utilizados nos ensaios variam entre 25 a 100 kHz

Tabela 1
Dimensões e índice de forma da faixa granulométrica

Classes granulométricas (mm)	Comprimento (c)	Largura (l)	Espessura (e)	Índice de forma (desvio padrão)	Esfericidade (desvio padrão)	Massa unitária (kg/m^3) (desvio padrão)	Índice de vazios
		Média (mm) (desvio padrão)					
6,3 - 9,5	15,96 (2,92)	10,08 (1,58)	5,09 (1,64)	3,29 (1,03)	0,59 (0,09)	1.374,01 (2,35)	0,544

e a velocidade de pulso ultrassônico (VPU) para o concreto convencional é diferente dependendo da constituição da mistura, de seu proporcionamento, e das características físicas dos agregados [31]. As normas para determinação da velocidade do pulso ultrassônico (VPU) no concreto seguem a ASTM C 597 [32].
O concreto permeável possui muitos poros, provocando uma atenuação da onda ultrassônica, e fazendo com que este comportamento seja diferente do concreto convencional que são inerentemente densos, sendo necessário um fator de amplificação para medir a VPU entre a faixa de 50 e 60 dB [33]. Verificou-se que para uma maior densidade do concreto permeável, menor porosidade e maior resistência à compressão, maior será a VPU. Destaca-se a viabilidade na utilização do método de ultrassom para realizar avaliações periódicas nos pavimentos de concreto permeável, preservando-o da necessidade da extração de testemunho, o que lhe causaria perturbações na estrutura porosa [34,35].
A partir do atual estado da arte, este artigo objetiva investigar as propriedades do concreto permeável com foco nos ensaios de caracterização pelo método do ultrassom.

2. Materiais e métodos

2.1 Materiais

Os agregados graúdos foram obtidos por um processo de peneiramento a partir de um conjunto granular de origem basáltica adquiridos em uma pedreira localizada na região de Apucarana/PR. O processo de peneiramento seguiu as recomendações da ABNT NBR NM 248 [36], obtendo a fração granulométrica entre 6,3 a 9,5 mm. Na Figura 1 pode ser observado o aspecto superficial dos agregados graúdos.
A fração granulométrica obtida foi caracterizada pelos seguintes ensaios: Massa unitária, ABNT NBR NM 45 [37]; Índice de forma (IF), ABNT NBR 7809 [38]; e Método de Zingg [39]. Para isso, foram realizados, com o auxílio de um paquímetro, as medições de três dimensões (comprimento, largura e espessura) de 200 agregados da fração granulométrica. Na Tabela 1 podem ser observadas as características físicas dos agregados.
Segundo a classificação de Zinng [39], obtida através dos valores de alongamento (relação entre espessura e largura) e planicidade (relação entre largura e comprimento) dos agregados, o aspecto predominante dos agregados é lamelar-alongado. A classificação do agregado é de fundamental importância para o entendimento das propriedades do concreto permeável, o qual suas características físicas influenciam no processo de compactação, afetando adversamente a área de contato entre os agregados e levando, assim, a diferentes densidades e resistências [10, 40, 44].
As composições utilizadas foram definidas com o intuito de emular dosagens típicas encontradas em aplicações de concreto permeável, sendo os agregados com diâmetro uniforme e dentro do encontrado na literatura [17, 22, 40-42]. Para as ralações Pasta/Agregado (P/Ag) os valores utilizados atendem a produção de um concreto com porosidade e permeabilidade compatíveis com a aplicação prática.
Na Tabela 2 podem ser observados os 3 traços produzidos, o qual variaram o volume de P/Ag de 0,45 a 0,65, atribuindo a nomenclatura aos três traços de T0.45, T0.55 e T0.65. A faixa granulométrica utilizada foi uniforme, com diâmetros entre 6,3 a 9,5 mm, a relação água/cimento (a/c) foi constante e igual a 0,3, e foi utilizado o Cimento Portland CP II-Z regulamentado pela ABNT NBR 16697 [43].
O processo de mistura do concreto permeável seguiu as recomendações de SCHAEFER et al. [44]. Após a confecção do concreto foi realizada uma inspeção visual e verificou-se que a relação a/c utilizada deixou os agregados inteiramente cobertos com pasta e no processo de moldagem a pasta não segregou, seguindo as recomendações de TENNIS et al. [1]. A moldagem foi realizada pelo lançamento do concreto no interior do molde cilíndrico em três camadas, sendo que cada camada foi compactada com 25 golpes com haste metálica, seguindo a normativa da ABNT NBR 45 [37]. Para realização dos ensaios foram produzidos, no total, 36 CPs, sendo estes cilíndricos (com 100 mm de diâmetro e 200 mm de altura).

Tabela 2
Traço do concreto permeável: primeira campanha experimental

Traço	Relação P/Ag em massa	Consumo de brita (kg/m^3)	Consumo de cimento (kg/m^3)	Traço em massa		
				Cimento	Brita	a/c
T0,45	0,45	1.305,91	452,26	1	2,9	0,3
T0,55	0,55	1.306,85	553,35	1	2,4	0,3
T0,65	0,65	1.218,81	609,40	1	2,0	0,3

(a) (b) (c)

Figura 2
Processo de montagem do ensaio de permeabilidade

Figura 3
Ensaio pelo método de ultrassom: leitura realizada pela transmissão direta na longitudinal

2.2 Métodos

Os ensaios utilizados para caracterização do concreto permeável foram: densidade e porosidade no estado fresco; densidade e porosidade no estado endurecido, permeabilidade; resistência à compressão e à tração; e determinação da VPU pelo Método do Ultrassom. A densidade e porosidade do concreto permeável no estado fresco foi obtida utilizando o procedimento descrito pela ASTM C1688 [27]. Também foi utilizado o procedimento proposto pela ASTM C1754 [25] para calcular a densidade e porosidade do concreto permeável no estado endurecido. A permeabilidade do concreto permeável foi obtida através do permeâmetro de carga constante, sendo este usualmente utilizado por alguns pesquisadores [12,15-19]. Na Figura 2 pode ser observado o permeâmetro de carga constante desenvolvido para a realização do ensaio. Os resultados de permeabilidade apresentados neste estudo foram calculados com uma carga hidráulica de 30 cm.

Após a amostra ser acoplada ao permeâmetro, a abertura inferior do tubo foi fechada. Em seguida, foi medido o volume de água necessário para encher o tubo inferior e os espaços porosos da amostra (q_1). Em seguida, o aparelho foi completamente preenchido com água e o tubo inferior foi aberto. Finalmente, o volume de água que passou pela amostra em 60 s foi medido (q_2).

A permeabilidade (k) foi estimada usando a Lei de Darcy de acordo com a Equação 1. Nesta equação, q é a diferença entre os dois volumes medidos de água (q_2 - q_1), h é a amostra de altura (L_s) mais a carga hidráulica (30 cm) , e t é o intervalo de tempo (60 s).

$$k = \frac{4.q.L_s}{\pi.\emptyset_s^2.h.t} \quad (1)$$

A resistência à compressão foi determinada através do rompimento de corpos de prova cilíndricos conforme estabelece a ABNT NBR 5739 [45], e o capeamento dos CPs para realizado com gesso, permitindo a regularização da superfície. A resistência à tração por compressão diametral foi determinada através do rompimento

Tabela 3
Propriedades do concreto permeável

Traços	Densidade estado fresco (kg/m³)	Densidade estado endurecido (kg/m³)	Porosidade total (%)	Resistência à compressão (MPa)	Resistência à tração (MPa)	Permeabilidade com altura de 30 cm (mm/s)	VPU (m/s)
T0,45	1.914,85 (23,48)	1.893,84 (23,71)	28,44 (1,05)	7,77 (0,46)	1,49 (0,20)	8,31 (0,77)	3,719,79 (48,91)
T0,55	2.046,04 (32,80)	2.026,20 (32,41)	20,97 (1,62)	10,65 (1,07)	2,36 (0,34)	2,37 (0,99)	4,063,50 (73,28)
T0,65	2.035,27 (42,38)	2.004,08 (42,21)	20,93 (2,14)	11,73 (1,72)	2,33 (0,41)	3,15 (0,82)	4,163,00 (97,70)

de corpos de prova cilíndricos conforme às recomendações da ABNT NBR 7222 [46].

Para cada corpo de prova foi determinado o tempo de propagação de pulso ultrassônico utilizando o aparelho de ultrassom da marca PROCEQ/Pundit Lab, seguindo as diretrizes da ASTM C597 [32]. A leitura dos CPs pelo ultrassom foi realizada pela transmissão direta na longitudinal (20 cm de comprimento), com frequência de vibração da onda ultrassônica de 24 kHz e com um ajuste no fator de amplificação do receptor de 500 (correspondente a 54 dB). A configuração do teste consistiu em duas placas com furos para apoiar os transdutores para aplicação direta, assegurando que os transdutores estavam concêntricos ao corpo de prova, como pode ser observado na Figura 3. Conforme recomendação de Chandrappa e Biligiri [34], como a superfície da amostra de concreto permeável é normalmente irregular devido à baixa relação P/Ag, foi aplicada uma camada espessa de gel entre as superfícies da amostra e os transdutores. Finalmente, a média de três medidas foi usada como um único valor da VPU.

3. Resultados e discussões

Na Tabela 3 pode ser observado as médias e desvios padrão (entre parênteses abaixo da média) de todas as propriedades ensaiadas, densidade (estados fresco e endurecido), porosidade, resistência à compressão, resistência à tração, permeabilidade e a VPU. A partir dos dados obtidos na caracterização pelo método do ultrassom, algumas correlações podem ser realizadas com o objetivo de entender o comportamento do concreto permeável utilizando um método não destrutivo.

Na Figura 4a pode ser observada a relação entre a VPU com a porosidade total, nota-se que a VPU aumenta à medida que a porosidade diminui. Esse comportamento é esperado pois os vazios de ar provocam atenuação da velocidade da onda ultrassônica. Além disso, quanto maior a relação P/Ag, aumenta a possibilidade da onda encontrar caminhos mais curtos para sua propagação, aumentando a velocidades da onda. A Equação 2 apresenta a relação para obter a porosidade total (P) através da variável independente VPU e da relação P/Ag.

$$\boldsymbol{P = 105.7576 + 11.8586 \cdot P/Ag - 0.022308 \cdot UPV} \tag{2}$$

A Figura 4b apresenta uma comparação entre a porosidade experimental e a estimada de todas as amostras, incluindo uma linha de tendência. Os resultados revelam um erro de previsão relativo de 0,24% e um coeficiente de correlação (R2) de 0,91.

A Figura 5a apresenta a relação entre a VPU e a densidade no estado endurecido. Como esperado, observa-se que quanto maior a densidade do material, maior a velocidade de pulso ultrassônico, pois a onda se propaga com maior velocidade na matéria do que em estrutura com muitos vazios. A Equação 3 apresenta a relação para obter a densidade no estado endurecido (DE) através da variável independente VPU e P/Ag.

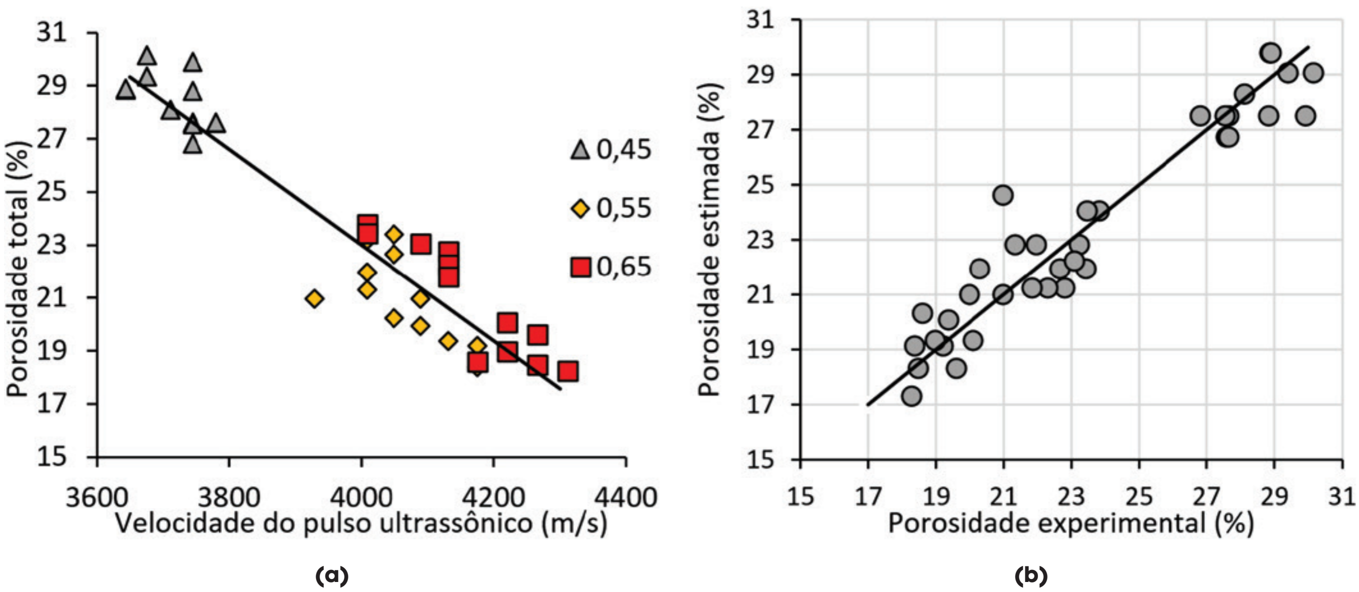

Figura 4
Relação entre a porosidade total e velocidade de pulso ultrassônico (a) e validação dos dados experimentais e estimados (b)

$$DE = 413,28 - 457,86 \cdot P/Ag + 0.45534 \cdot UPV \tag{3}$$

A Figura 5b retrata a comparação dos resultados experimentais com os estimados de todos CPs, incluindo uma linha de tendência. Os resultados revelam que um erro de previsão relativo de 0,01% e um coeficiente de correlação (R2) de 0,87.

A Figura 6a apresenta a comparação entre a permeabilidade (k), dependendo da VPU. Observa-se que os CPs com maior permeabilidade resultam em menores VPU, o que está relacionado a sua maior porosidade. Isso esclarece a possibilidade de estimar a permeabilidade do concreto permeável com testes não destrutivos. É possível estimar a permeabilidade (k) através das variáveis independentes VPU e razão P/Ag pela Equação 4.

$$k = 65.842 + 10.089 \cdot P/Ag - 0.01677 \cdot UPV \tag{4}$$

A Figura 6b apresenta uma comparação entre a permeabilidade

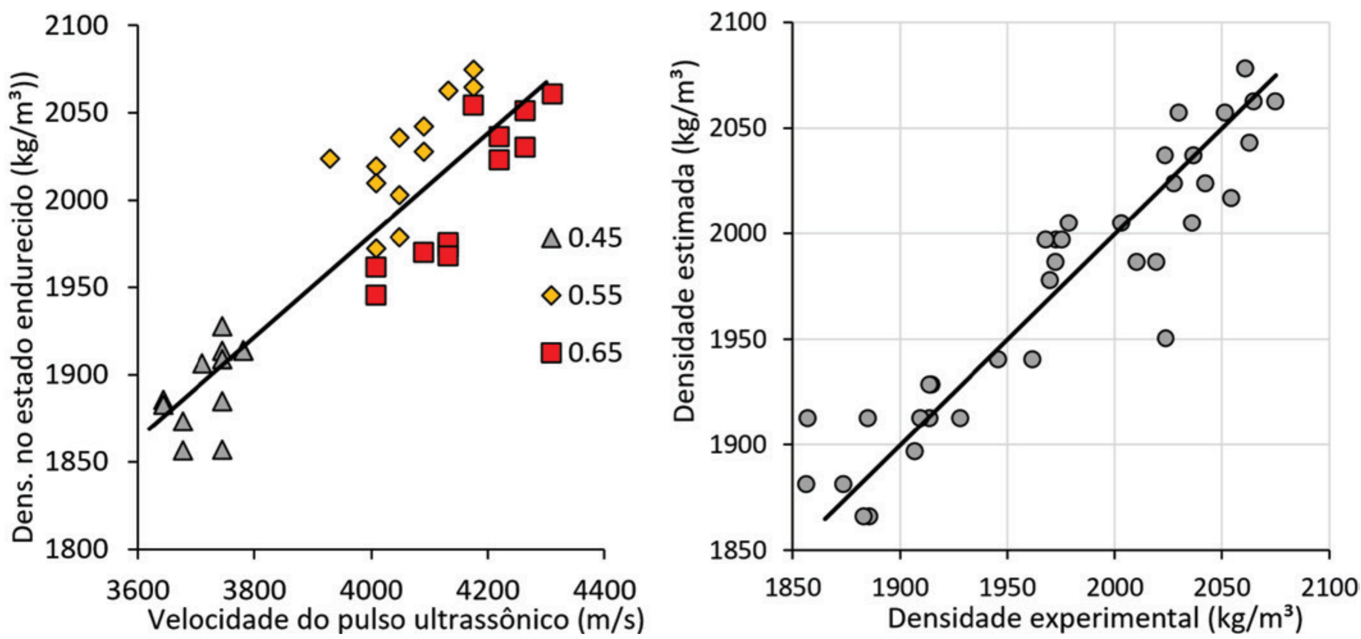

(a) (b)

Figura 5
Densidade no estado endurecido e velocidade de pulso ultrassônico (a) e validação dos dados experimentais e estimados (b)

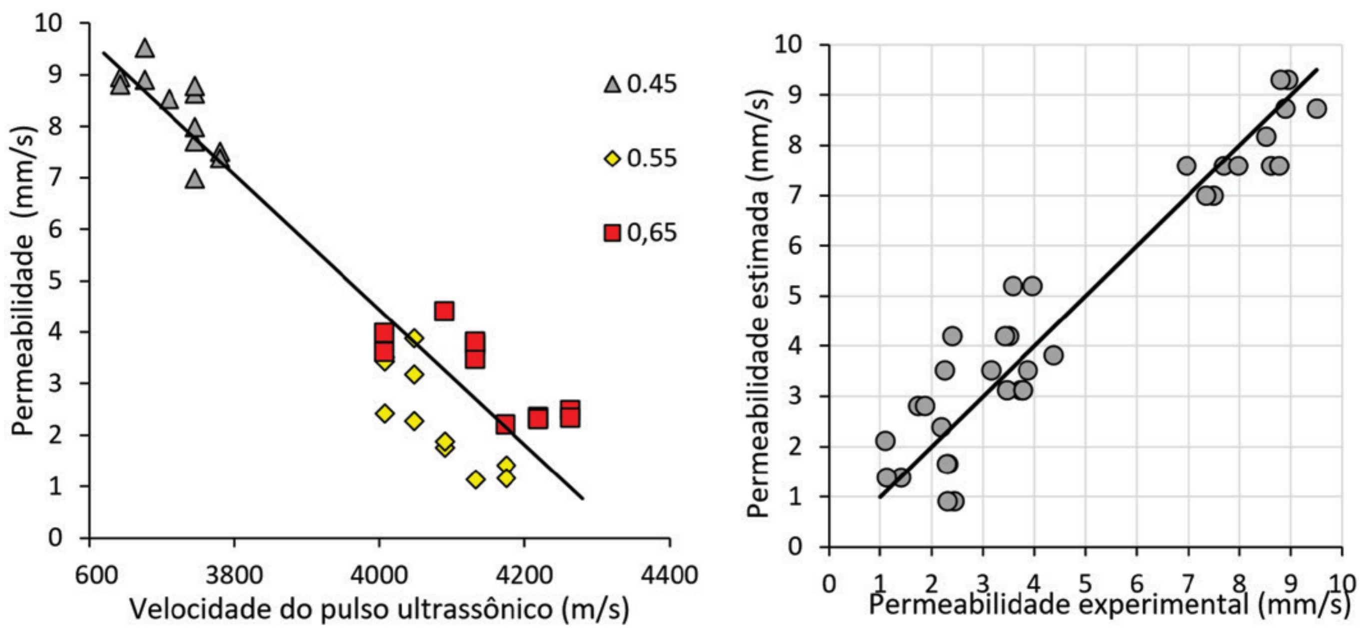

(a) (b)

Figura 6
Relação entre permeabilidade e velocidade de pulso ultrassônico (a) e validação dos dados experimentais e estimados (b)

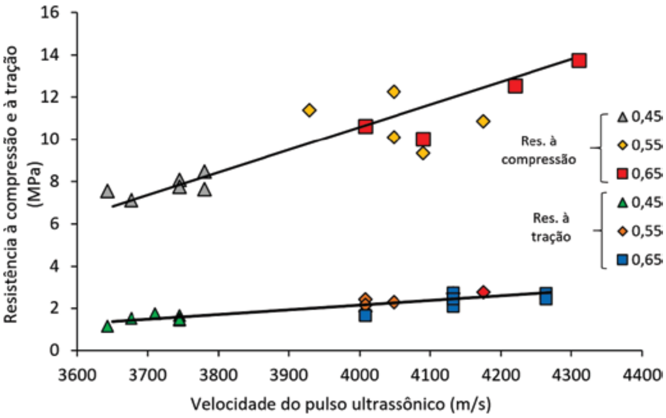

Figura 7
Relação entre resistência à compressão e tração com velocidade de pulso ultrassônico para três volumes P/Ag

experimental e a estimada de todas as amostras, incluindo uma linha de tendência. Os resultados revelam que um erro de previsão relativo de 5,06% e um coeficiente de correlação (R2) de 0,91. A Figura 7 mostra a comparação entre as forças de compressão e tração, dependendo da VPU. Essa correlação fornece uma estimativa dessas propriedades sem a necessidade de testes destrutivos. As Equações 5 e 6 apresentam as relações para obter a resistência à compressão e à tração, respectivamente, através das variáveis independentes VPU e razão P/Ag.
Na Figura 8 pode ser observado a linha de tendência retratando a concordância entre os resultados. A comparação dos resultados mostrou um erro de previsão relativo é de 0,63% e 0,81%, e um coeficiente de correlação (R^2) de 0,79 e 0,84, para a resistência à compressão e à tração, respectivamente.

$$\sigma_C = -18.56 + 6.418 \cdot P/Ag + 0.006297 \cdot UPV \tag{5}$$

$$\sigma_T = -9.4996 - 3.237 \cdot P/Ag + 0.003354 \cdot UPV \tag{6}$$

Vale destacar uma característica particular do concreto permeável em relação a sua ruptura, na qual predominantemente foram os agregados graúdos que sofreram falhas e não a camada de ligação P/Ag, comportamento também observado por outros autores [21].
As correlações apresentadas sugerem o potencial que a aplicação dos ensaios não destrutivos tem para caracterização do concreto permeável, evitando a necessidade de extração de testemunho e permitindo estabelecer correlações com suas propriedades. Assim, propõem-se estudos com maior profundidade afim de verificar a influência dos materiais constituintes do concreto permeável na VPU. Ressalta-se que as equações encontradas são apenas compatíveis com os materiais utilizados nesta pesquisa, assim, materiais de diferentes características físicas e químicas precisam ser testados e validados para as equações apresentadas.

4. Conclusões

A aplicação do Método do Ultrassom merece atenção especial para caracterização do concreto permeável, com carência de pesquisas e com potencial de desenvolver modelos analíticos de previsão das propriedades a partir da VPU como uma das variáveis independentes. Os resultados de velocidade de pulsos

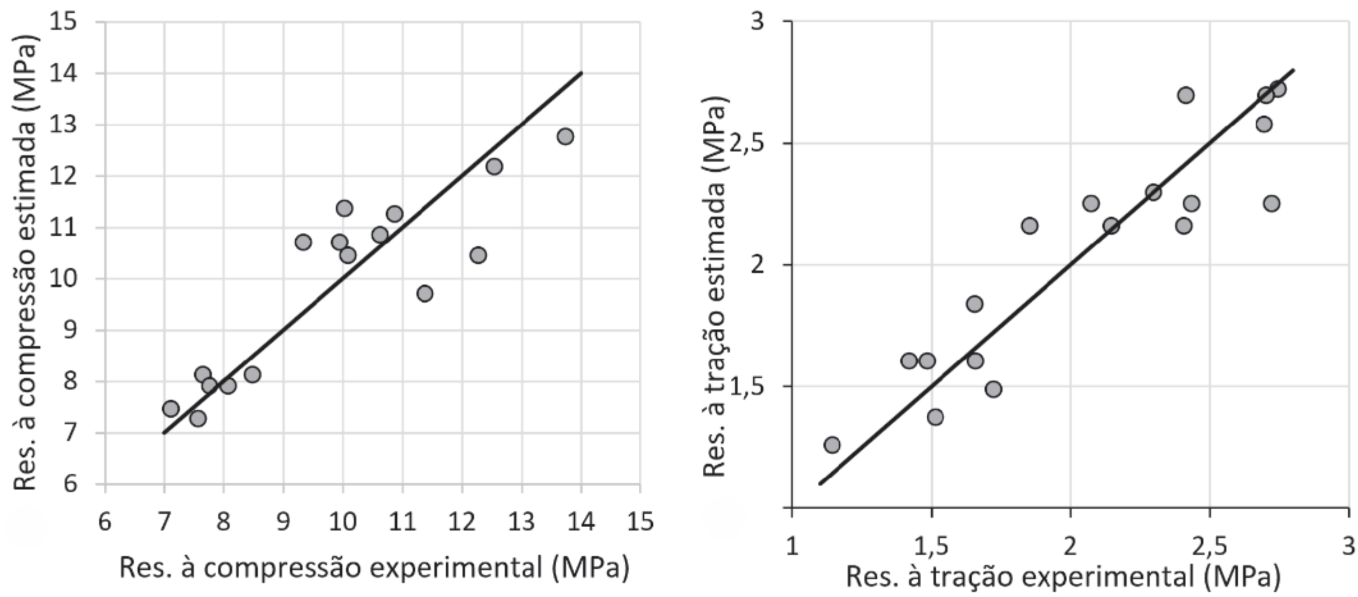

(a) (b)

Figura 8
Validação dos dados de resistência à compressão (a) e à tração (b) estimada e experimental

ultrassônicos (VPU) ficaram entre 3642 e 4262 m/s para uma variação de aproximadamente 12% na porosidade. À medida que a porosidade aumentou, a VPU diminuiu, uma vez que os vazios provocam atenuação da onda ultrassônica. Além disso, as medições da VPU retrataram valores maiores para os CPs com maiores densidades e maior desempenho mecânico. Com os valores de VPU de todas as amostras, foi realizado uma regressão linear para estimar as características e propriedades do concreto, obtendo alto coeficiente de correlação, sendo: 0,91 (Porosidade); 0,87 (Densidade); 0,91 (Permeabilidade); 0,79 e 0,84 (Resistência à compressão e tração, respectivamente).

5. Agradecimentos

Os autores agradecem ao Programa de Pós-graduação de Engenharia de Construção Civil, PPGECC, da UFPR. Ao Departamento de Engenharia Civil da UTFPR/Apucarana.

6. Referências bibliográficas

[1] TENNIS, P. D.; LEMING, M. L.; AKERS, D. J. Pervious concrete pavements. Technical report, EB302.02. Portland Cement Association, Skokie, Illinois, and National Ready Mixed Concrete Association, Silver Spring, Maryland, 32p, 2004.

[2] KIA, A.; WONG, H. S.; CHEESEMAN, C.R. Clogging in permeable concrete: A review. Journal of Environmental Management, v.193, p. 221-233, 2017.

[3] CAPUTO, H.P. Mecânica dos Solos e suas Aplicações-Fundamentos, v. 1, 234p, Rio de Janeiro, 1988.

[4] OSPINA, C. M. M.; ERAZO, C. H. B. Resistencia mecánica y condiciones de obra del concreto poroso en los pavimentos según el tipo de granulometría. Medellín, 2007.

[5] FERGUSON, B. K. Porous pavements, Boca Raton: CRC Press, London, 577p, 2005.

[6] KIM, H. K.; LEE, H. K. Influence of cement flow and aggregate type on the mechanical and acoustic characteristics of porous concrete. Applied Acoustics, v. 71, p. 607-615, 2010.

[7] HAGER, A. S. Sustainable Design of Pervious Concrete Pavements. PhD Dissertation, University of Colorado Denver, Department of Civil Engineering, Denver, CO, 2009.

[8] SABNIS G.M. Green building with concrete. Sustainable design and construction, 1nEd. Boca Raton, 320p, 2012.

[9] ASHLEY, E. Using Pervious Concrete to Achieve LEED Points. Concrete Infocus. National Ready Mixed Concrete Association, Silver Spring, MD, p. 1-6, 2008.

[10] AMERICAN CONCRETE INSTITUTE (ACI), 2010. Report on Pervious Concrete. ACI Committee 522. Report number: ACI 522R-10.

[11] NEITHALATH N.; DEO, O. Compressive response of pervious concretes proportioned for desired porosities. Construction and Building Materials, v. 25, p. 4181–4189, 2011.

[12] PIERALISI, R.; CAVALARO, S.H.P.; AGUADO. A Advanced numerical assessment of the permeability of pervious concrete. Cement and Concrete Research, v. 102, p. 149-160, 2017.

[13] MEININGER, R. C. No-Fines Pervious Concrete for Paving. Concrete International, v.10, p. 20-27, 1988.

[14] GHAFOORI, N.; DUTTA, S. Laboratory Investigation of Compacted No-Fines Concrete for Paving Materials. Journal of Materials in Civil Engineering, v. 7, n. 3, p. 183–191, 1995a.

[15] THO-IN, T.; SATA, V.; CHINDAPRASIRT, P.; JATURAPITAKKUL, C. Pervious highcalcium fly ash geopolymer concrete. Construction and Building Materials, v. 30, p. 366-371, 2012.

[16] SATA, V.; WONGSA, A.; CHINDAPRASIRT, P. Properties of pervious geopolymer concrete using recycled aggregates. Construction and Building Materials, v. 42, p. 33–39, 2013.

[17] ZAETANG, Y.; WONGSA, A.; SATA, V.; CHINDAPRASIRT, P. Use of lightweight aggregates in pervious concrete. Construction and Building Materials, v. 48, p. 585–591, 2013.

[18] BHUTTA, M. A. R.; HASANAH, N.; FARHAYU, N.; HUSSIN, M. W.; TAHIR, M. B. M.; MIRZA, J. Properties of porous concrete from waste crushed concrete (recycled aggregate). Construction and Building Materials, v. 47, p. 1243-1248, 2013.

[19] KUO, W. T.; LIU, C. C.; SU, D. S. Use of washed municipal solid waste incinerator bottom ash in pervious concrete. Cement and Concrete Composites, v.37, p. 328–335, 2013.

[20] NEITHALATH, N.; SUMANASOORIYA, M. S.; DEO, O. Characterizing pore volume, sizes, and connectivity in pervious concretes for permeability prediction. Materials Characterization, v. 61, p. 802-813, 2010.

[21] YAHIA, A.; KABAGIRE, D. New approach to proportion pervious concrete. Construction and Building Materials, v. 62, p. 38–46, 2014.

[22] NGUYEN, D. H.; SEBAIBI, N.; BOUTOUIL. M.; LELEYTER, L.; BARAUD, F. A modified method for the design of pervious concrete mix. Construction and Building Materials, v. 73, p. 271–282, 2014.

[23] COSTA, F. B. P.; LORENZI, A.; HASELBACH, L.; SILVA FILHO, L. C. P. Best practices for pervious concrete mix design and laboratory tests. REVISTA IBRACON DE ESTRUTURAS E MATERIAIS, v. 11, n. 5, p. 1151-1159, 2018.

[24] CAVALARO, S. H. P.; BLANCO, A.; PIERALISI, R. Holistic modelling approach for special concrete: from fresh-to hardened-state. RILEM Technical Letters, v. 3. p. 84-90, 2018.

[25] AMERICAN SOCIETY FOR TESTING AND MATERIALS.. ASTM C1754 / C1754M, Standard Test Method for Density and Void Content of Hardened Pervious Concrete, ASTM International, West Conshohocken, PA, 2012.

[26] AMERICAN SOCIETY FOR TESTING AND MATERIALS. ASTM C1747 / C1747M, Standard Test Method for Determining Potential Resistance to Degradation of Pervious Concrete by Impact and Abrasion, ASTM International, West Conshohocken, PA, 2013.

[27] AMERICAN SOCIETY FOR TESTING AND MATERIALS. ASTM C1688 / C1688M, Standard Test Method for Density and Void Content of Freshly Mixed Pervious Concrete, ASTM International, West Conshohocken, PA, 2014.

[28] AMERICAN SOCIETY FOR TESTING AND MATERIALS...ASTM C1701 / C1701M, Standard Test Method for Infiltration Rate of In Place Pervious Concrete, ASTM International, West Conshohocken, PA, 2017.

[29] ASSOCIAÇÃO BRASILEIRA DE NORMAS TÉCNICAS. NBR 16416: Pavimentos permeáveis de concreto - Requisitos e procedimentos, Rio de Janeiro, 2015.

[30] OHDAIRA, E.; MASUZAWA, N. Water content and its effect on ultrasound propagation in concrete —the possibility of NDE. Ultrasonics, v. 38, p. 546-552, 2000.

[31] MALHOTRA, V.M., N. J. E. CARINO, N. J. E. Handbook of Nondestructive Testing of Concrete, CRC Press, Boca Raton, FL, USA, 2nd edition, 2004.

[32] AMERICAN SOCIETY FOR TESTING AND MATERIALS. ASTM C597, Pulse velocity through concrete, ASTM International, West Conshohocken, PA, 1989.

[33] CHANDRAPPA, A. K.; BILIGIRI, K. P. Investigations on Pervious Concrete Properties Using Ultrasonic Wave Applications. Journal of Testing and Evaluation, v. 45, n.5, p.1736-1749, 2017.

[34] CHANDRAPPA, A. K.; BILIGIRI, K. P. Influence of mix parameters on pore properties and modulus of pervious concrete: an application of ultrasonic pulse velocity. Materials and Structures, v. 49, p. 5255-5271, 2016c.

[35] AMINI, K.; WANG, X.; DELATTE, N. Statistical Modeling of Hydraulic and Mechanical Properties of Pervious Concrete Using Nondestructive Tests. Journal of Materials in Civil Engineering, v. 30, n. 6, p. 1-8, 2018.

[36] ASSOCIAÇÃO BRASILEIRA DE NORMAS TÉCNICAS. NBR NM 248: Agregados -Determinação da composição granulométrica, Rio de Janeiro, 2003.

[37] ASSOCIAÇÃO BRASILEIRA DE NORMAS TÉCNICAS. NBR NM 45: Agregados – Determinação da massa unitária e do volume de vazios. Rio de Janeiro, 2006.

[38] ASSOCIAÇÃO BRASILEIRA DE NORMAS TÉCNICAS.. NBR 7809: Agregado graúdo - Determinação do índice de forma pelo método do paquímetro - Método de ensaio, Rio de Janeiro, 2006.

[39] ZINGG, T. Beiträg zur schotteanalysis. Diss.-Druckerei A.-O. Gebr. Leemann & Co., 107p., 1935.

[40] LIAN, C.; ZHUGE, Y. Optimum mix design of enhanced permeable concrete – An experimental investigation. Journal of Environmental Management, v.193, p. 221-233, 2017.

[41] LIM, E.; TWAN, K. H.; FWA, T. F. Effect of mix proportion on strength and permeability of pervious concrete for use in pavement. Journal of the Eastern Asia Society for Transportation Studies, v. 9, p. 1565-1575, 2013.

[42] IBRAHIM, A.; MAHMOUD, E.; YAMIN, M.; PATIBANDLA, V. C. Experimental study on Portland cement pervious concrete mechanical and hydrological properties, Construction and Building Materials, v. 50, p. 524–529, 2014.

[43] ASSOCIAÇÃO BRASILEIRA DE NORMAS TÉCNICAS.NBR 16697: Cimento Portland- Requisitos, Rio de Janeiro, 2018.

[44] SCHAEFER, V.; WANG, K.; SULEIMAN, M.; KEVERN, J. Mix design development for pervious concrete in cold weather climates. National Concrete Pavement Technology Center, 83p, 2006.

[45] ASSOCIAÇÃO BRASILEIRA DE NORMAS TÉCNICAS. NBR 5739: Concreto - Ensaio de compressão de corpos de prova cilíndricos, Rio de Janeiro, 1994.

[46] ASSOCIAÇÃO BRASILEIRA DE NORMAS TÉCNICAS. NBR 7222: Concreto e argamassa - Determinação da resistência à tração por compressão diametral de corpos de prova cilíndricos, Rio de Janeiro, 2011.

[47] CARRIÓN, A.; GENOVÉS, V.; GOSÁLBEZ, J.; MIRALLES, R.; PAYÁ, J. Ultrasonic signal modality: A novel approach for concrete damage evaluation. Cement and Concrete Research, v. 101, p. 25-32, 2017.

Volume 13, Number 3 (June 2020) p. 501 – 514 • ISSN 1983-4195
http://dx.doi.org/10.1590/S1983-41952020000300004

REVISTA IBRACON DE ESTRUTURAS E MATERIAIS
IBRACON STRUCTURES AND MATERIALS JOURNAL

Use of ornamental rock waste as a partial substitute for binder in the production of structural concrete

Uso do resíduo do beneficiamento de rochas ornamentais como substituto parcial ao aglomerante na produção de concretos estruturais

F. R. TEIXEIRA [a]
fernandoteixeira5400@gmail.com
https://orcid.org/0000-0001-8498-9263

F. C. MAGALHÃES [b]
fabiocmagalhaes@gmail.com
https://orcid.org/0000-0001-8463-1501

G. B. WALLY [b]
gustavo.wally@gmail.com
https://orcid.org/0000-0003-3008-3815

F. K. SELL JUNIOR [b]
felixsell@gmail.com
https://orcid.org/0000-0002-6286-5371

C. M. PALIGA [a]
charleipaliga@gmail.com
https://orcid.org/0000-0003-0521-4764

A. S. TORRES [a]
arielatorres@gmail.com
https://orcid.org/0000-0003-4686-9759

Abstract

Due to the population increase, to the improvement of life conditions, to the elevation of levels of consumption and the growing industrialization of developing countries, it is estimated that the production of concrete will present significant increase in the next decades. The process of producing cement is responsible for approximately 5 % of the emissions of CO_2, an expressive environment pollutant. In this context, this work presents an evaluation of the influence of partial substitution of cement by ornamental rock waste (ORW) on the physical and mechanical properties of concrete. ORW from a local marble and granite processing company was used. The waste was mineralogically characterized through X-ray diffraction (XRD) essays, energy-dispersive X-ray (EDX) microanalysis, and physically characterized through laser granulometry and specific mass. For this, was adopted a concrete trace as reference, produced with CP V-ARI cement (similar to ASTM Type III), from IPT dosage. Waste was used in proportions of 5 %, 7.5 %, 10 % and 12.5 % of substitution of cement by mass. Results were treated with ANOVA and multiple comparison of means, indicating a possibility of substitution of until 10% of cement by ORW, creating a concrete with proper resistance to Brazilian regulations regarding the classification as structural.

Keywords: waste management, ornamental rock waste, structural concrete, environmental impacts.

Resumo

Em decorrência do aumento populacional, da melhoria das condições de vida, da elevação dos níveis de consumo e da crescente industrialização dos países em desenvolvimento, estima-se que a produção de concreto apresentará expressivo crescimento ao longo das próximas décadas. O processo de produção do cimento é responsável por aproximadamente 5 % das emissões mundiais de CO_2, poluente que causa danos expressivos no meio ambiente. Neste contexto, este trabalho apresenta uma avaliação da influência da substituição parcial de cimento Portland por resíduo do beneficiamento de rochas ornamentais (RBRO) em propriedades físicas e mecânicas do concreto. Utilizou-se o RBRO proveniente de uma empresa beneficiadora de mármores e granitos localizada na região sul do Rio Grande do Sul. A caracterização mineralógica do resíduo foi realizada por meio de ensaios de difração de raios X (DRX), microanálise de raios X (EDX), enquanto suas características físicas foram analisadas por ensaios de granulometria a laser e de massa específica. Adotou-se um traço de concreto de referência produzido com cimento CP V-ARI, utilizando o método de dosagem do IPT/EPUSP. A substituição do cimento Portland pelo RBRO foi realizada nos teores de 5 %, 7,5 %, 10 % e 12,5 % em relação à massa de cimento. Os resultados foram tratados por ANOVA e comparação múltipla de médias, indicando a possibilidade da substituição de até 7,5 % do cimento pelo RBRO, gerando um concreto com resistência adequada às normas brasileiras e com potencial uso estrutural.

Palavras-chave: aproveitamento de resíduos, resíduo do beneficiamento de rochas ornamentais, concreto estrutural, impactos ambientais.

[a] *Universidade Federal de Pelotas, Programa de Pós-Graduação em arquitetura e urbanismo, Pelotas, RS, Brasil;*
[b] *Universidade Federal do Rio Grande, Programa de Pós-Graduação em Engenharia Oceânica, Rio Grande, RS, Brasil.*

Received: 05 Aug 2019 • Accepted: 10 Dec 2019 • Available Online: 26 May 2020

1. Introduction

Concrete is the most used construction material in the world, with an annual production estimated in 23 billion tons, which corresponds to average consumption of 10 kg of concrete per person per day [1]. The manufacture of cement in particular has considerable impact over the environment, due to the high energy consumption and the emission of greenhouse effect gases, mainly carbon dioxide [2-3]. In 2016, cement industries were responsible for 5.6 % of the world's entire CO_2 emission. Compared to 2013, emissions due to burning of fossil fuels for cement production have increased 1.2% [4]. The CO_2 emission in the production of common Portland cement is composed of two sources: the is decarbonising of calcium carbonate ($CaCO_3$), that releases approximately 528 kg of CO_2 per ton of cement, and the burning of fossil fuels, which releases approximately 367 kg of CO_2 per ton of cement, making a total of 895 kg of CO_2 per ton of cement [5].
The large environmental impacts generated by the cement industry foster the search for alternatives that make the production of concrete less aggressive to nature. Several studies have shown positive results in evaluating the incorporation of industrial waste into concrete, as this waste can increase the mechanical strength and durability-related properties of concrete.
Facing all that, the incorporation of industrial waste in concrete comes up as an alternative to minimize environmental impacts of cement production. Among such residuals, there is ornamental rock waste (ORW), a byproduct of the production of ornamental rocks, that has been showing potential to be used as a partial substitute for binder.
According to the Brazilian Association of Ornamental Rocks Industry (ABIROCHAS) [6], in 2017, the production of stones in Brazil was of about 9.24 Mt, of which 1.046 Mt were exported. It must be highlighted that 41 % of the blocks, in volume, were transformed into waste, producing 3.36 Mt of materials rejected during the processing of ornamental rocks. Thus, it is evident that the process of beneficiation of ornamental rocks is archaic, almost artisanal, and

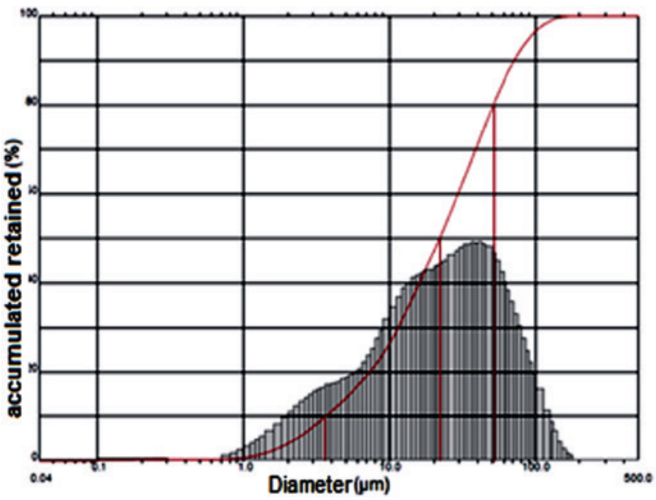

Figure 1
Granulometric distribution curves of ORW

that it has few investments in order to reduce the exorbitant waste generation during the process of rock processing.
In this context, the environmental issues exposed demonstrate the it is necessary to intensify studies on the ORW, with the objective of producing materials the incorporate it and, thus, mitigate its environmental impact.
Several researchers, like Ashish [7], Singh et al. [8], Rana et al. [9], Bacarji et al. [10] and Ergun [11], have demonstrated the viability of ORW as partial substitute for binder in the production of concrete. Most of these studies, however, focus only on mechanical properties. Considering that concrete is a hydrophilic material, studies that evaluate properties related to concrete durability, such as water absorption, are essential in the investigation of the feasibility of using ORW as a replacement for Portland cement in the production of structural concretes.
Thus, this work adopted a mixture of concrete produced with CP V-ARI cement (similar to ASTM Type III), as it contains the highest clinker content among the cements available in the regional market (southern Brazil) and, thus, consist of a "purer" cement in terms of mineral admixtures, and the feasibility of using the ORW as a partial replacement of cement was investigated. The waste was used in replacement of cement at the levels of 5 %, 7,5 %, 10 %, and 12.5 %.

2. Methods and materials

Following are presented the characteristics of the materials used to make the concretes that were studied, and the methods used to conduct the tests.

2.1 Ornamental rock waste

ORW, collected as mud, was generated by a local company that processes ornamental rocks. The collection was made according to NBR 10007 [12], directly from the company's decantation tank, and all the material used in the work was collected the same day. After collection, the material went through a homogenization and quartering process, to obtain a representative sample. Then, the ORW mud was put into an oven, where it remained for 48 h, under a temperature of 100 °C. Next, waste was passed in a 1.18 mm sieve, to remove possible impurities and harrowing, eliminating the need to grind it. After that, it was passed in a 300 μm mesh sieve and stored in sacks, ready to be used. The granulometry of ORW was determined with a Cilas laser granulometer, model 1064. Figure 1 presents the data obtained in the test. The curve analysis shows that the average diameter of the ORW particle is 30,95μm.
To identify the presence of crystalline elements in the ORW composition, X-ray diffraction (XRD) analysis was carried out using a Shimadzu diffractometer, model XRD 6000, operating under radiation of CuKα (=1.5418 Å) and graphite monochromator, operating under a 40 kV tension and current of 30 mA, in a scanning range from 5 to 80º and angular velocity of 2º/min. Figure 2 presents the X-ray diffractogram of the waste. Analysing the results obtained from the XRD, it is verified the the ORW used is mostly composed of quartz (Q) and albite (A). It is also possible to observe less

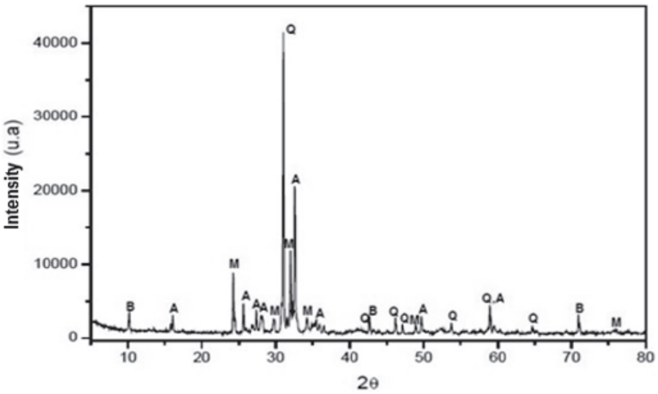

Figure 2
X-ray diffractogram obtained for the ORW sample

intense peaks of microcline (M) and biotite (B). Through this essay, the non-pozolanicity of ORW was found, as a result of its quite defined crystalline peak regarding quartz (SIO_2) and the absence of amorphous halo. So, ORW acts mainly as a nucleation agent within the microstructure.

To determinate ORW's chemical composition, an X-ray fluorescence spectrometer for energy dispersion, model Shimadzu EDX-720, was used. Table 1 presents the results of this test. According to NBR 12653 [13], the sum of oxides SiO_2, Al_2O_3 and Fe_2O_3 must be higher than 70 % for the analysed material to be considered pozzolanic. The sum of them was 62.42 %, so, according to NBR 12653 [13], the material is not considered pozzolanic, presenting only physical effect, which corroborates what was previously discussed.

Table 2 shows results of the essays of ORW specific real mass, through NBR NM 23 [14], and unitary mass, according to NBR NM 45 [15].

Table 1
Chemical composition of ORW

Element	Quantitative (%)
SiO_2	34.085
K2O	20.287
Al_2O_3	18.77
Fe_2O_3	12.57
CaO	12.181
TiO_2	1.444
MnO	0.178
ZnO	0.122
ZrO_2	0.118
SrO	0.103
CuO	0.101
Rb_2O	0.024
Y_2O_3	0.006

2.2 Cement

The cement used was CP V-ARI (similar to ASTMType III), as it possesses additions without reactivity, according to NBR 5733 [17], making it easy to understand the action of ORW and avoiding combined effects. That makes it possible to clearly visualize the effects of the substitution of cement by ORW in concrete.

2.3 Aggregates

A natural medium-sized quartz sand, fit into the usable zone of NBR 7211 [16], was used and oven-dried until mass constancy. Granite gravel was classified as gravel 1 according to NBR 7211 [16]. Results of physical characterization obtained in natural aggregates are presented in Table 2.

Table 2
Aggregate and ORW characterization

Test method		Fine aggregate	Coarse aggregate	ORW
Granulometric composition/ NBR NM 248 (ABNT, 2003)	Maximum Ø (mm)	4.75	19	—
	Fineness modulus	2.84	4.69	—
Specific mass (g/cm³) / NBR NM 52 (ABNT, 2009) and NBR NM 53 (ABNT,2009)		2.62	2.6	2.64
Loose unitary mass (g/cm³) / NBR NM 45 (ABNT, 2006)		1.55	1.41	1.16

Table 3
Unitary mixtures used in this study

Mix	Cement (kg)	ORW (kg)	Sand (kg)	Gravel (kg)	w/c ratio
Reference	1	0	2.4	3.28	0.60
5 %	0.95	0.05	2.4	3.28	0.60
7.50 %	0.925	0.075	2.4	3.28	0.60
10 %	0.9	0.1	2.4	3.28	0.60
12.50 %	0.875	0.125	2.4	3.28	0.60

Table 4
Methodology of the essays conducted

Properties		Details	Methodology
Mechanic	Compressive strength	5 samples by mixture at ages: 3, 7 and 28 days	NBR 5739 (2007)
Physical	Water absorption by immersion	3 samples by mixture at age: 28 days	NBR 9778 (2009)
	Sorptivity	3 samples by mixture at age: 28 days	NBR 9779 (2009)

Table 5
Analysis of variance results – p value – of compressive strength

ANOVA table					
Factor	**DF**	**Sum of squares**	**Average square**	**F-value**	**P-value**
Substitution level	4	78.88236	19.72059	6.928441737	0.000118253
Age	2	1241.111976	620.555988	218.0201509	3.01E-28
Substitution level x Age	8	20.215224	2.526903	0.887777709	0.532279889
Residuals	60	170.77944	2.846324	—	—

2.4 Concrete production and assessment

For concrete dosage, was used the dosing methodology by IPT/EPUSP [17]. Through an experimental procedure, the ideal percentage of dry mortar was set as 51% (α = 0,51) and the amount of water necessary to obtain the depletion of the marsh cone as 70 ± 10 mm.
Through dosage equations and the pre-established value of the relation water/cement of 0.60, we determined the concrete's reference trace, according to Table 3. The relation of water/cement of 0.60 was defined because it is the maximum value considered for a structural concrete located in urban environment (Class II of aggressiveness), according to NBR 6118 [18].
From the reference mixture, partial substitution of cement by ORW was carried out, in levels of 5 %, 7.5 %, 10 % and 12.5 %. The choice of these values was based in the studies by Singh et al. [8], Rana et al. [9] Bacarji et al. [10] and Ergun [11].
In Table 4, there are details about all properties studied in this work, as well as the number of samples and the regulations used in procedures. All specimens were moulded and cured according to the recommendations of NBR 5738 [19].
Finally, to understand the results obtained in terms of physical and mechanical properties of concrete, and if the independent variables analysed (age and replacement levels) are important in their alteration, they were submitted to statistical treatment by analysis of variance (ANOVA) and multiple comparison of means (Tukey's Test). The ANOVA, when indicates significance, makes sure that there are at least a couple of different averages, but not knowing how many and which ones. Thus, the Tukey's Test is necessary, where, in order to determine whether the pairs of means are different from each other, the comparison of means from two by two was made.

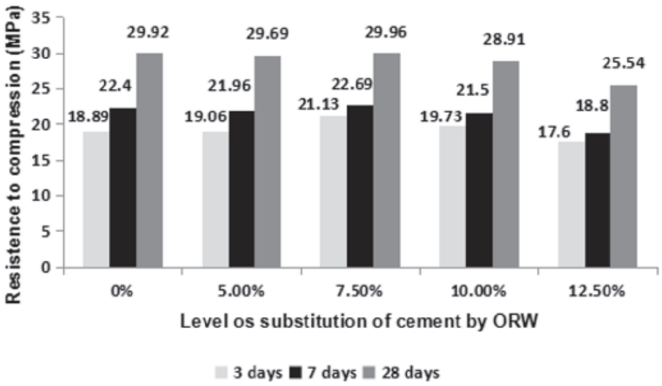

Figure 3
Compressive strength

3. Results and discussion

3.1 Compressive strength

The means of the results of compressive strength along the ages are presented in Figure 3. At the first ages, except with value of 12.5 %, the mixes with replacememnt of cement by ORW provided greater resistance than the reference one, which demonstrates the physical action of the waste, once in this moment the greater part of the pozzolanic reactions did not occur. ORW's physical effect accelerates cement hydration when it acts as a point of nucleation for calcium hydroxide, as it possesses extremely fine particles, accelerating reactions and forming less crystals of calcium hydroxide.
Through ANOVA, statistical significance of the related variables, which are replacement value and age in compressive strength was found. Table 5 presents the analysis of influence of these factors and possible interactions.
In Table 5, it is verified that the level of replacement and the age, when analysed separately, have significant effect over compressive strength.
However, there is no significant influence between the level of substitution and the age. The inexistence of interaction between

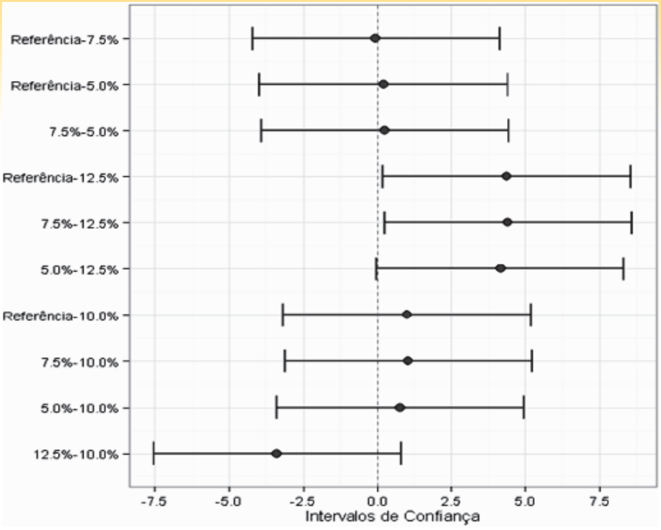

Figure 4
Tukey's Teat for concretes' compressive strength at 28 days

substitution level and age shows that substitution does not lead to significant increase throughout time. This behaviour was already expected, as the waste does not have pozzolanic activity.

Analysing the data in Table 5, it is possible to observe that the p value is lower than the expected level of significance (α = 0,05), so, the null hypothesis is rejected. This way, Tukey's Test was applied and the results obtained are shown in Figure 4.

Analysing the data obtained through Tukey's Test, Figure 4, it is possible to observe that, at 28 days, only the concrete with 12.5 % of replacement of cement by ORW can be considered statistically different from the reference concrete. At this level of substitution, the cementing effect has shown as preponderant regarding filler effect, causing a decrease of resistance, compared to the reference trace. Although the concrete with 10 % of substitution presents reduction in compressive strengthcompared to the reference concrete, this decrease in resistance cannot be considered significant, with a reliability level of 95 %.

The result obtained in the study corroborates with the results obtained by Ashish [7], Ergun [11], Agarwal; Gulati [20],Kockal [21], Ramos et al. [22]; Aliabdo et al. [23] and Munir et al. [24], who obtained increased compressive strength by replacing cement with ORW in the levels of 5 % and 7.5 %.

3.2 Absorption by capillarity

The results obtained in the test of sorptivity are presented in Figure 5. The essay demonstrated a reduction of the absorption tax in the substitution levels of 5 % and 7.5 %, with the content of 7.5 % presenting the best performance (reduction of 10 %).On the other hand, thereplacement of 12.5 % presented the worst results, with an increase of 22.70 % in the sorptivity tax. This result of sorptivity aids to explain the decrease in compressive strength in substitution levels above 7.5 %. In this substitution value, the cementing effect has shown as preponderant regarding the filler effect, causing an increase of the sorptivity tax.

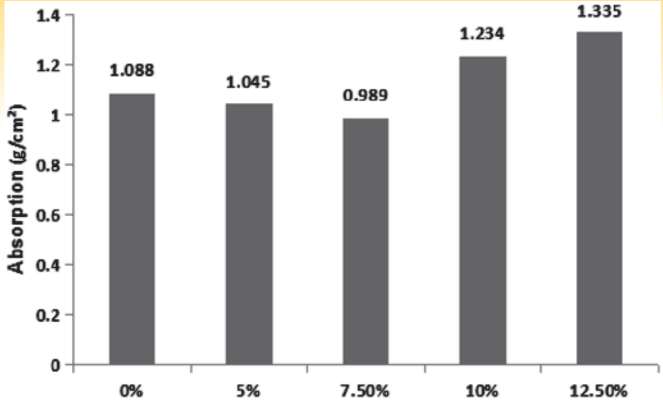

Figure 5
Water absorption by capillarity

Through ANOVA, statistical significance of the variable substitution level in sorptivity was found. Table 6 presents the analysis of influence of this factor.

In Table 6, it is verified that the level of substitution has significant effect over water absorption through capillarity.

It is possible to conclude, based on the analysis of variance, that the hypothesis of the means being equal was rejected and that the effect of the relation of the substitution level is significant, with reliability of 95 %.

Through Tukey's Test, Figure 6, it was found that concrete with 10 % and 12.5 % of replacement of cement by ORW can be considered statistically different from the reference one.

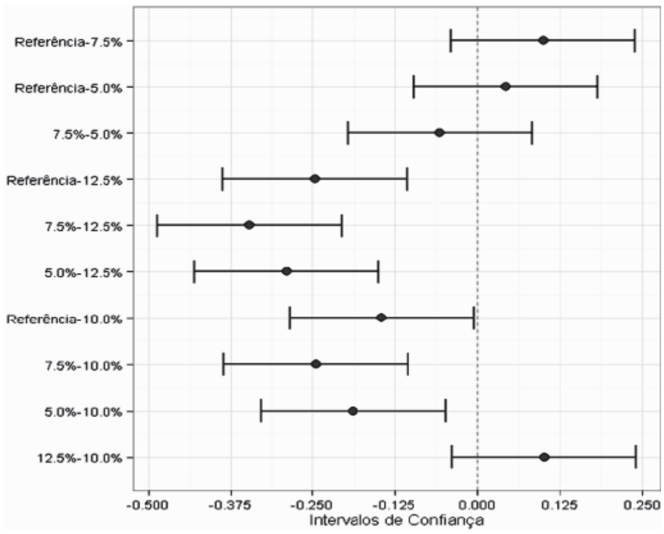

Figure 6
Tukey's test for absorption by capillarity

Table 6
Analysis of variance results – p value – of absorption by capillarity

ANOVA table					
Factor	**DF**	**Sum of squares**	**Average square**	**F-value**	**P-value**
Substitution levels	4	0.244210037	0.061052509	22.57819744	5.42E-05
Residuals	10	0.027040471	0.002704047	—	—

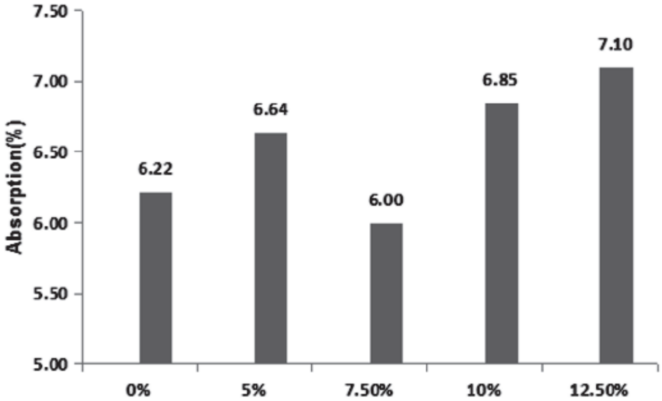

Figure 7
Water absorption by immersion

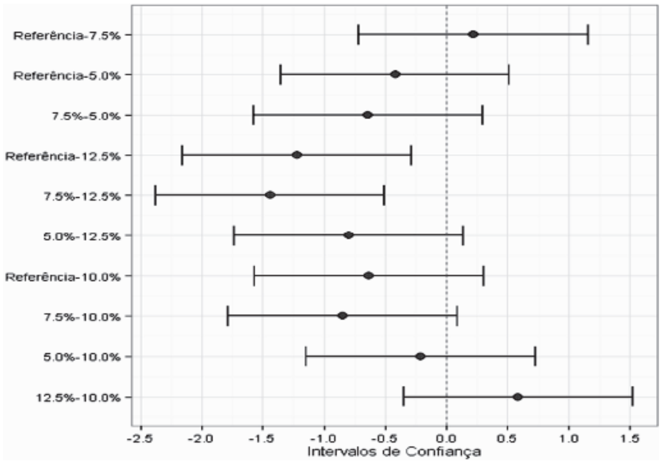

Figure 8
Tukey's Test for absorption by immersion

3.3 Absorption by immersion

Results of the measurement of water absorption by immersion are shown in Figure 7. The trace with 7.5 % substitution of cement by ORW presented better performance, with a decrease of absorption of 3.66 % compared to the reference mixture. All the other substitution levels promoted absorption increase, and the trace with 12.5 % substitution presented the worst performance, with increase of 14.14 % in the absorption tax, compared to the reference trace.
Through ANOVA, statistical significance of the variable replacement level in immersion absorption was found. Table 7 presents the analysis of influence of this factor.
In Table 7, it is verified that the level of replacement has significant effect over water absorption by immersion, indicated by the p-factor of 0.3956 %, below 5 %.
It is possible to conclude, based on the analysis of variance, that the hypothesis of the means being equal was rejected and that the effect of the relation of the substitution level is significant, with reliability of 95 %.
Through Tukey's Test, Figure 8, it was found that concrete with 12.5% of substitution of cement by ORW can be considered statistically different from the reference one.

4. Conclusions

In this work, we aimed to verify the influence of partial substitution of cement by ORW over the physical and mechanical properties of concretes. With the results obtained, it was possible to conclude that:

a) Although reduction of the mechanical properties of concretes with ORW in substitution for cement was observed in 28 days, there was no statistically significant difference regarding compressive strength in substitution values until 10 %;
b) In the sorptivity test, mixtures with 10 % and 12.5 % presented statistically significant differences. These levels promoted increase of the sorptivity tax, in comparison to the reference mix;
c) In the of absorption by immersion test, only the mix with 12.5 % replacement presented statistically significant difference in water absorption. This value promoted increase of the absorption tax, in comparison to the reference mixture;
d) Concretes with 5 % and 7.5 % substitution did not present statistically significant difference in the tests of compressive strength, sorptivity and water absorption by immersion, compared to the reference mixture;
e) The results show that the higher the waste content, the lower the compressive strength and the higher the water absorption rate. However, although smaller than the results obtained for the reference concrete, the compressive strength values indicate the possibility of use as a structural concrete. The results of the study demonstrate the partial replacement of the binder by OWR is satisfactorily feasible.

5. References

1. MEHTA, P. K.; MONTEIRO, P. J. M. kll. New York: McGraw-Hill, 2006. 659 p.
2. EPA - Environmental Protection Agency. National Ambient Air Quality Standards (NAAQS). 2014. Disponível em: https://www.epa.gov/ozone-pollution/2014-national-ambient-air-quality-standards-naaqs-ozone. Acesso em: 04 nov. 2017.

Table 7
Analysis of variance results – p value – of absorption by immersion

ANOVA table					
	Factor	DF	Sum of squares	Average square	F-value
Substitution Levels	4	3.8088	0.9522	7.841339555	0.003956086
Residuals	10	1.214333333	0.121433333	—	—

3. IPCC. Climate Change 2007: The PHysical Science Basis. Intergovernmental Panel on Climate Change (IPCC). Paris: Working Group I contribution to the IPCC Fourth Assessment Report, 2007.
4. Boden, T.A., G. Marland, and R.J. Andres. 2016. Global, Regional, and National FossilFuel CO2 Emissions. Carbon Dioxide Information Analysis Center, Oak Ridge National Laboratory, U.S. Department of Energy, Oak Ridge, Tenn., U.S.A. Disponívelem: Acessoem: 24/09/2017
5. SINDICATO NACIONAL DA INDÚSTRIA DO CIMENTO (Rio de Janeiro). Relatório Anual 2015. Disponível em: http://snic.org.br/assets/pdf/relatorio_anual/rel_anual_2015.pdfAcesso em: 10 mar. 2018.
6. ABIROCHAS (Associação Brasileira da Indústria de Rochas Ornamentais). O setor de rochas ornamentais e de revestimento. Informe 2017. São Paulo. 2017. Disponívelem: .Acessoem: 15 Abril. 2018.
7. ASHISH, D. K. Feasibility of waste marble powder in concrete as partial substitution of cement and sand amalgam for sustainable growth. Journal of Building Engineering, v. 15, n. September 2017, p. 236–242, 2018.
8. Singh, M., Srivastava, A., Bhunia, D., 2017. An investigation on effect of partial replacement of cement by waste marble slurry. Construct. Build. Mater. 134, 471- 488.
9. A. Rana, P. Kalla, L.J. Csetenyi, Sustainable use of marble slurry in concrete, Journal of Cleaner Production, 94 ,2015, 304-311.
10. Bacarji, R.D. Toledo Filho, E.A.B. Koenders, E.P. Figueiredo, J.L.M.P. Lopes, Sustainability perspective of marble and granite residues as concrete fillers, Construction and Building Materials, 45, 2013 1–10.
11. Ergün, A., 2011. Effects of the usage of diatomite and waste marble powder as partial replacement of cement on the mechanical properties of concrete. Construct. Build. Mater. 25, 806 -812.
12. ASSOCIAÇÃO BRASILEIRA DE NORMAS TÉCNICAS (2004d) NBR 10007 – Amostragem de resíduos sólidos. Rio de Janeiro, 21p.
13. ASSOCIAÇÃO BRASILEIRA DE NORMAS TÉCNICAS(2014a) NBR 12653 – Materiais pozolânicos – Requisitos. Rio de Janeiro, 6 p.
14. ASSOCIAÇÃO BRASILEIRA DE NORMAS TÉCNICAS (2001) NBR NM 23 – Cimento portland e outros materiais em pó – Determinação da massa específica. Rio de Janeiro, 5 p.
15. ASSOCIAÇÃO BRASILEIRA DE NORMAS TÉCNICAS (2006) NBR NM 45 – Agregados – Determinação da massa unitária e do volume de vazios. Rio de Janeiro, 8 p.
16. ASSOCIAÇÃO BRASILEIRA DE NORMAS TÉCNICAS (2009b) NBR 7211 – Agregados para concreto – Especificações. Rio de Janeiro, 9p.
17. Helene, P.R.L.; Terzian, P. Manual de dosagem do concreto. PINI: São Paulo (1992).
18. ASSOCIAÇÃO BRASILEIRA DE NORMAS TÉCNICAS (2014) NBR 6118 – Projeto de estruturas de concreto – procedimento. Rio de Janeiro.
19. ASSOCIAÇÃO BRASILEIRA DE NORMAS TÉCNICAS (1994) NBR 5738: Moldagem e cura de corpos-de-prova cilíndricos ou prismáticos de concreto. Rio de Janeiro.
20. AGARWAL, S. K.; GULATI, D. Utilization of industrial wastes and unprocessed microfillers for making cost effective mortars. Construction and Building Materials, v. 20, n. 10, p. 999–1004, 2006.
21. KOCKAL, N. U. Effects of Elevated Temperature and Re-Curing. Transactions of Civil Engineering, v. 37, n. C1, p. 67–76, 2013.
22. RAMOS, T. et al. Granitic quarry sludge waste in mortar: Effect on strength and durability. Construction and Building Materials, v. 47, p. 1001–1009, 2013.
23. ALIABDO, A. A.; ABD ELMOATY, A. E. M.; AUDA, E. M. Re-use of waste marble dust in the production of cement and concrete. Construction and Building Materials, v. 50, p. 28–41, 2014.
24. MUNIR, M. J.; KAZMI, S. M. S.; WU, Y. F. Efficiency of waste marble powder in controlling alkali–silica reaction of concrete: A sustainable approach. Construction and Building Materials, v. 154, p. 590–599, 2017.

Volume 13, Number 3 (June 2020) p. 501 – 514 • ISSN 1983-4195
http://dx.doi.org/10.1590/S1983-41952020000300004

REVISTA IBRACON DE ESTRUTURAS E MATERIAIS
IBRACON STRUCTURES AND MATERIALS JOURNAL

Use of ornamental rock waste as a partial substitute for binder in the production of structural concrete

Uso do resíduo do beneficiamento de rochas ornamentais como substituto parcial ao aglomerante na produção de concretos estruturais

F. R. TEIXEIRA [a]
fernandoteixeira5400@gmail.com
https://orcid.org/0000-0001-8498-9263

F. C. MAGALHÃES [b]
fabiocmagalhaes@gmail.com
https://orcid.org/0000-0001-8463-1501

G. B. WALLY [b]
gustavo.wally@gmail.com
https://orcid.org/0000-0003-3008-3815

F. K. SELL JUNIOR [b]
felixsell@gmail.com
https://orcid.org/0000-0002-6286-5371

C. M. PALIGA [a]
charleipaliga@gmail.com
https://orcid.org/0000-0003-0521-4764

A. S. TORRES [a]
arielatorres@gmail.com
https://orcid.org/0000-0003-4686-9759

Abstract

Due to the population increase, to the improvement of life conditions, to the elevation of levels of consumption and the growing industrialization of developing countries, it is estimated that the production of concrete will present significant increase in the next decades. The process of producing cement is responsible for approximately 5 % of the emissions of CO_2, an expressive environment pollutant. In this context, this work presents an evaluation of the influence of partial substitution of cement by ornamental rock waste (ORW) on the physical and mechanical properties of concrete. ORW from a local marble and granite processing company was used. The waste was mineralogically characterized through X-ray diffraction (XRD) essays, energy-dispersive X-ray (EDX) microanalysis, and physically characterized through laser granulometry and specific mass. For this, was adopted a concrete trace as reference, produced with CP V-ARI cement (similar to ASTM Type III), from IPT dosage. Waste was used in proportions of 5 %, 7.5 %, 10 % and 12.5 % of substitution of cement by mass. Results were treated with ANOVA and multiple comparison of means, indicating a possibility of substitution of until 10% of cement by ORW, creating a concrete with proper resistance to Brazilian regulations regarding the classification as structural.

Keywords: waste management, ornamental rock waste, structural concrete, environmental impacts.

Resumo

Em decorrência do aumento populacional, da melhoria das condições de vida, da elevação dos níveis de consumo e da crescente industrialização dos países em desenvolvimento, estima-se que a produção de concreto apresentará expressivo crescimento ao longo das próximas décadas. O processo de produção do cimento é responsável por aproximadamente 5 % das emissões mundiais de CO_2, poluente que causa danos expressivos no meio ambiente. Neste contexto, este trabalho apresenta uma avaliação da influência da substituição parcial de cimento Portland por resíduo do beneficiamento de rochas ornamentais (RBRO) em propriedades físicas e mecânicas do concreto. Utilizou-se o RBRO proveniente de uma empresa beneficiadora de mármores e granitos localizada na região sul do Rio Grande do Sul. A caracterização mineralógica do resíduo foi realizada por meio de ensaios de difração de raios X (DRX), microanálise de raios X (EDX), enquanto suas características físicas foram analisadas por ensaios de granulometria a laser e de massa específica. Adotou-se um traço de concreto de referência produzido com cimento CP V-ARI, utilizando o método de dosagem do IPT/EPUSP. A substituição do cimento Portland pelo RBRO foi realizada nos teores de 5 %, 7,5 %, 10 % e 12,5 % em relação à massa de cimento. Os resultados foram tratados por ANOVA e comparação múltipla de médias, indicando a possibilidade da substituição de até 7,5 % do cimento pelo RBRO, gerando um concreto com resistência adequada às normas brasileiras e com potencial uso estrutural.

Palavras-chave: aproveitamento de resíduos, resíduo do beneficiamento de rochas ornamentais, concreto estrutural, impactos ambientais.

[a] *Universidade Federal de Pelotas, Programa de Pós-Graduação em arquitetura e urbanismo, Pelotas, RS, Brasil;*
[b] *Universidade Federal do Rio Grande, Programa de Pós-Graduação em Engenharia Oceânica, Rio Grande, RS, Brasil.*

Received: 05 Aug 2019 • Accepted: 10 Dec 2019 • Available Online: 26 May 2020

1. Introdução

O concreto é o material de construção mais utilizado no mundo, com uma produção anual estimada em 23 bilhões de toneladas, o que corresponde a um consumo médio de aproximadamente 10 kg de concreto por pessoa por dia [1]. A fabricação de cimento, em particular, apresenta um considerável impacto ambiental devido ao elevado consumo energético e às emissões de gases do efeito estufa, principalmente o dióxido de carbono [2-3].
Em 2016, as indústrias cimenteiras foram responsáveis por 5,6 % da emissão de CO_2 de todo o mundo. Se comparado com dados do ano de 2013, as emissões devidas à queima de combustíveis fósseis para a produção do cimento apresentaram um crescimento de 1,2 % [4]. A emissão de CO_2 na produção do cimento Portland comum é composta de duas fontes: a descarbonatação do carbonato de cálcio ($CaCO_2$), que libera aproximadamente 528 kg CO_2/ton. de cimento, e a queima de combustíveis fósseis, responsável pela emissão de cerca de 367 kg CO_2/ton. de cimento, totalizando, aproximadamente, 895 kg de CO_2/t cimento [5].
Os grandes impactos ambientais gerados pela indústria cimenteira fomentam a busca por alternativas que tornem a produção do concreto menos agressiva à natureza. Diversas pesquisas têm apresentado resultados positivos ao avaliar a incorporação de resíduos do setor industrial em concretos, uma vez que esses resíduos podem aumentar a resistência mecânica e as propriedades relacionadas à durabilidade do concreto.
Diante do exposto, a incorporação de resíduos industriais no concreto desponta como uma alternativa para minimizar os impactos ambientais decorrentes da produção do cimento. Entre esses resíduos está o do beneficiamento de rochas ornamentais (RBRO), subproduto da produção de rochas ornamentais e que tem apresentado potencial para ser utilizado em concretos como substituinte parcial ao aglomerante.
Segundo a Associação Brasileira da Indústria de Rochas Ornamentais (ABIROCHAS) [6], em 2017 a produção de rochas no Brasil foi de aproximadamente 9,24 Mt, sendo 1,046 Mt para exportação. Deve se destacar que 41 % dos blocos, em volume, são transformados em rejeitos, produzindo 3,36 Mt de material a ser descartado durante o processamento das rochas ornamentais. Assim, é evidente que o processo de beneficiamento de rochas ornamentais é arcaico, quase artesanal, e que possui poucos investimentos com vistas à redução da geração exorbitante de resíduo durante o processo de processamento das rochas.
Nesse contexto, a problemática ambiental exposta demonstra que é necessário intensificar os estudos sobre o RBRO, com o objetivo de produzir materiais que o incorporem e, assim, propiciem a mitigação de seu impacto ambiental.
Vários pesquisadores, como Ashish [7], Singh *et al.* [8], Rana *et al.* [9], Bacarji *et al.* [10] e Ergun [11], têm demonstrado a viabilidade do RBRO como substituto parcial ao aglomerante na produção de concretos. A maioria desses estudos, no entanto, se concentram apenas na resistência mecânica. Considerando que o concreto é um material hidrófilo, estudos que avaliem propriedades relacionadas à durabilidade do concreto, como a absorção de água, são essenciais na investigação acerca da viabilidade do uso do RBRO como substituto ao cimento Portland na produção de concretos estruturais.
Desta maneira, neste trabalho adotou-se um traço de concreto produzido com cimento Portland de Alta Resistência Inicial (CP V-ARI), por conter o maior teor de clínquer dentre os cimentos disponíveis no mercado regional (sul do Brasil) e, assim, consistir em um cimento "mais puro" em termos de adições minerais, e investigou-se a viabilidade do uso do resíduo do beneficiamento de rochas ornamentais (RBRO) como substituinte parcial ao cimento na produção de concretos para fins estruturais. O resíduo foi utilizado em proporções de 5 %, 7,5 %, 10 % e 12,5 % de substituição em relação à massa de cimento.

2. Materiais e métodos

A seguir são apresentadas as características dos materiais utilizados na confecção dos concretos estudados e os métodos utilizados na realização dos ensaios.

2.1 Resíduo do beneficiamento de rochas ornamentais

O RBRO, coletado na forma de lama, foi gerado por uma empresa local de beneficiamento de rochas ornamentais. A coleta, segundo a NBR 10007 [12], foi feita diretamente do tanque de decantação da empresa, sendo que todo material utilizado no trabalho foi coletado no mesmo dia. Após a coleta, o material passou por um processo de homogeneização e quarteamento para a obtenção de uma amostra representativa. Na sequência, a lama do RBRO foi colocada em estufa, onde permaneceu por 48 h a uma temperatura de 100 °C. Em seguida, o resíduo foi passado na peneira de abertura 1,18 mm, para retirada de eventuais impurezas e destorroamento, eliminando, desta forma, a necessidade de moagem. Uma vez destorroado, o resíduo foi passado na peneira de abertura da malha de 300 μm e armazenado em sacos, estando pronto para ser utilizado.
A granulometria do RBRO foi determinada em granulômetro a laser marca Cilas modelo 1064. Na Figura 1 estão apresentados os dados obtidos no ensaio de granulometria a laser. A análise da curva mostra que o diâmetro médio de partícula do RBRO é de 30,95 μm.

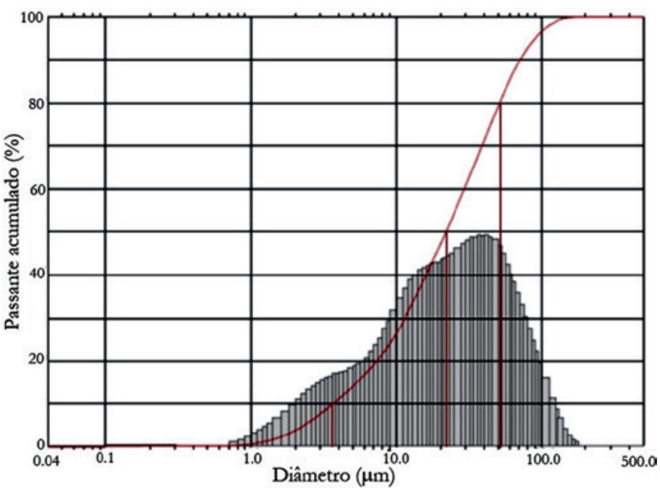

Figura 1
Curvas de distribuição granulométrica do RBRO

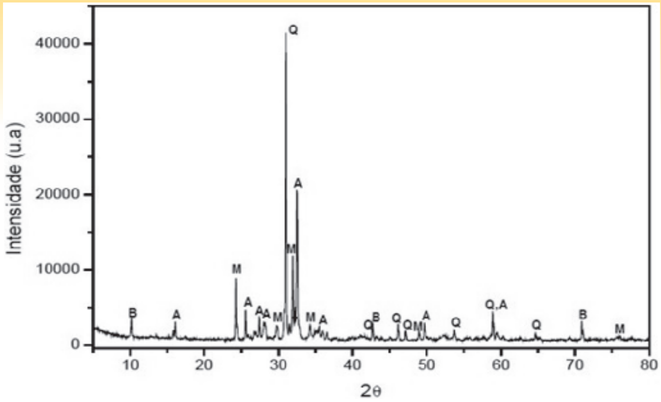

Figura 2
Difratograma de raios X obtido para amostra de RBRO

Tabela 1
Composição química do RBRO

Elemento	Teor (%)
SiO_2	34,085
K2O	20,287
Al_2O_3	18,77
Fe_2O_3	12,57
CaO	12,181
TiO_2	1,444
MnO	0,178
ZnO	0,122
ZrO_2	0,118
SrO	0,103
CuO	0,101
Rb_2O	0,024
Y_2O_3	0,006

Para identificar a presença de elementos cristalinos na composição do RBRO foi realizada análise de difração de raios X (DRX) utilizando difratômetro Shimadzu, modelo XRD 6000, operando com radiação de CuKα (=1,5418 Å) e monocromador de grafite, operando a uma tensão de 40 kV e corrente de 30 mA, na faixa de varredura de 5 a 80º e velocidade angular de 2º/min. A Figura 2 apresenta o difratograma de raios X do resíduo.
Analisando os resultados obtidos a partir do DRX, verifica-se que o RBRO utilizado é constituído principalmente por quartzo (Q) e Albita (A). Podem ser observados, também, picos menos intensos de Microclina (M) e Biotita (B). Através do ensaio é constatada a não pozolanicidade do RBRO em decorrência do mesmo apresentar um pico cristalino bem definido referente ao quartzo (SiO_2) e ausência de halo amorfo. Assim, o RBRO age principalmente como agente de nucleação no interior da microestrutura.
Para determinação da composição química do RBRO utilizou-se um espectrômetro de fluorescência de raios x por dispersão de energia, modelo Shimadzu EDX-720. Na Tabela 1 está apresentado o resultado deste ensaio. Segundo a NBR 12653 [13], a soma dos óxidos SiO_2, Al_2O_3 e Fe_2O_3 deve ser superior a 70 % para que o material analisado seja considerado pozolânico. A soma dos mesmos foi de 62,42 %, desta forma, de acordo com a NBR 12653 [13], o material não é considerado pozolânico, apresentando apenas efeito físico, o que corrobora com o que foi discutido anteriormente.
Na Tabela 2 estão os resultados dos ensaios de massa específica real do RBRO, através da NBR NM 23 [14] e da sua massa unitária conforme a NBR NM 45 [15].

2.2 Cimento

O cimento utilizado cimento Portland de Alta Resistência Inicial (CP V-ARI), tendo sido escolhido pelo seu uso difundido na região sul do Rio Grande do Sul devido ao fato de conter o maior teor de clínquer dentre os cimentos disponíveis e, assim, facilitar a compreensão da ação do RBRO, evitando efeitos combinados e possibilitando uma visualização mais clara dos efeitos da substituição do cimento pelo RBRO no concreto.

2.3 Agregados

Foi utilizada uma areia natural quartzosa de granulometria média, enquadrada na zona utilizável da NBR 7211 [16], seca em estufa até constância de massa. A brita granítica utilizada foi classificada como

Tabela 2
Caracterização dos agregados e do RBRO

Tipo de ensaio		Agregado miúdo	Agrega-do graúdo	RBRO
Composição granulométrica/ NBR NM 248 (ABNT, 2003)	Ø máximo (mm)	4,75	19	—
	Módulo de finura	2,84	4,69	—
Massa específica (g/cm³) / NBR NM 52 (ABNT, 2009) e NBR NM 53 (ABNT,2009)		2,62	2,6	2,64
Massa unitária solta (g/cm³) / NBR NM 45 (ABNT, 2006)		1,55	1,41	1,16

Tabela 3
Traços unitários utilizados

Traço	Cimento (kg)	RBRO (kg)	Areia (kg)	Brita (kg)	Fator a/c
Referência	1	0	2,4	3,28	0,60
5%	0,95	0,05	2,4	3,28	0,60
7,50%	0,925	0,075	2,4	3,28	0,60
10%	0,9	0,1	2,4	3,28	0,60
12,50%	0,875	0,125	2,4	3,28	0,60

Tabela 4
Metodologia dos ensaios realizados

Ensaio		Detalhes	Metodologia
Mecânico	Resistência à compressão	5 amostras por traço idades: 3, 7 e 28 dias	NBR 5739 (2007)
Físicos	Absorção de água por imersão	3 amostras por traço idade: 28 dias	NBR 9778 (2009)
	Absorção de água por capilaridade	3 amostras por traço idade: 28 dias	NBR 9779 (2009)

Tabela 5
Resultado de análise de variância – valor p – da resistência à compressão

Tabela da ANOVA					
Fator	**G.L.**	**Soma de quadrados**	**Quadrado médio**	**Estat. F**	**p-valor**
Teor de substituição	4	78,88236	19,72059	6,928441737	0,000118253
Idade	2	1241,111976	620,555988	218,0201509	3,01E-28
Teor de substituição x Idade	8	20,215224	2,526903	0,887777709	0,532279889
Resíduos	60	170,77944	2,846324	—	—

brita 1 segundo a NBR 7211 [16]. Os resultados da caracterização física obtidos dos agregados naturais estão apresentados na Tabela 2.

2.4 Produção e avaliação dos concretos

Para a dosagem dos concretos utilizou-se a metodologia do IPT/EPUSP [17]. Através de procedimento experimental definiu-se o teor de argamassa seca ideal em 51 % (α = 0,51) e a quantidade de água necessária para a obtenção do abatimento do tronco de cone em 70 ± 10 mm.
Através das equações de dosagem e do valor pré-estabelecido da relação água/cimento de 0,60, foi determinado o traço de referência do concreto, conforme Tabela 3. A relação água/cimento igual a 0,60 foi definida por ser o valor máximo considerado para um concreto estrutural, localizado em ambiente urbano (CAA II), de acordo com a NBR 6118 [18]. A partir do traço de referência foi realizada a substituição parcial do cimento pelo RBRO em teores de 5 %, 7,5 %, 10 % e 12,5 %. A escolha desses teores foi baseada em estudos realizados por Singh et al. [8], Rana et al. [9], Bacarji et al. [10] e Ergun [11].
Na Tabela 4 são detalhadas todas as propriedades estudadas neste trabalho, bem como a quantidade de amostras e as normas utilizadas nos procedimentos. Todos os corpos de prova foram moldados e curados conforme prescrito pela NBR 5738 [19].
Por fim, para se entender os resultados obtidos em termos de propriedades físicas e mecânicas dos concretos, e se as variáveis independentes analisadas (idade e teores de substituição) possuem importância na alteração dos mesmos, esses foram submetidos a tratamento estatístico por análise de variância (ANOVA) e comparação múltipla de médias (Teste de Tukey). A primeira análise, quando indica significância, dá a certeza de que existe no mínimo um par de médias diferentes, mas sem se saber quantas e quais. Assim, a segunda análise (Teste de Tukey) se faz necessária, onde, para se determinar quis os pares de médias são diferentes entre si, foi feita a comparação de médias de duas a duas.

3. Resultados e discussões

3.1 Resistência à compressão

As médias dos resultados de resistência à compressão ao longo das idades são apresentadas na Figura 3. Nas primeiras idades, com exceção do teor de 12,5 %, os traços com substituição do cimento pelo RBRO proporcionaram maior resistência que o traço de referência, o que demonstra a atuação física do resíduo, uma vez que nesse momento, a maior parte das reações pozolânicas ainda não ocorreu. O efeito físico do RBRO acelera a hidratação do cimento ao possuir partículas extremamente finas e atuar como ponto de nucleação para a formação do hidróxido de cálcio, acelerando as reações e formando menos cristais de hidróxido de cálcio.
Através da análise estatística ANOVA foi constatada a significância estatística das variáveis relacionadas, sendo elas o “teor de substituição” e “idade” na resistência à compressão axial. Na Tabela 5 estão apresentadas a análise de influência dos fatores e suas interações. Verifica-se que o teor de substituição e a idade de ensaio analisados separadamente possuem efeito significativo sobre a resistência à compressão axial. Entretanto, não existe influência significativa entre o teor de substituição e a idade. Essa inexistência de interação demonstra que a substituição não provoca aumentos significativos ao longo do tempo. Esse comportamento já era esperando, uma vez que o resíduo não possui atividade pozolânica. Ademais, é possível observar que o valor p é menor do que o nível de significância especificado (α = 0,05). Portanto a hipótese nula, que significa a igualdade entre as médias das resistências, é rejeitada. Deste modo, o teste de Tukey foi aplicado para se ter uma análise duas a duas das médias e se

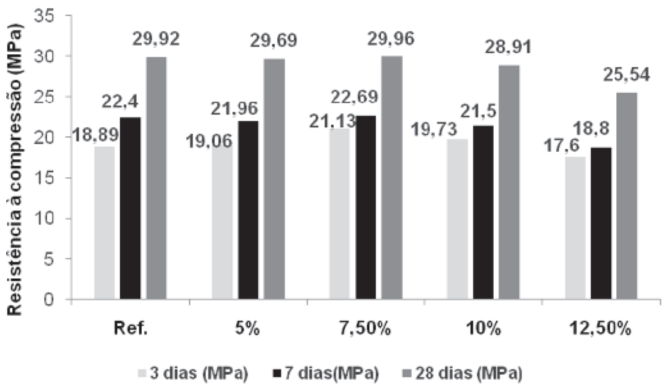

Figura 3
Resistência à compressão axial

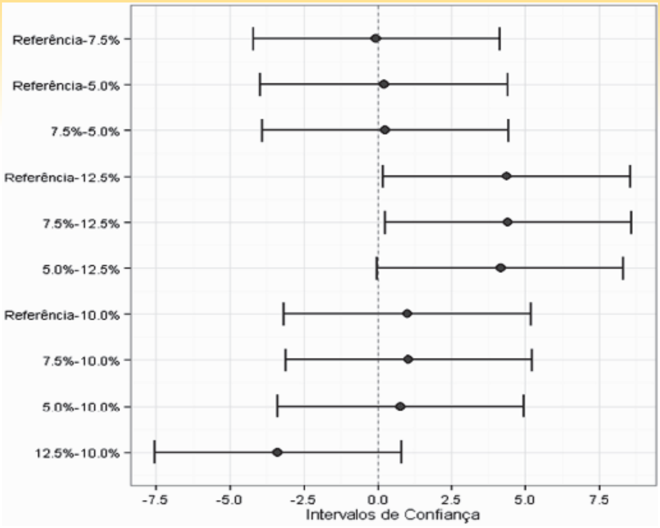

Figura 4
Teste de Tukey para a resistência à compressão aos 28 dias

chegar à conclusão de quais são diferentes entre si. Os resultados obtidos são exibidos na Figura 4.
Ao serem analisados os resultados obtidos pelo teste de Tukey (Figura 4) é possível observar que aos 28 dias, somente o concreto com 12,5 % de substituição do cimento pelo RBRO pode ser considerado estatisticamente diferente do concreto de referência, com significância superior a 95 %. Nesse teor de substituição, o efeito cimentante demonstrou ser preponderante em relação ao efeito *filler*, acarretando uma queda na resistência em comparação ao traço de referência. Apesar do concreto com 10 % de substituição apresentar redução na resistência à compressão em comparação ao concreto de referência, este decréscimo de resistência não pode ser considerado significativo quando adotado um nível de confiabilidade de 95 %.
Os resultados obtidos corroboram com os trabalhos de Ergun [11]; Agarwal; Gulati [20]; Kockal [21]; Ramos *et al.* [22]; Aliabdo *et al.* [23]; Munir *et al.* [24] e Ashish [7], que obtiveram aumento de resistência à compressão substituindo cimento por resíduo de rochas ornamentais nas porcentagens de 5 % e 7,5 %.

3.2 Absorção de água por Capilaridade

Os resultados do ensaio de absorção de água por capilaridade estão apresentados na Figura 5. O ensaio demonstrou uma redução na taxa de absorção nos teores de substituição de 5 % e 7,5 %, sendo o teor de 7,5 % o que apresentou melhor desempenho (redução de 10 %). Por outro lado, a substituição de 12,5 % apresentou os piores resultados, resultando em um aumento de 22,70 % na taxa de absorção. Nesse teor de substituição o efeito cimentante demonstrou ser preponderante em relação ao efeito *filler*, acarretando um aumento na taxa de absorção de água.

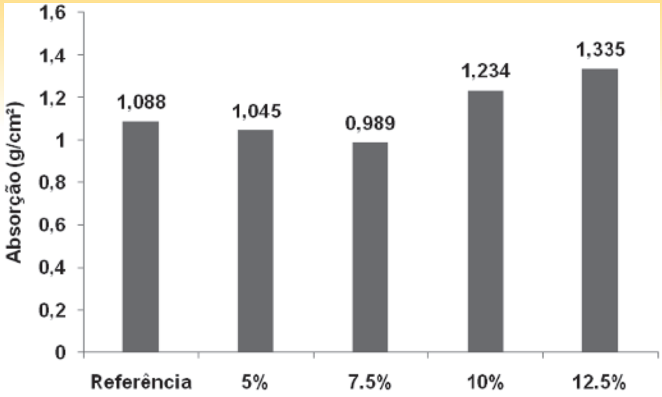

Figura 5
Absorção de água por capilaridade

Através da ANOVA foi constatada a significância estatística da variável “teor de substituição” na absorção capilar. Na Tabela 6 está apresentada a análise de influência dos fatores, verificando-se que o teor de substituição possui efeito significativo sobre a absorção de água por capilaridade, indicado pelo p-fator abaixo do limite de 5 %
Pode-se concluir, com base nas análises de variância, que a hipótese de as médias serem iguais foi rejeitada e que o efeito da relação teor de substituição é significante para um nível de confiabilidade de 95 %.
Através do teste de Tukey, apresentado na Figura 6, verifica-se que os concretos com 10 % e 12,5 % de substituição do cimento pelo RBRO podem ser considerados estatisticamente diferentes do concreto de referência. Todos os outros teores de substituição não podem ser considerados estatisticamente diferente do concreto de referência, com significância superior a 95 %.

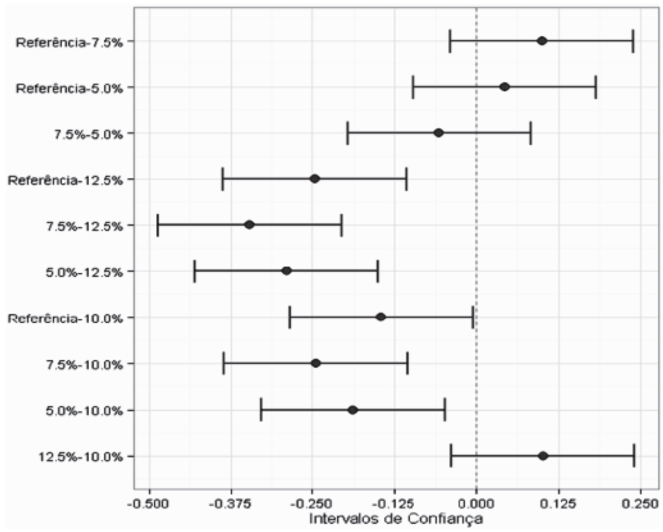

Figura 6
Teste de Tukey para a absorção por capilaridade

Tabela 6
Resultado de análise de variância – valor p – da absorção por capilaridade

Tabela da ANOVA					
Fator	**G.L.**	**Soma de quadrados**	**Quadrado médio**	**Estat. F**	**p-valor**
Teor de substituição	4	0,244210037	0,061052509	22,57819744	5,42E-05
Resíduos	10	0,027040471	0,002704047	—	—

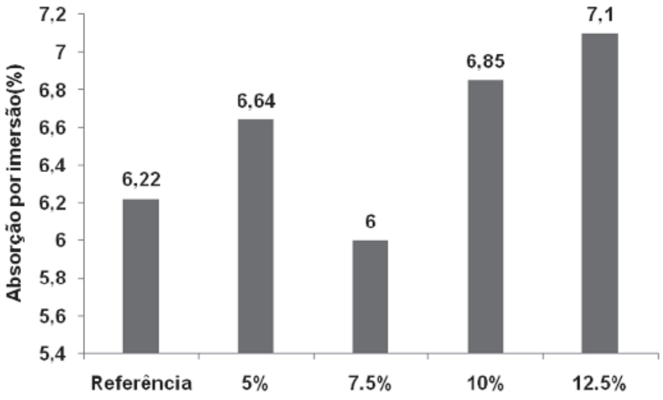

Figura 7
Absorção de água por imersão

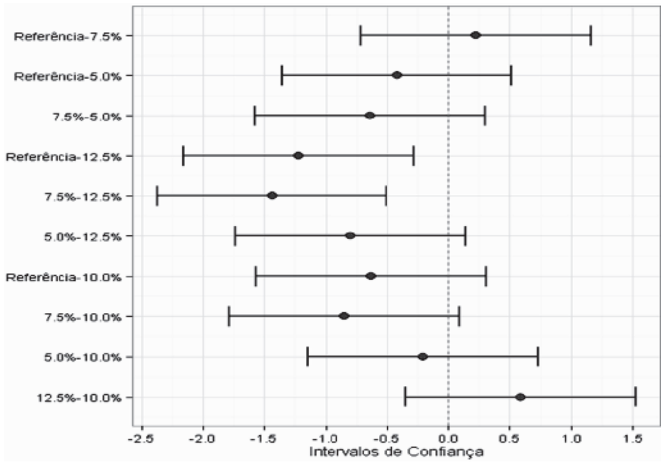

Figura 8
Teste de Tukey para a absorção por imersão

3.3 Absorção de água por imersão

Os resultados das medições de absorção de água por imersão são mostrados na Figura 7. O traço com substituição de 7,5 % do cimento pelo RBRO apresentou melhor desempenho, com diminuição da absorção de 3,66 % em relação ao traço de referência. Todos os outros teores de substituição promoveram um aumento na absorção, sendo que o traço com 12,5 % apresentou o pior desempenho, com um aumento de 14,14 % na taxa absorção em relação ao traço de referência.
Através da ANOVA foi constatada a significância estatística da variável “teor de substituição” na absorção por imersão. Na Tabela 7 está apresentada a análise de influência dos fatores, onde pode ser verificado que o teor de substituição possui efeito significativo sobre a absorção de água por imersão, indicado pelo p-valor de 0,3956 %, inferior a 5 %. Pode-se concluir, com base nas análises de variância, que a hipótese de as médias serem iguais foi rejeitada, e que os efeitos da relação teor de substituição são significantes ao nível de confiança de 95 %.
Através do teste Tukey, Figura 8, ficou constatado que somente o concreto com 12,5 % de substituição do cimento pelo RBRO pode ser considerado estatisticamente diferente do concreto de referência quanto à absorção de água por imersão.

4. Conclusões

Neste trabalho procurou-se verificar a influência exercida pela substituição parcial do cimento pelo RBRO nas propriedades físicas e mecânicas de concretos para fins estruturais. Vale ressaltar que para uso do RBRO em um estado físico adequado, se fez necessária uma preparação do material. No entanto, como a utilização desse resíduo está em estudo, para ser inserido em outros componentes, primeiro há necessidade de viabilizar seu uso para, após, novos estudos investigarem metodologias que proporcionem seu uso de maneira mais veloz. Tendo em vista os resultados obtidos, foi possível concluir que:

a) Apesar de ter sido observada aos 28 dias redução nas propriedades mecânicas dos concretos que empregaram RBRO em substituição ao cimento, não foram detectadas diferenças estatisticamente significativas na resistência à compressão em teores de substituição de até 10 %;
b) No ensaio de absorção de água por capilaridade, os traços com 10 % e 12,5 % apresentaram diferenças estatisticamente significativas, promovendo um aumento na taxa de absorção em relação ao traço de referência;
c) No ensaio de absorção de água por imersão, apenas o traço com 12,5 % de substituição apresentou diferença estatisticamente significativa na taxa de absorção promovendo um incremento na taxa de absorção em relação ao traço de referência.
d) Os concretos com 5 % e 7,5 % de substituição não apresentaram diferença estatística significativa nos ensaios de resistência à compressão, absorção de água por capilaridade e absorção de água por imersão, em relação ao traço de referência.
e) Os resultados demostram que quanto maior o teor de resíduo, menor a resistência à compressão e maior a taxa de absorção de água. Todavia, ainda que menores que os resultados obtidos para o concreto referência, os valores de resistência à compressão indicam a possibilidade de uso como concreto estrutural. Os resultados do estudo demonstram que a

Tabela 7
Resultado de Análise de Variância – valor p– da absorção por imersão

ANOVA table					
	G.L.	**Soma de quadrados**	**Quadrado médio**	**Estat. F**	**p-valor**
Teor de substituição	4	3,8088	0,9522	7,841339555	0,003956086
Resíduos	10	1,214333333	0,121433333	—	—

substituição parcial do aglomerante por RBRO é satisfatoriamente viável.

5. Referências bibliográficas

1. MEHTA, P. K.; MONTEIRO, P. J. M. kll. New York: McGraw-Hill, 2006. 659 p.
2. EPA - Environmental Protection Agency. National Ambient Air Quality Standards (NAAQS). 2014. Disponível em: https://www.epa.gov/ozone-pollution/2014-national-ambient-air-quality-standards-naaqs-ozone. Acesso em: 04 nov. 2017.
3. IPCC. Climate Change 2007: The PHysical Science Basis. Intergovernmental Panel on Climate Change (IPCC). Paris: Working Group I contribution to the IPCC Fourth Assessment Report, 2007.
4. Boden, T.A., G. Marland, and R.J. Andres. 2016. Global, Regional, and National FossilFuel CO2 Emissions. Carbon Dioxide Information Analysis Center, Oak Ridge National Laboratory, U.S. Department of Energy, Oak Ridge, Tenn., U.S.A. Disponívelem: Acessoem: 24/09/2017
5. SINDICATO NACIONAL DA INDÚSTRIA DO CIMENTO (Rio de Janeiro). Relatório Anual 2015. Disponível em: http://snic.org.br/assets/pdf/relatorio_anual/rel_anual_2015.pdfAcesso em: 10 mar. 2018.
6. ABIROCHAS (Associação Brasileira da Indústria de Rochas Ornamentais). O setor de rochas ornamentais e de revestimento. Informe 2017. São Paulo. 2017. Disponívelem: .Acessoem: 15 Abril. 2018.
7. ASHISH, D. K. Feasibility of waste marble powder in concrete as partial substitution of cement and sand amalgam for sustainable growth. Journal of Building Engineering, v. 15, n. September 2017, p. 236–242, 2018.
8. Singh, M., Srivastava, A., Bhunia, D., 2017. An investigation on effect of partial replacement of cement by waste marble slurry. Construct. Build. Mater. 134, 471- 488.
9. A. Rana, P. Kalla, L.J. Csetenyi, Sustainable use of marble slurry in concrete, Journal of Cleaner Production, 94 ,2015, 304-311.
10. Bacarji, R.D. Toledo Filho, E.A.B. Koenders, E.P. Figueiredo, J.L.M.P. Lopes, Sustainability perspective of marble and granite residues as concrete fillers, Construction and Building Materials, 45, 2013 1–10.
11. Ergün, A., 2011. Effects of the usage of diatomite and waste marble powder as partial replacement of cement on the mechanical properties of concrete. Construct. Build. Mater. 25, 806 -812.
12. ASSOCIAÇÃO BRASILEIRA DE NORMAS TÉCNICAS (2004d) NBR 10007 – Amostragem de resíduos sólidos. Rio de Janeiro, 21p.
13. ASSOCIAÇÃO BRASILEIRA DE NORMAS TÉCNICAS(2014a) NBR 12653 – Materiais pozolânicos – Requisitos. Rio de Janeiro, 6 p.
14. ASSOCIAÇÃO BRASILEIRA DE NORMAS TÉCNICAS (2001) NBR NM 23 – Cimento portland e outros materiais em pó – Determinação da massa específica. Rio de Janeiro, 5 p.
15. ASSOCIAÇÃO BRASILEIRA DE NORMAS TÉCNICAS (2006) NBR NM 45 – Agregados – Determinação da massa unitária e do volume de vazios. Rio de Janeiro, 8 p.
16. ASSOCIAÇÃO BRASILEIRA DE NORMAS TÉCNICAS (2009b) NBR 7211 – Agregados para concreto – Especificações. Rio de Janeiro, 9p.
17. Helene, P.R.L.; Terzian, P. Manual de dosagem do concreto. PINI: São Paulo (1992).
18. ASSOCIAÇÃO BRASILEIRA DE NORMAS TÉCNICAS (2014) NBR 6118 – Projeto de estruturas de concreto – procedimento. Rio de Janeiro.
19. ASSOCIAÇÃO BRASILEIRA DE NORMAS TÉCNICAS (1994) NBR 5738: Moldagem e cura de corpos-de-prova cilíndricos ou prismáticos de concreto. Rio de Janeiro.
20. AGARWAL, S. K.; GULATI, D. Utilization of industrial wastes and unprocessed microfillers for making cost effective mortars. Construction and Building Materials, v. 20, n. 10, p. 999–1004, 2006.
21. KOCKAL, N. U. Effects of Elevated Temperature and Re-Curing. Transactions of Civil Engineering, v. 37, n. C1, p. 67–76, 2013.
22. RAMOS, T. et al. Granitic quarry sludge waste in mortar: Effect on strength and durability. Construction and Building Materials, v. 47, p. 1001–1009, 2013.
23. ALIABDO, A. A.; ABD ELMOATY, A. E. M.; AUDA, E. M. Re-use of waste marble dust in the production of cement and concrete. Construction and Building Materials, v. 50, p. 28–41, 2014.
24. MUNIR, M. J.; KAZMI, S. M. S.; WU, Y. F. Efficiency of waste marble powder in controlling alkali–silica reaction of concrete: A sustainable approach. Construction and Building Materials, v. 154, p. 590–599, 2017.

Volume 13, Number 3 (June 2020) p. 515 – 542 • ISSN 1983-4195
http://dx.doi.org/10.1590/S1983-41952020000300005

IBRACON

REVISTA IBRACON DE ESTRUTURAS E MATERIAIS
IBRACON STRUCTURES AND MATERIALS JOURNAL

Experimental analysis of longitudinal shear of composite slabs

Análise experimental do cisalhamento longitudinal de lajes mistas

G. F. J. BRITTO [a]
guilhermino.f@hotmail.com
https://orcid.org/0000-0003-0705-1997

V. S. SILVA [a]
vanessass@ufba.br
https://orcid.org/0000-0003-2478-2353

J. P. GONÇALVES [a]
jardelpg@gmail.com
https://orcid.org/0000-0003-3484-3869

Abstract

The composite concrete slab systems with steel-deck incorporated has become an alternative to conventional slab models, since it often does not require the use of shoring, promoting several constructive practices, beyond operation of the reinforcement as a positive moment. The procedure of verification of composite slabs is based on the semi-empirical method m and k. The purpose of this paper was to investigate the application of the "m-k method" in a group of slabs with alternative dimensions as the usually adopted in the tests, even as to correlate the values obtained with the results found when testing the models as proposed by the ANSI 2011 test standard, since the normative method is costly and expensive. Therefore, four-point flexural tests were performed on slab models considering only one deck module, varying two spans, the same procedure was repeated in slabs with usual construction dimensions (normative models). The linear regression method was applied to the data found in order to obtain the parameters that would be analyzed. The main results show that the alternative model with the adopted dimensions does not present values that can be applied directly to the normative models, since the increase of the shear span reduces in a significant way the theoretical resistance of the slabs. Nevertheless, the values for the m and k obtained of both alternative and normative models can be adopted confidently as part of the sizing process of the respective models. The deviations between theoretical and experimental resistance satisfy the specifications of the ANSI 2011 standard for both models helped in the confirmation of the previous statement. The expectation of this paper is to assist in the search for new procedures for determining parameters m and k.

Keywords: alternative and normative models, m- k method, longitudinal shear, composite slabs.

Resumo

O sistema de lajes mistas de concreto com fôrma de aço incorporada tem se tornado uma alternativa aos modelos de lajes convencionais, pois muitas vezes dispensa o uso de escoramentos, promovendo diversas praticidades construtivas, além do funcionamento da fôrma como armadura de momento positivo. O procedimento de verificação das lajes mistas está fundamentado no método semi-empírico *m-k*. Este documento buscou investigar a aplicação do *"método m-k"* em um grupo de lajes com dimensões alternativas às usualmente adotadas nos ensaios, assim como correlacionar os valores obtidos com os resultados encontrados ao ensaiar os modelos conforme proposto pela norma de ensaio ANSI 2011, já que o método normativo é custoso e oneroso. Para tanto, foram realizados ensaios à flexão de quatro pontos em modelos de lajes considerando apenas um módulo de "*deck*", variando dois vãos; o mesmo procedimento foi repetido nas lajes com dimensões usuais de construção (modelos normativos). Aplicou-se o método de regressão linear nos dados encontrados a fim de obter os parâmetros que seriam analisados. Os principais resultados encontrados demonstram que o modelo alternativo não apresenta valores que possam ser aplicados aos modelos normativos, uma vez que o aumento do vão de cisalhamento reduz de forma significativa a resistência teórica das lajes. Porém os valores obtidos para *m* e *k*, tanto dos modelos alternativos, quanto normativos, podem ser adotados confiadamente como parte do processo de dimensionamento dos respectivos modelos. Os desvios entre a resistência teórica e experimental satisfazem as especificações da norma ANSI 2011 para ambos os modelos auxiliando a confirmação da afirmação anterior. Espera-se com esse trabalho auxiliar a pesquisa de novos procedimentos para determinação dos parâmetros *m* e *k*.

Palavras-chave: modelos alternativos e normativos, método *m-k*, cisalhamento longitudinal, sistema misto.

[a] *Universidade Federal da Bahia, Programa de Pós Gradução em Engenharia de Estruturas da Escola Politécnica, Salvador, BA, Brasil.*

Received: 19 Feb 2019 • Accepted: 08 Dec 2019 • Available Online: 26 May 2020

1. Introduction

The composite slab systems consist of a steel profield cold formed associated with the concrete. The composite behavior of slab is configured when the steel profield and the concrete, in the hardened state, if connect forming a single structure element. The interaction between cold formed profile and concrete cape was must be capable of transmitting forces at the interface being responsible for the effectiveness of the composite system. The geometry of the cross-section of the steel form and the arrangement of the dents surface slabs directly influence the structural behavior of the composite slabs, since the dents present on the form surface are fundamental for the mechanical connection between the concrete cape and the steel deck, Baião Filho [1]. The forces developed at the interface are main responsible for breaking this mechanical connection between the profield cold formed and the concrete cover. Currently, two methods are usually adopted to verify the interface shear strength of this system, which are the partial interaction method and the semi-empirical method *m-k*, which is the most used and main object of study of this work.

The use of the composite concrete slab systems with steel-deck incorporated requires a good comprehension of the behavior of the materials that compose the slab as well as the mechanical properties that guide it. Considering the usual profiles and spans, this system has a predominant collapse mode, the longitudinal shear, and it is necessary to use the methods mentioned above to calculate its resistant capacity. The "*m-k* method" consists in obtaining two sizing parameters, angular (*m*) and linear (*k*) coefficients of a line constructed from a semi-empirical equation that relates the nominal shear strength resistance with parameters obtained in the test. A variation of the application of the commonly used "m-k method" was proposed and developed in this work: the investigation and validation of the method applicability in models with only one deck

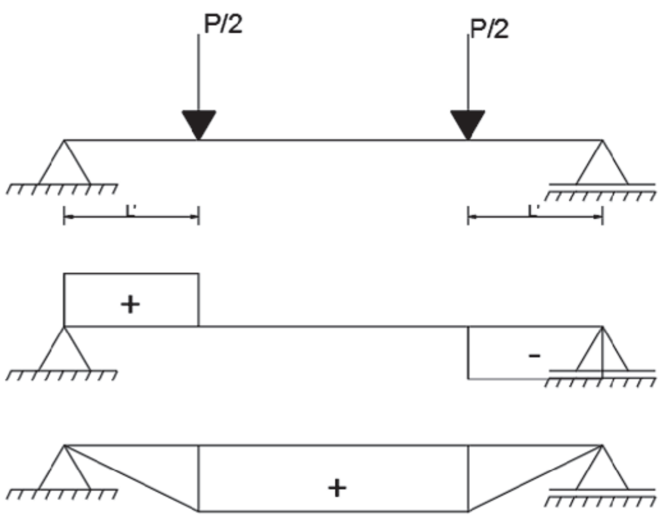

Figure 1
Four point bending test model with shear and bending diagrams
Source: The Author

module, observing the representativity of the values found when compared with the test values whose models are in accordance with the proposition of the ANSI standard [2]. As this is a new application of the "m-k method", it became necessary to correlate and compare the results and behaviors presented with those that occur in the application of the method to models proposed by norm, with purpose of verify the validity of the application of the results before models of different geometric characteristics. Several researchers have evaluated the influence of longitudinal shear on the composite system, based on normative scale models submitted to the four-point bending test. This test consists of submit a sample to the action of two concentrated loads of the same intensity, equidistant from the supports, where the region of the sample between the load and the support is submit to bending and shear forces while the region between the loads is subjected to pure bending (figure 1). Regarding the research done, Abdullah & Easterling [3] proposed a new method to model the horizontal shear connection in composite slabs; Campos [4] evaluated the effect of continuity in composite slabs; Costa [5] analyzed the influence of friction on the supports in the calculation of longitudinal shear strength. There are also studies on smaller scale models, such as the work of Daniels & Crisinel [6], which developed a numerical method of analysis that only requires push-off and pull-out shear tests. Although existing literature proposes that short and big height composite slabs can transfer loads directly to the supports, according to the connecting rod and tether pattern, and that extrapolation of results may against to safety values, Johnson & Anderson [7], it was not possible for the authors to find analysis and experimental results to secure these statements. Considering the research already carried and the above mentioned, it is intended in this work, as an unprecedented proposal of study, to analyze the longitudinal shear in composite slabs with alternative dimensions to those commonly used, submitting them to the four-point bending test, thus obtaining, values for the m and k parameters, verifying their application viability. Another objective also sought will be the extrapolation of its results to larger models, seeking to prove whether or not this extrapolation is viable.

1.1 Longitudinal shear strength of "steel deck" slabs

Several studies have shown, from semi-empirical procedures, that composite systems concrete slab with steel-deck incorporated, considering the usual profiles and spans, has a predominant mode of collapse, the longitudinal shear. Its occurrence is conditioned to a series of factors involving the geometrical characteristics such as: the embossing of the forms and the presence of superficial dents and indentations that help in the improvement of the mechanical connection. The yield strength of steel has little influence on occurs or not in that collapse mode. According to Araújo [8], the longitudinal shear strength allows full plastification of the maximum moment section only if complete interaction between the concrete and the steel form occurs, and then the flexural collapse occurs. On the other hand, if shear connection is not sufficient to promote complete interaction, slab collapse will occur by longitudinal shear. Seleim & Schuster [9] showed that the process of development of longitudinal shear collapse occurs gradually. Initially, when the shear transfer devices are no more capable of transferring all the longitudinal stress, cracking will begin at the critical point, a factor responsible for increasing the stress difference between concrete and steel deck, causing the crack propagation. The concrete slab and steel deck then begin to separate, decreasing the efficiency of the embossing and, consequently, the significant relative edge slippage between concrete and steel form begins. Thereafter, cracking and edge slippage are increased until complete failure of the transfer devices when the system will no more be able to withstand increased load.

A composite system may have all or partial shear interaction. The total shear interaction is defined according to EUROCODE 4 [10] when the increase in longitudinal shear strength no more corresponds to the increase in bending moment strength. Otherwise, the shear interaction will be partial. Except in situations where the shear gap is exceptionally large, the collapse of the composite system of steel and concrete will occur by longitudinal shear.

The solution usually adopted to verify the resistant capacity of the composite system consist in accomplishment on the laboratory testing program with models single-span under bending using the semi-empirical method *m-k*, as proposed by the ANSI standard [2], through equation (1) in the linear regression process of the test results.

$$Vut = b.d_f\left(m\frac{1}{L'}+k\right) \quad (1)$$

Being,

V_{ut} the total last transverse shear obtained in the tests at Newton for 1000 mm of slab width;

b the width of the slab in mm;

d_f the effective height of the slab in mm;

L' is the shear span in mm;

m and k are the parameters obtained in the linear regression process, in N/mm and N/mm^2, respectively.

Schuster [11], by establishing the original equation that gave rise to the formulation (1), verified the validity of the suggested equation by varying the geometric characteristics of the forms. In the first series of tests him fixed the thickness by varying the type of deck, dents and geometries. It was observed that neither the reinforcement rate nor the compressive strength of concrete has significant influence on the longitudinal shear strength of the followed models. The equation (1), recommended by the ANSI standard [2], has two unknown variables, *m* and *k*. Rewriting it as the equation of a straight line, is possible, from the linear regression of the test data, obtain the two unknown variables:

$$Y = mX + k \quad (2)$$

$$Y = \frac{Vut}{bdf} \quad (3)$$

$$X = \frac{1}{L'} \quad (4)$$

It is relevant to clear that the data processing method proposed by the ANSI standard [2] differs in some aspects from the proposition made by ABNT NBR 8800 [12], which adopts the EUROCODE 4 equation [10]. The equations adopted in the linear regression process to obtain *m* and *k* adopting different geometric parameters between the two standards. The units of measurement of *m* and *k*, presented by ABNT NBR 8800 [12], are given in units of stress, as presented in equation (5), while in ANSI [2] they are given in units as presented previously.

$$V_{l,R} = bd_f\left[\left(\frac{mA_{F,ef}}{bL_s}\right)\right]+k \quad (5)$$

Using the same equation (2), the variables X and Y are given by equations (6) and (7), respectively:

$$Y = \frac{V_{l,R}}{bdf} \quad (6)$$

$$X = \frac{AF_{ef}}{bL_s} \quad (7)$$

Where,

$V_{l,R}$ The resistant longitudinal shear force, given Newton, of the steel profile incorporated slabs relative to 1000 mm in width;

b the width of the slab in mm;

d_f is the distance from the upper face of the concrete slab to the geometric center of the effective section of the form expressed in mm;

L_s is the shear span in mm;

m and *k* are the parameters obtained in the linear regression process;

$A_{F,ef}$ the area of the effective section of the form.

It is easy to observe, by equation (7), that the geometric variations present in the form, resulting from the embossing process, directly influence the obtainment of the *m* and *k* parameters, since the cross section area is inversely proportional to the angular coefficient of the straight, in other words, the greater the area, the smaller it is angular coefficient *m*, unlike equation (4), where the cross section area of the form is not considered in the linear regression equation.

Beyond of the equations that define the strength of the composite slab system, it is important to emphasize its possible collapse modes. According to Brendolan [13], the collapse of the bending slab system is similar in nature to that of conventional reinforced concrete beams, differing only in the cold formed steel that provides the positive reinforcement. The bending collapse can be considered critical only when there is all interaction to shear at the interface between the metal deck and concrete cape, which occurs when have long spans and small slab thickness with high efficiency of the form dents, so that the shear force at the interface is not greater than the connection strength. Otherwise there will be no complete interaction and slab collapse is defined as longitudinal shear.

Vertical shear collapse occurs only in special cases of thick slabs with very short spans or by the application of high concentrated loads near the supports. The collapse by puncture occurs in cases

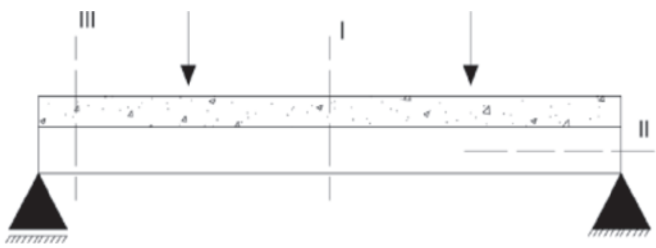

Figure 2
Composite system colapse modes
Source: SIEG, 2015, p. 30

Table 1
Geometric characteristics of the specimens tested

	Geometric characteristics			
Specimens	CP01	CP02	CP03	CP04
b (mm)	19.82	21.01	20.87	19.33
Lo (mm)	50.00	50.00	50.00	50
Lc (mm)	140.00	140.00	140	140
t (mm)	0.914	0.924	0.934	0.914
Lt (mm)	251.35	251.96	250.98	250.87
So (mm²)	18.12	19.41	19.49	17.67

Source: The Author

where high loads are concentrated in small areas, as in the case of pillars that born on the slab.

The collapse by longitudinal shear, among the others presented, if highlight for being the that occurs more frequently, being characterized by the formation of a crack by diagonal stress under or near one of the load points followed by relative slippage edge resulting in loss of system load capacity. Johnson [14] presents the three modes of collapse as can be seen in figure 2: section I (bending), section II (longitudinal shear) and section III (transverse shear).

Another fundamental feature to be observed for composite slabs is the influence of friction on the support region. Studies show that in models with relatively short shear spans, the influence of friction on the supports is relevant in the calculation of longitudinal shear strength, since smaller spans promote greater reaction on the supports. The intensity of the vertical force produced increase the mechanical contact between metal deck and concrete cover, making it difficult to slippage between them. This causes an increase in the force required for relative slippage and a total or partial loss of mechanical interaction. This effect is reduced when mean to larger spans, precisely because the contact force between concrete cover and steel deck, is reduced, facilitating the occurrence of relative slippage that occurs for lower force values. The *m-k* method doesn't take this effect directly into account and is implicit in the experimental results.

2. Experimental analysis of normative and alternative systems

The use of the incorporated steel profiles composite slab system requires a good understanding of the behavior of the composing materials as well as the mechanical properties that characterize it. This system has a predominant collapse mode, longitudinal shear, which requires its design to use a very widespread method, the semi-empirical method m-k, whereby it is possible to establish the resistant capacity of the composite slab.

The test proposed by the ANSI standard [2], adopted as a reference in this work, establishes the means that must be followed to evaluate the behavioral and quantitative relationship between slabs with different steel deck thickness and span. According to her, when a number of different deck thicknesses are produced for the project and only the smallest thickness is used in the test program, a minimum of four tests should be performed: two for a larger shear span and two for a smaller, this is the procedure adopted here to perform the experiments. The deck thickness made in the test program of this work was 0.8 mm, the other geometric characteristics were defined based on the design and testing needs.

2.1 Characterization of steel deck

The characterization of the steel deck consisted of the testing of four specimens following the standards specified by ABNT NBR 6892 [15]. The standard proposes that the dimensions of the specimen can be defined by considering the original metallic product, as well as it's cross section that can be square, rectangular, circular, among other shapes. It can therefore be subdivided into two groups: proportional and non-proportional. For this work, was chosen to use the non-proportional specimen, where the original measurement length (L_o) is independent of the original cross section area (S_o). As of the normative references, the dimensions of the specimens were measured, the thickness of the zinc cover was removed and the results found in Table 1 were presented.

As a consequence of the test performed, it was possible to determine the stress strength, *fu* (MPa), of the steel used to manufacture the steel deck (Table 2). During the procedure the real thickness of the steel was taken into consideration, disregarding the galvanization thickness of 0.04 mm. Due to variations in specimen dimensions and rupture loads, the mean stress value was accepted. The yield strength of the steel profile could not be obtained. Thus, the plastification located in the form that may appear in the assays can only be qualitatively evaluated.

2.2 Characterization of concrete

The concrete used to mold the slabs was produced by a concrete batching plant with characteristic strength, f_{ck}, estimated at 30 MPa after 28 days. Prior to the start of concreting, cylindrical specimens of 100 by 200 mm were molds; 3 specimens for axial compression test according to ABNT NBR 5739 specifications [16] and 4 specimens for determination of the modulus of elasticity using the test practice specified by ABNT NBR 8522 [17], whose results are presented in table 3.

3. Method

3.1 Alternative models consisting of only one steel deck module

The composite concrete slab systems with steel-deck incorporated,

Table 2
Mechanical properties of the steel deck

			Steel deck tensile test results		
Specimens	CP01	CP02	CP03	CP04	Middle
Rupture load (kN)	4.94	5.10	5.48	4.16	4.92
Rupture stress fu (MPa)	272.62	262.75	281.17	235.42	262.99
Yield stress fy (MPa)			180		
Elasticity module (MPa)			200000		

Source: The Author

Table 3
Axial compression resistence (MPa) and concrete Elasticity Module (Mpa)

Steel deck tensile test results				
Specimens	**CP01**	**CP02**	**CP03**	**Middle**
Axial compression strength (MPa)	36.12	38.63	45.64	40.13
Elasticity module (GPa)	—	—	—	21.88

Source: The Author

considering only one module steel deck, proposed as comparative to the normative scale model, has its length and width previously defined, for installation the test "setup" on the press used. Some limitations for the development of the trial, such as maximum dimensions of the press were responsible for choosing the dimensions of alternative models, especially their length. Height was establish, based on what was determined for the normative model, so that it allowed to analyze the dimensional compatibilities and incompatibilities came by to influence the comparative between the results obtained in both, the alternative and the normative model. The alternative composite system was then defined by a trapezoidal steel deck module with a nominal thickness of 0.8 mm and a height of 75 mm, a width of 350 mm and a length of 700 mm.

In addition to the steel deck, the model is made up of a 65 mm thick normal density concrete cover, specified 30 MPa fck, and welded steel mesh to restrict crack propagation and retraction during the curing process. It has 3.8 mm in diameter and 15 cm of wire spacing. The mesh was positioned in the region above the elastic neutral line of the cross section, ensuring, especially in alternative models, that the tensile stresses imposed on the specimen during the bending test were resisted only by the steel deck without participation of the metallic mesh. The nomenclature adopted for the models was: RM75-NI. Being RM, the steel deck manufacturer's, 75 the height of the deck and NI indicates that the position of the center table of the deck module is below its center of gravity. For the execution of the normative and alternative models, the use of stiffened U-type steel profile with specific width, thickness and lengths was adopted to delimit the slab dimensions (figure 3), which were removed before the tests. All models, normative and alternative, were supported only at the edges during their execution, allowing them to deform along the span during concreting.

The instrumentation of the models was basically composed of linear displacement measuring transducers (LVDT'S) with the objective of measuring the mid-span displacement and the relative edge slippage, besides the use of strain gauge to measure the state of deformation in the steel deck and concrete cover.

The test developed first in the 600 mm span specimens group followed by the 500 mm specimens group. The test was performed in sequential loading steps. First, 5% of the expected last load (W_t) was applied and maintained for a period of 5 minutes. Then the loading was removed and all measuring instruments zeroed. The same procedure was done for a load of 60% of the expected last load (W_t). After five minutes, the load was removed, all instruments zeroed and the specimen "rested" for 2 minutes. The final loading step was then initiated, entail the specimen to collapse. This was done for all specimens in each group. Figure 4 demonstrate the loading layout adopted in the test of alternative models.

3.2 Normative slabs models

Before presenting the dimensions adopted for the normative models, it is important to clarify that the L' shear span adopted for the composite concrete slab systems with steel-deck incorporated should be equivalent to ¼ of the theoretical slab span; This specification is justified by the fact that the test is done by applying two equidistant concentrated loads of the supports. However, when designing the composite system, loading is considered to be evenly distributed throughout the span of the slab. The equivalence between the two conditions is obtained by equality of the area underneath the shear stress diagram for evenly distributed load situations with the area

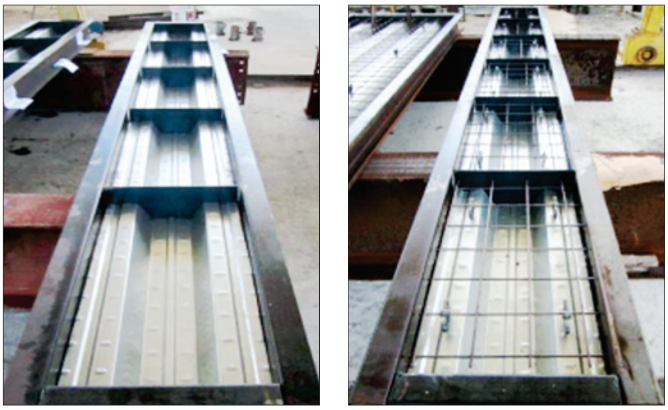

Figure 3
Mounted forms for the concreting; mold and shape for embedding
Source: The Author

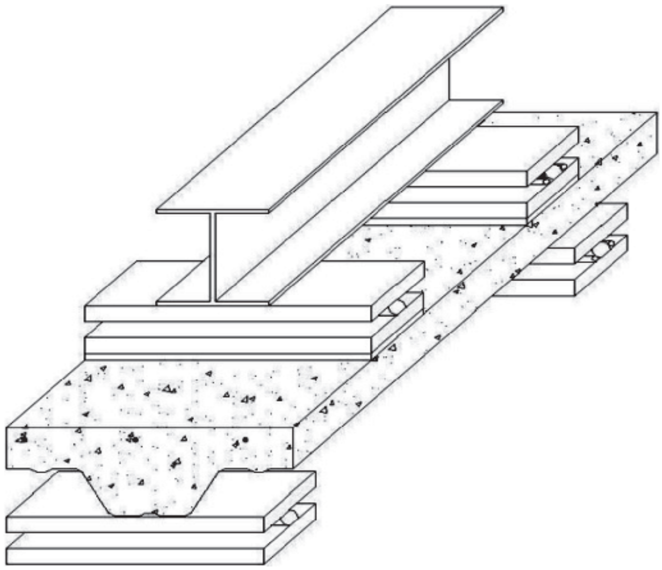

Figure 4
Alternative model load scheme
Source: The Author

underneath the shear stress diagram for symmetrically arranged concentrated loads, yielding the same maximum shear force value.

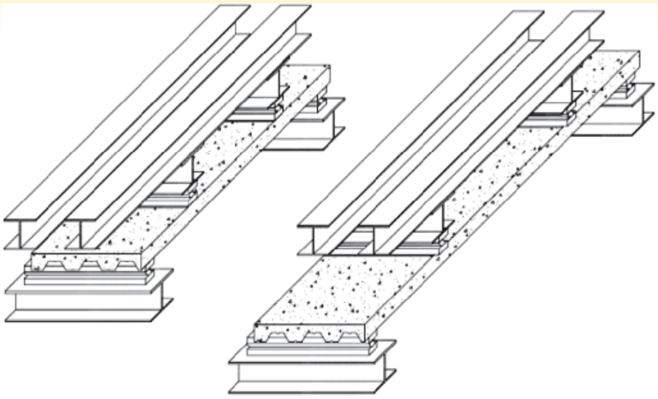

Figure 5
Normative model load scheme
Source: The Author

For the normative composite system tested in this work, the spans that are conventionally adopted in the construction processes with the RM 75 deck were defined. Two values for the spindle-to-spindle span were then adopted, these values being 2 m and 3 m. The nomenclatures adopted for specimens with these dimensions were defined as RM75-02 and RM75-03 respectively. Other geometrical characteristics, such as the deck thickness (t) and the width (b) of the model, were fixed by the choice of the deck as already mentioned in the "alternative model". The total height (h_t) of the slab was defined from the behavior presented by the steel profile for the concrete phase in the fresh state; under these conditions, it was possible to establish the steps measurements of the two normative models necessary to determine the parameters m and k. Thus, the adopted normative composite system is formed by a trapezoidal section steel profile with a nominal thickness of 0.8 mm and a height of 75 mm, width of 911 mm. These characteristics are defined by the manufacturer during the mechanical forming of the steel deck. The normal density concrete cover has a thickness of 65 mm and a specified *fck* of 30 MPa. The mesh used has a diameter of 3.8 mm, being positioned 20 mm below the upper face of the slab, ensuring

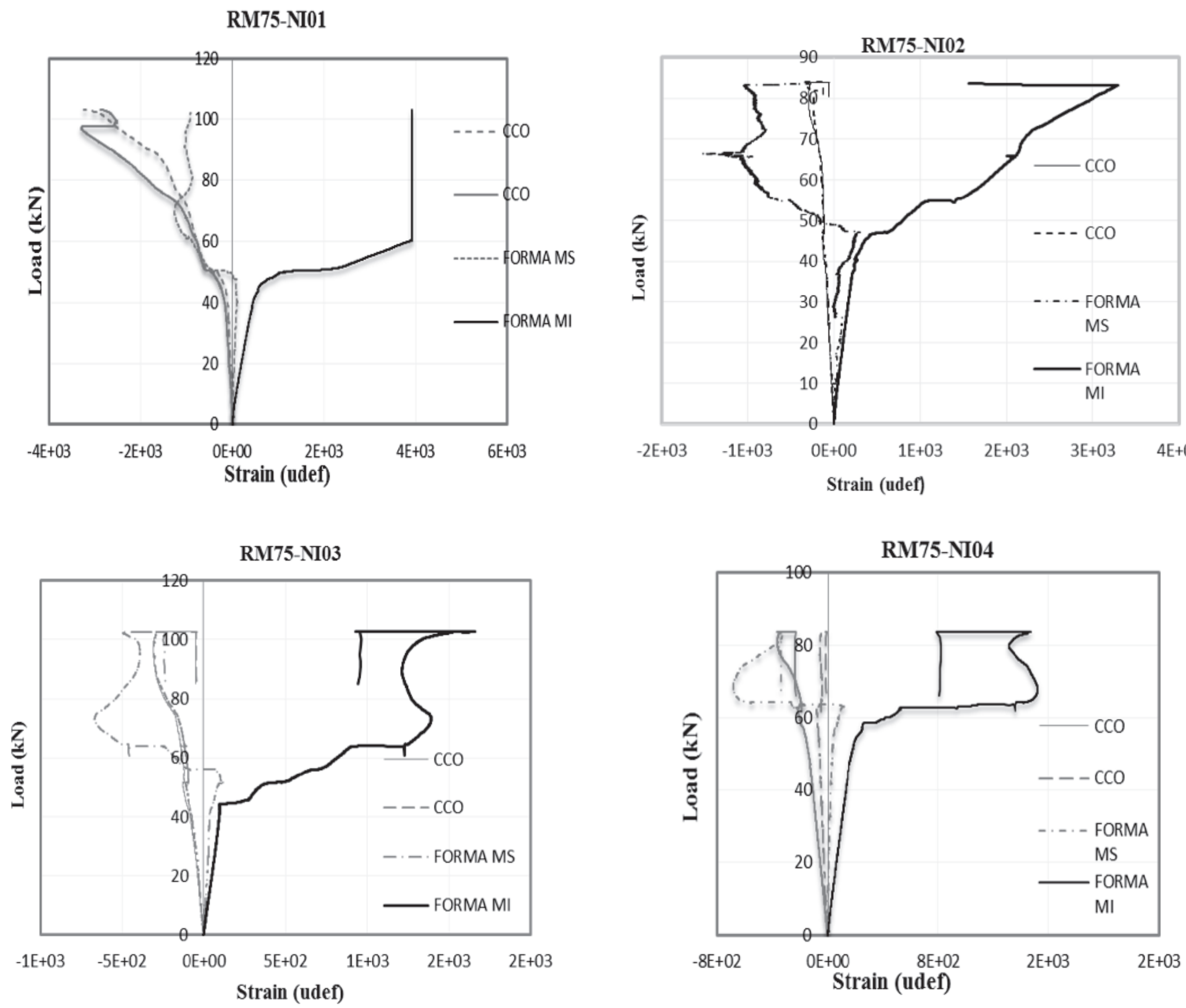

Figure 6
Load x Strain of the specimen RM75-NI 01 to 04
Source: The Author

its minimum coverage, besides being above the neutral line elastic, so that it doesn't participate in the resistance to tensile stresses arising from bending during the test run. The slabs of the normative models had strain gauges positioned on the concrete surface and of the steel profile as done with the alternative models. On the concrete surface were two strain gauges positioned in the center of the span, symmetrically disposed in relation to the lateral edge of the slabs. The other two, were similarly positioned in the center of the slab, one in the upper flange and the other in the lower steel deck flange. Displacement and relative slip measurements were made using indicator; two positioned in the middle of the span, on opposite sides of the slab edge and another positioned on the front face, attached to a magnetic base, which was fixed in the steel deck and the indicator cursor pressed against the concrete cover. Thus it was possible to follow whether or not there was relative slippage and the value of the load acting at this moment, besides measuring its maximum value until the collapse.

The evaluation of the normative slabs was carried out in compliance with most of the procedure proposed by ANSI standard [2], but the loading process was similar to the one carried out in a static load test, where the static forces were increasingly applied recording the displacements corresponding to each applied load value (Figure 5).

4. Results

4.1 Alternative models composed of a deck module

The graphs obtained in the tests of figures 03 and 4 exhibit the deformations measured in the RM75-NI specimen. The results indicate that the highest stress values, as expected, occurred at the extremities of the cross section of the models. The stress in the lower flange of the steel deck were higher than those stress observed in its upper flange. Both flanges presented tensile stress

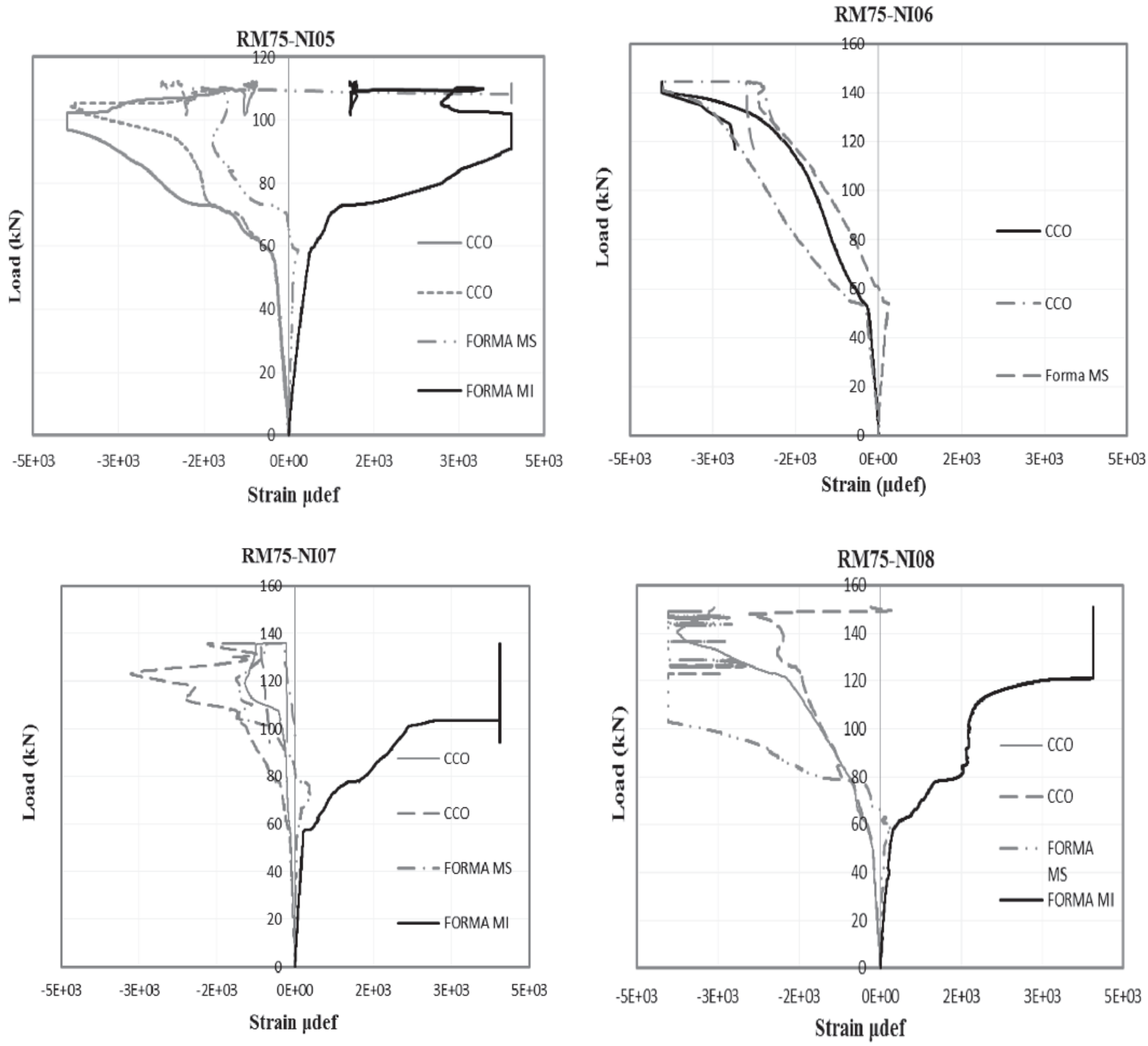

Figure 7
Load x Strain of the specimen RM75-NI 05 to 08
Source: The Author

during basically the whole test, until partial plasticization of the composite section, when the upper flange began to suffer compressive stress. The tests confirmed the expected result that the deformations measured by the strain gauges positioned on the surface of the concrete cover were compression, as seen in figures 6 and 7. In these figures the symbols CCO, Form MI and Form MS mean: concrete cover, flange lower deck and upper deck flange respectively. The composite section has elastic behavior up to a load of 40 kN and thereafter demonstrates inelastic behavior. The RM75-NI 01 and 02 specimens presented higher values of deformation until rupture if compared with the RM75-NI 03 and 04 specimens.

The difference in stiffness between steel and concrete in the interface zone of each model does not appear to influence their behavior while still in the elastic phase. It is possible to notice that the connection in the interface breaks after localized plasticization of the section, which can be noticed by the occurrence of plastic arrows and plastic deformations obtained by the strain gauges attached to the concrete cover and steel decks. It is possible to notice the relative slippage between the steel deck and the concrete cover, which characterizes a longitudinal shear failure. In addition, the change in tensile stress signal at the upper steel deck flange, for stress to compression, characterizes the formation of a second elastic line, typical behavior of partial interaction to longitudinal shear. Before, however, was observed the occurrence of cracks in the lower part of the cross section of the models in the region between the applied loads (pure bending region, null shear). The graphs indicated in figure 8 show that there was no wide variations between the elastic arrows of the RM75-NI 01 to 04 specimens subject to the same loading

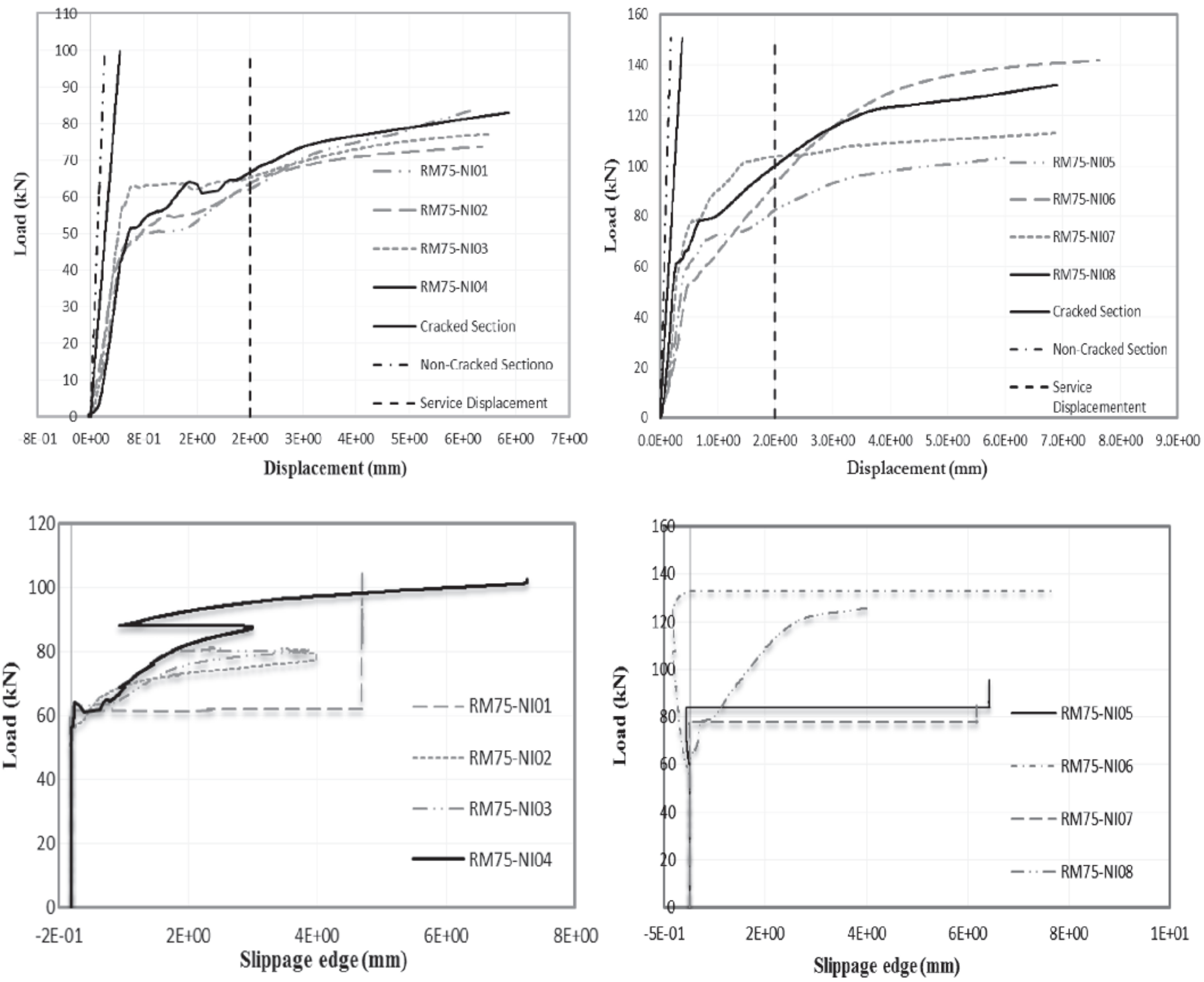

Figure 8
Load x displacement in the mid span and load relative slippage of specimens RM75-NI
Source: The Author

Table 4
Determination of transverse shear total finish of tests Vut

Specimens	b (mm)	ht (mm)	df (mm)	L (mm)	L' (mm)	P (kN)	Pue (kN)	P. Pslab (kN/m²)	Vut (kN)
RM75-NI01	352	143	126.618	600	150	104.84	105.26	2.563	52.899
RM75-NI02	353	145	128.618	600	150	83.93	84.35	2.563	42.445
RM75-NI03	355	148	131.618	600	150	83.79	84.21	2.563	42.376
RM75-NI04	355	147	130.618	600	150	102.66	103.08	2.563	51.811
RM75-NI05	356	145	128.618	500	125	112.27	112.69	2.563	56.572
RM75-NI06	350	145	128.618	500	125	144.55	144.97	2.563	72.708
RM75-NI07	353	146	129.618	500	125	135.88	136.30	2.563	68.375
RM75-NI08	355	148	131.618	500	125	150.80	151.22	2.563	75.836

Source: The Author

Table 5
Linear regression of datas

Specimens	X (1/mm)	Y (N/mm²)	Regression of results	Vus (kN)	Vus/Vut	Deviation (%)
RM75-NI01	0.0067	1.1869	m = 341.62 k = -1.241	46.195	0.873	-12.67
RM75-NI02	0.0067	0.9349		47.058	1.109	10.87
RM75-NI03	0.0067	0.9069		48.428	1.143	14.28
RM75-NI04	0.0067	1.1174		48.060	0.928	-7.24
RM75-NI05	0.0080	1.2355		68.314	1.208	20.76
RM75-NI06	0.0080	1.6151		67.163	0.924	-7.63
RM75-NI07	0.0080	1.4944		68.265	0.998	-0.16
RM75-NI08	0.0080	1.6230		69.711	0.919	-8.08

Source: The Author

layout, in the specimens 05 to 08, which may be an indication that there was no wide variation in the elasticity modulus of the concrete used. The elastic arrow occurs until a loading of the order of 40 kN, starting to present inelastic behavior. The allowable service arrow L / 250 and the theoretical arrows for cracked and non-cracked stages are also shown in this figure. The theoretical arrows of the cracked and non-cracked section approach the experimental arrows only at the initial load values. The service arrow was reached by the models already in the inelastic phase. The ductile behavior of the specimens can be observed by the large displacements presented until the moment of rupture, even after composite section plasticization. The presence of the mesh seems to influence the resistant capacity of the models.
The determination of the *m* and *k* parameters of the alternative models were performed according to the process presented in tables 4 and 5, based on the results obtained in the specimens tests with reference to the ANSI standard [2]. The straight obtained from the linear regression of the data is presented in figure 9.

4.2 Normative slabs models

The graphs shown in figure 10 exhibit higher tensile stress values in the lower flange of the specimens, while the concrete cover underwent compressive stress during all the test. It is also possible to observe that until the rupture is not noticed a chiseled change from the elastic phase to the inelastic phase, that is, there is an indication of the low interaction between steel deck and concrete cover since the collapse occurs before the plasticization of the composite section.
The graph load x displacement in the mid-span of specimen RM75-02 and RM75-03 are shown in Figure 11. The theoretical arrow of the cracked section follows the behavior of the experimentally measured arrow in the case of specimen RM75-02, which is an indication that the section cracked theoretical stiffness approximates the real stiffness. The theoretical arrow of the non-cracked

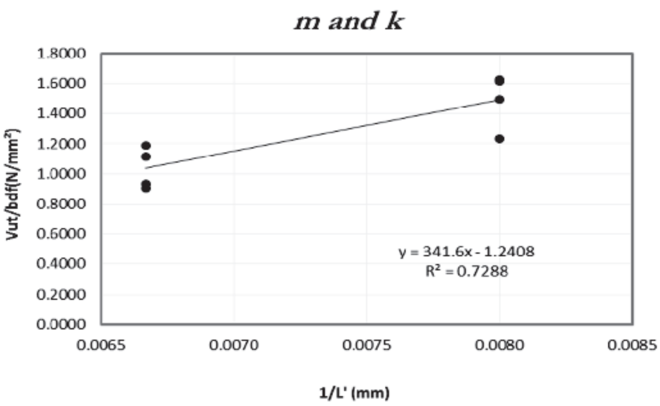

Figure 9
Linear regression of the test datesfrom alternative models
Source: The Author

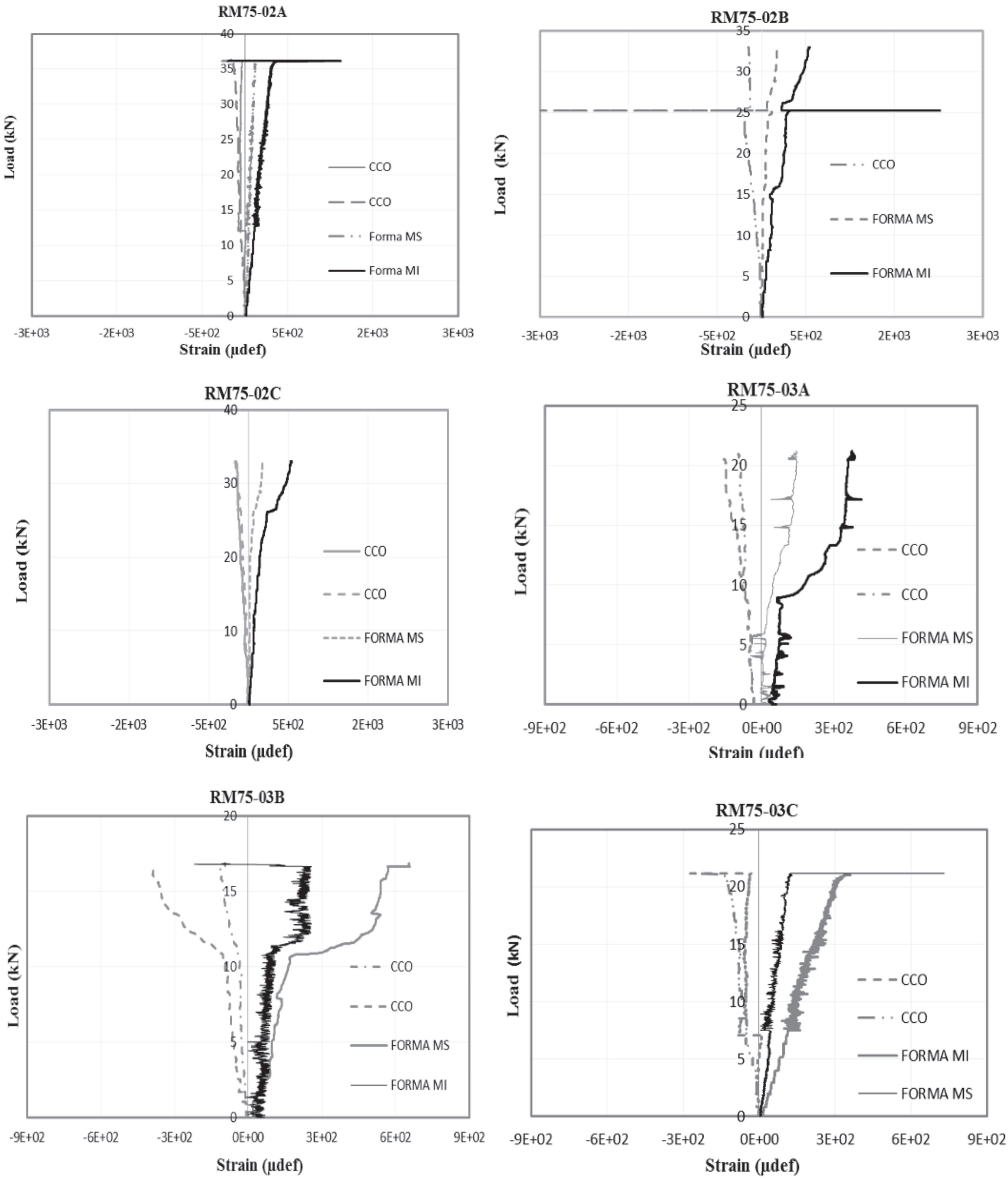

Figure 10
Load x Strain of the specimen RM75 Normative models
Source: The Author

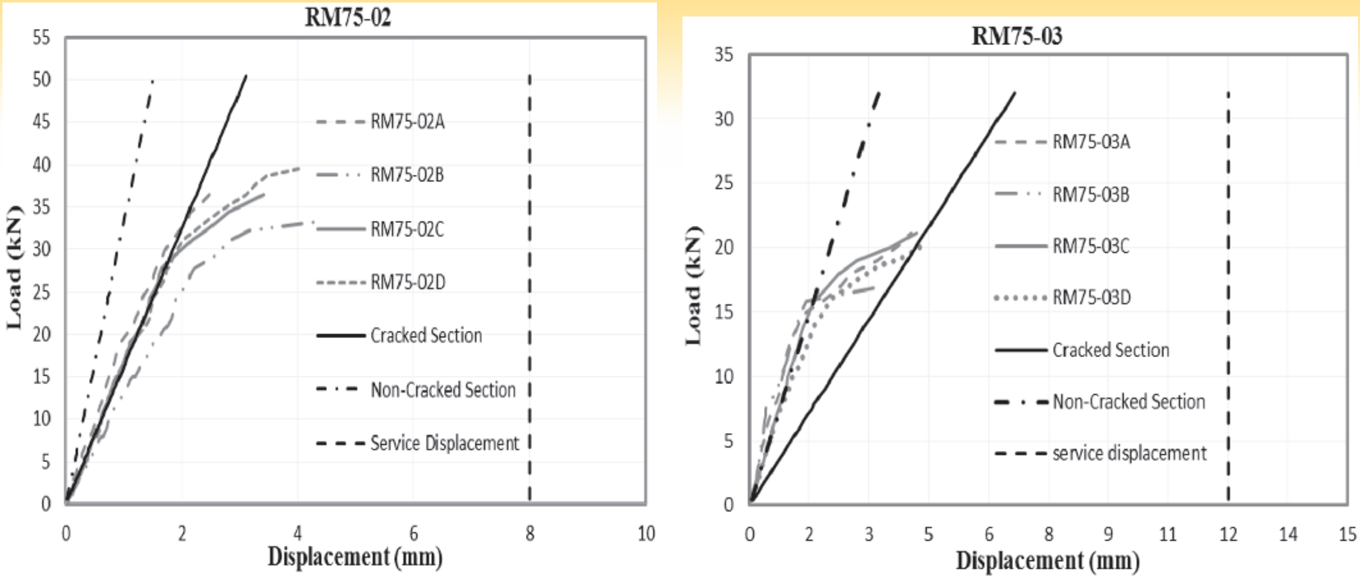

Figure 11
Load x Displacement in the mid span of the specimens RM75 normative models
Source: The Author

section follows the experimental only in the initial load values. The RM75-03 specimens presented an arrow of the non-cracked section with similar behavior to the experimental, thus demonstrating that its initial stiffness compare the theoretical stiffness of the non-cracked section, in contrast to the RM75 02 specimen. The specimens of both groups reached collapse before reaching the service arrow.

The presence of the mesh, positioned in the compressed region of the cross-section, didn't demonstrate to significantly inhibit or assist the system's carrying capacity, since, by losing the interaction, even if partial, between the concrete cover and the steel deck, the system immediately collapsed.

The determination of the parameters *m* and *k* of these models was according to the specification of ANSI 2011 standard, as of linear regression of the data obtained in the test. This is presented in tables 6, 7 and figure 12.

Table 6
Determination of transverse shear total finish of tests Vut

Specimens	b (mm)	ht (mm)	df (mm)	L (mm)	L' (mm)	P (kN)	Pue (kN)	P. Pslab (kN/m²)	Vut (kN)
RM75-02A	906	142	125.618	2000	500	36.200	41.828	2.563	23.232
RM75-02B	913	137	120.618	2000	500	32.986	38.606	2.563	21.643
RM75-02C	904	143	126.618	2000	500	36.208	41.828	2.563	23.231
RM75-02D	905	141	124.618	2000	500	39.430	45.050	2.563	24.844
RM75-03A	908	144	127.618	3000	750	21.172	26.792	2.563	16.886
RM75-03B	905	142	125.618	3000	750	16.876	22.496	2.563	14.726
RM75-03C	908	141	124.618	3000	750	21.172	26.792	2.563	16.886
RM75-03D	911	141	124.618	3000	750	21.300	26.920	2.563	16.962

Source: The Author

Table 7
Linear regression of datas

Specimens	X (1/mm)	Y (N/mm²)	Regression of results	Vus (kN)	Vus/Vut	Deviation (%)
RM75-02A	0.0020	0.2041	m = 93.748	23.444	1.009	0.916
RM75-02B	0.0020	0.1965		22.685	1.048	4.818
RM75-02C	0.0020	0.2030		23.579	1.015	1.500
RM75-02D	0.0020	0.2203		23.232	0.935	-6.488
RM75-03A	0.0013	0.1457	k = 0.0185	16.628	0.985	-1.528
RM75-03B	0.0013	0.1295		16.313	1.108	10.775
RM75-03C	0.0013	0.1492		16.237	0.962	-3.843
RM75-03D	0.0013	0.1494		16.291	0.960	-3.955

Source: The Author

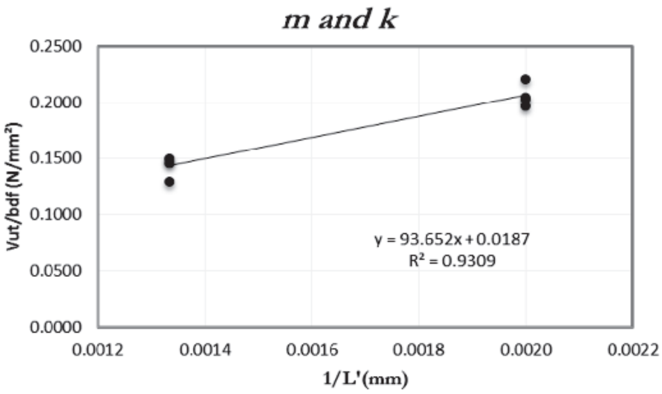

Figure 12
Linear regression of the test datesfrom normative models
Source: The Author

4.3 Comparative analysis of the normative and alternative models

The comparative analysis of the models requires some basic considerations of the main parameters that can influence their behavior during the test, being the collapse load and the geometrical characteristics. The latter is the main factor since directly influences the loading values and behavior of each model. For this reason, it is necessary a careful analysis of the differences presented by the models from the different geometric characteristics. The analysis began by applying the parameters *m* and *k* obtained by testing the alternative model in equation 01, varying its geometric characteristics, so that if approached the geometry of the normative model. And, then it was possible to find the relationship between the longitudinal shear strength of the composite system, Vus, and growing values of shear span and slab width. The results found for this situation were compared with the results found by adopting *m* and *k* of the normative model, as can be seen in figures 13 and 14. Although the parameters *m* and *k* obtained during studies on alternative models define the longitudinal shear strength of alternative models, they can't be adopted in the calculation of normative models, since they don't describe their resistance at the interface. By adopting the parameters *m* and *k* obtained in the test of the alternative slabs in larger span slabs, regardless of the adopted width, there is a sharp decrease in the theoretical slab strength until the zero value is reached. This value is reached for all specimens in the same shear span which characterizes a limiting span for adoption of this parameter.

5. Conclusions

In testing the alternative models, it was concluded that the sizing parameters longitudinal shear, *m* and *k,* obtained can be reliably used as part of the model sizing process. The deviations found by relating the experimental longitudinal shear resistance capacity (calculated through the presented equations) satisfy the normative requirements, thus allowing to confirm the statement that the found *m* and *k* values can be adopted in the procedure of calculation of the alternative model. However, by using the parameters *m* and *k*, obtained by testing alternative models as a procedure for calculating models in larger dimensional scales, it is possible to realize that there is a decrease in the resistant capacity of these models,

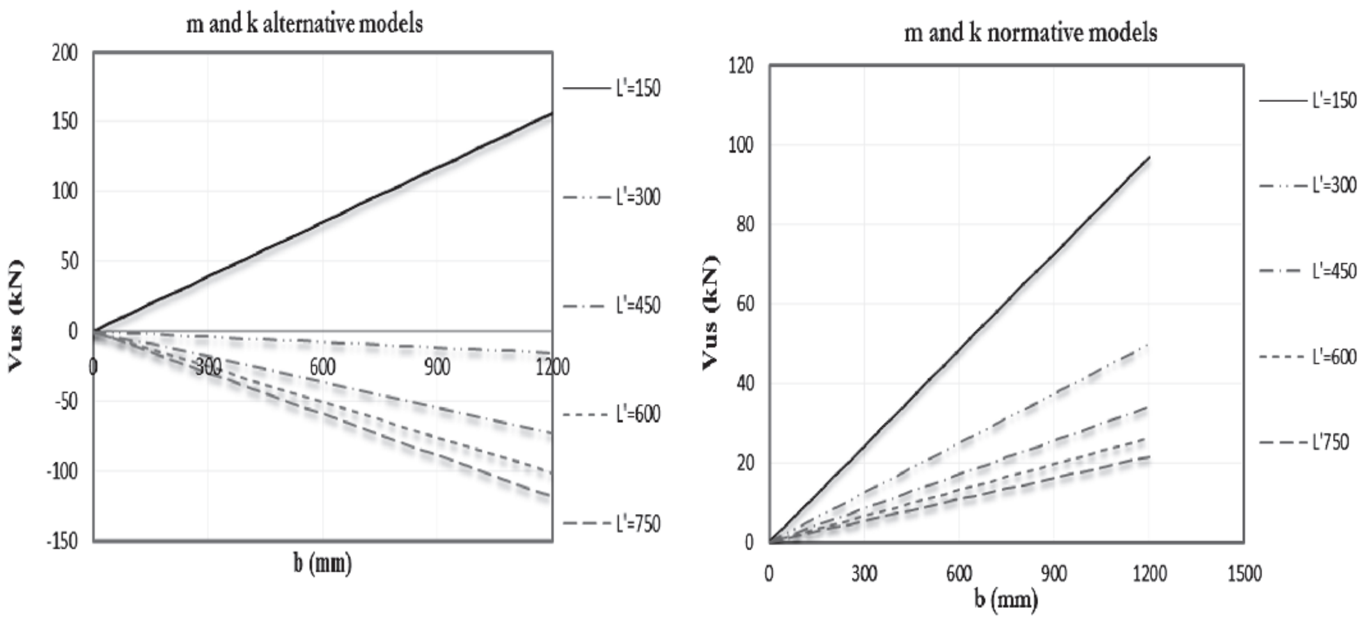

Figure 13
Longitudinal shear strenght when adopting m and k of the alternative and normative models change the width of specimens
Source: The Author

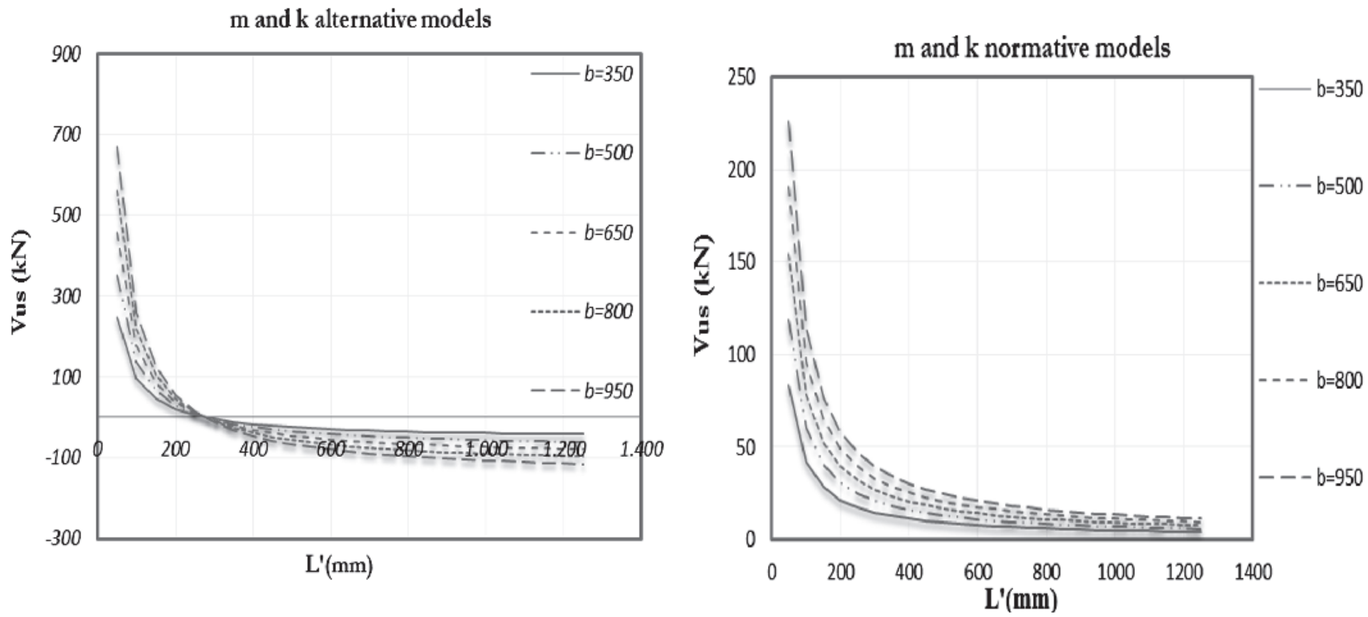

Figure 14
Longitudinal shear strenght when adopting m and k of the alternative and normative models change the shear span of specimens
Source: The Author

regardless of the variable dimension, width or length. It is also noticed the existence of a span limit to which these parameters can be adopted. It is inferred, then, that the *m* and *k* parameters found for the alternative models can't be adopted in the procedure of calculation of the normative model, since they present inconsistencies. The analysis of the behavior of the load x deformation graphs of the alternative models allowed that after partial plasticization of the section and approximation of the load that generates relative slippage edge, there is a change in the deformation behavior of the upper flange that spend suffer compression, namely, that the partial interaction between concrete and steel deck after relative slippage generates two neutral lines, one in concrete and one in steel deck, circumstances also confirmed in the bibliographies studied.
About the mode of collapse of alternative models, it is noticed a clear influence of the metallic mesh on its resistant capacity, even after the loss of mechanical interaction between steel deck and concrete cover. Moreover, after the appearance of the first cracks it is possible to notice large deformations until collapse, characterizing a ductile behavior.
A clear problem with alternative models is the distance between the applied load and the supports and the height of the models. These factors may cause the load to be transferred almost directly to the supports and not by longitudinal shear. Nevertheless, it is possible to observe in the alternative models the transfer of forces also through shear in the interface zone.
Through tests on normative models, it became possible to find values for *m* and *k* that reliably represent the interaction between the RM75 steel deck and the concrete cover, since the deviations between the theoretical and experimental relationship didn't exceed + -15% according to normative specifications. Nevertheless, the longitudinal shear-resistant capacity was of low intensity, demonstrating that there was a low interaction between steel deck and concrete cover. Is believed that be due to the low efficiency of the steel deck surface dents; It is therefore recommended to ensure a better arrangement of surface dents by adopting deeper and higher amount by linear meter. Or, evaluate the process of mechanical shaping of the steel deck in such a way that possible flaws in this step can be corrected.
The evaluation of the collapse of normative models shows that there was no considerable influence of the mesh on the obtained results. The collapse occurred with significant relative slippage only near the last load, that is, the rupture occurred in a fragile manner. Another unobserved characteristic compared to the alternative model was the occurrence of a process of continuous appearance of cracks before collapse.
Through this work, it is expected to assist research of new procedures to determine the parameters *m* and *k*.

6. Appreciation

The authors thank Pengec Engenharia e Consultoria, in the person of Dr Vinicius Maia Barreto de Oliveira. To the Laboratório de Estruturas S.P. TIMOSHENKO and Centro Tecnológico da Argamassa (CETA), of the UFBA Polytechnic School, for all the assistance available in the production and testing of the models.

7. Bibliography

[1] FILHO, O. T. B. Estudo comparativo de respostas estruturais antes da cura do concreto de fôrmas metálicas

incorporadas às lajes. Belo Horizonte: Dissertação de Mestrado Universidade Federal de Minas Gerais - Belo Horizonte, (2003).
[2] AMERICAN NATIONAL STANDARDS INSTITUTE/ STEEL DECK INSTITUTE ANSI. T-CD-2011 Test standard for composite steel deck- slabs, (2011).
[3] ABDULLAH, R. & EASTERLING, W. S., (2007). Determination of Composite Slab Strength Using a New Elemental Test Method. Journal of Structural Engineering, Vol. 133, Nº 9, September1, 2007. ASCE.
[4] CAMPOS, P. C. "Efeito da continuidade no comportamento e na resistência de lajes mistas com fôrma de aço incorporada". Belo Horizonte: Dissertação de Mestrado, Universidade Federal de Minas Gerais- Belo Horizonte, (2001).
[5] COSTA, R. S Análise de um sistema de lajes mistas considerando a influência do atrito dos apoios e a avaliação do momento de inércia efetivo. Belo Horizonte: Dissertação de Mestrado, Universidade Federal de Minas Gerais- Belo Horizonte, (2009).
[6] DANIELS, B., & CRISINEL, M. (1993.a). Composite Slab Behavior and Strength Anlysis. Part I: Calculation Produced. Journal of Structural Engineering, Vol. 119, Nº 1, January 1993. ASCE.
[7] JOHNSON, R. P.; ANDERSON, D. Designers´Guide to EN 1994-1-1 Eurocode 4: Design of Composite Steel and Concrete Structures – Part 1.1: General Rules and Rules for Buildings, first edition, Thomas Telford Publishing, London, 2004.
[8] ARAÚJO, G. S. Análise do comportamento e da resistência de um sistema de lajes mistas pelo método da interação parcial. Belo Horizonte: Dissertação de Mestrado Universidade Federal de Minas Gerais- Belo Horizonte, (2008).
[9] SELEIM, S. AND SCHUSTER, R. (1985). "Shear-Bond Resistance of Composite Deck-Slabs," *Canadian Journal of Civil Engineering*, National Research Council of Canada, Vol. 12, pp. 316-324.
[10] EUROPEAN STANDARD-EUROCODE 4: Design of composite steel and concrete structures-part 1-1: General rules and rules for buildings, (1994).
[11] SCHUSTER, R. M. Strength and behavior of cold-rolled steel-deckreinforced concrete floor slabs. Iowa State University of Science and technology Ames, Iowa, (1970).
[12] ASSOCIAÇÃO BRASILEIRA DE NORMAS TÉCNICAS. NBR 8800. Projeto de estruturas de aço e de estruturas mistas de aço e concreto de edifícios. Rio de Janeiro, (2008)
[13] BRENDOLAN, G. Análise comparativa da resistência de um sistema de lajes com fôrma de aço incorporada. Belo Horizonte: Dissertação de Mestrado, Universidade Federal de Minas Gerais- Belo Horizonte, (2007).
[14] JOHNSON, R. P. Composite structures of steel and concrete- Volume 1 Beams, Slabs, Columns, and frame for buildings, Second Edition. Blackwell Scientific Publications, (1994).
[15] ASSOCIAÇÃO BRASILEIRA DE NORMAS TÉCNICAS. NBR 6892 (Ensaio de tração à temperatura ambiente),2002.
[16] ASSOCIAÇÃO BRASILEIRA DE NORMAS TÉCNICAS. NBR 5739 (Concreto- Ensaio de compressão de corpos de prova cilíndricos).
[17] ASSOCIAÇÃO BRASILEIRA DE NORMAS TÉCNICAS. NBR 8522 (Concreto- Determinação dos módulos Estáticos de elasticidade e de deformação à compressão).

Volume 13, Number 3 (June 2020) p. 543 – 562 • ISSN 1983-4195
http://dx.doi.org/10.1590/S1983-41952020000300006

REVISTA IBRACON DE ESTRUTURAS E MATERIAIS
IBRACON STRUCTURES AND MATERIALS JOURNAL

Influence of the cementitious matrix on the behavior of fiber reinforced concrete

Influência da matriz cimentícia no comportamento de concretos reforçados com fibras

A. M. LEITE [a]
alexmacedoleite@gmail.com
https://orcid.org/0000-0003-4022-6787

A. L. DE CASTRO [a]
alcastro@sc.usp.br
https://orcid.org/0000-0002-7248-7327

Abstract

One of the main purposes of the addition of fibers to the concrete is the control of the plastic shrinkage cracking in the fresh state and the increase of the post-crack resistance in the hardened state. The cementitious matrix is one of the factors that influences the performance of fiber reinforced concrete, interfering in the fluidity of the mixture and in the adhesion between fiber and matrix. In this context, the present paper evaluates the behavior of two concrete, one of conventional strength and another of high-strength, without fiber and with a content of 1%, by volume, of fiber, being used steel fiber and macro-polymeric fiber. For this, the mechanical properties of the concrete were evaluated in the hardened state by the tests of compressive strength, Barcelona, flexure of prisms and punching of plates. From the experimental results, statistically analyzed, there were significant changes in toughness and residual strength due to change in the cementitious matrix. Finally, an equivalence of performance between the fibers as to the toughness was observed, with the change of the cementitious matrix.

Keywords: fiber reinforced concrete, cementitious matrix, steel fiber, macro-polimeric fiber, properties.

Resumo

Uma das principais finalidades da adição de fibras ao concreto é o controle da fissuração por retração plástica no estado fresco, e o aumento da capacidade resistente pós-fissuração no estado endurecido. A matriz cimentícia é um dos fatores que influencia no desempenho do concreto reforçado com fibras, interferindo na fluidez da mistura e na aderência entre as fibras e a matriz. Neste contexto, o presente trabalho avalia o comportamento de dois concretos, um de resistência convencional e outro de alta resistência, sem fibras e com teor de 1%, em volume, de fibras, sendo utilizadas fibras de aço e macrofibras polimérica. Para isso, foram avaliadas as propriedades mecânicas dos concretos no estado endurecido, a partir dos ensaios de resistência à compressão, Barcelona, flexão em prismas e punção em placas. A partir dos resultados experimentais, analisados estatisticamente, verificou-se alterações significativas da tenacidade e da resistência residual com a mudança da matriz cimentícia. Por fim, observou-se uma equivalência de desempenho entre as fibras quanto à tenacidade, com a alteração da matriz cimentícia.

Palavras-chave: concreto reforçado com fibras, matriz cimentícia, fibras de aço, macrofibras polimérica, propriedades.

[a] *University of São Paulo, Department of Structural Engineering, São Carlos School of Engineering, São Carlos, SP, Brazil.*

Received: 15 Oct 2018 • Accepted: 07 Apr 2019 • Available Online: 26 May 2020

1. Introduction

Fiber reinforced concrete is a composite material that has been used for several applications, such as tunnel lining, radier, industrial floors, precast elements, among others. The fibers improve the crack distribution and limit the crack openings in the Service Limit State, reducing the concrete exposure to the environment. Fiber reinforcement is suitable for structures with high stress distribution capacity. In the case of structures with localized stresses and dispersed stresses, local reinforcements with steel bars and fibers randomly arranged on concrete can be used simultaneously [1].

The addition of fibers to the concrete causes changes in the properties of the material, both in fresh and hardened states. In the fresh state, to improve the workability of the mixture, which is affected by the incorporation of fibers, superplasticizer admixture is generally used. However, in the case of concrete with higher fibers content, the addition of superplasticizer admixture may be impracticable, being necessary to change the cementitious matrix to improve the flowability of the concrete.

The main contribution of the fibers occurs in the hardened state of the concrete after the cement matrix failure, providing residual strength to the composite. The fibers act as a stress transfer bridge, reducing the stress concentration at the crack tip. Thus, the concrete becomes a pseudo-ductile material, presenting some ductility [2].

The cementitious matrix is one of the factors that interfere with the behavior of fiber reinforced concrete in the hardened state. The properties of the matrix affect the adherence between fibers and matrix, reflecting on the post-cracking performance of the concrete [2]. Thus, depending on the type and content of fibers added, and the properties of the cementitious matrix, fiber reinforced concrete may exhibit softening or hardening behavior after cracking. The softening behavior is characterized by deformations located in a single crack and by a reduction of the post-cracking resistant strength, while in the hardening behavior occurs the formation of multiple cracks and increased resistant capacity after concrete failure [3].

Nowadays there are fibers of different materials available in the construction market: steel, polymer, glass etc. The properties of the fibers material, such as modulus of elasticity and tensile strength, will define their function in concrete. Fibers with high modulus of elasticity and higher tensile strength than the matrix should act as primary reinforcement of the concrete, providing resistant capacity after matrix cracking. On the other hand, fibers that have low modulus of elasticity and tensile strength are more used in the control of cracking by plastic shrinkage of the concrete.

1.1 Justification and objective

The two main types of fibers used as primary reinforcement of the concrete are steel fibers and polymeric macrofibers. While the former is historically more used for this purpose, since it began to be marketed in the 1970s, and has more advantageous properties (higher modulus of elasticity modulus and higher tensile strength), the latter has a more recent commercialization and application, started in the 2000s [4], being object of several studies that seek to better understand its performance in concrete, especially in high strength concrete.

In addition, studies involving the influence of cementitious matrix on fiber reinforced concrete performance are still limited. It is known that a more resistant matrix has greater adherence to the fibers [2]. However, little is known about the impact of this greater adherence on the mechanical properties of fiber reinforced concrete. Thus, the present study aims to evaluate the influence of cementitious matrix on the behavior of fiber reinforced concrete, considering the use of steel fibers and polymeric macrofibers as reinforcement for ordinary and high strength concrete.

2. Materials and experimental program

2.1 Materials

For the production of the concrete, a pozzolan-modified Portland cement, with compressive strength class of 32 MPa (CPII Z 32) was used. In the high strength concrete it was also used silica fume derived from the production process of metallic silicon or iron-silicon alloys.

As fine aggregate two natural sands of quartzous origin, classified as fine sand and medium sand, were used. The coarse aggregate used was a crushed stone of basaltic origin, with a maximum characteristic particle size of 19 mm.

In all mixtures, water from the local water supply was used. To achieve the desired consistency, a polycarboxylate-based superplasticizer admixture was employed.

For the mixtures with fibers, two types of fibers were used as reinforcement for the concrete: steel fibers and polymeric macrofibers. The steel fibers had circular cross-section and anchor at the ends; the polymeric macrofibers were made of polypropylene, had a rectangular cross-section, straight shape, and grooved surface, so that the anchorage occurred along their length. Table 1 shows the main properties of the fibers used, according to the data provided by the manufacturers.

Table 1
Physical and mechanical properties of the fibers used in the study

Property	Fiber type	
	Steel fiber	Polymeric macrofiber
Specific gravity (g/cm³)	7.85	0.95
Length (mm)	50	50
Shape index	45	75
Modulus of elasticity (GPa)	210	7
Tensile strength (MPa)	1115	550

2.2 Mix design and production of the concrete

In the present study two concrete mixes design were produced: one mix design for an ordinary concrete, with mean compressive strength at 28 days of age ($f_{cm,28}$) of 40 MPa; and another for a high

Table 2
Consumption of materials (in kg/m³ of concrete) for the reference concrete (without fibers) used in the study

Material	Concrete type	
	Ordinary concrete (CCR)	High strength concrete (CARR)
Cement	382	468
Silica fume	—	39
Crushed stone	1032	936
Medium sand	528	531
Fine sand	358	354
Water	180	164
Superplasticizer	1.5	3.0

strength concrete with $f_{cm,28}$ of 70 MPa. As the water/cement ratio was kept constant, the desired consistency for all mixtures was achieved by adjusting the superplasticizer admixture. The slump value was set at (120 ± 20) mm for both concrete.
The mix design, by mass, for the reference ordinary concrete (without fibers) was 1: 2.30: 2.70: 0.47. In the reference high strength concrete (without fibers),it was used the mix design, by mass, 1: 1.70: 1.80: 0.35, with silica fume incorporated in the content of 10% in substitution to cement (by volume). The materials consumption for the reference concrete mixes design is presented in Table 2. In both mixes design, fine aggregate was composed of 40% of fine sand and 60% of medium sand.
For the production of ordinary and high strength fiber reinforced concrete mixtures, both steel fibers and polymeric macrofibers were added at the content of 1.0% by volume, which corresponds to the consumptions of 78.5 kg/m³ for steel fibers and 9.5 kg/m³ for polymeric macrofibers. Thus, in total six concrete mixtures were produced, varying the cementitious matrix and the type of fiber.
For the production of concrete, the same mixing procedure was considered for all concrete. At the end of the mixing, the concrete consistency was verified by the slump test, prescribed by NBR NM 67:1998 [5]. If the slump value was within the established range, the specimens were molded. Otherwise, the slump was adjusted by the superplasticizer. After 24 hours of molding, the specimens were demolded, transferred to a humid chamber and subjected to continuous cure until 28 days of age, when the mechanical tests were performed.

2.3 Test methods

The compressive strength was determined according to the specifications of NBR 5739:2007 [6] using a hydraulic testing machine. To analyze the toughness of the concrete it was performed the flexural test in prisms and the punching test in plates, besides the Barcelona test.
The Barcelona test, also known as double punching test, was performed according to the recommendations of the Spanish standard UNE 83515:2010 [7], considering a machine piston displacement speed of 0.5 mm/min. For the flexural test in prisms, the procedure prescribed by the Japanese standard JSCE-SF4 [8] was employed, with machine piston displacement speed equal to 0.15 mm/min. For the punching test in plates, the European recommendation EFNARC [9] was used, with machine piston displacement speed equal to 1.5 mm/min.
For the result of each test, the average corresponding to the individual results obtained in the specimens was considered, as well as the standard deviation and the coefficient of variation.
To verify the influence of the factors that affect the various properties of the concrete, analysis of variance (ANOVA) and Student's t-tests were performed. All statistical tests were performed considering a 95% confidence level, being ANOVA used to evaluate the relevance of adding different fiber types and contents to the concrete properties and the Student's t-test performed to investigate which factors were responsible for changes in such properties. Details of the statistical analysis performed can be found in Leite [10].

3. Results and discussions

3.1 Compressive strength

The value of the mean compressive strength at 28 days of age ($f_{cm,28}$), for each concrete mixture produced, is presented in Table 3. The values correspond to the average of five individual results obtained in cylindrical specimens, with 100 mm in diameter and 200 mm in height.
Both ordinary and high strength concrete increased the compressive strength with the addition of fibers. Although some studies are contradictory regarding the effect of fiber addition on the compressive strength of the concrete, some researchers state that high strength fiber reinforced concrete generally has higher compressive strength than fiber-free concrete [11; 12]. According to the fib Model Code 2010 [3], the elastic properties and compressive strength of the concrete do not change significantly with the addition of fibers, since low fiber contents are used. Song and Hawang [13] found an increasing compressive strength for a high strength concrete by adding steel fibers to the content of 1.5% by volume. For higher fibers contents, the value of compressive strength began to decrease.
In ordinary concrete, the mixture with polymeric macrofibers presented the highest compressive strength, while in the high strength concrete the mixture with steel fiber showed the highest value of such strength. This situation is different from that observed by Monte [14], whose ordinary concrete with polymeric macrofibers

Table 3
Values of the compressive strength values of the studied concrete

Concrete type	f_{cm28} (MPa)	
	Mean value	CV
CCR	41.66	1.42
CC10FA	42.63	4.65
CC10PP	44.08	3.73
CARR	70.24	3.64
CAR10FA	77.60	5.63
CAR10PP	73.52	1.60
Superplasticizer	1.5	3.0

presented a significantly lower compressive strength value than the mixture with steel fibers.

According to the statistical analysis [10], there was a significant variation of the compressive strength with the addition of fibers only in the high strength concrete, which may be due to the greater adherence between fibers and matrix in this type of concrete. Furthermore, it was found that the addition of steel fibers was the factor responsible for the significant variation of compressive strength in these concrete. According to Mehta and Monteiro [15], the use of low and moderate fibers contents should have little influence on the value of compressive strength of the concrete, with its main contribution occurring in the toughness of the composite.

The mixtures with fibers and with higher compressive strength values than those of reference concrete may have exhibited hardening behavior after the matrix failure, with increased resistant capacity of the composite. To confirm this hypothesis, the load *versus* displacement curve of the concrete under compression would be necessary; however, the test machine used did not provide such data for analysis.

3.2 Barcelona test

The Barcelona test was performed considering three cylindrical specimens (150 mm in diameter and 150 mm in height) for each concrete mixture produced. The curves of load *versus* total circumferential opening displacement (TCOD) obtained by testing the ordinary and high strength concrete, with steel fibers and polymeric macrofibers, are shown in Figure 1.

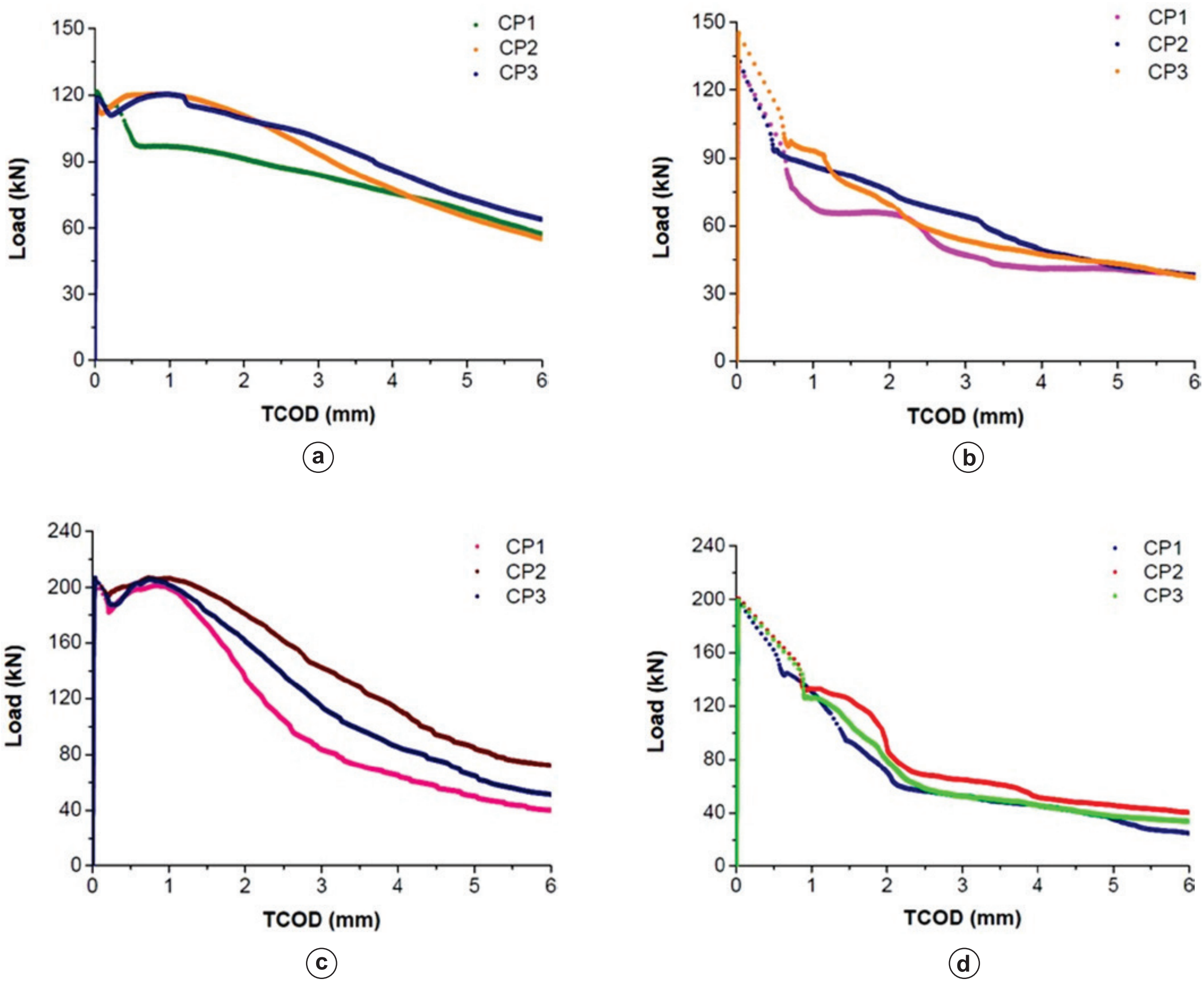

Figure 1
Barcelona test – load *versus* TCOD curves for samples of ordinary concrete with (a) steel fibers and (b) polymeric macrofibers, and high strength concrete with (c) steel fibers and (d) polymeric macrofibers, with a fiber content of 1% by volume

Table 4
Barcelona test results of the studied concrete

Concrete type	f_{ct} (MPa)		Toughness (J)		$f_{ct,TCOD=1.5}$ (MPa)		$f_{ct,TCOD=6}$ (MPa)	
	Mean	CV	Mean	CV	Mean	CV	Mean	CV
CCR	2.88	3.87	—	—	—	—	—	—
CC10FA	3.04	0.50	542.75	7.17	2.73	10.74	1.47	7.59
CC10PP	3.46	5.46	375.45	7.44	1.89	11.35	0.95	1.33
CARR	4.29	4.70	—	—	—	—	—	—
CAR10FA	5.19	0.55	750.90	14.20	4.63	6.57	1.37	30.00
CAR10PP	5.03	0.47	467.90	8.50	2.73	14.59	0.83	23.61

In the mixtures of concrete with steel fibers, both ordinary (Figure 1a) and high strength (Figure 1c), the resistant load remained constant until certain TCOD, from which they began to reduce this load, characterizing softening behavior. Polymeric macrofibers reinforced concrete showed softening behavior immediately after the matrix failure (Figures 1b and 1d). The post-peak instability phenomenon was practically nonexistent in mixtures with steel fibers; in concrete with polymeric macrofibers, such instability was observed up to TCOD values between 0.5 mm and 1.0 mm.

The Barcelona test results for all concrete mixtures are shown in Table 4. In addition to tensile strength (f_{ct}) and toughness up to a TCOD of 6 mm, it is presented the residual strength for the TCOD of 1.5 mm ($f_{ct,TCOD=1.5}$) and 6 mm ($f_{ct,TCOD=6}$), corresponding to the Service Limit State (SLS) and the Ultimate Limit State (ULS), respectively, as observed by Monte, Toaldo and Figueiredo [16].

Concrete mixtures with fibers had higher tensile strength values than the fiber-free concrete (reference). Such variation occurred due to the performance of the cementitious matrix, having little influence of the fibers in this aspect, since no mixture showed hardening behavior. However, from the statistical analysis [10], it was found that the addition of fibers significantly modified the tensile strength of ordinary and high strength concrete. In addition, the fiber type and the addition of polymeric macrofibers had a significant influence on the tensile strength of both ordinary and high strength concrete. On the other hand, in ordinary concrete the addition of steel fibers did not cause a significant change in such strength.

Regarding the toughness and the residual strength in the SLS and ULS, it was found that both ordinary and high strength steel fibers reinforced concrete showed higher values of these properties than those reinforced with polymeric macrofibers (Table 4). According to the statistical analysis [10], there was a significant variation of these properties with the fiber type in ordinary concrete, while in the high strength concrete there was a significant difference only in toughness and residual strength in the SLS.

Both steel fibers and polymeric macrofibers reinforced concrete showed an increase in the value of toughness and residual strength in the SLS with the change of the cementitious matrix. This increase was due to the better adherence between fibers and cementitious matrix that occurs in concrete with higher strength values, as highlighted by Figueiredo [2]. Due to the lower porosity, the contact area between the fibers and the matrix in the high strength concrete is larger, contributing to the formation of a stronger bond, which reflects in the mechanical behavior of the material [17].

According to the statistical analysis [10], the cementitious matrix had a significant contribution to the toughness of both steel fibers and polymeric macrofibers reinforced concrete. Further increase in the strength of concrete by using an ultra-high strength concrete, Abu-Lebdeh *et al.* [18] verified an increase of energy absorption in pullout tests, indicating an even better adherence between fibers and matrix.

It is interesting to highlight that the ordinary steel fiber reinforced concrete had a higher toughness and a residual strength in the SLS equal to the high strength concrete with polymeric macrofibers, which indicates the lower efficiency of these fibers compared to steel fibers even improving the characteristics of the cementitious matrix and, consequently, the fiber-matrix interaction. According to Student's t-test (Table 5), the difference between the toughness values is not significant, suggesting a possible performance equivalence between the fibers by changing the cementitious matrix in which they are immersed.

Table 5
Student's t-test to verify performance equivalence between fibers considering different cementitious matrices

Test method	Parameter analyzed	Concrete type	Fiber type	Fiber content	GL	t	t critical	Significant difference?
Barcelona	Toughness	CC	Steel fibers	1.0%	4	2.3294	2.7764	No
		CAR	Polymeric macrofibers	1.0%				
Flexure in prisms	Toughness	CC	Steel fibers	1.0%	4	0.0192	2.7764	No
		CAR	Polymeric macrofibers	1.0%				
Flexure in prisms	Residual strength in the SLS	CC	Steel fibers	1.0%	4	4.5327	2.7764	Yes
		CAR	Polymeric macrofibers	1.0%				
Punching in plates	Maximum load	CC	Steel fibers	1.0%	4	-0.7869	2.7764	No
		CAR	Polymeric macrofibers	1.0%				
Punching in plates	Toughness	CC	Steel fibers	1.0%	4	-0.5043	2.7764	No
		CAR	Polymeric macrofibers	1.0%				

With the change from ordinary concrete to high strength concrete, a reduction in the residual strength in the ULS was observed for both steel fibers and polymeric macrofibers reinforced mixtures. As there is a greater adherence between fibers and cementitious matrix in the high strength concrete, the fibers may have failure. Statistical analysis indicates that the change of the cementitious matrix is not significant for this parameter.

3.3 Flexural test in prisms

The flexural test in prisms was performed considering three prismatic specimens, with dimensions of 150 mm x 150 mm x 500 mm, for each concrete mixture produced. Figure 2 shows the load *versus* vertical displacement curves resulting from the flexural test on ordinary and high strength concrete prisms with steel fibers and polymeric macrofibers.

For ordinary concrete, in the CC10FA (Figure 2a) the hardening behavior predominated up to the vertical displacement of 0.25 mm, when it began to show resistant load drop. In the CC10PP (Figure 2b), an initial softening behavior was verified and, after the reduction of the resistant capacity due to the matrix failure, such concrete began to show a gain on the resistant capacity with increasing displacement (slip-hardening behavior). This result was also obtained in ordinary concrete (with compressive strength below 50 MPa) evaluated by Monte, Toaldo and Figueiredo [16] and Salvador and Figueiredo [19], who attributed this behavior to fibers defibrillation. Analyzing the ordinary concrete, only the sample with polymeric macrofibers presented post-peak instability.

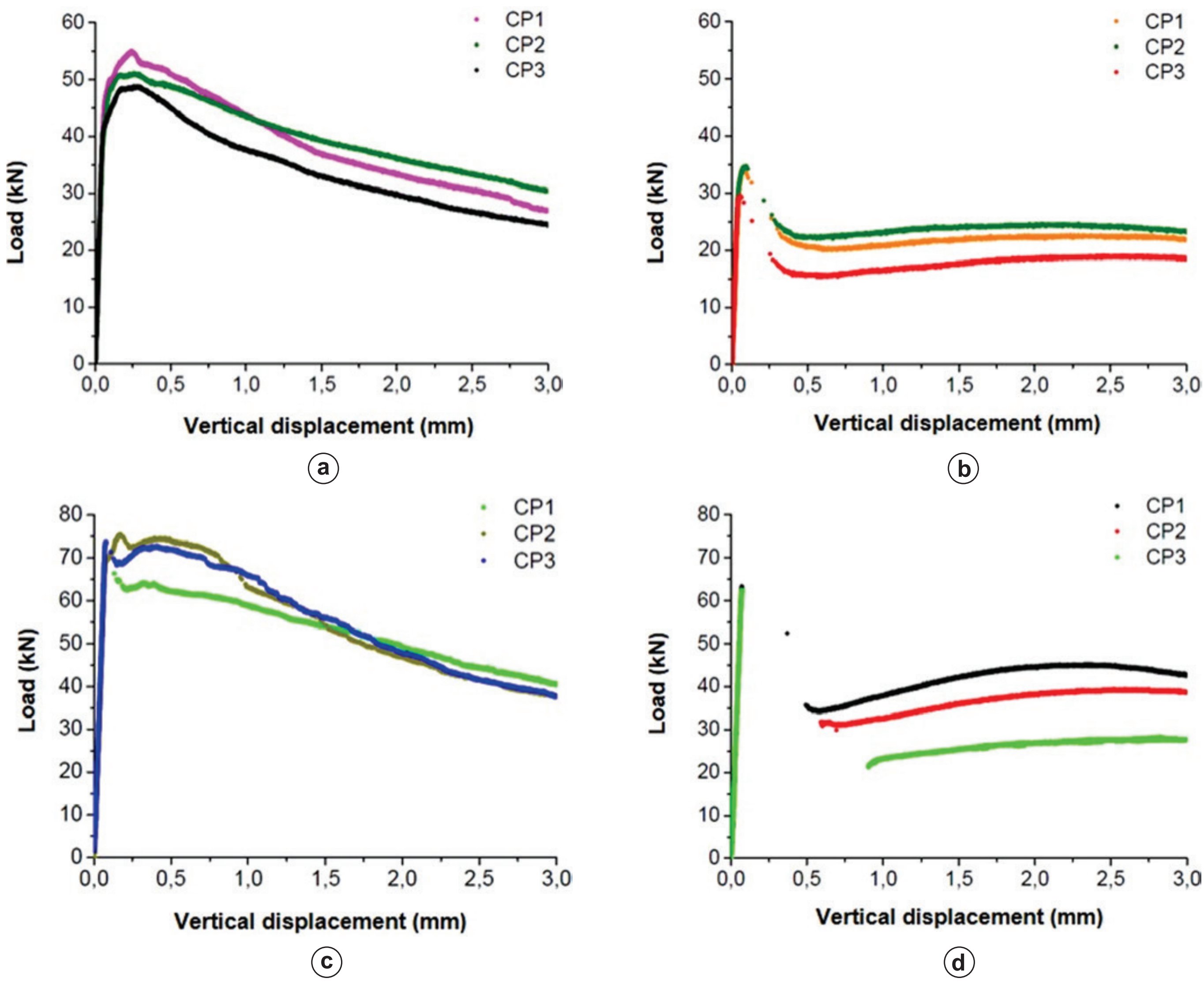

Figure 2
Flexural test in prisms – load *versus* vertical displacement curves for samples of ordinary concrete with (a) steel fibers and (b) polymeric macrofibers, and high strength concrete with (c) steel fibers and (d) polymeric macrofibers, with a fiber content of 1% by volume

For the high strength concrete, the CAR10FA curves (Figure 2c) showed a small instability after the matrix failure. In this case, the post-cracking resistant load was approximately constant and equal to the matrix load failure up to the vertical displacement of 0.75 mm. For higher displacement values, the resistant load was reduced, indicating a softening behavior. CAR10PP samples (Figure 2d) showed the highest post-peak instability, which extended to a vertical displacement of 1.0 mm in one of the prisms. It is interesting to highlight that, after the end of the instability, there was an increase of the resistant load with the increase of the displacement (slip-hardening behavior) in the mixture containing polymeric macrofibers.

The results of the flexural test in prisms for each concrete mixture are shown in Table 6. These results include flexural tensile strength ($f_{ct,f}$), toughness factor ($\overline{\sigma_b}$), and residual strength in the displacements of 0.75 mm (σ^D_{600}) and 3.00 mm (σ^D_{150}).

In most concrete, an increase in flexural tensile strength was observed with the addition of fibers. However, only the CC10FA mixture showed a hardening behavior, with increased resistant capacity after matrix failure. According to the statistical analysis [10], the addition of fibers caused significant changes in the tensile strength of both ordinary and high strength concrete. Furthermore, it was found that both type and presence of fibers had a significant influence on the value of such strength. The CC10FA concrete, which showed hardening behavior, had a flexural tensile strength value 35.9% higher than the reference concrete (CCR). This was due to the fact of having used a volume of fibers greater than the critical volume.

High strength steel fibers reinforced concrete had a flexural tensile strength value 22.8% higher than high strength concrete without fibers (CARR). End-anchored steel fibers have a more relevant contribution to flexural tensile strength compared to other types of fibers, as the use of mineral additions promotes greater adherence between matrix and steel fibers, reflecting the increased of such strength. The addition of synthetic fibers has a greater effect on the energy absorption and cracking control than on the maximum concrete load bearing [12].

Regarding the toughness factor and the residual strength in the SLS and ULS, it was found that in both ordinary and high strength concrete, the mixtures with steel fibers presented values of these properties superior to the mixtures with polymeric macrofibers. The statistical analysis of the results [10] confirmed the significant influence of the fiber type on the toughness factor and on the residual strength in the SLS of ordinary and high strength concrete, while the change in the residual strength in the ULS was considered non-significant.

By changing the cementitious matrix from ordinary to high strength concrete, the values of toughness and residual strength (SLS and ULS) had higher percentage increases in the concrete with polymeric macrofibers than in the concrete with steel fibers. According to the statistical analysis [10], the variation in the values of such properties due to the change of the cementitious matrix is considered significant for both steel fibers and polymeric macrofibers reinforced concrete. The increased strength of the matrix-fibers bond causes considerable changes in the flexural tensile strength and absorbed energy of fiberreinforced concrete [20; 21].

The values of toughness factor and residual strength in the SLS of ordinary steel fiber reinforced concrete were higher than those of high strength polymeric macrofibersreinforced concrete. Student's t-test (Table 5) indicates that the toughness factor results are statistically equivalent, while the difference between the results of residual strengthin the ULS is considered significant.

3.4 Punching test in plates

The punching test in plates was performed considering three plates, with plant dimensions of 600 mm x 600 mm and 100 mm in thickness, for each mixture produced. Figure 3 shows the load *versus* center displacement curves obtained in the test of ordinary and high strength concreteplates reinforced with steel fibers and with polymeric macrofibers.

In ordinary steel fibers reinforced concrete (Figure 3a) an increase in the resistant capacity (hardening behavior) was observed after the matrix failure. The increase of the resistant load was observed up to the center displacement of 2.5 mm, from which the load reduction was observed. The instability phenomenon was barely noticeable in this concrete. In ordinarypolymeric macrofibers reinforced concrete (Figure 3b) the predominant behavior was slip-hardening, being possible to verify successive losses and increments of the resistant capacity up to the center displacement of 7.5 mm, from which the load reduction began. Only one sample of the CC10PP concrete (Figure 3b) showed post-peak instability.

For the high strength concrete, for the steel fibers reinforced mixture (Figure 3c), the hardening behavior was verified, with increasing of the resistant load up to the center displacement of approximately 5 mm. After reaching the maximum load, the resistant capacity was reduced until the final displacement. Post-peak instability was nonexistent in this concrete. The high strength polymeric macrofibers reinforced concrete (Figure 3d) presented oscillations in the value of the resistant load after the cementitious matrix

Table 6
Results of the flexural test in prisms of the studied concrete

Concrete type	$f_{ct,f}$ (MPa)		$\overline{\sigma_b}$ (J)		σ^D_{600} (MPa)		σ^D_{150} (MPa)	
	Mean	CV	Mean	CV	Mean	CV	Mean	CV
CCR	5.07	1.34	—	—	—	—	—	—
CC10FA	6.89	6.05	5.01	7.72	5.97	8.26	3.64	11.17
CC10PP	4.37	8.66	2.87	14.39	2.59	16.87	2.82	11.70
CARR	7.97	2.49	—	—	—	—	—	—
CAR10FA	9.79	3.01	7.28	2.36	8.91	7.89	5.14	4.29
CAR10PP	8.36	0.80	5.00	16.74	4.23	10.55	4.83	21.23

Table 7
Results of the punching test in plates of the studied concrete

Concrete type	Maximum load (kN)		Toughness (J)	
	Mean	CV	Mean	CV
CCR	46.32	25.75	—	—
CC10FA	102.37	2.11	1679.83	2.59
CC10PP	68.27	13.13	1277.61	18.72
CARR	83.17	8.42	—	—
CAR10FA	171.66	11.48	2481.19	9.95
CAR10PP	107.23	9.77	1795.41	21.98

failure, being predominant the slip-hardening behavior. Figueiredo [2] attributes these oscillations to the formation of multiple cracks that occur in small displacements, and whose amount stabilizes at a given time. In this concrete, the maximum load was reached with a center displacement of approximately 7.5 mm and there was the occurrence of post-peak instability.
Regarding the maximum load values, the results obtained in the punching test in plates are presented in Table 7. It is verified that the addition of fibers caused an increase in the maximum load value of the concrete, with predominance of hardening and slip-hardening behavior. According to the statistical analysis [10], the addition of fibers caused significant changes in the maximum load value of ordinary and high strength concrete. The samples with steel fibers and poly-

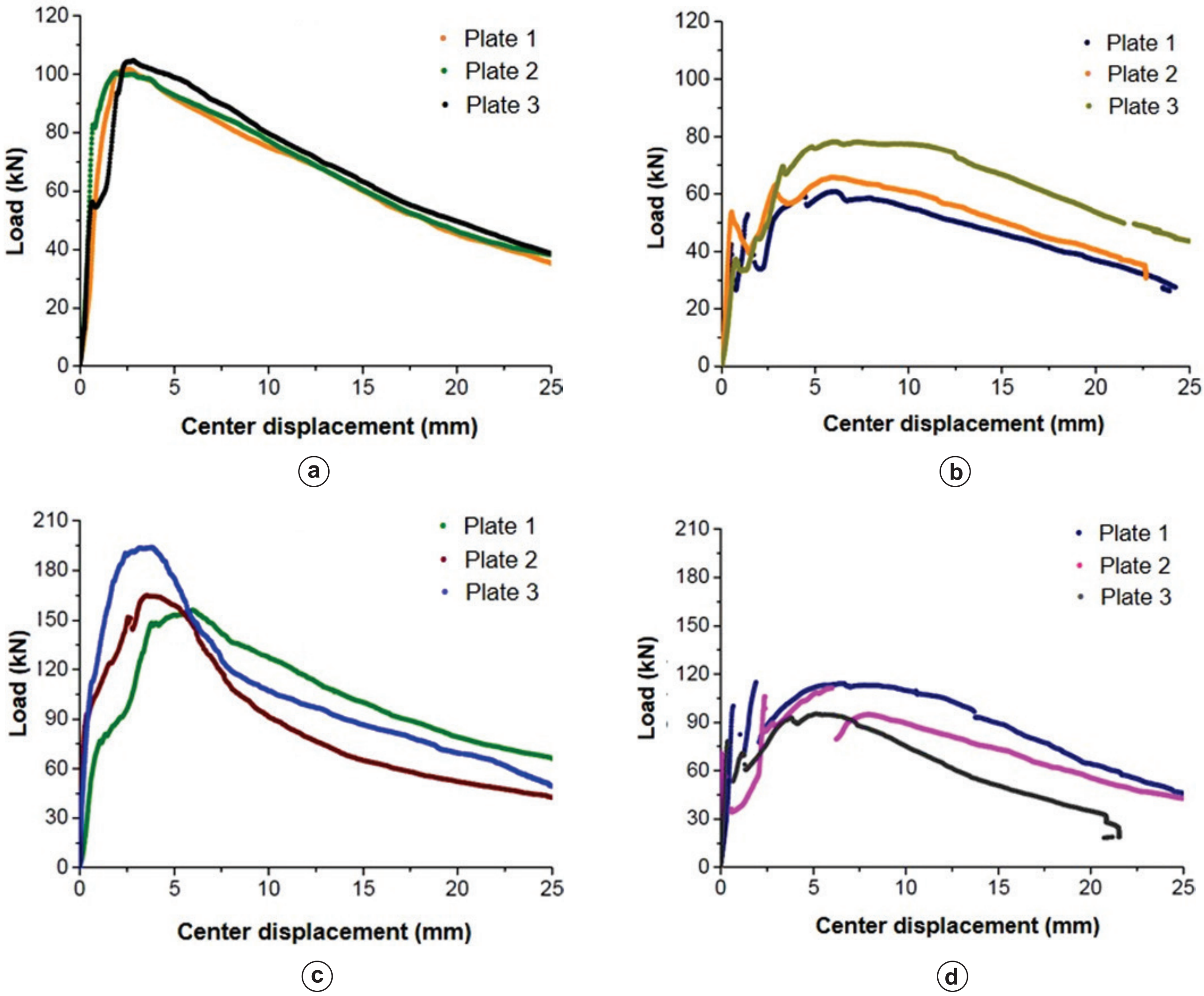

Figure 3
Punching test in plates – load *versus* center displacement curves for samples of ordinary concrete with (a) steel fibers and (b) polymeric macrofibers, and high strength concrete with (c) steel fibers and (d) polymeric macrofibers, with a fiber content of 1% by volume

meric macrofibers showed hardening and slip-hardening behavior, respectively, which contributed to present a higher maximum load than the reference concrete (CCR and CARR). In addition, the variation of the maximum load of concrete with the addition of steel fibers is considered significant for both ordinary and high strength concrete. The addition of polymeric macrofibers had a significant influence on the maximum load only of the high strength concrete.

The steel fibers reinforced concrete presented a higher maximum load than the polymeric macrofibers reinforced concrete in both cementitious matrices analyzed. Statistical analysis of the data indicates a significant influence of fiber type on the concrete maximum load value [10].

Regarding the toughness, as well as the maximum load, the values of this property obtained in the mixture with steel fibers were higher than those of the mixture with polymeric macrofibers in both ordinary and high strength concrete (Table 7). However, according to statistical analysis [10], there was a significant difference between the performance of the two fibers only in the ordinary concrete.

The percentage increase in toughness due to the change of the cementitious matrix was more relevant for steel fibers reinforced concrete than for polymeric macrofibers reinforced concrete. According to the statistical analysis [10], the change of the cementitious matrix had a significant influence on the toughness value only for steel fibers reinforced concrete.

Due to the hardening effect, both the maximum load and toughness of the ordinary steel fibers reinforced concrete were close to the values of these properties obtained in the high strength polymeric macrofibers reinforced concrete. Student's t-test (Table 5) confirms that these results are statistically equivalent, suggesting a performance equivalence between the fibers with the change of the cementitious matrix.

4. Conclusions

This paper evaluated the influence of cementitious matrix on the mechanical properties of concrete reinforced with different types of fibers. Thus, mixtures of ordinary and high strength concrete, without fibers and containing steel fibers or polymeric macrofibers, were analyzed.

The desired workability was not achieved in most ordinary fiber reinforced concrete mixtures, even with the increase in superplasticizer admixture content. By changing the cementitious matrix to a high strength concrete with a higher mortar content in the mixture, it was possible to achieve the required consistency, indicating that in some cases it is necessary to modify the cementitious matrix, and not just add superplasticizer to improve the workability of the mixture.

As for compressive strength, only the high strength concrete showed significant variation of this mechanical property with the addition of fibers, and the addition of steel fibers was the factor responsible for such variation. In high strength concrete there is a greater adherence between fibers and matrix, which may have caused this result.

In both Barcelona test and punching test in plates, there was no change in the behavior pattern of the mixtures with the change of the cementitious matrix. Only in the flexural test in prisms,the steel fiber reinforced concrete no longer exhibits hardening behavior, presenting a softening behavior with the change of the cementitious matrix. In addition, the mixtures showed different behaviors according to the test performed. While in the Barcelona test the predominant behavior was softening, in the toughness tests (flexural in prisms and punching in plates) the hardening and slip-hardening behaviors predominated.

Tensile strength and maximum load values showed significant variations with the addition of fibers, even in the case of mixtures that showed softening behavior. This may have been caused by the loss in homogeneity due to the addition of fibers.

The toughness in both Barcelona test and flexural test in prisms had a significant change with the change of the cementitious matrix of fiber reinforced concrete. In the punching test in plates, only the mixture with steel fibers showed a significant increase in toughness when using a high strength concrete.

Residual strength in the SLS of the Barcelona test and flexural test in prisms showed significant influence of the cementitious matrix. Regarding the residual strength in the ULS, only in the flexural test it was verified a significant variation of this property, indicating that the change of the cementitious matrix in the fiber reinforced concrete may not be effective in increasing the residual strength in larger displacements depending on the test performed.

It is important to highlight that statistically equivalent toughness values were obtained for ordinary steel fibersreinforced concrete and high strength polymeric macrofibers reinforced concrete. These results suggest a performance equivalence between the fibers, and indicate a lower efficiency of the polymeric macrofibers compared to steel fibers in this respect.

5. Acknowledgements

The authors thank the Coordenação de Aperfeiçoamento de Pessoal de Nível Superior (CAPES) for funding the research scholarship, and the companies Votorantim Cimentos, Grace Construction Products, Tecnosil and Belgo Bekaert Arames for donating the materials used in the study.

6. References

[1] DI PRISCO, M.; PLIZZARI, G.; VANDEWALLE, L. Fibre reincorced concrete: new desing perspectives. Materials and Structures, v.42, n.9, 2009, p.1261-1281.

[2] FIGUEIREDO, A. D. Concreto reforçado com fibras, São Paulo, 2011, Tese (Livre-Docência) – Escola Politécnica, Universidade de São Paulo, 248 p.

[3] INTERNATIONAL FEDERATION FOR STRUCTURAL CONCRETE – FIB. Model Code 2010: First complete draft – Bulletin 55. Germany: Document Competence Center Siegmar Kästl e.K., 2010, 292 p.

[4] THE CONCRETE SOCIETY. Guidance on the use of Macro-synthetic-fibre-reinforced Concrete. Trowbridge: Cromwell Press, 2007. 76 p.

[5] ASSOCIAÇÃO BRASILEIRA DE NORMAS TÉCNICAS – ABNT. Concreto - Determinação da consistência pelo abatimento do tronco de cone. – NBR NM 67, Rio de Janeiro, 1998.

[6] ASSOCIAÇÃO BRASILEIRA DE NORMAS TÉCNICAS - ABNT. Concreto – Ensaios de compressão de corpos-de-prova cilíndricos. – NBR 5739, Rio de Janeiro, 2007.

[7] ASOCIACIÓN ESPAÑOLA DE NORMALIZACIÓN Y CERTIFICACIÓN – AENOR. Hormigones con fibras - Determinación de la resistencia a fisuración, tenacidad y resistencia residual a tracción – Método Barcelona. – UNE 83515, Barcelona, 2010.

[8] THE JAPAN SOCIETY OF CIVIL ENGINEERS – JSCE. Method of tests for flexural strength and flexural toughness of steel fiber reinforced concrete. – JSCE-SF4, Tokyo, 1984.

[9] EUROPEAN FEDERATION OF PRODUCERS AND APPLICATORS OF SPECIALIST PRODUCTS FOR STRUCTURES – EFNARC. European Specification for Sprayed Concrete. Farnham, 1996.

[10] LEITE, A. M. Avaliação do uso da macrofibra polimérica na composição de concreto para fins estruturais. São Carlos, Dissertação (Mestrado em Engenharia de Estruturas) - Escola de Engenharia de São Carlos, Universidade de São Paulo, 257 p.

[11] MENDOZA, C. J.; AIRE, C.; DAVILA, P. Influencia de las fibras de polipropileno en las propriedades del concreto en estados plástico y endurecido. Concreto y cemento. Investigación y desarrollo, v.2, n.2, 2011, p.5-47.

[12] AFROUGHSABET, V.; BIOLZI, L.; OZBAKKALOGLU, T. High-performance fiber-reinforced concrete: a review. Journal of Materials Science, v. 51, n. 14, 2016, p. 6517-6551.

[13] SONG, P.S; HAWANG, S. Mechanical properties of high-strength steel fibre-reinforced concrete. Construction and Building Materials, v.18, n.9, 2004, p. 669-673.

[14] MONTE, R. Caracterização e controle do comportamento mecânico do concreto reforçado com fibras para tubos. São Paulo, Tese (Doutorado em Ciências) – Escola Politécnica, Universidade de São Paulo, 159 p.

[15] MEHTA, K.; MONTEIRO P. J. M. Concreto. Microestrutura, Propriedades e Materiais, São Paulo: Ibracon, 4ed, 2014. 751 p.

[16] MONTE, R.; TOALDO, G. S.; FIGUEIREDO, A. D. Avaliação da tenacidade de concretos reforçados com fibras através de ensaios com sistema aberto. Revista Matéria, v.19, n.2, 2014, p. 132-149.

[17] BUTTIGNOL, T. E. T; SOUSA, J. L. A. O.; BITTENCOURT; T. N. Ultra High-Performance Fiber-Reinforced Concrete (UHPFRC): a review of material properties and design procedures. Ibracon Structures and Materials Journal, v. 10, n. 4, 2017, p. 957-971.

[18] ABU-LEBDEH, T.; HAMOUSH, S.; HEARD, W.; ZORNIG, B. Effect of matrix strength on pullout behavior of steel fiber reinforced very-high strength concrete composites. Construction and Building Materials, v.25, n.1, 2011, p. 39-46.

[19] SALVADOR, R. P.; FIGUEIREDO, A. D. Análise comparativa de comportamento mecânico de concreto reforçado com macrofibra polimérica e com fibras de aço. Revista Matéria, v.18, n.2, 2013, p. 1273-1285.

[20] GRAY, R. J.; Johnston, C. D. The influence of fibre-matrix interfacial bond strength on the mechanical properties of steel fibre reinforced mortars. The International Journal of Cement Composites and Lightweight Concrete, v.9, n.1, 1987, p. 43-55.

[21] ABBAS, Y. M.; KHAN, M. I. Fiber–Matrix Interactions in Fiber-Reinforced Concrete: A Review. Arabian Journal for Science and Engineering, v.41, n.4, p. 1183-1198.

Volume 13, Number 3 (June 2020) p. 543 – 562 • ISSN 1983-4195
http://dx.doi.org/10.1590/S1983-41952020000300006

REVISTA IBRACON DE ESTRUTURAS E MATERIAIS
IBRACON STRUCTURES AND MATERIALS JOURNAL

Influence of the cementitious matrix on the behavior of fiber reinforced concrete

Influência da matriz cimentícia no comportamento de concretos reforçados com fibras

A. M. LEITE [a]
alexmacedoleite@gmail.com
https://orcid.org/0000-0003-4022-6787

A. L. DE CASTRO [a]
alcastro@sc.usp.br
https://orcid.org/0000-0002-7248-7327

Abstract

One of the main purposes of the addition of fibers to the concrete is the control of the plastic shrinkage cracking in the fresh state and the increase of the post-crack resistance in the hardened state. The cementitious matrix is one of the factors that influences the performance of fiber reinforced concrete, interfering in the fluidity of the mixture and in the adhesion between fiber and matrix. In this context, the present paper evaluates the behavior of two concrete, one of conventional strength and another of high-strength, without fiber and with a content of 1%, by volume, of fiber, being used steel fiber and macro-polymeric fiber. For this, the mechanical properties of the concrete were evaluated in the hardened state by the tests of compressive strength, Barcelona, flexure of prisms and punching of plates. From the experimental results, statistically analyzed, there were significant changes in toughness and residual strength due to change in the cementitious matrix. Finally, an equivalence of performance between the fibers as to the toughness was observed, with the change of the cementitious matrix.

Keywords: fiber reinforced concrete, cementitious matrix, steel fiber, macro-polimeric fiber, properties.

Resumo

Uma das principais finalidades da adição de fibras ao concreto é o controle da fissuração por retração plástica no estado fresco, e o aumento da capacidade resistente pós-fissuração no estado endurecido. A matriz cimentícia é um dos fatores que influencia no desempenho do concreto reforçado com fibras, interferindo na fluidez da mistura e na aderência entre as fibras e a matriz. Neste contexto, o presente trabalho avalia o comportamento de dois concretos, um de resistência convencional e outro de alta resistência, sem fibras e com teor de 1%, em volume, de fibras, sendo utilizadas fibras de aço e macrofibras polimérica. Para isso, foram avaliadas as propriedades mecânicas dos concretos no estado endurecido, a partir dos ensaios de resistência à compressão, Barcelona, flexão em prismas e punção em placas. A partir dos resultados experimentais, analisados estatisticamente, verificou-se alterações significativas da tenacidade e da resistência residual com a mudança da matriz cimentícia. Por fim, observou-se uma equivalência de desempenho entre as fibras quanto à tenacidade, com a alteração da matriz cimentícia.

Palavras-chave: concreto reforçado com fibras, matriz cimentícia, fibras de aço, macrofibras polimérica, propriedades.

[a] *University of São Paulo, Department of Structural Engineering, São Carlos School of Engineering, São Carlos, SP, Brazil.*

Received: 15 Oct 2018 • Accepted: 07 Apr 2019 • Available Online: 26 May 2020

1. Introdução

O concreto reforçado com fibras se trata de um material compósito que vem sendo utilizado para diversas aplicações, como revestimento de túneis, radier, pisos industriais, elementos pré-moldados, dentre outras. As fibras melhoram a distribuição das fissuras e limitam as aberturas destas no Estado Limite de Serviço, reduzindo a exposição do concreto ao ambiente. O reforço com fibras é apropriado para estruturas com alta capacidade de distribuição de tensões. No caso de estruturas com tensões localizadas e tensões dispersas, podem ser utilizados simultaneamente reforços locais com barras de aço e fibras dispostas aleatoriamente no concreto [1].

A adição de fibras ao concreto provoca alterações nas propriedades do material, tanto no estado fresco quanto no estado endurecido. No estado fresco, para melhorar a trabalhabilidade da mistura, que é afetada pela incorporação de fibras, geralmente utiliza-se aditivo superplastificante. No entanto, nos casos de concretos com maiores teores de fibras, a adição de aditivo superplastificante pode ser inviável, sendo necessário alterar a matriz cimentícia para melhorar a fluidez do concreto.

A principal contribuição das fibras ocorre no estado endurecido do concreto,após a ruptura da matriz cimentícia, fornecendo resistência residual ao compósito. As fibras agem como ponte de transferência de tensão, reduzindo a concentração de tensão nas extremidades das fissuras. Com isso, o concreto se torna um material pseudo-dúctil, apresentando certa ductilidade [2].

A matriz cimentícia é um dos fatores que interfere no comportamento do concreto reforçado com fibras no estado endurecido. As propriedades da matriz afetam a aderência entre as fibras e a matriz, refletindo no desempenho do concreto pós-fissuração [2]. Assim, dependendo do tipo e do teor de fibra adicionada, e das propriedades da matriz cimentícia, o concreto reforçado com fibras pode manifestar comportamento *softening* ou *hardening* após a fissuração. O comportamento *softening* é marcado por deformações localizadas em uma única fissura e por uma redução da carga resistente pós-fissuração, enquanto que no comportamento *hardening* ocorre a formação de múltiplas fissuras e aumento da capacidade resistente após ruptura do concreto [3].

Atualmente existem fibras de diversos materiais disponíveis no mercado da construção civil: aço, polímero, vidro etc. As propriedades do material que constitui as fibras, como módulo de elasticidade e resistência à tração, vão definir sua função no concreto. Fibras com elevado módulo de elasticidade e resistência à tração superior à da matriz devem atuar como reforço primário do concreto, proporcionando capacidade resistente após a fissuração da matriz. Já fibras que possuem baixo módulo de elasticidade e resistência à tração são mais utilizadas no controle da fissuração por retração plástica do concreto.

1.1 Justificativa e objetivo

Os dois principais tipos de fibras utilizadas como reforço primário do concreto são as fibras de aço e as macrofibras poliméricas. Enquanto a primeira é historicamente mais empregada para tal finalidade, visto que começou a ser comercializada primeiro, na década de 1970, e possui propriedades mais vantajosas (maior módulo de elasticidade e maior resistência à tração),a segunda tem uma comercialização e aplicação mais recente, na década de 2000[4], sendo alvo de vários estudos que buscam compreender melhor seu desempenho no concreto, principalmente em concretos de alta resistência.

Além disso, estudos envolvendo a influência da matriz cimentícia no desempenho do concreto reforçado com fibras ainda são limitados. Sabe-se que uma matriz mais resistente possuiu uma maior aderência com as fibras [2]. No entanto, pouco se conhece a respeito do impacto dessa maior aderência nas propriedades mecânicas do concreto reforçado com fibras. Com isso, o presente estudo busca avaliar a influência da matriz cimentícia no comportamento de concretos reforçados com fibras, considerando o uso de fibras de aço e macrofibras poliméricas como elemento de reforço aos concretos de resistência convencional e de alta resistência.

2. Materiais e programa experimental

2.1 Materiais

Para a produção dos concretos foi utilizado o cimento Portland composto com pozolana, com classe de resistência de 32 MPa (CPII Z 32). No concreto de alta resistência também foi utilizada sílica ativa derivada do processo de produção do silício metálico ou de ligas de ferro silício.

Como agregado miúdo foram utilizadas duas areias naturais, de origem quatzosa, classificadas como areia fina e areia média. O agregado graúdo empregado foi uma brita de origem basáltica, com dimensão máxima característica de 19 mm.

Em todas as concretagens foi utilizada água proveniente da rede de abastecimento local. Para se alcançar a consistência desejada foi empregado um aditivo superplastificante à base de policarboxilatos.

No caso das misturas com fibras foram utilizados dois tipos de fibras como reforço do concreto: fibras de aço e macrofibras poliméricas. As fibras de aço possuíam seção transversal circular e ancoragem nas extremidades; já as macrofibras poliméricas eram constituídas de polipropileno e possuíam seção transversal retangular, formato reto e com ranhuras na superfície, de maneira que a ancoragem ocorria ao longo do seu comprimento. Na Tabela 1 são apresentadas as principais propriedades das fibras utilizadas,

Tabela 1
Propriedades físicas e mecânicas das fibras utilizadas na pesquisa

Propriedade	Tipo de fibras	
	Fibras de aço	Macrofibras poliméricas
Massa específica (g/cm^3)	7,85	0,95
Comprimento (mm)	50	50
Fator de forma	45	75
Módulo de elasticidade (GPa)	210	7
Resistência à tração (MPa)	1115	550

Tabela 2
Consumo de materiais (em kg/m³ de concreto) para os traços de concreto de referência (sem fibras) utilizados na pesquisa

Material	Tipo de concreto	
	Concreto convencional (CCR)	Concreto de alta resistência (CARR)
Cimento	382	468
Sílicaativa	—	39
Brita	1032	936
Areia média	528	531
Areia fina	358	354
Água	180	164
Superplastificante	1,5	3,0

de acordo com dados fornecidos pelos fabricantes.

2.2 Dosagem e produção dos concretos

Na presente pesquisa foram elaborados dois traços de concreto: um traço para um concreto convencional, com resistência média à compressão aos 28 dias de idade ($f_{cm,28}$) de 40 MPa; e outro para um concreto de alta resistência, com $f_{cm,28}$ de 70 MPa. Como a relação água/cimento foi mantida constante, a consistência desejada para todas as misturas foi alcançada pelo ajuste do aditivo superplastificante. O abatimento foi fixado em (120 ± 20) mm para os dois concretos.
O traço em massa adotado para o concreto convencional de referência (sem fibras) foi 1: 2,30: 2,70: 0,47. Já no concreto de alta resistência de referência (sem fibras) foi utilizado o traço em massa 1: 1,70: 1,80: 0,35, com a sílica incorporada no teor de 10% em substituição volumétrica ao cimento. O consumo de materiais para os traços de concreto é apresentado na Tabela 2. Em ambos os traços, o agregado miúdo foi composto por 40% de areia fina e 60% de areia média.
Para a produção das misturas de concreto convencional e de alta resistência com fibras, tanto as fibras de aço quanto as macrofibras poliméricas foram adicionadas no teor de 1,0%, em volume, o que corresponde às dosagens de 78,5 kg/m³ para as fibras de aço e de 9,5 kg/m³ para as macrofibras poliméricas. Dessa forma, no total foram produzidas 6 misturas de concreto, variando-se a matriz cimentícia e o tipo de fibra.
Para a produção dos concretos foi adotado o mesmo procedimento de mistura para todos os concretos. Ao final da mistura a consistência do concreto era verificada por meio do ensaio de abatimento de tronco de cone, prescrito pela NBR NM 67:1998 [5]. Caso o valor do abatimento estivesse dentro do intervalo estabelecido, procedia-se com a moldagem dos corpos de prova. Caso contrário, o abatimento era ajustado pelo superplastificante. Após 24 horas da moldagem, os corpos de prova eram desmoldados, transferidos para câmara úmida e submetidos à cura contínua até os 28 dias de idade, quando foram realizados os ensaios mecânicos.

2.3 Métodos de ensaio

A resistência à compressão foi determinada de acordo com as especificações da NBR 5739:2007 [6], utilizando uma máquina de ensaio hidráulica. Para analisar a tenacidade dos concretos foram realizados os ensaios de flexão em prismas e de punção em placas, além do ensaio Barcelona.
O ensaio Barcelona, também conhecido como ensaio de duplo puncionamento, foi realizado de acordo com as recomendações da norma espanhola UNE 83515:2010 [7], adotando-se uma velocidade de deslocamento do pistão da máquina de 0,5 mm/min. Para o ensaio de flexão em prismas, foi empregado o procedimento prescrito pela norma japonesa JSCE-SF4 [8], com velocidade de deslocamento do pistão da máquina igual a 0,15 mm/min. Para o ensaio de punção em placas, utilizou-se a recomendação europeia EFNARC [9], com velocidade de deslocamento do pistão da máquina igual a 1,5 mm/min.
Para o resultado final de cada ensaio foi considerada a média referente aos resultados individuais obtidos nos corpos de prova, assim como o desvio-padrão e o coeficiente de variação.
Para verificar a influência dos fatores que afetam as diversas propriedades do concreto, foram realizadas análise de variância (ANOVA) e testes t de *Student*. Todos os testes estatísticos foram realizados considerando um nível de confiança de 95%, sendo a ANOVA usada para avaliar a relevância da adição de diferentes tipos e teores de fibras nas propriedades do concreto e o teste t de *Student* realizado para investigar quais os fatores responsáveis pelas alterações em tais propriedades. Detalhes da análise estatística realizada podem ser encontrados em Leite [10].

3. Resultados e discussões

3.1 Resistência à compressão

O valor da resistência média à compressão aos 28 dias de idade (f_{cm28}), referente a cada mistura de concreto produzida, é apresentado na Tabela 3. Os valores correspondem à média de cinco resultados individuais obtidos em corpos de prova cilíndricos, com 100 mm de diâmetro e 200 mm de altura.
Tanto no concreto convencional quanto no concreto de alta resistência houve um aumento da resistência à compressão com a adição de fibras. Apesar de alguns estudos serem contraditórios quanto ao efeito da adição de fibras na resistência à compressão do concreto, alguns autores afirmam que o concreto de alta resistência reforçado com fibras geralmente apresenta resistência à compressão maior em relação ao concreto sem fibras [11; 12]. De acordo com o *fib Model Code 2010* [3], as propriedades elásticas e a resistência à compressão do concreto não são alteradas significativamente com a adição de fibras, desde que sejam utilizados baixos teores. Song e Hawang [13] verificaram um aumento crescente da resistência à compressão de um concreto de alta resistência com a adição de fibras de aço até o teor de 1,5% em volume. Para teores superiores, o valor da resistência à compressão começou a diminuir.
No concreto convencional a mistura com macrofibras poliméricas apresentou a maior resistência à compressão, enquanto que no

Tabela 3
Valores do ensaio de resistência à compressão dos concretos estudados

Tipo de concreto	f_{cm28} (MPa)	
	Média	CV
CCR	41,66	1,42
CC10FA	42,63	4,65
CC10PP	44,08	3,73
CARR	70,24	3,64
CAR10FA	77,60	5,63
CAR10PP	73,52	1,60
Superplasticizer	1.5	3.0

concreto de alta resistência foi a amostra com fibras de aço que manifestou um maior valor de tal resistência. Esta situação é diferente da que foi verificada por Monte [14], cujo concreto convencional com macrofibras poliméricas apresentou valor de resistência à compressão significativamente menor do que a mistura com fibras de aço.

Segundo a análise estatística [10], houve uma variação significativa da resistência à compressão com a adição de fibras apenas no concreto de alta resistência, o que pode ter sido ocasionado pela maior aderência entre as fibras e a matriz neste tipo de concreto. Além disso, verificou-se que a adição de fibras de aço foi o fator responsável pela variação significativa da resistência à compressão nesses concretos. De acordo com Mehta e Monteiro [15], a utilização de baixos e moderados teores de fibras deve exercer pequena influência no valor da resistência à compressão do concreto, com sua principal contribuição ocorrendo na tenacidade do compósito.

As misturas com fibras com valores de resistência à compressão superiores aos dos concretos de referência podem ter apresentado comportamento *hardening* após a ruptura da matriz, com aumento da capacidade resistente do compósito. Para confirmar esta hipótese, seria necessária a curva carga *versus* deslocamento dos concretos sob compressão; no entanto, a máquina de ensaio utilizada não fornecia tal dado para análise.

3.2 Ensaio Barcelona

O ensaio Barcelona, também conhecido como ensaio de duplo puncionamento, foi realizado considerando três corpos de prova cilíndricos (com 150 mm de diâmetro e 150 mm de altura) para cada mistura de concreto produzida. Os gráficos das curvas carga *versus* aumento do perímetro circunferencial da amostra (TCOD) obtidos no ensaio do concreto convencional e de alta resistência com fibras de aço e com macrofibras poliméricas são apresentados na Figura 1.

Nas misturas de concreto com fibras de aço, tanto convencional (Figura 1a) quanto de alta resistência (Figura 1c), a carga resistente se manteve constante até determinado TCOD, a partir do qual começou a apresentar redução dessa carga, caracterizando o comportamento *softening*. Já os concretos com macrofibras poliméricas manifestaram comportamento *softening* imediatamente após a ruptura da matriz (Figuras 1b e 1d). O fenômeno de instabilidade pós-pico foi praticamente inexistente nas amostras com fibras de

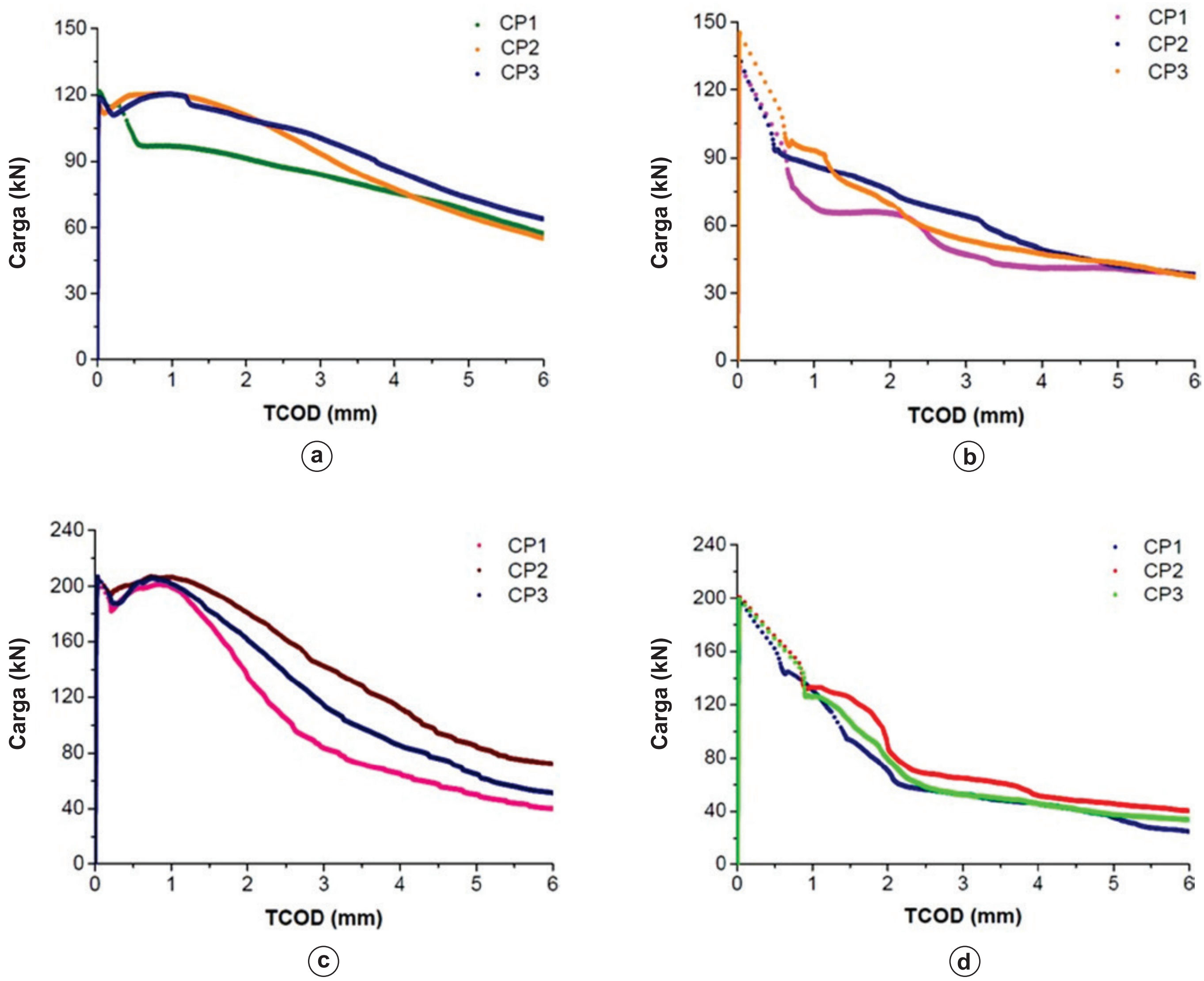

Figura 1
Ensaio Barcelona – curvas carga *versus* TCOD referentes às amostras de concreto convencional com (a) fibras de aço e (b) macrofibras poliméricas, e de concreto de alta resistência com (c) fibras de aço e (d) macrofibras poliméricas, com teor de fibrasde 1%, em volume

Tabela 4
Resultados do ensaio Barcelona dos concretos estudados

Tipo de concreto	f_{ct} (MPa)		Tenacidade (J)		$f_{ct,TCOD=1,5}$ (MPa)		$f_{ct,TCOD=6}$ (MPa)	
	Média	CV	Média	CV	Média	CV	Média	CV
CCR	2,88	3,87	—	—	—	—	—	—
CC10FA	3,04	0,50	542,75	7,17	2,73	10,74	1,47	7,59
CC10PP	3,46	5,46	375,45	7,44	1,89	11,35	0,95	1,33
CARR	4,29	4,70	—	—	—	—	—	—
CAR10FA	5,19	0,55	750,90	14,20	4,63	6,57	1,37	30,00
CAR10PP	5,03	0,47	467,90	8,50	2,73	14,59	0,83	23,61

aço; já no concreto com macrofibras poliméricas foi observada tal instabilidade até valores de TCOD entre 0,5 mm e 1,0 mm.
Os resultados do ensaio Barcelona para todas as misturas de concreto estão dispostos na Tabela 4. Além da resistência à tração (f_{ct}) e da tenacidade até um TCOD de 6 mm, também é apresentada a resistência residual referente ao TCOD de 1,5 mm ($f_{ct,TCOD=1,5}$) e de 6 mm ($f_{ct,,TCOD=6}$), correspondentes ao Estado Limite de Serviço (ELS) e ao Estado Limite Último (ELU), respectivamente, conforme observado por Monte, Toaldo e Figueiredo [16].
As misturas de concreto com fibras apresentaram valores de resistência à tração maiores do que os concretos sem fibras. Tal variação ocorreu devido ao desempenho da matriz cimentícia, possuindo pouca influência das fibras neste aspecto, visto que nenhuma mistura apresentou comportamento *hardening*. No entanto, por meio da análise estatística [10], foi constatado que a adição de fibras modificou significativamente a resistência à tração dos concretos convencional e de alta resistência. Além disso, o tipo de fibra e a adição de macrofibras poliméricas adicionadas tiveram uma influência significativa na resistência à tração tanto do concreto convencional quanto do concreto de alta resistência. Por outro lado, no concreto convencional a adição de fibras de aço não provocou uma alteração significativa em tal resistência.
Com relação à tenacidade e à resistência residual no ELS e ELU, verificou-se que as amostras de concreto com fibras de aço, tanto convencional quanto de alta resistência, apresentaram valores destas propriedades superiores aos concretos com macrofibras poliméricas (Tabela 4). De acordo com a análise estatística [10], houve uma variação significativa desses parâmetros com o tipo de fibras no concreto convencional, enquanto no concreto de alta resistência houve uma diferença significativa apenas na tenacidade e na resistência residual no ELS.
Tanto no concreto com fibras de aço quanto no concreto com macrofibras poliméricas foi verificado um acréscimo no valor da tenacidade e da resistência residual no ELS com a mudança da matriz cimentícia. Este aumento ocorreu devido à melhor aderência entre as fibras e a matriz cimentícia que acontece nos concretos de maiores resistências, conforme destacado por Figueiredo [2]. Devido a menor porosidade, a área de contato entre as fibras e a matriz no concreto de alta resistência é maior, contribuindo para a formação de uma ligação mais resistente, que reflete no comportamento mecânico do material [17].
De acordo com a análise estatística [10], a matriz cimentícia teve uma contribuição significativa para a tenacidade tanto do concreto com fibras de aço quanto do concreto com macrofibras poliméricas. Aumentando ainda mais a resistência do concreto, coma utilização de um concreto de ultra-alta resistência, Abu-Lebdeh *et al.* [18] verificaram um aumento da absorção de energia em ensaios *pull-out,* indicando uma melhor aderência das fibras com a matriz.
É interessante destacar que o concreto convencional com fibras de aço apresentou um valor de tenacidade superior e de resistência residual no ELS igual ao do concreto de alta resistência com macrofibras poliméricas, o que indica a menor eficiência destas fibras frente às fibras de aço mesmo melhorando as características da

Tabela 5
Teste t de *Student* para verificação daequivalência de desempenho entre as fibras considerando matrizes cimentícias diferentes

Método de ensaio	Parâmetro analisado	Tipo de concreto	Tipo de fibras	Teor de fibras	GL	t	t crítico	Diferença significativa?
Barcelona	Tenacidade	CC	Fibras de aço	1,0%	4	2,3294	2,7764	Não
		CAR	Macrofibras poliméricas	1,0%				
Flexão em prismas	Tenacidade	CC	Fibras de aço	1,0%	4	0,0192	2,7764	Não
		CAR	Macrofibras poliméricas	1,0%				
Flexão em prismas	Resistência residual no ELS	CC	Fibras de aço	1,0%	4	4,5327	2,7764	Sim
		CAR	Macrofibras poliméricas	1,0%				
Punção em placas	Carga máxima	CC	Fibras de aço	1,0%	4	-0,7869	2,7764	Não
		CAR	Macrofibras poliméricas	1,0%				
Punção em placas	Carga máxima	CC	Fibras de aço	1,0%	4	-0,5043	2,7764	Não
		CAR	Macrofibras poliméricas	1,0%				

matriz cimentícia e, consequentemente, a interação fibras-matriz. De acordo com o teste t de *Student* (Tabela 5), a diferença entre os valores de tenacidade é não significativa, o que sugere uma possível equivalência de desempenho entre as fibras alterando-se a matriz cimentícia na qual estão imersas.

Com a alteração do concreto convencional para o concreto de alta resistência foi observado uma redução da resistência residual no ELU tanto para a mistura com fibras de aço quanto com macrofibras poliméricas. Como há uma maior aderência entre as fibras e a matriz cimentícia no concreto de alta resistência, pode ter havido ruptura das fibras. A análise estatística indica que a alteração da matriz cimentícia é não significativa para este parâmetro.

3.3 Ensaio de flexão em prismas

O ensaio de flexão em prismas foi realizado considerando três corpos de prova prismáticos, com dimensões de 150 mm x 150 mm x 500 mm, para cada mistura de concreto produzida. A Figura 2 contém as curvas carga *versus* deslocamento vertical resultantes do ensaio de flexão em prismas de concreto convencional e de alta resistência com fibras de aço e com macrofibras poliméricas. Para os concretos convencionais, no CC10FA (Figura 2a) predominou-se o comportamento *hardening* até o deslocamento vertical de 0,25 mm, quando começou a apresentar queda da carga resistente. Já no CC10PP (Figura 2b) foi verificado um comportamento inicial de *softening* e, após a redução da capacidade resistente devido à ruptura da matriz, tal concreto começou a apresentar um ganho da capacidade resistente com o aumento do deslocamento (*slip-hardening*). Este resultado também foi obtido em concretos convencionais (com resistência à compressão inferior a 50 MPa) avaliados por Monte, Toaldo e Figueiredo [16] e Salvador e Figueiredo [19], os quais atribuíram este comportamento ao desfibrilamento das fibras. Analisando o concreto convencional, apenas a amostra com macrofibras poliméricas apresentou instabilidade pós-pico.

No caso dos concretos de alta resistência, as curvas referentes ao CAR10FA (Figura 2c) apresentaram uma pequena instabilidade após a ruptura da matriz. Neste caso, a carga resistente pós-fissuração ficou aproximadamente constante e igual à carga de ruptura da matriz até o deslocamento vertical de 0,75 mm. Para valores de deslocamentos superiores, houve redução da carga

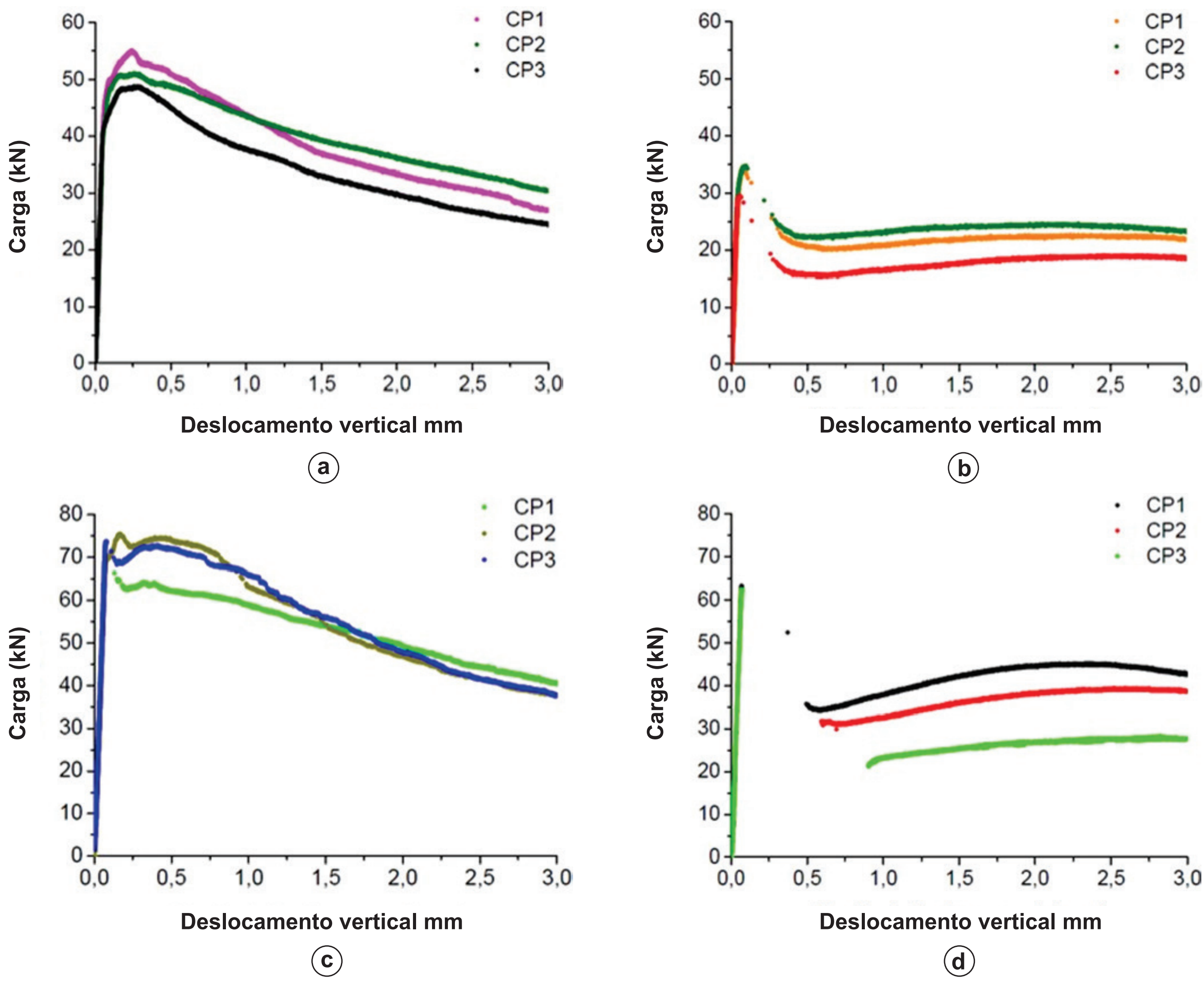

Figura 2
Ensaio de flexão em prismas – curvas carga *versus* deslocamento vertical referentes às amostras de concreto convencional com (a) fibras de aço e (b) macrofibras poliméricas, e de concreto de alta resistência com (c) fibras de aço e (d) macrofibras poliméricas, com teor de fibrasde 1%, em volume

resistente, indicando um comportamento *softening*. As amostras do CAR10PP (Figura 2d) apresentaram a maior instabilidade pós-pico, a qual se estendeu até um deslocamento vertical de 1,0 mm em um dos prismas. É interessante destacar que, após o fim da instabilidade, houve um aumento da carga resistente com o incremento de deslocamento (*slip-hardening*) na mistura contendo macrofibras poliméricas.

Os resultados do ensaio de flexão em prismas para cada mistura de concreto estão dispostos na Tabela 6. Tais resultados incluem resistência à tração na flexão ($f_{ct,f}$), fator de tenacidade ($\overline{\sigma_b}$) e resistência residual nos deslocamentos de 0,75 mm (σ_{600}^{D}) e de 3,00 mm (σ_{150}^{D}).

Na maioria dos concretos foi verificado um aumento da resistência à tração na flexão com a adição de fibras. No entanto, apenas a mistura CC10FA manifestou um comportamento *hardening*, com acréscimo da capacidade resistente após a ruptura da matriz. De acordo com a análise estatística [10], a adição de fibras provocou alterações significativas na resistência à tração tanto do concreto convencional quanto do concreto de alta resistência. Além disso, verificou-se que tanto o tipo quanto a presença de fibras tiveram uma influência significativa no valor de tal resistência. O concreto CC10FA, que manifestou comportamento *hardening*, apresentou um valor de resistência à tração na flexão 35,9% superior ao concreto de referência (CCR). Isto ocorreu devido ao fato de se ter utilizado um volume de fibras superior ao volume crítico.

O concreto de alta resistência com fibras de aço apresentou um valor de resistência à tração na flexão 22,8% superior ao concreto de alta resistência sem fibras (CAR). As fibras de aço com ancoragem nas extremidades têm uma contribuição mais relevante na resistência à tração na flexão comparadas a outros tipos de fibras, uma vez que a utilização de adições minerais promove uma maior aderência entre a matriz e as fibras de aço, refletindo no aumento de tal resistência. A adição de fibras sintéticas tem um maior efeito na absorção de energia e no controle da fissuração do que na carga máxima de suporte do concreto[12].

Com relação ao fator de tenacidade e à resistência residual no ELS e ELU, verificou-se que tanto no concreto convencional quanto no concreto de alta resistência, as misturas com fibras de aço apresentaram valores destas propriedades superiores às misturas com macrofibras poliméricas.A análise estatística dos resultados [10] confirmou a influência significativa do tipo de fibra no fator de tenacidade e resistência residual no ELS dos concretos convencional e de alta resistência, enquanto que a alteração da resistência residual no ELU foi considerada não significativa.

Com a alteração da matriz cimentícia de concreto convencional para concreto de alta resistência, os valores de tenacidade e de resistência residual (ELS e ELU) tiveram maiores aumentos percentuais no concreto com macrofibras poliméricas do que no concreto com fibras de aço. Segundo a análise estatística [10], a variação nos valores de tais propriedades devido à mudança da matriz cimentícia é considerada significativa tanto para o concreto com fibras de aço quanto para o concreto com macrofibras poliméricas. O aumento da resistência da ligação fibras-matriz provoca alterações consideráveis na resistência à tração na flexão e na energia absorvida do concreto reforçado com fibras [20; 21].

Os valores do fator de tenacidade e da resistência residual no ELS do concreto convencional com fibras de aço foram maiores do que os do concreto de alta resistência com macrofibras poliméricas. O teste t de *Student* (Tabela 5) indica que os resultados de fator de tenacidade são estatisticamente equivalentes, enquanto que a diferença entre os resultados de resistência residual no ELS é considerada significativa.

3.4 Ensaio de punção em placas

O ensaio de punção em placas foi realizado considerando três placas, com dimensões em planta de 600 mm x 600 mm e 100 mm de espessura, para cada mistura produzida. Na Figura 3 são apresentadas as curvas carga *versus* deslocamento central obtidas no ensaio de placas de concreto convencional e de alta resistência reforçado com fibras de aço e com macrofibras poliméricas.

No concreto convencional com fibras de aço (Figura 3a) foi observado um aumento da capacidade resistente (*hardening*) após a ruptura da matriz.O aumento da carga resistente foi observado até o deslocamento central de 2,5 mm, a partir do qual foi observada a redução da carga. O fenômeno de instabilidade foi pouco perceptível neste concreto. Já no concreto convencional com macrofibras poliméricas (Figura 3b) o comportamento predominante foi de *slip-hardening*, sendo possível verificar sucessivas quedas e incrementos da capacidade resistente até o deslocamento central de 7,5 mm, a partir do qual iniciou-se a redução da carga. Em apenas uma das amostras do concreto CC10PP (Figura 3b) foi verificada instabilidade pós-pico.

Para o concreto de alta resistência, para a mistura produzida com fibras de aço (Figura 3c) foi verificado o comportamento *hardening*, com aumento da carga resistente até o deslocamento central de aproximadamente 5 mm. Após atingir a carga máxima, houve redução da capacidade resistente até o deslocamento final.

Tabela 6
Resultados do ensaio de tenacidade em prismas dos concretos estudados

Tipo de concreto	$f_{ct,f}$ (MPa)		$\overline{\sigma_b}$ (J)		σ_{600}^{D} (MPa)		σ_{150}^{D} (MPa)	
	Média	CV	Média	CV	Média	CV	Média	CV
CCR	5,07	1,34	—	—	—	—	—	—
CC10FA	6,89	6,05	5,01	7,72	5,97	8,26	3,64	11,17
CC10PP	4,37	8,66	2,87	14,39	2,59	16,87	2,82	11,70
CARR	7,97	2,49	—	—	—	—	—	—
CAR10FA	9,79	3,01	7,28	2,36	8,91	7,89	5,14	4,29
CAR10PP	8,36	0,80	5,00	16,74	4,23	10,55	4,83	21,23

Tabela 7
Resultados do ensaio de tenacidade em placas dos concretos estudados

Tipo de concreto	Carga máxima (kN)		Tenacidade (J)	
	Média	CV	Média	CV
CCR	46,32	25,75	—	—
CC10FA	102,37	2,11	1679,83	2,59
CC10PP	68,27	13,13	1277,61	18,72
CARR	83,17	8,42	—	—
CAR10FA	171,66	11,48	2481,19	9,95
CAR10PP	107,23	9,77	1795,41	21,98

A instabilidade pós-pico foi inexistente neste concreto. Já a amostra de alta resistência com macrofibras poliméricas (Figura 3d) apresentou oscilações no valor da carga resistente após a ruptura da matriz cimentícia, sendo predominante o comportamento de *slip-hardening*. Figueiredo [2] atribui estas oscilações à formação de múltiplas fissuras que ocorre em pequenos deslocamentos e cuja quantidade se estabiliza em determinado momento. Neste concreto, a carga máxima foi atingida com o deslocamento central de aproximadamente 7,5 mm e houve a ocorrência de instabilidade pós-pico. Com relação aos valores de carga máxima, os resultados obtidos no ensaio de tenacidade em placas são apresentados na Tabela 7. Verifica-se que a adição de fibras provocou aumento no valor da carga máxima dos concretos, com predominância de comportamento *hardening* e *slip-hardening*. De acordo com a análise estatísti-

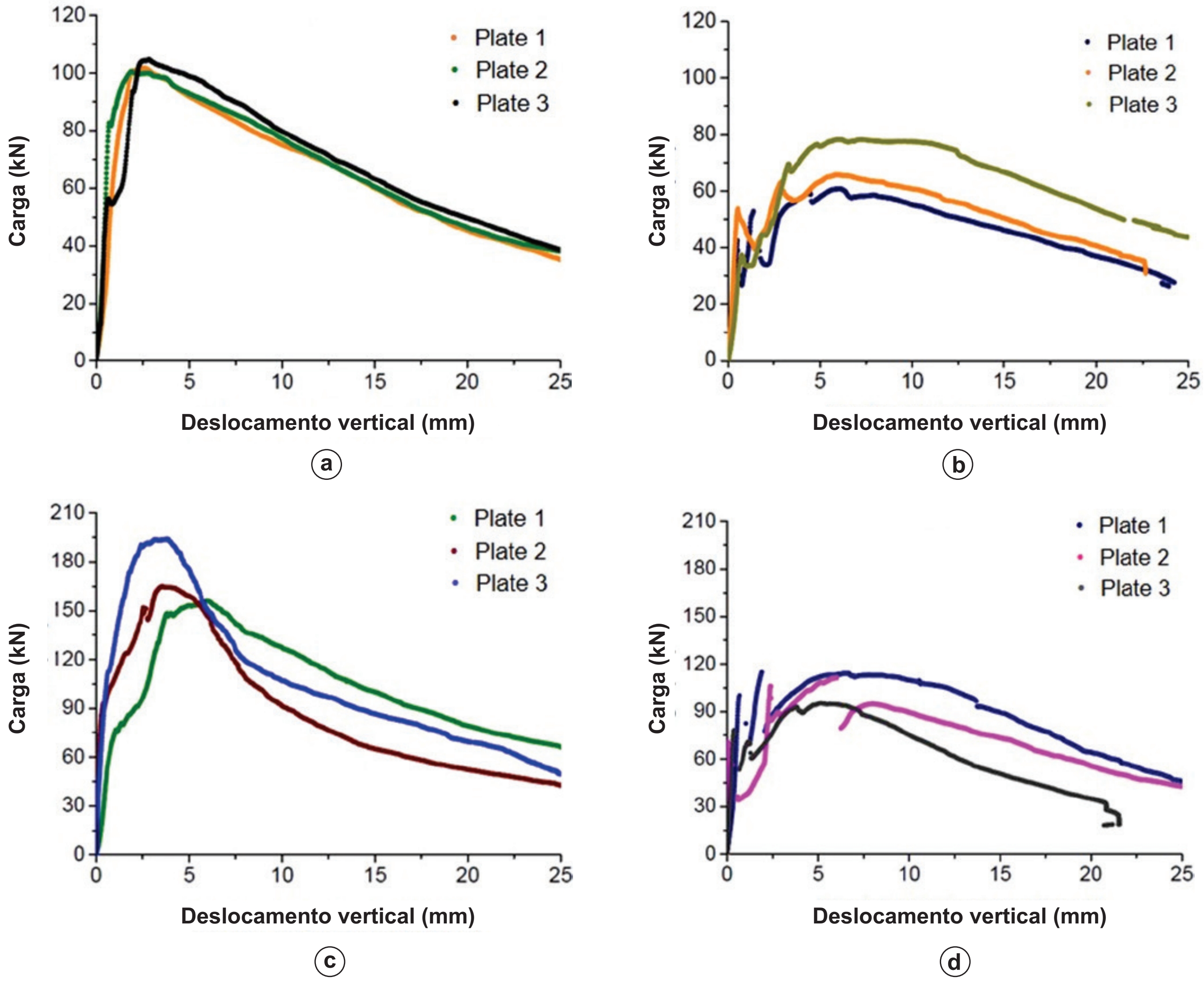

Figura 3
Ensaio de punção em placas – curvas carga *versus* deslocamento central referentes às amostras de concreto convencional com (a) fibras de aço e (b) macrofibras poliméricas, e de concreto de alta resistência com (c) fibras de aço e (d) macrofibras poliméricas, com teor de fibras de 1%, em volume

ca [10], a adição de fibras provocou alterações significativas no valor da carga máxima dos concretos convencional e de alta resistência. As amostras com fibras de aço e com macrofibras poliméricas manifestaram comportamento *hardening* e *slip-hardening*, respectivamente, o que constribuiu para apresentarem uma carga máxima superior a dos concretos de referência (CCR e CARR). Além disso, verificou-se que a variação da carga máxima do concreto com adição de fibras de aço é considerada significativa tanto para o concreto convencional quanto para o concreto de alta resistência. Já a adição de macrofibras poliméricas teve uma influência significativa da carga máxima apenas do concreto de alta resistência.

O concreto com fibras de aço apresentou carga máxima superior a do concreto com macrofibras poliméricas em ambas as matrizes cimentícias analisadas. A análise estatítica dos dados indica uma influência significativa do tipo de fibras no valor da carga máxima do concreto [10].

Com relação à tenacidade, assim como a carga máxima, os valores dessa propriedade obtidos na mistura com fibras de aço foram maiores do que os da mistura com macrofibras poliméricas tanto no concreto convencional quanto no concreto de alta resistência (Tabela 7). No entanto, de acordo com a análise estatística [10], houve uma diferença significativa entre o desempenho das duas fibras apenas no concreto convencional.

O aumento percentual da tenacidade devido à mudança da matriz cimentícia foi mais relevante para o concreto com fibras de aço do que para o concreto com macrofibras poliméricas. De acordo com a análise estatística [10], a alteração da matriz cimentícia teve uma influência significativa no valor da tenacidade apenas para o caso do concreto com fibras de aço.

Devido ao efeito *hardening*, tanto a carga máxima quanto a tenacidade do concreto convencional com fibras de aço ficou próximo dos valores dessas propriedades obtidos no concreto de alta resistência com macrofibras poliméricas. O teste t de *Student* (Tabela 5) confirma que tais resultados são estatisticamente equivalentes, sugerindo uma equivalência de desempenho entre as fibras com a alteração da matriz cimentícia.

4. Conclusões

Neste artigo foi avaliada a influência da matriz cimentícia nas propriedades mecânicas do concreto reforçado com diferentes tipos de fibras. Assim, foram analisadas misturas de concretos convencional e de alta resistência, sem fibras e contendo fibras de aço ou macrofibras poliméricas.

A trabalhabilidade desejada não foi obtida na maioria das misturas de concreto convencional com fibras, mesmo com o aumento do teor de aditivo superplastificante. Com a alteração da matriz cimentícia para um concreto de alta resistência e com maior teor de argamassa na mistura, foi possível alcançar a consistência requerida, indicando que, em alguns casos, torna-se necessário modificar a matriz cimentícia, e não apenas adicionar aditivo superplastificante para melhorar a trabalhabilidade da mistura.

Quanto à resistência à compressão, somente o concreto de alta resistência apresentou variação significativa dessa propriedade mecânica com a adição de fibras, sendo a adição de fibras de aço o fator responsável por tal variação. No concreto de alta resistência há uma maior aderência entre as fibras e a matriz, o que pode ter ocasionado tal resultado.

Tanto no ensaio Barcelona quanto no ensaio de tenacidade em placas não houve alteração do padrão de comportamento das misturas com a mudança da matriz cimentícia. Apenas no ensaio de tenacidade em prismas, o concreto reforçado com fibras de aço deixou de apresentar comportamento *hardening* para apresentar comportamento *softening* com alteração da matriz cimentícia. Além disso, as misturas apresentaram comportamentos diferentes de acordo com o ensaio realizado. Enquanto no ensaio Barcelona o comportamento predominante foi de *softening*, no ensaio de tenacidade predominaram os comportamentos de *hardening* e *slip-hardening*.

Os valores de resistência à tração e de carga máxima apresentaram variações significativas com a adição de fibras, inclusive no caso das misturas que manifestaram comportamento *softening*. Isto pode ter sido provocado pelo prejuízo na homogeneidade decorrente da adição de fibras.

A tenacidade, tanto no ensaio Barcelona quanto no ensaio de flexão em prismas, teve uma alteração significativa com a mudança da matriz cimentícia dos concretos com fibras. No caso do ensaio de tenacidade em placas, apenas a mistura com fibras de aço apresentou um aumento significativo de tenacidade ao utilizar um concreto de alta resistência.

As resistências residuais no ELS do ensaio Barcelona e de tenacidade em prismas apresentaram influência significativa da matriz cimentícia. Com relação à resistência residual no ELU, apenas no ensaio de flexão foi verificada variação significativa dessa propriedade, indicando que a alteração da matriz cimentícia no concreto reforçado com fibras pode não ser eficaz no aumento da resistência residual em maiores deslocamentos dependendo do ensaio realizado.

É importante destacar que foram obtidos valores de tenacidade estatisticamente equivalentes para o concreto convencional com fibras de aço e o concreto de alta resistência com macrofibras poliméricas. Tais resultados sugerem uma equivalência de desempenho entre as fibras, além de indicar uma menor eficiência das macrofibras poliméricas frente às fibras de aço neste aspecto.

5. Agradecimentos

Os autores agradecem à Coordenação de Aperfeiçoamento de Pessoal de Nível Superior (CAPES) pelo financiamento da bolsa de pesquisa, e às empresas Votorantim Cimentos, Grace Construction Products, Tecnosil e Belgo Bekaert Arames, pelos materiais utilizados na pesquisa.

6. Referências bibliográficas

[1] DI PRISCO, M.; PLIZZARI, G.; VANDEWALLE, L. Fibre reincorced concrete: new desing perspectives. Materials and Structures, v.42, n.9, 2009, p.1261-1281.

[2] FIGUEIREDO, A. D. Concreto reforçado com fibras, São Paulo, 2011, Tese (Livre-Docência) – Escola Politécnica, Universidade de São Paulo, 248 p.

[3] INTERNATIONAL FEDERATION FOR STRUCTURAL CONCRETE – FIB. Model Code 2010: First complete draft – Bulletin 55. Germany: Document Competence Center Siegmar Kästl e.K., 2010, 292 p.

[4] THE CONCRETE SOCIETY. Guidance on the use of Macro-synthetic-fibre-reinforced Concrete. Trowbridge: Cromwell Press, 2007. 76 p.

[5] ASSOCIAÇÃO BRASILEIRA DE NORMAS TÉCNICAS – ABNT. Concreto - Determinação da consistência pelo abatimento do tronco de cone. – NBR NM 67, Rio de Janeiro, 1998.

[6] ASSOCIAÇÃO BRASILEIRA DE NORMAS TÉCNICAS - ABNT. Concreto – Ensaios de compressão de corpos-de-prova cilíndricos. – NBR 5739, Rio de Janeiro, 2007.

[7] ASOCIACIÓN ESPAÑOLA DE NORMALIZACIÓN Y CERTIFICACIÓN – AENOR. Hormigones con fibras - Determinación de la resistencia a fisuración, tenacidad y resistencia residual a tracción – Método Barcelona. – UNE 83515, Barcelona, 2010.

[8] THE JAPAN SOCIETY OF CIVIL ENGINEERS – JSCE. Method of tests for flexural strength and flexural toughness of steel fiber reinforced concrete. – JSCE-SF4, Tokyo, 1984.

[9] EUROPEAN FEDERATION OF PRODUCERS AND APPLICATORS OF SPECIALIST PRODUCTS FOR STRUCTURES – EFNARC. European Specification for Sprayed Concrete. Farnham, 1996.

[10] LEITE, A. M. Avaliação do uso da macrofibra polimérica na composição de concreto para fins estruturais. São Carlos, Dissertação (Mestrado em Engenharia de Estruturas) - Escola de Engenharia de São Carlos, Universidade de São Paulo, 257 p.

[11] MENDOZA, C. J.; AIRE, C.; DAVILA, P. Influencia de las fibras de polipropileno en las propriedades del concreto en estados plástico y endurecido. Concreto y cemento. Investigación y desarrollo, v.2, n.2, 2011, p.5-47.

[12] AFROUGHSABET, V.; BIOLZI, L.; OZBAKKALOGLU, T. High-performance fiber-reinforced concrete: a review. Journal of Materials Science, v. 51, n. 14, 2016, p. 6517-6551.

[13] SONG, P.S; HAWANG, S. Mechanical properties of high-strength steel fibre-reinforced concrete. Construction and Building Materials, v.18, n.9, 2004, p. 669-673.

[14] MONTE, R. Caracterização e controle do comportamento mecânico do concreto reforçado com fibras para tubos. São Paulo, Tese (Doutorado em Ciências) – Escola Politécnica, Universidade de São Paulo, 159 p.

[15] MEHTA, K.; MONTEIRO P. J. M. Concreto. Microestrutura, Propriedades e Materiais, São Paulo: Ibracon, 4ed, 2014. 751 p.

[16] MONTE, R.; TOALDO, G. S.; FIGUEIREDO, A. D. Avaliação da tenacidade de concretos reforçados com fibras através de ensaios com sistema aberto. Revista Matéria, v.19, n.2, 2014, p. 132-149.

[17] BUTTIGNOL, T. E. T; SOUSA, J. L. A. O.; BITTENCOURT; T. N. Ultra High-Performance Fiber-Reinforced Concrete (UHPFRC): a review of material properties and design procedures. Ibracon Structures and Materials Journal, v. 10, n. 4, 2017, p. 957-971.

[18] ABU-LEBDEH, T.; HAMOUSH, S.; HEARD, W.; ZORNIG, B. Effect of matrix strength on pullout behavior of steel fiber reinforced very-high strength concrete composites. Construction and Building Materials, v.25, n.1, 2011, p. 39-46.

[19] SALVADOR, R. P.; FIGUEIREDO, A. D. Análise comparativa de comportamento mecânico de concreto reforçado com macrofibra polimérica e com fibras de aço. Revista Matéria, v.18, n.2, 2013, p. 1273-1285.

[20] GRAY, R. J.; Johnston, C. D. The influence of fibre-matrix interfacial bond strength on the mechanical properties of steel fibre reinforced mortars. The International Journal of Cement Composites and Lightweight Concrete, v.9, n.1, 1987, p. 43-55.

[21] ABBAS, Y. M.; KHAN, M. I. Fiber–Matrix Interactions in Fiber-Reinforced Concrete: A Review. Arabian Journal for Science and Engineering, v.41, n.4, p. 1183-1198.

Volume 13, Number 3 (June 2020) p. 563 – 577 • ISSN 1983-4195
http://dx.doi.org/10.1590/S1983-41952020000300007

IBRACON

REVISTA IBRACON DE ESTRUTURAS E MATERIAIS
IBRACON STRUCTURES AND MATERIALS JOURNAL

Assessment of the dynamic structural behaviour of footbridges based on experimental monitoring and numerical analysis

Avaliação do comportamento estrutural dinâmico de passarelas com base em monitoração experimental e análise numérica


G. L. DEBONA [a]
gilvanld@yahoo.com.br
https://orcid.org/0000-0001-8032-1813

J. G. S. DA SILVA [a]
jgss@uerj.br
https://orcid.org/0000-0002-2407-2127

Abstract

This research work aims to investigate the dynamic structural behaviour and assess the human comfort of footbridges, when subjected to pedestrian walking, based on experimental tests and tuning of finite element model. Therefore, the investigated structure is associated to a real pedestrian footbridge, spanning 24.4m, located at the campus of the State University of Rio de Janeiro (UERJ), Rio de Janeiro, Brazil. Initially, an experimental modal testing was conducted using two data acquisition strategies. After that the experimental forced vibration tests were performed on the footbridge, considering the pedestrians walking with different step frequencies. In sequence of the study, a finite element model was developed based on the ANSYS computational program. The experimental footbridge tests were used for the calibration of results on the numerical model. Finally, a human comfort assessment was performed, based on the comparisons between the results (peak accelerations), of the dynamic experimental monitoring and the recommendations provided by design guides SÉTRA, HIVOSS and AISC.

Keywords: footbridges, experimental monitoring, dynamic analysis, human comfort.

Resumo

Este trabalho de pesquisa tem como objetivo investigar o comportamento estrutural dinâmico e avaliar o conforto humano de passarelas, quando submetidas à caminhada de pedestres, com base em testes experimentais e calibrações dos modelos em elementos finitos. Assim sendo, a estrutura investigada corresponde a uma passarela de pedestres real, com vão de 24,4 m, localizada no campus da Universidade do Estado do Rio de Janeiro (UERJ), Rio de Janeiro, Brasil. Inicialmente, os ensaios para obtenção dos parâmetros modais foram realizados utilizando-se duas estratégias para aquisição dos dados. Em seguida, foram realizados testes experimentais de vibração forçada sobre a passarela, considerando os pedestres caminhando com diferentes frequências de passo. Na sequência do estudo, um modelo de elementos finitos foi desenvolvido com base no uso do programa computacional ANSYS. Os testes experimentais da passarela foram utilizados para a calibração dos resultados no modelo numérico. Finalmente, foi realizada uma avaliação do conforto humano, com base nas comparações entre os resultados (acelerações de pico), da monitoração experimental dinâmica e das recomendações fornecidas pelos guias de projeto SÉTRA, HIVOSS e AISC.

Palavras-chave: passarelas, monitoração experimental, análise dinâmica, conforto humano.

[a] *State University of Rio de Janeiro, Civil Engineering Postgraduate Programme, Faculty of Engineering, Rio de Janeiro, RJ, Brazil.*

Received: 04 Feb 2019 • Accepted: 20 Dec 2019 • Available Online: 26 May 2020

1. Introduction

Pedestrian footbridges are more and more becoming the modern landmarks of urban areas. On the other hand, structural engineers, with their experience and knowledge coupled with the use of newly developed materials and technologies, have produced pedestrian footbridges with daring structures. These facts have generated very slender pedestrian footbridges, sensitive to dynamic excitation, and, consequently, changed the serviceability and ultimate limit states associated with their design. A direct consequence of this design trend is a considerable increase in excessive vibration problems.
Several authors [1-8] have published important scientific works related to the vibration serviceability assessment of pedestrian footbridges, based on experimental data and modelling of the dynamic structural behaviour, considering finite element analysis. It is noteworthy that research papers [1-8] using experimental data and numerical analysis related to the human dynamic force associated with pedestrians walking confirm the ability of the people to act as a shock absorber for the structural system's dynamic response [2]. On the other hand, an increase of the structural system damping rate when a pedestrian crowd is crossing the footbridge in continuous flow was also reported [3-4]. However, Bocian et al. [5] and Silva [6] have observed that for different step frequency values, the structural damping can be influenced positively or negatively, resulting in different dynamic structural responses.
In his investigation, Ohlsson [9] reported that a moving pedestrian increased the mass and damping of the structural system and that the measured force on a rigid surface was different from the measurement on flexible structures. Baumann and Bachmann [10] reported that dynamic loading factors were 10% smaller on flexible surfaces when compared to rigid surfaces. This fact was also confirmed by Pimentel [11], who observed a reduction in the natural frequency of the footbridge when subjected to pedestrian walking. Ebrahimpour et al. [12] concluded from their experimental data that the damping and mass of the structure are dependent on the amount of people walking. Ebrahimpour and Sack [13] also concluded that dynamic loading factors decrease as the number of people increases over the structure.
Another relevant aspect that has been investigated is related to the differences in the pedestrian footbridges' natural frequency values when occupied by a crowd of people [14-15]. Other investigations [16] have demonstrated that the effects of the decisions assigned to each pedestrian to change its direction (trajectory), frequency, speed and step distance; to overcome other pedestrians; or even to change their attitude when walking, should be included in the dynamic analysis in addition to the pedestrian-structure dynamic interaction.
Hence, the frequencies of the actions associated with pedestrians (walking or running) may coincide with the fundamental frequency of the structure (resonance), and dynamic effects cannot be neglected. It is also known that the dynamic response of the footbridges in resonance with the human-induced dynamic loads is amplified when compared to the static response. This way, these structures may vibrate excessively and cause human discomfort.
Therefore, considering the increasing number of reported excessive vibration problems in pedestrian structures [16-17], this research study aims to develop an analysis methodology to investigate the dynamic structural behaviour of footbridges when subjected to the walking of pedestrians. The test structure is related to an existing pedestrian footbridge, based on an internal reinforced concrete footbridge, spanning 24.4 m, constituted by concrete beams and slabs and currently being used for pedestrian crossing, located on the campus of the State University of Rio de Janeiro (UERJ), Rio de Janeiro, Brazil.

2. Investigated pedestrian footbridge and finite element modelling

The investigated structure is related to an existing pedestrian footbridge located in the campus of the State University of Rio de Janeiro (UERJ), Rio de Janeiro/RJ, Brazil [1]. The structural system is based on a simply supported internal reinforced concrete pedestrian footbridge spanning 24.4 m, constituted by concrete beams and slabs, and being currently used for people crossing,

(a) Lateral view

(b) Lateral view

Figure 1
Investigated reinforced concrete pedestrian footbridge

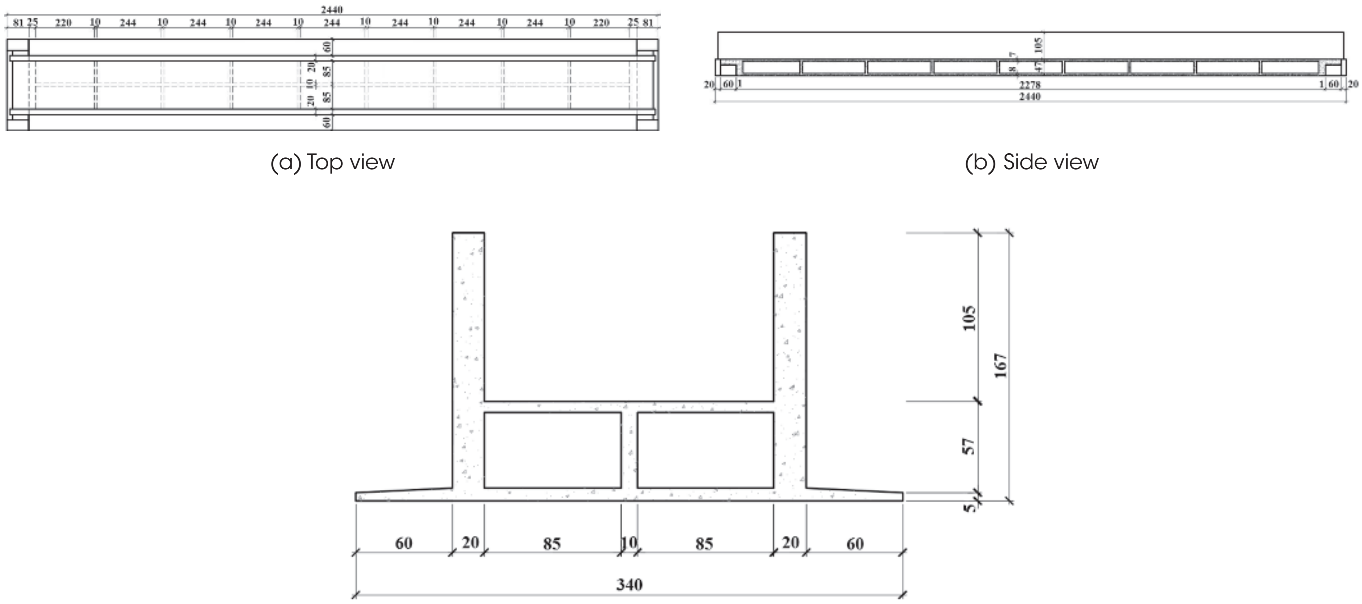

(a) Top view

(b) Side view

(c) Cross section

Figure 2
Structural model design (dimensions in cm)

see Figures 1 and 2. The concrete presents a 14 MPa specified compression strength and a 1.78 x 10^{10} N/m² Young's Modulus. The material properties of the concrete were obtained in the original drawings of the footbridge structural project. Is fair to mention that this pedestrian footbridge was constructed at the end of the 70's and the material properties are in fact real and were widely used in the design practice at Rio de Janeiro/RJ, Brazil, at that time. The total mass of the investigated structure is equal to 66200 kg [1].

The developed finite element model adopted the usual mesh refinement techniques present in finite element method simulations, based on the ANSYS computational program [18], as illustrated in Figure 3. In this computational model, all the reinforced concrete sections were represented by shell finite elements (SHELL63). This finite element has both bending and membrane capabilities. The element has six degrees of freedom at each node: translations in the nodal x, y, and z directions and also rotations about the nodal x, y, and z axes. The final computational model has presented 4104 nodes and 4074 finite elements, which resulted in a numeric model with 23364 degrees of freedom, see Figure 3. The boundary conditions (supports) were adopted according to the structural design and the footbridge supports were numerically modelled based on a traditional simply supported system.

3. Experimental modal analysis

The experimental modal analysis of the footbridge was conducted through dynamic monitoring, "in loco", through the installation of accelerometers on the structure connected to an ADS-2002 data acquisition system and through a Polytec PDV-100 laser vibrometry system, with the aid of a Dytran impact hammer, a modal exciter (shaker) TV 51140-M and the dynamic loadings of the people, see Table 1. Modal analysis tests were carried out in order to obtain the natural frequencies and vibration modes of the structure, the time functions associated with the accelerations in relevant structural sections of the footbridge, the damping coefficients and the experimental modal mass values.

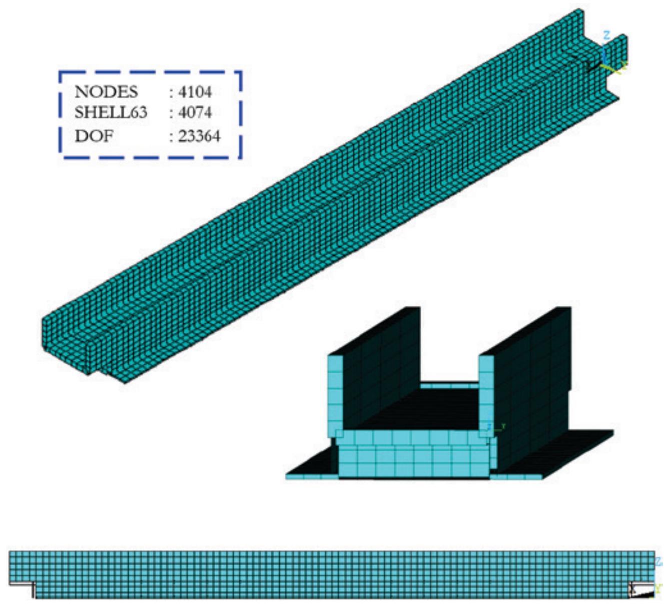

Figure 3
Finite element model of the footbridge: three-dimensional, front and lateral views

Table 1
Experimental tests

Experimental tests	Used reading equipment	Type of excitation	Points of interest (Figure 4)	
			Excitement	Reading
1	ADS2002 and accelerometers	Human (Jump)	Point 2 (1/2 of the span)	Point 1 (1/4 of the span) Point 2 (1/2 of the span) Point 3 (3/4 of the span)
2	PDV 100	Dytran impact hammer (red head)	Point 2 (1/2 of the span)	Point 1 (1/4 of the span) Point 2 (1/2 of the span) Point 3 (3/4 of the span)
3	PDV 100	TIRAvib S51140-M (shaker)	Point 1 (1/4 of the span)	Point 1 (1/4 of the span) Point 2 (1/2 of the span)

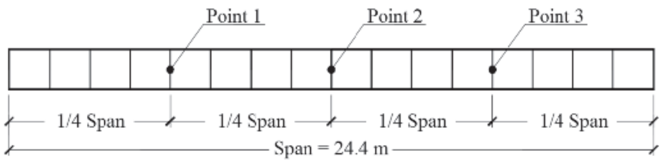

Figure 4
Investigated structural sections of the reinforced concrete pedestrian footbridge

This way, two different techniques commonly used in dynamic experimental monitoring of structures (Brandt [19], Cunha and Caetano [20]) was used in this study: single-input multiple-output (SIMO) and single-input single-output (SISO). Before the experimental modal tests, the behaviour of the main vibration modes of the structure was investigated, in order to find the common points on the footbridge that would excite as many modes as possible. After that, three points were chosen in this analysis, aiming to obtain the Frequency Response Functions (FRFs) and the Fast Fourier Transforms (FFTs) of the investigated footbridge.

In the experimental tests, several points of interest were used to study the footbridge dynamic behaviour. These sections were used to read or even to excite the structure (randomly modified, according to the results to be obtained and expected). These points on interest (1/4; 1/2 and 3/4 of footbridge span) are illustrated in Figure 4. It must be emphasized that numerous modal tests have been performed on the structure and only the most interesting test results will be presented in this research work.

Initially, the first modal analysis test (Test 1: ADS-2002 system) was carried out considering the simplest manner, i.e. one person (m_p = 95 kg) jumped at the footbridge central section (Point 2: see Figure 4). The modal analysis results were measured using three resistive Kyowa accelerometers (see Figure 5a), located at

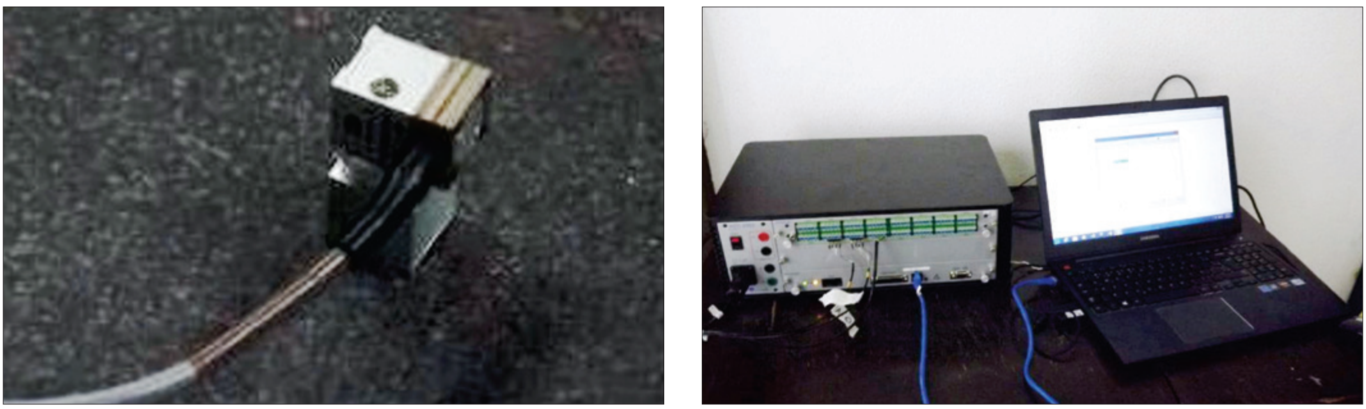

(a) Accelerometers Dytran

(b) ADS-2002 system and computer

Figure 5
Modal analysis experimental test (Test 1)

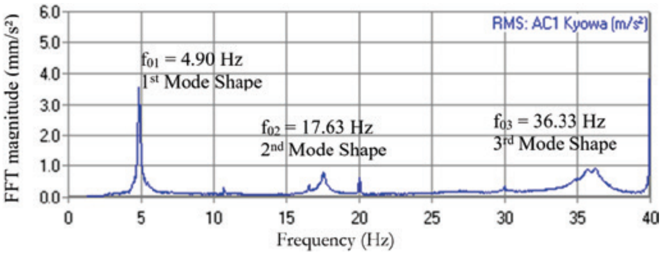

(a) Point 1 (1/4 of the span)

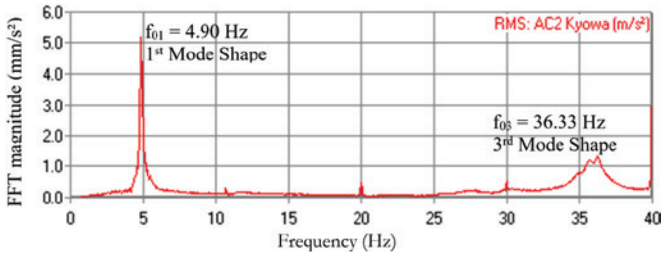

(b) Point 2 (1/2 of the span)

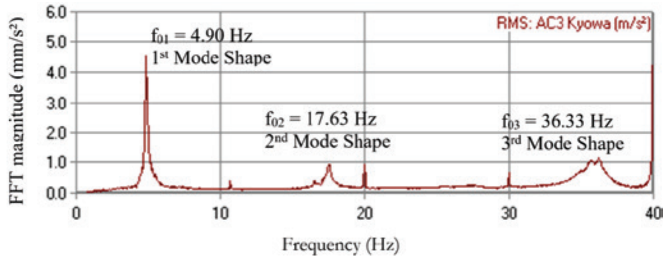

(c) Point 3 (3/4 of the span)

Figure 6
Experimental FFT magnitudes of the footbridge mode shapes

Points 1, 2 and 3 (1/4, 1/2 and 3/4 of the footbridge span, respectively: see Figure 4). A data acquisition system ADS-2002 manufactured by LYNX Electronic Technology was used in this investigation (see Figure 5b). This system is based on signal conditioners that return the sign of the variation in engineering value (specific deformation, acceleration and force), controlled by a computer. The FFT magnitudes corresponding to the output responses associated with the three accelerometers used in the experimental modal analysis of the investigated footbridge are presented in Figure 6.
After that, the second experiment (Test 2: PDV-100 and the Dytran impact hammer) was performed, based on a single-input single-output technique, combining the Polytec vibrometer PDV-100 and the Dytran impact hammer, as shown in Figure 7. In this test, the excitation provided by the Dytran impact hammer was located at footbridge middle span (Point 2: see Figure 4), and the velocities, in the time domain, were measured at Points 1, 2 and 3 (1/4, 1/2 and 3/4 of the footbridge span, respectively: see Figure 4). The input and output parameters of the dynamic response were properly measured, defining the vibrations of the footbridge. The basic functioning of the Laser Doppler Vibrometry (LDV) methodology is related to a laser beam focused on the tested structure so that the relative movement between the laser and the structure causes the presence of the Doppler Effect, i.e. the relative change in wavelength and frequency of a wave when the observer and the

(a) Polytec vibrometer PDV-100

(b) Dytran impact hammer

Figure 7
Modal analysis experimental test (Test 2)

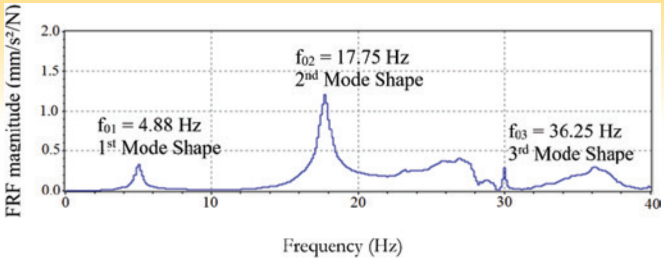

(a) Point 1 (1/4 of the span): FRF

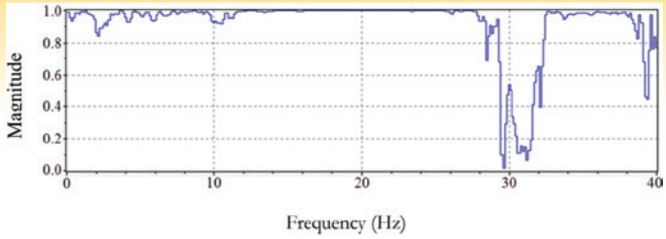

(b) Point 1 (1/4 of the span): Coherence

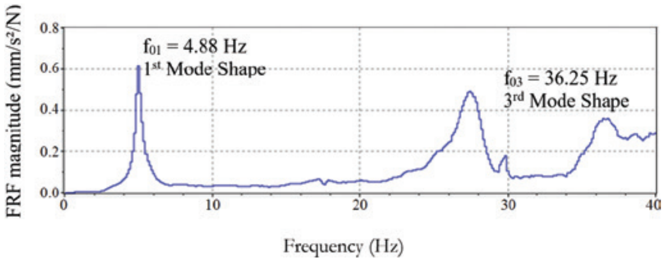

(c) Point 2 (1/2 of the span): FRF

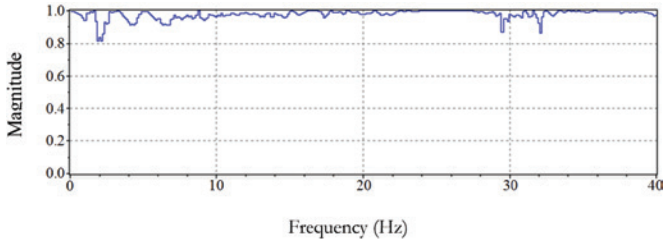

(d) Point 2 (1/2 of the span): Coherence

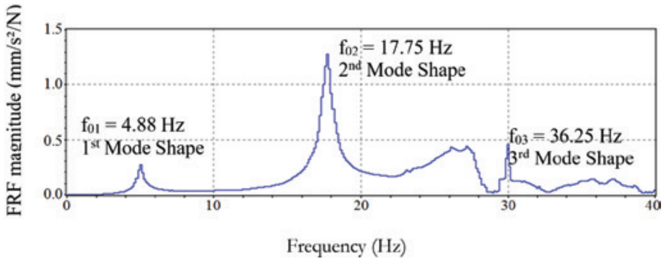

(e) Point 3 (3/4 of the span): FRF

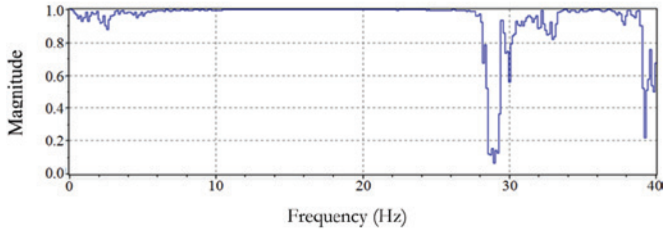

(f) Point 3 (3/4 of the span): Coherence

Figure 8
Experimental FRF magnitudes and consistency curves of the footbridge vibration modes (Test 2)

(a) PDV100 system

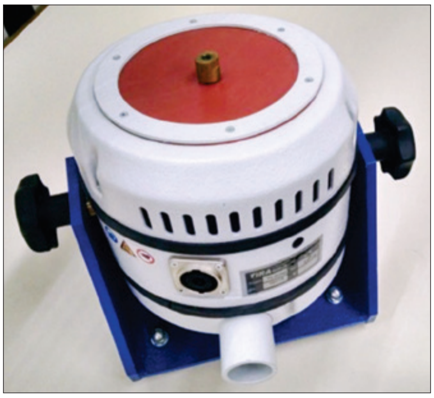

(b) Shaker S 511140-M

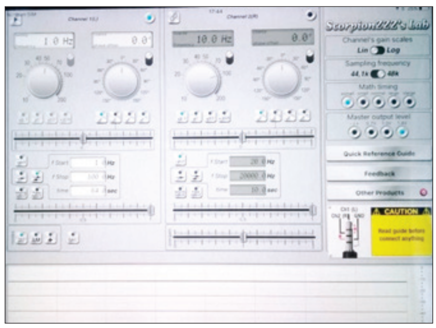

(c) SGenerator app

Figure 9
Modal analysis experimental test (Test 3)

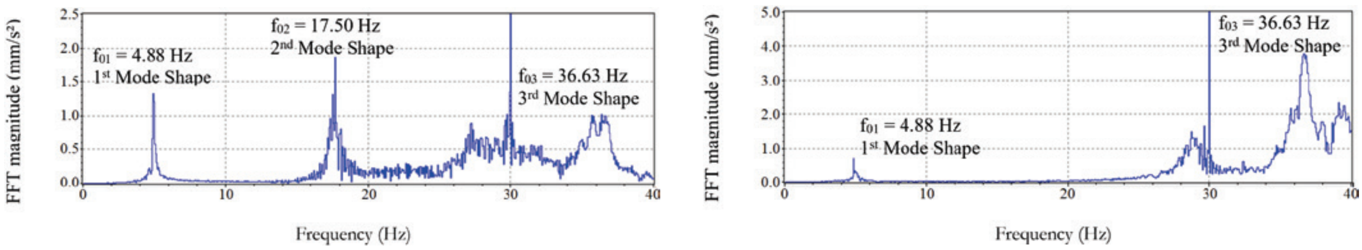

(a) Point 1 (1/4 of the span) (b) Point 2 (1/2 of the span)

Figure 10
Experimental FFT magnitudes of the footbridge vibration modes (Test 3)

source are moving [19]. To do this experimental test, the PDV-100 was positioned on the concrete slab of the investigated footbridge and properly isolated to avoid vibrations. In this situation, the upper footbridge was used as a non-vibrating reference system. The FRFs and the coherence curves of the dynamic response, based on 10 impacts on the footbridge for averaging, associated to the output signals obtained in the experimental modal analysis of the structure are presented in Figure 8. It is noteworthy that the coherence curves represent an very important data in the execution of the experimental tests, due to the fact that these curves show how the dynamic response can be representative of the reality or not. These coherence curves are based on a scale from 0 to 1, where 0 represents 0% of representativeness and 1 represents 100% of representativeness.

In sequence of the experimental analysis, the third modal vibration test (Test 3: Modal Exciter and PDV-100) was performed using the Modal Exciter (Shaker) TV 51140-M and the BAA 1000 power amplifier, as illustrated in Figure 9. The dynamic excitation was located at 1/4 of structure span (Point 1: see Figure 4), and the velocities, in the time domain, were obtained at Points 1 and 2 (1/4 and 1/2 of the footbridge span, respectively: see Figure 4), in modal analysis after the excitation. In this test, only the dynamic response parameters were measured and the impact input data was not obtained. The velocities in the time domain were measured using the Laser Vibrometry System PDV 100 (see Figure 9). The SGenerator app installed on the iPad A1459 was used to generate square wave signals connected to the power amplifier (BAA 1000) and the vibration exciter (Shaker) for this modal analysis test. The experimental FFT magnitudes of the pedestrian footbridge mode shapes are described by Figure 10.

The damping ratios were obtained via dynamic experimental monitoring of the tests previously described (Tests 1 to 3) and the results were summarized and presented in Table 2. In this investigation, the damping coefficients were obtained experimentally in Test 1 using the logarithm decrement filtering the respective vibration modes. In Tests 2 and 3, the “3Db Bandwidth” method [19] was used in the frequency domain, according to Equation (1). This equation is valid for low damping coefficients (ξ < 0.1) [19]. In this situation, the upper (f_s) and lower (f_i) frequencies were defined as half of the maximum peak value squared that occurs (or 3dB), as presented in Equation (1).

$$\xi = \frac{f_s - f_i}{2 f_d} \tag{1}$$

Where:
ξ = damping coefficient;
f_s = upper frequency in Hz;
f_i = lower frequency in Hz;
f_d = damped natural frequency in Hz.

In Tests 2 and 3, the critical damping corresponding to the vibration modes was obtained through the “Band Cursor” tool available in the “Polytec Vibrometer Software”. This tool has the extensive peak analysis capability enhanced by a band cursor that provides statistical parameters and harmonic oscillator curve adjustment,

Table 2
Modal analysis tests and numerical results

Test	Natural frequency (Hz)					Damping coefficient (%)	
	Experimental tests	Finite element model	Differences (%)	Concrete	Concrete		
1	f_{01}	4.90	f_{01}	4.90	0.00	ξ_{01} (1st mode shape)	1.80
	f_{02}	17.63	f_{02}	16.92	4.20	ξ_{02} (2nd mode shape)	1.15
	f_{03}	36.33	f_{03}	34.15	6.38	ξ_{03} (3rd mode shape)	1.02
2	f_{01}	4.88	f_{01}	4.90	0.41	ξ_{01} (1st mode shape)	1.60
	f_{02}	17.75	f_{02}	16.92	4.90	ξ_{02} (2nd mode shape)	1.24
	f_{03}	36.25	f_{03}	34.15	6.15	ξ_{03} (3rd mode shape)	1.04
3	f_{01}	4.88	f_{01}	4.90	0.41	ξ_{01} (1st mode shape)	1.80
	f_{02}	17.50	f_{02}	16.92	3.43	ξ_{02} (2nd mode shape)	1.12
	f_{03}	36.63	f_{03}	34.15	7.25	ξ_{03} (3rd mode shape)	0.86

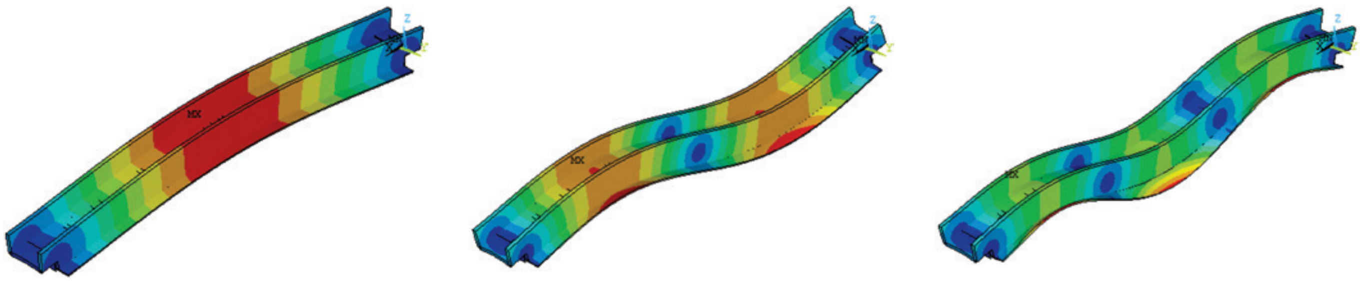

(a) 1st vibration mode (f_{01} = 4.90Hz) (b) 2nd vibration mode (f_{02} = 16.92Hz) (c) 3rd vibration mode (f_{03} = 34.15Hz)

Figure 11
Vertical vibration modes of the analysed pedestrian footbridge

adjusted to the vibration peaks of the dynamic response, by plotting the harmonic cursor up to 12 lines in the order of the base frequency of the structure.

In order to obtain the experimental modal mass values, some parameters need to be known from the experimental tests (the resonance peaks, the vibration mode magnitude and the vibration mode damping). In this investigation, these parameters were obtained through the VibSoft 5.1 software, based on the experimental data related to Test 2 (Test 2: PDV-100 and the Dytran impact hammer), in the frequency domain and also considering a bandwidth of 3dB [21]. Considering these parameters and based on the use of Equations (2) and (3) [21], the modal mass was calculated as the inverse of the modal constant at the point of maximum modal amplitude of the footbridge.

$$A_r = |H|\,\Omega_r^2\,2\,\xi_r \quad (2)$$

$$m_r = \frac{1}{A_r} \quad (3)$$

Where:
A_r = modal constant for the r mode;
|H| = Magnitude of the mode (displacement / force);
Ω_r = natural frequency in rad/s of the r mode;
x_r = damping of the r mode;
m_r = modal mass of the r mode.

The experimental modal mass values obtained for the first and second vertical vibration modes of the analysed pedestrian footbridge were equal to 33402 kg and 29529 kg, respectively. The modal mass value of the third vibration mode was not obtained due to the fact that this mode shape presents a resonance peak very close to other modes, falling under the restrictions of the adopted method utilised to obtain the modal mass.

Based on the two strategies used for the dynamic experimental monitoring of the footbridge, three natural frequencies of the structure were identified, corresponding to the vertical vibration of the system (bending mode shapes); the damping coefficients and the modal mass values were identified as well. It is worth emphasizing that the agreement between the dynamic structural responses

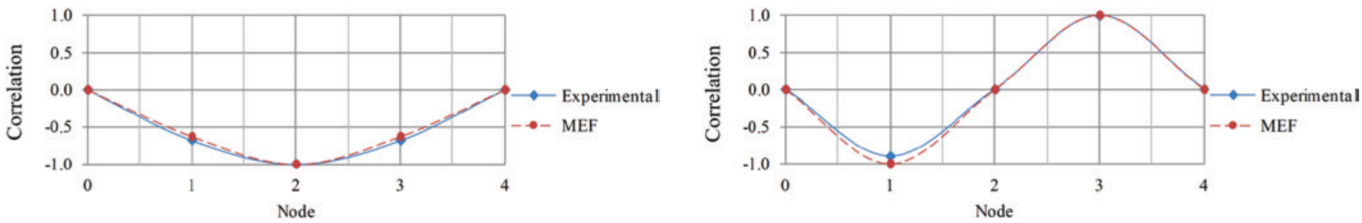

(a) 1st vibration mode (b) 2nd vibration mode

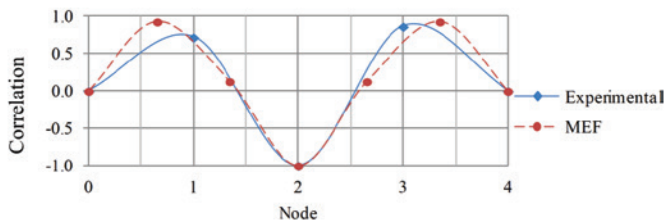

(c) 3rd vibration mode

Figure 12
Comparison between the experimental and numerical footbridge mode shapes

of the investigated footbridge obtained experimentally indicates a positive validation of the developed experimental tests.

4. Calibration of natural frequencies and vibration modes

The footbridge natural frequencies and vibration modes were determined with the aid of numerical simulations, based on the finite element method using the ANSYS computational program [18]. The numerical results were compared with the obtained experimental results, according to Tables 1 and 2 and also Figures 11 and 12.

The investigated footbridge dynamic response (modal analysis) was analysed and the numerical model was calibrated with the experimental results, through the addition of the mass corresponding to the finishing coat on the floor slab and longitudinal beams, which was included to the concrete structure right after its construction process, and was not predicted in the original structural design. Besides that, it can be emphasized that the dynamic behaviour of the footbridge was consistent in comparison with the experimental results, when the boundary conditions (supports) were modelled using a traditional simply supported model.

The numerical analysis carried out by Debona [1] showed natural frequencies of 4.90 Hz and 16.92 Hz for the first two vertical vibration modes of the structure, as presented in Table 2 and Figure 11, with modal mass of 31275 kg and 27488 kg for these modes shapes, respectively. The modal mass of the first vibration mode is equal to half of the total mass of the footbridge [1].

It must be emphasized that the natural frequency values of the investigated footbridge were coherent and reliable when compared with the experimental values, with differences between 1% and 7%, when the first, second and third vibration modes were investigated, as presented in Table 2. On the other hand, the modal mass values determined by the finite element modelling were compared with the experimental values (first and second vibration modes), obtained by the peak picking method. The analysed results presented small differences, 6% to 8%, demonstrating a very well correlation between the experimental and numerical values.

In sequence, Figure 11 illustrates the footbridge bending mode shapes, obtained based on numerical modelling, and Figure 12 presents the comparison between the first three experimental mode shapes, obtained via experimental monitoring, based on the modal analysis test (Test 1: ADS-2002 system), and the three corresponding vibration modes obtained by finite element modelling (Figure 11). This comparison is related to the correlation of the experimental amplitudes obtained in the frequency domain and the amplitudes of the numerical mode shapes.

It should also be noted that the experimental footbridge mode shapes obtained using the accelerometers precisely coincided with those generated through the numerical modal analysis, except for the third vibration mode, see Figure 12. However, it's important to point out that the modal curves were generated by point's approximation and these points coincide in both cases; showing that a better approximation between modes (experimental and numerical) can be obtained by increasing the number of the adopted reference points, see Figure 12.

Based on the results presented in Table 2 and Figures 11 and 12, it can be seen that the obtained experimental dynamic structural response agreed very well when the different strategies used in the experimental tests were investigated, as well as with the numerical results (Tests 1, 2 and 3: see Tables 1 and 2 and Figures 11 and 12). These results (experimental and numerical) are very important for the evaluation of the dynamic structural response of the investigated structural model to know its behaviour when subjected to walking human loads.

5. Experimental forced vibration analysis

Considering the experimental forced vibration analysis, the human walking excitation on the investigated reinforced concrete pedestrian footbridge was performed based on two control groups: the first one was intended to excite the structural model to cause a

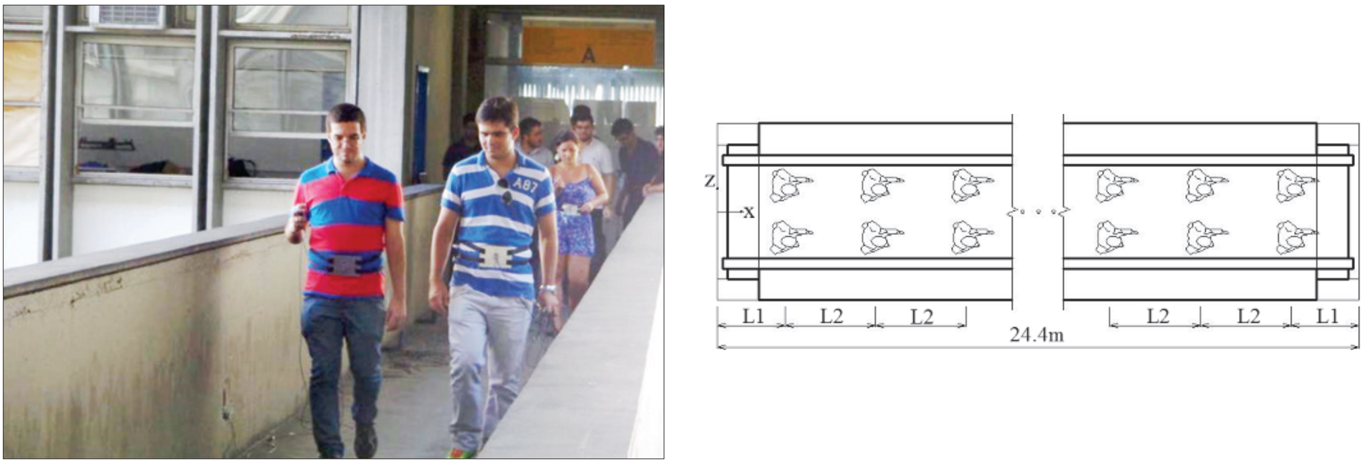

(a) Photo of the walking along the structure

Figure 13
Walking of 12 people on the footbridge

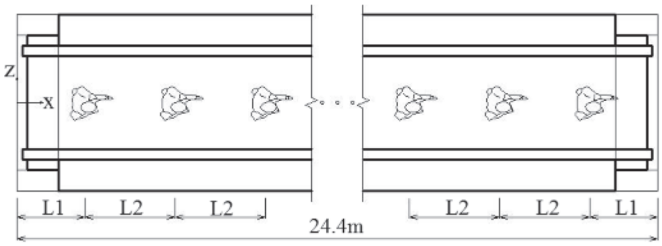

Figure 14
Walking of 8 people on the footbridge

resonance motion with a controlled step frequency; the second one was related to freely random people crossing the footbridge as it occurs normally during in service life. The obtained data related to these experimental tests were recorded by the acquisition system ADS-2002 using resistive Kyowa accelerometer located at Point 2 (see Figure 4). Figures 13 to 16 show the typical layouts (photos and typical walking paths) and Table 3 describes the forced vibration tests. To control the step of each pedestrian and to maintain the synchronization of the rhythm of the group of people that moved on the structure a metronome was used. This device was connected to a loudspeaker so that it was possible to produce sound pulses of regular duration. The representative unit of the metronome is the "bpm" (beats per minute). Therefore, each sound beating corresponds to the contact of each step of the pedestrian on the structure.
Initially, the value in the metronome was set at 96 bpm (f_p = 1.60 Hz, slow walking) and at 147 bpm (f_p = 2.45 Hz, fast walking), so that the second harmonic (2 x 2.45 Hz = 4.90 Hz) and the third harmonic (3 x 1.60 Hz = 4.80 Hz) of pedestrians walking that synchronously crossed the footbridge could force a resonant movement with the first vertical vibration mode (f_{01} = 4.90 Hz, see Table 2). Thereafter, in order to perform additional tests, the metronome value was changed: 102 bpm (f_p = 1.70 Hz) in order to induce pedestrians to cross the structure at a slow walk; 120 bpm (f_p = 2.00 Hz), inducing pedestrians to cross the structure at a normal walking pace and 138 bpm (f_p = 2.30 Hz) considering the pedestrians to cross the structure at a fast walk. After these experimental trials, pedestrians randomly walked on the studied footbridge. The forced vibration tests were performed in such a way that the structure was excited through human walking performed by people at slow, normal, fast or random walking paces with the measured frequencies in the metronome. The walking was distributed in such a way as to have equal spacing between individuals, measured by a timer with equal time between pedestrians.

Table 3
Investigated forced vibration tests: experimental tests

Tests	Experimental tests	
	Step frequency (f_p)	Number of people
1		1
2	1.60 Hz	8
3		12
4		1
5	1.70 Hz	8
6		12
7		1
8	2.00 Hz	8
9		12
10		1
11	2.30 Hz	8
12		12
13		1
14	2.45 Hz	8
15		12
16	Random walking	14

In relation to the data analysis (footbridge accelerations), the experimental signs were acquired with a sampling rate equal to 100 Hz. In addition, a fifth order Butterworth low pass filter with a cut-off frequency of 50 Hz was used in the investigation. The Fast Fourier Transform (FFT) functions of the experimental accelerations presented in this analysis were obtained based on the theory of signal processing [19-20]. The duration of each acquisition was in the range between 15 and 60s and the initial parts of each signal were discarded to collect only the part of in which the pedestrian flow was steady. It should be noted that a Hanning window was used to minimize the effects of using a non-integer number of cycles on an FFT, reducing the amplitude of the discontinuities at the edges of each finite sequence.
The experimental results associated to the dynamic structural response of the footbridge (vertical accelerations) are presented in Figures 17 to 21, considering 8 people walking on the concrete slab, aiming to illustrate the general behaviour of the dynamic response. These results were obtained in the time and frequency domain, respectively; corresponding to the output response associated with the Kyowa accelerometers (Point 2: see Figure 4). It should be emphasized that the horizontal axes of the graphs present the time in "hour: minute: second" and frequency in Hz,

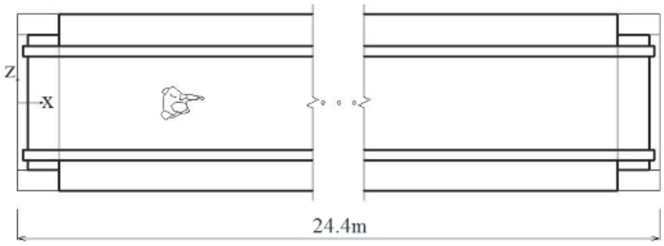

Figure 15
Walking of 1 individual on the footbridge

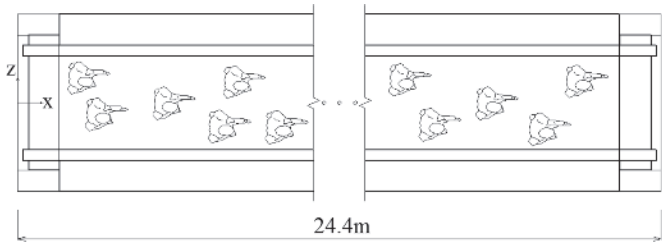

Figure 16
Typical random walking on the footbridge

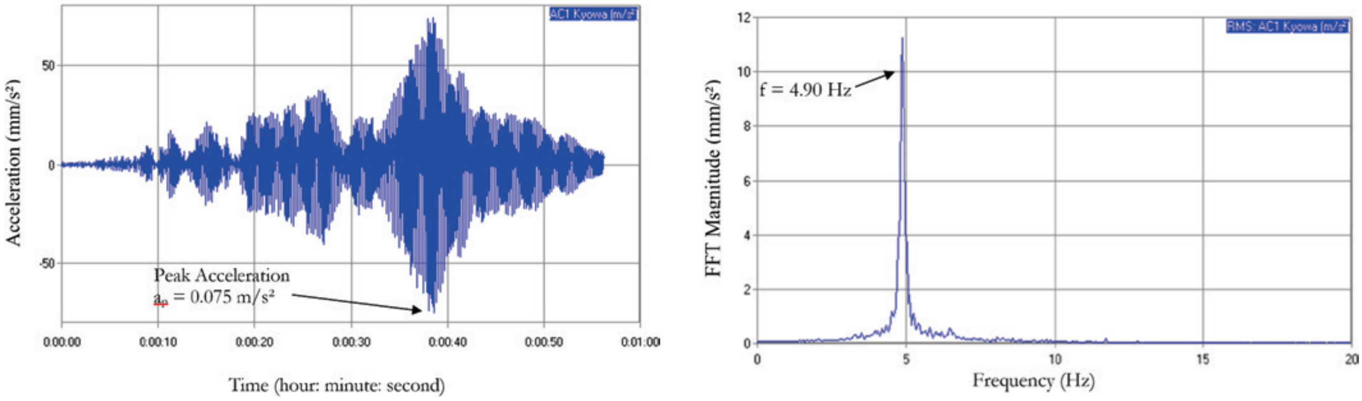

(a) Vertical acceleration

(b) Fast fourier transform

Figure 17
Dynamic structural response of the footbridge due to slow walking of 8 people (f_p = 1.60 Hz)

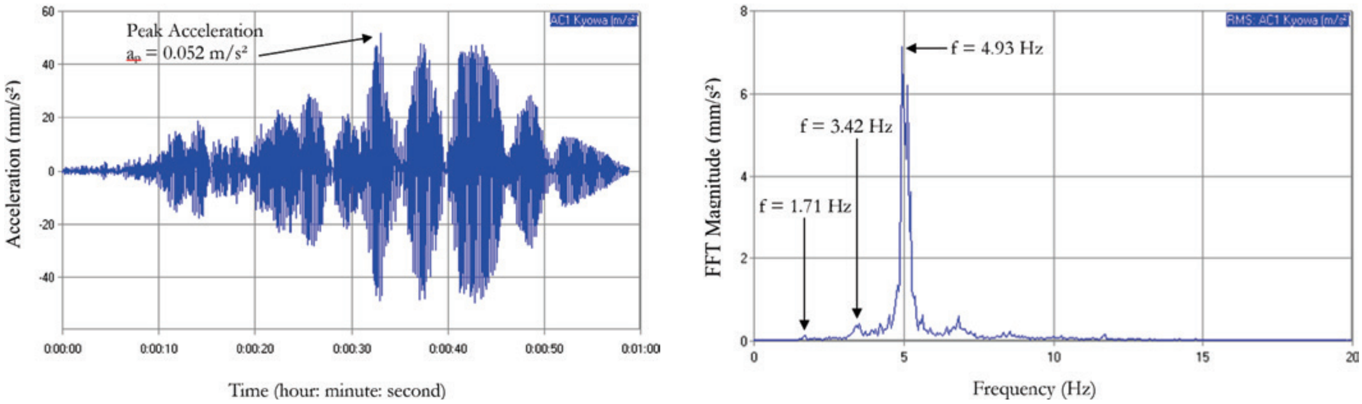

(a) Vertical acceleration

(b) Fast fourier transform

Figure 18
Dynamic structural response of the footbridge due to slow walking of 8 people (f_p = 1.70 Hz)

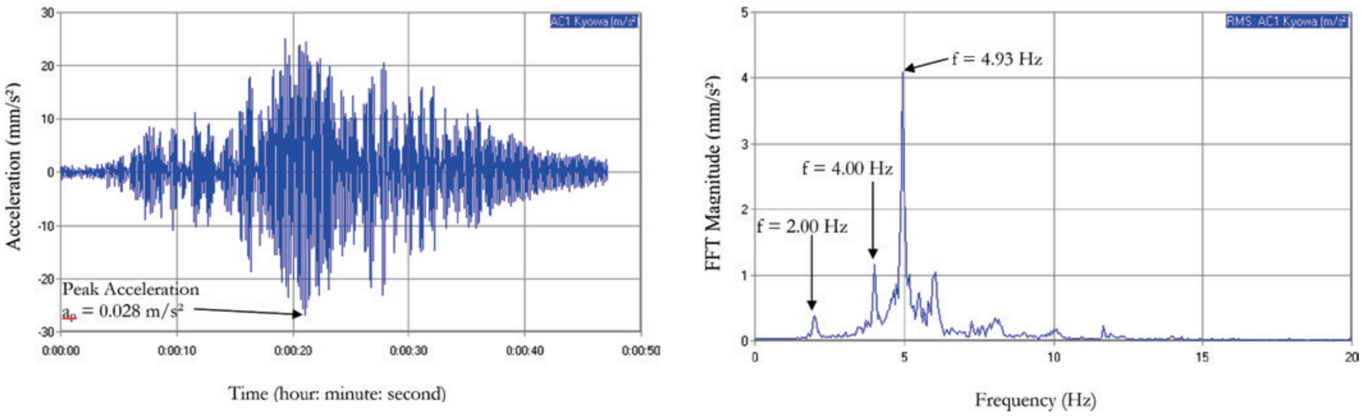

(a) Vertical acceleration

(b) Fast fourier transform

Figure 19
Dynamic structural response of the footbridge due to normal walking of 8 people (f_p = 2.00 Hz)

respectively and the vertical axes present the accelerations and the FFTs magnitude.
In sequence, Table 4 presents the peak accelerations values of the investigated footbridge, obtained through dynamic experimental monitoring. The maximum acceleration values found in this experimental investigation are respectively equal to 0.075 m/s² (f_p = 1.60 Hz: slow walking; see Figure 17) and 0.052 m/s² (f_p = 1.70 Hz: slow walking; see Figure 18), considering 8 people in slow walking on the structural model, respectively; 0.030 m/s² (f_p = 2.00 Hz: normal walking), for 12 pedestrians in normal walking on the footbridge; 0.114 m/s² (f_p = 2.30 Hz: fast walking), for 12 people in fast walking on the structure; 0.157 m/s² (f_p = 2.45 Hz: resonance) for 12 people in resonance walking on the footbridge and 0.046 m/s² for 14 people walking freely on the footbridge concrete slab (random walking), as presented in Table 4.
The results demonstrated that the maximum peak acceleration value occurred when the pedestrians are walking in resonance with relation to the second harmonic (2 x 2.45 Hz = 4.90 Hz) of the dynamic action. It should be noted that pedestrian synchronization difficulties occur in the step frequency and in the permanence of the distance between individuals. This fact is explained by the length of the step of each pedestrian being unique and the difficulty of some individuals to remain in synchronized movement. Another important factor was the logistical difficulty of the experimental tests performed using cable accelerometers, due to the fact that the cables coupled in the accelerometer of the first pedestrians walking on the footbridge were dragged along the structure span involuntarily, causing uncontrolled situations of the human step, due to the concern of the pedestrian in not stepping on the cables. The composition of humans walking in a single row and the number of pedestrians were limited, showing that in future experimental tests, accelerometers without cabling can be used for better synchronization.

6. Human comfort assessment

In this section of the paper, the footbridge human comfort levels are investigated. The results of all human walking tests are summarised in Table 4. It can be noted from Table 4 results that the

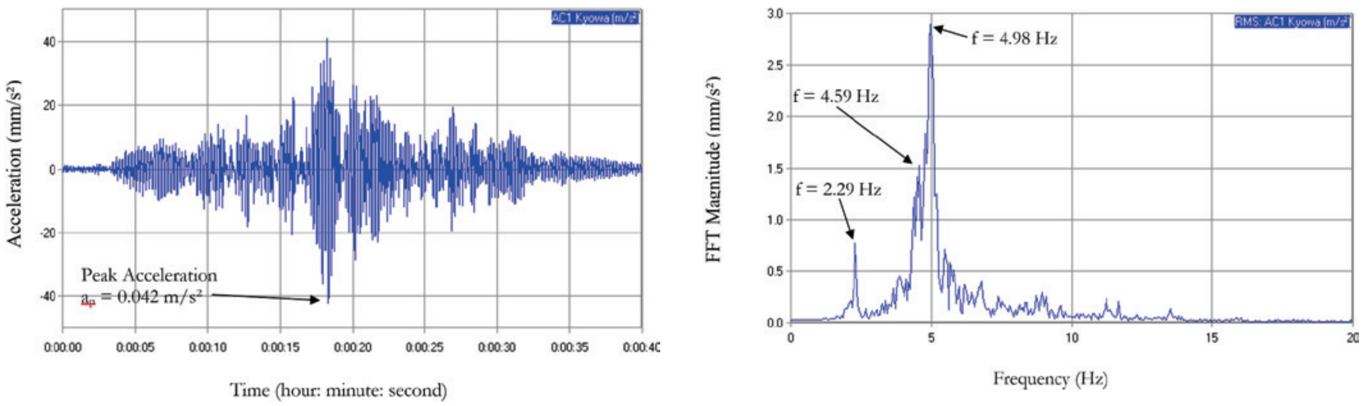

(a) Vertical acceleration (b) Fast fourier transform

Figure 20
Dynamic structural response of the footbridge due to fast walking of 8 people (f_p = 2.30 Hz)

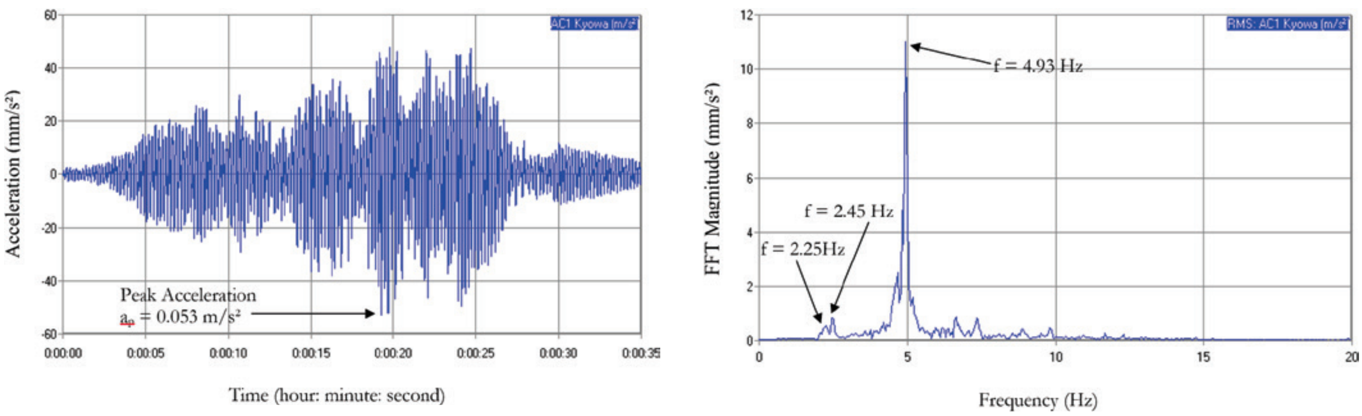

(a) Vertical acceleration (b) Fast fourier transform

Figure 21
Dynamic structural response of the footbridge due to fast walking of 8 people (f_p = 2.45 Hz)

Table 4
Peak acceleration of the experimental tests and human comfort assessment

Test	Step frequency (f_p)	Number of pedestrians (NP)	Peak accelerations a_p (m/s²)	Human comfort criteria		
				SÉTRA*[19]	HIVOSS*[20]	AISC**[21]
1	1.60 Hz	1	0.026	Maximum	Maximum	Acceptable
2		8	0.075	Maximum	Maximum	Acceptable
3		12	0.055	Maximum	Maximum	Acceptable
4	1.70 Hz	1	0.011	Maximum	Maximum	Acceptable
5		8	0.052	Maximum	Maximum	Acceptable
6		12	0.033	Maximum	Maximum	Acceptable
7	2.00 Hz	1	0.008	Maximum	Maximum	Acceptable
8		8	0.028	Maximum	Maximum	Acceptable
9		12	0.030	Maximum	Maximum	Acceptable
10	2.30 Hz	1	0.012	Maximum	Maximum	Acceptable
11		8	0.042	Maximum	Maximum	Acceptable
12		12	0.114	Maximum	Maximum	Acceptable
13	2.45 Hz	1	0.048	Maximum	Maximum	Acceptable
14		8	0.053	Maximum	Maximum	Acceptable
15		12	0.157	Maximum	Maximum	Unacceptable
16	Random	14	0.046	Maximum	Maximum	Acceptable

*Acceleration range of 0-0.50 m/s²: maximum comfort [19], [20]; **alim = 1.5%g = 0.15 m/s²: indoor footbridges [21]; **alim = 5.0%g = 0.49 m/s²: outdoor footbridges [21].

human comfort criterion proposed by the SÉTRA [22] and HIVOSS [23] technical guides was satisfied for the sixteen investigated walking situations. It means that the experimental acceleration values lie in range of 0.0 to 0.50 m/s² (see Table 4), which corresponds to a maximum human comfort for the investigated pedestrian footbridge.

On the other hand, regarding the AISC technical guide [24], even though the acceleration limit of 0.15 m/s² for indoor footbridges is respected in most of investigated situations (slow, normal, fast, resonance and random walking cases: see Table 4), the peak acceleration value of 0.157 m/s² for the resonance case slight overpass this limit (a_{lim}=0.15 m/s²). This way, it is interesting to point out that a person standing on the investigated structure can perceive an acceleration value equal to 0.034 m/s² (just perceptible), and 0.10 m/s² (clearly perceptible), based on the indication of human perceptibility thresholds for vertical vibrations (person standing) proposed by Bachmann et al. [25].

Finally, the authors would like to emphasize that this investigation will continue based on the development of a mathematical model, aiming to numerically simulate the pedestrian-structure dynamic interaction, considering the use of biodynamic models of people. This way, the results of the pedestrian walking vibration tests can also be validated and represented by FEM simulations. These models simulate the dynamic characteristics of the pedestrians (mass, stiffness and damping) and have been used as an efficient alternative to better evaluate human comfort rather than the traditional "force-only" model widely used for dynamic analysis of footbridges.

7. Conclusions

This research work analysed experimentally and numerically the dynamic structural behaviour of an internal reinforced concrete pedestrian footbridge spanning 24.4m, constituted by concrete beams and slabs and being currently used for pedestrian crossing located in the campus of the State University of Rio de Janeiro (UERJ), Rio de Janeiro/RJ, Brazil. Thus, the main conclusions of the present investigation are:

1. Modal Analysis: The modal analysis of the investigated structure was performed both experimentally and numerically. The modal testing of the footbridge was performed by dynamic monitoring through accelerometers installed on the concrete slab as well as by a vibrometer device based on a Laser Doppler Vibrometry methodology. Then, these experimental results were calibrated with a three-dimensional finite element model based on the use of ANSYS program. It must be emphasized that a good agreement between the experimental and numerical results was obtained. The highest energy transfer peak contribution related to the dynamic structural response of the analysed footbridge is associated to the vertical bending vibration mode with frequency equal to 4.90 Hz [f_{01} = 4.90 Hz].
2. Forced Vibration Experimental Tests: The maximum acceleration values (peak accelerations values), related to the central section of the investigated span (L = 24.4 m), respectively, are equal to 0.075 m/s² (f_p = 1.60 Hz; a_p = 0.075 m/s²; slow walking: 8 pedestrians); (f_p = 1.70 Hz; a_p = 0.052 m/s²; slow walking: 8 pedestrians); 0.030 m/s² (f_p = 2.00 Hz; a_p = 0.030 m/s²; normal walking: 12 pedestrians); 0.114 m/s² (f_p = 2.30 Hz; a_p = 0.114 m/s²; fast walking: 12 pedestrians); 0.157 m/s² (f_p = 2.45 Hz; a_p = 0.157 m/s²; resonance: 12 pedestrians) and 0.046 m/s² (a_p = 0.046 m/s²; random walking: 14 pedestrians).
3. Human Comfort Assessment: The experimental dynamic analysis, carried out by sixteen human walking loading cases (slow, normal, fast, resonance and random walking) have shown that the obtained accelerations values satisfied the current human comfort design criteria, apart from the resonance case

(a_p=0.157 m/s²), which slight overpass the AISC proposed limit equal to 0.15 m/s², when twelve persons crossed the footbridge. Based on the peak acceleration values (experimental tests), observations made at the footbridge location and also several interviews with the participants of the experimental tests, it was concluded that the investigated pedestrian footbridge attends the human comfort criteria. On the other hand, it is interesting to point out that a person standing on the footbridge concrete slab can perceive the accelerations values for vertical vibrations, as the traffic density on the footbridge increases.

Finally, the authors would like to emphasize the understanding of the necessity of a study based on the evaluation of the pedestrian footbridge dynamic interaction effect, associated to crowd situations, considering experimental tests and numerical modelling, using representative biodynamic models to simulate the pedestrians, aiming to contribute with a more realistic assessment of the dynamic structural behaviour and human comfort evaluation of footbridges subjected to pedestrian walking.

8. Acknowledgements

The authors gratefully acknowledge the financial support for this work provided by the Brazilian Science Foundation's CAPES, CNPq and FAPERJ.

9. References

[1] Debona GL. Experimental monitoring and numerical modelling on the dynamic structural response of pedestrian footbridges. PhD Thesis (In Portuguese). Civil Engineering Post-graduate Programme, PGECIV. State University of Rio de Janeiro, UERJ. Rio de Janeiro/RJ, Brazil, 2016.

[2] Brownjohn JMW, Fu, TN. Vibration excitation and control of a pedestrian footbridge by individuals and crowds. Shock and Vibration, 12: 333-347, 2005.

[3] Fernandes H. Dynamic behaviour of footbridges modelled as beams subjected to pedestrian-induced vertical direction vibrations. PhD Thesis (In Portuguese). Graduate Program in Mechanical Engineering, PPGEM, Federal University of Paraíba, UFPB, João Pessoa/PB, Brazil, 2007.

[4] Brownjohn JMW, Fok P, Roche M, Omenzetter, P. Long span steel pedestrian bridge at Singapore Changi Airport. Part 2: crowd loading tests and vibration mitigation measures. Structural Engineer; 82 (16): 28-34, 2004.

[5] Bocian M, Macdonald JHG, Burn JF. Biomechanically inspired modelling of pedestrian-induced vertical self-excited forces. American Society of Civil Engineers (ASCE), 2013.

[6] Silva JGS da, Debona GL. Effect of the pedestrian-structure dynamic interaction on the vibration serviceability of steel-concrete composite footbridges. Proceedings of the 8th International Conference on Advances in Steel Structures, ICASS 2015, Lisbon, Portugal; pp. 1-15, 2015.

[7] Pfeil MS, Costa NPA, Pimentel RL, Vasconcelos RP. Analytic-numerical model for walking person-footbridge structure interaction. Proceedings of the 9th International Conference on Structural Dynamics, EURODYN 2014, Porto, Portugal; pp: 1079-1085, 2014.

[8] Alonso JFJ, Saez A, Caetano E, Cunha A. Proposal and calibration of a human-structure interaction biomechanical model by the resolution of the inverse dynamic problem. Proceedings of the 9th International Conference on Structural Dynamics, EURODYN 2014, Porto, Portugal; pp: 975-982, 2014.

[9] Ohlsson S. Floor vibrations and human discomfort. PhD Thesis. Chalmers University of Technology, Switzerland, 1982.

[10] Baumann K and Bachmann H. Durch menschen verursachte dynamische lasten und deren auswirkungen auf balkentragwerke. Report 7501-3, Institute of Structural Engineering (IBK), Swiss Federal Institute of Technology (ETH), Switzerland, 1988.

[11] Pimentel RL. Vibration performance of pedestrian bridges due to human-induced loads. PhD Thesis, University of Sheffield, United Kingdom, 1997.

[12] Ebrahimpour RL, Sack PD, Cleek V. Computing crowd loads using a nonlinear equation of motion. Proceedings of the 4th International Conference on Civil and Structural Engineering Computing; pp: 47-52, Civil-Comp Press, United Kingdom, 1989.

[13] Ebrahimpour A, Sack RL. Design live loads for crowds in motion. Conference Proceedings of Building an International Community of Structural Engineers; pp: 420-427, 1996.

[14] Butz C, Feldmann M, Heinemeyer C, Sedlacek G, Chabrolin B, Lemaire A, Lukic M, Martin PO, Caetano E, Cunha A, Goldack A, Keil A, Schlaich M. Advanced load models for synchronous pedestrian excitation and optimised design guidelines for steel footbridges. European Comission; pp: 1-167, 2008.

[15] Barker C, Mackenzie D. Calibration of the UK National Annex. Proceedings of the International Conference Footbridge 2008: Footbridges for Urban Renewal, Porto, Portugal, 2008.

[16] Venuti F, Racic V, Corbetta A. Pedestrian-structure interaction in the vertical direction: coupled oscillator-force model for vibration serviceability assessment. Proceedings of the 9th International Conference on Structural Dynamics, EURODYN 2014, Porto, Portugal; pp: 915-920, 2014.

[17] Ingólfsson EL. Pedestrian-induced lateral vibrations of footbridges. PhD Thesis. DTU Civil Engineering. Technical University of Denmark - DTU. Lyngby, Denmark, 2011.

[18] ANSYS Swanson Analysis Systems, Inc., P. O. Box 65, Johnson Road, Houston, PA, 15342-0065. Release 11.0, SP1 UP20070830, ANSYS, Inc. is a UL registered ISO 9001:2000 Company. Products ANSYS Academic Research, Using FLEXlm v10.8.0.7 build 26147, Customer 00489194. 2007.

[19] Brandt A. Noise and vibration analysis. Signal analysis and experimental procedures. 1st Edition. John Wiley & Sons, Inc., 2011.

[20] Cunha A, Caetano E. Experimental modal analysis of civil engineering structures. Journal of Sound and Vibration; 40(6):12-20, 2006.

[21] Prislan R. Laser doppler vibrometry and modal testing. University of Ljubljana, 2008.

[22] Technical Guide Footbridges: Assessment of Vibrational

Behaviour of Footbridges under Pedestrian Loading. SÉTRA: Service d'Études Techniques des Routes et Autoroutes, 2006.
[23] HIVOSS "Human Induced Vibration of Steel Structures". Design of Footbridges Guideline. Research Fund for Coal and Steel, 2008.
[24] Murray TM, Allen DE, Ungar EE, Davis DB. Vibrations of Steel-Framed Structural Systems due to Human Activity. Second Edition. Steel Design Guide Series. American Institute of Steel Construction, AISC, 2016.
[25] Bachmann H et al., Vibration problems in structures - practical guidelines, Basel (Switzerland):Institut für Baustatik und Konstruktion, Birkhäuser, 1995.

IBRACON

Volume 13, Number 3 (June 2020) p. 578 – 592 • ISSN 1983-4195
DOI: http://dx.doi.org/10.1590/S1983-41952020000300008

REVISTA IBRACON DE ESTRUTURAS E MATERIAIS
IBRACON STRUCTURES AND MATERIALS JOURNAL

Experimental and numerical characterization of the interface between concrete masonry block and mortar

Análise teórica e experimental de ensaios de caracterização da interface entre bloco de concreto e argamassa




R. D. PASQUANTONIO [a]
r.pasquantonio@gmail.com
https://orcid.org/0000-0001-8289-4973

G. A. PARSEKIAN [a]
parsekian.ufscar@gmail.com
https://orcid.org/0000-0002-5939-2032

F. S. FONSECA [b]
fonseca@byu.edu
https://orcid.org/0000-0002-8945-8696

N. G.SHRIVE [c]
ngshrive@ucalgary.ca
https://orcid.org/0000-0003-3263-5644

Abstract

Masonry is a construction system that has been used since the beginning of civilization and is still used throughout the world. The finite element method is a recent development that allows complex problems, including structural masonry problems, to be solved. A vast amount of literature exists on finite element modeling, using software such as ABAQUS, to represent experimental masonry models. Based on this established pattern, an experimental and analytical research program was designed and implemented. Thus, a set of tests was conducted to determine the compressive and tensile strengths of the masonry components, i.e., block, mortar, and grout. Bond wrench tests, diagonal tension tests, and horizontal joint shear tests were conducted to characterize the interface between the blocks and the mortar. A finite element model was then developed to represent the physical models and the general conclusion is that the finite element model was able to represent reasonably well the physical models.

Keywords: masonry, concrete block, mortar, finite element analysis, block-mortar interface.

Resumo

A alvenaria é um sistema construtivo que tem sido usado desde o início da civilização e ainda é usado em todo o mundo. O método dos elementos finitos é um desenvolvimento recente que permite resolver problemas complexos, incluindo problemas de alvenaria estrutural. Existe uma vasta quantidade de literatura sobre modelagem de elementos finitos, usando software como o ABAQUS, para representar modelos experimentais de alvenaria. Com base nesse padrão estabelecido, um programa de pesquisa experimental e analítica foi projetado e implementado. Assim, um conjunto de testes foi realizado para determinar as forças de compressão e tração dos componentes de alvenaria, isto é, bloco, argamassa e graute. Foram realizados ensaios tipo bond wrench, de tração diagonal e cisalhamento de juntas horizontais para caracterizar a interface entre os blocos e a argamassa. Um modelo de elementos finitos foi desenvolvido para representar os modelos físicos e a conclusão geral é que o modelo de elementos finitos foi capaz de representar razoavelmente bem os modelos físicos.

Palavras-chave: alvenaria, bloco de concreto, análise em elementos finitos, interface de bloco-argamassa.

[a] *Federal University of São Carlos, Department of Civil Engineering, São Carlos, SP, Brasil;*
[b] *Brigham Young University, Department of Civil and Environmental Engineering, Provo, Utah, USA;*
[c] *University of Calgary, Schulich School of Engineering, Department of Civil Engineering Calgary, Alberta, Canada.*

Received: 29 May 2019 • Accepted: 13 Dec 2019 • Available Online: 26 May 2020

1. Introduction

A substantial volume of knowledge has been established with respect to individual masonry components (units, mortars and grouts) as well as the interaction between these components. For example, Barbosa (2005) investigated the shrinkage of concrete masonry units and of masonry walls constructed from those units; Santos (2014) examined the effects of the elastic properties of the block-grout interface on the stiffness of masonry walls; Izquierdo (2015) studied the interface between block and grout under direct compression and flexural compression; Barbosa (2000) and Madia (2012) studied the behavior and interaction of infill masonry walls and the surrounding concrete elements; Capuzzo Neto (2000), Maluf (2007) and Lopes (2014) investigated the behavior of masonry walls under compressive loadings; and Silva (2014) determined the distribution of vertical loads on masonry walls using experimental and numerical models. Studies have also been conducted on the behavior of masonry structural elements. Examples include Landini (2001) and Contadini (2014) where the behavior of masonry beams under flexural loads was studied, while Landini (2001) and Pasquantonio (2015) studied the behavior of masonry beams under shear loads.

Masonry has been used in the construction of tall buildings and in this application, masonry elements are subjected to high compressive stresses. Fortes (2017) determined the properties of masonry constructed with high strength units, which can be used when masonry is subjected to high compressive stresses. While there is a large body of literature on experimental research on structural masonry components and elements, there is a distinct lack of research and thus understanding, on the interaction between masonry elements, e.g., a masonry beam connected to a masonry wall.

The increase in computational capability over the last forty years has led to a large base of numerical modeling of masonry structural elements together with increasing sophistication in the modeling. To capture the capacity and behavior of masonry accurately, these sophisticated models require many material parameters, which are extracted from experimental research endeavors. Due to a lack of standardization in testing, differences in the manufacture of local masonry components from local materials, and differences in local construction techniques and skills, there is a large dispersion worldwide in the values of the material parameters of interest for numerical modelling. This is especially true for the parameters that control the behavior of the interface between blocks and mortar in concrete masonry and the parameters that control the post-peak behavior.

Herein we present a summary of three tests, namely, the bond wrench, diagonal tension, and horizontal joint shear as conducted on masonry constructed with half-scale (1:2) concrete blocks with dimension of 203 × 102 × 102 (length × width × height) mm and type S mortar (1:0.5:4.5 PC:Lime:sand by volume); some masonry specimens were hollow while others were grouted. In addition to the results of these masonry tests, results of tests conducted to the determine the compressive strength of the masonry materials are also presented.

Results from the tests are used to extract the parameters that are required for accurate numerical modeling of masonry elements and structures constructed from these materials. In addition to the results obtained from the tests described herein, the results obtained by other authors, who conducted similar tests, are also presented.

2. Tests to characterize the masonry and materials

In this section, the three tests that were conducted as part of this research to characterize the behavior and capacity of the block-mortar interface are described. The difficulty in representing the masonry behavior accurately lies in representing properly the block-mortar interface (Oliveira 2014, Bolhassani 2015, Santos 2016).

The tests that were conducted to determine the compressive strengths of the masonry materials are also described.

2.1 Flexural strength test (bond wrench test) – AS 3700 (2001)

The objective of this test is to determine the flexural tensile strength of the mortar-block interface. The tests are performed on stack-bonded prisms of masonry constructed as follows:

1. Set the first block on a firm, clean, flat surface.
2. Place a mortar bed on the face of the block. Use full bedding for solid or cored units and face-shell bedding for hollow units.
3. Wait 30 sec. before placing the next block on the mortar.
4. Repeat steps 2 and 3.
5. Strike off excess mortar with a trowel without disturbing the blocks.

In cases where grouted prisms are used, the following extra requirements must be observed:

1. Clean out the cores so that no mortar extrusions remain on the internal surfaces and the cores are free of mortar droppings.
2. Fill the cores with grout and compact in layers during filling by rodding, finishing to a height 25 mm above the top surface of the prism.
3. One hour after filling, strike the surplus grout off level with the top surface.

After construction, the prisms are to be fully wrapped in a single vapor-proof sheet and left undisturbed until transported for testing. Testing of the prisms is conducted 7 days after construction

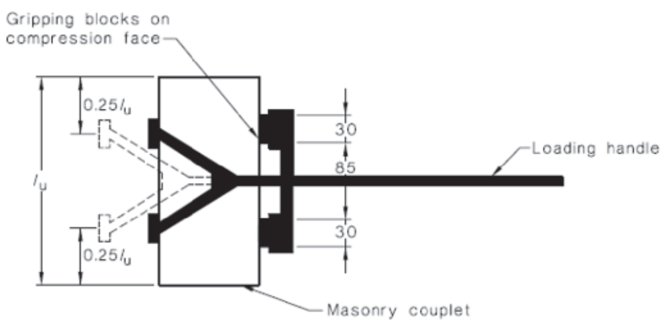

AS 3700 (2001) – Adapted

Figure 1
Bond wrench – plan view

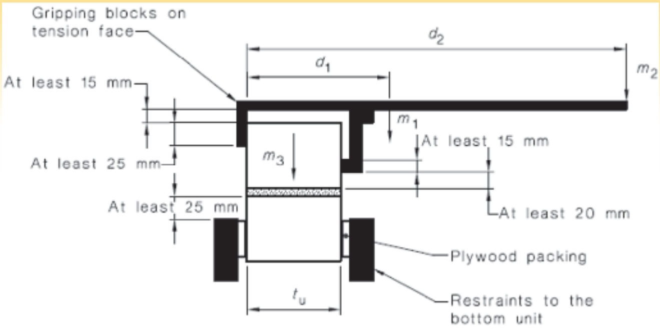

AS 3700 (2001) – Adapted

Figure 2
Bond wrench – elevation

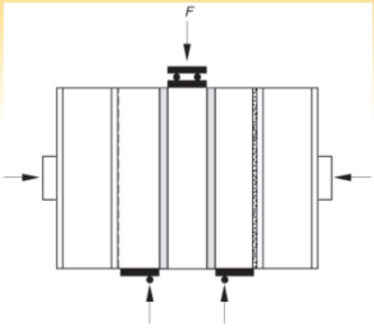

BS EN 1052-3 (2002) – Adapted

Figure 3
Precompression loading

or as soon as practicable after 7 days: grouted prisms are tested 28 days after filling the cores. Specimens are be transported to the testing location no more than 24 hours before the testing time. The testing apparatus or wrench, must be able to do the following:

- Apply a bending moment to the joint to be tested in the prism;
- Have a retaining frame into which the prism is clamped;
- Have the means of applying and measuring the load to determine the flexural stress at failure to an accuracy of within 0.01 MPa.

Sketches of a typical bond wrench apparatus are shown in Figures 1 and 2. The flexural moment is applied to the test joint by means of four gripping points at the quarter points along the length of the masonry unit on both the tension and compression faces. The wrench must have the following parameters calibrated:

- The mass of the wrench (m_1) to within ±25 g;
- The distance from the inside face of the tension gripping block to the center of mass of the bond wrench, d_1, to within ±2 mm;
- The distance from the inside face to the tension gripping block to the loading handle (d_2) to within ±2 mm.

The tensile strength of the specimen is calculated using Equation 1.

$$f_{sp} = \left(\frac{M_{sp}}{Z_d}\right) - \left(\frac{F_{sp}}{A_d}\right) \quad (1)$$

Where:

f_{sp} — Flexural tensile strength of the specimen, MPa;
M_{sp} — Bending moment about the centroid of the bedded the area of the test joint at failure, N·mm. This bending moment is calculated as $M_{sp} = 9.81 * m_2 * (d_2 - (t_u/2)) + 9.81 * m_1 * (d_1 - (t_u/2))$;
Z_d — Section modulus of the cross-sectional area A_d of the member;
F_{sp} — Total compressive force on the bedded area of the test joint, N. This compressive force is calculated as $F_{sp} = 9.81 * (m_1 + m_2 + m_3)$;
A_d — Cross-sectional area of the member, mm^2;
m_1, m_2 and m_3 – The mass of the wrench, the mass equivalent of the applied load and the mass of the block above the joint being tested, used in the flexural strength calculation, kg;

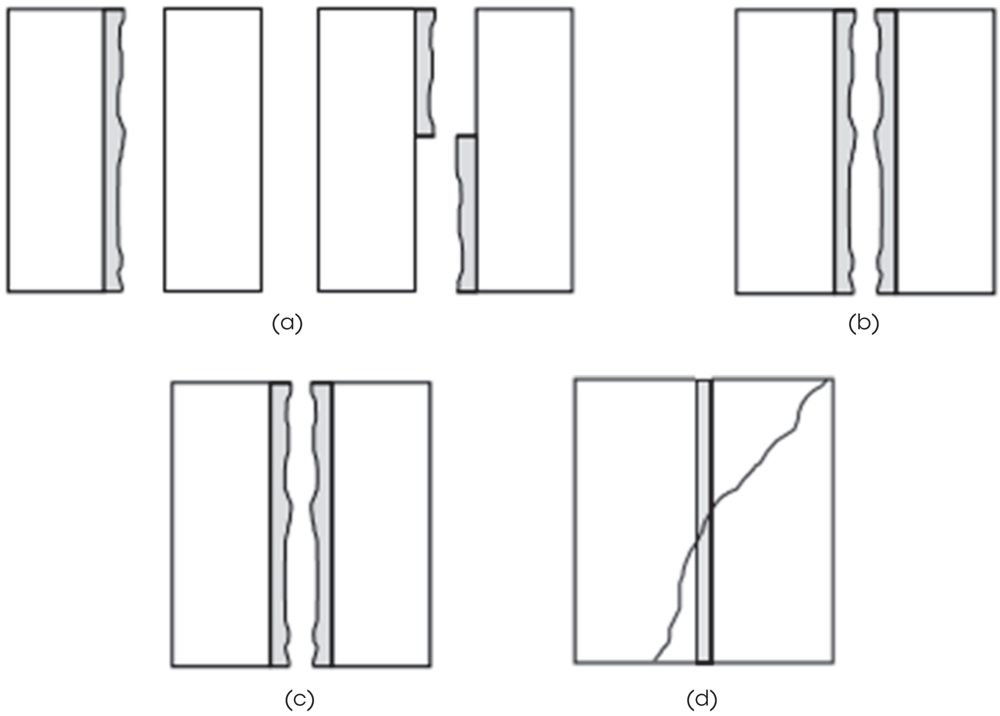

BS EN 1052-3 (2002) – Adapted

Figure 4
Typical shear rupture

d_1 — Distance from the inside edge of the tension gripping block to the center of mass, mm;
d_2 — Distance from the inside edge of the tension gripping block to the loading handle, mm;
t_u — Width of the masonry unit, mm.

2.2 Initial shear strength test – BS EN 1052-3 (2002)

Several authors (Araújo 2002, Oliveira 2014, Drysdale et al. 1999, Vermeltfoort 2012) have used the methodology presented in BS EN 1052-3 (2002) to determine the initial shear strength of mortar joints. The work presented herein follows this established pattern.

The initial shear strength of masonry is determined from the strength of small masonry specimens tested to failure. The specimens are tested in shear under four-point loading, with possible precompression perpendicular to the bed joints as shown in Figure 3.

Four different failure modes, shown schematically in Figure 4, are considered to give valid results to the test:

1. Rupture 1 (R1) – Figure 4.a. Debonding – occurs due to failure of the adhesion between one of the units and the mortar or the splitting of the mortar into two parts. In both cases there is complete or partial detachment of the mortar from the unit;
2. Rupture 2 (R2) – Figure 4.b. Debonding with mortar rupture – there is debonding of the mortar from both units together with failure of the mortar itself;
3. Rupture 3 (R3) – Figure 4.c. Unit failure – is due to failure of a unit in the direction parallel to the applied load and fragments of the unit remain attached to the mortar;
4. Rupture (R4) – Figure 4.d. Diagonal fracture – is due to diagonal cracking of the units.

The initial shear strength of the joint is obtained by linear regression of the stress-strain response to zero normal stress.

The testing machine must be able to apply the load while the specimen is subject to a pre-compression load. Two types of specimens can be used: type A consists of a prism assembled with three blocks with equal heights that are less than or equal to 200 mm and type B consists of a prism assembled with two blocks with unequal heights that are greater than 200 mm. Research (Araújo 2002, Oliveira 2014, Drysdale et al. 1999, Vermeltfoort 2012) indicates that type A specimens are preferred.

Specimens must be constructed as follows:

1. Set the first block on a firm, clean, flat, level surface;
2. Place a mortar bed on the face of the block with a final mortar joint thickness between 8 and 15 mm. In the research presented herein, the mortar thickness was 10 mm;
3. Place the next block on the mortar joint checking for linear alignment and level;
4. Repeat steps 2 and 3;
5. Strike off excess mortar with a trowel without disturbing the blocks;
6. Take samples (cubes) of the mortar.

Immediately after assembling a specimen, pre-compress the specimen with a uniformly distributed mass to give a vertical stress between 2.0×10^{-3} N/mm^2 and 5.0×10^{-3} N/mm^2. Then cure the specimens and maintain them undisturbed until testing. When lime-based mortar is used, specimens should be covered with a polyethylene sheet to prevent the mortar from drying out during the curing period. Specimens are to be tested, as shown schematically in Figure 3, when they reach an age of 28 days ± 1 day, unless otherwise specified when lime-based mortar is used. The compressive strength of the mortar is to be determined at the same time as the prisms are tested.

The standard specifies three precompression stresses and for each, a minimum of three specimens must be tested. Precompression stresses (f_{pi}) are determined based on the compressive strength of the units used. For units with compressive strength less than 10 MPa, precompression stresses should be approximately 0.1, 0.3, and 0.5 MPa. For units with compressive strength greater than 10 MPa, precompression stresses should be doubled.

The rate at which shear stress should be applied to the specimens is between 0.1 (N/mm^2)/min and 0.4 (N/mm^2)/min.

The following parameters must be recorded during a test:

1. The cross-sectional area of the specimen parallel to the shear force (Ai) with an accuracy of 1%;
2. The maximum applied load ($F_{i,max}$);
3. The precompression load;
4. The type of failure. If a specimen experiences rupture type R4, the standard recommends that further specimens be tested until three shear rupture of the other types are obtained.

For each specimen and precompression stress, the shear strength (f_{voi}) is calculated using Equation 2.

$$f_{voi} = \frac{F_{i,max}}{2 * A_i} \quad (2)$$

Shear strengths (f_{voi}) are plotted as a function of precompression stresses (f_{pi}) as shown in Figure 5 and a linear regression line is determined. The initial shear strength (τ_o) is the y-intercept of the regression line while the angle of internal friction (α) can be determined from the slope of the regression line.

The characteristic value of the initial shear strength is f_{vok} = 0.8 f_{vo} and the characteristic angle of internal friction can be obtained from $tan\ \alpha_k$ = 0.8 $tan\ \alpha$.

2.3 Diagonal tension (shear) test – ASTM E519-02

This test was developed to determine more accurately the diagonal tensile (shear) strength of masonry than was possible with

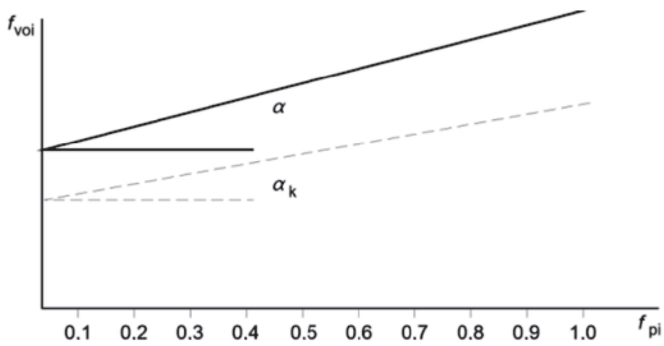

BS EN 1052-3 (2002) – Adapted

Figure 5
Typical f_{voi} x f_{pi} relationship

other available methods. The specimen size was selected as being the smallest that would be reasonably representative of a full-size masonry assemblage and that could be performed in the testing machines typical of laboratories.
The height and width of the specimen are 1200 mm and 1200 mm while the thickness depends on the thickness of the block. At least three specimens must be tested with all three constructed using the same type of block and mortar. When two types of mortar are to be evaluated, two sets of three specimens must be constructed. Specimens should not be moved for at least seven days after construction and should be stored for at least 28 days in a controlled environment with temperature of 24 ± 8˚C and relative humidity between 25 and 75%.
In addition to testing the masonry specimen, the mortar and the block must be also tested according to the following:

1. Mortar – for each mortar type, three 50-mm cubes must be tested to determine the compressive strength of the mortar;
2. Units – at least six units must be tested to determine their compressive strength.

The procedure to test the specimens are as follows:

1. Placement of the loading shoes – the upper and lower loading shoes are centered on the upper and lower bearing surfaces of the testing machine and are placed on a diagonal of the specimen;
2. Specimen placement – the specimen is positioned such that the diagonal to be tested is centered with the axis of the testing machine. In some cases it is necessary to cap the specimen with gypsum in the lower loading shoe to obtain full contact between the shoe and the specimen;
3. Instrumentation – extensometers or LVTDs are to be used to measure the shortening or elongation of the two diagonals of the specimen.

The shear stress is calculated using Equation 3.

$$S_s = \frac{0.707 * P}{A_n} \tag{3}$$

where:
S_s — shear stress, MPa;
P — applied load, N;
A_n — net area of the specimen, mm², calculated using equation 4.

$$A_n = \left(\frac{W + h}{2}\right) * t * n \tag{4}$$

where:
W — width of the specimen, mm;
h — height of the specimen, mm;
t — thickness of the specimen, mm;
n — percent of the gross area of the unit that is solid, expressed as a decimal.
The shear strain is calculated using Equation 5.

$$\gamma = \frac{\Delta V + \Delta H}{g} \tag{5}$$

where:
γ — shearing strain, mm/mm;
ΔV — vertical shortening, mm;
ΔH — horizontal shortening, mm;
g — vertical gage length, mm;
ΔH must be based on the same gage length as for ΔV.
The modulus of rigidity or the modulus of elasticity in shear is calculated using Equation 6.

$$G = \frac{S_s}{\gamma} \tag{6}$$

where:
G — modulus of rigidity, MPa.

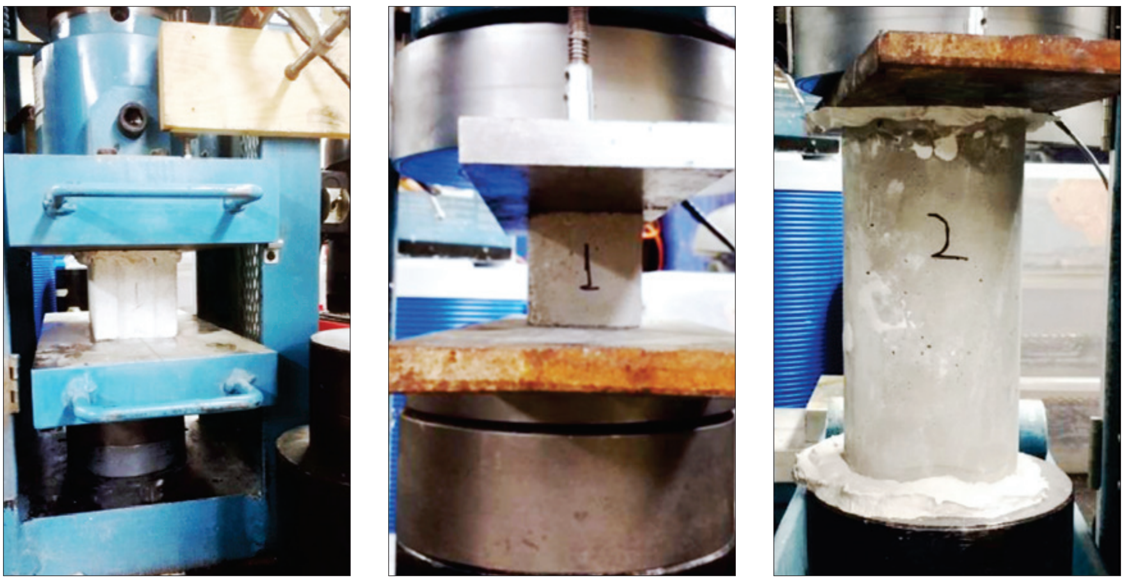

(a) (b) (c)

Figure 6
Material tests

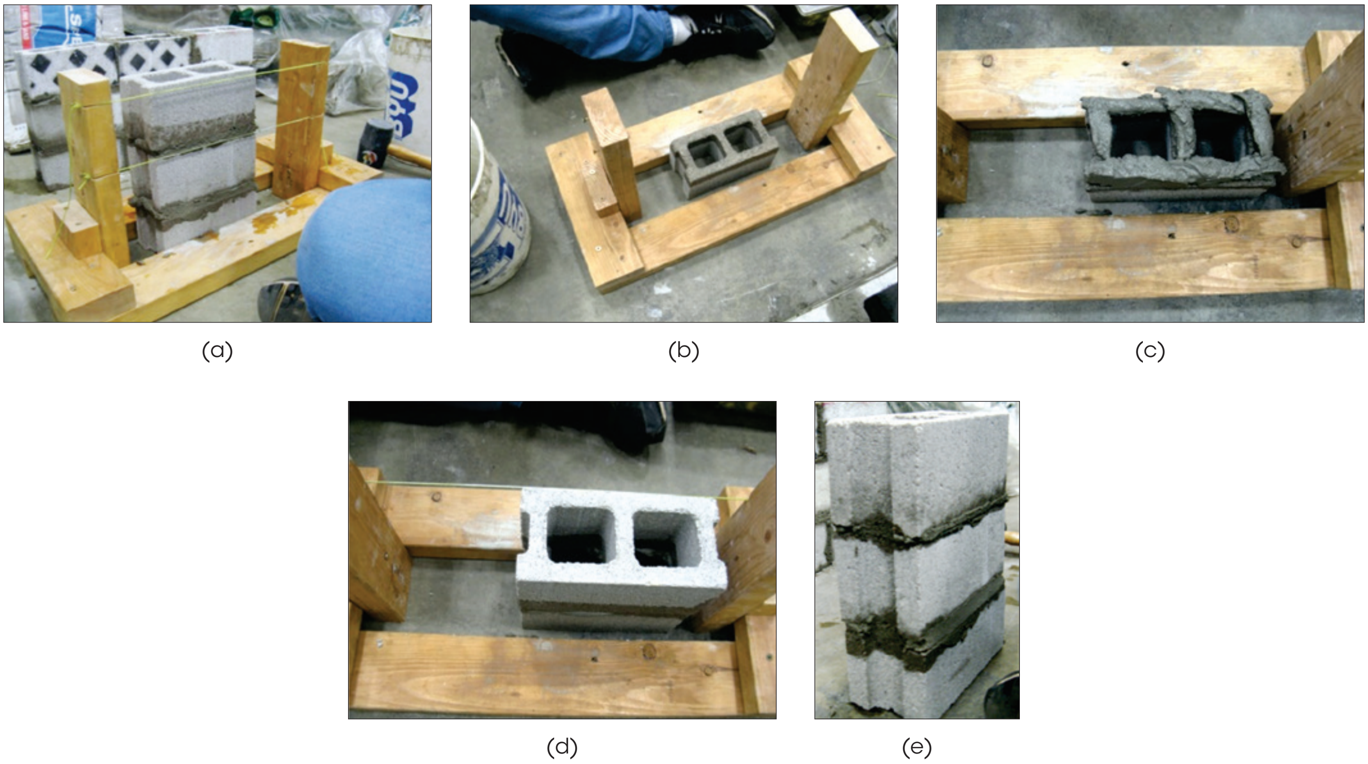
(a) (b) (c) (d) (e)

Figure 7
Wood jip used during construction of prisms (a) – Construction of the Prisms (b) to (e)

2.4 Materials test

To determine the compressive strength of the masonry units, tests were conducted according to ASTM C140. Six specimens were tested as shown in Figure 6.a; the loading rate used was 1.27 mm/min. To determine the compressive strength of the mortar, tests were conducted as outlined in ASTM C109. Six specimens were tested as shown in Figure 6.b. To determine the compressive strength of the grout, tests were conducted as specified in ASTM C1019 and ASTM C39. Four specimens were tested as shown in Figure 6.c.

3. Specimen construction

The construction of the specimens for the bond wrench and shear strength tests and the construction of the wallettes for the diagonal tension tests are summarized in this section.

3.1 Bond wrench and shear strength specimens

Prisms were constructed with three blocks for both types of test. A simple wood jig, shown in Figure 7.a, was built to facilitate the construction of the prisms.
The prisms were constructed as follows:
1. The top face of the block was moistened (to reduce absorption of the mortar water by the block) and the block was placed on the jig as shown in Figure 7.b;
2. A full bed of mortar was applied to the surface of the block as shown in Figure 7.c;
3. The next block was moistened and placed on the mortar bed as shown in Figure 7.d;
4. A line was used to aid the leveling the block and maintain the mortar bed thickness as close as possible to the specified thickness;
5. Steps 2 to 4 were repeated for the third block as shown in Figure 7.e;
6. The excess mortar was struck off with a trowel without disturbing the blocks.

3.2 Diagonal tension specimens

Ten wallettes were constructed: five hollow and five grouted. The wallettes were three blocks wide and six blocks high, constructed as follows:
1. The first course was constructed by buttering the webs of the blocks as shown in Figure 8.a;
2. The top face of the blocks was moistened, and a full bed of mortar applied as shown in Figure 8.b;
3. The second course of blocks was placed and the blocks leveled;
4. Steps 2 and 3 were repeated until the wallette was constructed. A complete wallette is shown in Figure 8.c.

Approximately 48 hours after being constructed, five wallettes were grouted as follows:
1. The grout space was cleaned from mortar droppings;
2. The wallettes were moistened;
3. Grout was placed in layers of approximately the height of the block. Each grout layer was rodded 15 times with a tamping rod.

The first layer was rodded to its bottom while the other layers were rodded to about half of the previous layer;

4. The process was repeated for the other wallettes.

4. Test results

In this section, the results of the tests conducted are presented.

(a) (b) (c)

Figure 8
Wallette construction

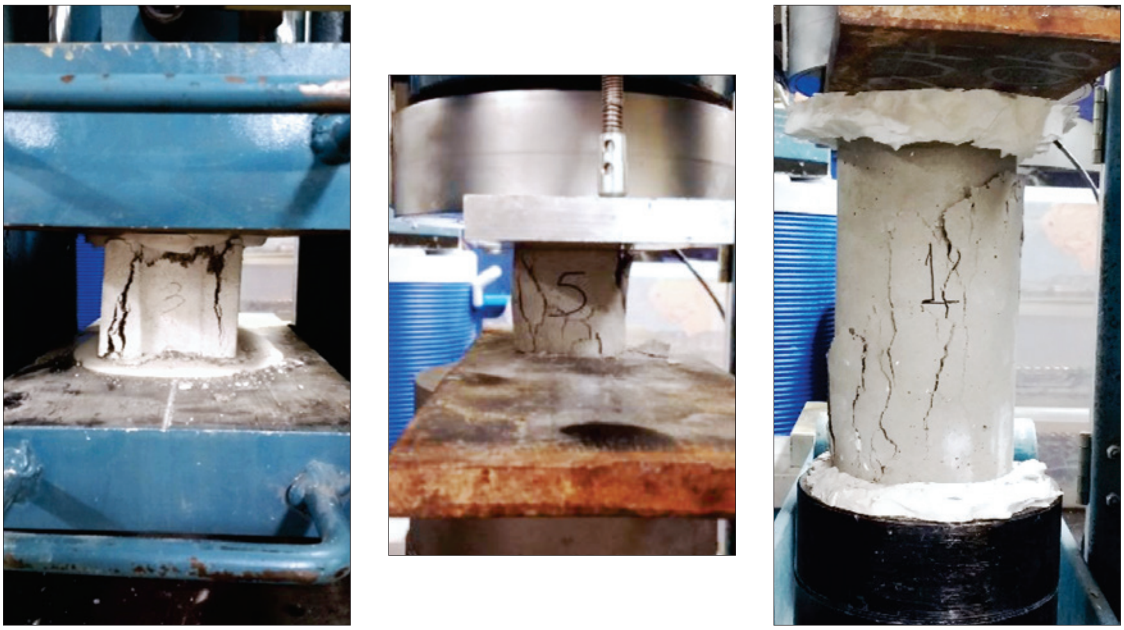

(a) (b) (c)

Figure 9
Typical failure mode of the materials

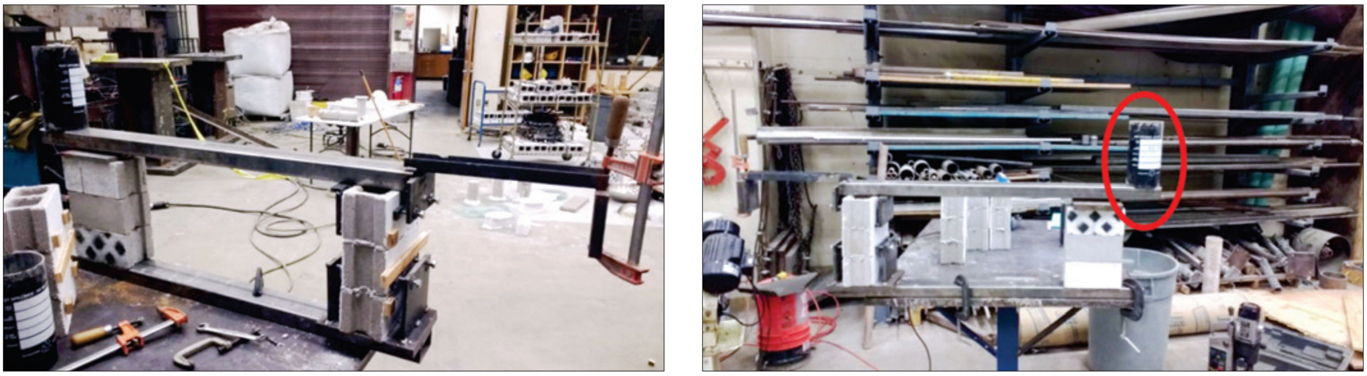

(a) (b)

Figure 10
Bond wrench test

4.1 Materials

In Figure 9a the typical mode of failure of the blocks is shown, which was separation of the face shells. The average compressive strength of the blocks was approximately 18.4 MPa with a Coefficient of Variation of 8.8%, and the average modulus of elasticity of the blocks was 65.7 GPa with a Coefficient of Variation of 13.8%. In Figure 9b the typical mode of failure of the mortar cube is shown. The average compressive strength of the mortar was approximately 20.8 MPa with a Coefficient of Variation of 15.6%. In Figure 9c the typical mode of failure of the grout is shown. The average compressive strength of the grout was approximately 25.8 MPa with a Coefficient of Variation of 30.4%.

4.2 Bond wrench

The testing apparatus is shown in Figure 10 with a specimen ready for testing. The specimen was loaded by means of slowly placing sand in the bucket located on the right side of the loading apparatus as shown in Figure 10b. The mortar separated from either the loaded block, as shown in Figure 11a, or from the block below, as shown in Figure 11.b. Thirty joints were tested in total. The average tensile resistance of the mortar joint was 0.08 MPa with a coefficient of variation of approximately 29.5%.

4.3 Initial shear strength

There were 30 specimens divided into three groups according to

(a) (b)

Figure 11
Typical mode of failure – bond wrench tests

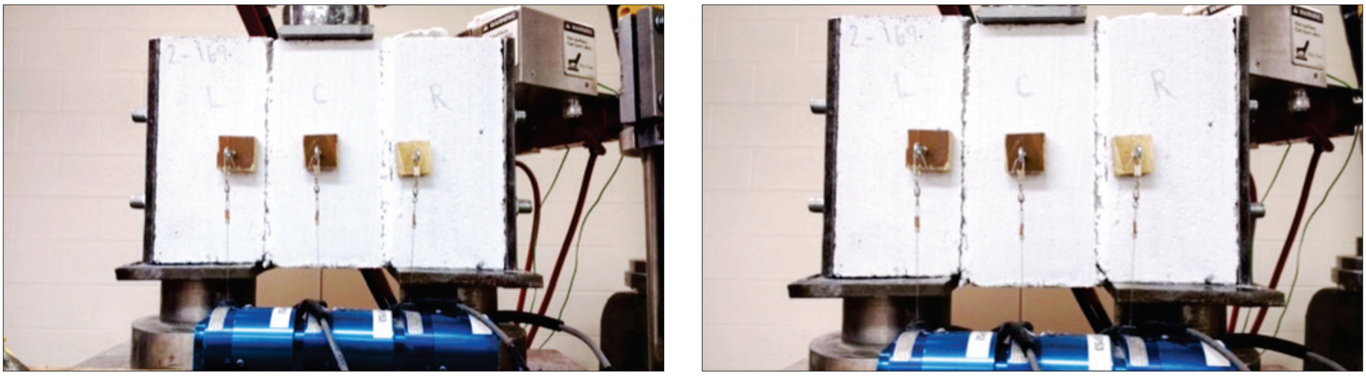

(a) (b)

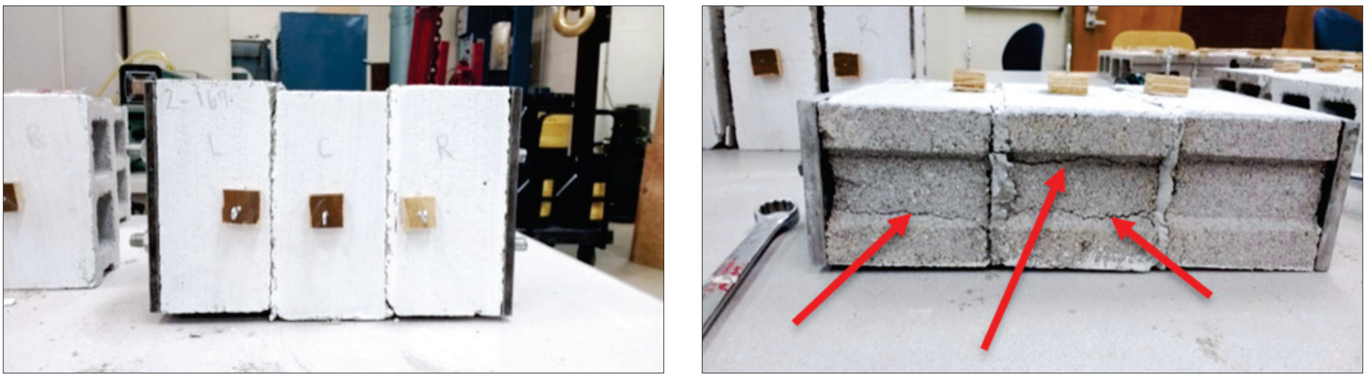

(c) (d)

Figure 12
Shear tests – before testing (a), After testing (b) and (c), Cracks of block webs (d)

the precompression loading. Since the blocks used had a compressive strength greater than 10 MPa, precompression stresses were approximately 0.2, 0.6, and 1.0 MPa. A specimen ready to be tested is shown in Figure 12a while specimens after testing are shown in Figures 12b and c. The underside of the same specimen is shown in Figure 12d: the cracks through the webs that developed during the testing are visible.

In Figures 13 to 15 the stress vs strain curves are presented for all specimens according to the applied precompression. Using the first peak stress and corresponding strain, an average shear strength and strain were determined; the values were approximately 0.52 MPa, 0.70 MPa and 1.01 MPa for each precompression level.

The average shear strength for each precompression stress as well as the regression line are shown graphically in Figure 16. The correlation between the regression line and the experimental data is excellent (R^2 = 0.9884.) Thus, from the regression line, a reasonable value for the initial shear strength, i.e., the shear strength for no precompression, can be obtained. The initial shear strength, τ_o, is 0.37 MPa and *tan* ϕ is 0.61, which corresponds to an angle of internal friction (α) of 0.552 rad.

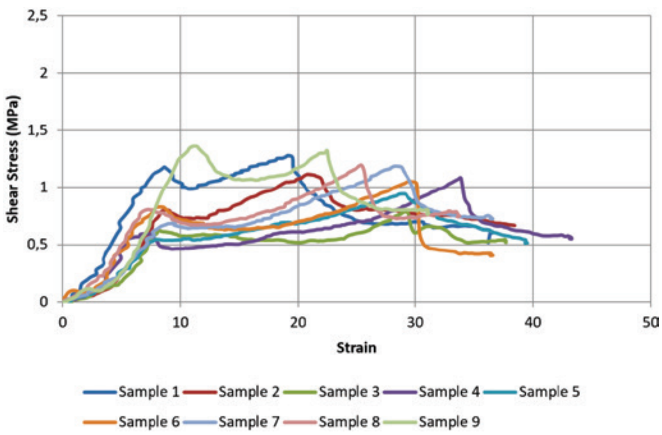

Figure 13
Shear stress x Strain – precompression of 0.2 MPa

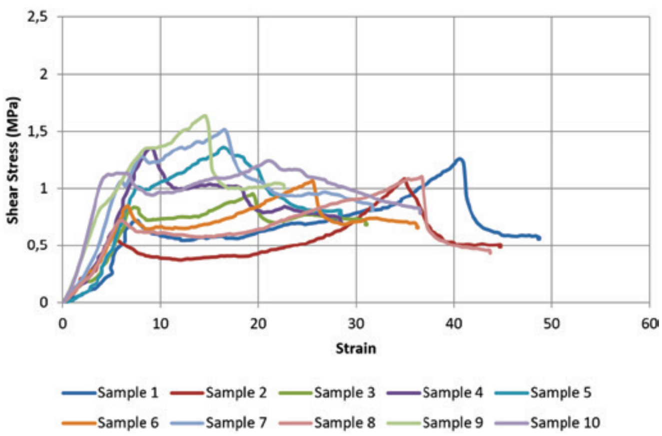

Figure 14
Shear stress x Strain – precompression of 0.6 MPa

4.4 Diagonal tension (shear)

Tests were conducted as shown in Figure 17. The positioning of the specimen is important since misalignment of the specimen can

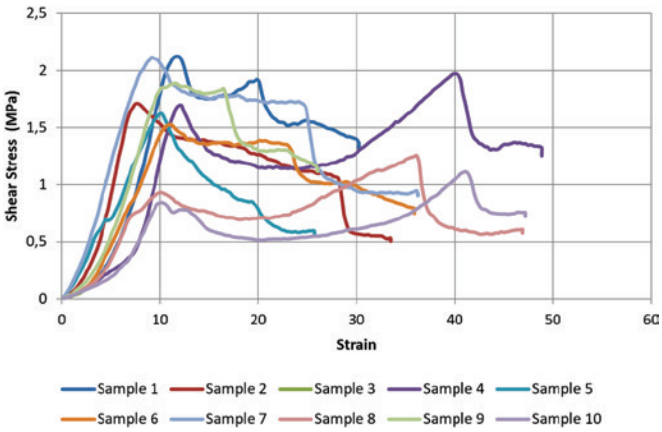

Figure 15
Shear stress x Strain – precompression of 1.0 MPa

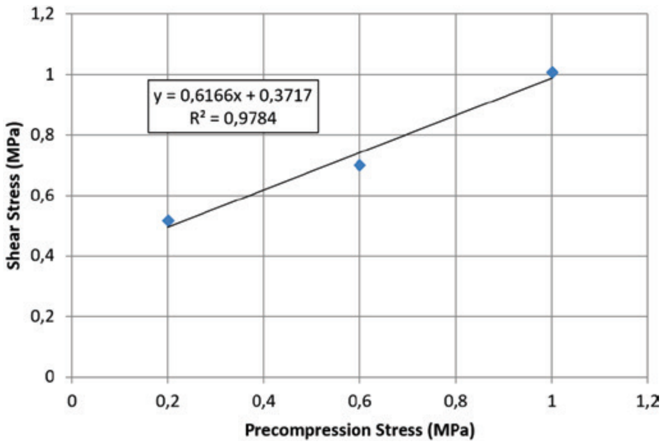

Figure 16
Average shear stress as a function of precompression

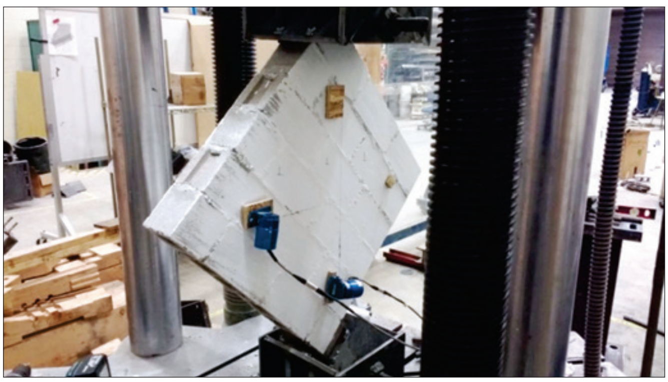

Figure 17
Diagonal tension testing

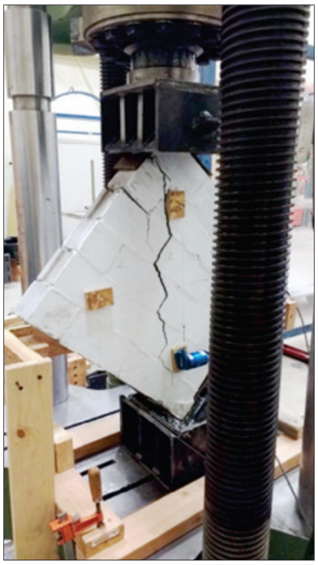

(a)

(b)

Figure 18
Typical rupture – diagonal tension testing

cause shear or bending moment to be applied to the specimen, which are undesirable. Positioning of the instruments measuring the deformations is also important because the modulus of rigidity of the masonry will be based on these measurements.

The failure mode observed for all specimens, like that observed by others (Bolhassani et al. 2015, Knox et al. 2018), was a crack along the vertical diagonal as shown in Figure 18.

In Figures 19 and 20 the shear stress vs shear strain is shown for the hollow and grouted specimens, respectively. The average shear stress and modulus of rigidity of the hollow masonry are approximately 2.8 MPa (CV = 17.1%) and 3,390 MPa (CV = 29.2%), respectively. For the grouted masonry, the average shear stress and modulus of rigidity are approximately 1.0 MPa (CV = 17.0%) and 1,360 MPa (CV = 12.2%), respectively.

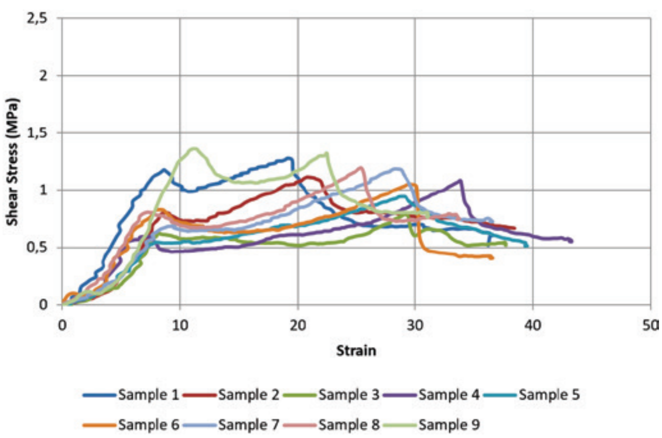

Figure 19
Shear stress vs Strain – hollow masonry

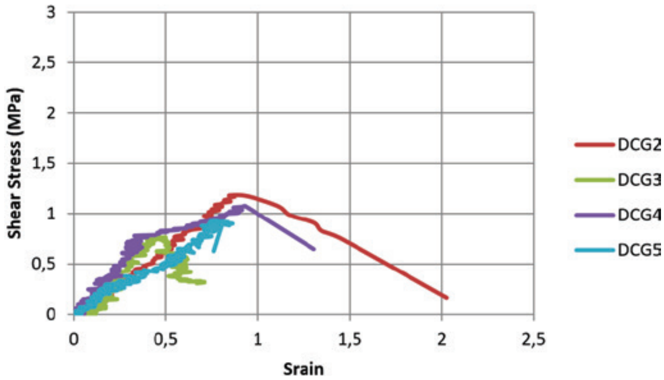

Figure 20
Shear stress vs Strain – grouted masonry

5. Analysis

In addition to the results obtained in this research, results from tests conducted by others are also presented and discussed.

5.1 Blocks

In Table 1, the results from compression tests conducted by several researchers on typical blocks, i.e., scale 1:1, and blocks of scales 1:2 and 1:3 are presented. The data show that the compressive strength of the block is independent of the block scale.

Using all the data obtained by others, the average compressive strength of the blocks is 24.2 MPa (CV = 46.9%) while the average compressive strength of the blocks used in this research is 18.4 MPa (CV = 8.8%), which is approximately 76% of 24.2 MPa.

Using the data for blocks of scale 1:2 only, as summarized in

Table 1
Compressive strength – scales 1:1, 1:2 and 1:3

Author	Scale	Strength (MPa)	S.D.	C.V.
Long et al. (2005)	1:2	24.4	2.8	11.4
Long et al. (2005)	1:1	29.2	1.6	5.4
Barbosa (2008)	1:1	24.7	5.8	23.7
Hughes (2010)	1:3	54.8	2.6	4.7
Wierzbicki (2010	1:3	54.8	2.6	4.7
Kaaki (2013)	1:3	19.2	1.2	6.2
Kaaki (2013)	1:3	14.1	1.6	11.3
Banting and El-Dakhakhni (2014)	1:2	26.5	3.5	13.2
Bolhassani et al. (2015)	1:1	21.6	—	—
Knox et al. (2018)	1:1	12.9	1.3	10.0
Knox et al. (2018)	1:2	16.9	4.9	28.0
Alotaibi and Galal (2018)	1:2	21.73	2.0	9.4
Average	—	24.2	—	—
This work	1:2	18.4	13.3	8.8

Table 2
Compressive strength – scale 1:2

Author	Strength (MPa)	S.D.	C.V.
Long et al. (2005)	24.4	2.7	11.4
Banting and El-Dakhakhni (2014)	26.5	3.4	13.2
Knox et al. (2018)	16.9	4.9	28.0
Alotaibi and Galal (2018)	21.73	2.0	9.4
Average	22.4	—	—
This work	18.4	13.3	8.8
This work/average	0.82	—	—

Table 3
Compressive strength – scale 1:1

Author	Strength (MPa)	S.D.	C.V.
Long et al. (2005)	29.2	1.57	5.4
Barbosa (2008)	24.7	5.84	23.6
Bolhassani et al. (2015)	21.6	—	—
Knox et al. (2018)	12.9	1.3	10.0
Average	22.1	—	—
This work	18.4	13.3	8.8
This work/average	0.83	—	—

Table 2, the value obtained in this research represents approximately 82% of the average compressive strength obtained using the values obtained by others. When using the data for blocks of scale 1:1 only, as summarized in Table 3, the value obtained in this research represents approximately 83% of the average compressive strength obtained by others. This simple analysis shows that the ratio of the compressive strength of the blocks obtained herein to that obtained using results of tests conducted by others is independent of the block scale. Further, the analysis confirms that in order to model a particular form of masonry, the data associated with that masonry need to be used – a single set of data for example, will not represent all concrete blockwork from all over the world.

5.2 Initial shear strength

The parameters considered in this analysis are described below:
1. The initial shear strength and the angle of internal friction – these values are obtained from the regression of the average shear strength for each precompression stress;
2. Modulus of rigidity of the interface – this value is obtained from stress vs strain curve. Herein, the modulus of rigidity will be considered the same for both shear directions;
3. Modulus of rigidity of the interface – considering the modulus of elasticity of the block, the modulus of elasticity of the mortar, and the Poisson's Ratio, this value will also be obtained using the equation proposed by Lourenço et al. (2004).

In addition to the results obtained herein for the initial shear strength and the angle of internal friction, the results from tests conducted by five other researchers are considered. The initial shear strength and the angle of internal friction results are summarized in Table 4.

Table 4
Angle of internal friction and initial shear strength – scale 1:1

Author	$\mu = \tan\varphi$	φ (rad)	τ_0 (MPa)
Lourenço et al. (2004)	1.03	0.8	1.39
Almeida et al. (2016)	1.15	0.855	—
Abdou et al. (2006)	1.05	0.81	1.27
Lizárraga and Perez-Gavillan (2017)	1.05	0.81	0.55
Lizárraga and Perez-Gavillan (2017)	1.2	0.87	0.46
Bolhassani (2015)	0.99	0.78	—
Average	1.07	0.82	0.91
Pasquantonio et al. (2018)	0.61	0.55	0.37
Pasquantonio et al. (2018)/average	0.56	0.67	0.40

The ratios between the initial shear strength and angle of internal friction obtained in this research and those obtained from tests by other researchers are 0.40 and 0.67, respectively. Most likely the reason for the smaller values obtained herein is that half scale blocks were used; the blocks used for the specimens in the other tests were full scale. Such a difference was also observed by

Table 5
Parameters for scale adjustment

Group	Quantity	Dimension	Scale 1:1	Model
Loading	Concentrated load	F	$S_oS_L^2$	S_L^2
	Bending moment	FL	$S_oS_L^3$	S_L^3
Geometry	Dimension	L	S_L	S_L
	Displacement	L	S_L	S_L
	Area	L^2	S_L^2	S_L^2
	Volume	L^3	S_L^3	S_L^3
Material property	Block compressive strength	FL^{-2}	S_o	1
	Block deformation	1	1	1
	Modulus of elasticity	F^{L-2}	S_o	1
	Poisson's ratio	1	1	1
	Stiffness	FL^{-1}	S_oS_L	S_L

Table 6
Modulus of rigidity for levels of precompression

f_{pi}	0.2	0.6	1.0
$K_{s,m}$	0.36	0.42	0.58
S.D.	0.09	0.17	0.18
C.V.(%)	24.5	40.5	31.0

Table 7
Coefficients of shear rigidity – in-plane and normal

Author	$K_{ss} = K_{tt}$ (MPa/mm)	K_{nn} (MPa/mm)
Vandoren et al. (2013)	124	222
Nasiri and Liu (2017)	320	1,011
Lourenço et al. (2004)	99	222
Lizárraga and Perez-Gavilan (2017)	103	153
Lizárraga and Perez-Gavilan (2017)	85	143
Massart et al. (2004)	191	351
Abdulla et al. (2017)	46	82
Abdulla et al. (2017)	62	110
Abdulla et al. (2017b)	27	62
Average	117	262
This work	118	197
This work/average	101	75

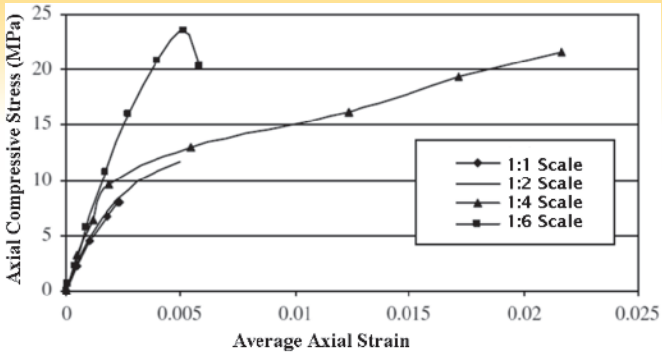

Mohammed et al (2011) – Adapted

Figure 21
Influence of block scale on stress x strain relationship

Mohammed et al. (2011), who investigated the influence of size on the shear strength and angle of internal friction of blocks. Hughes (2010) indicates that the size of the element may influence some properties of the material tested, as summarized in Table 5. Based on the values shown, the relationship between the shear strength for a half scale block and that of a full block is approximately 0.5; the same ratio is obtained for the angle of internal friction.
The values of modulus of rigidity for each level of precompression are summarized in Table 6.
In general, the stress-strain relationship is related to the size (or scale) of the block used and as the size increases or decreases, the behavior changes as depicted in Figure 21. Thus, the values obtained herein for the initial shear strength, the angle of internal friction, and the modulus of rigidity can be considered in good agreement with the values obtained when full scale blocks are used.
Lourenço et al. (2004) developed an analytical tool to determine the modulus of rigidity based on thickness of the mortar joint, Poisson's ratio, and the modulus of elasticity in the normal and in the transverse directions. The results of this analysis are summarized in Table 7 and the values obtained vary tremendously, again emphasizing the need for data for the particular masonry being modelled. These values have been used during numerical modeling, specifically for micro-modeling of the mortar-block interface.

5.3 Bond wrench

A literature search was conducted to find published results on the strength of the mortar to tension caused by flexure determined according to AS 3700 (2001). Unfortunately, not many published

Table 8
Strength of mortar to tension caused by flexure

Author	Strength (MPa)	C.V.	Observations
Thamboo et al. (2013)	0.42	Not given	Mortar with fiber and concrete blocks
Pavía and Hanley (2010)	0.27	32.6	Lime mortar and ceramic blocks
	0.19	24.6	
	0.32	33.9	
Barr et al. (2015)	0.11	7.9	Lime mortar. Testing right after construction of the specimens
	0.23	2.4	
	0.33	2.9	
Barr et al. (2015)	0.08	3.8	Lime mortar. Testing 1 minute after construction of the specimen
	0.19	2.7	
	0.31	1.7	
Barr et al. (2015)	0.07	19.4	Lime mortar. Testing 15 minute after construction of the specimen
	0.18	9	
	0.25	4.8	
Khalaf (2005)	0.12	14	—
	0.15	15	
	0.18	17	
Shabdin et al. (2018)	0.1	39	Ceramic blocks
Average	0.21	—	—
This work	0.08	29.4	—
This work/average	38.9	—	—

results were found, and the results obtained are for full scale blocks. The results are summarized in Table 8. When the number of specimens tested is less than 30, the standard specifies that the coefficient of variation must be less than 30%; the coefficient of variation for the results obtained during this research was 29.5%. Pavía and Henley (2010) concluded that the mortar strength depends on various factors including the block geometry, the mortar type, and the curing time of the specimen. Barr et al. (2015) conducted tests immediately after, 1 minute after, and 15 minutes after construction of the specimens, and concluded that the strength of the mortar is a function of the water absorbed by the block. Thus, although the average value obtained herein is only about 40% of the average value obtained from the results of the tests conducted by other researchers; the value can still be considered satisfactory.

5.4 Diagonal tension

The results of the analysis are summarized in Table 9 for the hollow masonry and in Table 10 for the grouted masonry. There is a large scatter in the results obtained for hollow masonry. The reason is that only the mortar joint is resisting the applied load, and as mentioned earlier, mortar strength varies tremendously and is difficult to determine using current testing methods. For grouted masonry, however, the values are more consistent because the grout prevents large relative displacement between the block and the mortar at their interface. Thus, the specimens resist larger applied load but displace significantly less than their hollow counterparts. Although the grouted specimens can resist more load, the shear strength is lower than that of their hollow counterpart because the area resisting the shear is significantly larger than that of their hollow counterparts.

Table 9
Diagonal tension – hollow masonry

Author	Strength (MPa)	C.V.	Observations
Long et al. (2005)	2.24	12.7	Concrete blocks – scale 1:2
Long et al. (2005)	1.77	10.2	Concrete blocks – scale 1:1
Kaaki (2013)	0.37	—	Concrete blocks – scale 1:1
Kaaki (2013)	0.38	—	Concrete blocks – scale 1:3
Bolhassani (2015)	0.51	17.8	Concrete blocks
Average	1.054	—	—
This work	2.79	—	—
This work/average	265	—	—

Table 10
Diagonal tension – grouted masonry

Author	Strength (MPa)	C.V.	Observations
Long et al. (2005)	2.2	2.9	Concrete blocks – scale 1:2
Long et al. (2005)	1.78	23.4	Concrete blocks – scale 1:1
Bolhassani (2015)	1	14.3	Concrete blocks
Average	1.66	—	—
This work	1.02	—	—
This work/average	61.44	—	—

6. Concluding remarks

Based on the results and analysis presented, the following conclusion can be made:

1. Blocks

- The stress-strain relationships of the tested blocks are in good agreement with each other;
- The compressive strength of the block is independent of the block scale;
- The modulus of elasticity of the block is within the values obtained by other researchers.

2. Initial shear strength

- The higher precompression level appears to change the mode of failure of the specimens slightly. Cracks developed in the webs of the block at a precompression of 1.0 MPa but no cracks were observed for the other two smaller precompression levels;
- Once one of the mortar joints fails, the central block of the specimen locks, causing an increase in capacity;
- Considering the scale effect, the values for the initial shear strength and angle of internal friction obtained in this research are consistent with those obtained in other studies.

3. Bond wrench

- The testing is very sensitive and must be conducted very carefully;
- The rupture observed was consistent with that observed by others;
- The flexural tensile strength of the block-mortar interface has significant variability;
- The value obtained herein differs slightly from those obtained by other researchers.

4. Diagonal tension

- The mode of rupture appears to be independent of the block scale used;
- The mode of rupture is independent of the type of masonry. Both hollow and grouted masonry experienced the same type of failure;
- The value obtained herein is slightly smaller than that obtained by other researchers due to the block size used;
- The moduli of rigidity obtained herein are smaller than those obtained by other researchers due to the block size used;
- The modulus of rigidity of hollow masonry varies tremendously because it is dependent significantly on the mortar-block interface strength.

5. Modelling

- There is so much variation in the data that the values of the parameters needed to model a particular form of masonry should be determined for that masonry.

7. Acknowledgements

The authors are grateful for the financial support of CAPES (Coordenação de Aperfeiçoamento de Pessoal de Nível Superior) through the PDSE program (Programa de Doutorado Sanduíche no Exterior). Most specially the authors acknowledge the half-scale blocks donated by the Canadian Masonry Design Centre.

8. References

[1] Abdou, L., Ami Saada, R., Meftah, F., Mebarki, A. (2006). Experimental investigations of the joint-mortar behaviour. Mechanics Research Communications. V33. 370-384.

[2] Abdulla, K. F., Cunningham, L. S., Gillie, M. (2017). Simulating masonry wall behaviour using a simplified micro-model approach. Engineering Structures, 151, 349-365.

[3] Abdulla, K., Cunningham, L., Gillie, M. (2017b). Non-linear simulation of masonry behaviour under cyclic loads. Proceedings of the 2017 MACE PGR Conference. University of Manchester, Manchester.

[4] Almeida, J. A. P. P., Bordigoni, D., Pereira, E. B., Barros, J. A. O., Aprile, A. (2016). Assessment of the properties to characterise the interface between clay brick substrate and strengthening mortar. Construction and Building Materials. v103. p47-66.

[5] Alotaibi, K. S., Galal, K. (2018). Experimental study of CFRP confined reinforced concrete masonry columns tested under concentric and eccentric loading. Elsevier Journal of Composites Part B: Engineering, 155:257-271.

[6] American Society for Testing and Material (ASTM 2008). Standard test method for compressive strength of hydraulic cement mortars (using 2-in. or [50-mm] Cube specimens. ASTM-C109, West Conshohocken, PA.

[7] American Society for Testing and Material (ASTM 2009). Standard test method for sampling and testing concrete masonry units and related units. ASTM-C140, West Conshohocken, PA.

[8] American Society for Testing and Material (ASTM 2009). Standard test method for sampling and testing grout. ASTM-C1019, West Conshohocken, PA.

[9] American Society for Testing and Material (ASTM 2014). Standard test method for compressive strength of cylindrical concrete specimens. ASTM-C39, West Conshohocken, PA.

[10] Araújo, A. F. (2002). Metodologia para Avaliação da Resistência de Aderência ao Cisalhamento de Prismas para Alvenaria Estrutural. Dissertação (Mestrado). Programa de Pós–Graduação em Engenharia de Estruturas, Universidade Federal de Minas Gerais (UFMG), Belo Horizonte. 149p.

[11] AS 3700 (2001). Masonry Structures, Australian Standard (AS), Sydney, NSW.

[12] Banting, B., El-Dakhakhni, W. (2014). Seismic performance quantification of reinforced masonry structural walls with boundary elements. J. Struct. Eng., 140(5), 1–15.

[13] Barbosa, C. S. (2008). Resistência e deformabilidade de blocos vazados de concreto, prismas e paredes e suas correlações com as propriedades mecânicas dos materiais constituintes. Tese (Doutorado). Escola de Engenharia de São Carlos. Universidade de São Paulo, São Carlos, SP. 262p.

[14] Barbosa, K. C. (2005). Avaliação Experimental do Fenômeno de Retração em Alvenaria de Blocos de Concreto. Dissertação (Mestrado). Programa de Pós-Graduação em Estruturas e Construção Civil – Universidade Federal de São Carlos (UFSCar) – SP. 252p.

[15] Barbosa, P. C. (2000). Estudo da interação de paredes de alvenaria estrutural com vigas de concreto armado. Dissertação (Mestrado) – Escola de Engenharia de São Carlos, Universidade de São Paulo, São Carlos. 110p.

[16] Barr, S., McCarter, W. J., Suryanto, B. (2015). Bond-strength performance of hydraulic lime and natural cement mortared sandstone masonry. Construction and Building Materials. V84, p128-135.

[17] Bolhassani, M. (2015). Improvement of Seismic Performance of Ordinary Reinforced Partially Grouted Concrete Masonry Shear Walls. Dissertation. 401p. Faculty of Drexel University, Drexel University.

[18] Bolhassani, M., Hamid, A. A., Lau, A. C. W., Moon, F. (2015). Simplified micro modeling of partially grouted masonry assemblages. Construction and Building Materials. v83. p159-173.

[19] BS EN 1052-3:2002 – Methods of test for Masonry: Part 3: Determination of Initial Shear Strength, Brussels.

[20] Capuzzo Neto, V. (2000). Estudo teórico e experimental da interação de paredes de alvenaria estrutural submetidas a ações verticais. Dissertação (Mestrado) - Escola de Engenharia de São Carlos, Universidade de São Paulo, São Carlos, 111p.

[21] Contadini, L. F. (2014). Análise teórica e experimental do comportamento de vigas de alvenaria estrutural armada sujeitas à flexão simples. Dissertação (Mestrado) – Departamento de Engenharia Civil – Universidade Estadual Júlio de Mesquita Filho (UNESP) – SP. 151p.

[22] Drysdale, R. G., Hamid, A. A., and Baker,L.R., (1999). Masonry Structures Behavior and Design. Prentice Hall, New Jersey.

[23] Fortes, E. S. (2017). Caracterização da alvenaria estrutural de alta resistência. Tese (doutorado). Pós-Graduação em Estruturas e Construção Civil (UFSCar). 350p.

[24] Hughes, K. J. (2010). Behaviour of Reduced-Scale Reinforced Concrete Masonry Shear Walls and Components. Thesis. Macmaster University, Hamilton, Ontario, Canadá. 216p.

[25] Izquierdo, O. S. (2015). Estudo da interface bloco/graute em elementos de alvenaria estrutural. Tese (Doutorado) – Escola de Engenharia de São Carlos, Universidade de São Paulo, São Carlos. 290p.

[26] Kaaki, T. (2013). Behavior and Strength of Masonry Prisms Loaded in Compression. Thesis. Dalhousie University, Halifax, Nova Scotia, Canadá. 112p.

[27] Khalaf, F. M. (2005). New test for determination of masonry tensile bond strength. Journal of materials in civil engineering, 17(6), 725-732.

[28] Knox, C. L., Dizhur, D., Ingham J. M. (2018). Experimental study on scale effects in clay brick masonry prisms and wall panels investigating compression and shear related properties. Construction and Building Materials. V163, p706-713.

[29] Landini, F. S. (2001). Comportamento à flexão e ao esforço cortante de vigas em alvenaria estrutural. 2001. Dissertação (Mestrado). Faculdade Engenharia Civil – Universidade Estadual de Campinas (UNICAMP) – SP. 135p.

[30] Lizárraga, J. F. and Pérez-Gavilán, J. J. (2017). Parameter estimation for nonlinear analysis of multi-perforated concrete masonry walls. Construction and Building Materials, 141, 353-365.

[31] Long, L., Hamid, A. A., Drysdale, R.G. (2005). Small-Scale Modelling of Concrete Masonry Using ½ - Scale Units: A Preliminary Study. 10th Canadian Masonry Symposium. Banff, Alberta. 2005

[32] Lopes, G. L., (2014) Estudo teórico e experimental de paredes esbeltas de alvenaria estrutural. Dissertação (Mestrado). Programa de Pós-Graduação em Estruturas e Construção Civil – Universidade Federal de São Carlos (UFSCar) – SP. 133p.

[33] Lourenço, P. B, Barros, J. A. O., Oliveira, J. T. (2004). Shear testing of stack bonded masonry, Construction and Building Materials. V18(2):125–132.

[34] Madia, F. C. A. R. (2012). Estudo de Pórticos Preenchidos com Alvenaria. Dissertação (Mestrado). Programa de Pós-Graduação em Estruturas e Construção Civil – Universidade Federal de São Carlos (UFSCar) – SP. 146p.

[35] Maluf D. R., (2007) Estudo de Painéis de Alvenaria Estrutural Sujeitos a Ações Perperncidculares ao Plano. Dissertação (Mestrado). Programa de Pós-Graduação em Estruturas e Construção Civil – Universidade Federal de São Carlos (UFSCar) – SP. 120p.

[36] Massart, T. J., Peerlings, R. H. J., Geers, M. G. D. (2004). Mesoscopic modeling of failure and damage-induced anisotropy in brick masonry. European Journal of Mechanics A/Solids. v23.

[37] Mohammed, A., Hughes T. G., Mustapha, A. (2011). The effect of scale on the structural behaviour of masonry under compression. Construction and Building Materials. V25, p303-307.

[38] Nasiri, E., Liu, Y. (2017). Development of a detailed 3D FE model for analysis of the in-plane behaviour of masonry infilled concrete frames. Engineering Structures. v143. p603-616.

[39] Oliveira, L., M. F. (2014). Estudo Teórico E Experimental Do Comportamento Das Interfaces Verticais De Paredes Interconectadas De Alvenaria Estrutural. Tese de Doutorado – Departamento de Estruturas, Escola de Engenharia de São Carlos, Universidade de São Paulo, São Carlos – SP. 272 p.

[40] Pasquantonio, R. D. (2015). Análise teórica e experimental de vigas de alvenaria estrutural sujeitas ao cisalhamento. Dissertação (Mestrado). Programa de Pós-Graduação em Estruturas e Construção Civil – Universidade Federal de São Carlos (UFSCar) – SP. 179p.

[41] Pasquantonio, R. D., Fonseca, F. S., Shrive, N. G., Parsekian, G. A. (2018). Caracterização De Alvenaria De Blocos De Concreto De Escala Reduzida. In: 60º Congresso Brasileiro Do Concreto, Foz Do Iguaçu. Anais do 60º Congresso Brasileiro Do Concreto. São Paulo: Ibracon. V. 1. P. 1-12.

[42] Pavía, S., Hanley, R. (2010). Flexural bond strength of natural hydraulic lime mortar and clay brick. Materials and Structures;43:913–922.

[43] Santos, C. F. R. (2016). Avaliação numérica da interação de paredes de alvenaria estrutural submetidas às ações verticais. Viçosa. Dissertação (Mestrado) – Universidade Federal de Viçosa. 213p.

[44] Santos, E. A. F. (2014). Estudo da influência das propriedades elásticas da interface bloco-argamassa na rigidez de paredes de alvenaria. Dissertação (Mestrado)– Escola de Engenharia de São Carlos, Universidade de São Paulo, São Carlos. 277p.

[45] Shabdin, M., Zargaran, M., Attari, N. K. (2018). Experimental diagonal tension (shear) test of Un-Reinforced Masonry (URM) walls strengthened with textile reinforced mortar (TRM). Construction and Building Materials, 164, 704-715.

[46] Silva, W. J. (2014). Análise experimental e numérica da distribuição das ações verticais entre paredes de alvenaria estrutural com a utilização de modelo físico reduzido na escala 1:5. Tese de Doutorado – Departamento de Estruturas, Escola de Engenharia de São Carlos, Universidade de São Paulo, São Carlos – SP. 331 p.

[47] Thamboo, J. A., Dhanasekar, M., Yan, C. (2013). Flexural and Shear Bond Characteristics of Thin Layer Polymer Cement Mortared Concrete Masonry. Construction and Building Materials. V46, p104-113.

[48] Vandoren, B., Proft, K., Simone A., Sluys, L. J. (2013). Mesoscopic modelling of masonry using weak and strong discontinuities. Computer Methods in Applied Mechanics and Engineering. V255. p167-182.

[49] Vermeltfoort, A. T. (2012). Shear Strength Variation due to Mortar Strength Variation and the use of a Triplet Shear Test Set-Up. 15th International Brick and Block Masonry Conference. Florianopolis.

[50] Wierzbicki, J. C. (2010). Behavior of Reduced-Scale Fully Grouted Concrete Block Shear Walls. Dissertação (Mestrado). Macmaster University, Hamilton, Ontario, Canada. 205p.

Volume 13, Number 3 (June 2020) p. 593 – 602 • ISSN 1983-4195
DOI: http://dx.doi.org/10.1590/S1983-41952020000300009

REVISTA IBRACON DE ESTRUTURAS E MATERIAIS
IBRACON STRUCTURES AND MATERIALS JOURNAL

Wind load effect on the lateral instability of precast beams on elastomeric bearing supports

Influência da ação do vento na instabilidade lateral de vigas pré-moldadas sobre almofadas de apoio elastoméricas


M. T. S. A. CARDOSO [a]
mariateresasacardoso@gmail.com
https://orcid.org/0000-0001-9762-8918

M. C. V. LIMA [a]
macris@ufu.br
https://orcid.org/0000-0001-9641-474X

Abstract

The behavior of slender precast beams related to lateral stability in the transitional and in service phases is worrying. The presence of geometric imperfections aggravates and makes the problems of instability more susceptible. The main objective of this work is to evaluate the behavior of concrete beams on elastomeric bearings and to analyze the influence of variables such as: concrete strength, wind load and bearing compression stiffness. For the numerical nonlinear analysis the software ANSYS based on the Finite Element Method was used. The analyses show that the influence of the strength of the concrete is significant in the lateral stability of the beam. The wind load represents a considerable decrease in the contact (lift off) between the beam and the bearing. Finally, the combination of these factors can result in a critical stress situation in the beam, and it is not possible to have equilibrium, causing its toppling.

Keywords: stability, bearing, stiffness, equilibrium, toppling.

Resumo

A estabilidade lateral de vigas pré-moldadas esbeltas durante as fases transitórias e em serviço deve ser avaliada, observando que a presença de imperfeições geométricas torna o problema da instabilidade mais susceptível. O objetivo principal deste trabalho é avaliar o comportamento de vigas de concreto sobre apoios elastoméricos, considerando a influência de variáveis como: a resistência do concreto, a ação do vento e a rigidez a compressão das almofadas de apoio. Para a análise numérica não-linear utiliza-se neste trabalho o programa computacional ANSYS, baseado no método dos elementos finitos. As análises mostram que a influência da resistência do concreto é significante na estabilidade lateral da viga. A ação do vento pode ser responsável pela redução da área de contato entre a viga e a almofada de apoio (efeito de lift-off). Finalmente, a combinação destes fatores pode resultar em uma situação crítica de tensões na viga, para a qual não há condição de equilíbrio, resultando no tombamento da viga.

Palavras-chave: estabilidade, apoio, rigidez, equilíbrio, tombamento.

[a] *Universidade Federal de Uberlândia, Faculdade de Engenharia Civil, Uberlândia, MG, Brasil.*

Received: 04 Oct 2018 • Accepted: 14 Jan 2019 • Available Online: 26 May 2020

1. Introduction

In recent years, there have been reported cases in the literature of occurrences involving the collapse of precast beams during transitory phases. Precast concrete elements are submitted, during their working life, to situations and stresses that are characteristic of these phases, which may not have been foreseen in their design.
In particular, in the case of beams destined to cover large spans, such as bridge beams, viaducts and large structures, the worrying problem of lateral stability arises. Due to the determinants of the lifting device and the transport vehicles, these cross sectional elements that are evermore optimized, present a considerable slenderness and great length. The mechanical length of the slender beams is different to non-slender beams. Beams that are very slender, along with those that are moderately slender are subject to the effects of lateral instability, which are inherent to cross section dimensions and design (Girija and Menon [1]).
In addition, the existence of initial geometric imperfections, due to failures in the concreting, in the application of prestressing and in the positioning of the lifting points, go onto aggravate the problem further. These imperfections generate additional eccentricities in the beam, which intensify the effects of the transitory phases.
The context of this study is found in the situation where the beam is supported on elastomeric bearing pads without any lateral bracing. In this case, there is no restriction to the rigid body rotation, and further still, the flexibility of the elastomeric support device together with some stresses (such as wind load) are capable of adding to the beam an extremely unstable configuration, which may lead to a possible collapse.
The accidents reported by Tremblay and Mitchell [2], Oesterle et al. [3] and Bairán and Cladera [4] relate to the phase in which the beam is positioned on supports. In Tremblay and Mitchell [2] and Oesterle et al. [3], the lateral bracing employed was insufficient to prevent the toppling of the beam. In Bairán and Cladera [4], the elastomeric support device does not offer sufficient stiffness in terms of the toppling of the beam due to the incorrect design of the pad, or that the pad was correctly designed, but positioned in an incorrect manner. The researchers Burgoyne and Stratford [5] along with Plaut and Moen [6], and Cardoso and Lima [7] deal with the lateral instability of beams from precast concrete on deformable supports. The authors show that the stiffness of the support significantly influences the equilibrium and stability of the beam, mainly when faced with wind loads.
Lee [8] studied the lateral instability of precast beams with initial sweep supported by elastomeric bearing pads with a regard to critical weight. In his article, the author has presented an equation to calculate the critical load that provides an unstable condition to the beam. As expected, the author concluded that the critical load decreased importantly as the initial sweep increased.
Lee et al. [9] analyzed precast beams during construction under wind loads. The authors investigated the influence of length and section properties on critical wind loads that provides rollover instability to the beam. The results have shown that the critical wind load was strongly influenced by the length of the girder, but with no influence by section properties.
In light of the above, this study aims at evaluating the lateral stability of the AASHTO beam Type IV positioned on FDOT pads Type A and FDOT Type B, taking into consideration wind loads. Furthermore, the intention is to evaluate the influence of the characteristic strength and of physical linearity of the concrete along with the compression stiffness of the pad, keeping in mind the loss of contact between the beam and the support and the compression limit of the employed bearing pad.

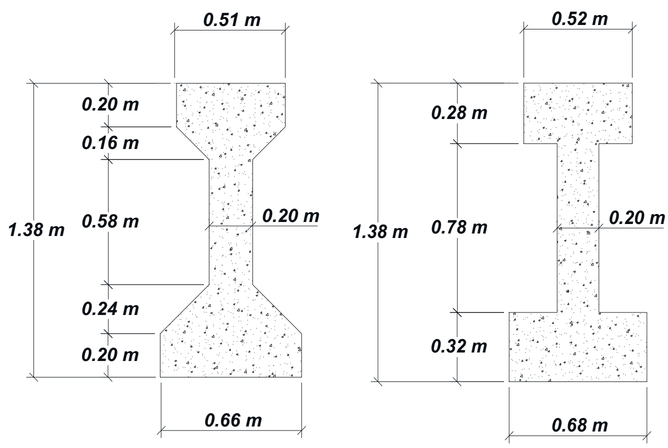

(a) Real section (b) Idealized section

Source: Authors (2017)

Figure 1
Cross section modified from the AASHTO beam Type IV

2. Material and methods

This study performs a numerical analysis through the computer modeling program ANSYS in finite elements. A simulation was run where the standardized section beam AASHTO Type IV, presented in Figure 1, with 32 m in length, is supported on pads also standardized FDOT Type A and FDOT Type B, for which the dimensions are presented on Table 1.
The AASHTO Type IV beam was fabricated with an initial geometric imperfection, which represented the maximum limit permitted by PCI [10]: 10 mm for every 10 m of beam length, which results in a total of 32 mm. The initial geometric imperfection is schematically represented in Figure 2.
In the case of steel-reinforced elastomeric bearing pads, the compression stiffness or roll stiffness is sometimes difficult to estimate

Table 1
Dimensions and characteristics of the analyzed bearing pads

Dimension/characteristic	Bearing pad	
	A	B
Length, L (cm)	60	60
Width, W (cm)	28	36
Height, H (cm)	4.8	6.5
Quantity of steel plates	3	4

Source: Authors (2017)

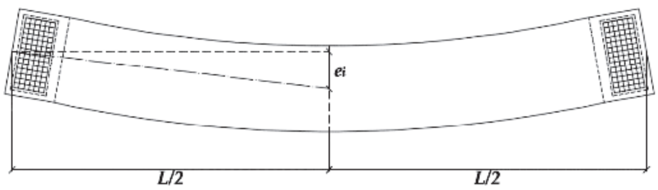

Source: Authors (2017)

Figure 2
Representation of the initial eccentricity on the beam (out of scale)

because of complex deformations of the elastomer. A method of numerical analysis for estimating the axial and roll stiffness of bearing pads is presented by Harper and Consolazio [11], which consider the pad modeled as a grillage of compression-only axial springs. The grillage method was partially derived from roll stiffness data measured in an experimental study, and accurately capture both the nonlinear moment-rotation behavior caused by lift off of the beam from the pad and the observed sensitivity of roll stiffness to initial compressive loading caused by self-weight of the beam. In order to numerically present the elastomeric bearing pads, the simplified model proposed by Harper and Consolazio [11] was adopted. The authors present a simplified model to calculate the axial stiffness and the rotation of the elastomeric rectangular bearing pads. According to the authors, when dealing with problems of lateral stability, torsional stiffness is not related directly and shear stiffness can be determined directly through basic principles that are already understood.

When the beam is placed in its service position on the padded supports, the pad is stretched and there is contact between the whole surface of the beam and the elastomer. In this situation, the roll stiffness of the pad presents a linear relationship. However, as the rate of the rotation angle on the beam increases, it loses part of its contact with the pad (lift off) and its roll stiffness is no longer linear, but rather non-linear (Figure 3) (Harper and Consolazio [11]).

The study of Harper and Consolazio [11] proposed a simplified numerical model for determining the roll stiffness of elastomeric pads. This model considers the pad as a rigid grid responsible for uniting compression springs of different stiffness, as presented in Figure 4. This grid model divides the pad into small rectangular

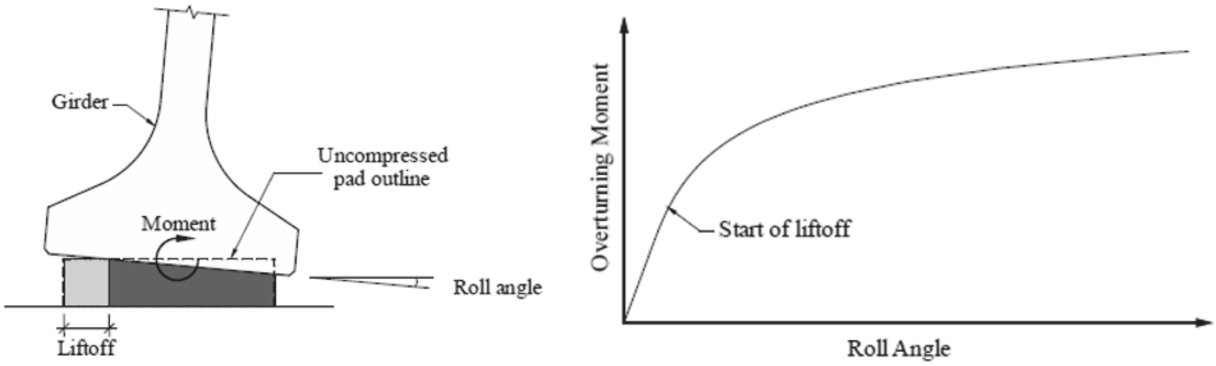

Source: Harper and Consolazio (2013)

Figure 3
Loss of contact of beam with the elastomer

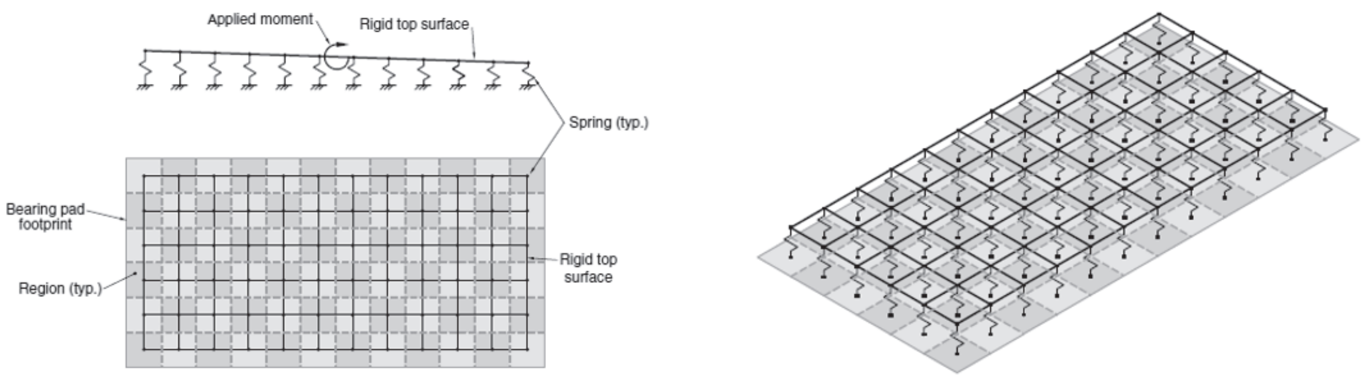

Source: Harper and Consolazio (2013)

Figure 4
Loss of contact of beam with the elastomer

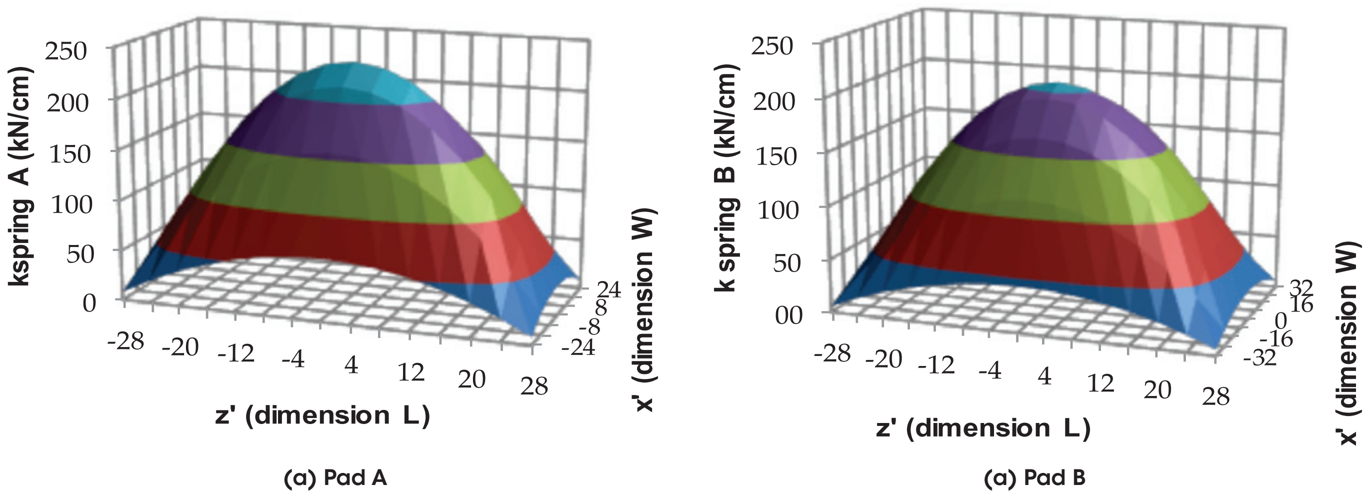

Source: Authors (2017)

Figure 5
Stiffness distribution

regions and each one is associated to a stiffness compression spring different to the others. Compression springs were used to represent the loss of contact of the beam with the pad.

According to the authors, at particular levels of compression, the behavior of the pad becomes non-linear, as the bulging caused by the compression reduces the thickness of the layer and stiffens the pad. In addition, the compression stiffness varies according to the distance in relation to the center of the pad. In this manner, the simplified model proposed by Harper and Consolazio [11] considers the different behaviors in relation to the distance from the center of the pad, as shown in Equation (1):

$$k_{spring}(x',z') = A_{region} \cdot \left(\frac{k_{bearing\ pad}}{A_{bearing\ pad}}\right) \cdot [1-(x')^2] \cdot [1-(z')^2] \quad (1)$$

Where: k_{spring} (x', z') is the value of the spring stiffness concerning its position relative to the center of the pad; A_{region} is the area of the region of influence of a spring; $k_{bearing\ pad}$ is the axial compression stiffness of the pad; $A_{bearing\ pad}$ is the area of the pad; x' and z' are the normalized coordinates of the pad.

The model proposed by Harper and Consolazio [11] was validated in this study by use of ANSYS. Starting out from the axial compression stiffness that is already known for pad A of 10991 kN/10^{-2} m and for pad B of 12512 kN/10^{-2} m, the pads were designed as stiff grids responsible for uniting the springs. The results obtained from displacement and rotating angles of the pad were close to those presented by the authors. Pad A was designed as a grid with 105 compression springs (7×15), with a region area equal to 16 cm^2. Pad B was designed as a grid with 135 compression springs (9×15), with a region area equal to 16 cm^2.

For the springs, the element LINK180 was used, with the “compress only” option activated, that is, in this situation, the springs do not work if they are tensioned, and thus they do not contribute numerically to the behaviour of the pad. In terms of the stiff grid, the element BEAM188 was used. The nodes on the lower parts of the model were embedded. As the element LINK180 is a truss element, so that the model does not become unstable, displacements were impeded on the longitudinal (UX) and transversal (UZ) on the upper nodes of the grid. In the interest of maintaining the grid rigid, an elasticity module was adopted that carried the same value as that of steel (2.0·10^8 kN/m^2). A rectangular transversal section was chosen, for which the dimensions were defined after various tests. The transversal section that provided rigidity to the grid was 25 mm × 90 mm. Through use of Equation (1), the calculation was made for the stiffness of each spring, taking into consideration its position that has been normalized in relation to the center of the pad. As affirmed by Harper and Consolazio [11], Equation (1) provides a satisfactory approximation of the format for the distribution of the axial stiffness on the pad; however, it does not provide values of the true magnitude of this stiffness. Therefore, it was necessary to include a correction factor (CF) to the stiffness of each spring, since the total value of the axial stiffness on the pad was less than the real value. This correction factor was obtained through adding the compression stiffness of each spring calculated using Equation (1) and then dividing this by the axial compression stiffness known through this sum. For pad A, the correction factor was equal to 2.2223 and pad B, 2.2312 (Cardoso [12]). Figure 5 presents the stiffness distribution on pads A and B.

In dealing with the element LINK180, the stiffness was considered in the definition of the modulus of elasticity (E) of each spring, since the stiffness of the truss element is given through Equation (2).

$$k_{spring} = \frac{E \cdot A}{L} \rightarrow E = \frac{k_{spring} \cdot L}{A} \quad (2)$$

Where: L is the length of the bar, which here is the height of the pad; A is the area of the cross section of the bar, defined as a unit set.

Table 2 presents the values of compression stiffness, corrected by the correction factor and the value of the elasticity module of the springs from the first quadrant of pad A. Similar procedures were made for the pad B in order to obtain the compression stiffness of their springs.

Once the simplified models for pads A and B were concluded, the beams were designed as an arc between two straight segments under which the pads were positioned. It was necessary to proceed in this manner, in order that the beam nodes coincide exactly with the nodes on the pad in accordance with the simplified model.

Lee et al. [9] presented an equation to estimate the critical wind load that provides an rollover instability to the beam (Equation (3)).

$$(wL)\left[y_c\theta_s+\frac{w\theta_s L^4}{120EI_y}+\frac{F_w L^4}{120EI_y}\right]+(F_w L)\left[y_c-\frac{F_w L^4}{120EI_y}\theta_s\right]=2k_r\theta_s \quad (3)$$

Where: (wL) is the total self-weight of the beam; y_c is the height of the centre of gravity of the beam; θ_s is the rotational angle at support; w is the self-weight of girder per unit length; L is the length of the beam; E is the modulus of elasticity of the beam; I_y is the smaller moment of inertia of the beam; F_w is the wind load per unit length; k_r is the rotational stiffness of bearing pad.

In order to model the beam, the three-dimensional element SOLID65 was employed. In the longitudinal direction, concerning the support regions, a more refined mesh was adopted, and in the region of the beam arc, a less discretized mesh was used.

From the standpoint of the beam on supports, one can state that the only load that acts on the structure is its self-weight, which was applied by the inertia command from ANSYS. In all the numerical analyses, emphasis was placed on geometric non-linearity. In cases of lateral instability, the emphasis placed upon large displacements is of great importance, in order that the problem is correctly represented.

Three characteristic strength for the concrete (f_{ck}) were adopted, namely, 27.5, 45 and 90 MPa. The modulus of elasticity of the concrete initially adopted for the beam were respectively, 29370, 37570 and 53130 MPa.

In an attempt to simulate the behavior of the cracked beam and the loss of its resistance capacity due to the physical non-linearity

Table 2

Corrected compression stiffness and elasticity module for the springs of the first quadrant of pad A

Spring	Node	x'	z'	kspring (kN/·10^{-2} m)	E (kN/·10^{-4} m^2)
1	1	-0.857	-0.933	7.954	38.181
2	3	-0.571	-0.933	20.192	96.921
3	5	-0.286	-0.933	27.534	132.165
4	7	0.000	-0.933	29.982	143.913
8	15	-0.857	-0.800	22.217	106.643
9	17	-0.571	-0.800	56.398	270.710
10	19	-0.286	-0.800	76.906	369.150
11	21	0.000	-0.800	83.742	401.963
15	29	-0.857	-0.667	34.286	164.573
16	31	-0.571	-0.667	87.034	417.762
17	33	-0.286	-0.667	118.682	569.676
18	35	0.000	-0.667	129.232	620.313
22	43	-0.857	-0.533	44.160	211.970
23	45	-0.571	-0.533	112.099	538.078
24	47	-0.286	-0.533	152.863	733.742
25	49	0.000	-0.533	166.451	798.964
29	57	-0.857	-0.400	51.840	248.834
30	59	-0.571	-0.400	131.595	631.656
31	61	-0.286	-0.400	179.448	861.349
32	63	0.000	-0.400	195.399	937.914
36	71	-0.857	-0.267	57.326	275.166
37	73	-0.571	-0.267	145.520	698.498
38	75	-0.286	-0.267	198.437	952.498
39	77	0.000	-0.267	216.076	1037.164
43	85	-0.857	-0.133	60.618	290.965
44	87	-0.571	-0.133	153.876	738.603
45	89	-0.286	-0.133	209.830	1007.186
46	91	0.000	-0.133	228.482	1096.714
50	99	-0.857	0.000	61.715	296.231
51	101	-0.571	0.000	156.661	751.972
52	103	-0.286	0.000	213.628	1025.416
53	105	0.000	0.000	232.618	1116.564

Source: Authors (2017)

of the concrete, a physical non-linear analysis was performed on ANSYS. In order to perform this analysis, the model for concrete from the element SOLID65 was used. The stress - strain curve was obtained through the definition of six points, for which the coordinates were calculated from parametric equations that relate the characteristic strength of the concrete with its initial or tangent modulus of elasticity.
To use the model for concrete on ANSYS, it was necessary to define four parameters relevant to the behavior of stressed concrete. The two parameters refer to the shear stress transferred to the open and closed cracks. For these variables, the values of 0.2 and 1.0 were adopted, respectively. The two remaining parameters relate to the stress on the cracks and crushing of the concrete, for which the values of one tenth of the strength of the concrete and (-1.0), were defined, respectively.
It is known that under pre-service conditions, even though not desirable, there can occur loads arising from wind in different magnitudes and directions. Therefore, the occurrence of wind loads on the AASHTO beam Type IV was analyzed, on the elastomeric pads A and B.
In the interest of representing the stress generated by wind loads, consideration was given to a horizontal stress load acting upon the direction of the initial eccentricity of the beam. The researchers Plaut and Moen [6] adopted a pressure of 2.4 kPa, which corresponds to the basic wind velocity of 45 m/s. In this study, a pressure of 2.0 kPa was adopted, corresponding to a basic velocity of 37.5 m/s, and the resulting stress was applied in a simplistic form to the upper surface of the beam in the middle of the span. The total wind stress (88 kN) was applied in four load steps, in order to obtain the structural behavior that is subject to different wind pressures, 0.5, 1.0, 1.5 and 2.0 kPa.

3. Results and discussions

Figure 6 presents the behavior of pads A and B, respectively, through consideration of an AASHTO beam Type IV, with eccentricity of 3.2 cm, considering only the non-linear geometric analysis. The shaded area represents the region where there is no support reaction on the pad, in other words, the region where there is no contact between the beam and the pad.
The stiffness of the beam plays an important role in terms of its stability. The wind represents a significant additional stress to the stability of the beam on pad A. In this sense, it is noteworthy to mention the stiffness limit of the elastomeric pad (Equation (4)), which has a value of 11 MPa. Hence, it is interesting to check it for the most unfavorable situation: beam with f_{ck} = 27.5 MPa subjected to wind pressure equal to 2.0 kPa.

$$\sigma_{c,lim} = \frac{N}{A} \rightarrow A = \frac{N}{\sigma_{c,lim}} \tag{4}$$

Where: $\sigma_{c,lim}$ is the compression stress limit on the pad, equal to 11 MPa; N is the normal stress that acts on the pad. In this case, we have the total weight of the beam placed on two pads, in other words, the normal stress is half of the total weight of the beam that adds up to approximately, 208 kN; A is the area being demanded from the pad.
The value of A is approximately $1{,}89 \cdot 10^{-2}$ m^2. The bearing pad A is $1{,}68 \cdot 10^{-1}$ m^2 and its area was discretized on the simplified model, with 105 area regions measuring $1{,}6 \cdot 10^{-3}$ m^2. Therefore, area A that is being demanded from the pad corresponds to 12 regions on the simplified model. Hence, as can be noted in Figure 6, in the last case for wind pressure equal to 2.0 kPa and f_{ck} equal to 27.5 MPa, still under the most unfavorable condition for the beam on bearing pad A, one was able to establish the equilibrium and

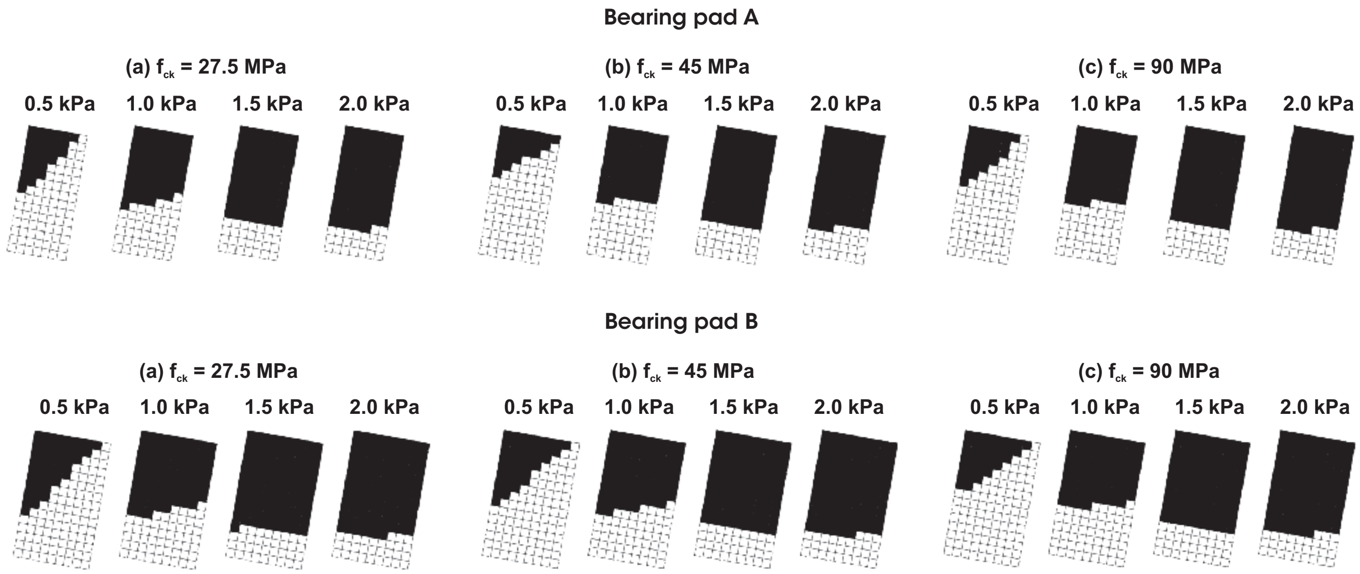

Source: Authors (2017)

Figure 6
Loss of contact on the AASHTO beam Type IV on pad A and B

Table 3
Maximum vertical displacement on the AASHTO beam Type IV

Wind load (kPa)	Maximum vertical displacement on the AASHTO beam Type IV (·10⁻² m)											
	Bearing Pad A						Bearing Pad B					
	27.5 MPa	27.5 MPa with PNL	45 MPa	45 MPa with PNL	90 MPa	90 MPa with PNL	27.5 MPa	27.5 MPa with PNL	45 MPa	45 MPa with PNL	90 MPa	90 MPa with PNL
0.0	2.6288	—	2.0512	—	1.4514	1.4737	2.5694	—	2.0053	—	1.4189	1.4428
0.5	2.7307	—	2.1333	—	1.5159	1.5417	2.6731	—	2.0899	—	1.4841	1.5118
1.0	2.9161	—	2.2907	—	1.6459	1.6792	2.8536	—	2.2396	—	1.6073	1.6425
1.5	3.3357	—	2.6463	—	1.9591	—	3.2299	—	2.5699	—	1.8867	—
2.0	3.6436	—	2.9236	—	2.1936	—	3.5258	—	2.8309	—	2.1549	—

Source: Authors (2017)

Table 4
Maximum horizontal displacement on the AASHTO beam Type IV

Wind load (kPa)	Maximum horizontal displacement on the AASHTO beam Type IV (·10⁻² m)											
	Bearing Pad A						Bearing Pad B					
	27.5 MPa	27.5 MPa with PNL	45 MPa	45 MPa with PNL	90 MPa	90 MPa with PNL	27.5 MPa	27.5 MPa with PNL	45 MPa	45 MPa with PNL	90 MPa	90 MPa with PNL
0.0	0.2789	—	0.2206	—	0.1624	0.1846	0.2653	—	0.2087	—	0.1521	0.1742
0.5	1.5716	—	1.2321	—	0.8964	1.0284	1.5314	—	1.2052	—	0.8721	1.0064
1.0	3.2790	—	2.6313	—	1.9795	2.2382	3.1590	—	2.5249	—	1.8936	2.1547
1.5	6.5847	—	5.4408	—	4.4064	—	6.1245	—	5.1200	—	4.0513	—
2.0	9.0760	—	7.7171	—	6.3519	—	8.5190	—	8.2641	—	6.2044	—

Source: Authors (2017)

stability of the beam and meet the compression limit of the elastomeric pad. As the pad region under demand corresponds to 23 regions, i.e., $3{,}68 \cdot 10^{-2}$ m².
By performing the same analysis for the compression limit on the elastomeric pad for bearing pad B under the situation of highest demand, one notes that here also this limit is met. Its most critical situation occurs when the wind pressure that acts upon it corresponds to 2.0 kPa. In this case, an area of $4{,}80 \cdot 10^{-2}$ m² (23 regions) still effectively functions to guarantee the stability of the beam and avoid toppling; this area is greater than the $1{,}89 \cdot 10^{-2}$ m² necessary in order that the limit is met.
Table 3 and Table 4 and Figure 7 and Figure 8 present the maximum vertical and horizontal displacements obtained on the AASHTO beam Type IV for the four wind pressures analyzed along with the physical and geometrical non-linear analyses. Due to the level of cracking reached in the physical non-linear analyses (PNL) with f_{ck} equal to 27.5 MPa and 45 MPa, there was no numerical convergence and no results were obtained for these strength

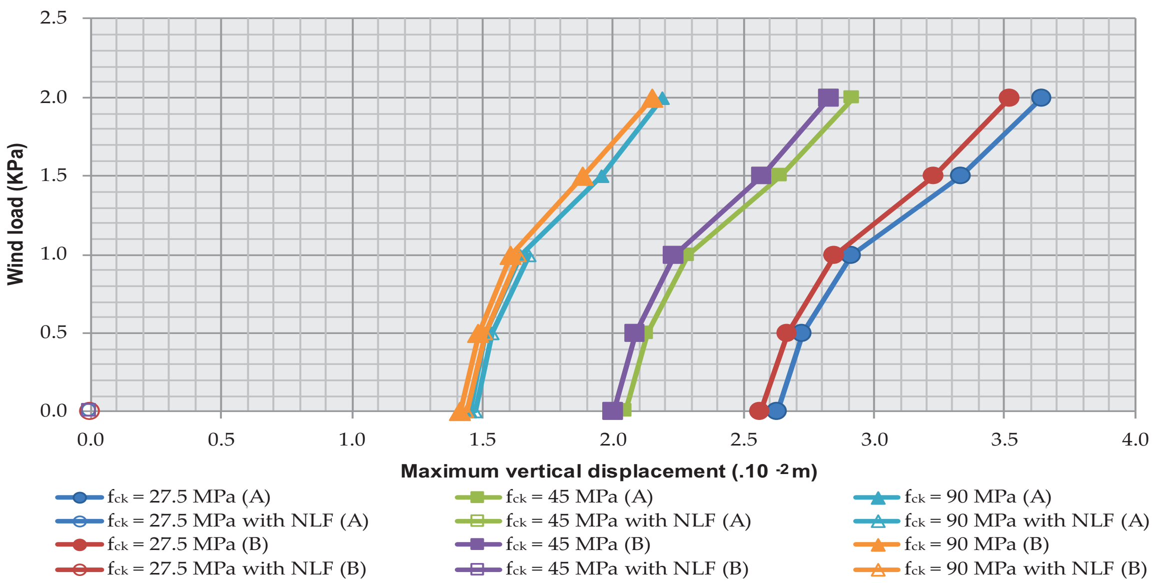

Source: Authors (2017)

Figure 7
Maximum vertical displacement on the AASHTO beam Type IV

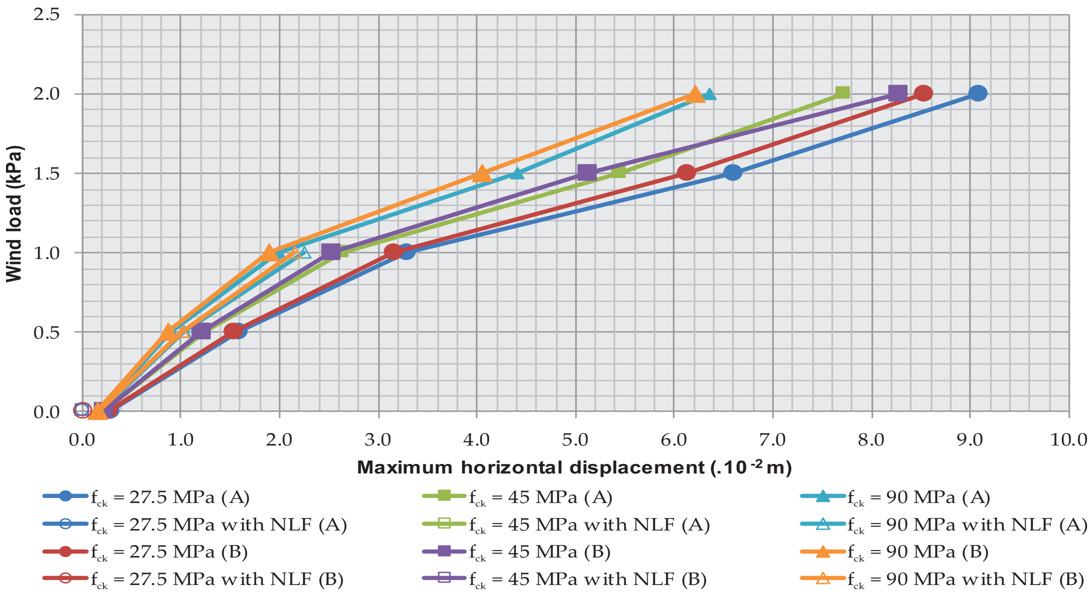

Source: Authors (2017)

Figure 8
Maximum horizontal displacement on the AASHTO beam Type IV

values of concrete. By considering the physical non-linearity for f_{ck} equal to 90 MPa, it was possible to obtain the displacements for wind pressure at a maximum of 1.0 kPa. For pressures of 1.5 and 2.0 kPa, the computer program ANSYS did not find equilibrium on the beam under analysis. The wind pressure equal to 0.0 kPa corresponds to the exclusive performance of the self-weight.
For the beam AASHTO Type IV with f_{ck} equal to 90 MPa and wind pressure of 1.0 kPa, the horizontal displacement obtained considering the geometric and physical nonlinearities was around 12% higher than that obtained only with nonlinear geometric analysis.
The influence from the wind was more significant on the horizontal displacement, in the direction of the smaller inertia of the beam, mainly when compared to the value of the displacement with and without wind load.
When dealing with the lifting of precast elements there exists a safety factor, that is already consolidated in the literature, equal to 4.0, i.e., needs to consider in the suspending device design, a stress equal to four times the weight of the structure. Making an analogy of this same value of the safety factor with the situation of the beam on elastomeric supports, in relation to the compression limits of the elastomeric pads, one arrives at that presented in Equation (5).

$$\sigma_{c,lim} = \frac{N}{A} \rightarrow A = \frac{4 \cdot \left(\frac{P}{2}\right)}{\sigma_{c,lim}} \tag{5}$$

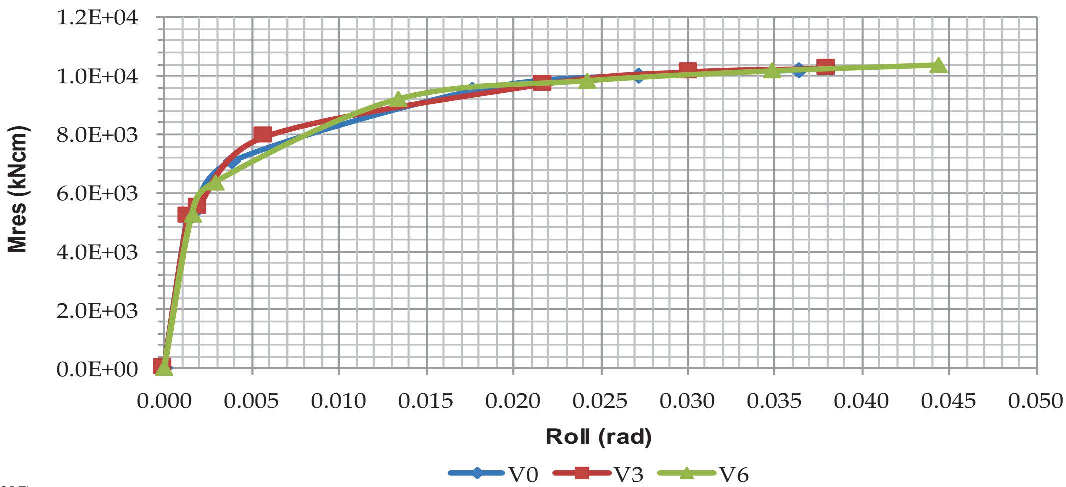

Source: Authors (2017)

Figure 9
Roll stiffness of bearing pad

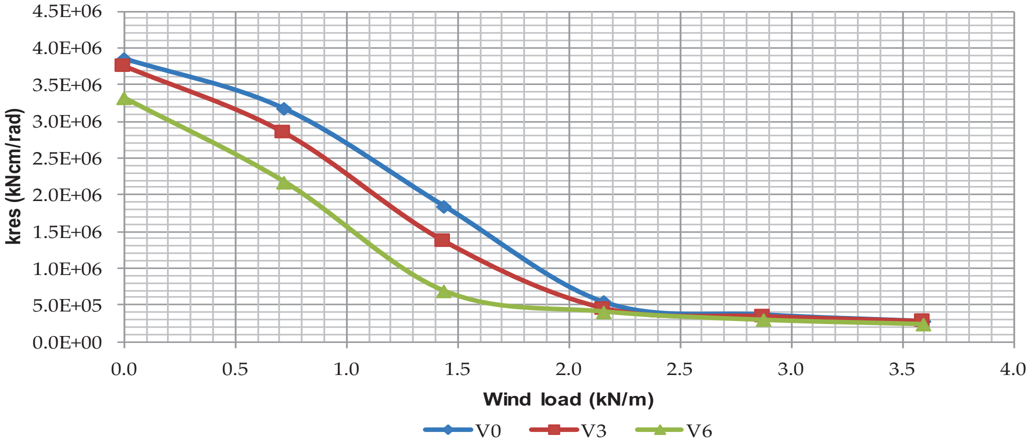

Source: Authors (2017)

Figure 10
Roll stiffness and wind load

Therefore, so that this limit be met it would be necessary an area of $7{,}57 \cdot 10^{-2}$ m^2 on the bearing pad, which corresponds to the 48 regions on the adopted simplified model. In this manner, for bearing pad A, from the configurations for the support reactions presented in Figure 6, only those that correspond to a wind load of 0.5 kPa met the compression limit of the elastomeric pad. For bearing pad B, wind stresses of up to 1.0 kPa can be used to meet the compression limit of the elastomeric pad.

The authors Burgoyne and Stratford (2001) mention in their study a safety factor equal to 10.0 (P_{crit}/P), in order to avoid the rotation of the beam on its supports. At first, one can consider the value to be too high for the safety factor. The authors, therefore justify that the geometric imperfections, which are not considered during the design, can introduce additional stresses to the beam, which can be avoided by the choice of an adequate support pad.

Comparing the previous beam (named V3) with similar beams, but with different geometric imperfections, it is possible to know the rotation behavior of the bearing pad, which roll stiffness is shown in Figure 9. The beam V0 is the same beam AASHTO Type IV, but with no initial eccentricity. The beam named V6 is the beam which initial imperfection approximates that recommended by Eurocode 2 [13], that is, L/300. Figure 10 shows the roll stiffness values for different wind loads. Significant reduction of roll stiffness of the bearing pad is noticed as the action of the initial imperfection and the increase of the wind pressure are considered together.

Lee et al. [9] concluded that a wind load of 3.6 kN/m would cause toppling of the beam. From Figure 10, considering the maximum roll stiffness 2.75E+05 kNcm/rad obtained for the beam V0 and substituting in Equation (3), one obtain a rotation of 0.019 rad that balances the acting moment with the resistant moment. According to Lee et al. [9], the rotation at the support of 0.0032 rad, equivalent to 0.001 rad every 10 m in length, would be sufficient to retain the beam and prevent its toppling. From the analyses carried out in this work, considering physical non-linearity (PNL) and the V3 beam with initial imperfection of 3.2 cm, the wind load that would cause its toppling would be 1.0 kPa, that is, 1.375 kN/m.

4. Conclusions

The study of the lateral stability of precast concrete beams is shown to be of extreme importance, especially in the transitory phases due to unforeseen demands on the design. Furthermore, the lateral stability has been pointed out as a cause of accidents already reported in the literature. In the case of the beam on flexible supports, such as elastomers, it is known that the pad is under greater demand in the region close to its center, as shown in the compression stiffness distribution.

The simplified model represented an extremely viable alternative for the elaboration of a pad model with solid elements associated with contact elements. The model with compression springs allowed the simulation of loss of contact between the beam and the elastomer, which produced a change in the position of the support reactions on the bearing pad.

The consideration made as to the wind load was shown to be a condition much more unfavorable in terms of contact loss between the beam and the pad. This was verified to be more stringent through the physical non-linear analysis, for which results were not possible for f_{ck} equal to 27.5 MPa and f_{ck} equal to 45 MPa.

For the beam AASHTO Type IV with f_{ck} = 90 MPa on bearing pad A, the total wind load produced loss of contact in 76% of the area of the bearing pad, whereas there was no loss of contact recorded when only the self-weight was acting on the beam . Regarding the horizontal displacements, for beam V3 with f_{ck} = 90 MPa on bearing pads A and B, the consideration of physical nonlinearity represented an increase of around 12% in these displacements in the middle of the span.

It is of the utmost importance to verify that the compressed area of the pad, reduced in the region of the beam with displacement (lift off), is capable of meeting its maximum compression limit.

5. Acknowledgements

The authors would like to thank CAPES for granting the scholarship on the Master Academic level and to FAPEMIG (Public Call 01/2015) for the financial support.

6. References

[1] Girija, K.; Menon, D. Reduction in flexural strength in rectangular RC beams due to slenderness. *Engineering Structures*, 33 (8), 2011, p.2398-2406.

[2] Tremblay, R.; Mitchell, D. Collapse during Construction of a Precast Girder Bridge. *Journal of Performance of Constructed Facilities*, 20 (2), 2006, p.113-125.

[3] Oesterle, R. G., Sheehan, M. J., Lotfi, H. R., Corley, W. G. & ROLLER, J. J. *Investigation of red mountain freeway bridge girder colapse*. Arizona Department of Transportation, Bridge Group, Skokie, Illinois. CTL Group Project No. 262291. 2007.

[4] Bairán, J. M.; Cladera, A. Collapse of a precast concrete beam for a light roof. Importance of elastomeric bearing pads in the element's stability. *Engineering Failure Analysis*, 39, 2014, p.188-199.

[5] Burgoyne, C. J.; Stratford, T. J. Lateral Instability of long-span prestressed concrete beams on flexible bearings. *The Structural Engineer*, 79 (6), 2001, p.23-26.

[6] Plaut, R. H; Moen, C. D. Stability of unbraced concrete beams on bearing pads including wind loading. *Journal of Structural Engineering*, 69, 2014, p.246-254.

[7] Cardoso, M. T. S. A.; Lima, M. C. V. Physical and geometrical non-linear behavior of precast beams on elastomeric supports. *Revista IBRACON de Estruturas e Materiais*, v. 1, n. 7, 2018, p. 183-202.

[8] Lee, J. H. Evaluation of the lateral stability of precast beams on an elastic bearing support with a consideration of the initial sweep. *Engineering Structures*, 143, 2017, p.101-112.

[9] Lee, J. H., Kalkan, I., Lee, J. J. & Cheung, J. H. (2017) Rollover instability of precast girders subjected to wind load. *Magazine of Concrete Research*, 69 (2), 68-83.

[10] Precast Concrete Institute. Committee on Tolerances. PCI Tolerance Manual for Precast and Prestressed Concrete Construction. 1st ed. Chicago, IL. 2000.

[11] Harper, Z. S.; Consolazio, G. R. (2013) Calculation method for quantifying axial and roll stiffnesses of rectangular steel-reinforced elastomeric bridge bearing pads. *Journal of the Transportation Research Board*, 2331, 3-13.

[12] Cardoso, M. T. S. A. *Instabilidade lateral de vigas pré-moldadas sobre apoios elastoméricos considerando o efeito das imperfeições geométricas*. Dissertação (Mestrado). Faculdade de Engenharia Civil, Universidade Federal de Uberlândia, 2017.

[13] Comité Européen de Normalisation. NF EN 1992 (Français): *Eurocode 2*: Calcul des structures en béton. CEN, Bruxelles, 2004.

Volume 13, Number 3 (June 2020) p. 603 – 612 • ISSN 1983-4195
DOI: http://dx.doi.org/10.1590/S1983-41952020000300010

REVISTA IBRACON DE ESTRUTURAS E MATERIAIS
IBRACON STRUCTURES AND MATERIALS JOURNAL

Early-age behavior of blast-furnace slag cement pastes produced with carbon nanotubes grown directly on clinker

Comportamento nas primeiras idades de pastas produzidas com cimento portland de alto forno fabricado com nanotubos de carbono crescidos diretamente sobre o clínquer

P. A. SOARES [a]
palomaassissoares@gmail.com
https://orcid.org/0000-0002-0688-9934

A. Z. BENEDETTI [a]
alicez.benedetti@gmail.com
https://orcid.org/0000-0001-7014-4876

T. C. SOUZA [a]
tarcizo.cruz@ctnano.org
https://orcid.org/0000-0001-6437-0009

J. M. CALIXTO [a]
jmfcalixto@gmail.com
https://orcid.org/0000-0003-2828-0967

L. O. LADEIRA [a]
loladeira@gmail.com
https://orcid.org/0000-0002-4935-6070

Abstract

Carbon nanotubes are a promising material to solve the low tensile strength and ductility of Portland cement-based materials. Carbon nanotubes (CNTs) synthesized directly on cement clinker particles can also reduce production costs and help dispersion. In this scenario, this paper analyzes the fresh state rheological behavior, as well as the initial hydration period of blast-furnace slag (Brazilian CP III 40 RS) cement pastes produced with CNTs grown directly on clinker. CP III 40 RS was selected since it is one of the most used cement by the construction industry in Brazil. Cement pastes containing 0.1% and 0.3% of CNTs with respect to cement content were compared with CNT-free pastes. No chemical admixtures were used as a dispersant in all cases. The yield stress, plastic viscosity, temperature profile and evolved accumulated heat during the initial hydration period as well as setting times are the properties investigated. The results show that the addition of CNTs does not alter the rheological behavior of the cement pastes considering the employed concentrations, although the yield stress values were larger. The presence of CNTs in the cement pastes did not change the evolved accumulated heat during the first 72 hours of the hydration period.

Keywords: carbon nanotubes, blast-furnace slag cement pastes, fresh state rheological behavior, hydration heat, setting times.

Resumo

Nanotubos de carbono são elementos promissores para melhorar a pequena resistência à tração e a dutilidade de materiais a base de cimento Portland. Nanotubos de carbono (NTC) sintetizados diretamente sobre o clínquer de cimento podem também reduzir custos de produção e melhorar a dispersão destes na matriz. Neste cenário, este artigo analisa o comportamento reológico no estado fresco, bem como o período inicial de hidratação de pastas produzidas com cimento Portland de alto forno (CP III 40 RS) contendo NTC sintetizados diretamente sobre o clínquer. O CP III 40 RS foi selecionado, pois é um dos cimentos mais utilizados pela indústria da construção civil no Brasil. As pastas de cimento contendo 0,1% e 0,3% das NTC em relação a massa de cimento foram comparadas com pastas sem nanotubos. Nenhum aditivo foi usado como dispersante em todos os casos. A tensão de escoamento, a viscosidade plástica, o perfil térmico e o calor acumulado durante o período inicial de hidratação, bem como os tempos de pega são as propriedades investigadas. Os resultados mostram que a adição de NTC não altera o comportamento reológico das pastas de cimento considerando as concentrações empregadas, embora os valores da tensão de escoamento terem sido maiores. A presença de NTC nas pastas de cimento não alterou o calor acumulado durante as primeiras 72 horas do período de hidratação.

Palavras-chave: nanotubos de carbono, cimento Portland de alto-forno, pastas de cimento, comportamento reológico, calor de hidratação, tempos de pega.

[a] *Federal University of Minas Gerais, Technological Center for Nanomaterials and Graphene, Belo Horizonte, MG, Brazil.*

Received: 25 Jan 2019 • Accepted: 23 Oct 2019 • Available Online: 26 May 2020

1. Introduction

Portland cement composites are the largest consumed construction materials worldwide. Among the reasons for this fact are the availability of raw materials and excellent compressive behavior. On the other hand, tensile characteristics of cementitious materials are poor due to their low tensile strength and brittle behavior. Recent investigations showed that the poor tensile behavior of cement-based materials is partly due to macroscopic defects (pores) and partly to the innate properties of calcium silicate hydrate (C-S-H), the main constituent of hardened cement paste.
Carbon nanomaterials, such as carbon nanotubes (CNTs) and graphene, have recently attracted tremendous scientific interest due to the remarkable and useful properties, such as exceptional tensile strength, elastic modulus, and electrical and thermal conductivity [1, 2]. These materials are promising candidates for next-generation high-performance structural and multi-functional cement composites [3, 4, 5, 6, 7].
Carbon nanotubes (CNTs) are graphene sheets rolled up to form cylinders or tubes. A single-walled CNT looks like a single sheet rolled up into a tube, while multi-walled CNTs look like multiple sheets rolled into a series of tubes, one inside the other. A single-walled CNT is typically 1-3 nm in diameter and a micrometer or more long. Multi-walled CNTs typically range in diameter from 10 to 40 nm but have the same length as the single-walled variety [8, 9]. According to Santra *et al.* [10], CNTs behave as one-dimensional materials. In addition, they present tensile strength and Young's modulus values ten times greater than steel and a density five times smaller [8, 9]. Consequently, CNTs have very high aspect ratios (length/diameter ratio) and can be distributed widely and densely at the microscopic scale yet covering longer lengths. These characteristics can be used in cement composites to bridge cracks and restrict them from increasing which can essentially create a new generation of crack-free cement materials [8, 9].
Many procedures have been used to promote an adequate dispersion of CNTs in cement-based composites [8, 9, 11]. However, these routes are not always compatible with the common processes used by the construction industry. In this context, a way that has proven viable is the CNTs synthesis *in situ*, directly on the clinker particle. This process, patented by Ladeira *et al.* [12], promotes a natural dispersion of CNTs making their application in the context of the construction industry more adequate. Investigations, that use this technology, show significative results in terms of gains in compressive and tensile strength [13, 14, 15].
In continuation of previous studies [13, 14, 15], the goal of this work is to present the results of the fresh state rheological behavior as well as of the initial hydration period of blast furnace slag (Brazilian CP III 40 RS) Portland cement pastes produced with carbon nanotubes grown directly on clinker. The yield stress, plastic viscosity, temperature profile and evolved accumulated heat during the initial hydration period as well as setting times are the properties investigated. Cement pastes containing 0.1% and 0.3% of CNTs with respect to cement content were compared with CNT-free pastes. No chemical admixtures were used as a dispersant in all cases. CP III 40 RS cement was selected since it is one of the most used cement by the construction industry in Brazil.

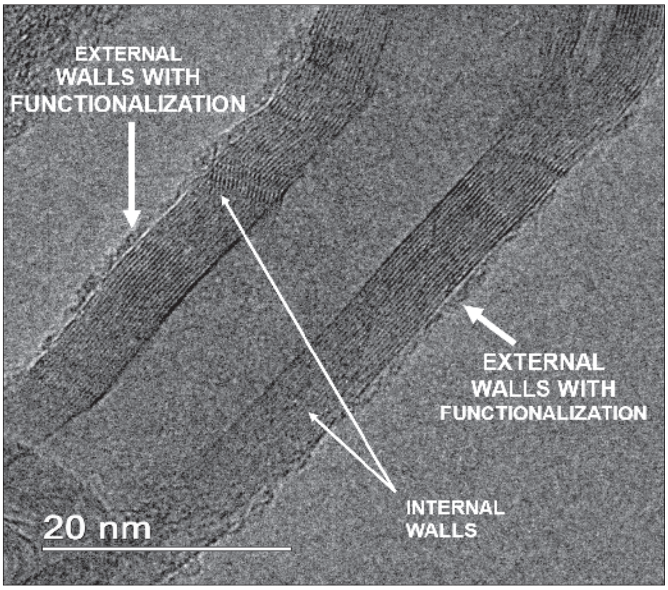

Figure 1
Transmission electron microscopy image of CNT grown directly on the cement clinker

2. Experimental methodology

2.1 Materials

According to Santra *et al*. [10], the effective reinforcement of cement with CNTs requires the consideration of the following factors: (1) the kind of CNT used and the aspect ratio; (2) the chemical functionality of the outer CNT wall; (3) the technique of dispersion in the cement matrix and (4) the workability of the fresh cement composite paste.
In this study, multi-walled carbon nanotubes (CNTs) were grown directly on cement clinker in a continuous process (Ladeira *et al.* [12]) at the Technological Center for Nanomaterials and Graphene (CTNano) of the Federal University of Minas Gerais, Belo Horizonte, Brazil. Ground iron oxide, a residue from mining exploration, was employed as a catalyst and a hydrocarbon gas as a carbon precursor in the chemical vapor deposition (CVD) process. This way, the produced CNTs have a natural functionality due to the defects they present in their shapes and outer walls, which, in turn, leads to no need for chemical functionalization. Figure 1 is a transmission electron microscopy (TEM) image, which illustrates this natural functionality: CNT outer walls have defects, which can provide a chemical and

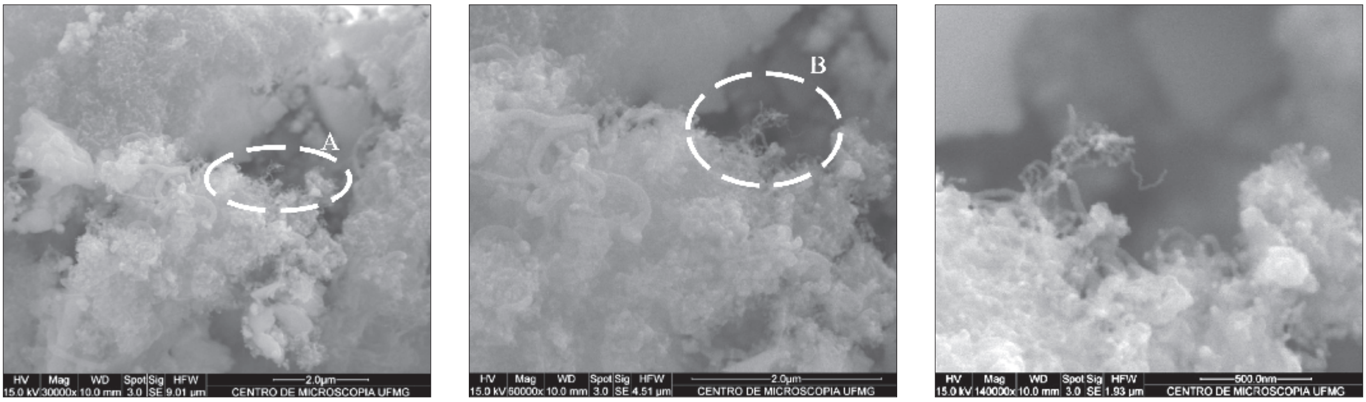

(a) (b) (c)

Figure 2
Scanning electron microscopy images of CNTs grown directly on the cement clinker

mechanical bond between the CNTs and the cement hydration products. The figure also shows that the CNTs are not perfectly straight. Thus, it is undoubtedly a much simpler, cheaper and lesser time-consuming way to produce functionalized CNTs to be used in cement composites. It also allows for large-scale production, which can be employed during cement manufacturing.
The maximum CNT length was in the order of tens of microns. The mean diameter of CNTs was between 15 and 40 nm. Thus, the average CNT aspect ratio was approximately 1000. Figure 2 shows scanning electron microscopy (SEM) images of the CNTs grown directly onto the cement clinker. From the figure, one can see that CNTs are well distributed in the clinker particles and are polydisperse in terms of length and diameter. The nanostructured clinker contained approximately 10.5 % of carbon nanotubes by weight, as determined by thermogravimetric analysis, as shown in Figure 3.

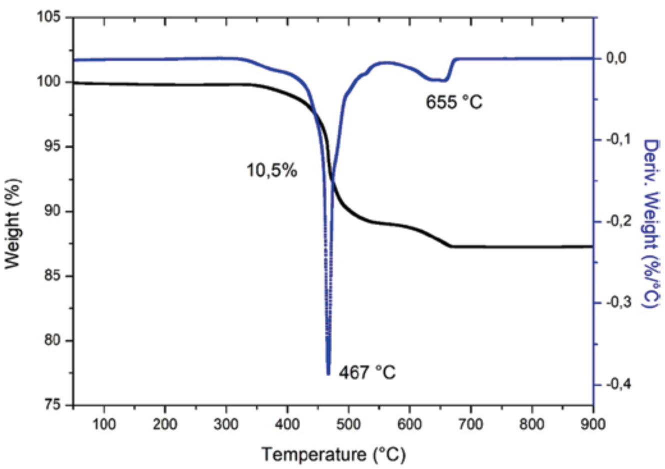

Figure 3
Thermo-gravimetrical analysis of the nanostructured clinker

Table 1 shows the physical and chemical characteristics of the Brazilian CP III 40 RS (blast-furnace slag) Portland cement used in these studies. These results were obtained from tests performed at InterCement Cement Plant in Pedro Leopoldo, Brazil.

2.2 Preparation of the cement pastes

The cement pastes were prepared at the CTNano laboratories in Belo Horizonte. The ambient temperature and relative humidity were monitored around 24 ± 2° C and 30%-50% respectively.

Table 1
Physical and chemical characteristics of Brazilian CP III 40 RS Portland cement

Physical characteristics	Sample	Standard requirements (Brazilian NBR-5735)
Residue in sieve 75 μm	0.467 %	≤ 8.0 %
Blaine finesse	4642 cm²/g	—

Chemical characteristics	Sample	Standard requirements (Brazilian NBR-5735)
Fire loss	3.47 %	≤ 4.5 %
Insoluble residue	1.40 %	—
SO_3	2.38 %	≤ 4.0 %
MgO	3.43 %	—
SiO_2	24.09 %	—
Al_2O_3	6.36 %	—
Fe_2O_3	3.30 %	—
CaO	54.81 %	—
Na_2O	0.14 %	—
K_2O	0.67 %	—

Table 2
Cement paste denomination and corresponding mix proportion used for a 0.6 – liter volume

Cement paste denomination	Cement* (g)	Water (g)	Nanostructured clinker (g)	Carbon nanotubes (g)
Reference	837	335	—	—
CNT01	831.4	335	5.6	0.84
CNT03	820.2	335	16.8	2.52

* Brazilian CP III 40 RS (blast-furnace slag) cement

The CNT cementitious material containing the anhydrous cement and the nanostructured clinker was first mixed together in a Y-type mixer. The mixing time was 20 minutes. This procedure was used to disperse and homogenize the nanostructured clinker into the pure cement.
The volume of each cement paste batch was always equal to 0.6 liters. For the production of this volume, the amount of cement used in each composition was always equal to 837 grams and the water/cement ratio equal to 0.4. The CNTs synthesized directly on cement clinker ratio corresponded to 0.1% and 0.3% of the binder weight (bwoc). This amount of CNTs was based on results obtained by Souza [16]. No chemical admixtures were used as a dispersant in all cases. Three different pastes were prepared and tested. Table 2 shows the mix proportion of each paste as well as its corresponding denomination, which will be referred to throughout this paper.
A Chandler Engineering ™ mixer was employed to prepare the cement pastes. The dry cementitious material was added to the water evenly through the central opening of the lid of the mixer up to 15 seconds. In this time interval, the mix rotation was 5000 rpm ± 200 rpm. After that, the lid was completely closed and the stirring process continued for another 15 seconds at the same rotation. Then the paste was manually agitated with a stick for approximately 15 seconds. Finally, the paste was stirred for another 30 seconds at a rotation of 5000 rpm ± 200 rpm.

2.3 Rheological behavior tests

The rheological behavior tests were conducted using a rheometer RHEOTEST (Medingen GmbH) totally controlled by software that monitors and analyzes the obtained data. Right after the cement pastes were mixed, they were placed inside a cup, which was inserted into the rheometer to start the rheological behavior tests. The shear rate was applied from 0.6 s^{-1} to 100 s^{-1} for 120 seconds and then back from 100 s^{-1} to 0.6 s^{-1} for another 120 seconds (Soares, [17]). The downslope curve data was employed in the calculation of the rheological parameters. Four specimens were used for each cement paste composition. The apparent viscosity, shear stress and shear rate of each cement paste with and without CNTs were measured by the rheometer. The yield stress ($\mathbf{t}_0$) and plastic viscosity ($\mathbf{m}_p$) were then calculated using the Bingham and Modified Bingham models.
Bingham is the most widely used model to evaluate the yield stress and plastic viscosity of cement pastes (Papo, [18]). It corresponds to a mathematical equation, which is linear (Equation [1]) and is a function of the yield shear stress $\mathbf{t}_0$ and the plastic viscosity $\mathbf{m}_p$. In general, the Bingham model does not fit well the nonlinear portion of the flow curve at low shear rates. In order to overcome this fact, the modified Bingham model is used, which corresponds to a second-order polynomial (Equation [2]) where ***c*** is a fitting regression constant. In both of these models, τ is the shear stress while Ÿ is the shear rate.

$$\boldsymbol{\tau} = \boldsymbol{\tau}_0 + \boldsymbol{\mu}_{\boldsymbol{p}} \text{Ÿ} \qquad (1)$$

$$\boldsymbol{\tau} = \boldsymbol{\tau}_0 + \boldsymbol{\mu}_{\boldsymbol{p}} \text{Ÿ} + \boldsymbol{c}\text{Ÿ}^2 \qquad (2)$$

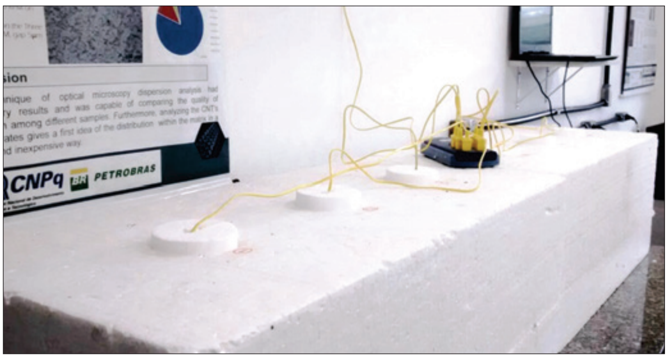

Figure 4
Details of the semi-adiabatic chambers made of expanded polystyrene blocks

2.4 Heat of hydration

According to ASTM C1753 [19], non-conventional differential thermal analysis (NCDTA) can be employed to evaluate the heat of hydration of hydraulic cementitious mixtures, through the measurement of the temperature difference between a sample and an inert reference, when both are submitted to the same environmental conditions. In this case, the system operates semi-adiabatically and the temperature difference is measured due to the exothermal effects promoted by the spontaneous cement hydration reactions. ASTM C1753 still prescribes that the inert material temperature throughout the test period is of paramount importance since this tends to account for the effects of the change of the ambient temperature during the measurement period, as well as possible interference from a sample to the other. This way it specifies that the inert reference has a maximum

Table 3
Specific heat capacity of each component of the cement paste

Component	Specific heat capacity (T in °C)
Brazilian type III 40 RS cement	C_c = 0.0045.T + 0.4807
Nanostructured clinker	C_{nc} = 0.0035.T + 0.5509
Water	C_w = 4.18 J/(g.°C)

variation of 3° C throughout the test period. This method was used in this investigation.
The semi-adiabatic chambers consisted of two blocks made of expanded polystyrene. Each block had dimensions of 93.5 cm (length) x 42.5 cm (width) x 36 cm (height). In each block, three cylindrical holes were drilled where the aluminum cans surrounded by Styrofoam cups were placed. Each cup had an expanded polystyrene lid with a small hole from which the leads from the thermocouples passed through as shown in Figure 4 (Benedetti [20]).
Right after the cement pastes were mixed, they were placed inside the aluminum cans, capped and then inserted into the expanded polystyrene blocks. Each can contain 0.2 liters of each cement paste batch. In a certain can was placed an inert reference material, which in this case consisted of sand and water in the same amount of cement and water used in the pastes. A thermocouple was placed inside the fresh cement paste or the reference material. This way it measured the reference material or the cement paste temperature. Ten specimens were used for each cement paste composition. The temperature data acquisition was done by a controller device connected to a computer. The data was collected during the first 72 hours of hydration, every 30 seconds.
The specific heat capacity, in the range from 10 to 80°C, of the raw materials used in the cement pastes, was determined by differential scanning calorimetry (DSC) analysis. These values are presented in Table 3 for each component. For each cement paste composition, the cumulative evolved heat, in arbitrary units, was calculated according to the equations presented in Table 4.
The consistency change of the cement pastes with respect to time was evaluated employing the Vicat analysis, performed according to Brazilian Standard Method NBR NM 65 [21].

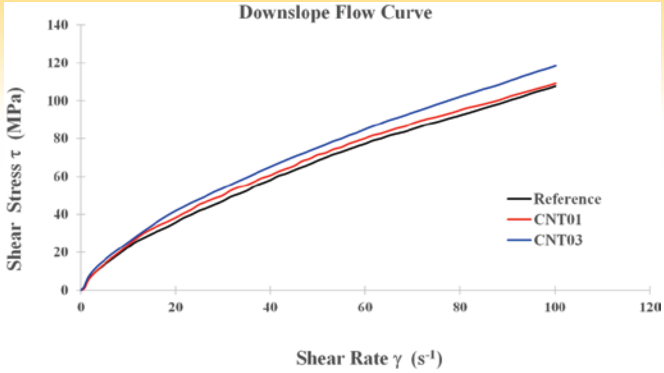

Figure 5
Shear stress versus shear rate relationships for the investigated cement pastes

The procedure measures the Vicat needle penetration in the pastes as their setting processes occur. The only difference in this case with respect to NBR NM 65 specifications was the water/cement ratio: 0.4 was used since this was the value adopted in the NCDTA evaluation. This way the initial and final setting times could be correlated with the evolved accumulated heat during the hydration period. Three specimens for each cement paste composition were used.

3. Results and discussion

Figure 5 presents the most representative downslope flow curve for each of the three cement paste compositions (Reference, CNT01, and CNT03). The flow curves are almost equal for both the Reference and CNT01 cement pastes. For the CNT03 composition, there is a difference with respect to the other two: for the same shear rate, the corresponding yield stress is larger.
The calculated values of mean yield stress and plastic viscosity using the Bingham and Modified Bingham models are shown in Table 5 and Figure 6. The comparison between both mathematical models shows that for all pastes the modified Bingham, which fits better the nonlinear portion of the flow curve at low shear rates, has smaller values for the yield stress and larger values for the plastic viscosity. The addition of CNT leads to larger yield stress values with respect

Table 4
Cumulative evolved heat for each cement paste composition used for a 0.2 – liter volume

Cement paste denomination	Cumulative evolved heat (arbitrary units-a.u.)
Reference	[279 • (0.0045 • T + 0.4807) + 112 •4.18)] • ΔT*
CNT01	[277.1 • (0.0045 • T + 0.4807) + 1.9 • (0.0035 • T + 0.5509) + 112 • 4.18] • ΔT*
CNT03	[273.4 • (0.0045 • T + 0.4807) + 5.6 •(0.0035 • T + 0.5509) + 112 • 4.18] • ΔT*

*$\Delta T = (T_{sample} - T_{inert\ material})$ (in °C)

Table 5
Rheological parameters for the three cement compositions

Cement paste denomination	Bingham model			Modified Bingham model		
	Yield stress (Pa)	Plastic viscosity (Pa.s)	Regression r^2 value	Yield stress (Pa)	Plastic viscosity (Pa.s)	Regression r^2 value
Reference	18.2 ± 1.24	0.99 ± 0.06	0.988	10.2 ± 0.92	1.39 ± 0.02	0.999
CNT01	20.8 ± 1.12	0.98 ± 0.07	0.984	11.4 ± 0.58	1.46 ± 0.03	0.999
CNT03	21.3 ± 1.81	1.01 ± 0.05	0.988	12.4 ± 1.12	1.47 ± 0.03	0.999

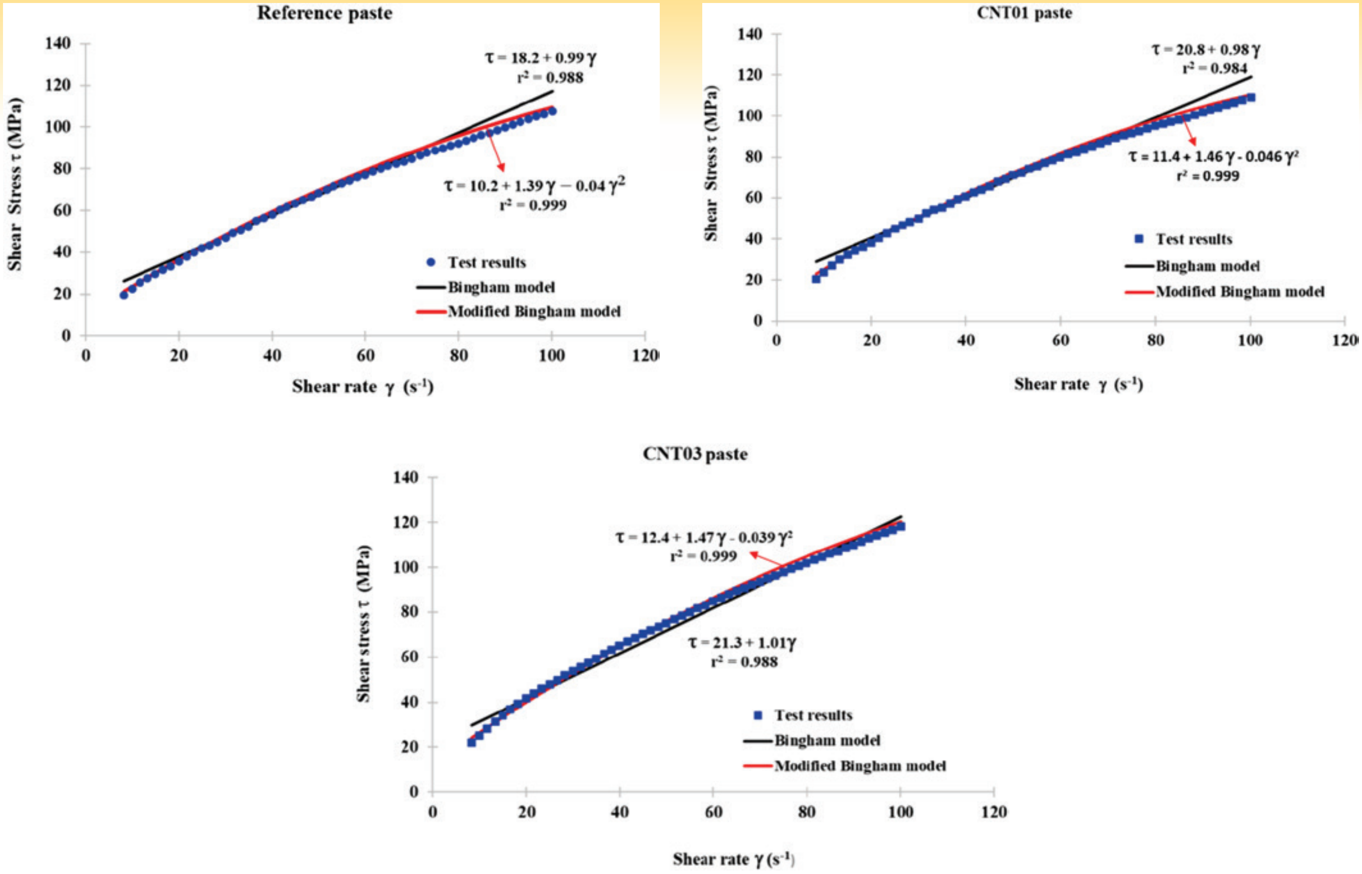

Figure 6
Bingham and modified Bingham model for the investigated cement pastes

to the reference pastes in both models. On the other hand, no change was observed in the plastic viscosity of all pastes. This way, comparative analysis of these results shows the equivalence of these rheological parameters. The modified Bingham model represents much better the observed behavior as shown in Figure 6 for all pastes.

It has been reported in the literature that like any most nanomaterials, the workability of cement paste is often reduced with the addition of CNTs due to their large surface area (Kowald and Trettin [22]). The results obtained in this study show otherwise: with CNTs directly grown on clinker, no significant changes were found in the rheological behavior of the cement pastes.

Figure 7 shows the thermal profile versus time relationships for the most representative specimen of each cement paste composition. The analysis of the thermal profiles indicates

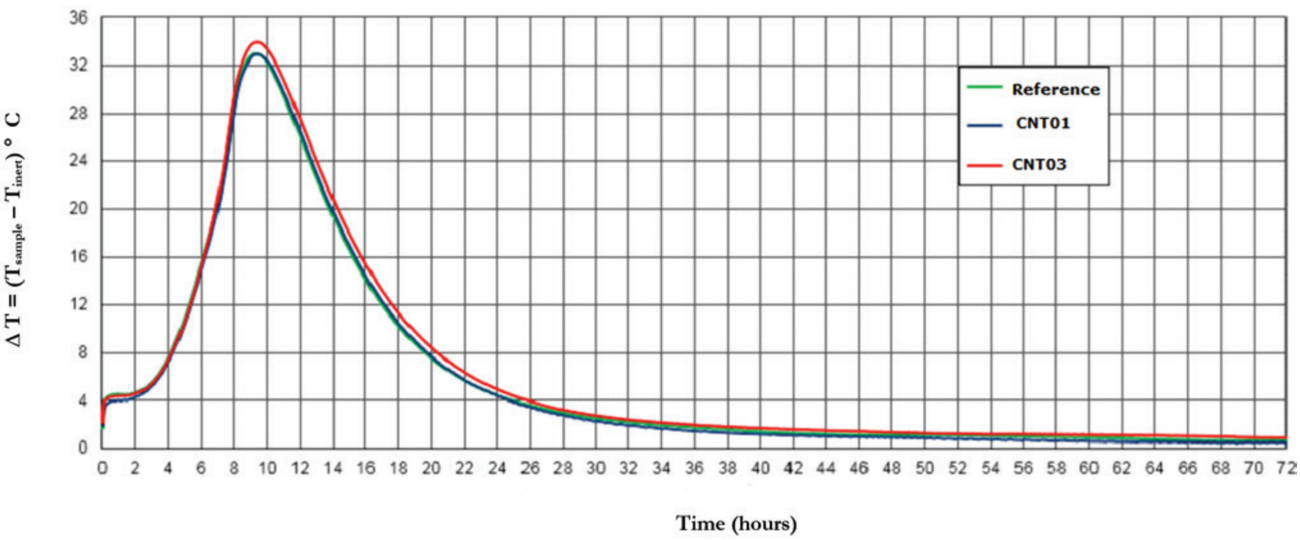

Figure 7
Representative thermal profiles of the cement pastes

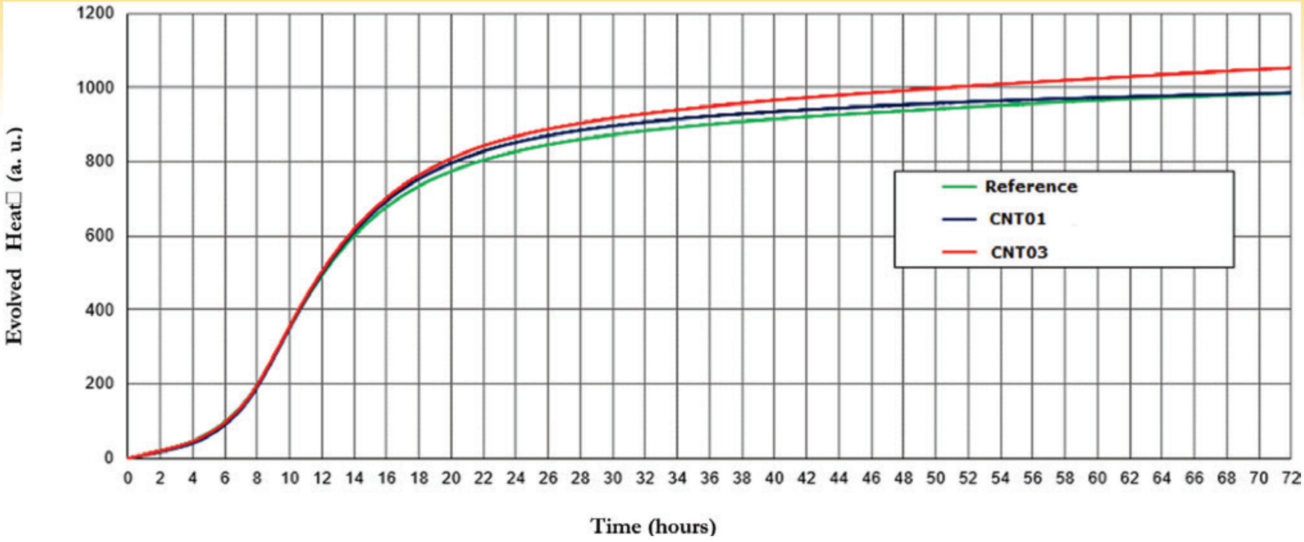

Figure 8
Evolved accumulated heat (a. u.) of the cement pastes

that they are very similar and that the main peak of cement paste with carbon nanotubes (CNT01 and CNT03) occurs practically at the same time in comparison with the reference without CNTs. Therefore, the effect of the presence of CNTs on the thermal profiles of cement pastes made with cement CPIII-40 RS was not significant.

The evolved heat versus time relationships for the most representative of each type of cement paste investigated are presented in Figure 8. Table 6 shows the average accumulated heat values with the respective standard deviation values of the three different cement pastes up to 24 and 72 hours. The analysis of these results indicates that the addition of 0.1% and of 0.3 % of CNT on the accumulated heat of pastes produced with CPIII- 40 RS was not significant up to 72 hours. The differences between the values are within 10% of each other.

Table 6
Evolved accumulated heat, in arbitrary units, for each cement paste composition

Cement paste denomination	Evolved heat up to 24 hours (a.u.)	Evolved heat up to 72 hours (a.u.)
Reference	823 ± 14	969 ± 30
CNT01	845 ± 18	984 ± 19
CNT03	864 ± 24	1049 ± 34

In addition to Vicat analysis, a procedure, developed by HU *et. al* [23], was employed to evaluate the initial and the final setting times. The methodology is based on the first derivative of the temperature profile along the time. According to

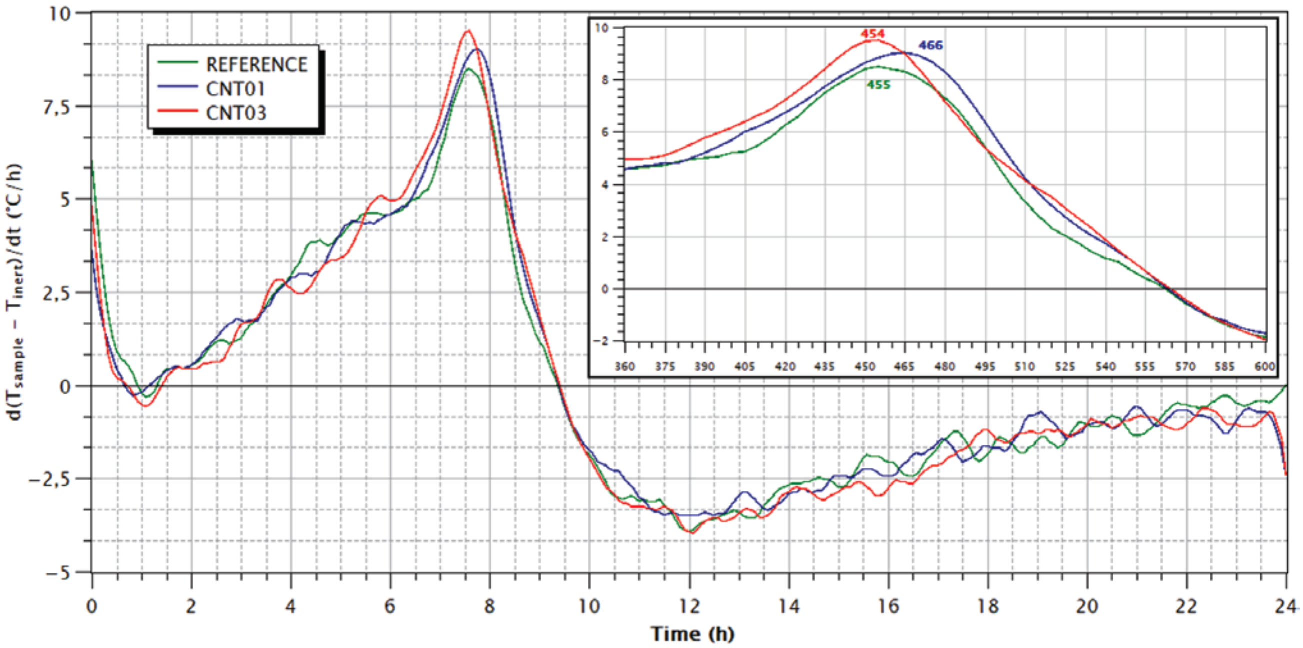

Figure 9
First derivative of the temperature profile *versus* time relationships for each type of cement paste investigated

Table 7
Vicat analysis: average initial and final setting times and corresponding evolved accumulated heat for each cement paste composition

Cement paste denomination	Average initial setting time Vicat analysis (min)	Corresponded accumulated heat (a. u.)	Average final setting time Vicat analysis (min)	Corresponded accumulated heat (a. u.)
Reference	336 ± 1	65 ± 4	370 ± 5	83 ± 4
CNT01	305 ± 2	68 ± 4	332 ± 5	91 ± 5
CNT03	297 ± 3	75 ± 4	345 ± 8	96 ± 5

Table 8
First derivative procedure: average initial and final setting times and corresponding evolved accumulated heat for each cement paste composition

Cement paste denomination	Average initial setting time First derivative analysis (min)	Corresponded accumulated heat (a. u.)	Average final setting time First derivative analysis (min)	Corresponded accumulated heat (a. u.)
Reference	458 ± 3	174 ± 4	565 ± 5	306 ± 8
CNT01	469 ± 4	180 ± 6	568 ± 5	303 ± 5
CNT03	456 ± 2	170 ± 7	562 ± 8	308 ± 4

HU *et. al* [23], the initial setting time is defined as the time when the first derivative reaches its highest value. At this point, the increase in the rate of heat generation is the fastest. After this initial setting time, the first derivative values start to decrease. The time when the first derivative drops to zero is defined as the calorimetry of the final setting time. This point corresponds to the time when the highest rate of hydration is achieved; after this point, the rate of hydration will be reduced. The most representative of the first derivative of the temperature profile versus time relationships for each type of cement paste investigated are presented in Figure 9. Closer detail of the initial and final setting times is also shown in the figure.
The average initial and final setting times, as well as, their corresponding evolved accumulated heat for each type of investigated cement paste are presented in Tables 7 and 8. Table 7 corresponds to the values determined according to the Vicat analysis, while in Table 8 the values were calculated from the first derivative of the temperature profile along the time.
The Vicat analysis, determined according to NBR NM 65 [21], indicates that the addition of CNTs in both contents reduced significantly the initial and final setting times of the cement pastes with respect to the reference. The initial and final setting times were reduced by 10% approximately for cement pastes containing CNTs with respect to the CNT-free paste. This difference in the setting times does not correlate well with the corresponding evolved accumulated heat: in the first 10 hours of the hydration period, the evolved accumulated heat is about the same for all cement pastes regardless of the presence or not of CNTs.
The analysis according to the first derivative of the temperature profile versus time shows otherwise. The initial and final setting times, as well as, their corresponding evolved accumulated heat are basically the same for all cement pastes. This indicates a good correlation between these parameters as should be expected. These results also reveal that the presence of CNTs made no difference in the first 72 hours of the cement hydration process.
The values of the initial and final setting times obtained with the Vicat analysis and the first derivative of the temperature profile along the time are significantly different. The values with the Vicat method are much smaller. This finding was also obtained by HU *et. al* [23]. This fact, as explained by Hu, is due to the very different mechanisms and test setups in determining setting times. Vicat method is a physical procedure while the first derivative methodology is related to thermodynamics of the hydration process.

4. Conclusions

The goal of this work was to present the results of the early-age behavior of blast furnace slag (Brazilian CP III 40 RS) Portland cement pastes produced with carbon nanotubes grown directly on clinker. This way, the produced CNTs have a natural functionality due to the defects they present in their shapes and outer walls. Thus, it is undoubtedly a much simpler, cheaper and lesser time-consuming way to produce functionalized CNTs to be used in cement composites. It also allows for large-scale production, which can be employed during cement manufacturing. CP III 40 RS cement was selected since it is one of the most used cement by the construction industry in Brazil. The yield stress, plastic viscosity, evolved accumulated heat, and the initial and final setting times of the cement pastes were the investigated characteristics. The main conclusions are:

1. The results show that the addition of CNTs in both contents (0.1 and 0.3% bwoc) does not alter the rheological

behavior, although the yield stress values were larger. It has been reported in the literature that like any most nanomaterials, the workability of cement paste is often reduced with the addition of CNTs due to their large surface area. The results herein show otherwise, which indicates that with the procedure used in this investigation to include CNTs in cement pastes and the employed CNT/cement ratios no significant changes were found in the rheological behavior of the cement slurries.

2. All cement pastes presented a nonlinear behavior of the downslope flow curve at low shear rates. Due to this fact, the modified Bingham model represents much better this observed behavior.
3. The Vicat analysis indicates that the addition of CNTs in both contents reduced significantly the initial and final setting times of the cement pastes with respect to the reference. On the other hand, the results according to the first derivative of the temperature profile versus time show that the initial and final setting times, as well as, their corresponding evolved accumulated heat are basically the same for all cement pastes regardless of the presence or not of CNTs. This fact is due to the very different mechanisms and test setups in determining setting times. Vicat method is a physical procedure while the first derivative methodology is related to thermodynamics of the hydration process.

5. Acknowledgments

The authors would like to acknowledge the financial aid and invaluable support of CENPES/PETROBRAS, Intercement Brasil S/A, BNDES, FAPEMIG, CNPq, CAPES, INCT, and the Center of Microscopy at UFMG.

6. References

[1] DRESSELHAUS, M.S., DRESSELHAUS, G., EKLUNG, P.C., 1996, Science of Fullerenes and Carbon Nanotubes (USA), Elsevier Science Imprint, California, ⟨http://www. academicpress.com⟩.

[2] HUANG, X., QI, Y., BOEY, F., ZHANG, H., 2012, Graphene-based composites. Chemical Society Reviews, 41, p. 666–686, http://dx.doi.org /10.1039/c1cs15078b.

[3] LI, G.Y., WANG, P.M. and ZHAO, X., 2005, Mechanical behavior and microstructure of cement composites incorporating surface-treated multi-walled carbon nanotubes, Carbon, Vol. 43, pp. 1239-1245, doi:10.1016/j.carbon.2004.12.017.

[4] MAKAR, J.M. and CHAN, G.W., 2009, Growth of cement hydration products on single-walled carbon nanotubes, Journal American Ceramic Society Vol. 92, pp. 1303-1310, doi: 10.1111/j.1551-2916.2009.03055.x.

[5] MUSSO, S.; TULLIANI, J.-M.; FERRO, G. and TAGLIAFERRO, A., 2009, Influence of carbon nanotubes on the mechanical behavior of cement composites, Composites Science and Technology, Vol. 69, pp. 1985-1990, doi:10.1016/j.compscitech.2009.05.002.

[6] KONSTA-GDOUTOS, M. S., METAXA, Z. S. and SHAH, S. P., 2010, Multi-scale mechanical and fracture characteristics and early-age strain capacity of high-performance carbon nanotube/cement nanocomposites, Cement & Concrete Composites, Vol. 32, pp. 110-115. doi:10.1016/j.cemconres.2010.02.015.

[7] KUMAR, S., KOLAY, P., MALLA, S., MISHRA, S., 2012. Effect of multiwall carbon nanotubes on mechanical strength of cement paste. J. Mater. Civil Eng. (ASCE) 24, 84–91. http://dx.doi.org/10.1061/(ASCE)MT.1943-5533.0000350.

[8] RASHAD, A. M., 2017, Effect of carbon nanotubes (CNTs) on the properties of traditional cementitious materials, Construction and Building Materials., vol. 153, pp. 81–101. http://dx.doi.org/10.1016/j.conbuildmat.2017.07.089.

[9] REALES, O. M. and TOLEDO FILHO, R. D., 2017, A review on the chemical, mechanical and microstructural characterization of carbon nanotubes-cement based composites, Construction and Building Materials, vol. 154, pp. 697–710. http://dx.doi.org/10.1016/j.conbuildmat.2017.07.232.

[10] SANTRA, A., BOUL, P.J., PANG, X., 2012. Influence of nanomaterials in oil well cement hydration and mechanical properties. In: Proceedings of the SPE International Oilfield Nanotechnology Conference held in Noordwijk. Netherlands, 12–14 June, SPE 156937.

[11] S. PARVEEN, S. RANA, and R. FANGUEIRO, 2013, A review on nanomaterial dispersion, microstructure, and mechanical properties of carbon nanotube and nanofiber reinforced cementitious composites, Journal of Nanomaterials, pp. 1–19, http://dx.doi.org/10.1155/2013/710175

[12] LADEIRA, L. O.; SILVA, E. E.; OLIVEIRA, S.; LACERDA, R. G.; FERLAUTO, A. S.; ÁVILA E.; LOURENÇON, E., 2015, Large-scale production of carbon nanotubes in Portland cement, US Patent, 9085487 B2.

[13] LUDVIG, P., CALIXTO, J. M., LADEIRA, L. O., and GASPAR, I. C. P., 2011, Using Converter Dust to Produce Low-Cost Cementitious Composites by in situ Carbon Nanotube and Nanofiber Synthesis, Materials (Basel), vol. 4, no. 12, pp. 575–584, http://dx.doi.org/10.3390/ma4030575.

[14] PAULA, J. N.; CALIXTO, J. M.; LADEIRA, L. O.; LUDVIG, P.; SOUZA T. C. C.; ROCHA, J. M.; MELO, A. V., 2014, Mechanical and rheological behavior of oil-well cement slurries produced with clinker containing carbon nanotubes, J. of Petroleum Sci. and Eng., 122, p. 274-279, http://dx.doi.org/10.1016/j.petrol.2014.07.020.

[15] LUDVIG, P., CALIXTO, J. M., LADEIRA, L. O., SOUZA T. C. C. and PAULA, J. N., 2017, Analysis of cementitious composites prepared with car-

bon nanotubes and nanofibers synthesized directly on clinker and silica fume, Journal of Materials in Civil. Engineering (ASCE), v. 29, http://dx.doi.org/10.1061/(asce)mt.1943-5533.0001836.

[16] SOUZA, T.C.C., 2015, Síntese contínua e caracterização de cimento Portland fabricado com nanotubos de carbono, Master´s Dissertation, Universidade Federal de Minas Gerais, Belo Horizonte, Brazil, 184 p.

[17] SOARES, P.A., 2019, Caracterização da reologia no estado fresco de pastas de cimento Portland fabricadas com nanotubos de carbono sintetizados diretamente sobre o clínquer, Master´s Dissertation, Universidade Federal de Minas Gerais, Belo Horizonte, Brazil, 138 p.

[18] PAPO, A., Rheological models for cement pastes, 1988, Materials Structure, vol. 21, p. 41-46.

[19] AMERICAN SOCIETY FOR TESTING AND MATERIALS, 2015, ASTM C1753: Standard Practice for Evaluating Early Hydration of Hydraulic Cementitious Mixtures Using Thermal Measurements ASTM International, West Conshohocken, PA, USA.

[20] BENEDETTI, A.Z., 2018, Avaliação da temperatura gerada pelo calor de hidratação de pastas de cimentos Portland fabricados com nanotubos de carbono, Master´s Dissertation, Universidade Federal de Minas Gerais, Belo Horizonte, Brazil, 161 p.

[21] ASSOCIAÇÃO BRASILEIRA DE NORMAS TÉCNICAS, 2003, NBR NM 65: Cimento Portland - Determinação do tempo de pega. Rio de Janeiro.

[22] KOWALD, T., TRETTIN, R., 2009, Improvement of Cementitious Binders by Multiwall Nanotubes, in Zdenêk. B. et al. (Eds.), Proceedings of the 3rd International Symposium on Nanotechnology and Construction (NICOM 2009), Prague, Czech Republic, Berlin, Heidelberg, 31 May–2 June.

[23] HU, J., GE, Z., and WANG, K., 2014, Influence of cement fineness and water-to-cement ratio on mortar early-age heat of hydration and set times, Construction and Building Materials, vol. 50, pp. 657–663, http://dx.doi.org/10.1016/j.conbuildmat.2013.10.011.

Volume 13, Number 3 (June 2020) p. 613 – 627 • ISSN 1983-4195
DOI: http://dx.doi.org/10.1590/S1983-41952020000300011

REVISTA IBRACON DE ESTRUTURAS E MATERIAIS
IBRACON STRUCTURES AND MATERIALS JOURNAL

Performance of concrete with the incorporation of waste from the process of stoning and polishing of glass as partial replacement of cement

Desempenho de concretos com a incorporação de resíduo do processo de lapidação e polimento do vidro como substituto parcial ao cimento



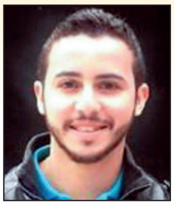


G. C. GUIGNONE [a]
gcgarquiteto@gmail.com
https://orcid.org/0000-0002-1007-8739

G. L. VIEIRA [a]
geilma.vieira@gmail.com
https://orcid.org/0000-0001-6148-3307

R. ZULCÃO [a]
robsonzulcao@gmail.com
https://orcid.org/0000-0003-3381-0360

M. K. DEGEN [a]
maxdegen@hotmail.com
https://orcid.org/0000-0002-6453-797X

S. H. M. MITTRI [a]
sergio-mittri@hotmail.com
https://orcid.org/0000-0001-6038-8463

C. R. TELES [a]
clauteles@hotmail.com
https://orcid.org/0000-0002-5639-389X

Abstract

The incorporation of waste glass as a partial replacement for cement in concrete can provide an alternative destination for the waste, reduce the consumption of cement (minimizing CO_2 emissions and consumption of natural resources), and improve the concrete performance. Thus, this research evaluated the performance of concrete incorporating waste glass sludge (GS), resulting from the process of stoning and polishing of soda-lime flat glass, as a supplementary cementing material. Mechanical strength and durability properties were assessed through compressive strength, alkali-silica reactivity, electrical resistivity and chloride permeability, diffusivity and migration tests. Mixtures containing metakaolin (ME) were also evaluated. The results indicated that the use of the waste ground to an adequate size can replace up to 20% of cement. At this content, it caused a reduction of chloride penetration of over 80%, reduced ASR and conserved compressive strength. The combination of waste with metakaolin replacing 20% of cement also improved all the concrete properties, increasing the compressive strength up to 12% at 28 days.

Keywords: waste glass. pozzolan. metakaolin. chloride. alkali-aggregate reaction.

Resumo

A incorporação de resíduos de vidro em concretos como substitutos parciais ao cimento pode proporcionar um destino alternativo aos resíduos, reduzir o consumo de cimento (minimizando as emissões de CO_2 e o consumo de recursos naturais) e melhorar o desempenho do concreto. Assim, esta pesquisa avaliou o desempenho de concretos com a incorporação de lama de resíduo de vidro (GS), resultante do processo de lapidação e polimento de vidros planos sodo-cálcicos, como material cimentício suplementar. As propriedades de resistência mecânica e de durabilidade foram avaliadas por meio de testes de resistência à compressão, reatividade álcali-sílica, resistividade elétrica e permeabilidade aos íons cloreto por meio de mecanismos de transporte de difusividade e migração de cloretos. Misturas contendo metacaulim (ME) também foram avaliadas. Os resultados indicaram que o uso do resíduo de vidro moído, adotando-se dimensões de partículas adequadas, pode substituir até 20% de cimento. Proporcionando assim, uma redução na penetração de cloretos acima de 80%, reduzindo a ASR e conservando a resistência à compressão. A combinação de resíduos de vidro com metacaulim, substituindo 20% do cimento, também melhorou todas as propriedades do concreto, aumentando a resistência à compressão em até 12% em 28 dias.

Palavras-chave: resíduo de vidro. pozolana. metacaulim. cloreto. reação álcali-agregado.

[a] *Universidade Federal do Espírito Santo, Civil Engineering Department, Vitória, ES, Brazil.*

Received: 25 Jan 2019 • Accepted: 23 Oct 2019 • Available Online: 26 May 2020

1. Introduction

The increase of natural resources and energy consumption correlates with the increase of population. This has generated concerns regarding the finitude of resources, waste generation and gaseous emissions. Alternative technologies and waste reutilization emerge as possible solutions to these issues [1-4], the construction sector being of major importance due to its high consumption of energy and resources and waste generation. Portland cement used in concrete production has clinker as its main component, which is produced by burning limestone with other ingredients at high temperatures, consuming natural resources and emitting CO_2. In the chemical reaction to dissociate 1 ton of limestone, 440 kg of CO_2 is emitted, and only 560 kg goes into the clinker composition [5].

According to Shi and Zheng [6], among the urban solid wastes, glass can be considered the most suitable as a cement replacement due to its physical properties and chemical composition. Waste glass generation worldwide has not been precisely quantified, mainly due to the lack of data in several countries, such as those situated in the Middle East. Jani and Hogland [7] state that the world production of glass in 2007 was about 89.4 million tons, and it is expected to rise due to industrialization and improvement of the quality of life. Saito and Shukuya [8] estimate that for each kg of float glass produced, 1.73 kg of raw materials and 0.15 m³ of water are used. Additionally, due to the need for elevated temperatures (up to 1600 ºC) to produce the glass, they estimate 16.9 MJ of waste heat for each kg of glass sheets.

Several studies indicate that the use of glass powder (or waste glass) in concrete production can improve the mechanical and durability properties. Regarding the mechanical properties, an increase in concrete compressive strength after 56 days is noted when replacing 20% of cement by glass powder with particles size smaller than 20 µm [9-11]. Using particle sizes between 75 and 100 µm, a strength loss is verified at the same replacement level [12-13]. For durability, an improvement in chloride penetration resistance is reported, by means of chloride migration tests, for the same replacement level [11-16]. It noted that the pozzolanic activity of the glass powder increases with grinding and that the ideal particle size should be smaller than 40 µm for use as a partial replacement for cement [17]. Nevertheless, there is discussion regarding the use of materials with alkalis content above the normative limits for concrete production, as the alkalis can react with the siliceous compounds present in the reactive aggregates, causing deleterious expansive mechanisms in the hardened concrete [18]. Studies point out that the use of supplementary cementitious materials (SCM) can help reduce this mechanism called the alkali-silica reaction (ASR). The use of SCM can help to reduce the calcium hydroxide content in the pores solution by causing pozzolanic activity [11-12]. Research has also revealed that the particles size influences the occurrence of these reactions [12, 19].

There is little literature regarding the analysis of chloride penetration by different transport mechanisms and the ASR assessment of concrete mixtures with waste glass combined with metakaolin. Authors have mainly assessed the chloride penetration resistance by migration tests (rapid migration test - RMT) [11-20] and no diffusion by immersion tests have been performed. Thus, an evaluation of chloride resistance by different tests is regarded as relevant, due to the discussion related to the tests procedures and the diffusion coefficients obtained from chloride diffusion tests (bulk diffusion test - BDT) and migration tests (RMT) [21-23]. Additionally, there is a lack of studies concerning the durability of concrete incorporating wastes from the process of stoning and polishing soda-lime flat glass (waste glass sludge). A study by Kim et al. [24] evaluated the use of glass stoning waste in concrete, aiming at improving the durability properties in freezing and thawing cycles. Improvements were noted in the compressive strength and chloride penetration resistance of mixtures combining 10% glass powder and 10% fly ash compared to those with only fly ash as SCM.

Regarding the use of glass sludge waste in concrete production, the literature is even scarcer. Pignaton [25] assessed the properties of concrete containing waste from the process of stoning of glass (without subsequent grinding) and noticed a reduction in compressive strength with the increase of partial cement replacement by waste. Furthermore, Lee et al. [26] replaced 20% of cement with the stoning glass waste and verified a decrease in the compressive strength of concrete at 28 days, while noticing an increase at 91 days.

Thus, due to its fine particle size, waste glass is considered as a viable option for incorporation into concrete, with little or no further processing (grinding). Therefore, this study aims to contribute to the studies related to the performance of concrete incorporating the waste generated by the stoning and polishing of soda-lime flat glass as a cement replacement, for the mitigation of environmental impact. The influence of further grinding of the waste prior to cement replacement was assessed. Mechanical and durability properties (chloride penetration by different transport mechanisms – migration and diffusion; ASR) were evaluated. Furthermore, metakaolin in isolation and combined with waste glass sludge was used for comparative purposes.

2. Materials and experimental program

2.1 Materials

High early-strength Portland cement, CPV-ARI (equivalent to CEM I 52.5 R) was used in this study. As high mineral additions content can influence test results, this cement was used as it is the commercially available cement in Brazil with the lowest percentage of additions (up to 5% limestone powder). Natural quartz sand and granitic coarse aggregate were used as aggregates in the mixtures. The coarse aggregate had maximum grain size of 19 mm, true density of 2.77 g/cm³, bulk density of 1.45 g/cm³ and water absorption of 0.73%. The fine aggregate had maximum grain size of 2.4 mm, fineness modulus of 1.92 and true density of 2.57 g/cm³. The physical and chemical characterization of cement, metakaolin (ME), glass sludge without grinding (GS1) and ground glass sludge (GS2) are presented in Table 1. Grinding of the waste glass was used to intensify the material reactivity.

Figure 1a shows the particle size gradation curve of GS1, GS2, cement and metakaolin used in the experimental program. Additionally, Figure 1b presents the X-ray diffraction (XRD) of the ground waste, where an amorphous state can be verified, due to the absence of visible peaks in its spectrum. Studies have pointed out that the pozzolanic reactivity increases if more amorphous phases are present in the supplementary cementing materials [27,28].

Table 1
Physical and chemical properties of GS1, GS2, metakaolin and cement

Composition (%), by mass	Glass sludge (GS1)	Ground glass sludge (GS2)	Metakaolin (ME)	Cement
Silica (SiO_2)	64.77	64.77	58.7	19.42
Alumina (Al_2O_3)	2.81	2.81	33.1	4.87
Iron oxide (Fe_2O_3)	0.44	0.44	1.8	2.93
Calcium oxide (CaO)	6.92	6.92	0.2	63.69
Magnesium oxide (MgO)	4.49	4.49	0.2	0.86
Sodium oxide (Na_2O)	19.36	19.36	0.2	—
Potassium oxide (K_2O)	0.11	0.11	1.8	0.8
Sulphur trioxide (SO_3)	0.21	0.21	0.2	3.02
% retained # 400 mesh	—	—	—	2.2
% retained # 325 mesh	19.65	7.64	8.14	—
% retained # 200 mesh	10.63	4.08	0.92	—
Average particle size (μm)	42.17	35.02	23.8	16.06
Median particle size – d50 (μm)	16.06	10.28	16.65	13.75
Specific gravity (g/cm³)	2.51	2.51	2.55	3.07
Blaine specific surface area (cm²/g)	6121	8015	18549	4751

2.2 Waste from the process of stoning and polishing of glass

The glass powder used in this study is a waste originated in the process of stoning and polishing flat glass. It is obtained through the water recycling process, according to Figure 2. In summary, ducts crossing the glass manufacturing area collect the slurry that contains the water used in the stoning process along with the glass powder. This waste output is then conducted by pipes to reservoirs, where submerged pumps raise it to vertical silos for decantation (Figure 2b). Subsequently, the sludge (water and glass powder) is pumped to vertical silos, where chemical products (compounds of ethanol, oxides and polar solvents) are added for decantation. The excess water is then transported to another reservoir where is pumped back to the manufacturing process. Afterwards, the waste proceeds to the sludge mixer, and it is pumped to the filter press for dehydrating. The sludge is pressed, the excess water returns to the manufacturing process, and the final waste is obtained (Figure 2c). With this system, approximately 95 to 97% of the water is re-used in the process [25].

The waste used in this study was obtained from a factory which generates around 290 kg of the final waste daily, totaling approximately 84 tons yearly. After collection, the waste was partially air dried, and then oven dried at 100 ºC until mass constancy

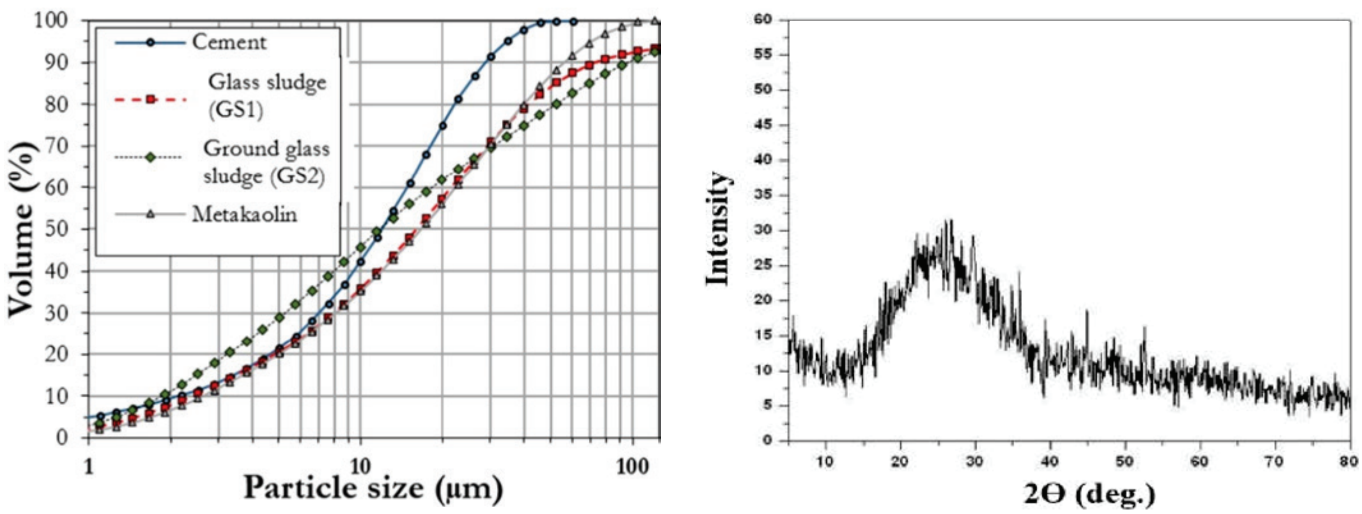

(a) (b)

Figure 1
(a) Size gradation curve of cement, GS1, GS2 and metakaolin. (b) X-ray diffraction (XRF) of GS2

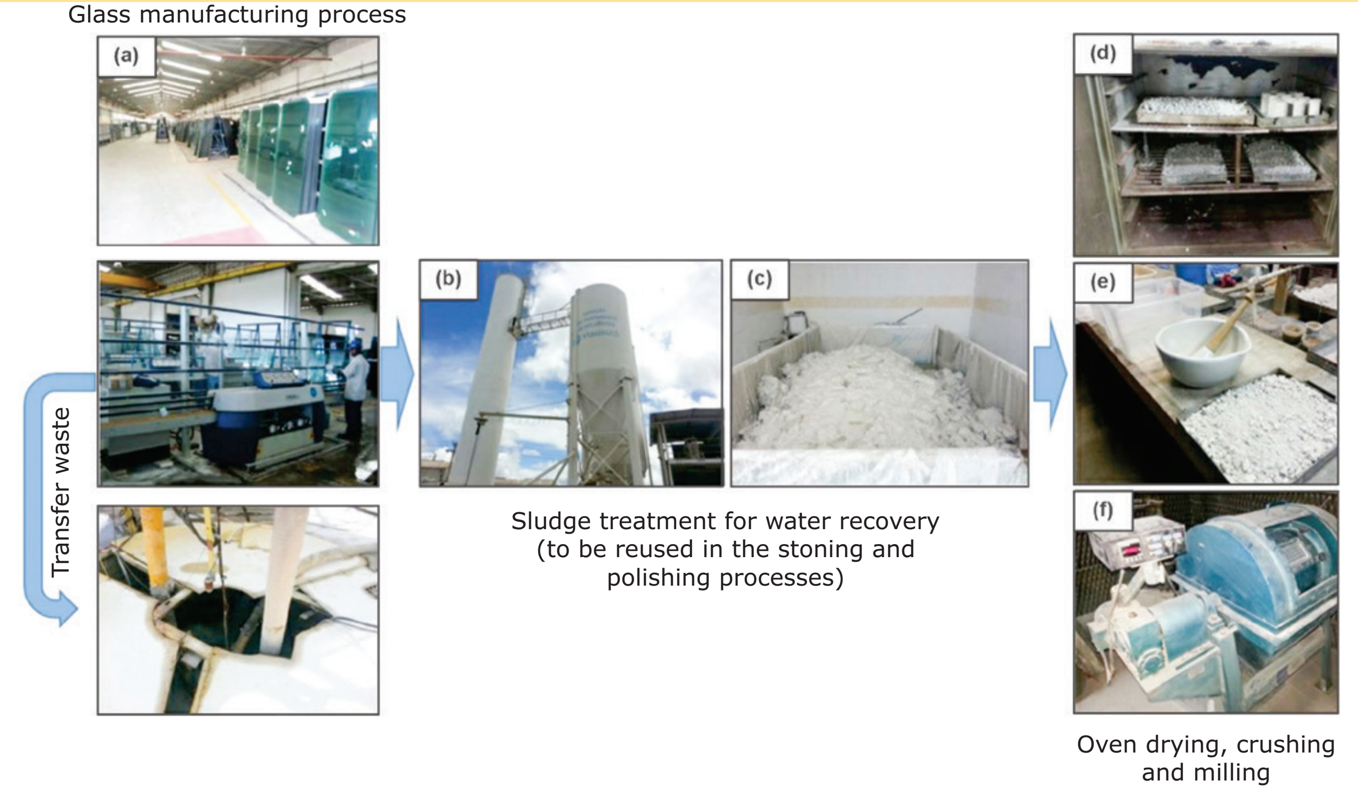

Figure 2
(a) Glass before stoning and polishing; (b) Silo for decantation; (c) Final waste after filter press; (d) Oven drying; (e) Crushing for breaking the lumps, GS1; (f) Ball mill for grinding, GS2

(Figure 2d). Subsequently, the waste was crushed to break the lumps using a ceramic mortar and pestle (Figure 2e). Additionally, aiming to intensify its reactivity, the waste was also ground. For the grinding process, a ball mill was used, composed of steel balls of 40 mm diameter and 0.278 kg. The internal diameter of the mill was 380 mm with a volume of 47 litres with the capacity of 14 kg per batch (Figure 2f). Thus, two types of glass powder were produced: GS1, without grinding, and GS2, ground.

2.3 Pozzolanic activity

The premises from the ABNT NBR 12653 [29] standard were used to assess the pozzolanic activity of the materials, where limits regarding the physical and chemical properties are established, as per Table 2. The standard classifies the materials in three classes (N, C and E) according to their nature. The glass waste fits in class E, comprising percentage amounts of $SiO_2 + Al_2O_3 + Fe_2O_3$ greater than 50%, whereas metakaolin fits into class N, comprising percentage amounts greater than 70% for the same compounds. The method according to Luxán *et al.* [30] was also used for complementing the information regarding the materials' pozzolanic activity. This method, which can be rapidly executed, is based on measuring the conductivity of a saturated solution with calcium hydroxide, before and after adding the potential pozzolanic material. According to Rodrigues [31], variation of the conductivity occurs due to the pozzolanic reaction with the ions Ca^{2+} and $(OH)^-$; that is,

Table 2
Limits for classification of pozzolanic materials according to NBR 12653 [29]

Properties	Limits ABNT NBR 12653 [29] Class E	Limits ABNT NBR 12653 [29] Class N	Glass sludge (GS1) (class E)	Ground glass sludge (GS2) (class E)	Metakaolin (ME) (class N)
Fineness by sieve #325 (45µm) (% retained)	< 20	< 20	19.65	7.64	8.14
Pozzolanic activity with lime (MPa) [32]	≥ 6	≥ 6	4.14	6.28	11.53
Pozzolanic activity with cement (%) [33]	≥ 90	≥ 90	83	90	137
$SiO_2 + Al_2O_3 + Fe_2O_3$ (%)	≥ 50	≥ 70	68.02	68.02	93.6
SO_3 (%)	≤ 5	≤ 4	0.21	0.21	0.2
Loss on ignition (%)	≤ 6	≤ 10	0.55	0.55	2.5
Available alkalis in Na_2O_{eq}* (%)	≤ 1.5	≤ 1.5	19.43	19.43	1.38

* $Na_2O_{eq} = Na_2O + 0.658\ K_2O$

the pozzolan reduces the quantity of free ions in the solution and, consequently, diminishes its conductivity. From the difference of conductivity, it was possible to classify the material according to its pozzolanic activity, where materials which presented a variation of conductivity above 0.4 mS/cm can be classified as pozzolans. Figure 3 shows that the ground glass sludge (GS2), as well as metakaolin, can be classified as materials containing pozzolanicity materials according to the method of Luxán et al. [30]. It is also possible to compare the materials used in this research with other materials commonly used in concrete structures, such as: ornamental rock residues and active silica.

It can be observed that the glass powder did not comply with the standard ABNT NBR 12653 [29] regarding the available alkalis content, presenting significantly higher values (Table 2). This observation motivated the execution of tests to assess the ASR, which can cause expansive mechanisms and concrete cracking. The ASR occurs during the hydration process, due to the reaction between reactive aggregates and the alkalis present in the cement and glass powder [14]. Furthermore, it was noted that the GS1 did not fulfill the pozzolanic activity tests with lime [32] and cement [33], fact that was corroborated by the Luxán et al. [30] method. Therefore, a preliminary study was performed to assess the necessary grinding time in a ball mill. The required time reached was 2 h, reducing the retained percentage in sieve # 325 (45 µm) from 19.65 to 7.64% (maximum reduction obtained) (Figure 4a). The GS2 (Figure 4b) and GS1 aspect (Figure 4c) are also presented. Figures 4d and 4e show the microscopic analysis of the ground residue where its angular geometry and particle sizes ranging from 2 µm to 10 µm can be identified.

After this process, the resulting product was a ground waste, called GS2, finer than metakaolin, which complied with the required limits to be classified as a pozzolanic material according to all tests performed [30,32,33] (Table 2).

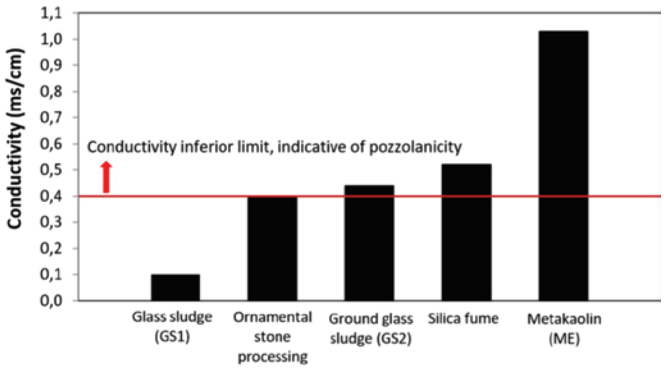

Figure 3
Pozzolanicity test as according to Luxán *et al.* [30] for the materials used in this study (GS1, GS2, ME) and other similar materials

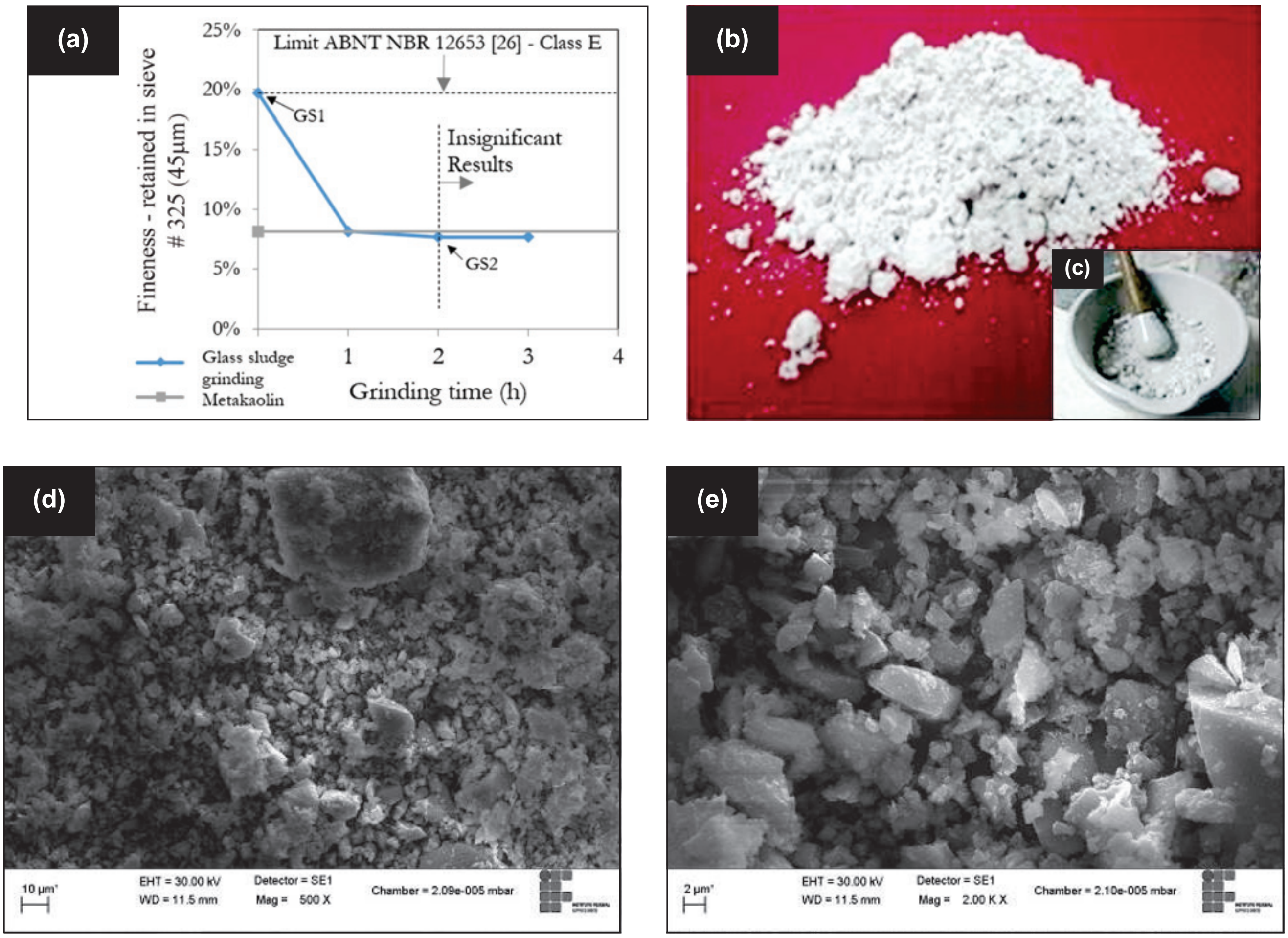

Figure 4
(a) Waste grinding time study; (b) GS2 (ground sludge), (c) GS1 (without grinding), (d) GS2 micrograph 500x; and (e) GS2 micrograph 2000x

2.4 Specimens preparation

Mixtures containing 10 and 20% of glass sludge waste as partial substitute for cement (by volume) were used, adopting the waste without grinding (GS1) and after grinding (GS2) (Table 3). The cement replacement by metakaolin (ME) was also evaluated at the same contents, for comparative reasons, and the metakaolin combined with both glass powders (GS1ME and GS2ME) (Table 3) with aim of intensifying the mechanical and durability properties. The water/cementitious materials ratio (w/cm) used was 0.60, this being the highest accepted in the standard ABNT NBR 6118 [34] in urban applications. Furthermore, at this w/cm ratio, a concrete of high porosity could be obtained, making it easier assess the possible pore-filling effects of the cement replacement by waste glass. Since the density of the waste glass powder and metakaolin is less than that of the cement, a volumetric compensation was used. It is important to note that the amount of water was maintained from the control mixture, considering the water/cement ratio of 0.60, changing the water/binder ratio for the other mixtures thereafter. The dosage method adopted was the IPT-EPUSP Method. Cylindrical specimens of 100 × 200 mm (diameter x height) were prepared, according to standard ASMT C192 [35], and cured in a moist chamber with relative humidity higher than 95% and temperature of 23 ± 2 ºC, until the testing day. The concrete fresh properties were assessed using slump test, according to ASMT C143 [36], and density measurement, according to ASMT C138 [37]. The slump value used for the control mixture was 200 ± 10 mm. This value, from the batching and consistency study, was adopted to compensate the reduction of the slump caused by the incorporation of fine and not immediately reactive materials (metakaolin and glass powder). Thereby, an appropriate workability was obtained for the preparation of specimens, since the use of superplasticizer was not considered for the study in order to not add new variables that might hamper the results identification.

2.5 Methods

2.5.1 Mechanical strength tests

The specimens were cured in a moist chamber until the testing ages of 28, 56 and 91 days. The upper and lower parts were polished for levelling, and then the specimens were submitted to the compressive test, according to standard ABNT NBR 5739 [38].

2.5.2 Rapid chloride permeability test (RCPT)

The rapid chloride permeability test (RCPT) was idealized by Whiting [39], and it is recommended by standard ASTM C1202 [40]. For each mixture, three specimens – 50 mm thick and 100 mm in diameter, extracted from the central part of the single original cylinder specimen – were tested at 28 and 91 days. The test consisted in exposing one side of the specimen to a sodium chloride solution (3% NaCl by mass) and the other to a sodium hydroxide solution (0.3 N NaOH). In each solution, a conducting copper electrode was introduced, and connected to a 60 V ± 0,1 V source, creating an electrical current that induced the chlorides to migrate through the concrete specimen. Amperage readings were taken every 30 min, totaling 6 h of testing. The sum of the electrical current by time, expressed in coulombs, specified the total charge passed through the specimen, indicating the chloride penetration resistance of the concrete.

2.5.3 Rapid migration test (RMT)

Proposed by Luping and Nilsson [41] and consolidated in the standard NT BUILD 492 [42], this method uses as procedures the potential difference and a colorimetric indicator (spray of $AgNO_3$ – 0.1 M). It provides quantitative data on the final chloride penetration depth and chloride diffusion coefficient. Specimens 50 mm thick and 100 mm in diameter, extracted from the central part of the single original cylinder specimen, were tested at 56 and 91 days. The specimens were exposed to sodium chloride solution (2N NaCl) on one side

Table 3
Mixture proportions for 1 m³ of concrete

Mix design	Cement replacement (%) (by volume)	Cement (kg/m³)	Glass sludge (GS1) (kg/m³)	Ground glass sludge (GS2) (kg/m³)	Metakaolin (ME) (kg/m³)	Fine aggregates (kg/m³)	Coarse aggregates (kg/m³)	Mixture density (kg/m³)	Water content (kg/m³)
Control	0	302.85	—	—	—	875.24	1133	2420	181.71
GS1-10	10	272.57	24.77	—	—	875.24	1133	2402	181.71
GS1-20	20	242.28	49.57	—	—	875.24	1133	2371	181.71
GS2-10	10	272.57	—	24.77	—	875.24	1133	2391	181.71
GS2-20	20	242.28	—	49.57	—	875.24	1133	2430	181.71
ME-10	10	272.57	—	—	25.17	875.24	1133	2396	181.71
ME-20	20	242.28	—	—	50.30	875.24	1133	2396	181.71
GS1ME-10	10	272.57	12.42	—	12.72	875.24	1133	2423	181.71
GS1ME-20	20	242.28	24.77	—	25.17	875.24	1133	2409	181.71
GS2ME-10	10	272.57	—	12.42	12.72	875.24	1133	2409	181.71
GS2ME-20	20	242.28	—	24.77	25.17	875.24	1133	2412	181.71

and on the other to sodium hydroxide solution (0.3 N NaOH). The test duration and the voltage adopted depended on the initial passing current reading in the concrete specimen when applying a different potential of 30 V. Usually, the test can last from 24 h, for ordinary concrete, to 96 h, for high performance concrete. To calculate the apparent chloride ion migration coefficient, Equation 1 was used.

$$D_{nssm} = \frac{0.0239\,(273+\mathrm{T})\mathrm{L}}{(\mathrm{U}-2)\mathrm{t}}\,\left(X_d - 0.0238\sqrt{\frac{(273+\mathrm{T})Lx_d}{(\mathrm{U}-2)}}\,\right) \quad (1)$$

Where: D_{nssm} is the non-steady-state migration coefficient multiplied by 10-12 (m^2/s); U is the absolute value of the applied potential (V); T is the average value of the initial and final temperatures in the anolyte solution (ºC); L is the thickness of the specimen (mm); x_d is the average value of the chloride penetration depth (mm), and t is the test duration (h).

2.5.4 Bulk diffusion test (BDT)

The method for determining the apparent chloride diffusion coefficient on cementitious mixtures by bulk diffusion is based on the NT BUILD 443 [43] and consists in keeping the concrete specimens immersed in a chloride solution (165g of NaCl by litre) to induce accelerated diffusion mechanisms. The immersed test specimens (100 mm thick and 100 mm in diameter) were placed in a hermetically sealed plastic container, the solution being agitated weekly. The specimens were cured for 28 days in a moist chamber and subsequently immersed in the solution for 60, 120 and 180 days. The chlorides profile was obtained by milling the material in layers parallel to the exposed surface. The thickness of the layers was adjusted according to the expected chloride profile, such that at least six places encompassed the profile between the exposed surface and the depth reached by the chlorides. The content of chloride soluble in acid in the specimens was determined according to NT BUILD 208 [44]. The test results, superficial chlorides concentration (C_s) and non-steady-state chlorides diffusion coefficient (D_{ns}) – also entitled chloride apparent diffusion coefficient (D_a) [21] – were determined by adjusting Equation 2 for the chlorides content measured, using a linear regression analysis according to the least squares.

$$C_{(x,t)} = C_s - (C_s - C_i)\,.\,erf\left(x/\sqrt{4.D_a.\mathrm{t}}\right) \quad (2)$$

Where: C (x, t) (mass, %) is the chlorides concentrations, measured at the depth x at the exposure time t; Cs (mass, %) is the boundary condition of the exposed surface; Ci (mass, %) is the initial chlorides concentration measured; x is the depth below the exposed surface (m); Da is the chloride apparent diffusion coefficient (m^2/s); t is the exposure time (s); erf is the Gauss error function.

2.5.5 Alkali-silica-reaction (ASR) - expansion measurement

This test provides means of detecting the alkali-silica reactivity potential in concrete, which can cause harmful expansion mechanisms and deleterious processes, such as concrete cracking. Three prismatic specimens (25 x 25 x 285 mm) were used for each mixture, as according to ABNT NBR 15577-4 [45]. The specimens were demolded 24 h after their casting, and submerged in water at 80 ºC for 24 h. Subsequently, they were submerged in a solution of

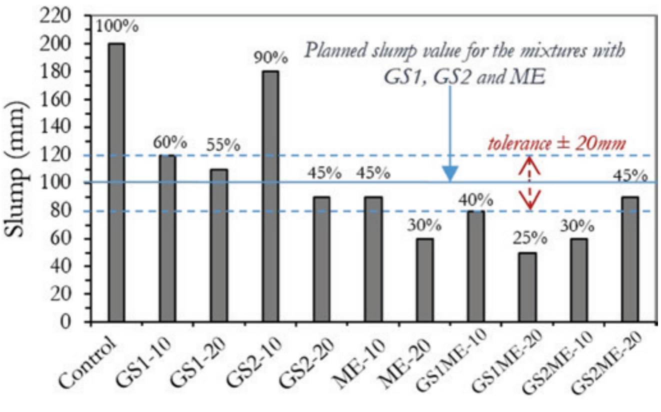

Figure 5
Slump values of the analyzed concrete mixtures

NaOH (1N) at 80 ºC and their initial lengths were registered. During 30 days, length readings were performed with the frequency of 3 days. The mentioned standard considers that if the expansion is higher or equal to 0.19% at 30 days, the aggregate is considered potentially reactive.

3. Results and discussions

3.1 Slump tests

The Figure 5 presents the slump values of the concrete mixtures. By using the glass sludge without grinding (GS1) and after grinding (GS2) there is a reduction in the slump value in comparison with the control mixture, as also found in other studies [46-48]. However, it was still an adequate workability (100 ± 20 mm) to produce the concrete specimens and for the conventional applications of reinforced concrete, placed without pumping (ABNT NBR 8953 [49]). The use of materials with elevated superficial area and which do not react immediately in the mixture increases the demand for water in the fresh concrete. Thus, the use of very fine materials, as it is the case of the glass powder (average particle size 35-45 µm) used in this study, confirms this mentioned effect, which can also be related to the poor geometry of the waste glass.
According to Ismail and Al-Hashmi [46], the reduction in the slump value can also be attributed to the geometry of the glass powder, resulting in a lower fluidity of the mixtures. Furthermore, mixtures with glass powder (GS1 and GS2) presented higher slump value than those mixtures that used metakaolin, indicating the lower demand for water of the glass sludge compared to metakaolin.

3.2 Mechanical strength tests

A compressive strength loss was identified at 28 days by replacing the cement by GS1 (Figure 6), as also verified in previous studies [10-13, 25]. Nevertheless, the concrete using the ground waste at 10 and 20% cement replacement (GS2-10 and GS2-20), presented similar values to the control mixture, without significant statistical variation. It is also observed that the combination of the glass sludge waste with metakaolin, at 10% cement replacement

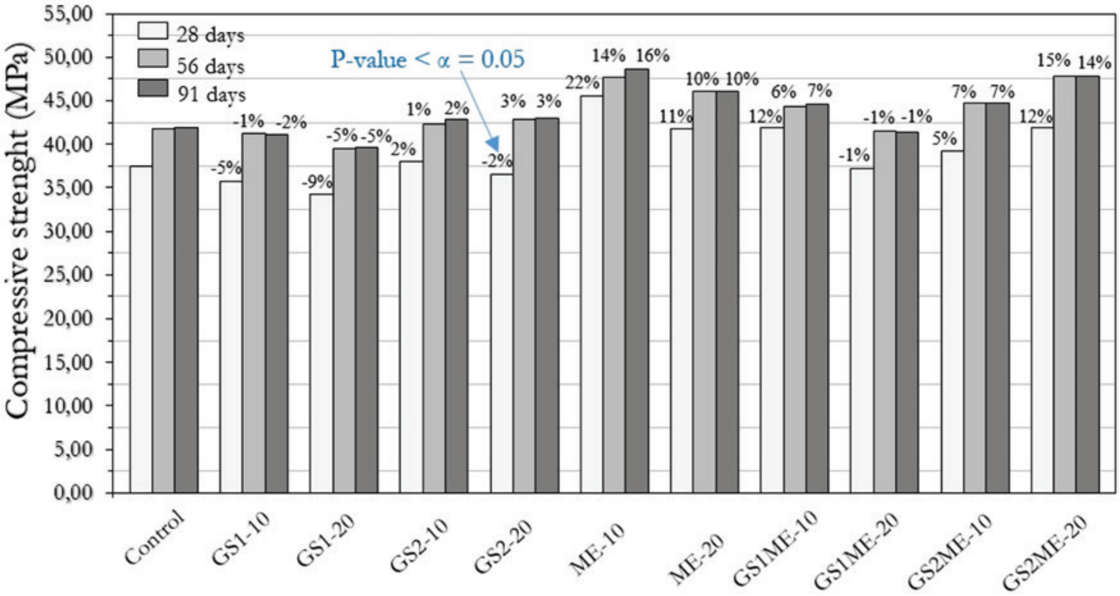

Figure 6
Concrete compressive strength results

each (GS2ME-20), presented an increase in compressive strength of 12% at 28 days, compared to the control mixture. Moreover, the positive effect of using glass powder can be seen at more advanced ages. At 56 and 91 days, the mixture with 20% ground glass powder (GS2-20) had results slightly higher than those of the control mixture. These results can be explained by the physical effect of pore-filling, where the empty pores left by the cement paste are filled by the glass particles, reducing the porosity, and contributing to the retention of the mixture water, enhancing the cement hydration process. Another process that may have contributed to the compressive strength gain is the possible pozzolanic effect of the glass waste. This possible chemical reaction between the glass powder and the cement (due to the formation of more stable compounds, such as the production of C-S-H originated from the reaction of calcium hydroxide and water) diminishes the empty spaces in the transition zone between the paste and the aggregates. Moreover, the GS2ME-20 presented superior values to that of the control mixture at all ages, and at 56 and 91 days, its values were similar to the mixture containing only metakaolin as a cement replacement, at 20% (ME-20). Thus, replacing the use of 10% metakaolin by glass waste is justified, promoting also possible economic and environmental aspects.

The ANOVA showed that there is a statistically significant (p-value < 0.05) reduction in the compressive strength as the glass sludge without grinding (GS1) content increases (Fig. 7a). Thus, initially indicating that the cement replacement by glass powder

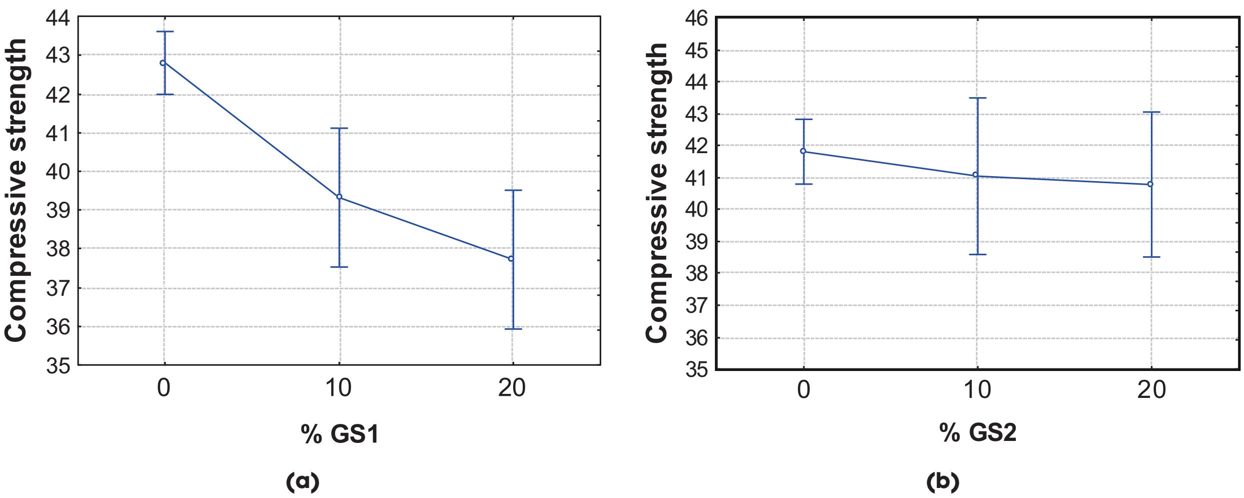

Figure 7
Statistical analysis of concrete with glass wastes. (a) mixtures with GS1 (b) mixtures with GS2

Table 4
Statistical analysis of the compressive strength of concrete with GS2

Factors	SS	DF	MS	F	p-value	Results
GS2 content	10.30	2	5.15	0.447	0.641849	Non-Significant
Age	199.92	2	99.96	8.676	0.000550	Significant
Error	610.66	53	11.52	—	—	—

without grinding did not cause a positive effect on the compressive strength. This is possibly due to the non-pozzolanic effect of the material (as observed in the pozzolanic activity tests – Table 2), combined with the fact the pore-filling effect was not sufficient to compensate the strength loss caused by the cement content reduction. It became necessary the identification of which treatments presented the variation; thus, the Tukey's test verified that the GS1 provided similar results to that of the control mixture. Therefore, indicating that it is possible to replace the cement by the GS1 without reducing the concrete strength, at up to 10%, whereas at 20% replacement, a loss in compressive strength is verified. Additionally, using this statistical analysis to the GS2, it is noted that there is no significant difference between the concrete with and without the waste, since the GS2 content in the compressive strength presented p-value of 0.642 (> 0.05) (Fig. 7b and Table 4). Hence, it is possible to replace the cement by up to 20% of ground glass powder without negative effects in the compressive strength. This performance can be justified due to the pozzolanic reaction with the cement hydrated compounds, as identified in the pozzolanic activity tests performed in the ground waste (Table 2).

3.3 Rapid chloride permeability test (RCPT)

The use of glass powder in the contents of 10 and 20% increased the chloride penetration resistance of the mixture, by reducing the total charge passed (Figure 8), as noted in previous studies [11-16]. It is noted that both GS1, by the pore-filling effect, and GS2, by the pore-filling and the possible pozzolanic activity effect, produced a reduction in the total charge passed in the mixtures in comparison with the control, being the GS2 the most effective. The mixture with 10% glass sludge without grinding (GS1-10) did not reach a moderate level of chloride penetrability; nevertheless, it reduced the charge passed by 13 and 30% at 28 and 91 days, respectively, in comparison with the control. For 20% content (GS1-20), at 91 days it is verified a reduction of 83% compared to the control, being equivalent to the reduction obtained by the mixtures with ground waste (GS2-20, with 80% reduction) and metakaolin (ME-10, with 84% reduction, and ME-20, with 79%). Figure 8 presents the qualitative classification used by the test standard and classifies GS1ME-20 and ME-10 as of very low chloride penetrability level, a significant reduction from the high level observed for the control mixture. This may be due to the combined effect of the metakaolin pozzolanic activity and the pore-filling effect caused by the waste. Furthermore, at 10% glass powder, the chloride resistance is improved with the grinding of the glass waste (GS2-10), and the increase of glass powder content also improves the chloride resistance.
According to the qualitative assessment proposed by Gjørv [50], the GS1-10 did not reach a moderate resistance to chloride

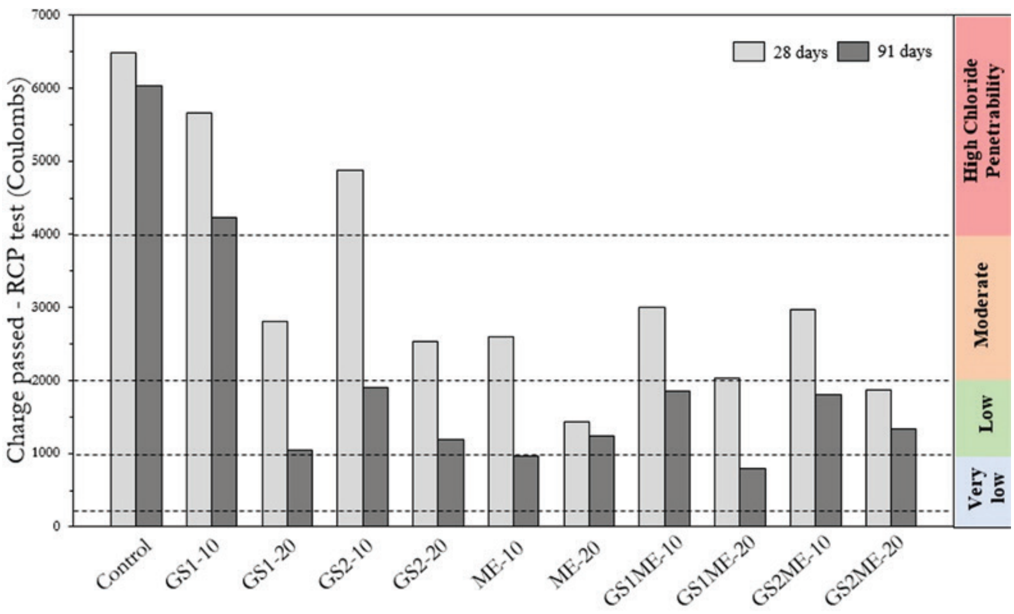

Figure 8
Total charge passed results and chloride resistance classification

penetration (Figure 9), corroborating the results from total charge passed (ASTM C 1202 [40]). Thus, to improve the resistance to chloride penetration with 10% glass sludge waste addition, it was needed to grind the material (GS2-10), or to use it in combination with 10% metakaolin (GS1ME-20), replacing 20% of cement. The increase of glass sludge content to 20% (GS1-20) provided improvements in chloride resistance, advancing the classification to high chloride resistance at 56 days and very high at 91 days. At 56 days, the reductions in the chloride migration coefficient in comparison to the control mixture were 18% for GS1-10 and 78% for GS1-20; whereas at 91 days, these reductions were 22 and 85% for GS1-10 and GS1-20, respectively. This evolution can be attributed to the mechanism of pore-filling. Furthermore, the use of ground glass sludge waste in the contents of 10 and 20% (GS2-10 and GS2-20) provided improvements in chloride resistance comparable to those caused using metakaolin.

Thus, it can be confirmed, just as previous studies [11,12,15] that have used the RMT test (NT BUILD 492 [42]), that the glass powder use as a cement replacement at 20% content provides an improvement in chloride penetration resistance, mainly at 56 days. This delayed influence in the improvement of concrete microstructure can be attributed to the pozzolanic effect or to the pore-filling effect. For the control mixture, no variation in chloride resistance from 56 to 91 days is noted, whereas for the glass sludge and metakaolin mixtures, increases in chloride resistance are observed.

Pignaton [25] performed a microstructural analysis in concrete containing a glass sludge waste equivalent to the one used in this study at similar replacement contents; but without grinding the waste. The analysis focused on assessing the interfacial transition zones between the coarse aggregate and the cement paste after 28 days age. It was noted that the partial replacement of cement by GS1 at 20% content provided a reduction in the cement matrix porosity and the interfacial transition zones were reinforced by crystalline formations due to the chemical reaction with the glass powder in the hydration process. Furthermore, the concrete have not presented any cracking that could indicate the production of expansive gel or ASR.

This study assessed the microstructure of concrete with the ground waste (GS2) and metakaolin (ME) focusing on the improvement of the interfacial transition zone between cement paste and aggregate (Figure 10). 500x, 1000x and 3000x enlargements were used. The scanning electron microscope (SEM) images (Figure 10) shows that the mixtures with GS2 and ME presents a more compact structure with fewer pores in relation to the REF. The formation of fibrous C-S-H crystals filling the pores among the hydrated cement particles is verified, explaining the improvement in the durability properties of the mixtures. In the GS2-2- and ME-20 mixtures, the GS2 and ME particles were encapsulated and dispersed in the gel hydrated compounds (Figure 10f and 10i). Furthermore, no cracking due to the possible expansive reaction of the waste glass was found.

3.5 Bulk diffusion test (BDT)

Figure 11 presents the linear regression analysis of the chloride content through the concrete depths, from the diffusion by immersion test according to NT BUILD 443 [43]. The use of GS1 and GS2 provided a reduction in the chloride content through the concrete, and these reductions are greater for increased contents of glass powder (Figure 11a and 11b). In Figure 11c, by analyzing the mixtures with glass powder at 20% content (GS1-20 and GS2-20), the grinding presented itself as a determinant factor, the ground waste being

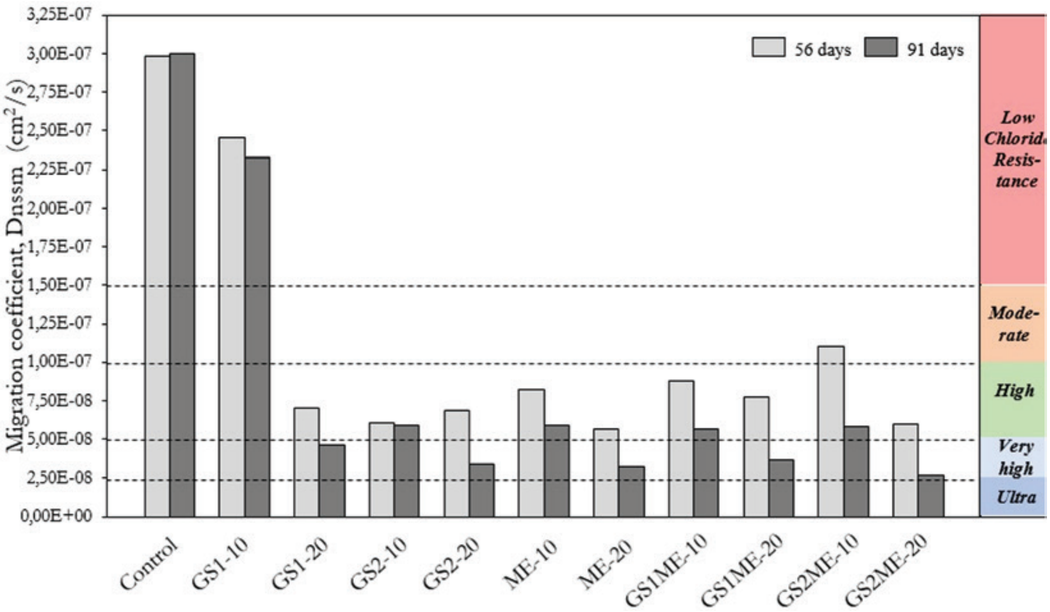

Figure 9
Non-steady-state chloride migration coefficient and chloride resistance classification

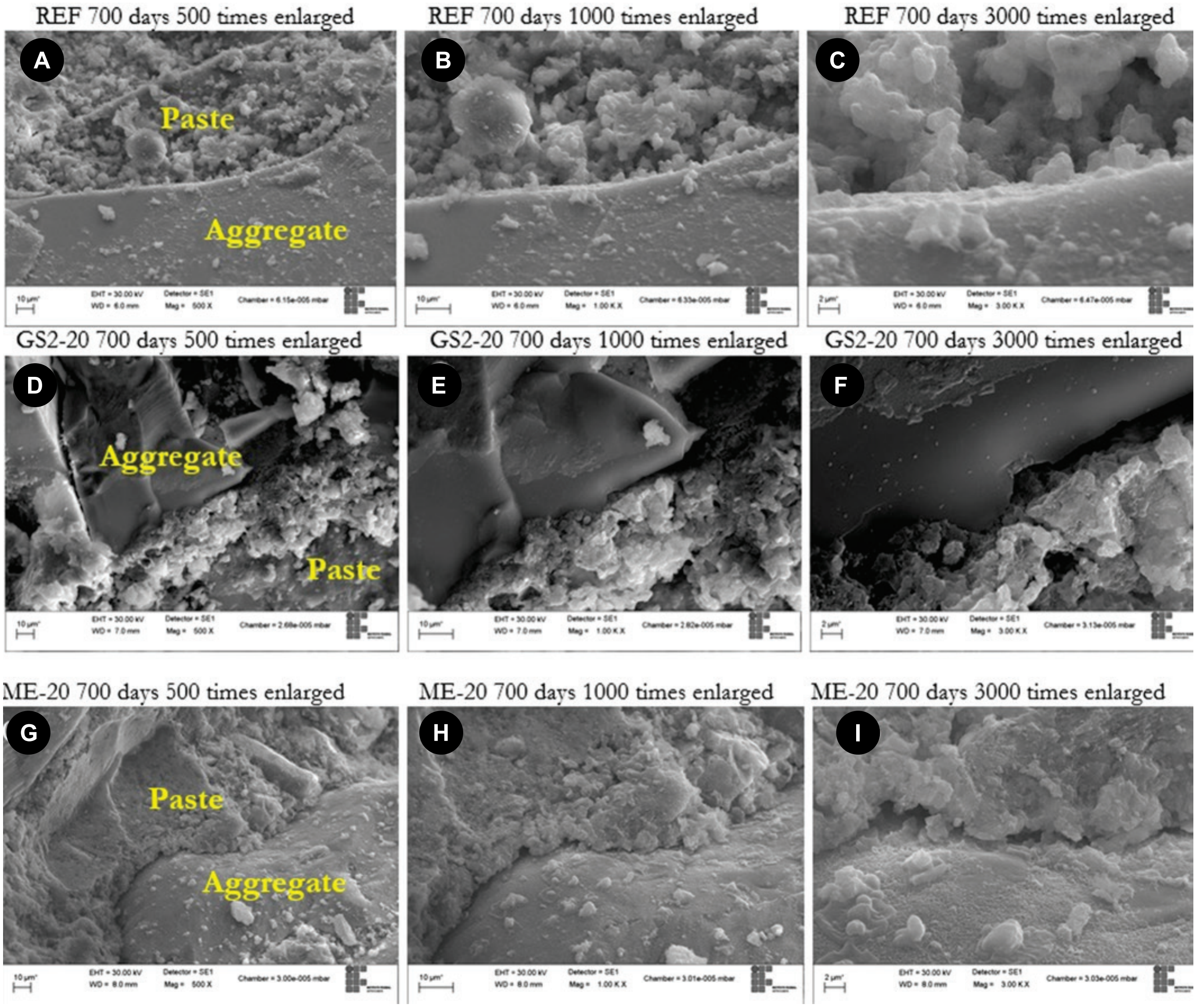

Figure 10
Microstructure analysis of concrete mixtures with GS2 and ME. (a) REF (500x magnification); (b) REF (1000x magnification); (c) REF (5000x magnification); (d) GS2-20 (500x magnification); (e) GS2-20 (1000x magnification); (f) GS2-20 (5000x magnification); (e) ME-20 (500x magnification); (f) ME-20 (1000x magnification); (g) ME-20 (5000x magnification)

more efficient for chloride resistance.

From the liner regression analysis, it was possible to calculate the diffusion coefficients identified in Figure 12, as defined in NT BUILD 443 [43]. For comparative purposes, Figure 12 also presents the results of chloride diffusion coefficients obtained from NT BUILD 492 [42] test for the age of 56 days. Additionally, the limits for the qualitative assessment proposed by Gjørv [50] are also presented. From the test results of chloride diffusion (NT BUILD 443 [43]) and migration (NT BUILD 492 [42]), it is verified that the use of glass powder and metakaolin provided an increase in chloride resistance, especially in the mixtures using the ground glass powder and 10 and 20% (GS2-10 and GS2-20). Additionally, the GS2 provided similar values to those of metakaolin. The GS2ME-20 mixture (GS2 and ME at 10% each) presented the lowest diffusion coefficients, surpassing even the mixtures with only metakaolin. This mixture presented as very effective due to the combination of pozzolanic effect of both materials along with the pore-filling effect. According to Zibara et al. [51], the chloride diffusion through the concrete depends mainly on its microstructure and ions fixation capability. For mixtures with ordinary Portland cement, the key fixation mechanism is the formation of Friedel's salt and aluminates related complexes [52]. The anhydrous compounds of cement which react quickly with the chloride ions producing the Friedel's salt is the tricalcium aluminate (C3A). In concrete with SCM, it is indicated that the fixation capability is function of the aluminates content [53]. Thus, the metakaolin, by having in its chemical composition 33.10% alumina (Al_2O_3) (Table 1), fosters the formation of C_3A compounds and helps to increase the chloride ions fixation.

It was also observed that the chloride diffusion coefficients obtained from NT BUILD 443 [43] were higher than the chloride migration coefficients obtained from NT BUILD 492 [42] (Figure 14). This can be explained by the time difference of testing, where for the migration test the mixtures were cured for 56 days (concrete age with a more developed microstructure), and for the diffusion test, the specimens were cured for 28 days and then exposed 180 days to the chloride solution, providing more time for the chloride to propagate; a different adopted time frame from the used in studies that aimed at assessing the correlation between both tests [21, 23]. The BDT (NT BUILD 443) is relevant for the comparison among different concrete of the same study due to be an alternative accelerated method which do not require the use of electrical currents and the adoption of colorimetric indicators – procedures used by RMT (NT BUILD 492 [42]) which are criticized by some researchers [21-23]. From this comparison of results, it can be noted that by adopting a content of cement replacement of 20%, the glass powder can be used without grinding (GS1), presenting increases in chloride penetration resistance, comparable to the values obtained in the mixtures with metakaolin use. Moreover, this chloride resistance can be further increased if the waste is ground (GS2).

3.6 Alkali-silica-reaction (ASR) –

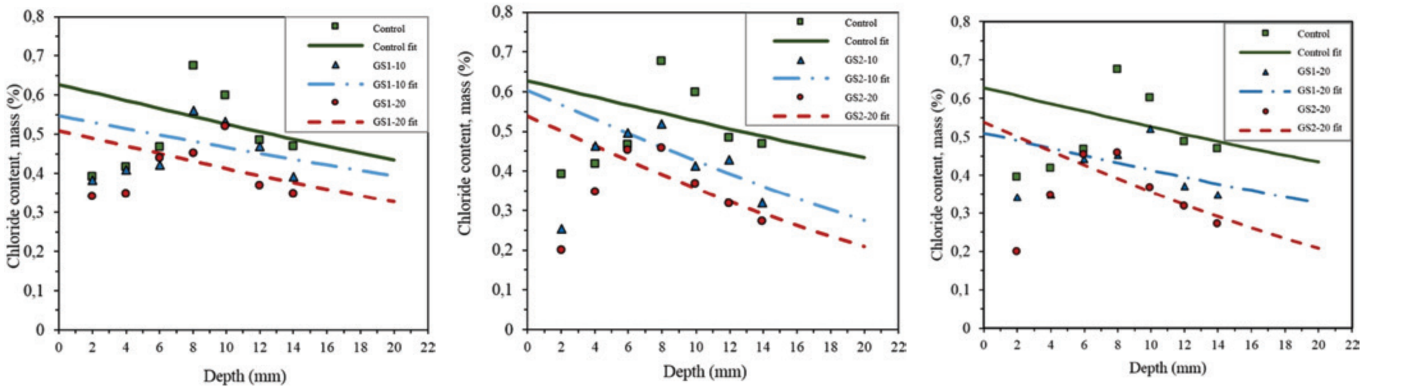

Figure 11
Linear regression analysis of chloride content through concrete depths. (a) Glass sludge waste without grinding (GS1); (b) Ground glass sludge waste (GS2); (c) GS1 and GS2 at 20% content

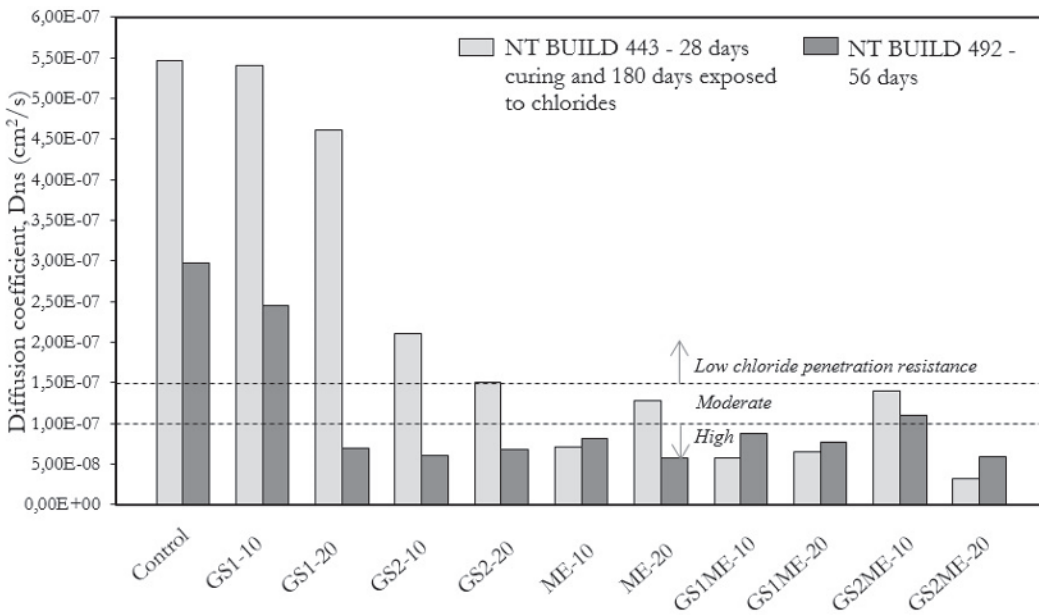

Figure 12
Chloride diffusion coefficient results as according to NT BUILD 443 and NT BUILD 492

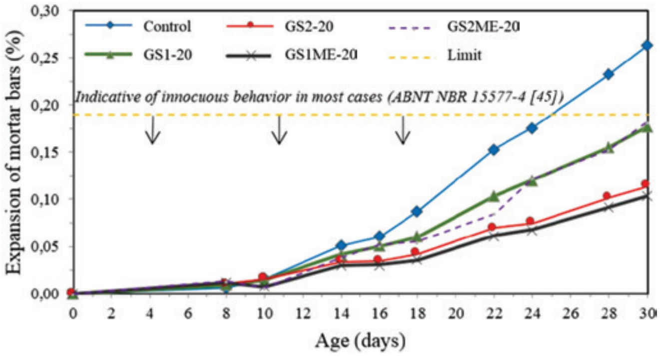

Figure 13
Expansion of mortar bars produced with waste glass and metakaolin

Expansion measurement

The expansion results of mortar bars immersed for 30 days, as according to ABNT NBR 15577-4 [45], can be seen in Figure 13. It its verified that the glass powder, despite presenting a greater quantity of available alkalis than is required by the standard to be classified as a pozzolanic material, did not cause an increase in ASR related expansion. In fact, there was a reduction in the expansion due to the use of glass powder, and this was more prominent in the GS2. This behavior supports the results from other studies [16, 19], which stated that the glass powder, as a function of its particle dimensions, can cause a mitigation of ASR in concrete. According to Shayan and Xu [16], the use of glass microparticles tends to inhibit the ASR, thereby indicating that the quantity of available alkalis in the glass powder does not necessarily contribute to ASR. This is explained by the encapsulation of alkalis in the paste, which are unable to react. Additionally, the high silica content is circumvented by the fact that the high surface area and the amorphous state of the glass induced the silica to react with the calcium hydroxide in the early ages. Thus, there was not enough silica in advanced ages for further reactions. Furthermore, the GS1ME-20 favored the reduction of the ASR related expansive behavior. According to Matos and Sousa-Coutinho [12], the use of SCM can reduce the deleterious effect of the expansion caused by ASR. This is attributed to the reduction of calcium hydroxide concentration in the pores solution, due to pozzolanic reactions, resulting in a densification of the microstructure, fostering lower alkali mobility and quantity in the pores solution.

4. Conclusions

1. The mixtures containing glass sludge waste presented a reduction in workability in comparison with the control mixture, further noticed with increase of the content. Nevertheless, the slump values were higher than the mixtures containing only metakaolin.
2. The use of glass waste, originated from stoning and polishing of glass, generally did not cause a reduction in compressive strength with statistical significance (with exception to the glass without grinding at 20%, GS1-20), and provided durability improvements. The resistance to chloride penetrability was improved, evidenced by chloride ions diffusion and migration tests. Additionally, the ASR potential was reduced by using the glass powder, and further diminished by grinding the glass waste.
3. Many advantages in incorporating the ground glass sludge waste as a cement replacement at 20% (GS2-20) were verified. Its use did not cause significant influence on compressive strength and provided significant improvements in chloride penetration resistance. The reductions obtained in comparison with the control mixture were 80% in total charge passed, 89% in chloride migration coefficient, 73% in chloride diffusion coefficient and 58% in ASR related expansion.
4. The combined use of metakaolin and ground glass sludge waste at 10% each (GS2ME-20) presented the best performance among the mixtures which contained glass sludge waste, providing more than 12% increase in compressive strength and more than 74% reduction in chloride penetrability. It can also be an alternative to the isolated use of metakaolin (ME-20), since equivalent values of compressive strength and chloride resistance were observed. Thus, financial and environmental benefits may be attained.
5. This study concludes that the incorporation of ground glass sludge waste, a waste from the process of stoning and polishing of glass, can be adopted in reinforced concrete structures without detriments in the mechanical properties and providing an increase in durability in structures in an urban maritime environment. The material can replace the cement up to 20%, without affecting the compressive strength at 28 days, and reducing the chloride penetration by up to 90%, besides providing a reduction in ASR-related expansion.

5. Acknowledgements

This work was supported by the Coordination for the Improvement of Higher Education Personnel (CAPES). The authors would like to express their sincere thanks to LEMAC-UFES (Building Materials Tests Laboratory) and IFES for the testing equipment and to the companies Holcim, Viminas and Metacaulim do Brasil for providing the cement, waste glass and metakaolin, respectively, used in this study.

6. References

[1] A. André, J. Brito, A. Rosa, D. Pedro, Durability performance of concrete incorporating coarse aggregates from marble industry waste, J. Clean. Prod. 65 (2014) 389-396.

[2] D.F. Aponte, M. Barra, E. Vàzquez, Durability and cementing efficiency of fly ash in concrete. Constr. Build. Mater. 30 (2012) 537-546.

[3] M.C. Bignozzi; A. Saccani, L. Barbieri, I. Lancelloti, Glass waste as supplementary cementing materials: The effects of glass chemical composition, Cem. Concr. Compos. 55 (2015) 45-52.

[4] T. Gupta, S. Chaudhary, R.K. Sharma, Mechanical and durability properties of waste rubber fiber concrete with and without silica fume, J. Clean. Prod. 112 (2016) 702-711.

[5] L. Bernstein et al., Chapter 7: Industry, in: B. Metz et al.

(Eds.), Climate Change 2007: Mitigation-Contribution of Working Group III to the Fourth Assessment Report of the Intergovernmental Panel on Climate Change, Cambridge University Press, Cambridge, United Kingdom and New York, USA, 2007, pp. 447-496.
[6] C. Shi, K. Zheng, A review on the use of waste glasses in the production of cement and concrete, Resour. Conserv. Recycl. 52 (2007) 234-247.
[7] Y. Jani, W. Hogland, Waste glass in the production of cement and concrete – A review, J. Environ. Chem. Eng. 2 (2014) 1767–1775.
[8] M. Saito, M. Shukuya, Energy and material use in the production of insulating glass windows, Sol. Energy 58 (1996) 247–252.
[9] A.M. Matos, Estudo de argamassas com substituição parcial de cimento por resíduos de vidro moídos, Engineering School, Universidade do Porto, Porto, Portugal (2010). (In Portuguese)
[10] R. Nassar, P. Soroushian, Strength and durability of recycled aggregate concrete containing milled glass as partial replacement for cement, Constr. Build. Mater. 29 (2012) 368-377.
[11] M. Kamali, A. Ghahremaninezhad, Effect of glass powders on the mechanical and durability properties of cementitious materials, Constr. Build. Mater. 98 (2015) 407-416.
[12] A. M. Matos, J. Souza-Coutinho, Durability of mortar using waste glass powder as cement replacement. Constr. Build. Mater. 36 (2012) 205-215.
[13] N. Schwarz, H. Cam, Influence of fine glass powder on the durability characteristics of concrete and comparison to fly ash, Constr. Build. Mater. 30 (2008) 486-496.
[14] J. Cassar, J. Camiller, Utilization of imploded glass in structural concrete, Constr. Build. Mater. 29 (2012) 299-307.
[15] J.A. Jain, N. Neithalath, Chloride transport in fly ash and glass powder modified concrete – Influence of test methods on microstructure, Cem. Concr. Compos. 32 (2010) 148-156.
[16] A. Shayan, A. Xu, Performance of glass powder as a pozzolanic material in concrete: a field trial on concrete slabs, Cem. Concr. Res. 36 (2006) 457–68.
[17] A. Khmiri, B. Samet, M. Chaabouni, A cross mixture design to optimise the formulation of a ground waste glass blended cement, Constr. Build. Mater. 28 (2012) 680-686.
[18] W. Jin, C. Meyer, S. Baxter, "Glascrete" – concrete with glass aggregate, Am. Concr. Inst. Mater. J. 97 (2000) 208-213.
[19] K. Hwee, H. Du, Use of waste glass as sand in mortar: Part II –Alkali-silica reaction and mitigation methods, Cem. Concr. Compos. 35 (2013) 118-126.
[20] A.M. Matos, T. Ramos, S. Nunes, J. Souza-Coutinho, Durability Enhancement of SCC with Waste Glass Powder, Mater. Res. 19 (2016) 67-74.
[21] D. Henry, V. Baroghel Bouny, T. Chaussadent, Evaluation of chloride penetration into concrete by various methods, Proceeding of the Second International RILEM Workshop on Testing and Modelling the Chloride, Paris, France, 2000, pp. 471-486.
[22] T. Luping, H.E. Sørensen, Evaluation of the Rapid Test Methods for Measuring the Chloride Diffusion Coefficients of Concrete, NORDTEST Project Nº 1388-98, Swedish National Testing and Research Institute Building Technology, 1998.
[23] T. Luping, H.E. Sørensen, Precision of the Nordic test methods for measuring the chloride diffusion/migration coefficients of concrete, Mater. Struct. 34 (2001) 479-485.
[24] J. Kim, J.-H. Moon, J.W. Shim, J. Sim, H.-G. Lee, G. Zi, Durability properties of a concrete with waste glass sludge exposed to freeze-and-thaw condition de-icing salt. Constr. Build. Mater. 66 (2014) 398-402.
[25] A.A. Pignaton, Potencialidades do aproveitamento do resíduo de estação de tratamento de efluentes do processo de lapidação do vidro sodo - cálcico na produção de concretos, Technological Center, Universidade Federal do Espírito Santo, Vitória, Brazil (2012). (In Portuguese)
[26] H. Lee, A. Hanif, M. Usman, J. Sim, H. Oh, Performance evaluation of concrete incorporating glass powder and glass sludge wastes as supplementary cementing material, Journal of Cleaner Production, 170 (2018) 683-693
[27] P. Chindaprasirt, C. Jaturapitakkul, T. Sinsiri, Effect of fly ash fineness on compressive strength and pore size of blended cement paste, Cem Concr Compos 27 (2005) 425–428.
[28] H. Jun-yuan, B.E. Scheetz, Della M. Roy, Hydration of fly ash-Portland cements, Cem Concr Res 14 (1984) 505–512.
[29] Associação Brasileira de Normas Técnicas, ABNT NBR 12653: Materiais Pozolânicos – Especificação, Rio de Janeiro, Brazil. (2015). (In Portuguese)
[30] M.P. Luxán, F. Madruga, J. Saavedra, Rapid evaluation of pozzolanic activity of natural products by conductivity measurement, Cem. Concr. Res. 19 (1989) 63-68.
[31] C.S. Rodrigues, Efeito da adição de cinza de casca de arroz no comportamento de compósitos cimentícios reforçados por polpa de bambu, Pontifícia Universidade Católica do Rio de Janeiro, Rio de Janeiro, Brazil. (2004). (In Portuguese)
[32] Associação Brasileira de Normas Técnicas, ABNT NBR 5751: Materiais pozolânicos - Determinação de atividade pozolânica com cal aos sete dias, Rio de Janeiro, Brazil, 2015. (In Portuguese).
[33] Associação Brasileira de Normas Técnicas, ABNT NBR 5752: Materiais pozolânicos — Determinação do índice de desempenho com cimento Portland aos 28 dias, Rio de Janeiro, Brazil, 2014. (In Portuguese)
[34] Associação Brasileira de Normas Técnicas, ABNT NBR 6118 NB1: projeto de estruturas de concreto – procedimento, Rio de Janeiro, Brazil, 1968, rev. 2014. (In Portuguese)
[35] American Society for Testing and Materials, Standard Practice for Making and Curing Concrete Test Specimens in the Laboratory: ASTM C 192, Philadelphia, USA, 2018.
[36] American Society for Testing and Materials, Standard Test Method for Slump of Hydraulic-Cement Concrete: ASTM C 143, Philadelphia, USA, 2015.
[37] American Society for Testing and Materials, Standard Test Method for Density (Unit Weight), Yield, and Air Content (Gravimetric) of Concrete: ASTM C 138, Phila-

delphia, USA, 2017.

[38] Associação Brasileira de Normas Técnicas, ABNT NBR 5739: Concreto – Ensaio de compressão de corpos-de-prova cilíndricos, Rio de Janeiro, Brazil, 2018. (In Portuguese)

[39] D. Whiting, Rapid determination of the chloride permeability of concrete, Final Report Portland Cement Association, Skokie, IL, USA, 1981.

[40] American Society for Testing and Materials, Standard test method for electrical indication of concrete's ability to resist chloride ion penetration: ASTM C 1202, Philadelphia, USA, 1992.

[41] T. Luping, L. Nilsson, Rapid determination of the chloride diffusivity in concrete by applying an electrical field, Am. Concr. Inst. Mater. J. 89 (1992) 49-53.

[42] Nordtest method, Concrete, mortar and cement-based repair materials: chloride migration coefficient from non-steady-state migration experiments: NT BUILD 492, Oslo, Norway 1999.

[43] Nordtest method, Concrete, hardened: accelerated chloride penetration, NT BUILD 443, Oslo, Norway, 1995.

[44] Nordtest method, Concrete, hardened: Chloride content by volhard titration, NT BUILD 208, Oslo, Norway, 1996.

[45] Associação Brasileira de Normas Técnicas, ABNT NBR 15577-4: Agregados - Reatividade álcali-agregado, Parte 4: Determinação da expansão em barras de argamassa pelo método acelerado, Rio de Janeiro, Brazil, 2018. (In Portuguese)

[46] Z.Z. Ismail, E.A. Al-Hashmi, Recycling of waste glass as partial replacement for fine aggregate in concrete, Waste Manag. 29 (2008) 655-659.

[47] S.B. Park, B.C. Lee, J.H. Kim, Studies on mechanical properties of concrete containing waste glass aggregates, Cem. Concr. Res. 34, (2004) 2181-2189.

[48] S. Castro, J. Brito, Evaluation of the durability of concrete made with crushed glass aggregates. J. Clean. Prod. 41 (2013) 7-14.

[49] Associação Brasileira de Normas Técnicas, ABNT NBR 8953: Concreto para fins estruturais - Classificação pela massa específica, por grupos de resistência e consistência, Rio de Janeiro, Brazil, 2015. (In Portuguese)

[50] O.E. Gjørv, Service life of concrete structures and performance-based quality control, International Workshop on Innovations in Concrete Materials, Whistler, Canada, 2001, 13 p.

[51] H. Zibara, R.D. Hooton, M.D.A. Thomas, K. Stanish, Influence of the C/S and C/A ratios of hydration products on the chloride ion binding capacity of lime-SF and lime-MK mixtures, Cem. Concr. Res. 38 (2008) 422-426.

[52] N. Saikia, S. Kato, T. Kojima, Thermogravimetric investigation on the chloride binding behaviour of MK-lime paste, Thermochimica Acta 444 (2006) 16-25.

[53] R. Talero, L. Trusilewicz, A. Delgado, C. Pedrajas, R. Lannegrand, V. Rahhal, Comparative and semi-quantitative XRD analysis of Friedel's salt originating from pozzolan and Portland cement, Constr. Build. Mater. 25 (2011) 2370-80.

Volume 13, Number 3 (June 2020) p. 628 – 643 • ISSN 1983-4195
http://dx.doi.org/10.1590/S1983-41952020000300012

REVISTA IBRACON DE ESTRUTURAS E MATERIAIS
IBRACON STRUCTURES AND MATERIALS JOURNAL

From numerical prototypes to real models: a progressive study of aerodynamic parameters of nonconventional concrete structures with Computational Fluid Dynamics

De protótipos numéricos a modelos reais: Um estudo progressivo de parâmetros aerodinâmicos de estruturas não convencionais de concreto utilizando a Dinâmica dos Fluidos Computacional

C. V. S. SARMENTO [a]
carlos.vitor@ufpe.br
https://orcid.org/0000-0002-2808-5996

A. O. C. FONTE [a]
antoniooscardafonte@gmail.com
https://orcid.org/0000-0003-2943-2184

L. J. PEDROSO [b]
lineu@unb.br
https://orcid.org/0000-0002-2734-3260

P. M. V. RIBEIRO [a]
paulo.vribeiro@ufpe.br
https://orcid.org/0000-0002-9261-8953

Abstract

The practical evaluation of aerodynamic coefficients in unconventional concrete structures requires specific studies, which are small-scale models evaluated in wind tunnels. Sophisticated facilities and special sensors are needed, and the tendency is for modern and slender constructions to arise with specific demands on their interaction with the wind. On the other hand, the advances obtained in modern multi-core processors emerge as an alternative for the construction of sophisticated computational models, where the Navier-Stokes differential equations are solved for fluid flow using numerical methods. Computations of this kind require specialized theoretical knowledge, efficient computer programs, and high-performance computers for large-scale calculations. This paper presents recent results involving two real-world applications in concrete structures, where the aerodynamic parameters were estimated with the aid of computational fluid dynamics. Conventional quad-core computers were applied in simulations with the Finite Volume Method and a progressive methodology is presented, highlighting the main aspects of the simulation and allowing its generalization to other types of problems. The results confirm that the proposed methodology is promising in terms of computational cost, drag coefficient estimation and versatility of simulation parameters. These results also indicate that mid-performance computers can be applied for preliminary studies of aerodynamic parameters in design offices.

Keywords: aerodynamics, computational fluid dynamic, special structures, wind.

Resumo

A avaliação prática dos coeficientes aerodinâmicos em estruturas de concreto não convencionais demanda estudos específicos, que consistem em modelos em escala reduzida, em túnel de vento, para estimativa desses parâmetros. Instalações sofisticadas e sensores especiais são necessários, e a tendência é que as construções modernas, cada vez mais esbeltas e arrojadas, surjam com demandas específicas em relação a sua interação com o vento. Por outro lado, o avanço obtido em processadores modernos do tipo multi-núcleo, emerge como uma alternativa para a construção de modelos computacionais sofisticados, onde as equações diferenciais de Navier-Stokes são resolvidas para o escoamento do fluido por meio de métodos numéricos. Análises deste tipo demandam conhecimento teórico especializado, programas computacionais eficientes e computadores de alta performance para cálculos em larga escala. Este artigo apresenta resultados recentes envolvendo duas aplicações reais em estruturas de concreto, onde os parâmetros aerodinâmicos foram estimados com o auxílio da dinâmica dos fluidos computacional. Computadores convencionais do tipo quad-core foram empregados em simulações com o Método dos Volumes Finitos e uma metodologia progressiva é apresentada, destacando os principais aspectos da simulação e permitindo a sua generalização a outros tipos de problemas. Os resultados confirmam que a metodologia proposta é promissora em termos de custo computacional, estimativa do coeficiente de arrasto e versatilidade dos parâmetros da simulação. Esses resultados confirmam que computadores de média performance podem ser aplicados a estudos preliminares de parâmetros aerodinâmicos em escritórios de projeto.

Palavras-chave: aerodinâmica, dinâmica dos fluidos computacional, estruturas especiais, vento.

[a] *Universidade Federal de Pernambuco, Departamento de Engenharia Civil, Recife, PE, Brasil;*
[b] *Universidade de Brasília, Departamento de Engenharia Civil e Ambiental, Brasilia-DF, Brasil.*

Received: 26 Sep 2018 • Accepted: 14 Nov 2019 • Available Online: 26 May 2020

1. Introduction

Nowadays the design of slender concrete structures emerges as a current trend. These structures, with irregular geometry, more flexible and susceptible to wind spectra are demanding detailed analysis of aerodynamic effects. These forces affect several structural elements, including modern facades. In this way, the evaluation of wind forces acting on modern concrete structures requires detailed analysis procedures, some not even covered by design prescriptions (Tapajos et al [2], Oda [3], Adnan and Suradi [4], Bhandari et al [5] and Biasioli et al [6]).

Aerodynamics is a field of study widely explored by aerospace and automotive industries in search of optimized solutions and user safety. Similarly, aerodynamics applied to buildings aims to attenuate dynamic effects in structures, ensuring safety and comfort to users, as well as maintaining structural integrity. To measure wind actions in structures, several countries have developed technical standards with examples described in Table 1.

These standards provide values for pressure and drag coefficients for standard geometries with the use of tables and abacuses. In the scenario of concrete reinforced structures of irregular geometries, such as special buildings, bridges, towers, and other special structures, wind tunnel tests (as depicted in Figure 1) must be carried out. In these tests, reduced models (including the structure itself, nearby buildings and topography) are built in specific and sophisticated facilities, which are properly instrumented through electronic sensors.

Another way to acquire aerodynamic parameters is through Computational Fluid Dynamics (CFD). The aerospace and automotive industries were the pioneers in Computational Wind Engineering (CWE) (Blocken [9]), due to the possibility of performing several numerical simulations of the flow for the same prototype, requiring only the calibration with a few wind tunnel tests. Thus, from a valid computational model it is possible to replace experimental tests, having as main advantages: (i) the low cost of a numerical wind tunnel using computers; (ii) speed of simulations for valuable data acquisition. Recent advances in computer software and hardware have inspired researchers in numerical solutions acting as feasible alternatives to wind tunnel tests. Despite this progress, wind tunnel remains as a reliable choice for structural projects. This is partly due to uncertainties in developing a reliable numerical model. On the other hand, numerous studies have dealt with CWE applied to

Table 1
Wind design provisions in some countries

Country	Standards	Year	Title
Germany	DIN 1055-4	2005	Einwirkungen auf tragwerke – Teil 4: Windlasten
Brazil	NBR 6123	1988	Forças devido ao vento em edificações
Canada	NBCC	2010	National building code of Canada
USA	ASCE/SEI 7-05	2006	Minimum design loads for buildings and other structures
Italy	NTC	2008	Technical rules for construction
European Countries	EM 1991 - 1- 4	2005	Actions on structures- Part 1 – 4: general actions – wind actions
Russia	SNIP 2.0107	1985	Loading and excitations
Taiwan	ABRI	2006	Specifications for building wind-resistant design

(a)

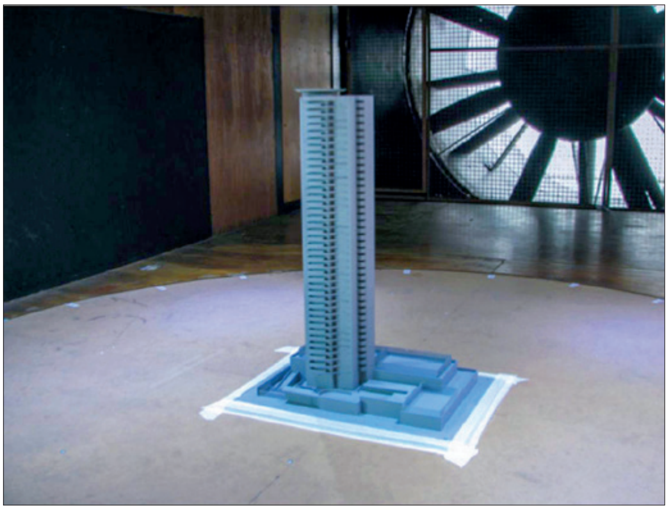

(b)

Figure 1
Wind tunnel lab (a) LAC [7] and (b) IPT [8]

wind flow around buildings, with a further comparison to experimental data and search for optimal simulation parameters.
Akins et al. [10] presented experimental results of mean force and moment coefficients for a series of thirteen flat-roofed rectangular buildings made with plexiglass. Braun and Awruch [11], using CWE, analyzed viscous incompressible flows over one of these models, and presented a good agreement between numerical and experimental data.
CAARC (Commonwealth Advisory Aeronautical Research Council) building is also an excellent example of extensive numerical simulation and was analyzed in the works of Braun [12], Dagnew and Bitsuamlak [13] and Dagnew and Bitsuamlak [14], among others.
In the above-cited cases, the computational domain mimics the wind tunnel aerodynamic test. Therefore, prescriptions must be made to the numerical model regarding length, width, and depth, as well as the position of the target building (or structure). The choice of adequate turbulence model and convergence criteria is also important. These numerical simulations, mostly performed to structures with regular geometry and in the presence of experimental, data serve as a benchmark for advances in CWE. However, a problem arises whenever experimental data is unavailable at the project stage.
Facing the increased application of CFD, some procedures, guides and good practices were presented for computational simulations, as seen in Oberkampf and Trucano [15], Chen and Srebric [16], Moonen et al. [17], Franke et al [18], Reiter [19], Schatzmann and Britter [20], Kim [21] and Rong et al. [22].
With the focus on the advantages of CWE and its application to structural engineering practice, this article proposes a step-by-step procedure for aerodynamic analysis of structures using simple numerical prototypes (with known theoretical or experimental values) for calibration of the final numerical model.
The analysis procedures are based on the use of finite element or finite volume software and address the steps of (i) computational domain construction and structural representation; (ii) mesh generation (domain refinement and mesh quality criteria); (iii) configuration of the problem physics; (iv) convergence study; (v) results analysis.
These procedures allow structural engineers to perform simulations using conventional computers available in design offices and to obtain an initial estimate of aerodynamic parameters(with error minimization and low computational cost). Finally, real-world examples including an aqueduct and a high-rise building are presented and analyzed with the proposed prescriptions.

2. Governing equations and numerical solution

2.1 Governing equations in differential form

Initially a fixed volume in space is observed with $\vec{V}$, μ and ρ. Figure 2a presents a control volume, with contour S.
If conservation is guaranteed in $d\upsilon$, then it can also be extended to the whole domain υ. To guarantee mass conservation the differential form presented in equation (1) is defined as the continuity equation:

$$\frac{\partial \rho}{\partial t} = \vec{\nabla} \cdot (\rho \vec{V}) = 0 \qquad (1)$$

Momentum conservation is based on the principle that the sum of forces acting in $d\upsilon$ will be equal to the momentum rate of change. Basically, two forces act on an infinitesimal volume: (i) body forces and (ii)surface forces. The governing equation is defined as Navier-Stokes equation for an incompressible fluid and it is described in Cartesian components by:

$$\rho\left[\frac{\partial u}{\partial t} + u\frac{\partial u}{\partial x} + v\frac{\partial u}{\partial y} + w\frac{\partial u}{\partial z}\right] = -\frac{\partial \rho}{\partial x} + \rho g_x + f_{\upsilon x} \qquad (2)$$

$$\rho\left[\frac{\partial v}{\partial t} + u\frac{\partial v}{\partial x} + v\frac{\partial v}{\partial y} + w\frac{\partial v}{\partial z}\right] = -\frac{\partial \rho}{\partial y} + \rho g_y + f_{\upsilon y} \qquad (3)$$

$$\rho\left[\frac{\partial w}{\partial t} + u\frac{\partial w}{\partial x} + v\frac{\partial w}{\partial y} + w\frac{\partial w}{\partial z}\right] = -\frac{\partial \rho}{\partial z} + \rho g_z + f_{\upsilon z} \qquad (4)$$

The set of equation (2)-(4) combined with equation (1) form a system of nonlinear partial differential equations composed of 04 unknowns

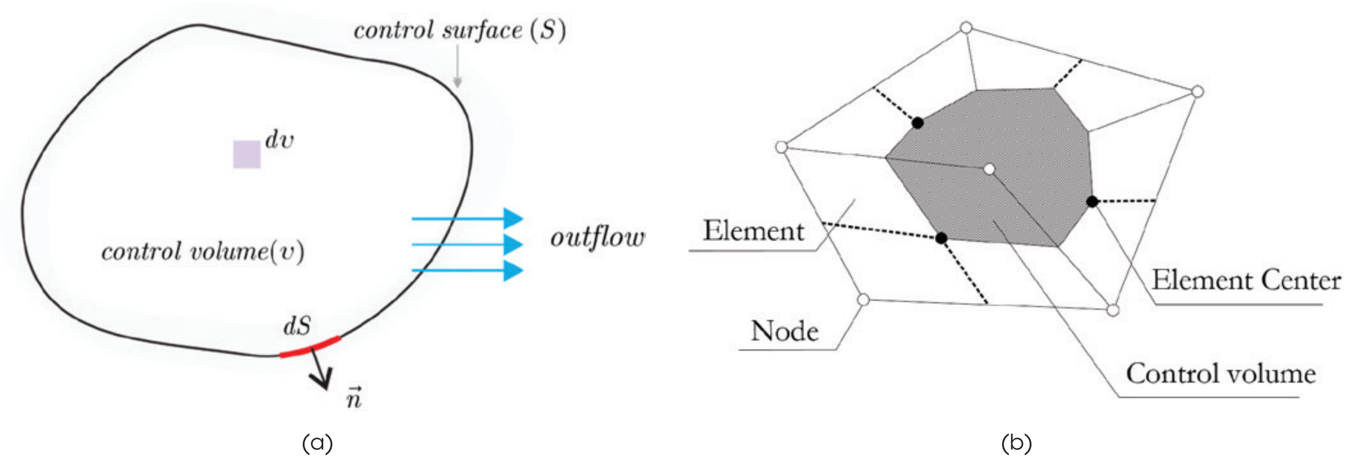

Figure 2
Control volume 2D: (a) Fluid flowing through the generic control volume; (b) Typical mesh for a generic control volume

(u, v, w and p). The inherent difficulties to this problem often require the use of numerical methods for practical solutions.

2.2 Numerical strategies for computational solution

A suitable discretization method must be chosen to approximate equation (1)-(4) to a system of discrete algebraic equations in space and time. The most applied and indicated methods to solve Navier Stokes equation with the Eulerian descriptions in computational simulations of flow around structures is the Finite Volume Method (FVM), as described by Patankar [23], Prakash and Patankar [24], Versteeg and Malalasekera [25] and Ferziger and Peric [26].This method is one of the cornerstones of computational mechanics, due to its versatility and ability to solve differential equations.The FVM comprises a domain discretized through control volumes, as seen in Figure 2b.In these volumes the mass, the

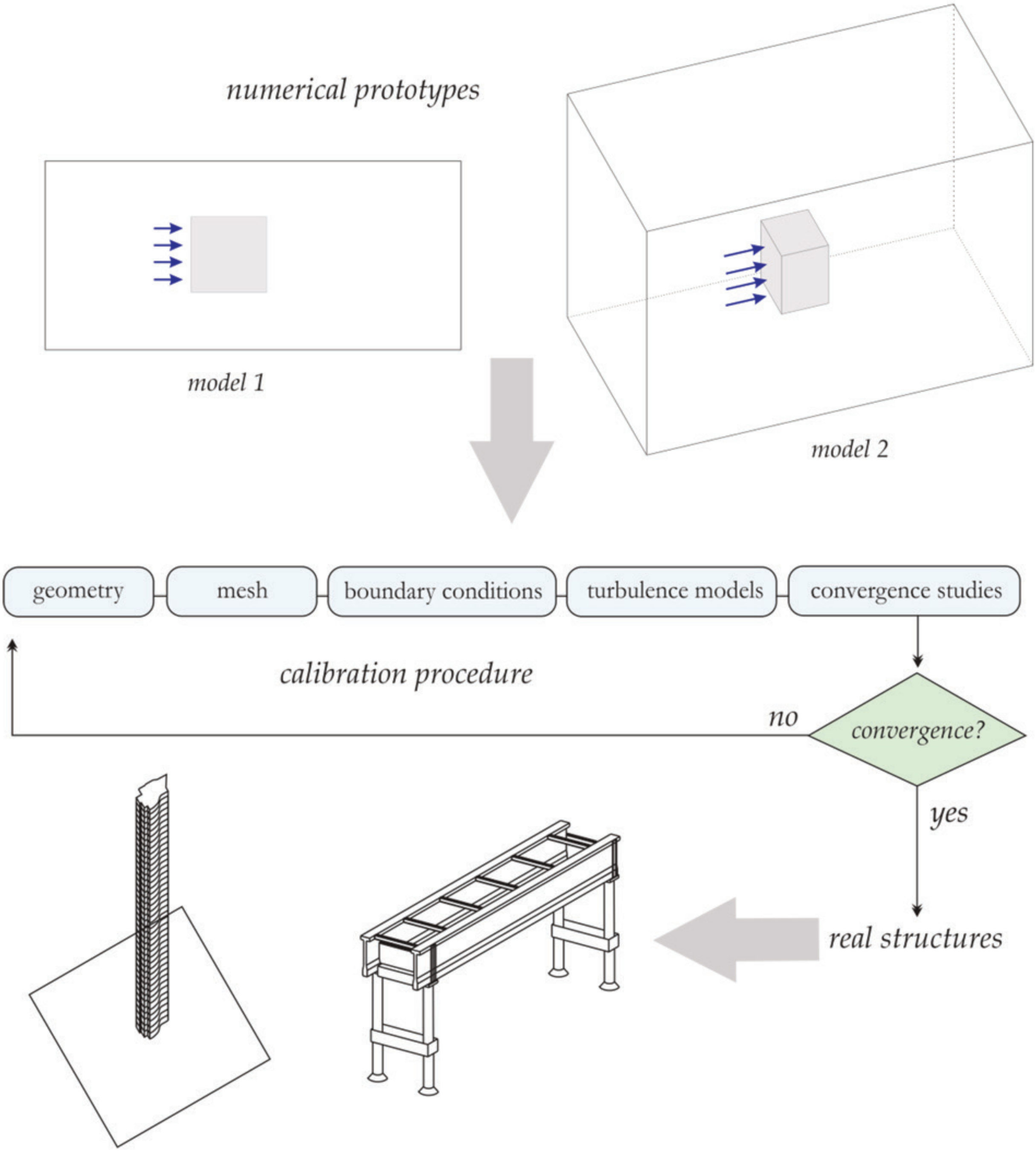

Figure 3
Proposed methodology

momentum, and the energy quantities (Equations 1-4) are conserved and based on the nodal variables of the mesh (pressure and velocity). Interpolations are performed for field evaluation at a subdomain (finite volume). This method is conservative and the solution is based on surface integrals, and finite volumes share their surfaces with adjacent ones. The FVM represents convective and diffusive fluxes and in this way this method is one of the most employed methods in CFD.

The above cited numerical methods require turbulence treatment because the contribution of fluctuations to velocity plots in the Navier-Stokes equations may be practically unpredictable in turbulent flows, and this is due to the large-scale of space and time to be solved (Kundu and Cohen [27]). Aerodynamic flows in structures are commonly quite turbulent, with a high(>10^5) Reynolds number, defined by:

$$Re = \frac{\rho V D}{\mu} = \frac{V D}{\nu} \quad \textbf{(5)}$$

There are basically three ways to solve turbulence in CFD simulations:

(I) DNS — Direct Numerical Simulation, which solves numerically, in the smallest time scales, the Navier Stokes equations. In this way, the average Reynolds obtained computationally determines the average flow. For the DNS, the meshes must be extremely refined, restricting applications to supercomputers.

(II) LES — Large Eddy Simulation is based on large-scale solution of turbulent energy. So, the idea is to solve only the large eddies accurately and the effects are approximate of the small scales. The LES model requires less refinement than a DNS model.

(III) RANS — Reynolds Averaged Navier Stokes, based on the Reynold average equations. This model was proposed by Reynolds in 1895 where the approach is based on the decomposition of the variable into mean and fluctuating parts in time. The RANS model solves the turbulent fluctuation for all the scales on each node. When the target is reducing computational cost, the RANS model is usually the first choice.

RANS is the most common choice for fluid dynamic analysis and

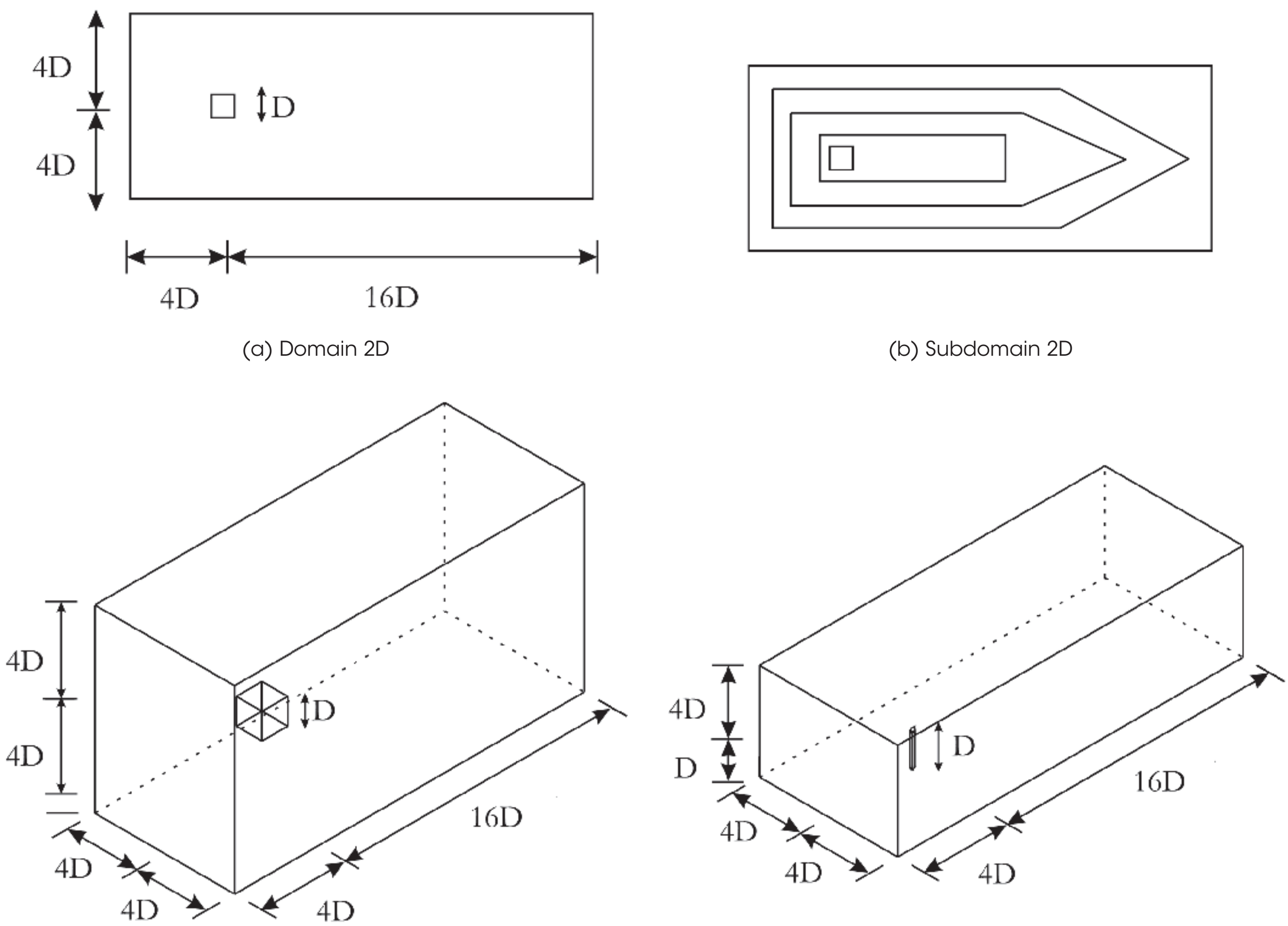

(a) Domain 2D

(b) Subdomain 2D

(c) Domain 3D

(d) Structures in floor

Figure 4
General dimensional domain

will be used on this paper. It can be further divided into a series of models, such as Zero Equation Model, Eddy Viscosity Transport Equation, Standard k -ε Model, RNG, k-ω, SST, SSG, BSL.
Procedures required estimating the aerodynamic coefficients using numerical methods are described in the next section.

3. Methodology: from numerical prototypes to the final model

This procedure starts with a progressive evolution of simple computational models (here defined as numerical prototypes), where numerical calibration is initially performed with reference or experimental results. This step precedes the final computational model, which represents the real structure, and provides the required reliability for numerical simulations. Thus, the reasoning is not only to solve the numerical problem but to construct a numerical model that approximates real conditions and can be used as a numerical wind tunnel.
An overview of the major steps evolved in the current proposal are depicted in Figure 3. These will be detailed in the following sections.

3.1 Geometry domain

This procedure mimics the wind tunnel test. The structure is positioned at a given distance from the inlet, thus allowing the generation of turbulence. As for the dimensions, the prescriptions available in Franke et al. [18] are recommended, where the proposed dimensions are shown in Figure 4. It is treated as a Boolean operation, where a computational domain is generated, and the structure is subtracted.
In general, the domain length is selected between 15D and 20D, where D is the characteristic dimension of the section. In this case, there is a greater refinement of volumes in the user-defined region (closer to the object), since the flow is more sensitive to boundary conditions. Because of this, subdomains must be created around the objects and at regions of the floor, to allow different mesh scales for rugosity prescription. Another strategy (commonly seen in the literature for laminar flows) is the use of symmetry. However, it should be noted that the wind flow has turbulent characteristics, so for a given time t, what occurs in one half of the domain will not necessarily occur in other.
For two-dimensional flows using 3D codes, a thickness must be imposed to the domain. In practice, a small value is prescribed, avoiding excessive computational cost. The authors propose a value of D/20. For three-dimensional simulations, it is important to maintain a 4D distance from the object to the walls, resulting in a thickness of 8D. This is necessary for the development of vortices and to capture relevant information of the flow (velocity and pressure).

3.2 Mesh

In this step, the computational domain is refined following the criteria of the element type, local grid refinement, element quality, and mesh quality.

3.3 Boundary conditions

Prescribed boundary conditions are given by (i) pressure and velocity at the inlet and outlet, (ii) zero normal velocity (no-slip condition) for structural boundary and ground, (iii) free to slide condition for the remaining boundaries. A general scheme is presented in Figure 5.

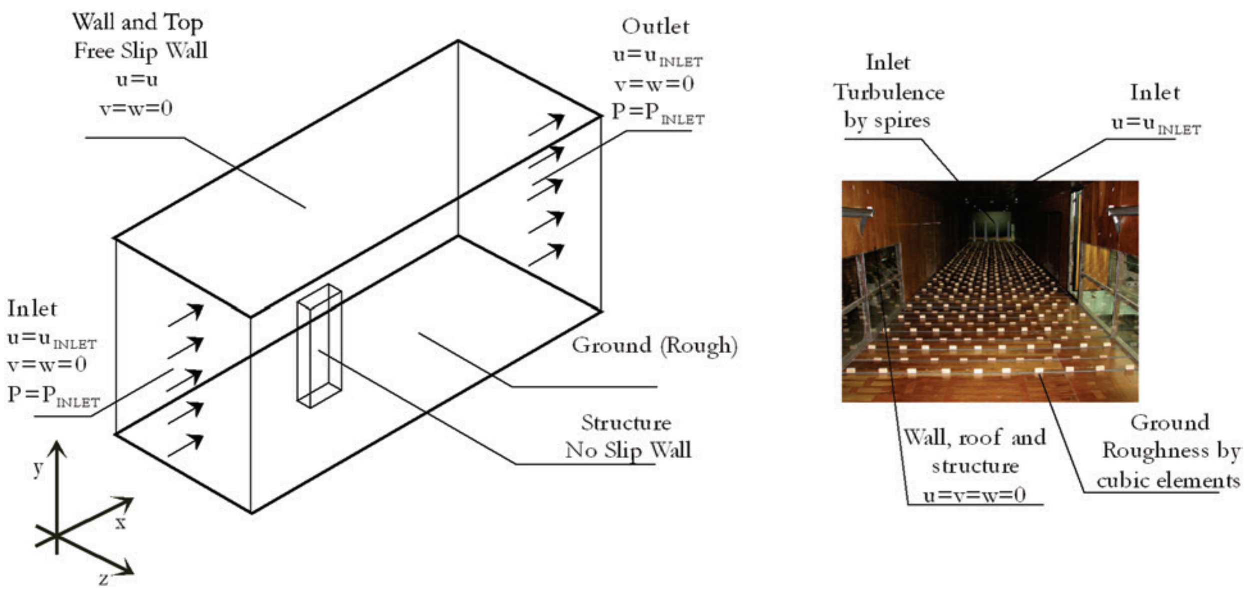

(a) Wind tunnel numerical

(b) Wind tunnel experimental

Figure 5
Boundary conditions

3.3.1 Inlet

The input face is selected and the wind speed at the inlet is considered. To insert the velocity, two main methods are highlighted. The first is to consider speed input as a function of height (Z), according to the logarithmic law in equation (6), with u_+ defined by $\sqrt{\tau/\rho}$.

$$\frac{V}{u_+} = \frac{1}{k} ln\left(\frac{Z}{Z_0}\right) \tag{6}$$

Another possible strategy, resembling wind tunnel tests, is to apply constant speed at the inlet. In this way ground roughness causes the speed profile to develop naturally. However, when using this method, two essential points should be emphasized: the mesh refinement in the floor and the size of the upstream and downstream computational domains must be large enough to capture flow effects.

3.3.2 Outlet

At the outlet, it is possible to define speed or pressure (gauge or atmospheric). In practice, the outer pressure is prescribed, allowing velocity to be developed naturally along the domain.

3.3.3 Wall and ceiling (top wall)

On walls (side faces) and ceiling (top face) it is admitted that the fluid is free to flow.

3.3.4 Ground and structure

Simulations of structures located far from the ground (Figure 4a), such as aqueducts and bridges allow considering the floor as free-slip wall condition. However, for ground-based structures, as is the case of buildings, the no-slip condition must be considered, and the roughness of the floor must be specified. This parameter is calibrated from speed profiles or design values.
Depending on the design, the roughness of the structure should be considered, however additional studies must be performed in this case. Due to the surface finish of the structures applied in this work, the roughness of the object walls could be neglected. In this way, the no-slip condition was adopted in these models.

3.4 Turbulence model

A RANS turbulence model, described in section 2, is selected based on two criteria for a selected global variable: (i) smaller amplitudes over time and (ii) greater proximity to the theoretical value on the numerical prototype. Models with large amplitudes should be avoided, even if their mean value is close to the theoretical one, because, at a given stopping point of the simulation, peak values may not represent the global variable. To perform these simulations, an intermediate mesh is employed, avoiding high computational costs. Therefore, no more than 50,000 nodes for the two-dimensional flow and 200,000 nodes in the three-dimensional case are sufficient at this preliminary stage.

3.5 Convergence studies

In a broad sense, convergence on this proposal is based on asymptotic curves tending to a number (Lewis et al. [28]), providing mesh independence in time, number of iterations and space. The numerical model is said to be convergent when average values of the selected global variable remain approximately constant over time.

3.5.1 Independence of time

The numerical model is submitted to studies in the transient regime using the following criteria: (i) total time of flow simulation and (ii) time step. The duration of the flow should be such that the fluid crosses ‘n’ times the domain, where ‘n’ should be enough for the stabilization of the global variable. The time step is selected based on the Courant number:

$$Courant = \frac{u\,\Delta x}{\Delta t} \tag{7}$$

For solvers with implicit schemes, it is possible for the Courant number to be greater than 1. In the absence of an initial estimate, it is pointed out the need for a convergence analysis of this variable,

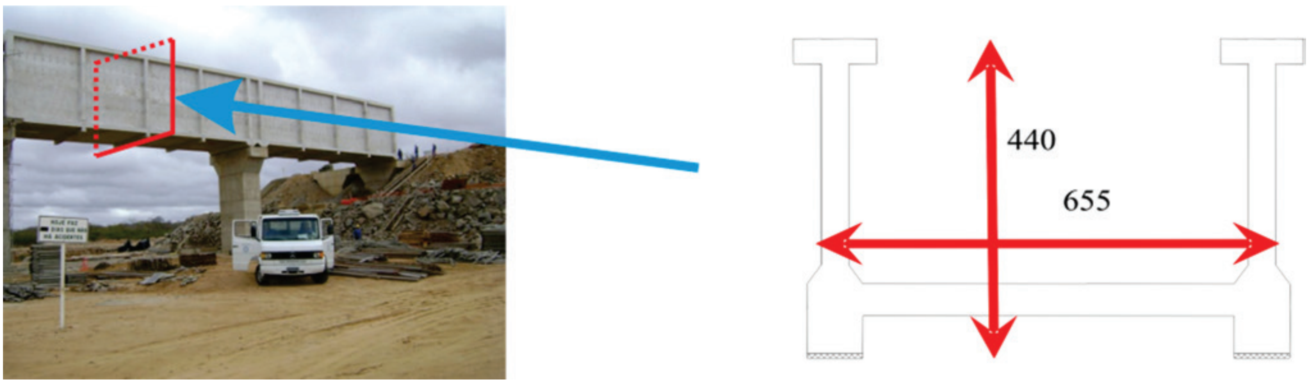

(a) Aquedut

(b) Cross section

Figure 6
Concrete aqueduct details (units in centimeter)

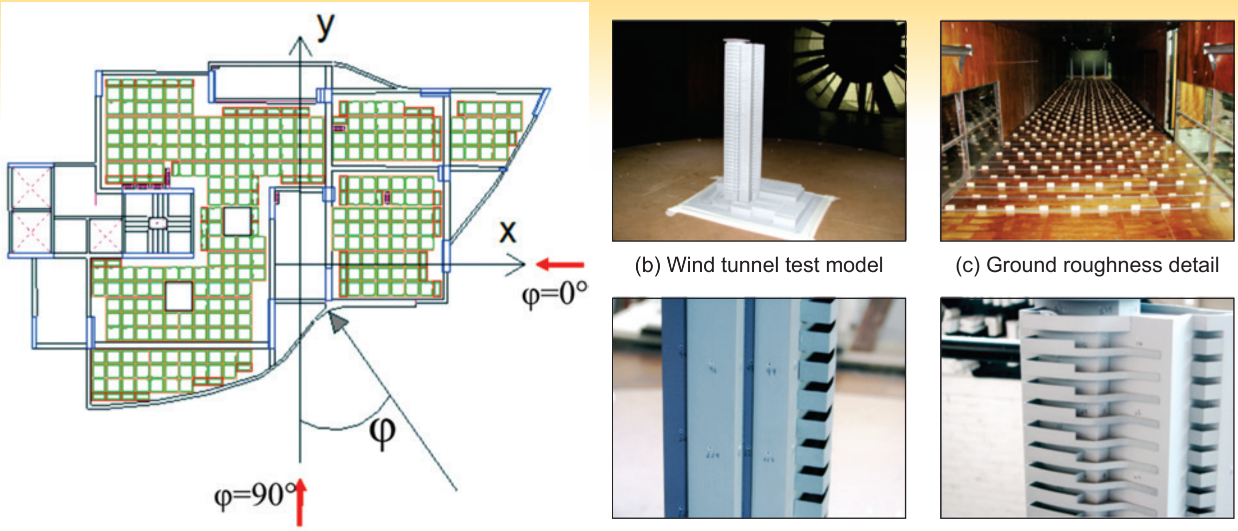

(a) Floor plan and wind incidence angle φ

(b) Wind tunnel test model

(c) Ground roughness detail

(d) Pressure sensors

(e) Building details

Figure 7
Wind tunnel test and details (Model 04) (IPT [8])

using different time steps. In this convergence study, an upper bound must be verified for this parameter, so that time independence is achieved for the flow.
A point to be highlighted is that equation 7 shows the relation between temporal and spatial domains. Thus, in reducing element sizes, time step values should also be reduced, guaranteeing the same Courant number. The authors point out that this will increase mesh complexity and simulation costs, making the numerical model infeasible on average computers.

3.5.2 Number of iterations

Another variable in CFD is the number of iterations that are performed in each time step, where linearization of the non-linear terms of the Navier-Stokes equations is performed. Since this parameter influences computational cost, a convergence study must be made. For a given mesh, the number of iterations must range from 1 to 50, providing the smallest value for a global parameter estimate at the lowest computational cost.

3.5.3 Simulation stop criteria

The total simulation time is selected so that the global variable exhibits cyclic behavior, with the mean result providing agreement with reference values. This is necessary for stabilization of the global variable and validation of the numerical prototype.

3.5.4 Independence of space

Mesh convergence study is performed by reducing element size, thus verifying the behavior of the global variable as the number of elements increases. In turbulent flows, mesh improvement may cause the appearance of localized phenomena, initially not present. This spatial criterion guarantees the accuracy of the computational model.

3.5.5 Final model – real structure

The evaluation of a real structure arises after calibration of a numerical prototype. Thus, turbulence models, convergence criteria and computational domain, among others, are applied or adapted to the final model. This procedure allows a progressive evolution to the simulation of a real structure, where theoretical or experimental values are unknown. Figure 3 illustrates this procedure.
On this paper, two numerical prototypes (square section and cube, models 01 and 02) were selected for simulation of real structures, exemplified by an aqueduct and a building (models 03 and 04). These will be analyzed in the next section.

4. Implementation of the proposed procedures in concrete structures: study of aqueduct and high-rise building

Simulations were performed using Ansys v.14.0[29] with its computational fluid module CFX. This module implicitly solves the nonlinear system of equations described in Section 1 for pressure and flow velocity in space and time, through the finite volume method. Mesh refinements were performed with tetrahedral or hexahedral elements. Simplifications in structural geometry were necessary to reduce computational cost. Hardware features include a desktop PC with quad-core processor Intel® i7-4770, 3.40GHz, 8.00GB RAM memory, 64-bit operating system.Simulations were initially performed for numerical prototypes according to Figure 3 (models 1 and 2). In a sequence, the real models were studied (models 3 and 4).
In structures like aqueducts or bridges (Figure 6), where one dimension prevails over the other and velocity profile along the longitudinal length is substantially constant, it is possible to approach the drag value to a section cut (two-dimensional). Therefore, the geometry of the aqueduct (model 03) is defined by a U section, as indicated in Figure 6b. This cross-section will be simplified to a rectangle with dimensions of 655x440 cm. For this section, a theoretical drag coefficient is C_D = 1.95 (with linear interpolation; provided by Çengel and Cimbala [30]).
Model 04 simulates a reinforced concrete building of 40 floors (130.30 m). The geometry of this structure is shown in Figure 7a, along with the floor plan and the wind incidence angle. In this work, only winds with φ = 0° and φ = 90° are analyzed, knowing that the methodology will be the same for any other angle φ.
Reference values for Model 04 were obtained from an experimental test with a 1:200 scale model (Figure7b-e), conducted in the

Table 2
Simulations parameter — aqueduct and building

Parameter		Model 03	Model 04
Air	Temperature	25° C	
	ρ	1.185 kg/m³	
	μ	1.831 x 10^5 kg/ms	
	Velocity inlet	30m/s (108km/h)	30m/s (108km/h)
Reynold		7.2 x 10^6	3.9 x 10^6 in $\varphi = 0°$ 5.8 x 10^6 in $\varphi = 90°$
Element type		Hexahedral	Tetrahedral
Pressure outlet		0 Pa	0 Pa
Wall conditions	Free-slip wall	Top, bottom and sides	Top and sides
	No slip wall	Structure	Structure and bottom
Turbulence model		k–ε	SST
Total simulation time		10s	20s
Courant number		Between 10 and 20	
Number of interactions		10	10
Roughness		0	0.32m
RMS		10^{10}	10^{10}

Atmospheric Boundary Wind Tunnel of the Technological Research Institute (IPT [8]). Force values on each floor were computed by means of 285 pressure sensors (Figure 7d).

Numerical simulations required some adjustments to produce a feasible computational model. In this way, rooftop elements (helipad, water tank, among others) and ground level floor details were neglected. This simplified model has 40 identical floors ranging from 0 to 130.30m elevation.

Table 2 describes the main parameters adopted in the simulations. The Courant number, turbulence model, number of interactions and RMS (root mean square) were obtained with a numerical prototype, and its details are presented in the next sections.

4.1 Geometry

Details of the geometric domain are given in Figure 8. Transition regions were prescribed for mesh refinement according to Section 4.1. A scale factor 1:10 was adopted for the real building (model 4), only as a verification of the scale analysis, assuming that the software will perform mathematical operations and such a strategy will not lead to errors in the simulation.

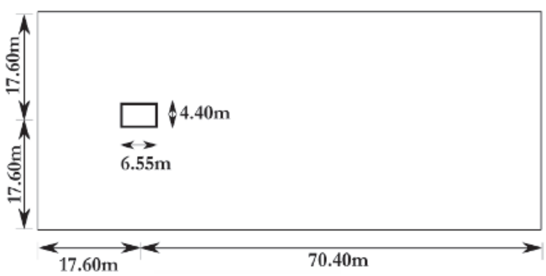

(a) Aqueduct domain

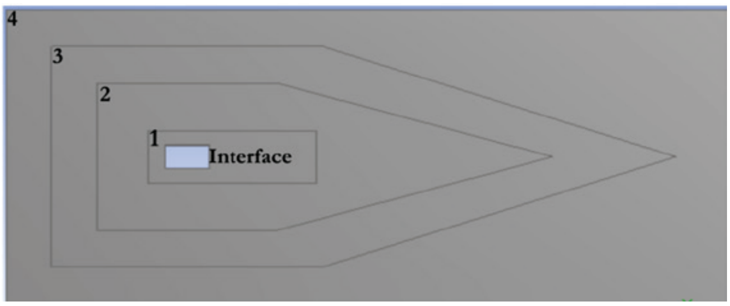

(b) Aqueduct subdomain

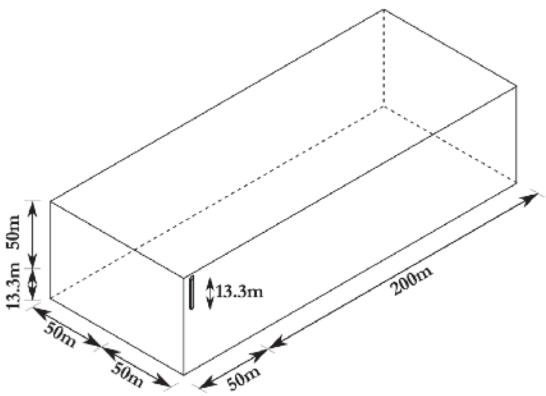

(c) Building domain

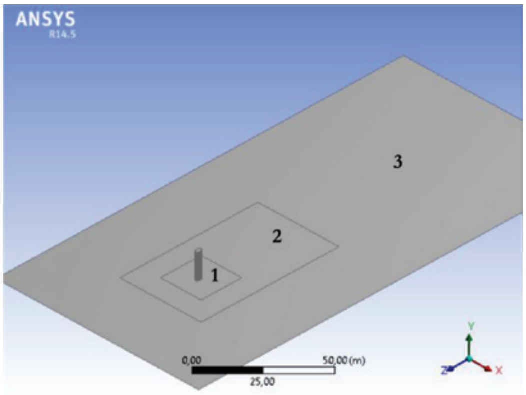

(d) Building subdomain

Figure 8
Domains and subdomains

Table 3
Mesh refinement – element size in meters (m)

	Subdomain	Mesh 01	Mesh 02	Mesh 03	Mesh 04	Mesh 05
Model 03	1	D	0.2D	0.1D	0.05D	0.02D
	2	2D	0.4D	0.2D	0.1D	0.05D
	3	4D	0.8D	0.4D	0.2D	0.1D
	4	8D	1.6D	0.8D	0.4D	0.2D
				Number of nodes		
	Aqueduct	3,042	10,551	20,665	47,727	178,043

	Subdomain	Mesh 01	Mesh 02	Mesh 03	Mesh 04	Mesh 05
Model 04	1	D	0.5D	0.25D	0.125D	0.0625D
	2	2D	D	0.5D	0.25D	0.125D
	3	4D	2D	D	0.5D	0.25D
	Interface	0.1D	0.05D	0.025D	0.0125D	0.00625D
				Number of nodes		
	Building	23,212	32,656	56,264	203,282	658,007

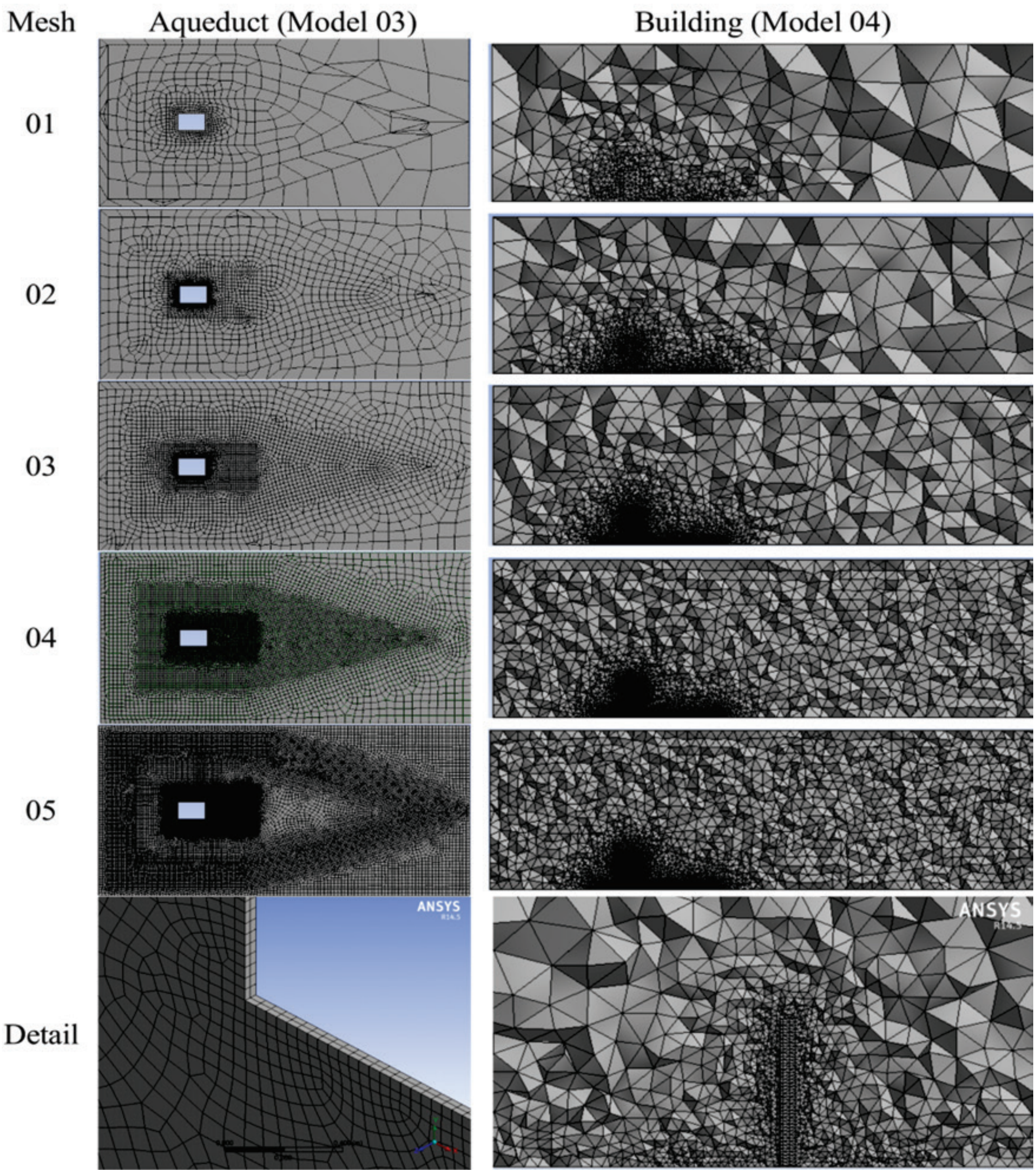

Figure 9
Mesh refinement details

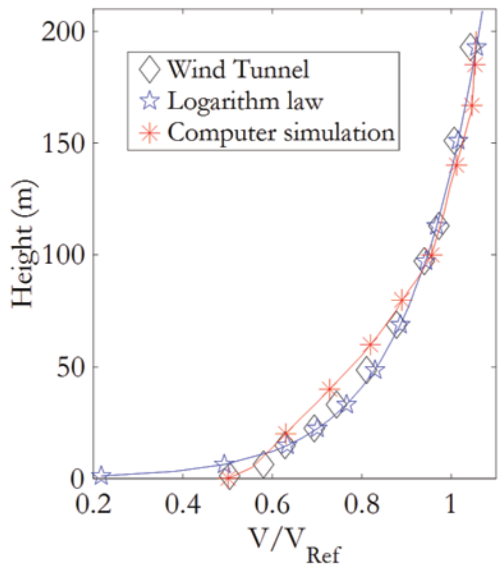

Figure 10
Velocity profile – Model 04

4.2 Computational mesh

4.2.1 Domain refinement

Due to the high computational cost, the use of small volumes in the entire computational domain is avoided. However, specific regions, such as the boundary layer and wake, require localized refinement to capture flow relevant effects. Figure 4b shows a proposal for subdomains where the smallest element sizes are located near the structure. Transition regions are required, enabling progressive refinement towards the center. A total of five computational meshes were employed for each model. Element size was selected based on the characteristic dimension of the structure, with D=4.40m for Model 03 and D = 2.00m for Model 04 (20.0m in a real building without scale factor). Additional mesh parameters and details are given in Table 3 and Figure 9. The meshes must be generated for elements with aspect ratio and orthogonality close to 1 (one) and skewness close to 0 (zero). The use of conforming meshes is recommended. Mesh quality criteria were verified in both models, focused on low-quality elements only in regions that are not very sensitive to the flow.

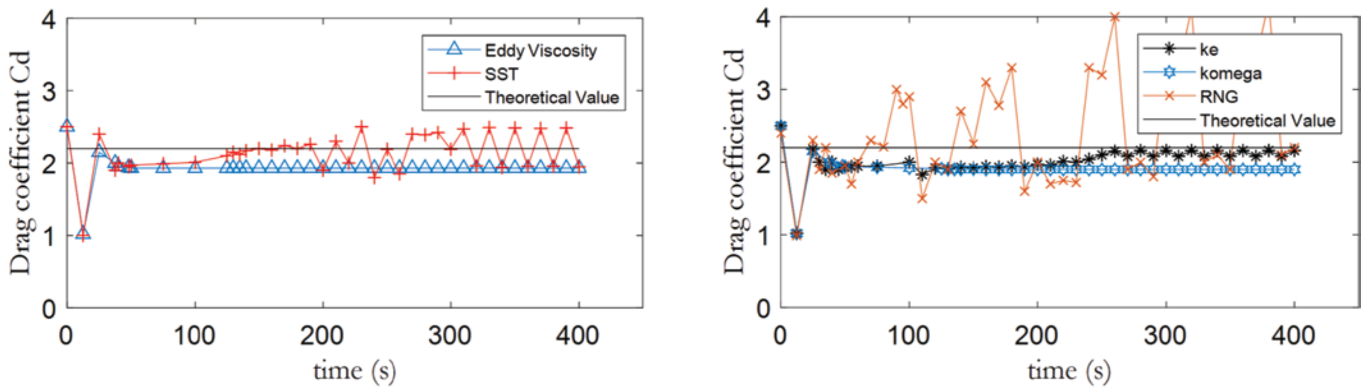

Figure 11
Convergence of test of different turbulence models — square section (Model 1)

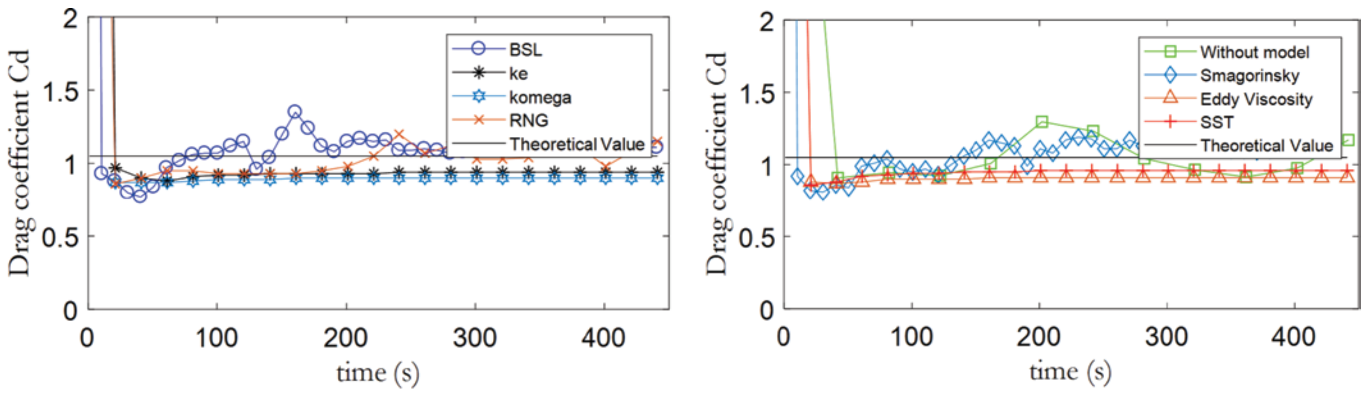

Figure 12
Convergence test of different turbulence models — cube (Model 2)

Table 4
Mean drag coefficients for different turbulence models (Models 1 and 2)

	SST	RNG	SSG	Whitout model	k-ω	BSL	k-ε	Smagorinsky	Eddy viscosity	Theoretical value	Average
Square	2.14	2.44	2.27	—	1.91	—	2.01	—	1.93	2.20	2.00
Cube	0.95	1.04	—	1.05	0.90	1.11	0.94	1.08	0.91	1.05	1.00

— not simulated for this case

4.3 Boundary conditions

For Model 03, wind velocity was prescribed according to design data(IPT [8]). In Model 04, it was considered as 30m/s, which is the reference value on the wind tunnel report. In this last case, wind speed acting on the structure is presented by Figure 10 using three different approaches: (i) wind tunnel test results, (ii) equation (6) with parameters given by u_+ 0.97m/s;
k = 0.40 and Z = 0.32m, (iii) computational simulation. The selected roughness value provides a good agreement with experimental or theoretical results. Remaining boundary conditions (floor and walls) are given in Table 2.

4.4 Turbulence model

A study of the turbulence models described in Section 2 was carried out to verify which of these models best represents the target parameter (experimental or literature values for the drag coefficient). These analyses were performed on the numerical prototypes (square section and cube) shown in Figure 11 and Figure 12. A list of mean drag coefficient values is summarized in Table 4. For Model 1 (square section) most of the mean values are in agreement with the theoretical reference (C_D=2.2), with relative errors at a maximum of 12%. For model 2 (cube section) the maximum relative error is given by 10%. Therefore, it is concluded that in terms of the mean values for the drag coefficient, any turbulence model will provide a good estimate when compared to the reference value. On the other hand, some of the models may exhibit varying amplitudes, which are of secondary nature, since only mean values are required for drag force computations in real structures. For the real structures, k-ε and SST turbulence models were selected for the aqueduct and high-rise building, respectively.

4.5 Convergence

4.5.1 Temporal discretization

A Courant number convergence test was performed for reference models 01 and 02. Values in the range 10-20 resulted in satisfactory results. The flow duration was defined as 3 times the time required for the fluid to flow the entire domain.

4.5.2 Number of iterations

In the numerical prototypes, a number of iterations over 10 per time step resulted in a good agreement with theoretical values. Therefore, this value was selected for Models 03 and 04.

4.5.3 Independence of space

Computational meshes were studied according to the refinement provided by Table 3. Figure 13 shows the mesh convergence analysis for Model 03.
In Model 04, simulations were performed for two incidence angles, where several data were computed. Among them: global drag and average force on each floor. Figure 14 illustrates mesh independence studies of this model on floors 25, wind at 90°. The remaining floors were also verified, showing similar behavior.

4.6 Results

The numerical models obtained after application of the proposed procedure are the best estimate of the real scenario. For validation, these results were compared to experimental or theoretical values.

4.6.1 Aqueduct

Figure 13 presented the converged drag coefficient value for the aqueduct (C_D=1.93), where the simulation error for the last mesh was 1.03% and the processing time was 40.8h.

4.6.2 High-rise building

From the simulations carried out in the high-rise building, Table 5 was elaborated for analysis on each floor for the 0° and 90° incidence angles.
The error was calculated considering the wind tunnel test results

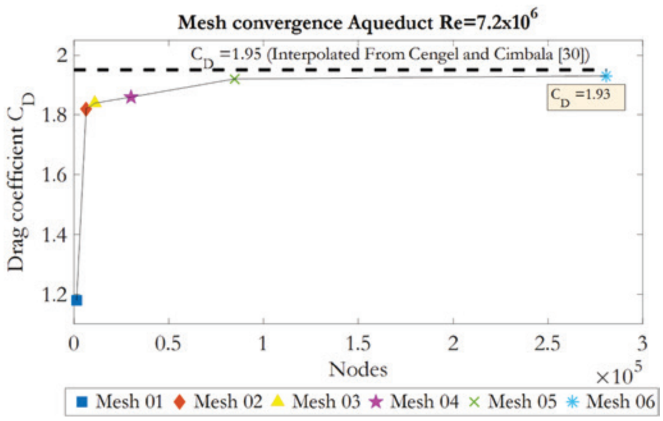

Figure 13
Mesh convergence — average drag — Model 03

as a reference. In this table, besides the errors per floor, it is also indicated if the value of the computational simulation was superior or inferior to the experimental one (arrows), verifying that there is no pattern in the whole floor, that is, the CFD was not always an upper or lower estimate when compared to the experimental results. In Figure 15, it can be verified that the largest errors are in the floors that were neglected in modeling: upper and lower level. This figure is a global analysis, verifying the sum of the forces in the whole building for each incidence angle, allowing to quantify the global error and verify the force distribution along the structural height.

It is possible to summarize the simulations from the values obtained for the drag coefficients. Table 6 presents these results.

The average time required to perform the methodology for a given discretization (mesh 04) is shown in Table 7. It is known that this time is only an estimate since it depends on the complexity of the geometry and boundary conditions.

Table 5
Wind force resultant — incident angles at 0° and 90°

Floor	Height-z (m)	Force (N) at 0°		Force (N) at 90°		Error (%) wind at 0°	Error (%) wind at 90
		Wind tunnel	Computer simulation	Wind Tunnel	Computer simulation		
1	13.3	32,678.0	34,396.0	11,659.9	17,697.8	5.3 ↑	51.8 ↑
2	16.3	33,927.6	34,965.5	11,659.9	17,764.6	3.1 ↑	52.4 ↑
3	19.3	33,179.8	35,251.8	13,120.3	17,701.6	6.2 ↑	34.9 ↑
4	22.3	32,258.5	35,511.7	14,398.0	17,557.8	10.1 ↑	21.9 ↑
5	25.3	32,677.9	35,806.2	14,398.0	17,213.4	9.6 ↑	19.6 ↑
6	28.3	32,349.2	35,713.6	14,558.1	17,119.3	10.4 ↑	17.6 ↑
7	31.3	31,847.3	35,816.6	14,741.1	17,105.5	12.5 ↑	16.0 ↑
8	34.3	30,570.4	35,794.9	14,741.1	16,648.8	17.1 ↑	12.9 ↑
9	37.3	31,148.2	35,746.6	15,202.7	16,685.6	14.8 ↑	9.8 ↑
10	40.3	32,068.4	35,623.0	15,895.1	16,682.9	11.1 ↑	5.0 ↑
11	43.3	31,769.1	35,953.1	15,895.1	16,398.6	13.1 ↑	3.2 ↑
12	46.3	32,167.3	35,817.4	16,087.6	16,172.2	11.4 ↑	0.5 ↑
13	49.3	32,660.9	35,957.9	16,472.7	16,348.8	10.1 ↑	0.8 ↓
14	52.3	32,887.2	36,113.9	16,472.7	16,074.2	9.8 ↑	2.4 ↓
15	55.3	33,392.6	35,991.9	16,632.4	16,083.3	7.8 ↑	3.3 ↓
16	58.3	34,165.7	36,030.8	17,071.6	16,180.2	5.5 ↑	5.2 ↓
17	61.3	34,402.9	35,917.6	17,071.6	16,393.5	4.4 ↑	4.0 ↓
18	64.3	34,839.2	35,853.2	17,221.3	16,937.2	2.9 ↑	1.6 ↓
19	67.3	35,901.3	35,760.5	17,820.2	17,060.3	0.4 ↓	4.3 ↓
20	70.3	36,094.2	35,829.2	17,820.2	17,268.8	0.7 ↓	3.1 ↓
21	73.3	36,334.1	36,025.3	17,932.0	16,740.1	0.9 ↓	6.6 ↓
22	76.3	37,390.0	36,070.5	18,658.6	16,517.6	3.5 ↓	11.5 ↓
23	79.3	37,642.5	36,252.9	18,658.6	16,787.5	3.7 ↓	10.0 ↓
24	82.3	37,736.2	36,571.2	18,708.3	16,903.9	3.1 ↓	9.6 ↓
25	85.3	38,453.7	37,153.3	19,404.3	17,023.5	3.4 ↓	12.3 ↓
26	88.3	38,730.3	37,715.5	19,404.3	17,621.5	2.6 ↓	9.2 ↓
27	91.3	38,999.8	38,604.0	19,404.3	18,332.5	1.0 ↓	5.5 ↓
28	94.3	40,014.1	39,582.6	19,750.7	18,338.1	1.1 ↓	7.2 ↓
29	97.3	40,354.2	40,770.9	19,750.7	18,059.1	1.0 ↑	8.6 ↓
30	100.3	40,438.2	42,120.0	19,750.7	18,872.8	4.2 ↑	4.4 ↓
31	103.3	41,894.0	43,444.9	20,125.2	17,762.0	3.7 ↑	11.7 ↓
32	106.3	42,359.6	44,842.5	20,151.9	18,196.2	5.7 ↑	9.7 ↓
33	109.3	42,555.2	46,099.2	20,151.9	17,948.9	8.3 ↑	10.9 ↓
34	112.3	43,462.6	47,072.3	20,835.4	17,543.8	8.3 ↑	15.8 ↓
35	115.3	43,768.3	47,874.4	20,940.5	17,405.1	9.4 ↑	16.9 ↓
36	118.3	44,063.9	48,214.2	20,940.5	17,216.1	9.4 ↑	17.8 ↓
37	121.3	44,552.7	48,580.9	21,394.8	17,041.3	9.1 ↑	20.3 ↓
38	124.3	44,868.9	47,900.1	21,507.9	16,739.1	6.8 ↑	22.2 ↓
39	127.3	44,676.7	45,863.7	21,507.9	14,715.0	2.7 ↑	31.6 ↓
40	130.3	21,445.4	30,355.5	10,484.2	8,781.6	41.5 ↑	16.2 ↓
Global		1,460,726	1,544,965	698,402	675,640	5.77 ↑	3.37 ↓

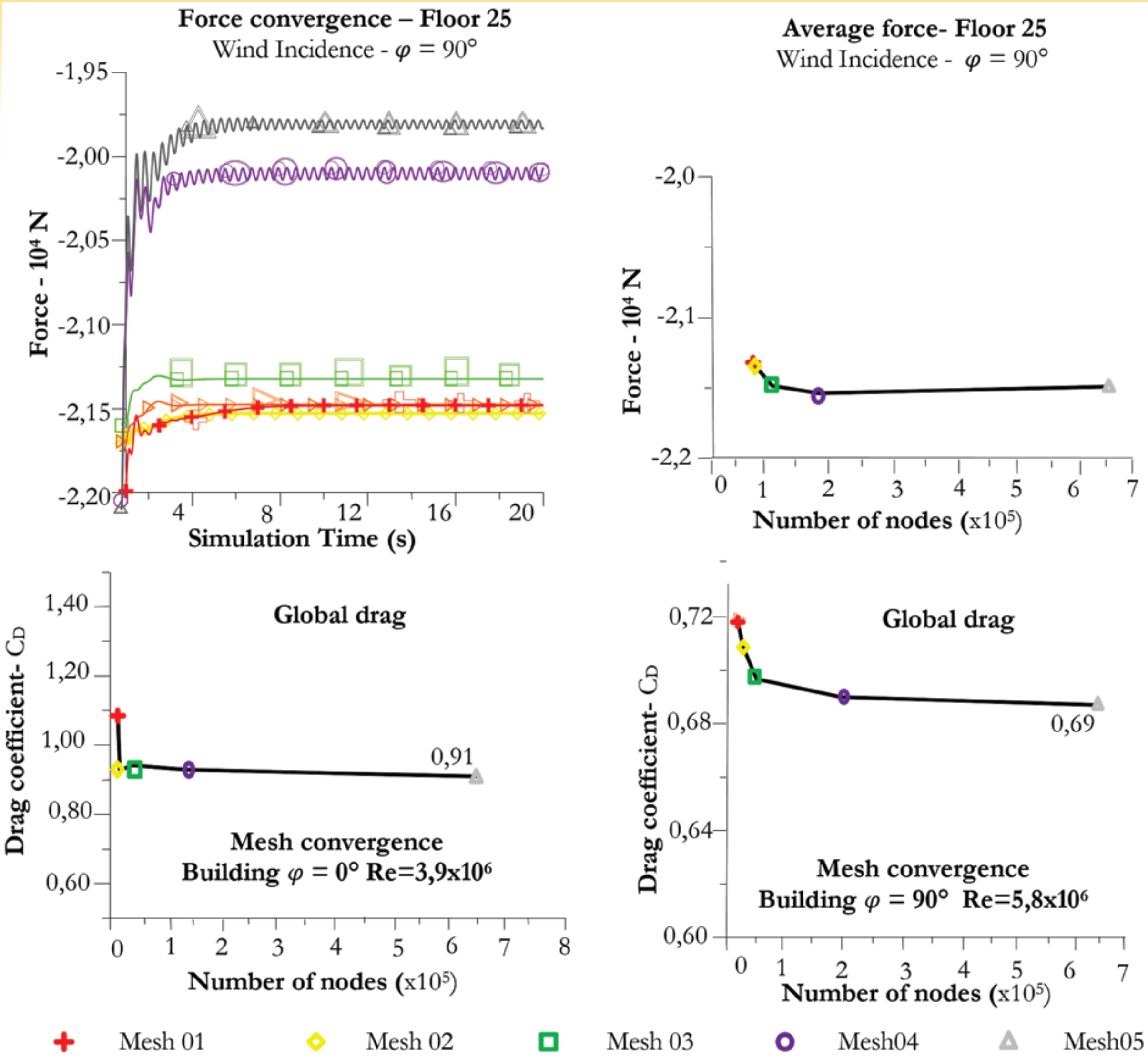

Figure 14
Mesh convergence — Model 04

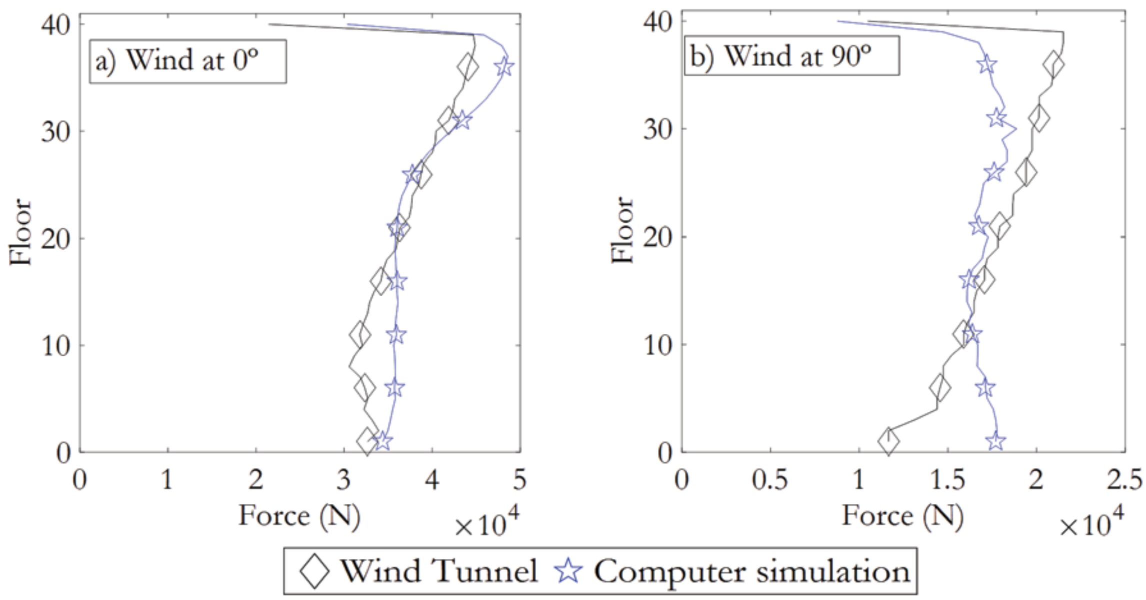

Figure 15
Drag force per floor: CFD and wind tunnel - wind incidence: a)φ = 0° and b) φ =90°

Table 6
Summary of simulations - 2D and 3D flow

Model	Drag coefficient (C_D)			
	CFD	Wind tunnel	Theoretical value Çengel and Cimbala[30]	Error (%)
01 — Square section	2.17	—	2.20	1.36
02 — Cube	1.02	—	1.05	2.86
03 — Real aqueduct	1.93	—	1.95	1.03
04 — Real building wind at 0°	0.91	0.86	—	5.81
04 — Real building wind at 90°	0.69	0.72	—	4.17

Table 7
Average time for each step — Mesh (04)

Case	Geometry	Mesh	Data and premises	Processing	Analysis of results	Total time
Model 3	0.5 h	2.0 h	0.5 h	13.0 h	1.0 h	17h
Model 4	1.0 h	3.0 h	1.0 h	41.0 h	2.0 h	48h

5. Conclusions

The proposed procedures resulted in a very efficient and objective guide, being recommended for preliminary analysis of buildings and special structures.

One of the requirements for the elaboration of this proposal was to carry out simulations using average computers. In this way, simplifications were necessary to meet hardware limitations. Another requirement imposed by this work was the use of numerical prototypes. The objective was to establish a series of criteria for several relevant variables in two and three-dimensional simulation of real structures.

This methodology was applied to the reference section (Model 01) where it presented an error of 1%. Then, it was possible to apply these parameters to an aqueduct submitted to real wind inputs (Model 03), whose drag values presented an error of 1% in relation to the estimated theoretical value.

Flow simulations of the 3D reference model (Model 02) converged to a drag coefficient C_D = 1.02, resulting in an error of only 3% over the theoretical value.

The real building (Model 04) presented an overall error of 6% for the incident wind at 0° and 3% for the wind at 90°. In modeling, simplifications were made in the geometry described in Section 5 for the upper and lower floors. These approximations are confirmed in Figure 15, where the smaller error amplitudes appear at the intermediate floors, leaving the upper and lower ones with the largest errors, already highlighted in Table 5. It is noteworthy that for such building there were no reference values for the aerodynamic parameters. To reduce computational costs, it would be possible to carry out simulations using only mesh 04, resulting in errors (in relation to mesh 05) of 1% for the incident wind at 0° and 2% for incident wind at 90°. This would reduce simulation time by 40%, about 48 hours, which proves to be a feasible value for design offices. In this way, the proposed procedures are very promising in terms of computational cost, drag estimation and versatility in changing problem variables, enabling a fast, low-cost companion to traditional wind tunnel tests.

6. List of symbols

$\vec{V}$ — Velocity vector
μ — Dynamic Viscosity
ρ — Density
$\mathcal{v}$ — Control volume
$d\mathcal{v}$ — Infinitesimal volume
S — Control surface
υ — Control domain
$\vec{\nabla}$ — Divergence
$\vec{f}$ — Effective force per unit mass within
u — Velocity in x
v — Velocity in y
w — Velocity in z
p — Pressure
$g_{x,y,z}$ — Body accelerations
$f_{\mathcal{v}}$ — Viscous forces acting on dv
V — Averaged speed
v — Kinematic viscosity
D — Characteristic dimension of the immersed body
Z — Height
Z_0 — Roughness of the floor
u_+ — Friction velocity
C_D — Drag coefficient
k — Von Karman constant
Δt — Time interval
Δx — Element size
φ — Wind incidence angle
τ — Shear stress of the wind acting on the surface

7. References

[1] HALLEBRAND, E; JAKOBSSON, W. Structural design of high-rise buildings, Master dissertation, Department of construction sciences, LUND University, 2016.

[2] TAPAJÓS, L.S.; FERREIRA, J.A.T.; LIMA NETO,

A.F.; REIXEIRA, M. R.; FERREIRA, M. P. Effect of Wind in the design of reiforced concrete buildings.*In*: RIEM- Ibracon structures and materials journal. V.9, 2016, p.883-910.

[3] ODA, D.A. Wind design loads on high-rise reinforced concrete buildings in Maysan province ShouthernIrac. *In*: International journal of innovative researche in science engineering and technology. V.6, n.7, 2017, p.12451-12471.

[4] ADNAN, A.; SURADI, S. Comparison on the effect of earthquake and wind loads on the performance of reinforced concrete buildings. *In*: Word conference on earthquake engineering. v.14, 2008.

[5] BHANDARI, N.M.; KRISHNA, P. ; KUMAR, K.. An explanatory handbook on proposed IS 875 (Part3) Wind load on buildings and structures. Shri G.S Institute of technology and science Indore. Document n IITK-GSDMA- Wind 06-v3.0. 2011.

[6] BIASIOLI, F.; POLJANSEK,B.;NIKOLOVA, B.; DIMOVA, S and PINTO, A. Eurocode 2:Background and applications: Design of concrete buildings. Publications office, 2014.

[7] LAC- Laboratório de aerodinâmica de construções. Edifício Alfredo Volpi- João Pessoa, Túnel de vento Prof. Joaquim Blessmann, Porto Alegre, UFRGS, 2012.

[8] IPT- Instituto de Pesquisas Tecnológicas. Análise dinâmica da ação do vento no empreendimento Terra Brasilis Caruaru, CTMETRO- Centro de Metrologia mecânica, elétrica e de fluidos, São Paulo, 2014, relatório 138 649-205.

[9] BLOCKEN, B. 50 years of Computational Wind Engineering: Past, present and future, *In*: Journal of Wind Engineering and industrial Aerodynamics, 129, Cambridge, 2014 p.69-102.

[10] AKINS, R.E.; Peterka, J.A, CERMAK, J.E. Mean force and moment coefficiens for buildings in turbulent boundary layer, *In:*Journal of wind Engineering and Industrial Aerodynamics, v.2, 1977, p.195-209.

[11] BRAUN, A.L. e AWRUCH, A.M. Aerodynamic analysis of buldings using numerical tools from computational wind engineering, *In*: Associación Argentina de mecânica computational, v.26, 2007 p.1236-1251.

[12] BRAUN, A.L.; AWRUCH, A.M. Aerodynamic and aeroelastic analyses on the CAARC standard tall building model using numerical simulation. *In*: Computers and Structures, v.87, Porto Alegre, 2009, p.564-581.

[13] DAGNEW, A.K.; BITSUAMLAK, G.T. LES evaluation of Wind pressures on a standard tall building with and without a neighboring building. *In*: CWE-Computational Wind Engineering, Chapel Hill, North Carolina, 2010.

[14] DAGNEW, A.K.; BITSUAMLAK, G.T. Computational evaluation of Wind loads on a standard tall building using LES. *In*: Wind and structures, Techno-Press, 2014, p.567-598.

[15] *OBERKAMPF*, *W.L.*; *T.G. TRUCANO*, Verification and validation in computational fluid dynamics. *Progress in Aerospace Sciences, v.38, 2002. p.209*-272.

[16] CHEN, Q.; SREBRIC, J. A procedure for verification, validation , and reporting of indoor environment CFD analyses, *In:* HVAC&R Research, v.8, n.2, 2002, p. 201-216.

[17] MOONEN, P.; BLOCKEN, B.; ROELS, S.; CARMELIET J. Numerical modeling of the flow conditions in a closed-circuit low-speed wind tunnel, *In*: International Journal of Wind Engineering and Industrial Aerodynamics, v.94, 2006, p.699-723.

[18] FRANKE, J.; HELLSTEN, A.; SCHLÜNZEN, H.; CARISSIMO, B., (Eds.). Best practice guideline for the CFD simulation of flows in the urban environment, *In*: COST- European Cooperation in Science and Technology, Action 732, 2007.

[19] REITER, S. Validation process for CFD simulations of Wind around buildings, *In*: EBECC- European Built Environment CAE (Computer-Aited Engineering) Conference, London, 2008.

[20] SCHATZMANN, M.; BRITTER, R. Quality assurance and improvement of micro-scale meteorological models, *Int. Journal of environment and pollution*, v.44, n.1-4, 2011, p.139-146.

[21] KIM, D. The application of CFD to building analysis and design: a combined approach of an immersive case study and wind tunnel testing, Dissertation, Faculty of the Virginia Polytechnic institute, Virginia, 2013.

[22] RONG, L.; NIELSEN, P.V.; BJERG, B. ZHANG, G.. Summary of best guidelines and validation of CFD modeling in livestock buildings to ensure prediction quality, *In:* Computers and Electronics in Agriculture, v.121, 2016, p.180-190.

[23] PATANKAR, V. Numerical heat transfer and fluid flow. Hemisphere publish corporation, 1980.

[24] PRAKASH, C.; PATANKAR, S.V. A control volume-based finite-element method for solvingthe Navier-Stokes equations using equal-order velocity-pressure interpolation, *In*: Numerical heat transfer, 8, 1985, p.229-280.

[25] VERSTEEG, H.K. MALALASEKERA,W. An excellent introduction to theory of CFD with well-presented derivations of the equations, Longman, Harlow, 1995.

[26] FERZIGER, J.H; PERIC, M. Computational Methods for Fluid Dynamics, 3, Springer, 2002.

[27] KUNDU, P.K.; COHEN, I.M. Fluid Mechanics, 2, Academic Press, 2002.

[28] LEWIS, R.W.; NITHIARASU, P.; SEETHARAMU, K.N. Fundamentals of the finite element method for heat and fluid flow. Wiley, 2004, p.217-218.

[29] ANSYS 14.0. Training Manual, Ansys, Incorporation, 2012.

[30] ÇENGEL, Y.A.; CIMBALA, J.M. Fluid Mechanics: Fundamentals and Applications. Mc Graw Hill, AMGH. 2007.

Volume 13, Number 3 (June 2020) p. 644 – 655 • ISSN 1983-4195
http://dx.doi.org/10.1590/S1983-41952020000300013

REVISTA IBRACON DE ESTRUTURAS E MATERIAIS
IBRACON STRUCTURES AND MATERIALS JOURNAL

Evaluation of external sulfate attack (Na_2SO_4 and $MgSO_4$): Portland cement mortars containing fillers

Avaliação do ataque externo por sulfato (Na_2SO_4 e $MgSO_4$): Argamassas de cimento Portland contendo fíleres



D. J. DE SOUZA [a]
diegojesusdesouza@hotmail.com
https://orcid.org/0000-0002-7531-0084

M. H. F. MEDEIROS [b]
medeiros.ufpr@gmail.com
https://orcid.org/0000-0003-3112-9715

J. HOPPE FILHO [c]
juarez.hoppe@gmail.com
https://orcid.org/0000-0002-9645-6808

Abstract

Sulfate attack is a term used to describe a series of chemical reactions between sulfate ions and hydrated compounds of the hardened cement paste. The present study aims to evaluate the physical (linear expansion, flexural and compressive strength) and mineralogical properties (X-ray diffraction) of three different mortar compositions (Portland Cement CPV-ARI with limestone filler and, with a quartz filler, in both cases with 10% replacement of the cement by weight) against sodium and magnesium sulfate attack (concentration of SO_4^{2-} equal to 0.7 molar). The data collected indicate that the replacing the cement by the two fillers generate different results, the quartz filler presented a mitigating behaviour towards the sulfate, and the limestone filler was harmful to Portland cement mortars, in both physical and chemical characteristics.

Keywords: durability, sulfate attack, sodium sulfate, magnesium sulfate.

Resumo

Ataque por sulfato é um termo utilizado para descrever uma série de reações químicas que ocorrem entre os íons de sulfato com os produtos da hidratação do cimento Portland. O presente estudo tem por objetivo avaliar de maneira física (expansão linear, resistência à compressão e tração na flexão) e mineralógica (DRX), três diferentes composições de argamassa, alterando a composição dos finos (CPV – ARI, CPV – ARI com substituição parcial do cimento por 10%, em massa, de fíler calcário, e, CPV – ARI com substituição parcial por 10%, em massa, de fíler quartzoso) frente ao ataque por sulfato de sódio, bem como, por sulfato de magnésio (concentração da solução de 0.7 molar). Os resultados obtidos indicam que a substituição parcial do cimento Portland pelos dos diferentes fíleres geram diferentes resultados, o fíler quartzoso apresentou um comportamento mitigativo frente ao ataque por sulfato, porém, o fíler calcário apresentou comportamento deletério tanto pela avaliação física, quanto mineralógica.

Palavras-chave: durabilidade do concreto, ataque por sulfato, sulfato de sódio, sulfato de magnésio.

[a] *University of Ottawa (uOttawa), Department of Civil Engineering, Ottawa, ON, Canada;*
[b] *Federal University of Parana, Graduate Program in Civil Construction Engineering, Curitiba, PR, Brazil;*
[c] *Federal University of Western Bahia, Centre of Exact Sciences and Technologies, Barreiras, BA, Brazil.*

Received: 26 Jun 2019 00000 • Accepted: 14 Nov 2019 • Available Online: 26 May 2020

1. Introduction

Sulfate attack is a term used to describe a series of chemical reactions between sulfate ions and hydrated compounds of the hardened cement paste [1,2]. The typical form of sulfate attack, associated with the formation of gypsum and the secondary ettringite formation, is the most common, resulting from the diffusion of sulfate ions from an external source [1,3,4]. The interaction between SO_4^{2-} ions and hydrated Portland cement products, such as calcium hydroxide, to form gypsum; and, with aluminates, to form ettringite, which can increase the volume in about 1.2 to 2.2 times more than the initial products. Moreover, causing internal stresses in the bulk cement paste, which can form crack resulting in distress of the hydrated cement matrix [2,5,6].

An important aspect in studies related to external sulfate attack (ESA) is regarding to the associated cation to SO_4^{2-} (i. e., Na^+, K^+, Mg^{2+}, Ca^{2+}, etc.) since the physical and chemical behaviour of the matter depends on the way in which the atoms interact, all the components in pores solution should be considered in the reaction, some of them can act as a catalyst or actively on the damage [3–6]. The mechanism of attack for the anion (SO_4^{2-}) is very close for each of the associated cation, on the other hand, each cation has a distinct interaction with the cementitious matrix. Also, the ratio anion/cation in solution for each salt (Na_2SO_4, $MgSO_4$, $CaSO_4$, etc.) is also variable, since the molecular mass is dependent on the mass of each of the atoms.

Several studies indicate that $MgSO_4$ solutions are more aggressive than Na_2SO_4 at the same concentration level [1,3,4,7–12]. In sodium sulfate solution the main reaction is between SO_4^{2-} ions and Ca(OH)2, forming gypsum, and then between gypsum and calcium monosulfoaluminate hydrate (AFm) to form secondary ettringite [3,4,8,13,14]. Magnesium sulfate solutions, besides the formation of gypsum and ettringite, also develop brucite [$Mg(OH)_2$] (from the reaction between Mg^{2+} and Portlandite) and Magnesium Silicate Hydrate (MSH) due to the decalcification of the C-S-H. MSH has negligible binding capacity and no cementitious properties [9,12,15].

The use of fillers in the composition of cementitious products is widely discussed in the literature [2,16–18]. It is known that such materials can influence the physical, mechanical and chemical characteristics of the concrete, even if it is an inert material. Three physical effects of fillers can be observed when used in cementitious materials [16]. Two of these, cement dilution and improved particle packing, are direct consequences of the substitution or addition of these fineness particles, while the third effect is related to the improvement of the nucleation of the cement grain. Regarding the hydration of Portland cement, such materials can modify the kinetics of this phenomenon, especially at lower ages due to the heterogeneous nucleation [16].

However, the blended cements containing fillers are more vulnerable to sulfate attack distresses (at longer exposure periods) when compared with supplementary cementitious materials [12,19–23]. Mostly because fillers do not consume part of the portlandite generated in the cement hydration process, favoring the formation of gypsum and later, secondary ettringite [17,24,25].

An example of the long-term exposure of fillers, Tosun-Felekoglu [26] presented results from samples with different amount of C_3A (4.6% and 11.2%) and limestone filler (0%, 5%, 10%, 20% and 40% % in partial replacement of the cement) exposed to both magnesium and sodium sulfate at two different temperatures (5 and 20 °C). The author concludes that the deterioration of the

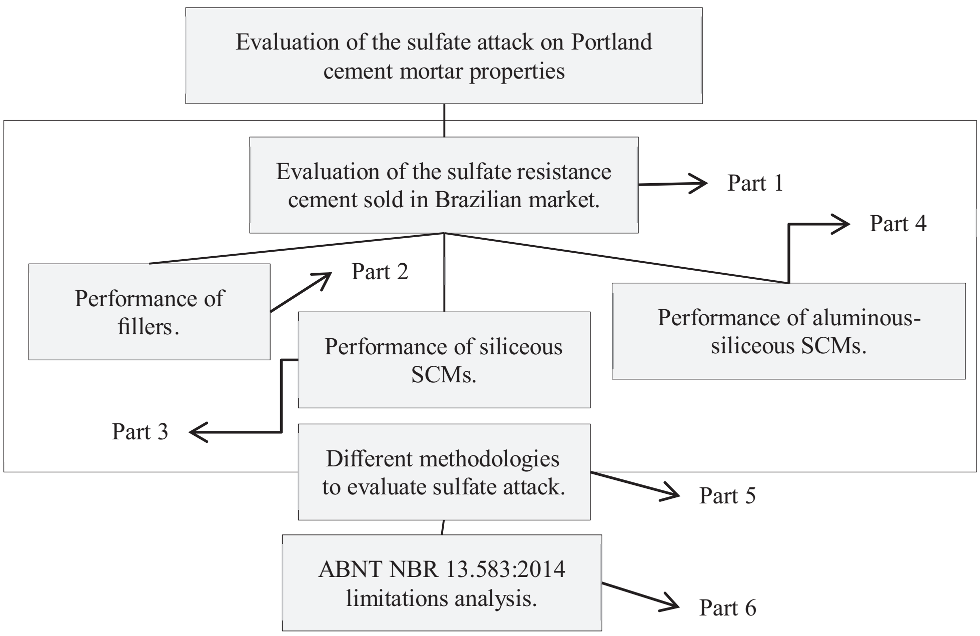

Figure 1
Division of the research project to evaluate sulfate attack on the properties of Portland cement mortars

samples was much more significant in concretes containing C_3A content in the range of 11.2% in both solutions, and this has become even more critical in conditions where there are higher cement substitution levels Portland by limestone filler. The increase in the amount of limestone filler had increased the permeability of the samples, and, there was an increase in the formation of thaumasite that had been aggravated at low temperatures.
The limestone filler added may also present some reactive activity with Portland cement [27]. A small portion of this material can be consumed and form calcium monocarboaluminate hydrated, which can influence and delay the conversion of AFt into AFm [28].
The presence of limestone filler can also be harmful when exposed to sulfate ions, especially when exposed at lower temperatures (below 15 ºC). Due to the release of carbonates from the filler particles, which combinate with sulfate and potentially form thaumasite [14,17,19,20,24,25].
The present paper is the second part of a research project to evaluate the sulfate attack on the physical-chemical properties of Portland cement composites, developed at the Federal University of Paraná (Figure 1). Part one can be seen in [29].

2. Research significance

The use of different types of fillers with different chemical compositions could also produce different concrete behaviours when exposed to different sulfate salts, affecting cement paste properties differently, which require different remedial actions and mix design depending on the exposure conditions. The present study aims to evaluate the performance of physical and mineralogical properties of three different mortar compositions (OPC, with limestone and quartz filler) exposed to sodium and magnesium sulfate attack. The approach of the problem will involve the manipulation of two independent variables, the type of binder material used and the aggressive solution of exposure of the mortars.

3. Materials and methods

In order to detect the influence of the cement type on sulfate attack damage degree, the present research has as a main concern, the evaluation of the interference of the sulfate ions in the physical properties intrinsic to the proposed objective.

Table 1
Chemical composition of the cement

Chemical composition (%)		Clinker composition (%)	
CaO	60.97	C_3S	52.00
SiO_2	18.77	C_2S	14.60
Al_2O_3	4.36	C_3A	6.60
Fe_2O_3	2.93	C_4AF	8.91
MgO	3.50	Gypsum	6.71
SO_3	3.12	$CaCO_3$	4.9
Na_2Oeq	0.68	Physical properties	—
Free lime	0.90	BET (m^2/kg)	1,070
Insoluble res.	0.77	Specific gravity	3.13
Loss on ignition	3.55	—	—

3.1 Materials

Portland cement with high early age strength CPV - ARI (PC) was used as a control group (containing 4.9% of carbonaceous material) and also replaced partially (10% by weight) by the limestone filler and quartz filler.
The PC used has no influence of any supplementary cementitious materials (SCM) or even addition of fillers (just clinker + gypsum) on the reference system to be evaluated; however, should be mentioned that the PC has just a small amount of carbonaceous material as allowed by Brazilian's standards (maximum of 5%, according to ABNT NBR 5733/2010). The Portland cement was characterized by performing loss on ignition; specific gravity and BET tests. Chemical analyses were also performed, using X-ray fluorescence; and, particle size distribution was measured using laser diffraction in a measurement range of 0.04-500 µm. Table 1 shows the chemical, mineralogical and physical composition of the PC according to the results obtained from the X-ray fluorescence and the physical characteristics of the cement.
In this study, two different types of filler were selected, limestone filler (LF) and quartz filler (QF), which correspond to different total amount of carbonaceous materials in the mixes, i.e. control group equal to 5%, LF group equal to 15% (5% from the cement + 10% of limestone filler, corresponding to the new regulations regarding the use of limestone filler in blended cement), and QF group equal to 5% of carbonaceous materials + 10% of quartz filler. Both fillers were characterized for loss on ignition, specific gravity, BET and particle size distribution. The mineralogical properties of both fillers were also characterized using XRD tests. The analysis was performed from 5º to 75º 2θ, with an angular pitch of 0.02º 2θ and time per step of 1 second. It was used copper anode tube, 40 kV / 30 mA and divergent slot of 1º. Minerals were identified by comparison with the standards of the International Centre for Diffraction Data, ICDD. Finally, the chemical characterization of the samples was performed using X-ray fluorescence (XRF) method.
The fine aggregate used for the design of the mortar bars was natural quartz sand with SiO_2 content of 96% and free of contaminants, which means that it is negligible the chemical influence of this material on final results. Finally, the fine aggregate was sieved, and the particle size distribution was fixed as 25% of the total mass of sand between each of the following ranges 0.15-0.30 mm, 0.30-0.60 mm, 0.6-1.2 mm and 1.2-2.4 mm.

3.2 Methods to evaluate sulfate attack

In this section will present the procedures used to evaluate the sulfate attack in different prismatic mortars bars, such as preparing procedure of the samples; solutions; conditions of exposure; length variation test and compressive strength test.

a) Preparing of the sample for mortar bar tests

The degree of sulfate attack on mortars was analyzed in general by two main groups samples:
- Group 1: composed of 36 specimens measuring 25 mm x 25 mm x 285 mm (to evaluate induced expansion), divided into 3 different mix-designs (PC, PC + LF and PC + QF) and

3 final exposure solutions: Control (water + calcium hydroxide), Na_2SO_4 and $MgSO_4$ solutions;

- Group 2: composed of 108 specimens with dimensions of 40 mm x 40 mm x 160 mm (to evaluate compressive and flexural tensile strength) and divided into 3 compositions and 3 final exposure solutions.

The mortars bars were designed based on Brazilian standard ABNT NBR 13.583/2014 with binder (cement + filler)-to-sand ratio of 1.0/3.2, by mass, and water to "binder" ratio of 0.60. After casting and moulding, all bars were subject to 48 h in the mold in moist cabinet, later the samples were cured for 12 days in lime water at 23±2 °C before, finally, immersed in sulfate solutions at 40 °C, in accordance with ABNT NBR 13.853/2014, for a period of 140 days.

b) Exposure solutions

The concentration of anhydrous sodium sulfate, in accordance with ABNT NBR 13.853/2014, was 100g of Na_2SO_4/L of solution (0.704 mol/L); which means that the concentration of SO_4^{2-} (also 0.704 mol/L) can be defined as 67,630 ppm (67.63 g/L). Fixing the total amount of sulfate ions, the magnesium sulfate solution was prepared as 0.704 mol/L as well, (84.74g of $MgSO_4$/L of solution). Finally, the solution volume-to-samples volume ratio was fixed as 4.0/1.0 [13,14,29,30], along the whole exposure period.

c) Length variation

The evaluation of the induced expansion followed NBR 13.583/2014, after the first and second curing procedures (48 h and 12 days, respectively), the samples had their initial lengths measured just before the exposure to the final solutions.

The measurements were performed after 2, 4, 6, 8, 10, 15 and 20 weeks of exposure. For this purpose, the samples were placed at the micrometre, always with the same face upwards, and the measurements were taken always referring to the smaller length indication identified by the apparatus after 360° rotation of the bar. The individual expansion or shrinkage of the samples are given by the difference between the value measured at the corresponding exposure time and the initial reading minus the difference of the same group of samples exposed to the lime-water solution, divided by its initial length and multiplied by 100.

d) Compressive and flexural tensile strength

The tests of flexural tensile and compression strength were made at times of exposure of 0; 2; 6; 10; and, 20 weeks. ABNT NBR 13.279 [27] recommendations were followed and the tests were carried out in an equipment with a load capacity of 100 kN, and the tensile strength tests were performed in the bars before the compression.

For the flexural tensile strength test the load application rate was 50 ± 10 N/sec until failure, thus, the strength was calculated according to ABNT NBR 13.279 [27].

In compressive strength test, 6 specimens were obtained after tensile tests of 3 samples and the load application rate was 505 ± 5 N/sec until failure, thus, the strength was calculated.

Table 2
Chemical and physical properties of the limestone filler and quartz filler

	Limestone filler	Quartz filler
CaO	42.77	—
SiO_2	1.62	94.45
Al_2O_3	0.95	2.76
Fe_2O_3	0.24	—
MgO	8.25	—
SO_3	0.66	1.18
K_2O	0.17	0.29
Insoluble residue	0.14	0.05
Loss on ignition	45.2	1.3
BET (m^2/kg)	1,413	1,227
Specific gravity	2.70	2.60

4. Results and discussions

The results of the tests will be presented and discussed in this section, firstly length variation of and then the results related to mechanical properties.

4.1 Physical and chemical characterization of the filler materials

Table 2 reports the chemical compositions measured by XRF and the results of BET specific surface area, LOI and the specific gravity of the mineral additions.

Both fillers have higher surface specific area and lower specific gravity than PC. The limestone filler had magnesium oxide content of 8.25% according to its chemical composition, which means that this material is not classified as limestone, but as magnesian limestone, since the MgO content is in between 5% and 12% [31] and it can be classified as Type B of Fillers (ASTM C1797). On the other hand, the chemical composition of the quartz filler (Type C of Fillers according to ASTM C1797), as expected, had a high content of silicon dioxide, close to 95%. The XRD patterns of the limestone and quartz filler, respectively, are shown in Figure 2. Calcite ($CaCO_3$), dolomite ($CaCO_3.MgCO_3$) and quartz (SiO_2) were identified as the main mineralogical phases in the samples.

In Figure 3, the particle size distributions of the cement and fillers are presented. The limestone and quartz fillers have D50 around 10-15 μm, both higher than the cement average, around 6 μm. However, this does not necessarily mean that the fillers grains will not influence the nucleation and hydration of the cement particles [16,32,33]. As an example, for all anhydrous cement particles larger than 10 μm (approximately 31% of the cement grains), 50% of the QF particles and approximately 40% of LF will be equal to or lower than those of Portland cement grains, which means that some fillers particles can still change the hydration kinetics of the cement. However, the randomization of the mixture between the binder particles should be considered as well.

4.2 Length variation analysis

The results of the analysis of length variation of the samples over

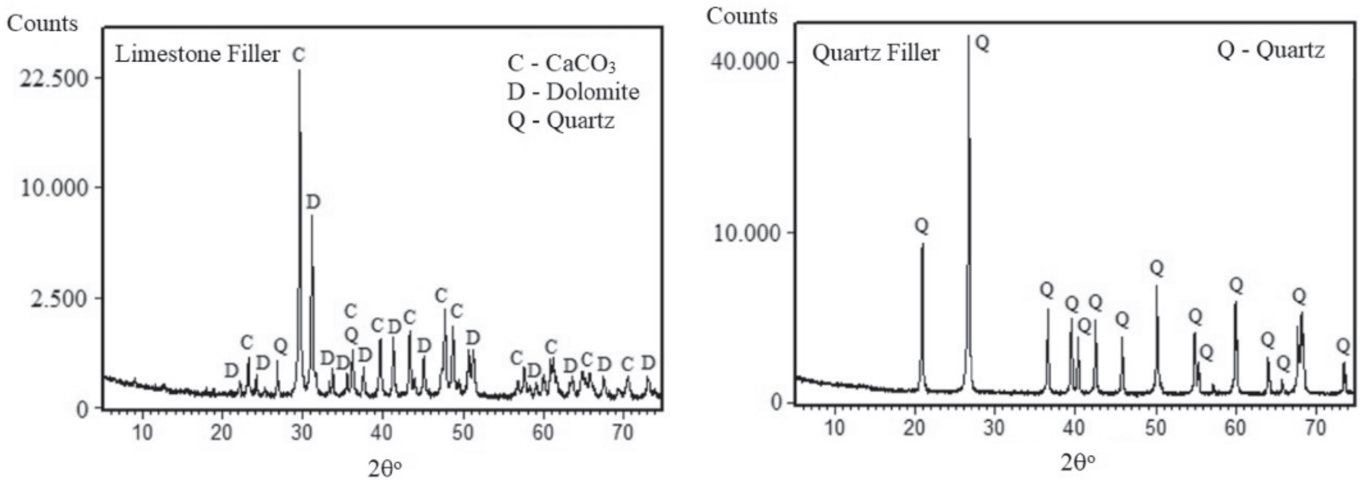

Figure 2
X-ray diffractograms of limestone filler and quartz filler

the 20 weeks of exposure (140 days) in both aggressive solutions are presented in Figure 4.

The methodology of the discussion will initially debate the length variations presented for an exposure period of 42 days (6 weeks) since the test was based on NBR 13.583. Then, the discussion of the behaviour of the studied groups will be discussed individually for the extended time of exposure (20 weeks).

It should be noted that NBR 13.583 does not specify a value to which a composition can be considered resistant or not to sulfate attack since it is only a comparative analysis. However, according to Marciano [34], compositions with expansion equal to or less than 0.030% at the 42 days of exposure (6 weeks) may be considered resistant to sodium sulfate. However, considering that SO_4^{2-} content in solution was kept constant at 6.76%, it was observed that only the FQ series exposed to sodium sulfate presented resistance (expansion equal to 0.02%), considering the limit of 0.03% at 42 days (6 weeks).

On the other hand, the expansion of mortars bars exposed to magnesium sulfate was more harmful until the 42nd day. This behaviour is associated with the higher solubility of $MgSO_4$ when compared to Na_2SO_4, which results in a higher sulfate ions content in the solution. Also, for one mole of magnesium sulfate the available amount of SO_4^{2-} in solution also becomes higher due to the influence of the sulfate ion on the molar mass of the $MgSO_4$ molecule. Moreover, in $MgSO_4$ the brucite precipitation also acts a pH-buffer in the sulfate solution.

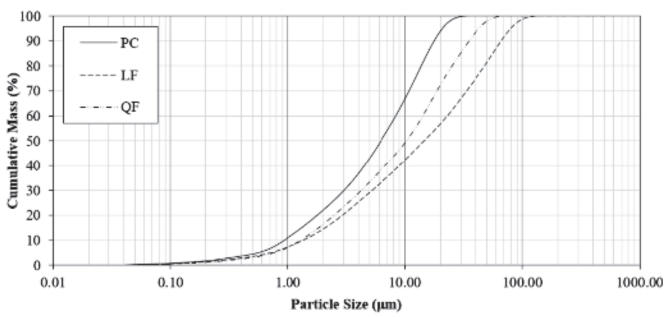

Figure 3
Particle size distribution of the cement, limestone filler and quartz filler

The comparative analysis between the averages results, Tukey's test, for 6 weeks of exposure, can be seen in Figure 5. Thus, it should be mentioned that the PC and LF groups exposed to sodium sulfate, as well as PC and QF for exposed to magnesium sulfate can be considered statistically equivalent. Therefore, the decision-making should be based on the economic and non-technical benefits for these cases (when the analysis is based on NBR 13.583, at 42 days of exposure). However, in the PC x QF and LF x QF comparisons exposed to sodium sulfate presented significant differences in the results, the QF had 59% lower induced expansion than the other samples. The PC x LF and LF x QF samples exposed to magnesium sulfate also showed significant variations in the results. For magnesium sulfate, the QF samples presented statistical similarity to the control group and the samples containing LF showed worse results (66% greater than the control group).

As can be seen in Figure 4 the groups LF and QF, have mitigated the effect of sodium sulfate attack or at least have shown results similar to the control group at 140 days of exposure, as can be seen in Figure 6, which shows the comparative analysis of the averages, Tukey's Test. The impact of the fillers, at least for low replacement levels, such as 10%, was more significant for exposure to sodium sulfate solution so that the QF presented a good performance to induced expansion when compared with the control group (50% lower expansion values) and LF decreases the expansion to values close to 14%. On the other hand, for exposure to magnesium sulfate attack, all series can be considered as equivalents (Figure 6). However, such similarities are positive, since the replacement of the Portland cement did not cause losses in performance.

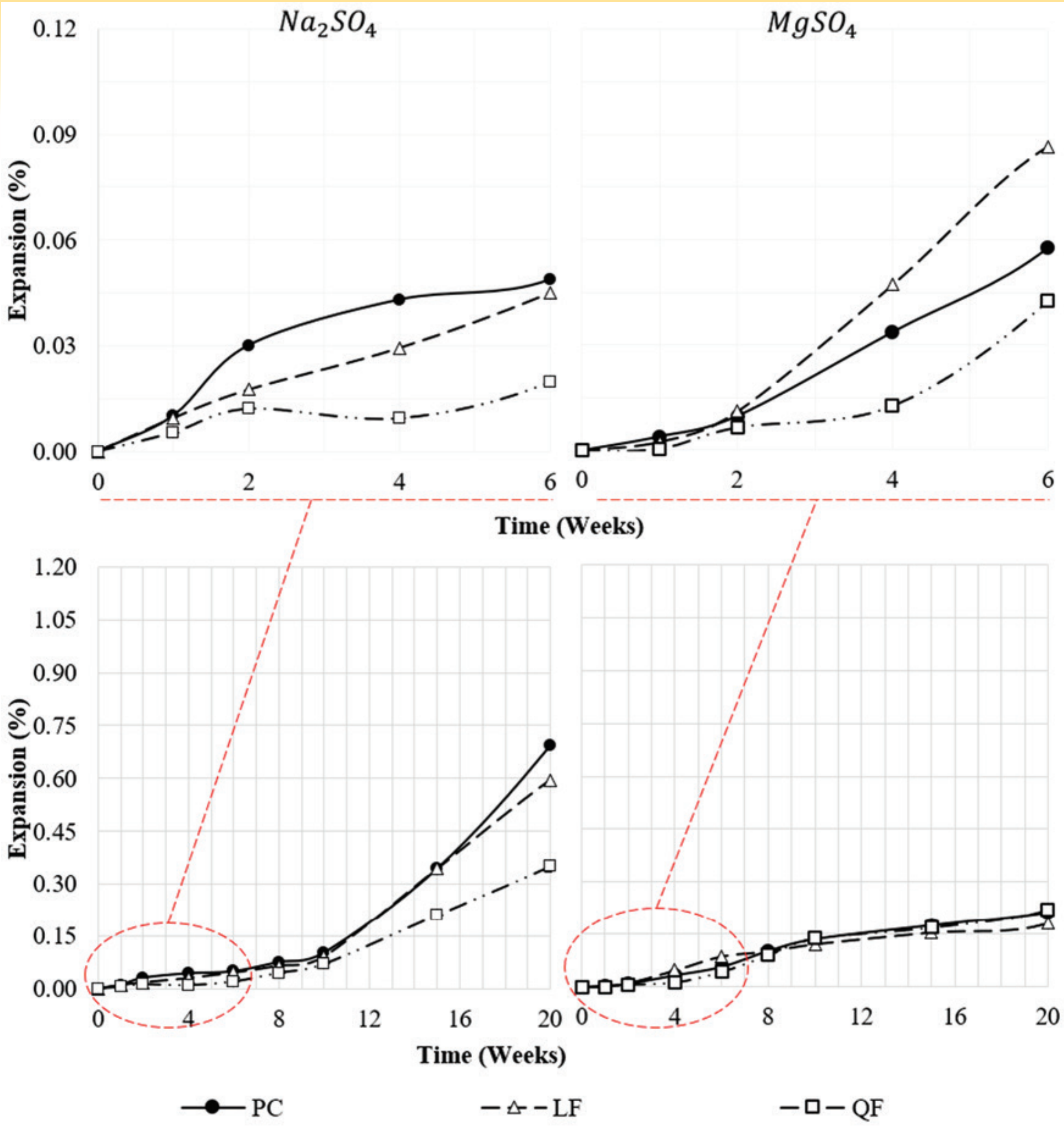

Figure 4
Expansion of the mortar bars ARI, LF and QF exposed to solutions of Na_2SO_4 and $MgSO_4$ (0.7 mol/L) for 42 and 140 days (6 and 20 weeks)

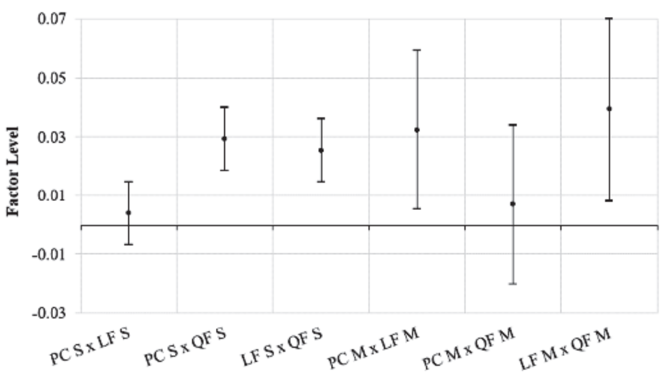

Figure 5
Comparative analysis of the averages, Tukey's test, for 6 weeks of exposure among the series studied, for a significance level of 5% (S-sodium sulfate and M-Magnesium sulfate)

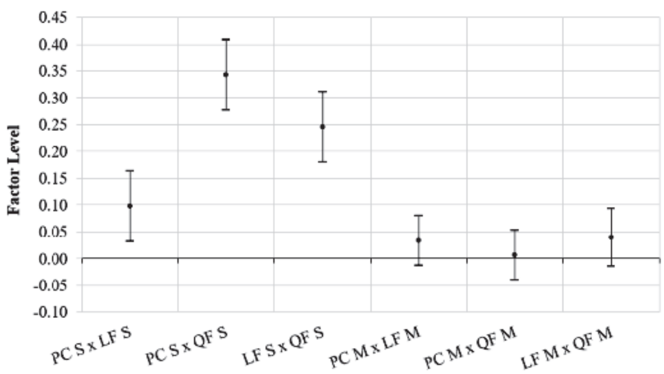

Figure 6
Comparative analysis of the averages, Tukey's test, for 20 weeks of exposure among the series studied, for a significance level of 5% (S-sodium sulfate and M-Magnesium sulfate)

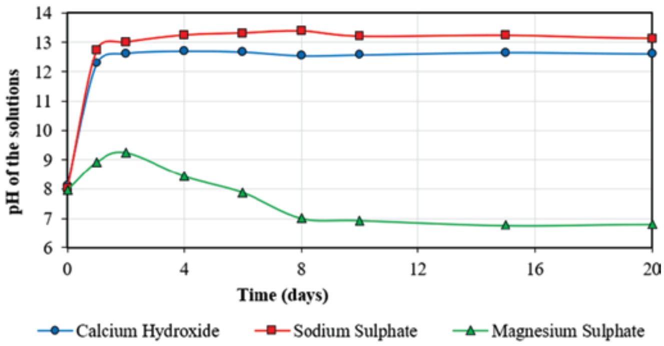

Figure 7
Comparative pH analysis of $Ca(OH)_2$, Na_2SO_4 and $MgSO_4$ solutions over 20 weeks (140 days)

The first product formed from the interaction between magnesium sulfate and Portland cement hydrated products is brucite (magnesium hydroxide), in which the electron affinity magnesium ion replaces the portlandite calcium ions. Such material is presented as a gel filling the voids of the mortars and can precipitate on the surface along with the gypsum and compositions of hydrated magnesium sulfate [2,3,8,11,17,35–37].
According to authors [3,8,37], after the mortar bars are immersed in the solution, it tends to have an increase in the pH of the solution (initially close to 7-8) for a range of 9 - 10 due to the interaction with the portlandite of the pores of the samples, and, parallel with this phenomenon, there is the formation of brucite, gypsum and ettringite on the surface of the mortar bars. With the excessive formation of brucite and gypsum, the pH of the pore solution begins to decrease, since such these materials have lower solubility than the portlandite. Therefore, releasing less OH^- to the solution. Then, at lower pH in mortar pores solution (around 7) there is the destabilization of the C-S-H, which begins to release calcium ions to increases the pH. However, this process, besides the decalcification of calcium silicate hydrate (CSH), allows the

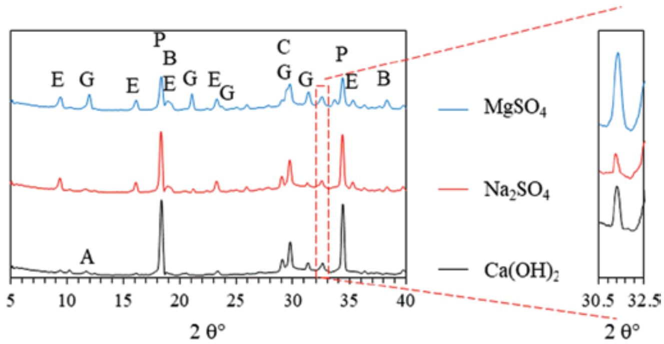

Figure 9
LF diffractograms after 20 weeks of exposure to $Ca(OH)_2$, Na_2SO_4 and $MgSO_4$.
Monocarboluminate (A), brucite (B), calcite (C), ettringite (E), gypsum (G) and portlandite (P)

formation of magnesium silicate hydrate (MSH) that does not have the cementitious capacity.
Nevertheless, the calcium ions cannot stimulate the increases in pH of the solution, because the Ca^{2+} ends up interacting with sulfate ions and precipitate due to the low solubility of the calcium sulfate. To analyze such statement, for the present study, pH measurements were carried out along the analyzed periods of exposure, and Figure 7 presents the comparative pH along the evaluation between three studied solutions (i.e. control, sodium sulfate and magnesium sulfate).

4.3 Mineralogical analysis

The obtained diffractograms for all series for each exposure conditions can be seen in Figure 8, Figure 9 and Figure 10. Compared to calcium hydroxide exposure solution, it can be observed that PC, LF, and QF presented a higher intensity the peaks related to ettringite crystals (E) for exposure in

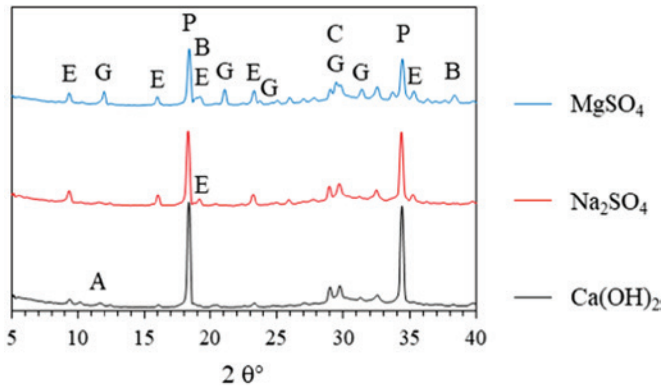

Figure 8
PC diffractograms after 20 weeks of exposure to $Ca(OH)_2$, Na_2SO_4 and $MgSO_4$.
Monocarboluminate (A), brucite (B), calcite (C), ettringite (E), gypsum (G) and portlandite (P)

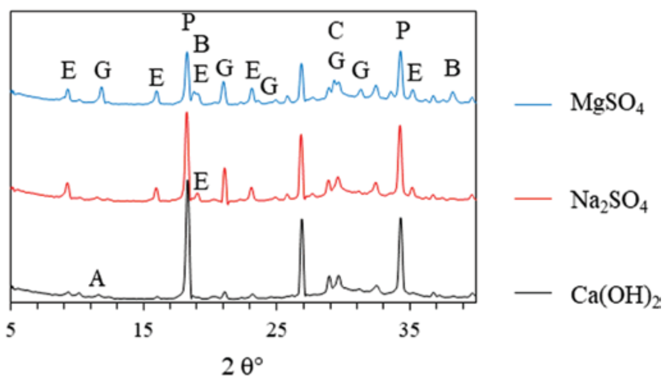

Figure 10
QF diffractograms after 20 weeks of exposure to $Ca(OH)_2$, Na_2SO_4 and $MgSO_4$.
Monocarboluminate (A), brucite (B), calcite (C), ettringite (E), gypsum (G) and portlandite (P)

both sulfate solutions, as well as consumption of the portlandite. In the position close to 12.00° 2θ related to gypsum (11.65° 2θ, card number 03-0044) and calcium monocarboaluminate hydrate (11.68° 2θ, card number 14-0083) formation, can be seen an increase for exposure of the sample in a magnesium sulfate solution. The formation of gypsum in this condition of exposure can be associated, among other factors, to the destabilization of the ettringite and C-S-H due to the lower pH in the pore solution of the samples and with the reaction between $MgSO_4$ and calcium hydroxide [17,36]. The later can be easily explained by the higher consumption of the portlandite (34.19° 2θ, card number 02-0968) due to the exposure to magnesium sulfate, leading to a higher gypsum formation, reduction of the pH, destabilization of CSH and ettringite (9.14° 2θ, card number 13-0350), suitable with data presented in the literature [3,10–12,36].

The groups containing fillers materials (LF and QF), in general, mitigated or, at least, kept similar the effects in the induced expansion of sodium sulfate attack when compared to PC. The fact that the composition LF presented greater degradation than QF due to Na_2SO_4, can be plausibly explained by the high pH of the sodium sulfate solution after reaction with mortar samples. After formation of gypsum and ettringite, Na_2SO_4 releases a large amount of Na+ in the pore solution of the mortar bars. As seen the LF group presented higher peak count at 31.33° 2θ (Figure 9) in comparison with PC and QF, this peak is be associated with the presence of two main minerals: gypsum and dolomite (i.e. from the mineralogical formation of the magnesian limestone filler used). Comparing the three diffractograms showed in Figure 9, the exposure to sodium sulfate presented a significant consumption of Dolomite (at 31.33 ° 2θ) when compared with the different exposure conditions, as well as there is an increase in the peak of calcite at 29.5° 2θ. One of the possible explanations for dolomite consumption can be the "dedolomitization" process caused by ion exchange between the Ca^{2+}, Mg^{2+} and CO_3^{2-} ions in the solid phase and alkali ions (i.e. Na+) in the pore solution, as the occurrence in alkali-carbonate reaction [38–43]. As already mentioned, the source of the limestone filler can be classified as magnesian limestone rock, and, based on CSA A23.2-26A, "Determination of Potential Alkali-Carbonate Reactivity of Quarried Carbonate Rocks by Chemical Composition", this rock (source of the limestone filler) can be classified as potential to the reactivity of alkali-carbonate reaction, as indicated in Figure 11, the red zone indicated is the potential reactivity zone of ACR occurrence, based on the chemical composition of the material. Then, the red dot indicated is related to the chemical combination of the magnesian limestone filler used (i.e. CaO content of 42.77%, MgO content of 8.25% and Al_2O_3 content of 0.95%, with CaO/MgO ratio equal to 5.18), placed in the red zone.

Also, carbonate molecules from the limestone filler can also be "consumed" to reacts with the ettringite particles (replacing the sulfate ions), or with unhydrated aluminate particles, to form of calcium monocarboaluminate hydrate [27,28]. In the comparison between the diffractograms, it is possible to see a slightly decreases on ettringite peaks, which may confirm the above statement.

4.4 Mechanical properties

The compressive strength is an essential parameter to be considered regarding the degree of sulfate attack [11,44], as well as the flexural strength which gives important data regarding the microcrack propagation within the cement paste [19,45]. According to Marciano [28] publication, tensile strength is not a good parameter for monitoring the degradation due to sulfate attack, either flexural strength or splitting tensile strength (Brazilian test), especially for short exposure time. However, Biczók [1] and Irassar [29] commented that the flexural strength test shows that the strength increases with exposure to sulfate attack up to a limit point, from which it starts to decrease. According to Irassar [29], it is possible to take from this parabolic behavior of the results the micro-cracking start time point of the samples. Which matches with the point at derivate is equal to zero. Is common in the literature that samples exposed to the sodium sulfate solutions have their strength increased at an initial exposure time and then, for a long time of exposure, there are strength loss (Figure 12 and Figure 13).

Figure 12 and Figure 13 show an increase in early strength comparing both sulfate solutions with the control solution, attributable to pore filled by sulfate attack products, (i.e. gypsum, ettringite, brucite, etc.), once these "empty" void are now filled with "solid" material, they have their density increased and also there is more contact area to absorb the applied load. However, the formed sulfate attack products continue to gain volume so far, at the point that tensile strength is overcome and then there is the beginning of micro-cracks on cement paste [44]. So, at 6 weeks of exposure, the strength of the mortar bars, even for flexural tensile or compressive, is still increasing, which became difficult to compare the "damage" caused by the sulfate attack.

In general, it was observed during the 20 weeks of exposure to sodium and magnesium sulfate solutions that the individual

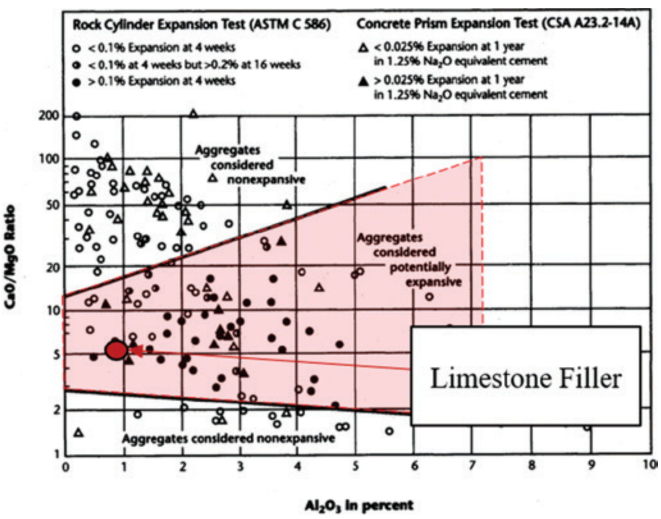

Figure 11
Illustration of the division between non-expansive and potentially expansive aggregates on basis of chemical composition. Source: CSA A23.2-26A

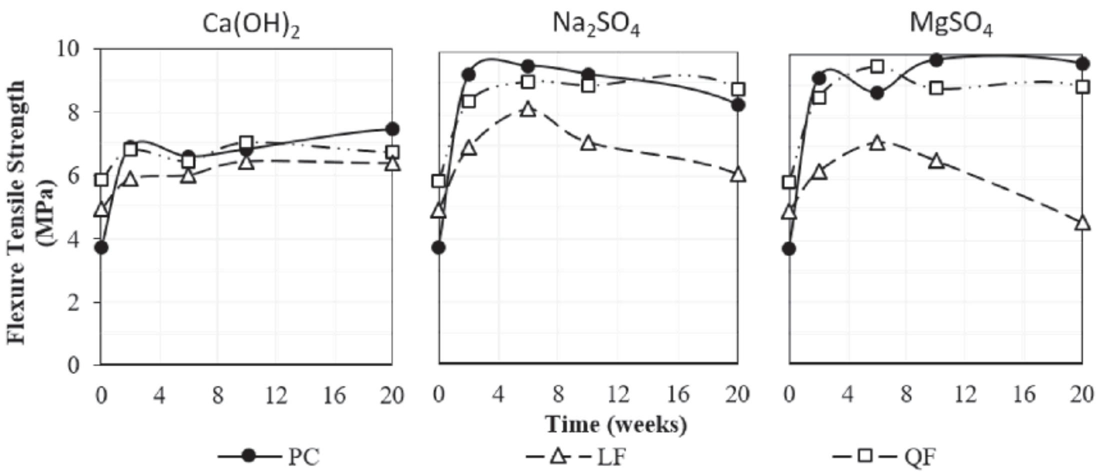

Figure 12
Flexural Tensile strength of the samples up to 20 weeks of exposure in the three different solutions [$Ca(OH)_2$, Na_2SO_4 and $MgSO_4$]

behaviour of each filler group distinguishes between them, even considering that both materials are inert fillers with close physical properties. When exposed to Na_2SO_4, QF showed results statistically similar to the control group PC (Figure 14 and Figure 15), as well as the same behaviour in flexural tensile strength can be seen for QF when exposed to magnesium sulfate attack; however, for compressive strength, QF and PC are not statistically similar, indicating that the behaviour of QF was slightly better than PC.

On the other hand, LF has not shown any similarities with QF and PC (Figure 14 and Figure 15) and based on the flexural and compressive strength data presented in Figure 12 and Figure 13, the use of the magnesian limestone filler was worse in terms of mechanical losses. In one hand, replacing the Portland cement by LF decreases the total amount of aluminates, as result, decreases the potentiality of ettringite formation, which can explain the similarities in the induced expansion results. Though, considering that the water-to-cement ration changed, (from 0.60 to 0.66) since it was kept the water-to-"binder" ratio constant (as 0.60), there are changes in the microstructure of the mortar bars; however, the same behaviour should be addressed to QF as well, but both fillers behave differently. Therefore, a plausible explanation for the obtained results for LF can be its physical and chemical properties. Physically, as presented in Figure 3, the limestone filler has a larger average for particle size distribution, which increases, even more, the porosity and replacing the finer Portland cement particles, decreasing the quality of the microstructure of the mortar bars. Chemically, as already discussed, the significant amount of magnesium in the limestone filler may contribute to a process of dedolomitization of the LF in the mortar bars, especially when exposed to Na_2SO_4.

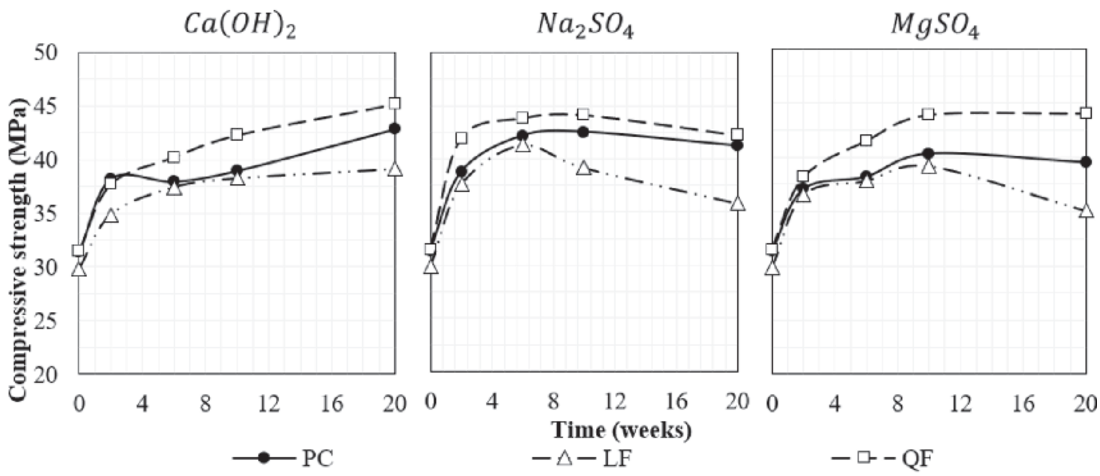

Figure 13
Compressive strength of the samples up to 20 weeks of exposure in the three different solutions [$Ca(OH)_2$, Na_2SO_4 and $MgSO_4$]

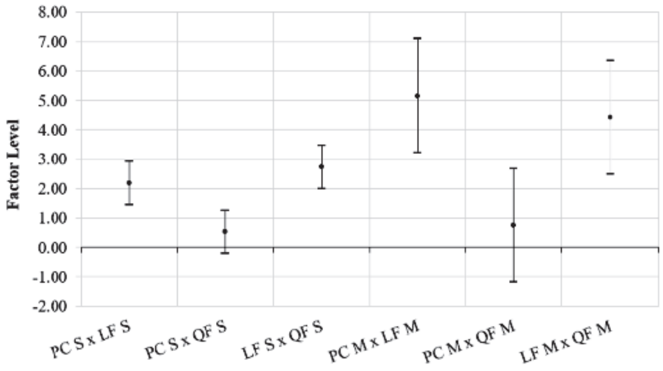

Figure 14
Comparison between averages of flexural tensile strength losses (tukey test for a significance level of 5%) of the same series for different aggressive solutions (S - sodium sulfate and M - magnesium sulfate) for 20 weeks of exposure

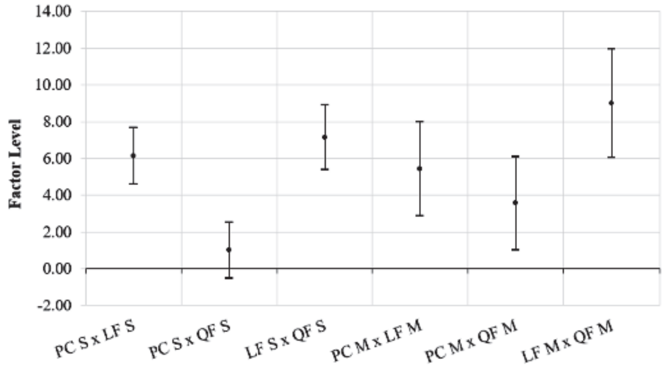

Figure 15
Comparison between averages of compressive strength losses (tukey test for a significance level of 5%) of the same series for different aggressive solutions (S - sodium sulfate and M - magnesium sulfate) for 20 weeks of exposure

The loss in strength for exposure to magnesium sulfate attack (comparatively higher than sodium sulfate attack for PC and LF) is associated with the decalcification of CSH, and, consequently, formation of MSH particles, which have little or no binding characteristics [3,10,11,17,36]. Thus, these results are consistent with the theory and experiments analyzed in the literature. The losses in strength are much more significant than the actual linear induced expansion of samples exposed to magnesium sulfate attack. Therefore, the evaluation only of length variation can lead to erroneous conclusions that, since magnesium sulfate attack does not generate great expansions values in concrete, mortars or cement pastes, when compared in the same exposure period for the solution of Na_2SO_4. However, such results show a contrary reality, leading to the analysis of the sulfate attack may be insufficient when evaluated only by linear dimensional variation.

5. Conclusions

Based on the results of this experimental investigation under tidal environment, the following conclusions are drawn:

- The partial replacement (10% by mass) of the cement by filler particles in the mortars mitigated the induced expansion due to sodium sulfate attack, on higher values for quartz and smaller for limestone fillers. The exposure to magnesium sulfate solution did not show the same behaviour, the replacement of the cement by fillers did not mitigate the expansion, but at least QF and LF were statistically similar to the control group;
- When exposed to sodium sulfate attack, the pH increased along time and has an influence on the test results (i.e. length variation and mechanical analysis), since higher pH maintains the stability of CSH and Ettringite particles. For $MgSO_4$ the pH decreases to values close to 7, which decreases the flexural tensile and compressive strength of the samples due to instability and decalcification of the CSH, plus the damage caused by gypsum and ettringite formation;
- Sodium sulfate solution affected differently the induced expansion and strength loss of Quartz Filler and the Limestone Filler groups. The fine particles of LF show more instability due to the presence of Na^{2+} ions (for Na_2SO_4 exposure) and the XRD analysis showed that the peak of dolomite decreased and there was also increase in the peak of calcite (LF released Mg into the solution) due to sodium sulfate attack;
- Comparing the expansion caused by Na_2SO_4 with $MgSO_4$, for the shorter exposure time (6 weeks as NBR 13,583 recommendations) the different mixes presented higher induced expansion values for the latest. On the other hand, with long-term exposure conditions (i.e. 20 weeks) this behaviour has changed, so that exposure to Na_2SO_4 causes higher values of induced expansion.

Sulfate attack tests with long exposure period, such as 20 weeks or more, are important to better understand and characterize degradation processes of Portland cement composites due to different types of sulfate (sodium sulfate attack, magnesium sulfate attack, etc.).

6. Acknowledgment

The authors would like to thank the support of the Graduation Program in Civil Construction Engineering at Federal University of Paraná (DCC-PPGECC-UFPR), the Ponta Grossa State University (UEPG), the Federal University of Western Bahia (UFOB), the National Council for Scientific and Technological Development (CNPq) and the Coordination for the Improvement of Higher Education Personnel (CAPES), De Souza benefits from a Vanier scholarship financed by NSERC (Natural Science and Engineering Research Council of Canada).

7. References

[1] N.M. Al-Akhras, Durability of metakaolin concrete to sulfate attack, Cem. Concr. Res. 36 (2006) 1727– 1734. doi:10.1016/j.cemconres.2006.03.026.

[2] P.K. Mehta, P.J.M. Monteiro, Concrete: Microstructure, Properties, and Materials, 3rd Edition, 2013. doi:10.1036/0071462899.

[3] M. Santhanam, M.D. Cohen, J. Olek, Mechanism of sulfate attack: A fresh look - Part 2. Proposed mechanisms, Cem. Concr. Res. 33 (2003) 341–346. doi:10.1016/S0008-8846(02)00958-4.

[4] A. Neville, The confused world of sulfate attack on concrete, Cem. Concr. Res. (2004). doi:10.1016/j.cemconres.2004.04.004.

[5] P.J.M. Monteiro, K.E. Kurtis, Time to failure for concrete exposed to severe sulfate attack, Cem. Concr. Res. (2003). doi:10.1016/S0008-8846(02)01097-9.

[6] W. Müllauer, R.E. Beddoe, D. Heinz, Sulfate attack expansion mechanisms, Cem. Concr. Res. 52 (2013) 208–215. doi:10.1016/j.cemconres.2013.07.005.

[7] M. Santhanam, M.D. Cohen, J. Olek, Sulfate attack research - Whither now?, Cem. Concr. Res. 31 (2001) 845–851. doi:10.1016/S0008-8846(01)00510-5.

[8] M. Santhanam, M.D. Cohen, J. Olek, Mechanism of sulfate attack: A fresh look Part 1: Summary of experimental results, Cem. Concr. Res. 32 (2002) 915–921.

[9] B. Chatveera, P. Lertwattanaruk, Evaluation of sulfate resistance of cement mortars containing black rice husk ash, J. Environ. Manage. 60 (2009) 435–1441. doi:10.1016/j.jenvman.2008.09.001.

[10] K. Behfarnia, O. Farshadfar, The effects of pozzolanic binders and polypropylene fibers on durability of SCC to magnesium sulfate attack, Constr. Build. Mater. 38 (2013) 64–71. doi:10.1016/j.conbuildmat.2012.08.035.

[11] A.M. Diab, A.E.M. Awad, H.E. Elyamany, A.E.M. Abd Elmoaty, Guidelines in compressive strength assessment of concrete modified with silica fume due to magnesium sulfate attack, Constr. Build. Mater. 36 (2012) 311–318. doi:10.1016/j.conbuildmat.2012.04.075.

[12] N. Saca, M. Georgescu, Behavior of ternary blended cements containing limestone filler and fly ash in magnesium sulfate solution at low temperature, Constr. Build. Mater. 71 (2014) 246–253. doi:10.1016/j.conbuildmat.2014.08.037.

[13] J. Hoppe Filho, D.J. De Souza, M.H.F. Medeiros, E. Pereira, K.F. Portella, Concrete attack by sodium sulfate: mineral additions as a mitigation tool, Cerâmica. 61 (2015) 168–177. doi:10.1590/0366-69132015613581905.

[14] D.J. Souza, L.Y. Yamashita, F. Dranka, M.H.F. Medeiros, R.A. Medeiros-Junior, Repair Mortars Incorporating Multiwalled Carbon Nanotubes: Shrinkage and Sodium Sulfate Attack, J. Mater. Civ. Eng. 29 (2017) 1–12. doi:10.1061/(ASCE)MT.1943-5533.0002105.

[15] M.D. Cohen, A. Bentur, Durability of Portland Cement-Silica Fume Pastes in Magnesium Sulfate and Sodium Sulfate Solutions, ACI Mater. J. 85 (1988) 148–157.

[16] P. Lawrence, M. Cyr, E. Ringot, Mineral admixtures in mortars, Cem. Concr. Res. 33 (2003) 1939 – 1947. doi:10.1016/S0008-8846(03)00183-2.

[17] S.T. Lee, R.D. Hooton, H.S. Jung, D.H. Park, C.S. Choi, Effect of limestone filler on the deterioration of mortars and pastes exposed to sulfate solutions at ambient temperature, Cem. Concr. Res. (2008). doi:10.1016/j.cemconres.2007.08.003.

[18] B. Lothenbach, K. Scrivener, R.D. Hooton, Supplementary cementitious materials, Cem. Concr. Res. 41 (2011) 1244–1256. doi:10.1016/j.cemconres.2010.12.001.

[19] E.F. Irassar, M. González, V. Rahhal, Sulphate resistance of type V cements with limestone filler and natural pozzolana, Cem. Concr. Compos. 22 (2000) 361–368. doi:10.1016/S0958-9465(00)00019-6.

[20] E.F. Irassar, Sulfate attack on cementitious materials containing limestone filler - A review, Cem. Concr. Res. (2009). doi:10.1016/j.cemconres.2008.11.007.

[21] N. Mavropoulou, N. Katsiotis, J. Giannakopoulos, K. Koutsodontis, D. Papageorgiou, E. Chaniotakis, M. Katsioti, P.E. Tsakiridis, Durability evaluation of cement exposed to combined action of chloride and sulphate ions at elevated temperature: The role of limestone filler, Constr. Build. Mater. 124 (2016) 558–565. doi:10.1016/j.conbuildmat.2016.07.134.

[22] J. Sun, Z. Chen, Influences of limestone powder on the resistance of concretes to the chloride ion penetration and sulfate attack, Powder Technol. 338 (2018) 725–733. doi:10.1016/j.powtec.2018.07.041.

[23] F. Abubaker, C. Lynsdale, J. Cripps, Investigation of concrete-clay interaction with regards to the thaumasite form of sulfate attack, Constr. Build. Mater. 67 (2014) 88–94. doi:10.1016/j.conbuildmat.2013.10.033.

[24] A. Skaropoulou, K. Sotiriadis, G. Kakali, S. Tsivilis, Use of mineral admixtures to improve the resistance of limestone cement concrete against thaumasite form of sulfate attack, Cem. Concr. Compos. 37 (2013) 267–275. doi:10.1016/j.cemconcomp.2013.01.007.

[25] A. Skaropoulou, S. Tsivilis, G. Kakali, J.H. Sharp, R.N. Swamy, Long term behavior of Portland limestone cement mortars exposed to magnesium sulfate attack, Cem. Concr. Compos. 31 (2009) 628–636. doi:10.1016/j.cemconcomp.2009.06.003.

[26] K. Tosun-Felekoğlu, The effect of C 3A content on sulfate durability of Portland limestone cement mortars, Constr. Build. Mater. 36 (2012) 437–447. doi:10.1016/j.conbuildmat.2012.04.091.

[27] T. Matschei, B. Lothenbach, F.P. Glasser, The role of calcium carbonate in cement hydration, Cem. Concr. Res. 37 (2007) 551–558. doi:10.1016/j.cemconres.2006.10.013.

[28] G. Kakali, S. Tsivilis, E. Aggeli, M. Bati, Hydration products of C 3 A, C 3 S and Portland cement in the presence of CaCO 3, Cem. Concr. Res. 30 (2000) 1073–1077. doi:10.1016/S0008-8846(00)00292-1.

[29] D.J. De Souza, M.H.F. Medeiros, J. Hoppe Filho, Evaluation of the SR Portland cement against sodium and magnesium sulfate attack: a physical and comparative analysis of mortars, Rev. IBRACON Estruturas e Mater. 11 (2018) 1053–1075. doi:10.1590/s1983-41952018000500009.

[30] M.H.F. de Medeiros, D.J. Souza, J.H. Filho, C.S. Adorno, V.A. Quarcioni, E. Pereira, Red-clay waste and limestone filler added in Portland cement composite: effects on sulfate attack and alkali-silica reaction, Rev. Mater. 21 (2016) 282–300. doi:10.1590/S1517-707620160002.0028.

[31] J.L. Wilson, Limestone and dolomite reservoirs, 1st Editio, U.S. Dept. of the Interior, Bureau of Mines, 1980.
[32] M. Cyr, P. Lawrence, E. Ringot, Efficiency of mineral admixtures in mortars: Quantification of the physical and chemical effects of fine admixtures in relation with compressive strength, Cem. Concr. Res. 36 (2006) 264–277. doi:10.1016/j.cemconres.2005.07.001.
[33] M. Cyr, P. Lawrence, E. Ringot, Mineral admixtures in mortars: Quantification of the physical effects of inert materials on short-term hydration, Cem. Concr. Res. 35 (2005) 719–730. doi:10.1016/j.cemconres.2004.05.030.
[34] Z.A. Marciano, Desenvolvimento de um método acelerado para avaliação da resistência de argamassas de cimento Portland expostas à solução de sulfato de sódio., 1993.
[35] D. Bonen, M.D. Cohen, Magnesium sulfate attack on portland cement paste-I. Microstructural analysis, Cem. Concr. Res. 22 (1992) 169–180. doi:10.1016/0008-8846(92)90147-N.
[36] S.T. Lee, H.Y. Moon, R.N. Swamy, Sulfate attack and role of silica fume in resisting strength loss, Cem. Concr. Compos. 27 (2005) 65–76. doi:10.1016/j.cemconcomp.2003.11.003.
[37] Z. Makhloufi, S. Aggoun, B. Benabed, E.H. Kadri, M. Bederina, Effect of magnesium sulfate on the durability of limestone mortars based on quaternary blended cements, Cem. Concr. Compos. 65 (2016) 186–199. doi:10.1016/j.cemconcomp.2015.10.020.
[38] S.W. Forster, G.S. Barger, R.L. Boone, M.S. Hammer, J.F. Lamond, D.S. Lane, R.E. Miller, S.E. Parker, A. Pergalsky, J.S. Pierce, M.Q. Robert, J.W. Schmitt, D.C. Stark, R.E. Tobin, Report on Alkali-Aggregate Reactivity Reported by ACI Committee 221, (1998).
[39] P. Štukovnik, M. Marinšek, B. Mirtič, V. Bokan Bosiljkov, Influence of alkali carbonate reaction on compressive strength of mortars with air lime binder, Constr. Build. Mater. 75 (2015) 247–254. doi:10.1016/j.conbuildmat.2014.11.024.
[40] T. Prinčič, P. Štukovnik, S. Pejovnik, G. De Schutter, V. Bokan Bosiljkov, Observations on dedolomitization of carbonate concrete aggregates, implications for ACR and expansion, Cem. Concr. Res. 54 (2013) 151–160. doi:10.1016/j.cemconres.2013.09.005.
[41] M. Beyene, A. Snyder, R.J. Lee, M. Blaszkiewicz, Alkali Silica Reaction (ASR) as a root cause of distress in a concrete made from Alkali Carbonate Reaction (ACR) potentially susceptible aggregates, Cem. Concr. Res. 51 (2013) 85–95. doi:10.1016/j.cemconres.2013.04.014.
[42] A.M. López-Buendía, V. Climent, P. Verdú, Lithological influence of aggregate in the alkali-carbonate reaction, Cem. Concr. Res. 36 (2006) 1490–1500. doi:10.1016/j.cemconres.2006.05.032.
[43] B. Fournier, M.-A. Bérubé, Alkali-aggregate reaction in concrete: a review of basic concepts and engineering implications, Can. J. Civ. Eng. 27 (2000) 167–191. doi:10.1139/cjce-27-2-167.
[44] W. Ouyang, J. Chen, M. Jiang, Evolution of surface hardness of concrete under sulfate attack, Constr. Build. Mater. (2014). doi:10.1016/j.conbuildmat.2013.11.107.
[45] E.F. Irassar, Prediction and Relation With Flexural Strength, 20 (1990) 209–218. doi:10.1197/j.aem.2005.06.022.

REVISTA IBRACON DE ESTRUTURAS E MATERIAIS
IBRACON STRUCTURES AND MATERIALS JOURNAL

Volume 13, Number 3
June 2020
ISSN: 1983-4195

Contents